Water Science and Technology Library

Vikas Garg
Vijay P. Singh
Vijay Raj *Editors*

Development of Water Resources in India

Springer

Water Science and Technology Library

Volume 75

The aim of the Water Science and Technology Library is to provide a forum for dissemination of the state-of-the-art of topics of current interest in the area of water science and technology. This is accomplished through publication of reference books and monographs, authored or edited. Occasionally also proceedings volumes are accepted for publication in the series.

Water Science and Technology Library encompasses a wide range of topics dealing with science as well as socio-economic aspects of water, environment, and ecology. Both the water quantity and quality issues are relevant and are embraced by Water Science and Technology Library. The emphasis may be on either the scientific content, or techniques of solution, or both. There is increasing emphasis these days on processes and Water Science and Technology Library is committed to promoting this emphasis by publishing books emphasizing scientific discussions of physical, chemical, and/or biological aspects of water resources. Likewise, current or emerging solution techniques receive high priority. Interdisciplinary coverage is encouraged. Case studies contributing to our knowledge of water science and technology are also embraced by the series. Innovative ideas and novel techniques are of particular interest.

Comments or suggestions for future volumes are welcomed.

Vijay P. Singh, Department of Biological and Agricultural Engineering & Zachry Department of Civil Engineering, Texas A&M University, USA
Email: vsingh@tamu.edu

More information about this series at http://www.springer.com/series/6689

Vikas Garg · Vijay P. Singh
Vijay Raj
Editors

Development of Water Resources in India

Springer

Editors
Vikas Garg
Department of Civil Engineering
University of Petroleum and Energy Studies
Dehradun
India

Vijay Raj
Department of Civil Engineering
University of Petroleum and Energy Studies
Dehradun
India

Vijay P. Singh
Department of Biological and Agricultural
Engineering and Zachry Department
of Civil Engineering
Texas A&M University
College Station, TX
USA

ISSN 0921-092X ISSN 1872-4663 (electronic)
Water Science and Technology Library
ISBN 978-3-319-55124-1 ISBN 978-3-319-55125-8 (eBook)
DOI 10.1007/978-3-319-55125-8

Library of Congress Control Number: 2017934443

Printed on acid-free paper

This Springer imprint is published by Springer Nature
The registered company is Springer International Publishing AG
The registered company address is: Gewerbestrasse 11, 6330 Cham, Switzerland

Contents

About the Editors

Dr. Vikas Garg is working as a Professor and Head in Civil Engineering Department at University of Petroleum & Energy Studies, Dehradun (India). He received B.E. in civil engineering, M.Tech and PhD in water resources engineering. He is having more than 18 years of teaching experience.

He is a recipient of Indian Patent for developing "*Multiple Collar Plates: A Composite scour Protection Device*" in 2006. He has received G M. Nawathe Award twice for Best Research Paper by Indian Society for Hydraulics (ISH) at CWPRS PUNE in HYDRO 2005 and HYDRO 2015. He had been honoured with Young Engineer Award by Institution of Engineers (India) in 2008. He had been selected as a Young Researcher in Lisbon to attend river flow conference in Lisbon, Portugal, in 2006. He had visited several countries such as Iran, Portugal, Turkey, Bangladesh, Mauritius, Bangkok, Dubai and Taiwan for the presentation of a research work. He has published more than 40 research papers in his research area in National Journal/International Conferences/National Conferences. He had handled a research project on Modernization of Fluid Mechanics Laboratory sponsored by AICTE, New Delhi (2007–09). He is a reviewer of Journal of Pipeline, ASCE.

He had organized a National Conference on Water Resources and Hydropower in 2016 at UPES, Dehradun. Earlier, he had organized various National Conferences on River Hydraulics (2012), National Conference on Hydraulics, Water Resources, Coastal and Environmental Engineering (HYDRO 2010), National Specialty Conference on River Hydraulics (2009) and National Conference on Civil Engineering: Advancement and Challenges (2007). He had delivered several talks on "*Scour Protection around bridge pier*" in National Cheng Kung University Taiwan (2011). He had also delivered lecture during Master Classes in International Conference on River Flow-2008 (Turkey) and several talks in other universities.

Prof. V.P. Singh is a Distinguished Professor and the inaugural holder of the Caroline and William N. Lehrer Distinguished Chair in Water Engineering in the Department of Biological and Agricultural Engineering as well as the Zachry

Department of Civil Engineering at Texas A&M University. He received his B.S., M.S., Ph.D. and D.Sc. degrees in engineering. He is a registered professional engineer, a registered professional hydrologist and an Honorary diplomate in water resources engineering, American Academy of Water Resources Engineers.

Prof. Singh had extensively published the results of an extraordinary range of his scientific pursuits. He had published more than 853 journal articles; 24 textbooks; 58 edited reference books, including the massive Encyclopedia of Snow, Ice and Glaciers and Handbook of Applied Hydrology; 100 chapters; 314 conference papers; and 72 technical reports in the areas of hydrology, ground water, hydraulics, irrigation engineering, environmental engineering and water resources.

For his scientific contributions to the development and management of water resources and promoting the cause of their conservation and sustainable use, he has received more than 74 national and international awards and numerous honours, including the Arid Lands Hydraulic Engineering Award, Ven Te Chow Award, Richard R. Torrens Award, Norman Medal, EWRI Lifetime Achievement Award, and Distinguished Member all given by American Society of Civil Engineers; Ray K. Linsley Award and Founder's Award, given by American Institute of Hydrology; and Crystal Drop Award, given by International Water Resources Association, among others. He has received three honorary doctorates. He is a Distinguished Member of ASCE, and a fellow EWRI, AWRA, IWRS, ISAE, IASWC and IE and holds membership in 16 additional professional associations. He is a fellow/member of 10 international science/engineering academies. He has served as President and Senior Vice President of the American Institute of Hydrology (AIH).

Dr. Vijay Raj graduated in B. Tech. civil engineering from Indian Institute of Technology Kanpur, India, in 1976. He was awarded certificate of Merit for Academic Proficiency, as well as the General Proficiency Prize for being the best graduate of the year in Civil Engineering, by IIT Kanpur. After graduation, he served with the Bureau of Indian Standards (B.I.S.), New Delhi, for over 7 years, and contributed significantly towards the development of many pertinent Indian Standards in civil engineering. Later on, he relinquished his job of Deputy Director in B.I.S. to adopt teaching and research as his career. He shifted to Madan Mohan Malaviya University of Technology, Gorakhpur, India, in 1984, completed his Ph.D. degree in the year 1987, continued till the year 2012, and took voluntary retirement thereafter. He also holds a management diploma from IGNOU, New Delhi.

The areas of interest are multidimensional that include engineering, accounting and financial management and meteorology. He has been teaching civil engineering subjects at UG and PG levels, and guided 19 postgraduate research works. He has 40 publications to his credit and has also coordinated many academic, research and consultancy projects. He has attended 18 training programs/conferences/workshops/seminars and has organized twelve such events. He has also acted as reviewer for several technical books. He has been the Academic Guide for the Diploma in Business Finance (DBF) program for

engineering students run by The Institute of Chartered Financial Analysts of India (ICFAI) and delivered special lectures on accounting, economics and financial management.

After voluntary retirement in 2012 from Madan Mohan Malaviya University of Technology, Gorakhpur, India, he has rendered his services as Director of Uttaranchal Institute of Technology (U.I.T.), Dehradun, Uttarakhand, for 3 years till 2015. The complete department of Civil Engineering was established at U.I.T. under his guidance. He has also delivered special lectures on meteorology to students of engineering and agriculture, and has also set up a Meteorological station at U.I.T. Dr. Vijay Raj has a total experience of over 40 years and is presently providing expert technical guidance at University of Petroleum and Energy Studies as Adjunct Professor.

Part I
Water Resource Planning Management

Hydrological Planning of Watershed of RGSC, Mirzapur, UP, Using GIS Techniques

Nikita Shivhare, Atul Kumar Rahul, Shishir Gaur, Manvendra Singh Chauhan, Prabhat K.S. Dikshit, Shyam B. Dwivedi and Chandra S.P. Ojha

Abstract Water is the remarkable natural resource which is essential for every form of life on the planet "Earth," and nowadays India is facing major water scarcity problems. These problems are due to climate change and urbanization. As the urbanization is increasing, the percentage of impervious land is increasing which is leading to increase in urban runoff and lesser recharge of underlying aquifers, leading to water scarcity at local scale as runoff is not tapped and utilized. Watershed modeling is considered as one of the most important aspects of planning and development for natural resources for water conservation measures. Watershed modeling is useful for completing and implementing plans, programs, and projects to sustain and increase watershed utilities that directly affect the biotic and abiotic communities within watershed boundary. In this paper, we have taken Rajiv Gandhi South Campus (RGSC), Barkachha, which is the extension of Banaras Hindu University and facing serious water scarcity problems. Here, firstly runoff was

N. Shivhare · A.K. Rahul (✉) · S. Gaur · P.K.S. Dikshit · S.B. Dwivedi
Department of Civil Engineering IIT(BHU), Varanasi 221005, UP, India
e-mail: atulcivil.iitbhu@gmail.com

N. Shivhare
e-mail: nikitas.rs.civ15@itbhu.ac.in

S. Gaur
e-mail: shishir.gaur@gmail.com

P.K.S. Dikshit
e-mail: pksdikshit.civ@itbhu.ac.in

S.B. Dwivedi
e-mail: sbd.civ@itbhu.ac.in

M.S. Chauhan
Department of Civil Engineering, Chitkara University, Chandigarh 174103, HP, India
e-mail: manvendra.hbti@gmail.com

C.S.P. Ojha
Department of Civil Engineering IIT, Roorkee 247667, Uttarakhand, India
e-mail: cspojha@gmail.com

V. Garg et al. (eds.), *Development of Water Resources in India*,
Water Science and Technology Library 75, DOI 10.1007/978-3-319-55125-8_1

calculated by SCS-CN method using 10 years of rainfall data, and then flow accumulation and sink map were created using DEM. Watershed investigation has been done to suggest some hydraulic structures using flow accumulation, sink map, and runoff data, for the study area, mainly to enhance the availability of water for agricultural activity and university development.

Keywords DEM · SCS-CN · ArcGIS · RGSC · Runoff

1 Introduction

The study area is situated in Barkachha which is located at Vindhyan region. This area mainly consists of sandstone. The climate of this region is mostly dry. Duration of the winter season is between December and February, whereas summer extends between March and November. The temperature varies from 48 °C (May–June) to 80 °C (December–January). The maximum rainfall in the study area is received by Southwest monsoon, where the monsoon period exists from the second week of June to end of September. Highly erratic and unpredictable behavior of the climate and cyclonic disturbance from the Bay of Bengal causes extension of the rainy season and correspondingly drought spells of varying degrees and durations. Therefore, the imbalance between rains received and vegetation water demand occurred due to the trend of monsoon rains including existing topo-sequence.

Insufficient availability of water is the most limiting factor in agricultural and rural development, particularly in semiarid regions of Indian subcontinent. Those regions receive, on an average, 400–1,000 mm rainfall annually, which if harvested and used judiciously, could support a higher cropping intensity than the existing one [1]. Therefore, watershed management is essential to enhance land, groundwater, and agriculture productivity. Approaches to man aging a watershed should encompass a holistic approach of land, water, and people, with programs implemented to check erosion, harvest rainwater, and improve the crop position [2]. The water demand is increasing to help agricultural and industrial development and correspondingly to enhance incomes and wealth in rural areas, which also contribute to the sustainable development of water resources. Management of water resources at watershed scale generates various benefits such as increased food production, improved livelihoods, environment protection, and addressing gender and equity issues along with biodiversity [3–6]. Formulation of a comprehensive land use plan for sustainable development requires liable and adequate information on the availability of natural resources. The different natural resources, viz. land, water, minerals, and biomass, are under huge threat in the context of highly competing and conflicting demands of increasing population of the region which leads to exploitation and mismanagement of resources. Watershed planning has been studied by various researchers from different regions of the world. It is evident that water resource planners are aware that the watershed gives the best planning unit for developing water resource plans [7]. Earlier watershed modeling uses the

river basin as a general planning unit. Watershed management fundamentally includes the data regarding the use of natural resources within a watershed. The main objectives of water resource management are to increase agricultural productivity and to provide a better standard of livelihood for its residents.

2 Study Area

Banaras Hindu University acquired the RGSC in the year 1979. It has an area of about 2700 acres and is situated at Barkachha near Mirzapur town. The Majhawati river flows in this area. This area is the developing part of BHU, but it is facing a problem of water scarcity; thus, water harvesting is very much required in this area; otherwise, development in this area would be useless. The study area (Fig. 1) consists of Vindhyan sandstone and soil of three different types typically clay loam, sandy loam, and silty clay.

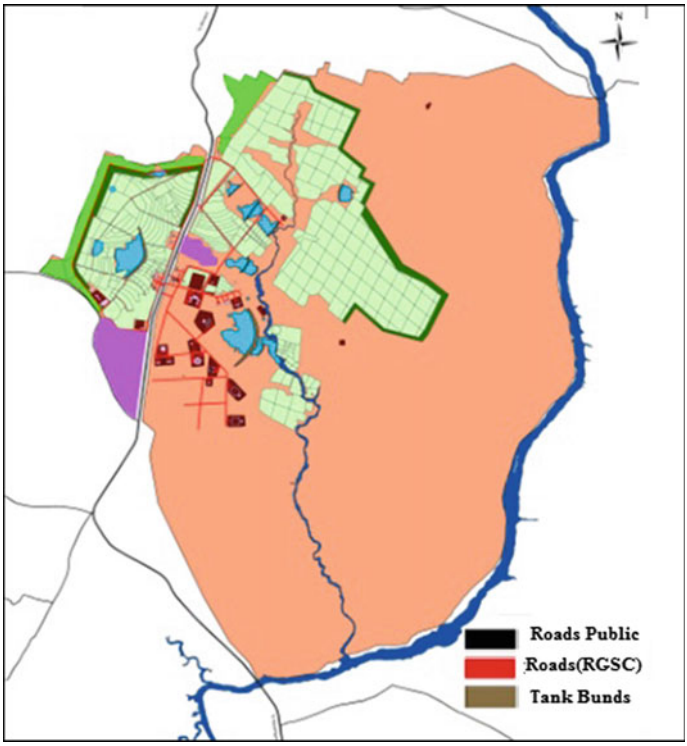

Fig. 1 Study area and LULC of RGSC

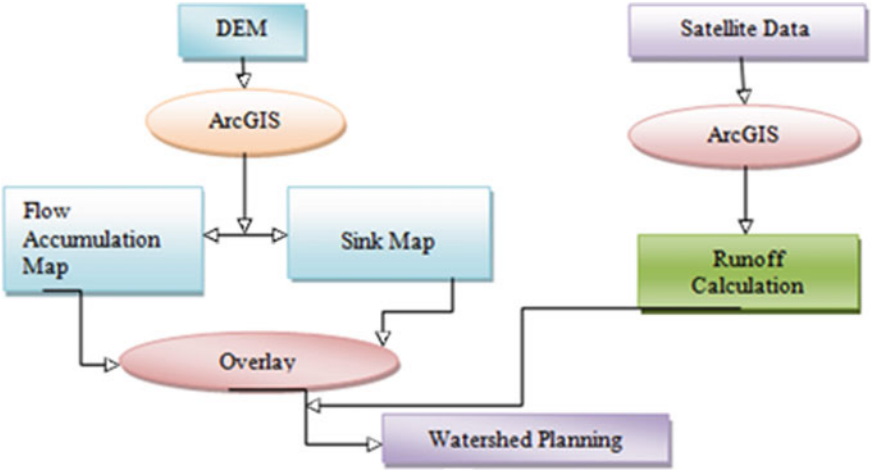

Fig. 2 Flow diagram for watershed planning

3 Materials and Methods

The efficient utilization and management of available rainwater is the core issue to enhance cropping intensity and production of any particular area. In a developing country like India, due to the problem of awareness in people and irresponsible behavior, a lot of running water gets wasted. Therefore, it is imperative to implement the technologies of watershed modeling to solve the problem of water scarcity and urban flood. For watershed modeling, the key requirements are the expert knowledge, appropriate and reliable data, simulation model, and a perfect decision-making algorithm. Nowadays, with the help of GIS and remote sensing, the experts can develop best models for watershed planning. Flow diagram in Fig. 2 shows the various steps involved in watershed planning.

4 Soil Conservation Service-Curve Number (SCS-CN) Method

The primary data required for watershed planning are the precipitation data, the discharge data, soil type, and data regarding demand of natural resources in the watershed. Various methods like SCS-CN method and rational method are used for the estimation of discharge data at a watershed level. But the most popular method is SCS-CN method, which computes the volume of surface runoff for a given

rainfall event. This method is based on a key input called as curve number (CN), which depends on the land use, precipitation, and soil characteristics of the watershed. This method is one of the most reliable methods, and with the help of remote sensing and GIS, it becomes very easy to estimate discharge.

This method is based on the fundamental equation, which states that:

$$P = Ia + F + Q \tag{1}$$

where

P precipitation/rainfall in this case,
Ia initial abstraction,
F actual infiltration,
Q discharge

This method is also based on two hypotheses.

The first hypothesis states that:

$$\frac{Q}{P} - Ia = \frac{F}{S} \tag{2}$$

where

S potential maximum retention or infiltration

The second hypothesis states that:

$$Ia = \lambda S \tag{3}$$

where λ = some fraction.

In the current study, the value of λ is taken as 0.2, which means that the amount of initial abstraction is 20% of the total potential maximum retention. In theory, λ can take any value between 0 and ∞ [8].

Combining Eqs. (1) and (2), we obtain

$$Q = \frac{(P - Ia)2}{(P - Ia + S)}, \quad \text{for } P > Ia \tag{4}$$

$$Q = 0, \quad \text{for } P < Ia \tag{5}$$

$$Ia = 0.2S. \tag{6}$$

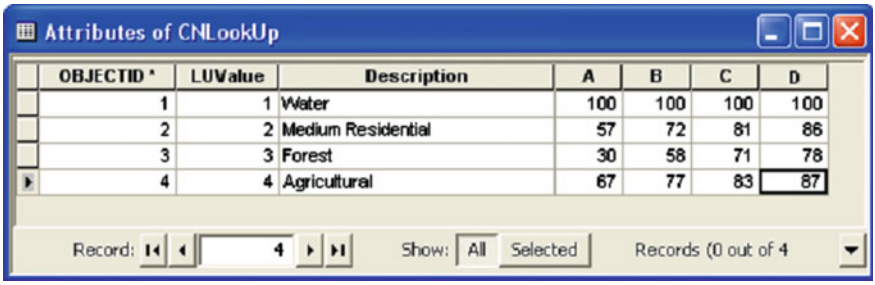

Fig. 3 CN lookup table

By putting the value of Ia in Eq. (4), from Eq. (6) we get:

$$Q = \frac{(P - 0.2S)^2}{(P + 0.8S)} \tag{7}$$

S can be obtained according to the CN value.

$$S = \left(\frac{25400}{CN}\right) - 254 \tag{8}$$

These equations are based on the trends in observed data obtained from the study areas, so these are empirical equations rather than equations based on physical laws. The CN is a hydrologic factor that relies completely on the assumptions of extreme runoff events and represents a convenient representation of the potential maximum soil retention [9]. The curve number is used in the determination of S, and values for the CN for different land use, soil types, and soil moisture conditions were taken from CN lookup table created in ArcGIS shown in Fig. 3. This table was created using TR 55 report. The CN grid map (Fig. 4) and runoff map of RGSC (Fig. 5) were prepared to evaluate the required data for estimation of surface runoff of the study area.

The surface runoff is a very important parameter for this area, and the estimation of the total surface runoff as compared to the rainfall is also an important parameter. It shows the actual runoff quantity. Runoff starts when the excess rainfall is available for any area, and Fig. 6 shows the rainfall versus runoff graph of BHU South Campus.

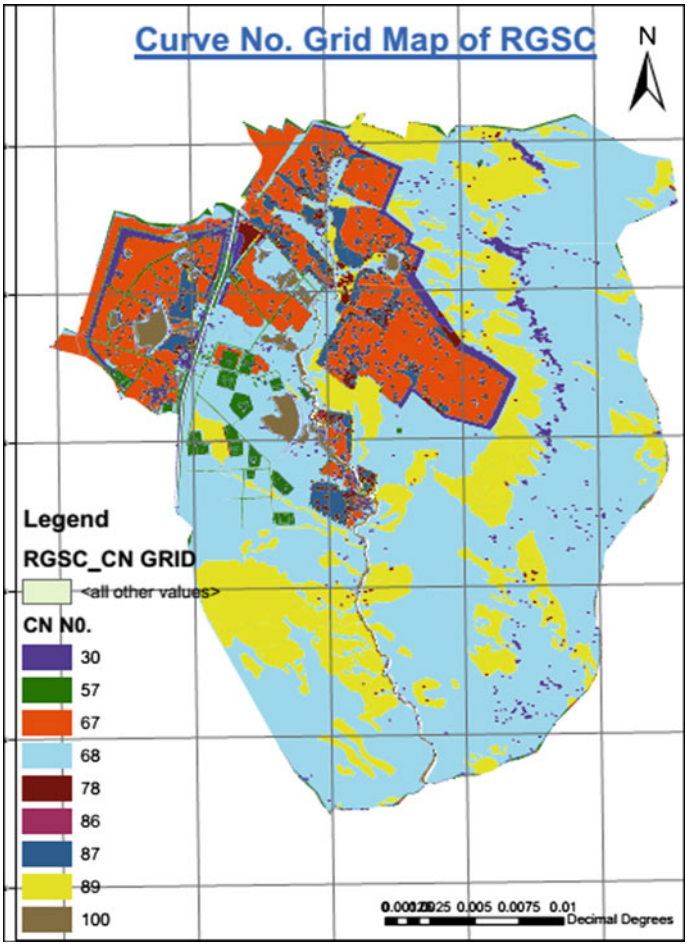

Fig. 4 CN grid map

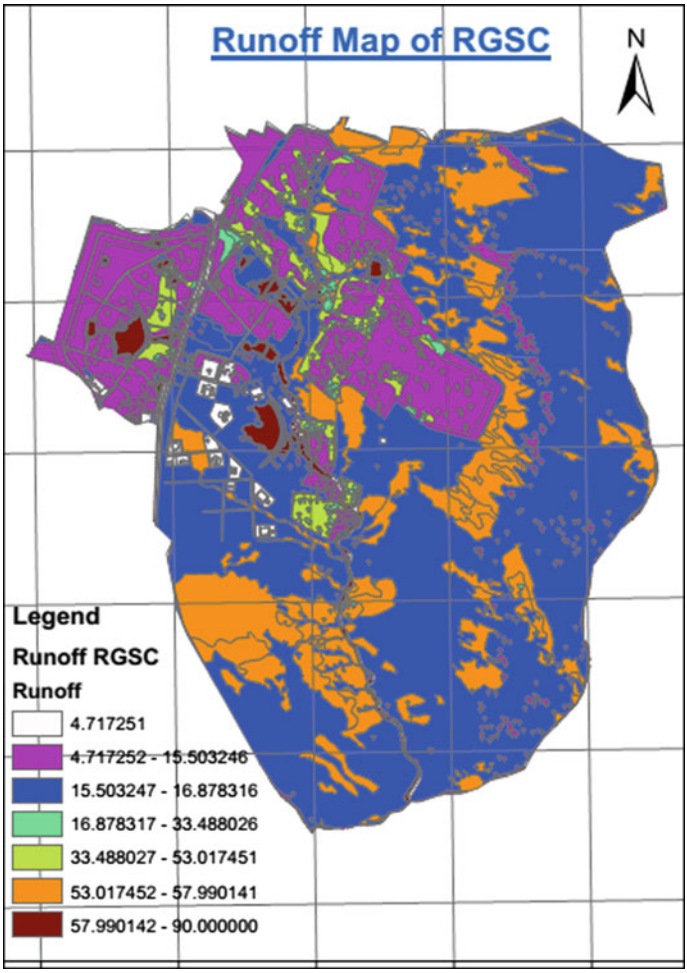

Fig. 5 Runoff map of RGSC

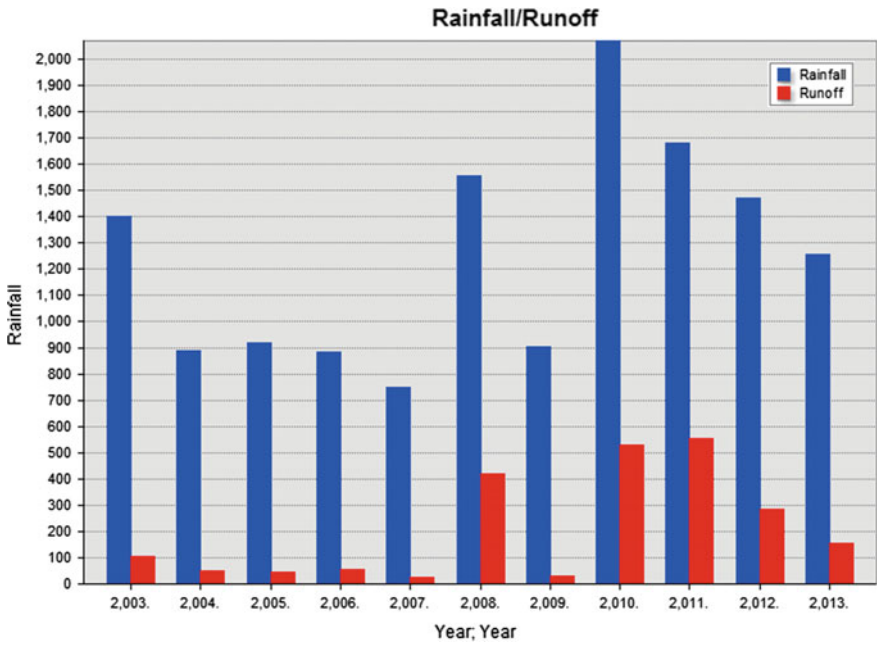

Fig. 6 Rainfall versus runoff (unit—mm) graph of RGSC

Table 1 Description of metadata of satellite imageries of study area

Satellite imagery	SENSOR_ID	Resolution	Acquisition date
Liss 4	ETM+	5.8 m × 5.8 m	2015-10-25

5 Data Used

5.1 Satellite Data

The details of primary data in the form of digital data (procured from NRSC) for interpretation and analysis of satellite imagery are given in Table 1. The entire catchment area of the watershed was covered in one tile (Fig. 7).

5.2 Digital Elevation Model (DEM)

As the runoff depends on the slope of the watershed, the DEMs can be used for estimating areas of enhanced runoff [10, 11], drainage areas [12], flow directions [13, 14], and channelized flow [15]. Flow accumulation can be generated using

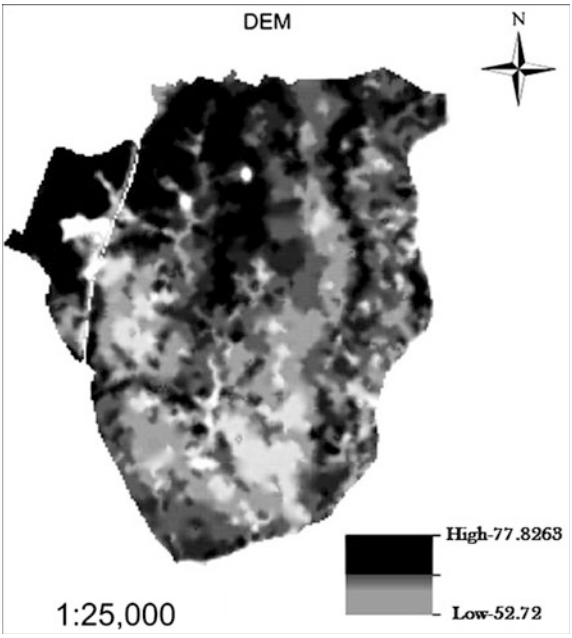

Fig. 7 Digital elevation model (DEM) of study area

DEM and hydrology tool of ArcGIS software. This map along with the flow direction data can be used to prepare a drainage network map [16]. Flow accumulation has been useful for predicting locations of headwater and perennial streams and threshold values of flow accumulation can predict channelized stream sections. Terrain and GIS-based modeling approaches have also been proposed for assigning the widths of no cropping zones ("buffers") [17–21]. In ArcGIS software, there are various tools for processing the elevation data, and the elevation data procured using GPS, total station, or any other sources can be used to create TIN and DEM. For perfect watershed modeling, the DEM should be hydrologically correct, which means that all the pixels should have appropriate elevation data. If a pixel has lower elevation value than the nearby pixels, then it starts acting as "sink." Previously, contour map was used for visualizing the existence of closed depressions, and GIS tools were used for digitizing these depressions manually [22, 23]. Flow accumulation and sink map (Fig. 8) were generated from DEM imagery using ArcGIS software.

Flow accumulation map was used to study flow accumulation of surface water flow in the study area. In this study, sink map is used to determine the locality of depressed point and these depressed points were useful for locating a suitable site for placing farm ponds. In other words, these maps were very useful for visualization of surface runoff and placing the suitable structure in the stream. All maps which are essential for the watershed management were developed for study

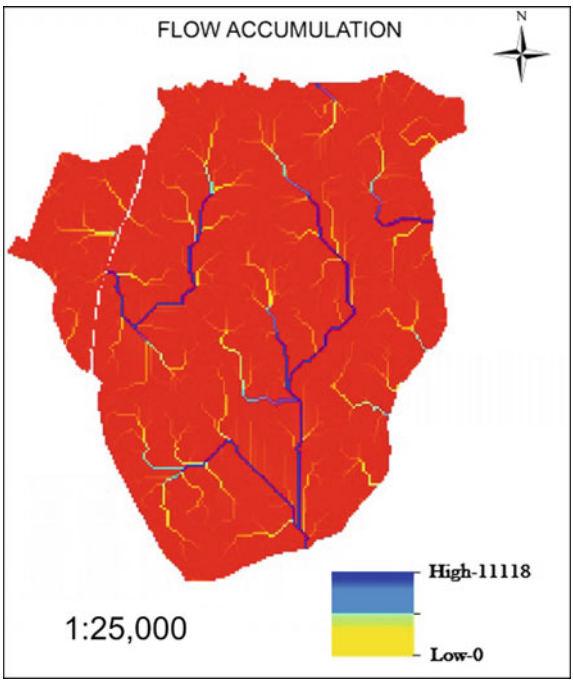

Fig. 8 Flow accumulation map of RGSC

Table 2 Details of structures proposed for water harvesting

Type of structure	Gabion	Check dam	Bund	Farm ponds
No. of structures	6	5	4	4

area through DEM by using ArcGIS. Watershed has been grouped into several subwatersheds, which has been used as the main key for modeling of the watershed. These maps have been used for deciding the locations of appropriate water harvesting structures (WHS). Details of Structures are shown below (Table 2).

6 Results

Hydraulic structures are the small manmade structures which are used to interrupt, reroute, or completely stop the flow of water. Based on the runoff estimation, flow accumulation map, sink map, and runoff versus runoff diagram, different hydraulic structures have been proposed (Fig. 9) for the study area. The detailed number of structures, location with runoff per unit area, and cost of each structure are mentioned in Tables 3 and 4, respectively.

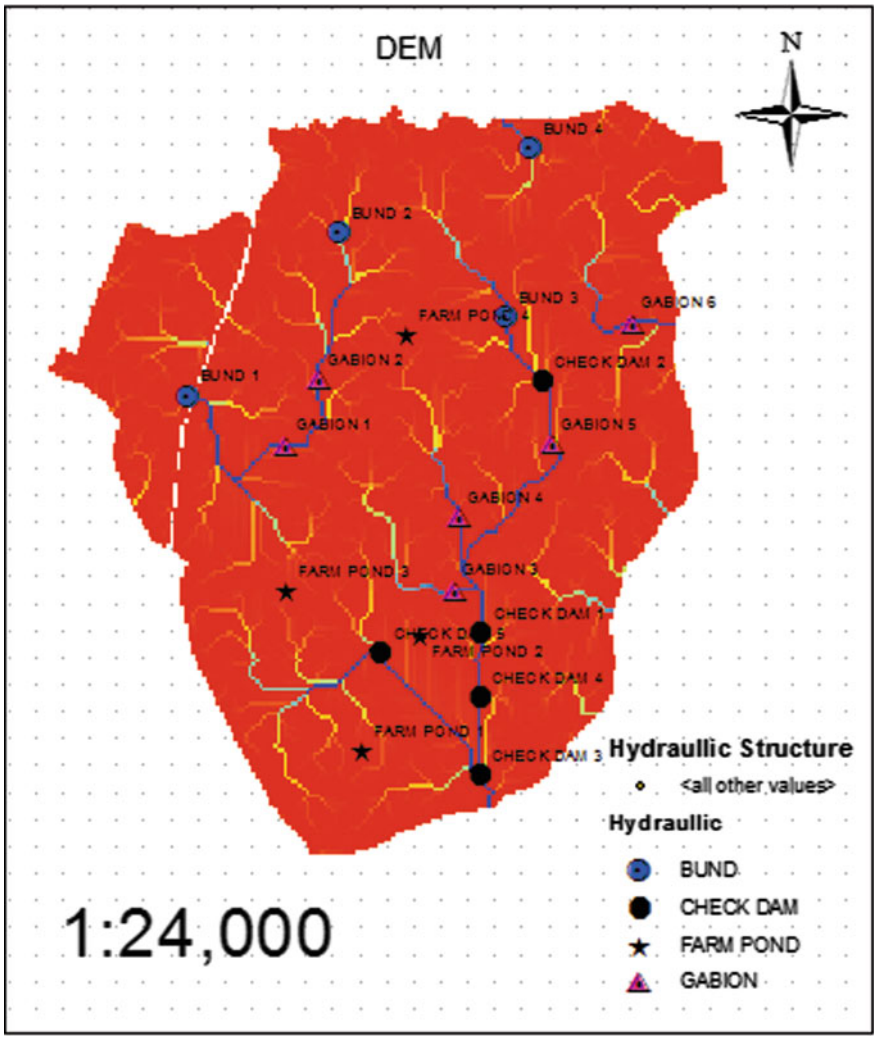

Fig. 9 Proposed hydraulic structure plan for RGSC

The proposed hydraulics structures with cost estimations are given below:

6.1 Gabion Weirs

It is a partially permeable obstruction, which is prepared by boulders in a mesh of steel wires. Gabion permits water to go through, but it increased the retention time

Table 3 Detailed location of structures and maximum runoff/day per area for each structure

S. no	Structure	Location	Maximum runoff/area
1	Check dam 1	82° 36′ 30.399″ E 25°1′ 58.239″ N	57.990141
2	Check dam 2	82° 36′ 31.345″ E 25° 2′ 3.259″ N	57.990141
3	Check dam 3	82° 36′ 31.849″ E 25° 2′ 23.16″ N	36.878316
4	Check dam 4	82° 36′ 11.577″ E 25° 2′ 21.329″ N	57.990141
5	Check dam 5	82° 36′ 44.846″ E 25° 3′ 10.843″ N	57.990141
6	Bund 1	82° 35′ 35.062″ E 25° 3′ 8.18″ N	16.878316
7	Bund 2	82° 36′ 4.694″ E 25° 3′ 37.58″ N	33.488026
8	Bund 3	82° 36′ 37.111″ E 25° 3′ 21.516″ N	33.488026
9	Bund 4	82° 36′ 42.825″ E 25° 3′ 52.218″ N	57.990141
10	Farm pond 1	82° 36′ 7.308″ E 25° 2′ 2.972″ N	55.524141
11	Farm pond 2	82° 36′ 19.721″ E 25° 2′ 24.06″ N	15.503246
12	Farm pond 3	82° 35′ 52.594″ E 25° 2′ 32.124″ N	16.878316
13	Farm pond 4	82° 36′ 17.485″ E 25° 3′ 19.081″ N	15.503246
14	Gabion 1	82° 36′ 27.372″ E 25° 2′ 32.047″ N	16.878316
15	Gabion 2	82° 36′ 28.199″ E 25° 2′ 45.19″ N	16.878316
17	Gabion 3	82° 35′ 53.919″ E 25° 2′ 58.412″ N	90.020000
18	Gabion 4	82° 36′ 0.32″ E 25° 3′ 11.196″ N	33.488027
19	Gabion 5	82° 36′ 46.422″ E 25° 2′ 58.742″ N	57.990141
20	Gabion 6	82° 37′ 3.1″ E 25° 3′ 19.483″ N	16.878316

Table 4 Area and cost of each structure

S.no	Structure	Area of structures (m^2)	Cost of structure (Indian rupees)
1	Check dam 1	180,000	3,50,000
2	Check dam 2	180,000	3,50,000
3	Check dam 3	140,000	2,50,000
4	Check dam 4	180,000	3,50,000
5	Check dam 5	180,000	3,50,000
6	Bund 1	16	10,000
7	Bund 2	16	10,000
8	Bund 3	16	10,000
9	Bund 4	16	10,000
10	Farm pond 1	50 × 50 = 2500	1,58,182
11	Farm pond 2	50 × 50 = 2500	1,58,182
12	Farm pond 3	100 × 100 = 10,000	6,32,727
13	Farm pond 4	50 × 75 = 3750	2,37,272
14	Gabion 1	30	35,000
15	Gabion 2	30	35,000
17	Gabion 3	40	40,000
18	Gabion 4	40	40,000
19	Gabion 5	30	35,000
20	Gabion 6	30	35,000

of water in a small watercourse. Its work is to infiltrate groundwater and help prevent soil erosion.

We have proposed six gabion weirs, out of which gabion weirs 1, 2, 5, and 6 have the same area of about 30 m^2 and cost of building per structure was Rs 35,000/-, and gabions 3 and 4 have the same area of about 40 m^2 and cost of building per structure was Rs 40,000/-.

6.2 Check Dams

Check dams are a small structure, sometimes permanent or temporary. They are normally low-cost structures. They are constructed to prevent rainwater along small drains, check the flow of water, reduce the velocity of water, control the soil erosion, recharge the groundwater, and store the water for various purposes for future necessity [24]. This stored water is very useful of irrigation for the neighboring agriculture land, through the straight lift of water and also use for ground water percolation [25]. These are very small level treatments, and characteristics are dependent on the various specific spots. They are shallow structures and provide a large area, and water logging does not take place [26].

We have proposed five check dams, out of which check dams 1, 2, 4, and 5 have the same area of about 180,000 m^2, the cost of building per structure was Rs 350,000/- each, and total amount of water harvesting per structure is 5 cumecs. Check dam 3 has an area of about 140,000 m^2, the cost of building per structure was Rs 250,000/-, and the total amount of water harvesting per structure is 3 cumecs.

6.3 Farm Pond

It is a deep opening dug out from the earth surface of any shape and depth but generally rectangular or square in shape, which harvests rainwater, collects groundwater, and stores it for upcoming use or water problems. It has an inlet to regulate the inflow and an outlet to discharge excess water. It is one of the most important rainwater harvesting structures constructed at the lowest relief of the farm area. The stored water must be used for irrigation only.

We have proposed four farm ponds, out of which farm ponds 1 and 2 have the same area of about 2500 m^2. The cost of building per structure was Rs 158,182/-, and the total amount of water harvesting per structure is 1.5 cumecs. Farm pond 3 has an area of about 10,000 m^2, cost of building per structure was Rs 632,727/-, and the total amount of water harvesting per structure is 6 cumecs. Farm pond 4 has an area of about 3750 m^2, cost of building per structure was Rs 237,272/-, and the total amount of water harvesting per structure is 2 cumecs.

6.4 Bund

Bunds are basically an outside catchment, long slant system of water collection system. Commonly, agriculturists expand u-shaped structure of earthen bunds on their developed terrains to reap the spillover from adjoining upslope catchments. This framework is ordinarily utilized where slants are above 0.5%, and there is noteworthy overflow to be collected. It is a long incline catchment framework where water going in little gulleys is redirected onto a ranch region.

We have proposed four bunds having area of about 16 m^2, and cost of building per structure is Rs 10,000/-.

The six gabions, five check dams, four farm ponds, and four bunds have been proposed with their cost as shown in Table 4. The total cost required for the improvement of the groundwater quantity of the RGSC, Mirzapur, UP, is Rs 3,096,363/- only.

7 Conclusion

Watershed modeling is essential and vital aspects of planning, management, and enlargement for real assets for water conservation measures. The surface water, as well as groundwater potential of subwatershed of the study, has been impounded by the modeling of watershed. Through this planning, the scarcity of water can be minimized, and the river will flow throughout the year with improved discharge. The six gabion, five check dams, four farm ponds, and four bunds have been proposed with their cost per structure of Rs 220,000, Rs 1,650,000, Rs 40,000, and Rs 1,186,363, respectively, for the improvement of the groundwater quantity of the RGSC, Mirzapur, UP. It shows the effectiveness of remote sensing and GIS techniques in demonstrating of watersheds. These techniques are particularly valuable for decision makers and planners to apply management strategies at subwatershed level.

References

1. Jagawat, H., Alagh, Y.: Transforming the Dry Lands, 1st edn. India Research Press, New Delhi (2005)
2. Rao, S.: Watersheds Comprehensive Development, 1st edn. B.S Publishers, New Delhi (2000)
3. Sharma, R.: Watershed development adaptation strategy for climate. Change. Presented in South Asia Expert Workshop on Adaptation to Climate Change for Agricultural Productivity. Organized by the Government of India, UNEP and CGIAR, New Delhi (2002)
4. Wani, S.P., Singh, H.P., Sreedevi, T.K., Pathak, P., Rego, T.J., Shiferaw, B., Iyer, S.R.: Farmer-Participatory Integrated Watershed Management: Adarsha Watershed, Kothapally India: An Innovative and Upscalable Approach. Case **7**, 123–147 (2003)

5. Joshi, P.K., Jha, A.K., Wani, S.P., Joshi. L., Shiyani, R.L.: Meta-analysis to assess impact of watershed program and people's participation. Comprehensive Assessment Research Report 8, Colombo, Sri Lanka. Comprehensive Assessment of Water Management in Agriculture (2015)
6. Rockstrom, J., Hatibu, N., Oweis, T., Wani, S., Barron, J., Bruggeman, A., Qiang, Z., Farahani, J., Karlberg, L.: Managing water in rain-fed agriculture. In: Molden, D. (ed.) Water for Food, Water for Life. A Comprehensive Assessment of Water Management in Agriculture. International Water Management Institute. Earthscan, London (2007)
7. Loucks, D.P.: Watershed planning: changing issues, processes and expectations. Water Resour. Update **111**, 38–45 (1998)
8. Mishra, S.K., Singh, V.P.: Another look at SCS-CN method. J. Hydrol. Eng. **4**, 257–264 (1999)
9. Ponce, V.M., Hawkins, R.H.: Runoff curve number: Has it reached maturity. J. Hydrol. Eng. **1**, 11–19 (1996)
10. Bernier, P.Y.: Variable source areas and storm-flow generation: an update of the concept and a simulation effort. J. Hydrol. Eng. **79**, 195–213 (1985)
11. Richards, P.L., Brenner, A.J.: Delineating source areas for runoff in depressional landscapes: implications for hydrologic modeling. J. Great Lakes Res. **30**, 9–21 (2004)
12. Jenson, S.K., Domingue, J.O.: Extracting topographic structure from digital elevation data for geographic information system analysis. J. Photo. Eng. Remote Sensing. **54**, 1593–1600 (1988)
13. Quinn, P.F., Beven, K.J., Chevallier, P., Planchon, O.: The prediction of hillslope flow paths for distributed modeling using digital terrain models. J. Hydrol. Processes. **5**, 59–80 (1991)
14. Tarboton, D.G.: A new method for the determination of flow directions and upslope areas in grid digital elevation models. J. Water Resour. Res. **33**, 309–319 (1997)
15. O'Callaghan, J.F., Mark, D.M.: The extraction of drainage networks from digital elevation data. Comput. Vis. J. Grap. Img. Proc. 323–344 (1984)
16. Donia, N.: Application of remotely sensed imagery to watershed analysis: a case study of Lake Karoun catchment, Egypt. In: Thirteenth International Water Technology Conference, pp. 1035–1049. Hurghada, Egypt (2003)
17. Narumalani, S., Yingchun, Z., Jensen, J.R.: Application of remote sensing and geographic information systems to the delineation and analysis of riparian buffer zones. J. Aquat. Bot. **58**, 393–409 (1997)
18. Bren, L.J.: The geometry of a constant buffer-loading design method for humid watersheds. Forest Eco. Manag. **110**, 113–125 (1998)
19. Herron, N.F., Hairsine, P.B.: A scheme for evaluating the effectiveness of riparian zones in reducing overland flow to streams. Aust. J. Soil Res. **36**, 683–699 (1998)
20. Endreny, T.A.: Forest buffer strips: mapping the water quality benefits. J. Forestry **100**, 35–40 (2002)
21. McGlynn, B.L., Seibert, J.: Distributed assessment of contributing area and riparian buffering along stream networks. Water Resour. Res. **29**, 1082–1099 (2003)
22. Angel, J.C., Nelson, D.O., Panno, S.V.: Comparison of a new GIS-based technique and a manual method for determining sinkhole density: an example from illinois sinkhole plain. J. Cave Karst Stud. **66**, 9–17 (2004)
23. Seale, L.D., Florea, L.J., Vacher, H.L., Brinkmann, R.: Using ALSM to map sinkholes in the urbanized covered karst of Pinellas County, Florida-1, methodological considerations. J. Env. Geol. **35**, 995–1005 (2008)
24. Murty, J.V.S.: Watershed Management, 2nd edn. New Age International Publisher, New Delhi (1998)
25. Shingi, P.M., Asopa, V.N.: Independent Evaluation of Check dams in Gujarat. Centre for Management in Agriculture, Indian Institute of Management, Ahmedabad (2002)
26. Fromant, E.: Study of Workings of Check Dams in MP. Action for Social Advancement. State Planning Commission, Madhya Pradesh (2009)

Hydrological Simulation of a Large Catchment Using the Variable Infiltration Capacity Model

Hengade Narendra, T.I. Eldho and Ghosh Subimal

Abstract Understanding the hydrological response of the larger catchment/river basin is a challenge under the changing environment/climate change. In the present study, the Variable Infiltration Capacity (VIC) model, a macroscale hydrological model, is applied over the Tekra catchment (with area of 108780 km^2), a part of Godavari river basin in India. The characteristic of the VIC model are: consideration of variability of soil moisture storage within the grid, nonlinear representation of baseflow and explicit representation of vegetation class. All these characteristics strengthen its suitability to simulate the hydrological changes. In this paper, the performance assessment of the VIC model to simulate the hydrology of the considered large catchment is done. Result shows reasonable agreement between the observed and simulated daily stream flows for the monsoon season of 2009. The gridwise computation of the VIC model allows the meteorological data directly from gridded dataset or General Circulation Models (GCMs) for climate change assessment.

Keywords Tekra catchment · Godavari river basin · Hydrological simulation · Variable infiltration capacity model

1 Introduction

Macroscale hydrological model (MHM) has been developed to study the hydrological responses to the changing climate and land cover. They also deal with the interaction between the land surface schemes and General Circulation Models

H. Narendra · T.I. Eldho (✉) · G. Subimal
Department of Civil Engineering, Indian Institute of Technology Bombay, Mumbai 400076, India
e-mail: eldho@civil.iitb.ac.in

T.I. Eldho · G. Subimal
Interdisciplinary Program in Climate Studies, Indian Institute of Technology Bombay, Mumbai 400076, India

V. Garg et al. (eds.), *Development of Water Resources in India*,
Water Science and Technology Library 75, DOI 10.1007/978-3-319-55125-8_2

(GCMs) to predict the hydrological implication of future climate scenarios. MHMs also provide a link between GCMs and hydrological systems [15]. The VIC model [5, 6] is one of the semi-distributed macroscale hydrological models which have been widely used to study different aspect of water resources management including implications of land cover and climate change over the larger river basins [1, 13–15, 17]. As a hydrological model, VIC solves the water as well as surface energy budgets within the specified grid. Equation 1 shows the water balance components in the VIC model:

$$\frac{\partial \mathrm{S}}{\partial \mathrm{t}} = PR - ET - RF \tag{1}$$

where $\partial S/\partial t$—water storage change, PR—precipitation, ET—evapotranspiration and RF—runoff. The distinguishing hydrological features of the VIC model are: (a) variability of vegetation within a grid, the vegetation classes are represented by its fraction within a grid with its canopy resistance, leaf area index (LAI) and corresponding root fraction in different soil layers; (b) the variability in soil moisture storage capacity within a grid associated with surface runoff; and (c) nonlinear baseflow from the bottom soil layer. The Penman–Monteith formulation is employed to calculate the evapotranspiration (ET) from each vegetation type. Vertical moisture transfer between the two soil layers is formulated by the one-dimensional Richards equation. ARNO baseflow formulation [18] is employed to obtain the subsurface runoff from the bottom layer. The variable infiltration curve [19] represented by Eq. 2 is adopted to account for the runoff generation.

$$i = i_m(1 - (1 - A)^{1/b_i}) \tag{2}$$

where i = infiltration capacity, $\mathrm{i_m}$ = maximum infiltration capacity, A = fraction of an area for which the infiltration capacity is less than i; and b_i = infiltration shape parameter, θ_s = soil porosity and z = soil depth (m). The VIC model generated fluxes (runoff, evapotranspiration, baseflow, soil moisture) are employed as input fluxes to the stand-alone routing model [10]. A routing model is formulated by adopting unit hydrograph to generate the overland flow and linear Saint-Venant equation to derive channel flow [9]. The surface runoff and baseflow is routed to river through grid cells and drainage network to compute the streamflows at specified runoff gauging station.

In this study, the VIC model was adopted to simulate water fluxes at Tekra runoff gauging stations within Godavari river basin. The daily observed streamflows were compared with the VIC simulated daily streamflows for the monsoon period (JJAS) of 2009. The main scope of the present study is to evaluate the performance of the VIC model in estimating the hydrological responses.

2 Literature Review

The literature review mainly refers to acceptance of the VIC model in different aspects of water resources such as evaluation of catchment/basin hydrological processes, effects of land cover and climate change on hydrology.

Hamlet and Lettenmaier [3] used the suite of linked models (global climate model, the VIC hydrology model, ColSim reservoir model) to evaluate the climate/hydrology/water resources systems. The VIC model was employed at 1/8° resolution to assess the hydrological response over the Columbia basin. The future climate records from four climate models (CCCma, HC, GFDL and MPI) were adopted to run the VIC model over the Columbia River. The streamflow simulated by the VIC model was used to drive a reservoir model. The study suggests that streamflow reduction in summer is caused due to increased temperatures which may results in loss of mountain snowpack irrespective of changes in precipitation.

Nijssen et al. [13] used four GCMs (HCCPR-CM2, HCCPR-CM3, MPI-ECHAM4 and DOE-PCM3) to assess the impact of climate change on the nine continental river basins around the globe (Amazon, Amur, Mackenzie, Mekong, Mississippi, Severnaya Dvina, Xi, Yellow and Yenisei). The monthly downscaled precipitation and temperature were used as input to the hydrological model at the river basin level. The VIC model was employed to evaluate the hydrological responses. All GCMs predicted increase in precipitation and temperature for all the basins. The extreme heating was predicted for the area at the highest latitudes during the winter season. The significant implication on the hydrological cycle was observed in the snow-dominated basins. In most of the cases, the increase in annual flow volume was observed for the high-latitude basins, whereas decrease in annual streamflow was observed for the tropical and mid-latitude basins.

Liang et al. [7] proposed a new methodology to describe the dynamic interaction between surface and groundwater. The new parameterization coupled with VIC-3L model termed as VIC-ground accounts the implication of the interaction on hydrological variables such as runoff, evapotranspiration, soil moisture and recharge. The proposed model was applied to two watersheds in Pennsylvania. The results emphasized that the dynamic exchange between the surface and groundwater hydrology impacts the surface fluxes and soil moisture significantly which needs attention.

Meng and Quiring [11] employed three models to compare the results of simulated soil moisture conditions. The VIC model, Decision Support System for Agrotechnology Transfer (DSSAT) and climatic water budget (CWB) models are employed to simulate the soil moisture. The results are compared with observed soil moisture data (1997–2005) at different sites. It is found that the VIC and DSSAT are more accurate in simulating soil moisture than CWB at all sites. Both the

models simulate the soil moisture and its response to weather conditions, accurately. It is also observed that the VIC model is less sensitive in simulating the soil moisture conditions.

Mishra et al. [12] evaluated the hydrological implications due to the land cover pattern and climate change. Historic and projected land cover data along with observed meteorological forcing data (1983–2007) were used to run the VIC model over Wisconsin (USA). The current land cover data are compared with the projected (2030) land cover data. The projected land cover was generated using land transformation model (LTM). The projected climate forcing was downscaled and bias-corrected for three GCMs (HadCM3, PCM and GFDL) and further used to run the VIC model. It is observed that conversion from forested area to cropland caused the increase in surface runoff, baseflow and latent heat, and decrease in evapotranspiration.

Liu et al. [8] used the VIC model to study the land use and climate change over Qingyi river basin in China. They found that the impact of climate change on the hydrological process is more prominent than the land use changes.

Quio et al. [15] estimated the impact of climate change on water quality, water availability and ecosystem by using statistically and dynamically downscaled climate projections. The VIC model is employed to evaluate the hydrological response to climate change at Oologah Lake watershed. The evaluation and comparison show that the dynamically downscaled projection performed better in capturing a rainfall as compared to the statistically downscaled projections, and the annual water availability (precipitation, runoff and baseflow) would increase by 3–4%.

3 Case Study Area and Database

The Godavari river basin extends over the catchment area of 312,800 km^2. It is the second-largest (with a length of 1470 km) perennial river which joins the Bay of Bengal. The Godavari basin is bounded by several hills such as Ajanta range, Satmala hills, Mahadeo hills, Eastern Ghats and the Western Ghats. The river originates at an altitude of 1,067 m near Triambakeshwar in Nasik District, Maharashtra State. The average rainfall over the Godavari basin is 1100 mm/year which vary largely in space and time. The basin receives more than 85% rainfall from the southwest monsoon during the months of June–July–August–September. The Tekra gauge station is established at latitude 18°58′42″ and longitude 79°56′49″ on Pranhita tributary by Central Water Commission (CWC) in 1963. The total catchment area discharging to Tekra station is 108780 sq. km. Geographic setting of Godavari basin, Tekra station and Tekra catchment is shown in Fig. 1.

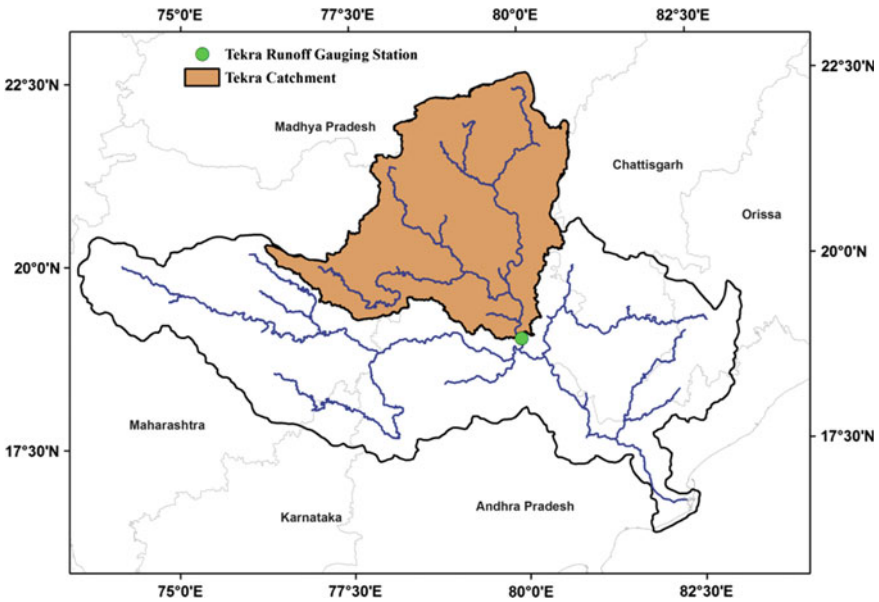

Fig. 1 Geographic setting of Tekra catchment within Godavari river basin

The daily precipitation, daily maximum and minimum temperature and daily wind speed are the forcings to run the VIC model. The 0.25° × 0.25° daily precipitation and 1° × 1° minimum and maximum daily temperature gridded data for the monsoon period of 2009 were obtained from Indian Meteorological Department [16]. The reanalysis data [4] are employed for wind speed at 2.5° × 2.5° resolutions obtained from National Centers for Environment Prediction (NCEP).

Figure 2 represents digital elevation model (DEM) of 90-m spatial resolution extracted from Shuttle Radar Topography Mission (SRTM) dataset to delineate the Tekra catchment boundary. Figure 3 represents the soil types that are extracted from digitized soil map of the world [2] which indicate the dominance of clay and sandy clay loam within the Tekra catchment. Figure 4 represents global land cover map of 1 km resolution for the Tekra catchment as generated by University of Maryland, Department (UMD) of Geography, from Advanced Very-High-Resolution Radiometer (AVHRR) data generated. It showed the dominance of wooded grassland (78.1%) and woodland (17.7%) within Tekra catchment area.

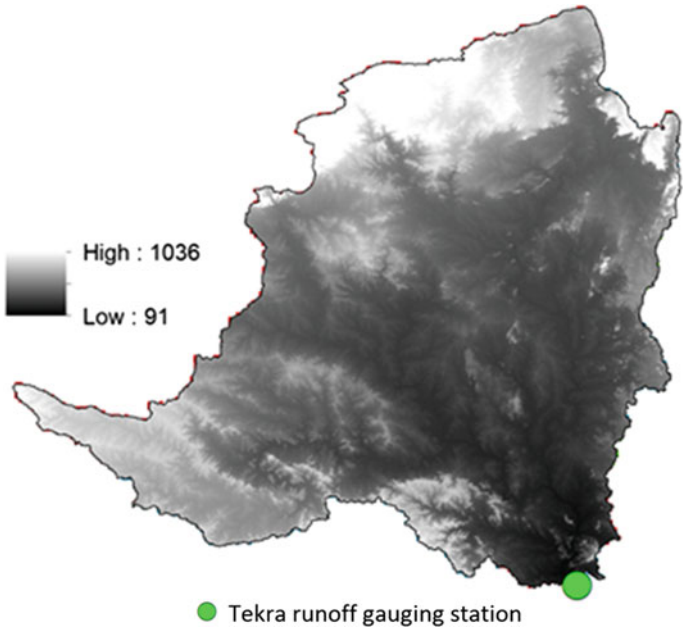

Fig. 2 Digital elevation model (SRTM) for Tekra catchment

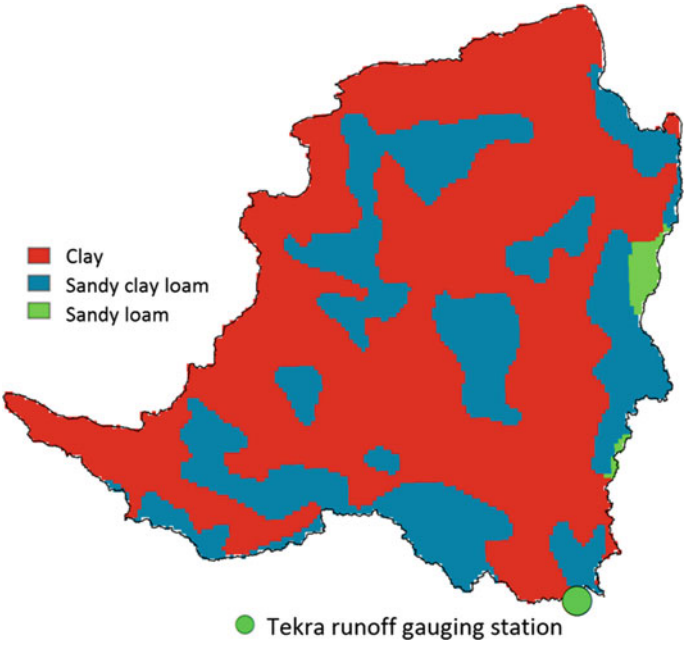

Fig. 3 Soil map (FAO) for Tekra catchment

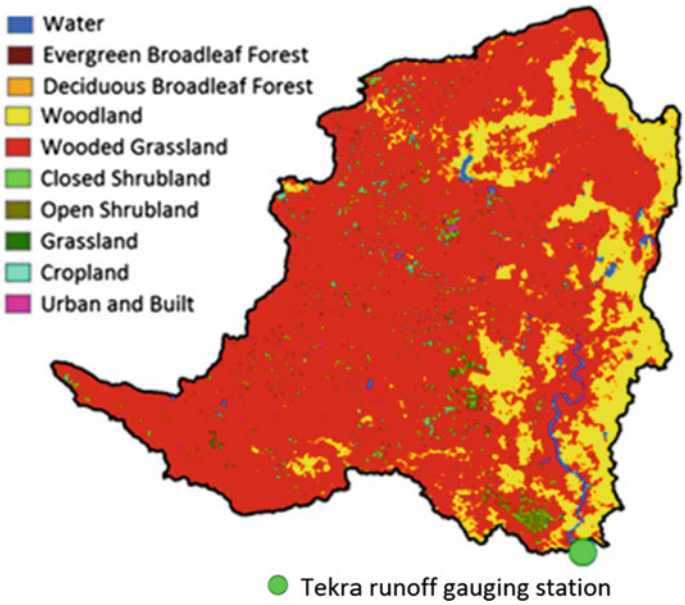

Fig. 4 Land cover map (AVHRR) for Tekra catchment

4 Establishing the VIC Model for the Tekra Catchment

In this paper, the VIC-2L model was employed to evaluate the performance of the model over the Tekra catchment. Since the VIC model computation works on grid basis, the Tekra catchment is divided into multiple uniform grid cells of 25 km 25 km as shown in Fig. 5.

Gridwise daily inputs of DEM, soil parameters, vegetation parameters and daily meteorological forcing parameters are used to run the VIC model in water balance mode. For each grid, forcing file containing meteorological variables (daily precipitation, daily max. and min. temperature and daily wind speed) for monsoon period of 2009 has been generated as input to the VIC model. The thematic layers such as DEM, soil and land cover grids were used to overlay on the generated grids to extract the gridwise parameters. The number of vegetation types, their fraction within the grid, root depth and its fraction in different soil layers were derived at each grid cell. Standard soil properties are obtained for the respective soil type. All soil parameter has been obtained at each grid cell for two soil layers (300 and 700 mm). Thus, the gridwise distribution of parameters and properties of two soil layers is defined over the Tekra catchment as per the input format required to run the VIC model.

The VIC model derived fluxes such as surface runoff, evapotranspiration and baseflow along with the direction of flow and the fraction of flow at each grid are adopted as input flow routing model [10]. The flow direction of each grid was

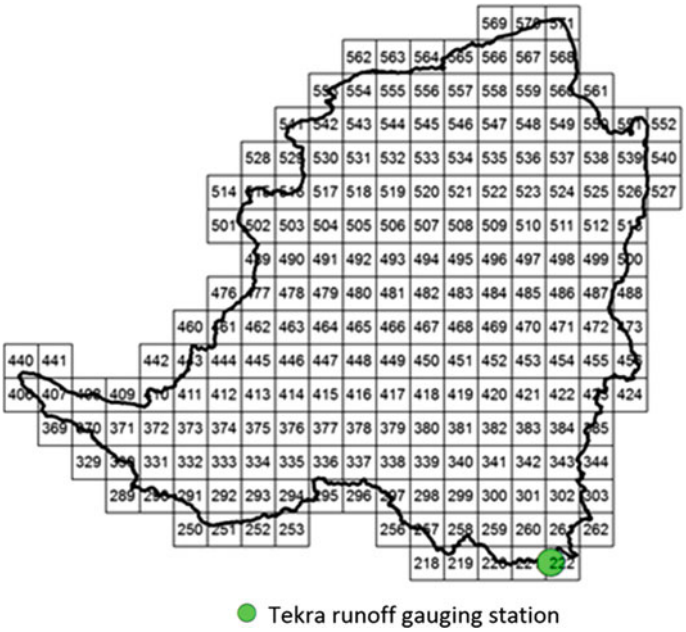

Fig. 5 Grids (25 km × 25 km) over Tekra catchment

extracted using DEM, and flow fraction of boundary grids was extracted to process the actual catchment area during the flow routing. The simulated streamflow by the VIC model is compared with observed streamflow at the Tekra runoff gauging station. The observed streamflows at Tekra station were obtained from Central Water Commission (CWC), Government of India. The routing model permits to evaluate the efficiency and performance of the VIC model using the observed streamflow hydrographs.

Remote sensing data and geographic information system (GIS) techniques played a vital role to retrieve the required gridded hydrological parameters from the global dataset (DEM, land cover map and soil map) over the Tekra catchment.

5 Results and Discussion

In this study, the hydrological response of the Tekra catchment is estimated using the VIC-2L model and evaluated the model parameters. The model parameters play a crucial role to simulate the streamflow closer to the observed streamflow. Hence, the understanding and selection of these parameters are inevitable. The VIC model accounts for many parameters like other physically based hydrological models. Most of the hydrological variables can be obtained from in situ observations and remote sensing data. The VIC-2L model accounts five parameters for model

Table 1 Adopted VIC-2L model parameter values for Tekra catchment

Parameter	Description	Adopted value
b_i	Shape parameter for Soil moisture capacity curve	0.2
Dsmax	The maximum baseflow velocity of the lowest soil layer (mm/day)	10
Ds	Fraction of Dsmax.	0.01
W_s	Fraction of max. soil moisture in which nonlinear baseflow occurs	0.8

calibration: (1) the infiltration parameter (b_i), which governs the variable infiltration capacity curve shape and control the partitioning of rainfall into direct runoff and infiltration. The value of b_i is ranging from 0 to 0.4 and directly proportionate to yield of surface runoff; (2) the thickness bottom soil layer (D_2) which control the amount of water for transpiration and baseflow. Thicker bottom soil layer causes higher evapotranspiration, longer soil moisture retention and higher baseflow; (3) the baseflow max. velocity (Ds_{max}) from the lowest soil layer (mm/day). The value ranges from 0 to 30 depending on the hydraulic conductivity of soil; (4) the fraction of Ds_{max} (Ds) where the rapidly increasing nonlinear baseflow starts. It ranges from 0 to1. Higher value of Ds causes higher baseflow; and (5) the fraction of the max. soil moisture of the lowest soil (Ws) when the rapidly increasing baseflow begins. The higher value of Ws tends to delay the peak runoff. The selection of these parameters plays a vital role in controlling the infiltration and baseflow which eventually governs the streamflow hydrograph at the outlet location. The adopted values of the above parameters for the Tekra catchment are shown in Table 1 to get reasonable agreement with observed and estimated streamflow.

The daily observed and simulated streamflows are compared at Tekra runoff gauging station for the June–July–August–September (JJAS) or monsoon period of 2009. Figure 6 shows that the estimated and observed streamflows are in reasonable agreement.

The Nash–Sutcliffe coefficient (N_s), relative error (RE) and coefficient of determination (R^2) are selected as the performance criteria to evaluate the model performance. The performance indicators are obtained by comparing daily simulated and observed streamflows at Tekra station and given in Table 2.

At Tekra runoff gauging station, the Nash–Sutcliffe value is 0.66. The value of efficiency coefficient of 1 indicates a perfect match between simulated output and the observed data. Value of efficiency coefficient of 0 corresponds to the match of mean values of the simulated output to the observed data. The coefficient of determination (0.83) shows good agreement between the simulated and observed runoff (Fig. 6b). It is observed that the simulated flows are overestimated than the observed flows. The VIC model simulated streamflow following the same trend of the daily streamflow observed; however, overestimated simulated streamflow is determined which is indicated by the relative error of 30.03%. Nevertheless, overestimations or underestimations are inevitable in the simulation because of the uncertainties in the used data, model and estimating the parameters. Using the VIC

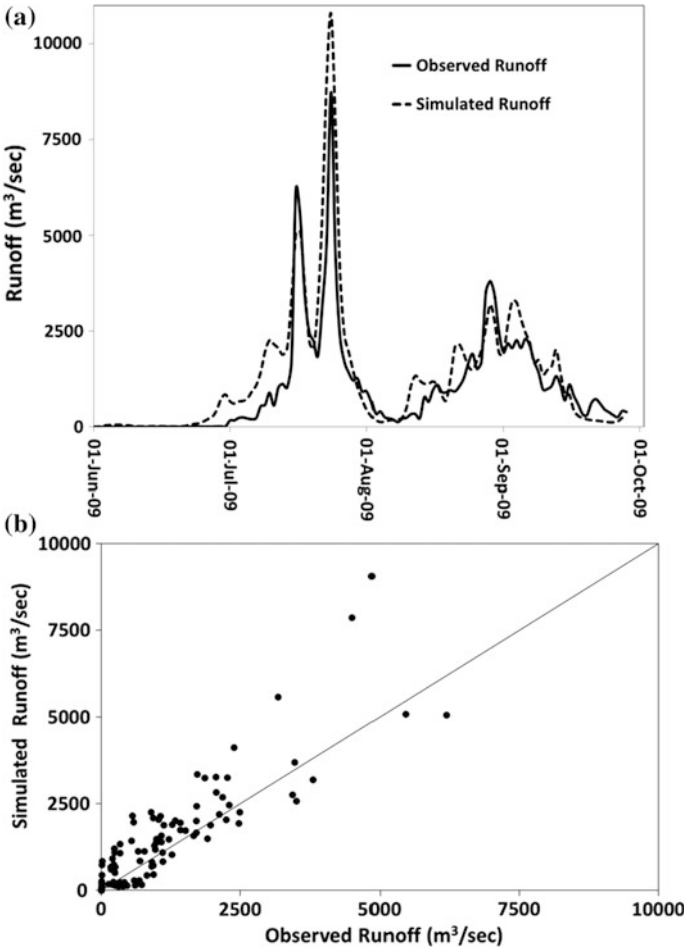

Fig. 6 Comparison of simulated and observed runoff for monsoon period of 2009 at Tekra station

Table 2 Model performance indicators during calibration and validation

Station	Period	Ns	RE (%)	R^2
Tekra	JJAS-2009	0.66	30.03	0.83

model, various fluxes are derived for the study area for the year of simulation. The obtained fluxes are surface runoff = 147.65 mm, evapotranspiration = 547.94 mm and baseflow = 28.87 mm for monsoon rainfall of 827.57 mm for the year 2009. The difference between the rainfall and fluxes mentioned above is due to other losses such as soil moisture storage and interception.

The VIC model accounts several land cover characteristics such as leaf area index (LAI), albedo, stomatal resistance, height, canopy resistance and fraction of

roots of plants in different soil layers. It also accounts evapotranspiration (ET) as one of main hydrological parameters which is sensitive to land cover change. The VIC model computation works on grids and accepts gridded meteorological input directly from the global database or from GCMs. Hence, the VIC model is one of the powerful tools to estimate the hydrological responses to land use/cover and climate change within the catchment/river basin.

6 Conclusions

In the present study, the VIC model is used for hydrological simulations and the performance is evaluated by comparing the daily VIC model estimated and observed streamflow at Tekra station. The estimation of sensitive model parameters is also discussed. The conclusions drawn from the study are as follows:

- The VIC model considers a large number of vegetation parameter, soil parameters, daily/sub-daily meteorological forcing data. It adopts the physical models for runoff generation. Hence, the model is suitable to estimate the hydrological processes for large catchments.
- The reasonable agreement between the VIC model simulated and observed runoff at Tektra station shows the capability of the model over larger catchments or river basin.
- The acceptability of the VIC model is strengthened by the easy parameter estimation during calibration; adaptation of readily available global datasets such as meteorological forcing, land cover, soil and topography; and use of GIS techniques.
- Measured streamflow are easily available and the effective indication of the change in hydrological cycle. Further coupling of the VIC model with a routing model allows the comparison between the observed and simulated streamflow in order to access model capacity and efficiency.

Acknowledgements The authors sincerely acknowledge Central Water Commission (CWC) for providing streamflow data at Tekra gauging station in Godavari river basin.

References

1. Cuo, L., Zhang, Gao, Y., Hao, Z., Cairang L.: The impacts of climate change and land cover/use transition on the hydrology in the upper Yellow River Basin, China. J. Hydrol. **502**, 37–52 (2013)
2. FAO: The digitized soil map of the world and derived soil properties (version 3.5). FAO Land and Water Digital Media Series 1, FAO, Roam (2003)
3. Hamlet, A.F., Lettenmaier, D.P.: Effects of climate change on hydrology and water resources in the Columbia river basin. J. Am. Water Resour. Assoc. **35**, 1597–1623 (1999)

4. Kalnay, E., Kanamitsu, M., Kistler, R.: The NCEP/NCAR 40-years reanalysis project. Bull. Am. Meteorol. Soc. **77**, 437–471 (1996)
5. Liang, X., Lettenmaier, D.P., Wood, E.F., Burges, S.J.: A simple hydrologically based model of land surface water and energy fluxes for general circulation models. J. Geophys. Res. **99**, 14415–14428 (1994)
6. Liang, X., Lettenmaier, D.P., Wood, E.F.: One-dimensional statistical dynamic representation of subgrid variability of precipitation in the two-layer variable infiltration capacity model. J. Geophys. Res. **101**, 403–421 (1996)
7. Liang, X., Xie, Z., Huang, M.: A new parameterization for surface and groundwater interactions and its impact on water budgets with the variable infiltration capacity (VIC) land surface model. J. Geophys. Res. **108**, 8-1–8-17 (2003)
8. Liu, Y., Zhang, X., Xia, D., You, J., Rong, Y., Bakir, M.: Impacts of land-use and climate changes on hydrologic processes in the Qingyi River Watershed, China. J. Hydrol. Eng. **18**, 1495–1512 (2013)
9. Lohmann, D., Nolte-Holube, R., Raschke, E.: A large scale horizontal routing model to be coupled to land surface parameterization schemes. Tellus **48A**, 708–721 (1996)
10. Lohmann, D.R., Raschke, E., Nijssen, B., Lettenmaier, D.P.: Regional scale hydrology: I Formulation of the VIC-2L model coupled to a routing model. Hydrol. Sci. J. **43**, 131–141 (1998)
11. Meng, Quiring: A comparison of soil moisture models using Soil Climate Analysis Network observations. J. Hydrometeorol. **9**, 641–659 (2008)
12. Mishra, V., Keith, A.C., Dev, N., Ming, L., Bryan, C.P., Deepak, K.R., Bowling, L., Guoxiang, Y.: A regional scale assessment of land use/land cover and climatic changes on water and energy cycle in the upper Midwest United States. Int. J. Climatol. **30**, 2025–2044 (2010)
13. Nijssen, B., Greg O'Donnell, M., Lettenmair, D.P.: Predicting the discharge of global rivers. J. Clim. **14**, 3307–3323 (2000)
14. Nijssen, B., Greg O'Donnell, M., Hamlet, A.F., Lettenmaier, D.P.: Hydrologic sensitivity of global rivers to climate change. Clim. Chang. **50**, 143–175 (2001)
15. Qiao, L., Hong, Y., Renee, M.R., Mark, S., David, G.D., David, W.D., Chen, S., Lilly, D.: Climate Change and Hydrological Response in the Trans-State Oologah Lake Watershed-Evaluating Dynamically Downscaled NARCCAP and Statistically Downscaled CMIP3 Simulations with VIC Model BCSD. Water Resour. Manag. **28**, 3291–3305 (2014)
16. Rajeevan, M., Bhate, J., Kale, J.D., Lal, B.: Development of a high resolution daily gridded rainfall data for the Indian region: analysis of break and active monsoon spells. Technical Report, India Meteorological Department (2005)
17. Savary, S., Rousseau, A. N., Quilbe, R.: Assessing the effects of historical land cover changes on runoff and low flows using remote sensing and hydrological modeling. J. Hydrol. Eng. 575–587 (2009)
18. Todini, E.: The ARNO rainfall-runoff model. J. Hydrol. **175**, 339–382 (1996)
19. Zhao, R.J., Zhang, Y.L., Fang, L.R., Zhang, Q.S.: The Xinanjiang model. Hydrological Forecasting. In: Proceedings Oxford Symposium, vol. 129, pp. 351–356 (1980)

Rainfall Assessment Through Space and Time from 1999 to 2014 in Salem District, South India

Arulbalaji Palanisamy and Gurugnanam Balasubramanian

Abstract The present study deals with the rainfall assessment using geospatial techniques in Salem District, South India. The rainfall assessment was carried over a period of 16 years from 1999 to 2014. The research methodology has been adopted based on the literature study and has given accurate results. Therefore, the output shows that the study area received 1%, 19%, 41% and 39% of precipitation in winter season, summer season, southwest and northeast monsoon, respectively, and the average annual rainfall was relatively more in north and northeast, and it gradually decreased at eastern, western and southern parts of the study area. The precipitation ratio has less abnormality during southwest and northeast season and high abnormality during summer and winter season. Finally, rainfall variation assessment shows that the rainfall conditions in Salem District are normal and fluctuation depends on time and space.

Keywords Variability · Precipitation ratio · Time · Space

1 Introduction

Rainfall plays a vital role for socioeconomic growth of an area, region and country. Generally, rainfall has a fluctuating character in year-to-year. Rainfall is a dynamic input for hydrologic studies, and it is serious for obtaining accurate results Suk et al. [9]. Forecasting and monitoring of precipitations are very important for management of future droughts or floods [3, 7]. Rainfall is exclusive variable, which

A. Palanisamy (✉) · G. Balasubramanian
Centre for Applied Geology, Gandhigram Rural Institute-Deemed Unviersity, Dindigul, Tamil Nadu, India
e-mail: arulbalajigeo@gmail.com

V. Garg et al. (eds.), *Development of Water Resources in India*,
Water Science and Technology Library 75, DOI 10.1007/978-3-319-55125-8_3

reflects numerous factors regionally and globally [4, 5]. Therefore, this study will assist the people to predict meteorological condition and its variation in spatial and temporal of Salem District. Rainfall variation and the detection of rainfall extremes are a function of scale, so high space and time resolution data are ideal to identify extreme events and exact prediction of future variability [6, 13]. Climatology is one of the main factors, which is directly or indirectly influenced by hydrology predictions [1, 8, 11]. Remote sensing and geographical information system has been used to create model in identification of rainfall-based assessment [2]. India receives more rainfall during SW monsoon than the other seasons [10, 12], have analyzed that the Salem District received average rainfall of less than 200 mm during 1998–2007, which was very less than actual rainfall.

2 Materials and Methods

The rainfall data were collected from State Ground and Surface Water, Resource Data Centre, Chennai. The collected data were attributed by using statistical tools; then, Arc GIS 10.2.1 software was used for deriving the spatial distribution maps and results. The 16 years of rainfall data were analyzed for season and annual rainfall, seasonal and annual precipitation ratio. All these parameters have been assessed in spatial and temporal methods. The detailed flowchart methodology of the present study is shown in Fig. 1.

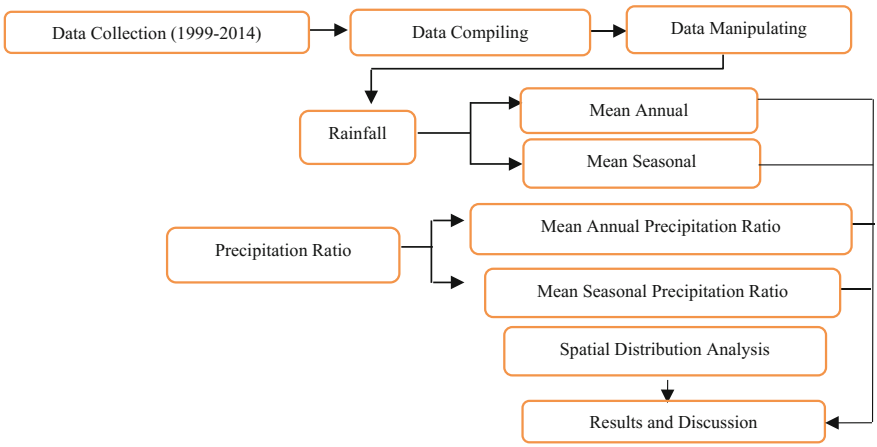

Fig. 1 Flowchart methodology

3 Study Area

The present study concentrated on Salem District (Fig. 2), which is located between 11°10′ and 12°10′ north latitudes and between 77°35′ and 78°55′ east longitudes and the total area covered by 5232 km^2. The average mean sea level is 278 m. The study area is situated at north side of Nagaramalai hill, west side of Kanjamalai hill, east side of Godumalai hill, south side of Jarugumalai hill, northeast side of Shevaroy hills and southwest side of Kariyaperumal Hills.

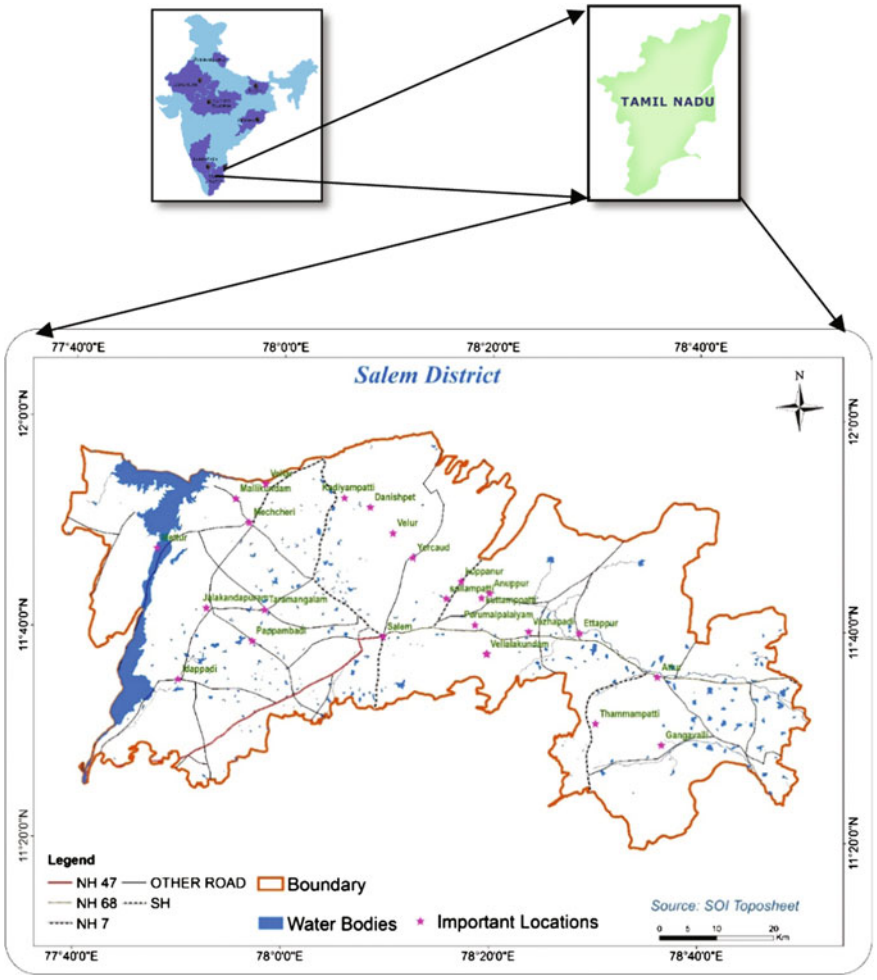

Fig. 2 Study area

4 Results and Discussion

4.1 Mean Annual Rainfall

Since 1999 to 2014, the study area received an average annual rainfall of 816 mm. The average annual rainfall ranges varied from 329 to 1492 mm. The spatial map (Fig. 3) is clearly representing the mean annual rainfall variation between one station to another station, and the distribution was divided into five categories with 250-mm interval. The northern part of study area, especially in Yercaud station, received a very high (>1250) rain fall, which covered an area of 109 km^2; the Mettur and surrounding of Yercaud hill received high (1000–1250) rainfall, which covered an area of 579 km^2. The very high and high rainfall categories occurred in the high elevation area. Most parts of the study area received moderate (750–1000) mean annual rainfall. Nangavalli, Omalur, Kullampatti, Salem city, Valapadi, Anaimadu Reservoir, Athur and Thammampatti areas found under the moderate rainfall category covered an area of 3664 km^2. Low (500–750) level of rainfall located in Gangavalli, Salem Junction, Pillukuruchi, Sankagiri, Edapadi and Kolathur. These locations are situated in east and western part of the study area. Low rainfall covered an area of 710 km^2. Very low (<500) level rainfall covered an area of 168 km^2 of the study area, and it was mainly found in Veeraganoor and its surrounding areas. Moderate to very low rainfall occurred in low elevation and plain regions of the study area.

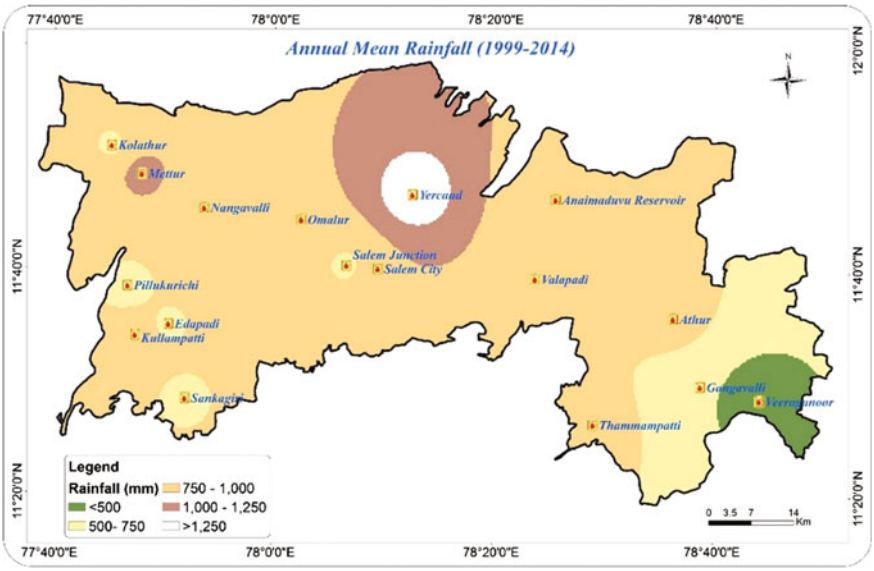

Fig. 3 Spatial distribution map of annual mean rainfall

4.2 Seasonal Rainfall

4.2.1 Winter Season

The winter season contributed very less (1%) percentage of rainfall than other season. The average winter season rainfall ranges varied from 1 to 12 mm. The spatial distribution map of the winter season is shown in Fig. 4. The spatial distribution of winter season rainfall was divided into five classes with 2.5-mm interval. The very low (<2.5) level rainfall occurred in Nangavalli, Salem Junction and Veeraganoor stations, which covered an area of 323 km^2. Low (2.5–5) level rainfall covered an area of 3711 km^2, and the locations were Kolathur, Mettur, Omalur, Salem city, Sankagiri, Valapadi, Anaimaduvu reservoir, Athur and Gangavalli stations. Moderate (5–7.5) level rainfall covered an area of 905 km^2, and the locations were surrounding parts of Yercaud, Edapadi and Kullampatti. High (7.5–10) level rainfall found in Pillukurichi and some parts of Yercaud covered an area of 269 km^2. The very high (>10) level rainfall occurred in Yercaud, and it covered an area of 24 km^2.

4.2.2 Summer Season

The summer season contributed 19% of rainfall, and it is higher than winter season rainfall. The summer season rainfall ranges varied from 47 to 264 mm. The spatial

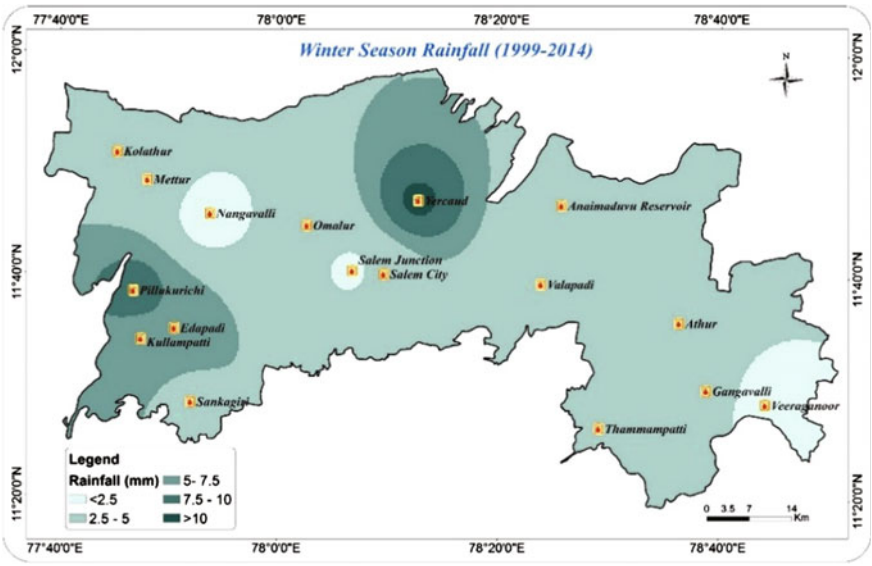

Fig. 4 Spatial distribution map of annual winter season rainfall (1999–2014)

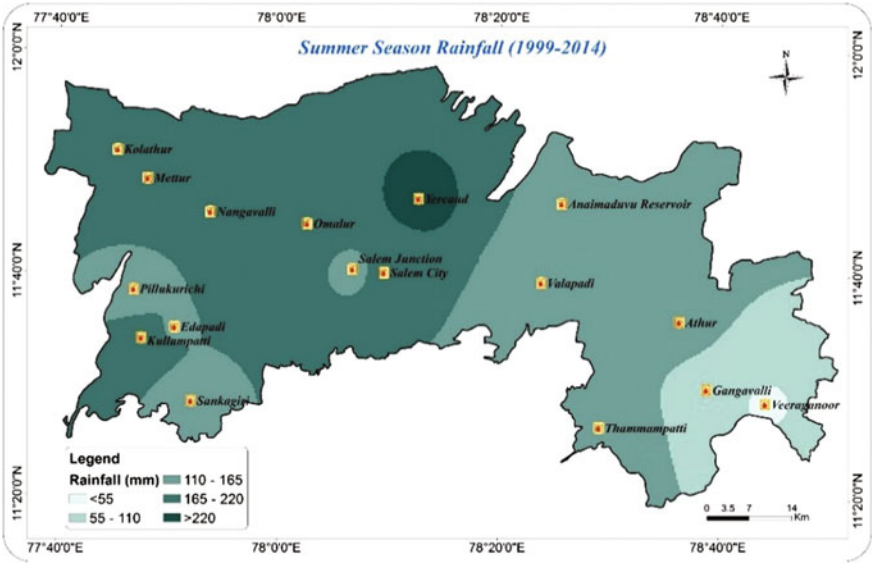

Fig. 5 Spatial distribution map of annual summer season rainfall (1999–2014)

distribution map of the summer season is shown in Fig. 5. The summer season rainfall was divided into five classes with 55-mm interval. The very low rainfall (<55) station was Veraganoor, and it covered an area of 30 km^2. Low rainfall (55–110) occurred in Gangavalli and surrounding parts of Veraganoor stations, which covered an area of 497 km^2. Moderate rainfall (110–165) occurred in Pillukurichi, Edapadi, Sankagiri, Salem Junction, Anaimaduvu, Valapadi, Athur and Thammampatti stations, which covered an area of 1968 km^2. High rainfall (165–220) occurred in Kullampatti, Kolathur, Mettur, Nangavalli, Omalur and Salem city, which covered an area of 2604 km^2. Very high rainfall (>220) occurred in Yercaud station, and it covered an area of 129 km^2.

4.2.3 Southwest Monsoon (SW)

The SW monsoon contributed 41% of rainfall, and it is higher than summer season rainfall. The SW monsoon rainfall ranges varied from 92 to 718 mm. The spatial distribution map of the SW monsoon is given in Fig. 6. The SW monsoon was divided into five classes in 150-mm interval. The very low (<150) rainfall occurred in Gangavalli and Veeraganoor stations, which covered an area of 134 km^2. Low (150–300) rainfall covered an area of 1089 km^2, and the areas were Kolathur, Pillukurichi, Sankagiri, Thammampatti and surrounding areas of Gangavalli station. Moderate (300–450) rainfall covered an area of 3299 km^2, and the areas were Mettur, Nangavalli, Kullampatti, Edapadi, Salem Junction, Anaimaduvu reservoir,

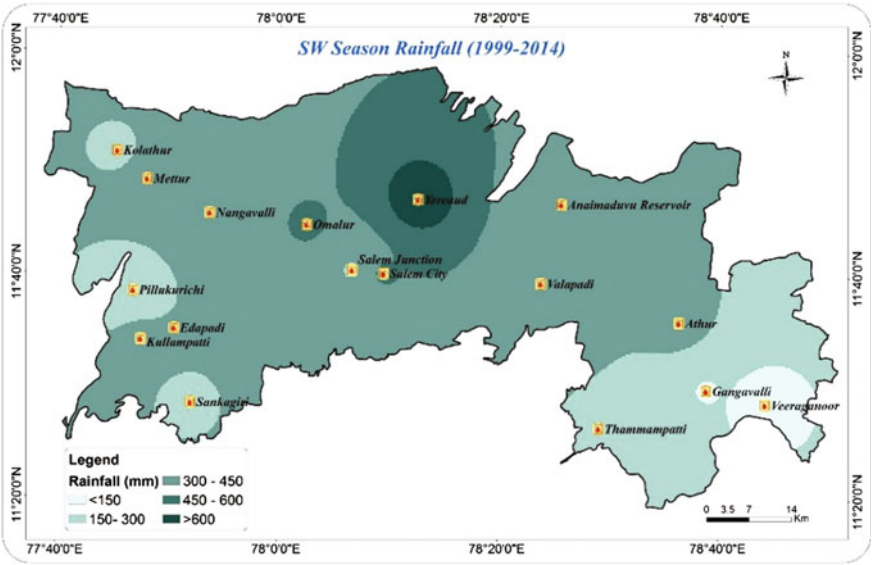

Fig. 6 Spatial distribution map of annual SW season rainfall (1999–2014)

Valapadi and Athur. High (450–600) rainfall located in Omalur, Salem city and surrounding parts of Yercaud and covered an area of 615 km^2. The very high (>600) rainfall region was Yercaud station, and it covered an area of 93 km^2.

4.2.4 Northeast Monsoon (NE)

The NE monsoon contributed 39% of rainfall which is higher than winter and summer season. The NE monsoon rainfall ranges varied from 190 to 496 mm. The spatial distribution map of the NE monsoon is given in Fig. 7. The NE monsoon was divided into five classes in 80-mm interval. The very low (<240) rainfall occurred in Veeraganoor station, which covered an area of 130 km^2 (Table 1).

Low (240–320) rainfall covered an area of 2141 km^2, and the locations were Kolathur, Pillukurichi, Edapadi, Sankagiri, Omalur, Salem Junction, Anaimaduvu reservoir and Gangavalli station. Moderate (320–400) rainfall covered an area of 2663 km^2, and the locations were Mettur, Nangavalli, Kullampatti, Salem city, Valapadi and Athur. High (400–480) rainfall located in Thammampatti and surrounding parts of Yercaud and covered an area of 280 km^2. The very high (>480) rainfall region was Yercaud station and covered an area of 15 km^2.

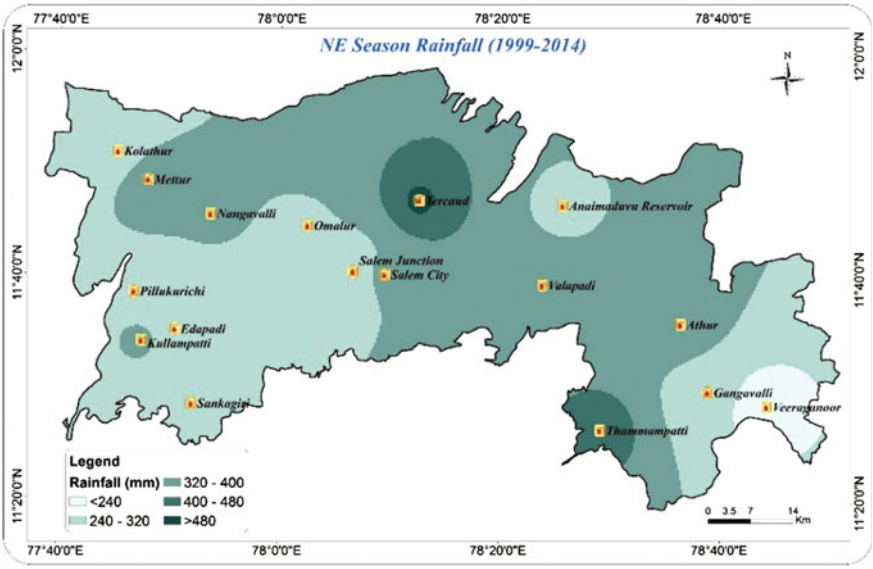

Fig. 7 Spatial distribution map of annual NE season rainfall (1999–2014)

Table 1 Annual and seasonal rainfall

Station	Winter	Summer	SW	NE	Mean annual
Veeraganur	0.821429	46.81	91.88929	189.7557	329.2764
Yercaud	12.4625	264.1575	718.9288	495.9513	1491.5
Thammampatti	6.525	132.27	288.1563	448.605	875.5563
Valapadi	2.675	119.20833	358.5475	355.335	835.7658
Omalur	4.4	179.75375	472.3756	316.7669	973.2963
Pillukurichi	10.08125	142.51688	240.3969	309.2056	702.2006
Salem	4.63125	173.92688	464.7563	346.815	990.1294
Athur	3.90625	129.56188	359.4181	391.9813	884.8675
Gangavalli	4.923077	97.410769	144.6369	254.8723	501.843
Salem Rly	1.6625	157.10375	288.5894	244.2313	691.587
Edapadi	8.538462	164.07769	302.0615	259.7692	734.4469
Kolathur	3.923077	175.20308	286.1369	257.8577	723.1208
Anaimaduvu-RES	3.307692	160.38462	350.4615	300.4	814.5538
Kullampatti	7	183.45688	318.3519	334.3088	843.1176
Mettur	5.7875	203.875	333.1119	366.9381	909.7125
Nangavalli	0	174.69786	345.2064	327.0157	846.92
Sankagiri	4.925	155.945	287.7438	282.5856	731.1994
Average	5.033529	156.491757	332.39818	322.4938	816.4173
Percentage	1	19	41	39	

4.2.5 Precipitation Ratio (PR)

The abnormalities of rainfall have been calculated using a simple ratio of precipitation. Precipitation ratio is the difference between maximum and minimum rainfall over the study period of mean value. The precipitation ratio may give the stability of rainfall with spatial pattern. Higher value of PR has high abnormality in rainfall, and the lower PR value has less abnormality in rainfall. The PR formula is given below.

$$\text{Precipitation Ratio} = (\text{Px} - \text{Pn})/\text{Pm} \times 100$$

where

Px Maximum of Rainfall
Pn Minimum of Rainfall
Pm Mean Rainfall

The result of precipitation ratio analysis is given in Table 2.

Mean Annual Precipitation Ratio

The mean annual precipitation ratio of the study area was 132%. The spatial distribution of the mean annual precipitation ratio is shown in Fig. 8. The precipitation ratio was divided into five classes in 50% intervals. The very low (<100) PR

Table 2 Annual and seasonal precipitation ratio

Station	Winter (%)	Summer (%)	SW (%)	NE (%)	Mean annual (%)
Veeraganur	1437.5	486.4345	330.652174	269.870883	301.382061
Yercaud	783.1809	143.8144	78.3814611	122.955943	71.8739524
Thammampatti	521.0728	180.5398	118.616305	112.325988	54.9365015
Valapadi	336.4486	246.6443	62.9485116	134.740456	102.687854
Omalur	1250	205.5076	112.073163	107.791142	53.6725465
Pillukurichi	765.873	207.0175	102.000915	224.256145	129.73511
Salem	535.6371	232.1182	101.245831	48.0946946	70.7685278
Athur	548.7179	209.4782	99.2181631	169.881116	138.992561
Gangavalli	595.9184	206.139	231.957409	278.965747	204.207251
Salem Rly	1325.301	226.5436	188.322938	268.640216	170.687154
Edapadi	831.3817	246.7089	110.574058	223.364126	131.86794
Kolathur	576.5306	164.8374	195.848186	235.712042	183.413541
Anaimavu-RES	484.8485	142.1446	86.4479315	191.078562	110.489939
Kullampatti	828.5714	159.2371	183.320245	240.146575	181.315178
Mettur	539.1395	225.683	83.5705706	210.820387	114.220702
Nangavalli	0	227.5329	100.463499	243.149847	124.309262
Sankagiri	1359.026	70.85832	163.955509	139.578173	96.4853089
Mean	748.1852	210.6611	138.211581	189.492473	131.8262

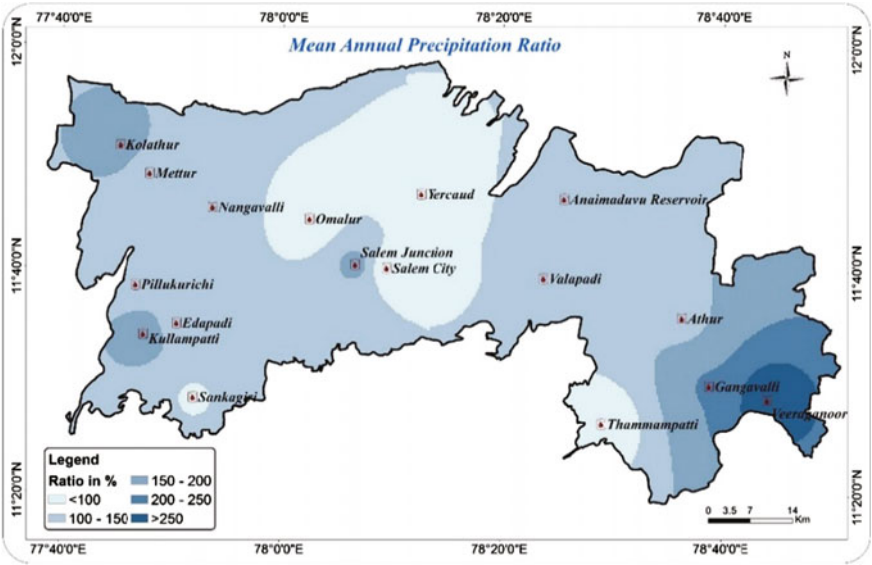

Fig. 8 Spatial distribution map of annual mean precipitation ratio

occurred in Yercaud, Omalur, Salem city, Sankagiri and Thammampatti Stations, which covered an area of 1150 km^2. Low (100–150) PR covered an area of 3143 km^2, which occurred in Pillukurichi, Mettur, Nangavalli, Edapadi, Valapadi, Anaimaduvu reservoir and Athur stations. Moderate (150–200) PR covered an area of 626 km^2, which occurred in Kolathur, Kullampatti, Salem junction and surrounding parts of Gangavalli station. High (200–250) PR located in Gangavalli station, which covered an area of 205 km^2. The very high (>250) PR region was Veeraganoor station, and it covered an area of 104 km^2.

4.2.6 Winter Season Precipitation Ratio

The mean winter season precipitation ratio of the study area was 748%, and it varied from 0 to 1437.5%. The spatial distribution of the winter season PR is shown in Fig. 9. The precipitation ratio was divided into five classes in 300% intervals. The very low (<300) PR occurred in Nangavalli and Salem city station, which covered an area of 67 km^2. Low (300–600) PR covered an area of 1563 km^2 and occurred in Kolathur, Mettur, Valapadi, Anaimaduvu reservoir and Athur stations. Moderate (600–900) PR covered an area of 2666 km^2 and occurred in Pillukurichi, Edapadi, Kullampatti, Yercaud and Gangavalli stations. High (900–1200) PR located in surrounding parts of Omalur, Salem junction, Sankagiri and Veeraganoor

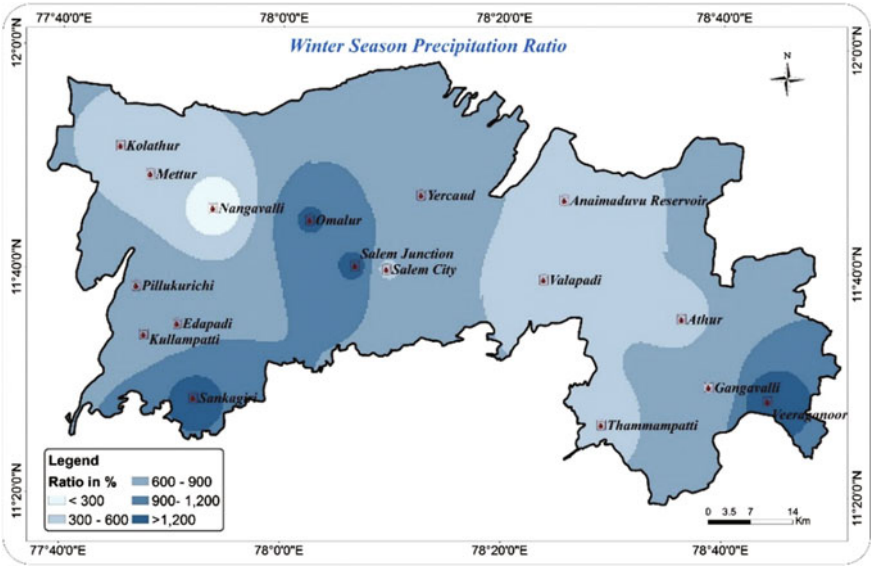

Fig. 9 Spatial distribution map of annual winter season precipitation ratio

stations, which covered an area of 765 km^2. The very high (>1200) PR regions were Veeraganoor, Omalur, Salem junction, and Sankagiri stations, which covered an area of 170 km^2.

4.2.7 Summer Season Precipitation Ratio

The mean summer season precipitation ratio of the study area is 210%, and it varied from 70 to 486%. The spatial distribution of the summer season PR is shown in Fig. 10. The precipitation ratio was divided into five classes in 100% intervals. The very low (<100) PR occurred in Sankagiri, which covered an area of 48 km^2. Low (100–200) PR covered an area of 1864 km^2, which occurred in Kolathur, Kullampatti, Yercaud, Anaimaduvu reservoir and Thammampatti stations. Moderate (200–300) PR covered an area of 3075 km^2, which occurred in Mettur, Nangavalli, Omalur, Pillukurichi, Edapadi, Salem Junction, Salem city, Valapadi, Athur and Gangavalli stations. High (300–400) PR located in surrounding parts of Veeraganoor stations, which covered an area of 158 km^2. The very high (>400) PR region was Veeraganoor station, and it covered an area of 85 km^2.

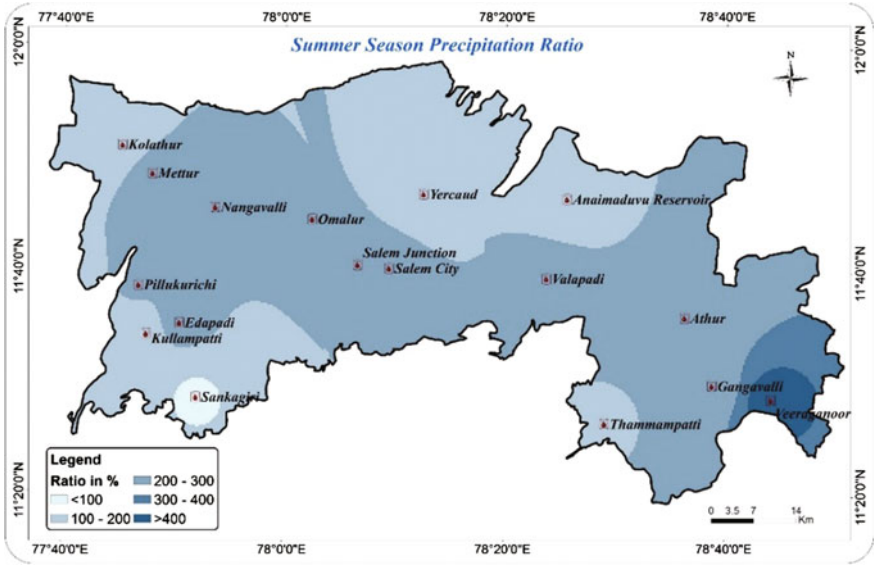

Fig. 10 Spatial distribution map of annual summer season precipitation ratio

4.2.8 Southwest (SW) Monsoon Precipitation Ratio

The mean SW monsoon precipitation ratio of the study area was 138%, and it varied from 62 to 330%. The spatial distribution of the SW monsoon PR is shown in Fig. 11. The precipitation ratio was divided into five classes in 80% intervals. The very low (<80) PR occurred in Valapadi and Yercaud, which covered an area of 110 km^2. Low (80–160) PR covered an area of 4285 km^2, which occurred in Mettur, Nangavalli, Omalur, Pillukurichi, Edapadi, Anaimaduvu reservoir, Athur and Thammampatti stations. Moderate (160–240) PR covered an area of 634 km^2 and occurred in Kolathur, Kullampatti, Sankagiri, Salem junction and Gangavalli stations. High (240–320) PR located in surrounding parts of Veeraganoor stations covered an area of 185 km^2. The very high (>320) PR region was Veeraganoor station, and it covered an area of 15 km^2.

4.2.9 Northeast (NE) Monsoon Precipitation Ratio

The mean NE monsoon precipitation ratio of the study area is 189%, and it varied from 48 to 278%. The spatial distribution of the NE monsoon PR is shown in Fig. 12. The precipitation ratio was divided into five classes in 60% intervals. The very low (<60) PR occurred in Salem city covered an area of 7 km^2. Low (60–120)

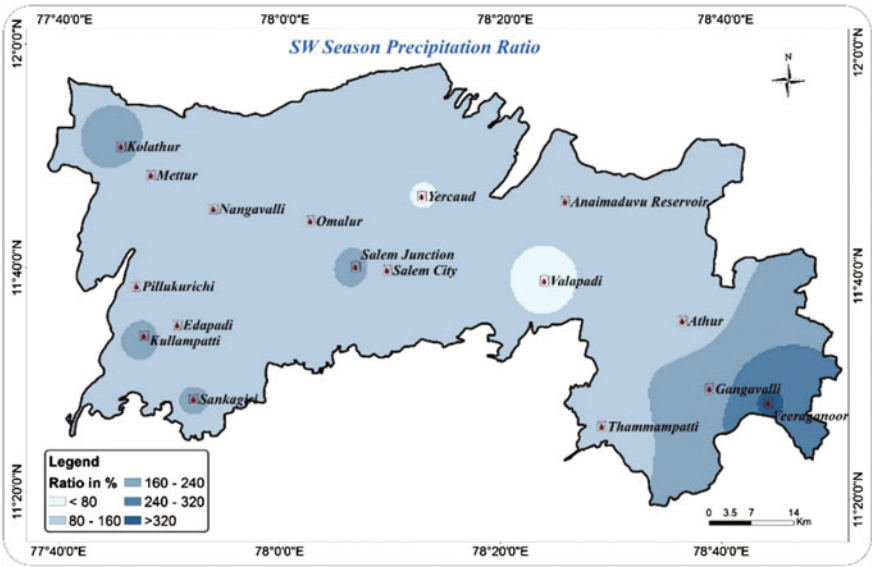

Fig. 11 Spatial distribution map of annual SW season precipitation ratio

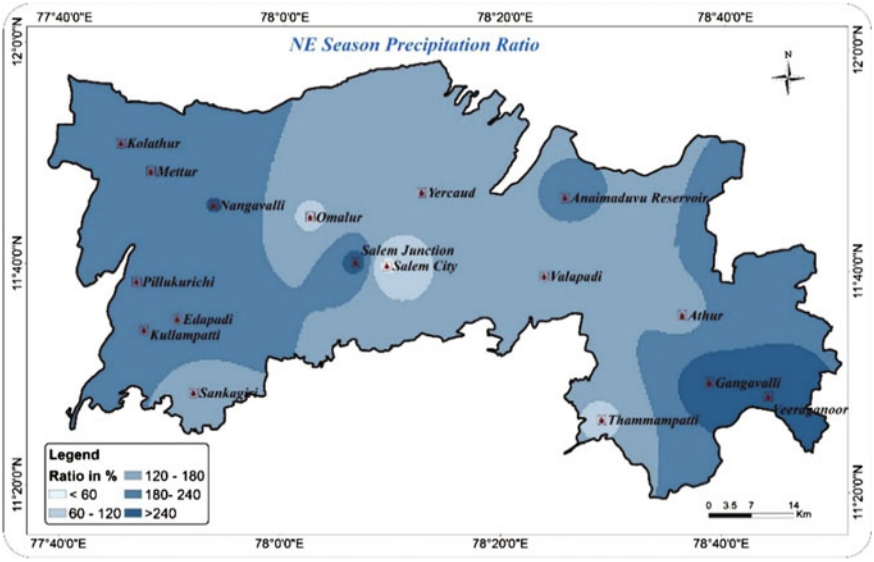

Fig. 12 Spatial distribution map of annual NE season precipitation ratio

PR covered an area of 131 km^2 and occurred in Omalur, Thammampatti and surrounding parts of Salem city stations. Moderate (120–180) PR covered an area of 2515 km^2 and occurred in Yercaud, Valapadi, Athur and Sankagiri stations. High

(180–240) PR located in Kolathur, Mettur, Nangavalli, Pillukurichi, Edapadi, Kullampatti and Anaimaduvu reservoir stations, which covered an area of 2281 km^2. The very high (>240) PR regions were Veeraganoor and Gangavalli station, and it covered an area of 296 km^2.

5 Conclusion

The analysis of the rainfall data has shown that the average rainfall ranges vary from 329 to 1492 mm. It is clearly evidenced that the high-altitude area like Yercaud station has received more rainfall than plain regions. In general, the rainfall was found to be relatively higher in the hilly regions and lower in the plain regions. The average annual rainfall was relatively more in N and NE, and it gradually decreased in the eastern, western and southern parts. It was found that the southwest monsoon was considerably more active in northern, northeastern and northwestern part than other direction, whereas the northeast monsoon was more active in north and northeastern part. The relative percentage of rainfall during summer season was relatively more on northern, northeastern and eastern part, whereas during winter season it was relatively more on northern and eastern part. The southwest monsoon contributed more than the other season of rainfall. The precipitation ratio has less abnormality during southwest and northeast monsoon and high abnormality during summer and winter season. Based on mean annual precipitation ratio, eastern part of the study area had high abnormality, and central and western part of the study area had less abnormality. Finally, rainfall variation assessment depicts that the rainfall conditions in Salem District were normal and fluctuation depends on time and space. Therefore, the rainfall assessment study illustrates the climate changes because rainfall is the main parameter for climate change.

References

1. Ahmadi, A., Moridi, A., Lafdani, E.K., Kianpisheh, G.: Assessment of climate change impacts on rainfall using large scale climate variables and downscaling models–a case study. J. Earth Syst. Sci. 123 (2014)
2. Fistikoglu, O., Harmancioglu, N.B.: Integration of GIS with USLE in Assessment of Soil erosion. Water Resour. Manage. **16**, 447–467 (2002)
3. Hong, W.-C., Pai, P.-F.: Potential assessment of the support vector regression technique in rainfall forecasting. Water Resour. Manage. **21**, 495–513 (2007)
4. Jegankumar, R., Nagarathinam, S.R., Kannadasan, K.: Spatial distribution of rainfall in Salem and Namakkal Districts. Int. J. Geomat. Geosci. **2**(4) (2012)
5. Mahalingam, B.: Rainfall variability in space and time, a case of Mysore District, Karnataka, India. Curr. Trends Technol. Sci. **3**(3) (2014)
6. Remesan, R., Holman, I.P.: Effect of baseline meteorological data selection on hydrological modelling of climate change scenarios. J. Hydrol. **528**, 631–642 (2015)

7. Rico-Ramirez, M.A., Liguori, S., Schellart, A.N.A.: Quantifying radar-rainfall uncertainties in urban drainage flow modelling. J. Hydrol. **528**, 17–28 (2015)
8. Sen, Z., Habib, Z.: Spatial precipitation assessment with elevation by using point cumulative semivariogram technique. Water Resour. Manage. **14**, 311–325 (2000)
9. Suk, W., Steven, H., Marshall, J.B.J.: Assessment of satellite-based rainfall estimates in urban areas in different geographic and climatic regions. Nat. Hazards **56**, 733–747 (2011)
10. Thilagavathi, N., Subramani, T., Suresh, M., Ganapathy, C.: Rainfall variation and groundwater fluctuation in Salem Chalk Hills area, Tamil Nadu, India. Int. J. Appl. Innov. Eng. Manage. **3**(1) (2014)
11. Tye, M.R., Cooley, D.: A spatial model of examine rainfall extremes in Colorado's Front Range. J. Hydrol. **530**, 15–23 (2015)
12. Venkatesan, T., Krishnomoorthy, S.: A comparative assessment on ground water quality of rural and city locations of Salem District, Tamil Nadu, India. J. Chem. Pharm. Res. **6**(2) (2014)
13. Williams, C.J.R., Kniveton, D.R., Layberry, R.: Assessment of a climate model to reproduce rainfall variability and extremes over Southern Africa. Theoret. Appl. Climatol. **99**, 9–27 (2010)

Assessing Stormwater Harvesting Potential in Dehradun City Using Geospatial Technology

Shray Pathak, C.S.P. Ojha, Chris Zevenbergen and R.D. Garg

Abstract Assessment of surface runoff using Natural Resources Conservation Service-Curve Number (NRCS-CN) method is the most extensively globally adopted method. With the availability of geospatial techniques, the surface runoff can be estimated accurately. In this study, effort has been made to assess the applicability of NRCS-CN method by incorporating the geospatial tools on the study area. The land-use maps are generated by supervised classification, and soil map is prepared by applying this method. Land-use map and soil group map are integrated, and the CN values are assigned to form reclassified image from NRCS Standard tables. The runoff curve number (CN), thus assigned to different subareas, was utilized to estimate monthly runoff for the city of Dehradun. The paper also looks into the gap between runoff and precipitation for different months in a year, and this subsequently helps identifying the need for harnessing rainwater or surface runoff during these critical months. Considering the demand patterns along with runoff generated can be helpful in dimensioning storage tanks in available utilized patches in the city.

Keywords Rainfall · Surface runoff · LULC · NRCS curve number · GIS

S. Pathak (✉) · C.S.P. Ojha (✉) · R.D. Garg
Civil Engineering Department, Indian Institute of Technology, Roorkee, India
e-mail: shraypathak@gmail.com

C.S.P. Ojha
e-mail: cspojha@gmail.com

C. Zevenbergen
Water Engineering Department, UNESCO-IHE, Delft, Netherlands

V. Garg et al. (eds.), *Development of Water Resources in India*,
Water Science and Technology Library 75, DOI 10.1007/978-3-319-55125-8_4

1 Introduction

1.1 General

Urban areas are confronted with the urge to expand their water supply sources to deal with developing populace-driven demand and concern of supply from water catchments because of climate change and droughts [5, 8]. The long-term sustainability of current urban water systems is increasingly questioned due to high demand for limited natural water assets for all uses [10]. This impels the requirement of re-configuration of current urban water systems and development toward more sustainable arrangements by incorporating the allocation and management of water supply, wastewater resources, and stormwater [4]. To solve these challenges, decentralized water supply system is increasingly being promoted. Stormwater harvesting is also useful in reducing flooding, and it reduces pressure from water supply network during peak demand [1, 6].

As there is no separate water supply in most of the cities, stormwater is an important option for urban water source to reduce demand on freshwater assets [9]. Because of the shortcomings of the centralized water supply system, the stormwater harvesting proves to be the best alternative. These surface-based systems also provide other benefits such as pollutant removal and enhancing the livability [1, 14].

Collection, treatment, storage, and distribution of stormwater streams are the processes involved in stormwater harvesting and reuse. Therefore, the most crucial step is the optimal selection of a site for urban stormwater harvesting as there is a direct involvement of social, public, environmental impact, topography, political interference, technical aspects, and legislative issues which increases the difficulties in selecting the suitable sites. Initially, the choice for selecting the suitable sites for stormwater harvesting (SWH) depends upon the soil type, land-use characteristics, water, and runoff availability. Local data can be collected through in situ measurements that provide site-specific information at a certain point in time [13]. These measurements are generally representative for a small area. Urban areas are often highly dynamic and require high-resolution data [3]. An alternative approach is to collect data through the use of remote sensing measurements. RS is able to produce continuous time series of images on a large spatial scale covering the surface area of entire cities.

Geomatics techniques such as remote sensing and GIS are proven to be very useful for this purpose [7] as it enables to get various parameters in spatial format which is required for the study. Satellite images, DEM, and soil map are required for getting the complete knowledge of the study area and assist in finding out the parameters suitable for SWH sites. With the impact of climate change and the advantages discussed above, SWH plays an important role in achieving the sustainable water resources management.

Design capacity of reservoirs and potential sites for water harvesting can be suggested by knowing the water demand and runoff availability of a particular area.

With GIS techniques, spatial maps of LULC, soil, topography, runoff can be prepared. Thus, by applying various geomatics techniques, hydrological parameters can be computed and analyzed to cope for the increase in demand of water.

With the knowledge of LULC and soil texture of the study area, the runoff map can be prepared by the use of NRCS-CN method which helps the proposers to plan the location and design of water storage tanks to reduce the pressure on existing water supply.

2 Study Area

2.1 Geography of the Area

Dehradun is the district of national importance and also a capital city of state Uttarakhand. It is situated in northwest side of Uttarakhand and extends from Latitude 29° 58′ N to 31° 02′ 30″ N and Longitude 77° 34′ 45″ E to 78° 18′ 30″ E. It lies in Survey of India (SOI) Toposheets number 53E, 53F, 53G, 53J and 53K. Uttarkashi lies on north, Pauri Garhwal and Tehri Garhwal on east, Saharanpur (UP) on south, and Sirmour (HP) on west. Dehradun district is on an average altitude of 640 m above MSL and covers an area of approximately 3088 km^2. Six tehsils, namely Dehradun, Vikasnagar, Tiuni, Chakrata, Kalsi, and Rishikesh, are in the Dehradun district. The district comprises of 17 towns and 764 villages, and the administrative map is shown in Fig. 1.

2.2 Drainage

Dehradun is a district which is drained by two major rivers and their tributaries, i.e., Ganga and Yamuna. A ridge which starts from Mussoorie and passes through Dehradun separates the two basins. All the rivers on the east side of the district merge into River Ganga, and on the west side, all rivers merge into River Yamuna. River Ganga has two main tributaries, i.e., Suswa and Song, and it enters the district through River Chandrabhaga near Rishikesh. Eastern part of the district is drained by the River Suswa and its tributaries, i.e., Rispana Rao and Bindal Rao. Song River originates from district Tehri and joins with River Suswa on southeast of Doiwala.

Yamuna River originates from Yamnotri which falls in Uttarkashi district. It enters district at a point called Khat Bhondar which lies east of Deoban. Major portion of the water is received from Rupin and Supin which are the tributary of River Tons which splits Uttarakhand from Himachal Pradesh and also the main tributary of River Yamuna. River Yamuna divides the district roughly into two halves, hilly region in the north and Doon valley in the south.

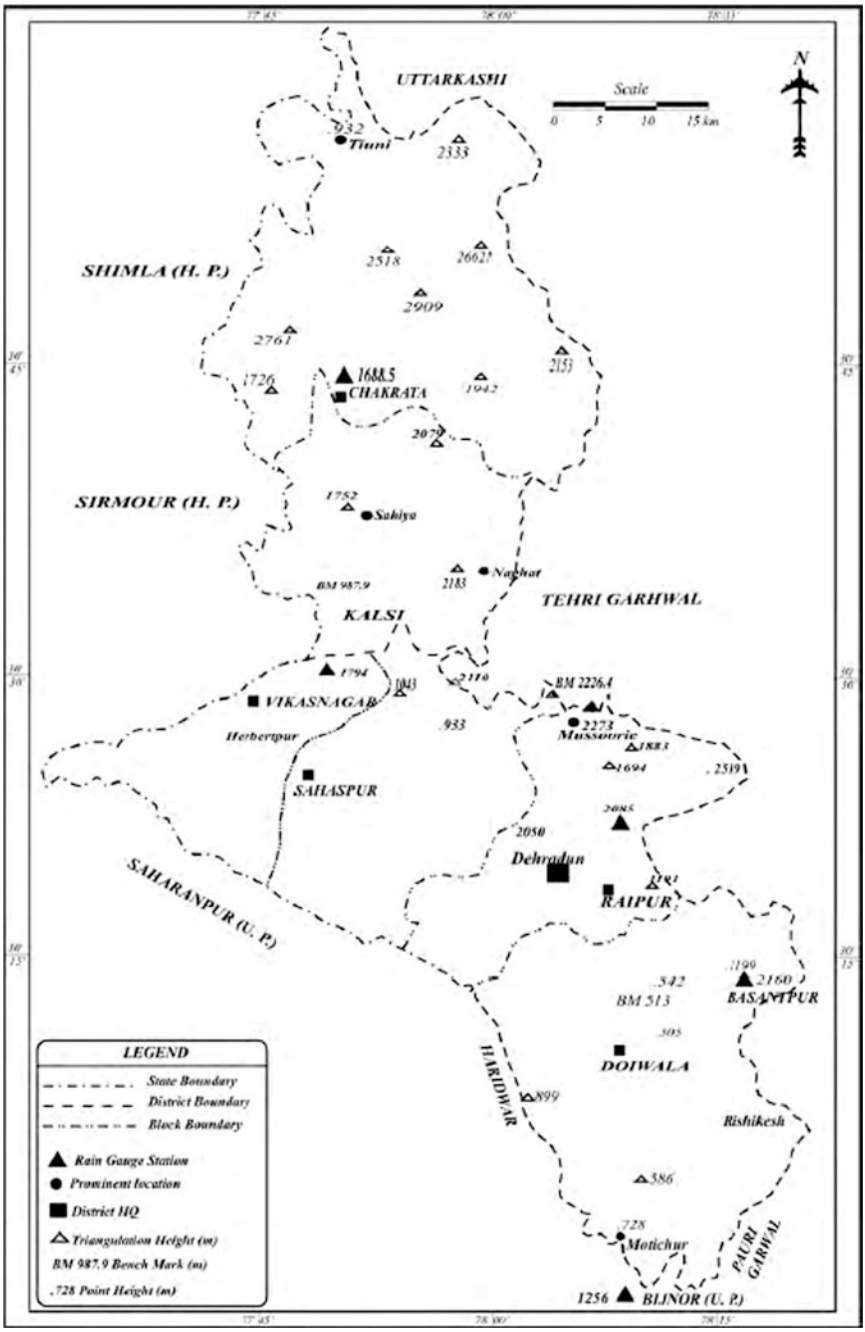

Fig. 1 Administrative map, district Dehradun (*Source* Ground Water Brochure, Dehradun, CGWB [2])

2.3 Climate and Rainfall

With the large variation in the topography of the district, it has climatic conditions of both Himalayas and plains. Temperature also has a very wide range, and the hottest month is May with the mean temperature rise of up to 42 °C for Dehradun and up to 36.2 °C for Mussoorie. During summers, the hilly regions are generally pleasant, but in the Doon valley the heat is often intense. During winters when the higher peaks are under snow, the temperature drops below freezing point not only for the higher altitudes but also for the plains like Doon. The district receives an average annual rainfall of 2051.4 mm. Most of the rainfall received is during the period from June to September, and July and August are the wettest months. The southern part of the district receives the least rainfall, and the region around Raipur receives the maximum amount of rainfall in the district.

2.4 Soil Types

The type and nature of soil plays a vital role in the estimation of surface runoff and groundwater recharge. Various factors such as climate, geology, physiography, and drainage of the area influence the type and nature of soil and soil cover. The soil type also depends upon the slope of the area and its erosion rate. The soil types of district Dehradun are referred from Central Ground Water Board (CGWB), Dehradun [2].

3 Methodology

3.1 Spatial Data Collection

All the criteria that account for the availability of water in the area (as follows) are analyzed in GIS environment, and spatial map is prepared.

(a) Land use
(b) Soil depth
(c) Soil texture
(d) Runoff coefficient

The work flowchart of methodology is shown in Fig. 2.

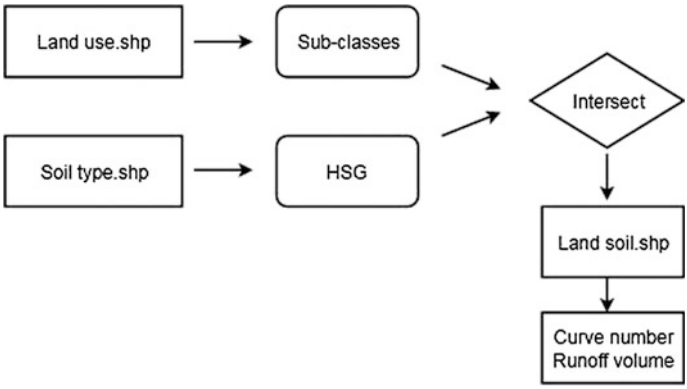

Fig. 2 Flowchart of methodology

3.1.1 Land-Use Map

Landsat 8 TM/ETM images of the grid having study area are taken as raw data from USGS. These data are available in the form of 11 different bands with a cell size of 30 m × 30 m. Four bands are stacked in ERDAS, and a new stacked image is generated. This image is now classified using supervised classification in ERDAS in five different classes, i.e., forest, water, agricultural, wasteland, and built-up land. Classification of the area is based upon their similar response under different bands. Each class is then recognized with the help of ground truth and high-resolution satellite images.

3.1.2 Soil Depth and Soil Texture

Spatial data of soil are collected from National Bureau of Soil Survey and Land-Use Planning (NBSSLUP) at 1:250,000. The cell size of these data is 1200 m × 1200 m which is different from that of land-use data which have a cell size of 30 m × 30 m. So these data are resampled using "resample" tool in ArcGIS. The attribute table of the vector layer contains fields like soil depth, soil texture, percentage carbon content, drainage, slope, erosion, soil temperature, and mineralogy. The relevant features of soil depth and soil texture are converted into the raster image. The study area is extracted using the shape file of Dehradun district.

3.1.3 Runoff Coefficient

The runoff coefficient is computed with the help of LULC and the soil map of the area by applying Natural Resources Conservation Service (NRCS)-CN method [12].

$$P = I_a + F + Q \tag{1}$$

$$Q/\ P - I_a = F/S \tag{2}$$

$$I_a = \lambda S \tag{3}$$

In the above equation, P denotes total precipitation (mm), F is cumulative infiltration (mm), I_a is initial abstraction (mm), S denotes potential maximum retention (mm), Q is direct runoff (mm), and λ is the coefficient of initial abstraction (0.2).

The NRCS-CN equation derived from the above relations is stated below,

$$Q = (P - Ia)^2/(P - Ia + S) \tag{4}$$

Above equation is valid only for $P \geq Ia$ or else Q = 0. S can be derived from P-Q data by taking the constant value of I_a (0.25).

$$S = 25{,}400/CN - 254 \tag{5}$$

The value of curve number (CN) which is a dimensionless number ranging from 0 to 100 is obtained from a table which is based upon the type of land use/land cover, hydrological soil group (HSG) [11]. HSG is of four types as HSG A, HSG B, HSG C, HSG D based on the infiltration rate of soil which can be obtained only for bare soil after prolonged wetting. In this study, the curve number is determined by the following formula.

$$CN_w = \sum (CN_i * A_i)/A \tag{6}$$

In above equation, CN_w denotes weighted curve number, A_i represents the area associated with curve number CN_i, A denotes total area, and CN_i denotes the range of curve number from 1 to any number N.

Based on this technique, a table of runoff coefficient which takes into consideration the land-use type and soil type for Indian condition is referred from AMC-II [11]. Hydrological soil group is classified according to soil texture.

4 Results

With the use of above-mentioned methodology for the study area Dehradun, the following LULC and soil maps are prepared, and with the use of these maps, the NRCS-CN method is applied for computing runoff for the study area.

The land-use/land-cover map of the Dehradun is prepared by applying supervised classification and is shown in Fig. 3. It is evident from the map that the major portion of land is covered with forest and agricultural land. The forest contributes

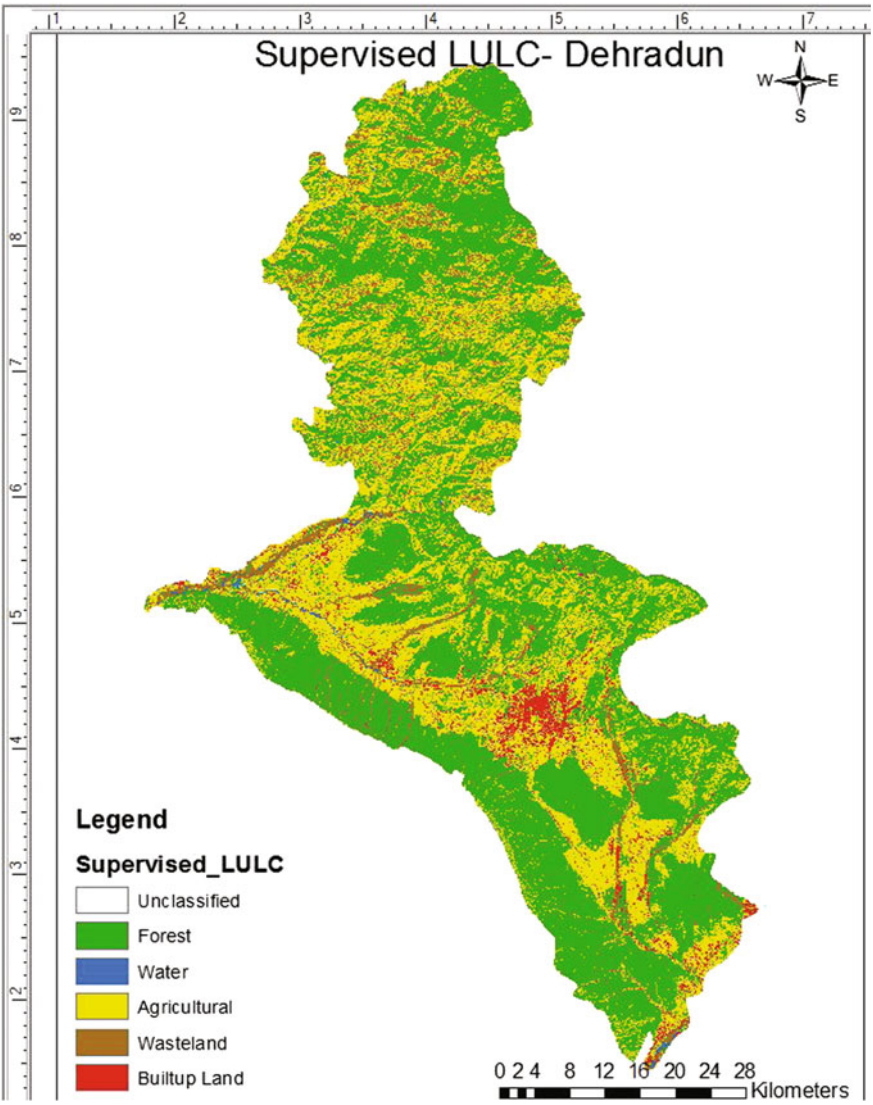

Fig. 3 LULC of Dehradun district

55%, agricultural 33%, wasteland 8.5%, built-up land 2.5%, and water body 0.5% of the Dehradun district. The land use infers the amount of water that will contribute as runoff.

The soil map is clipped for the Dehradun district, and then, the vector file is converted into raster format by selecting taxonomy from the attribute table. The soil type has a major contribution in determining the infiltration rate of water. The soil-type distribution for the Dehradun city is shown in Fig. 4. It is evident from the

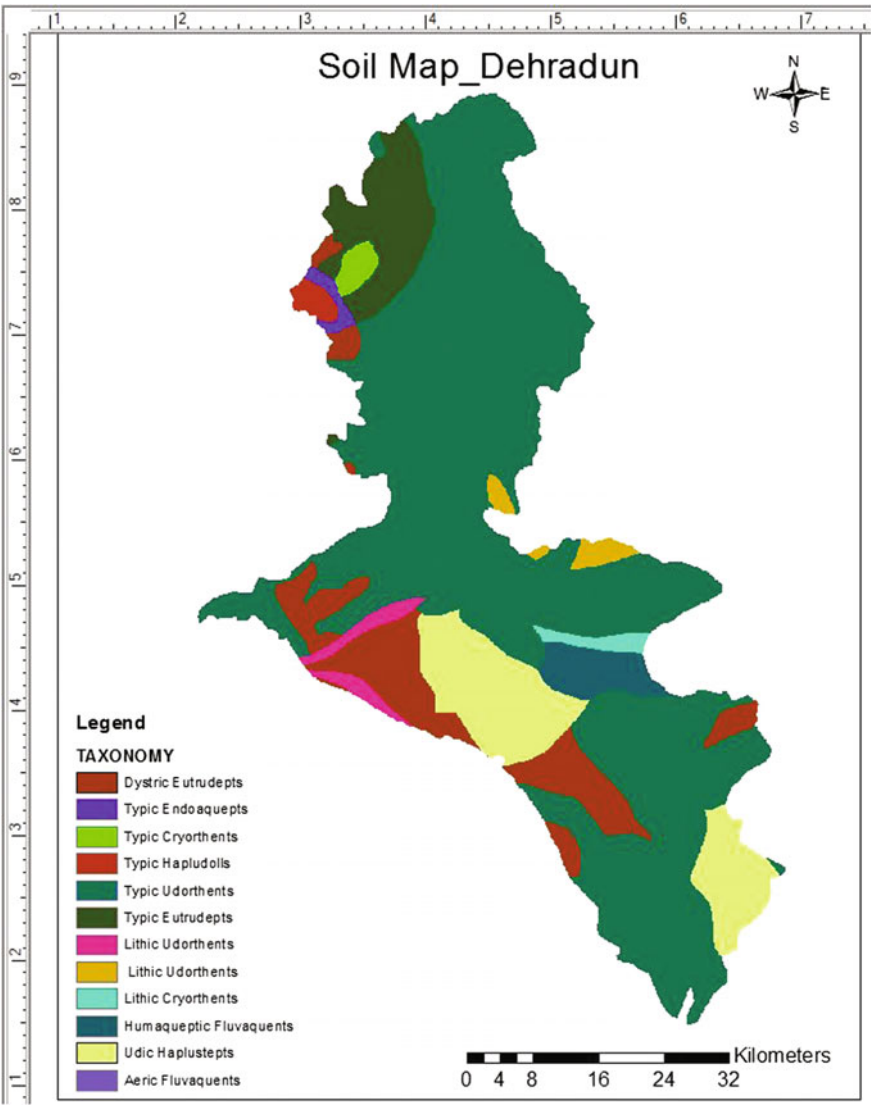

Fig. 4 Soil map of Dehradun district

map that the soil type, Typic Udorthents, covers major portion of approximately 66% of the area.

After preparing the soil map, the soil and land use are then overlaid to create polygons. A lookup table to contain SCS CN for all land use and soil group is also created. A reclassified image is prepared by integrating the LULC and soil type for the study and is shown in Fig. 5.

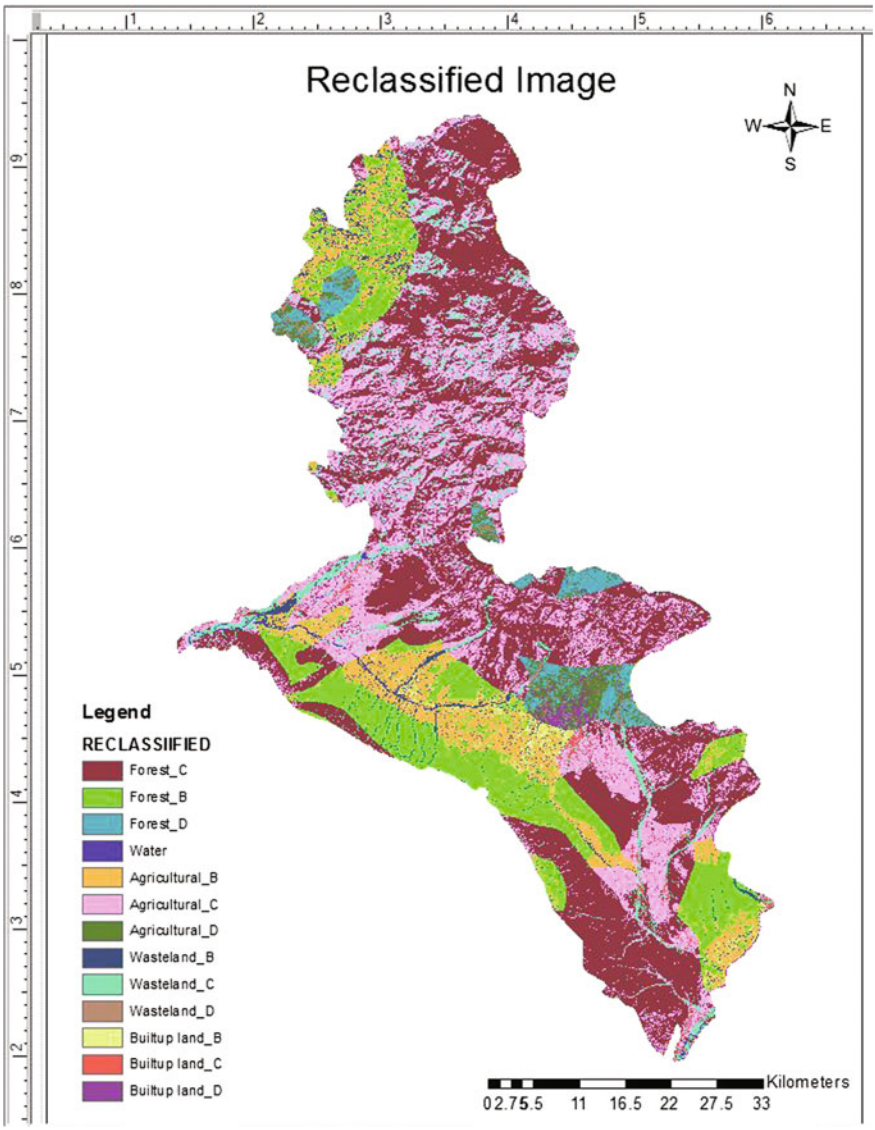

Fig. 5 Integrated LULC and soil map of Dehradun district

The appropriate NRCS-CN values for each reclassified land use were assigned according to soil group in Table 2, for the study area as shown in Fig. 6.

Thus, the low value of CN represents less stormwater runoff, and high value of CN represents more stormwater runoff. So the areas where the CN is higher indicate the potential zones for providing the storage tanks for the reuse of runoff water for various aspects.

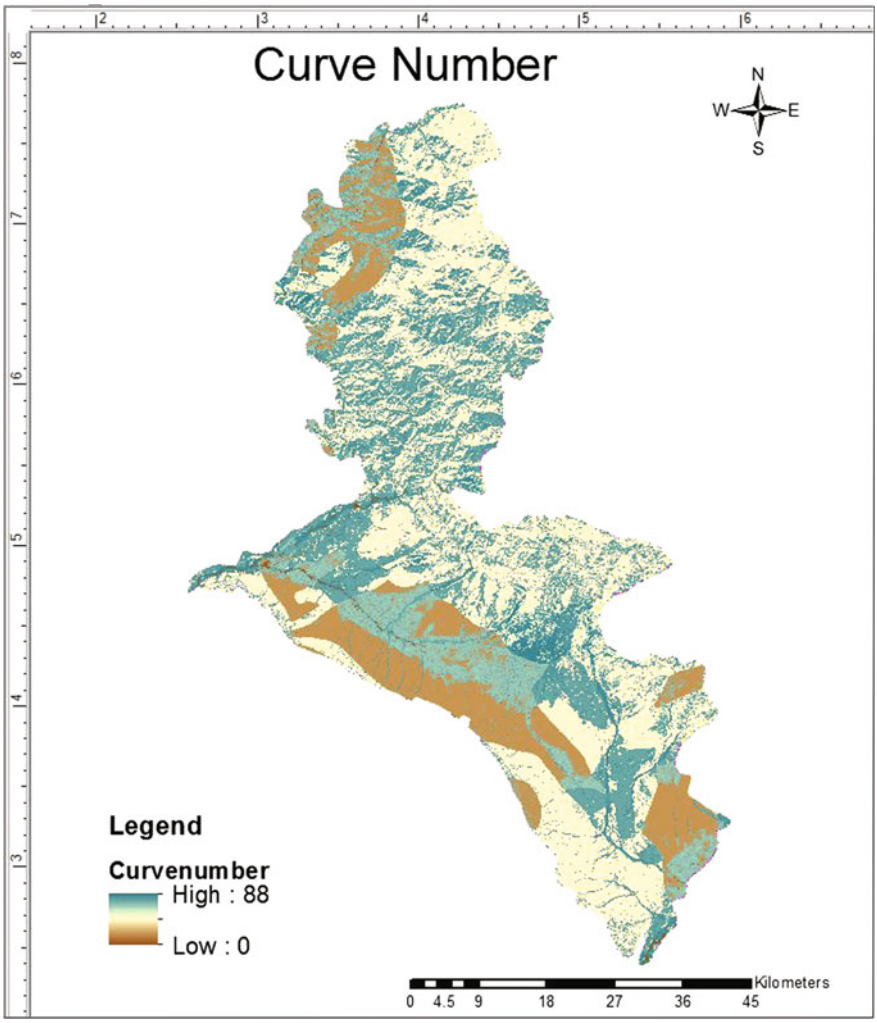

Fig. 6 Curve number map of Dehradun district

The data for the study area as shown in Table 1 represent the area of different combinations of land use and soil type and also the CN value assigned to groups for computing the weighted CN value.

By calculating the CN-weighted value, the maximum potential retention (S) is computed. With the knowledge of monthly rainfall data for 25 years, monthly runoff (mm) is computed for the study area and is shown in Table 2. If runoff is multiplied by the known area of the agricultural or built-up land, it will give the exact figure of runoff volume for which the storage tank can be designed/proposed for that area.

Table 1 NRCS-CN of Dehradun district

Type	Group	CN value	Area (km^2)	CN-weighted
Forest	B	40	430.15	17205.98
Forest	C	58	1186.56	68820.65
Forest	D	61	80.38	4903.06
Agricultural	B	74	270.43	20012.10
Agricultural	C	80	688.15	55051.99
Agricultural	D	82	57.69	4731.02
Wasteland	B	80	67.01	5360.54
Wasteland	C	85	181.03	15387.36
Wasteland	D	88	15.53	1367.07
Built-up land	B	75	29.57	2217.44
Built-up land	C	83	31.98	2654.31
Built-up land	D	87	15.19	1321.55
Total			3053.67	199033.10

Table 2 Monthly runoff of Dehradun district

Month	Rainfall (mm)	Runoff (mm)
January	46.90	2.51
February	54.90	4.71
March	52.40	3.96
April	21.20	0.27
May	54.20	4.49
June	230.20	121.72
July	630.70	492.77
August	627.40	489.58
September	261.40	148.33
October	320	0.17
November	10.90	2.21
December	29.20	0.03
Annual	2051.40	1897.09

With the installation of storage tanks, there will be less dependency on urban water supply which is a better sustainable approach. By considering only the population water demand per month for the district, it comes out to be 7650×10^6 l of demand per month and 10780×10^6 l of surface runoff volume per month is generated for the Dehradun district. If one looks at Table 2, maximum precipitation is confined to months of June, July, August, and September. Thus, if the runoff during these months is harvested, it can lead to reduced pressures on water supply.

5 Conclusion

A methodology for predicting runoff based on integrated GIS and remote sensing technique is successfully applied on the Dehradun district. The NRCS-CN method is a universally adopted method to generate the surface runoff volume from the available rainfall data. The key factor of applying geomatics techniques for computing surface runoff is that more precise spatial information and features of the catchment can be obtained. Moreover, the computations could be achieved quickly particularly in the case of complex mix of diverse soil types and land-use classes. NRCS-CN approach based on geospatial techniques is used to calculate the weighted curve number for Dehradun district. It may be concluded that based on the findings of this study, rainfall, land use/land cover, soil condition, and type data obtained with integrated RS provide sufficient detailed information for the computation of surface runoff. By considering only the population water demand per month for the district, it comes out to be 7650×10^6 l of demand per month, and 10780×10^6 l of surface runoff volume per month is generated for the Dehradun district. The figures clearly indicate that the urban water demand can be met to a large extent on the surface runoff in Dehradun district.

References

1. Ashley, R.M., Nowell, R., Gersonius, B., Walker, L.: Surface water management and urban green infrastructure: a review of potential benefits and UK and international practices (2011). http://fwr.org. Accessed Dec 2012
2. Central Ground Water Board (CGWB), Dehradun. http://www.cgwb.gov.in/. Accessed Aug 2016
3. Ebrahimian, M., See, L.F., Ismail, M.H., Malek, I.A.: Application of natural resources conservation service–curve number method for runoff estimation with GIS in the Kardeh watershed, Iran. Eur. J. Sci. Res. **34**(4), 575–590 (2009)
4. Fletcher, T.D., Andrieu, H., Hamel, P.: Understanding, management and modelling of urban hydrology and its consequences for receiving waters: a state of the art. Adv. Water Resour. **51**, 261–279 (2013)
5. Goonrey, C.M., Lechte, P., Perera, B., Maheepala, S., Mitchell, V.: Examining the technical feasibility of using stormwater as an alternative supply source within an existing urban area-a case study. Aust. J. Water Resour. **11**, 13 (2007)
6. Harremös, P.: Integrated urban drainage, status and perspectives. Water Sci. Technol. **45**(3), 1–10 (2002)
7. Kahinda, J.M., Jaighbenu, A., Sejamoholo, B., Lillie, E., Boroto, R.: A GIS based decision support system for rain water harvesting (RHADESSS). Phys. Chem. Earth **34**, 767–775 (2009)
8. Lloyd, S., Wong, T., Chesterfield, C.: Opportunities and impediments to water sensitive urban design in Australia. In: Proceedings of the Second South Pacific Stormwater Conference, Auckland, New Zealand, pp. 302–309 (2001)
9. Maheepala, S., Blackmore, J., Diaper, C., Moglia, M., Sharma, A., Kenway, S.: Integrated Urban Water Management Planning Manual, pp. 1–165. Water Research Foundation, Denver, CO (2010)

10. McDonald, R.I., Weber, K., Padowski, J., Flörke, M., Schneider, C., Green, P.A., Gleeson, T., Eckman, S., Lehner, B., Balk, D., Boucher, T.: Water on an urban planet: urbanization and the reach of urban water infrastructure. Glob. Environ. Change **27**, 96–105 (2014)
11. Mishra, S.K., Jain, M.K., Pandey, R.P., Singh, V.P.: Catchment area-based evaluation of the AMC-dependent SCS-CN-based rainfall–runoff models. Hydrol. Process. **19**(14), 2701–2718 (2005)
12. Ojha, C.S.P., Bhunya, P., Berndtsson, R.: Engineering Hydrology, 1st edn, pp. 1–459. Oxford University Press, UK (2008)
13. Saptarshi, P.G., Raghavendra, R.K.: GIS-based evaluation of micro-watersheds to ascertain site suitability for water conservation structures. J. Indian Soc. Rem. Sens. **37**(4), 693–704 (2009)
14. USEPA: Case studies analyzing the economic benefits of low impact development and green infrastructure programs. U.S. Environmental Protection Agency (2013). https://www.epa.gov/green-infrastructure. Accessed Oct 2013

Derivation of Geomorphology-based IUH Using GIS-supported GIUH Model for the Barak River Basin

Shahneen Nazreen Ali and Briti Sundar Sil

Abstract The present study was carried out to generate the instantaneous unit hydrograph for estimation of peak discharge from the geomorphological resource characterization and a timing component, the velocity parameter, using geomorphological instantaneous unit hydrograph (GIUH) model for the ungauged Barak River Basin of north-east India. Application of channel and basin morphometry for determining peak discharge in the selected river basin establishes good relation with the unavailability of sufficient hydrological data for many rivers. To achieve this objective, morphometric analysis for the whole basin area has been performed in GIS environment using different spatial analyst tools and extensions with an aim to produce a predictive tool for short-term imminent flood forecasting. The peak discharge, time to peak, and base time calculated by this model is 0.105/h, 5.34 h, and 18.9 h, respectively. This might become successful application for flood forecasting and for management of the different ungauged watersheds of Barak River Basin.

Keywords IUH · GIUH · Horton's ratios and GIS

1 Introduction

Flooding is a natural disaster that endangers human lives and public health, impacts essential services, and can transport pathogens over large vicinity. It is basically impractical to put a stop to flooding, but it is likely to get out of the way and to calculate approximately the level of flows in the imminent time from existing and precedent rainfall data. An established alternative is to use hydrological methods to formulate such predictions. This study involves methods developed from existing research for ungauged watersheds in north-east region and evaluates the utility of the approach for instantaneous unit hydrograph computation which can be further

S.N. Ali (✉) · B.S. Sil
Civil Engineering Department, NIT Silchar, Silchar 788010, Assam, India
e-mail: shahneenali24@gmail.com

V. Garg et al. (eds.), *Development of Water Resources in India*,
Water Science and Technology Library 75, DOI 10.1007/978-3-319-55125-8_5

studied for the development of unit hydrographs of required duration. These methods are particularly useful because of effortless computations, and also sufficient observed values of flow rates and depths are not required for design and early warning.

Several empirical relations were introduced by the previous studies to provide a better understanding of the relationship between the conceptual geomorphology parameters and hydrology. The speculative model of geomorphological instantaneous unit hydrograph (GIUH) consists of Horton's morphometric parameters as an input for a river hydrograph determination [1]. This quantitative perceptive establishes a different element in the analysis of hydrological studies, especially for the river basins which are ungauged and turns out to be effective for the study of rainfall–runoff relationships for the selected study area. Geomorphological instantaneous unit hydrograph (GIUH) approach was employed for the derivation of the flood hydrograph for an ungauged catchment located in Rajasthan, India [2]. The GIUH was developed based on Clark and Nash model [3]. The Clark model parameters for GIUH approach were estimated using the mathematical model developed at the National Institute of Hydrology. The values for hydrological parameters for the selected study area were predicted by combining the empirical formulae based on measurable watershed parameters and are a function of Horton's order ratios [4]. Kirpich formula for estimating the dynamic parameter velocity in GIUH and applicability of the model was carried out by using a standard unit hydrograph executed earlier by different researchers [5]. The concept of GIUH is probability density function (pdf) of the instant required for an arbitrarily selected drop of excess rainfall to enter into the outlet of a theoretical basin.

1.1 Database and Drainage Network Development

The data set employed in this study for carrying out the desired objective is as follows:

(i) ***Geological Map***: DEM (digital elevation model) data were downloaded from the website http://gdex.cr.usgs.gov/ and was subsequently utilized for preparation of digital elevation model to extract the basin parameters using product NGA SRTM (finished) 3 arcsec (90-m spatial resolution) in GeoTiff format.

The delineated sub-basin area taking Badarpur Ghat (92.58° E, 24.87° N) as the main outlet lies in the states of Manipur, Mizoram, Assam, and Nagaland with an area of approximately 25039 km^2. It lies between east longitudes 92.34° E to 94.31° E and north latitudes 23.00° N to 25.66° N. The principal tributaries of Barak include the Jiri, the Chiri, the Madhura, and the Jatinga on the north bank, and the Sonai, the Katakhal, and the Dhaleswari on the south, flowing in a north–south and south–north orientation, respectively, and Longai, Sonai, Rukni, and Singla are the main tributaries of the valley (source: India WRIS). The tributaries are mainly rain fed and cause flood problems when precipitation occurs. It is liable to floods, mainly because it receives heavy rainfall within a short time and is very

active agents of erosion. The Barak flows in an east–west direction through the valley. The drainage system of the basin was confirmed based on drainage flow direction and a threshold area of 45.5 km^2. The stream network was defined based on the collective number of the upstream cells draining to each cell. Critical threshold in flow accumulation of 5000 is used for defining streams. However, to examine the most appropriate stream threshold as required by the GIS software, Melton number approach is employed [6]. Strahler stream order technique [7] was followed and is found out to be sixth ordered basin (Fig. 1).

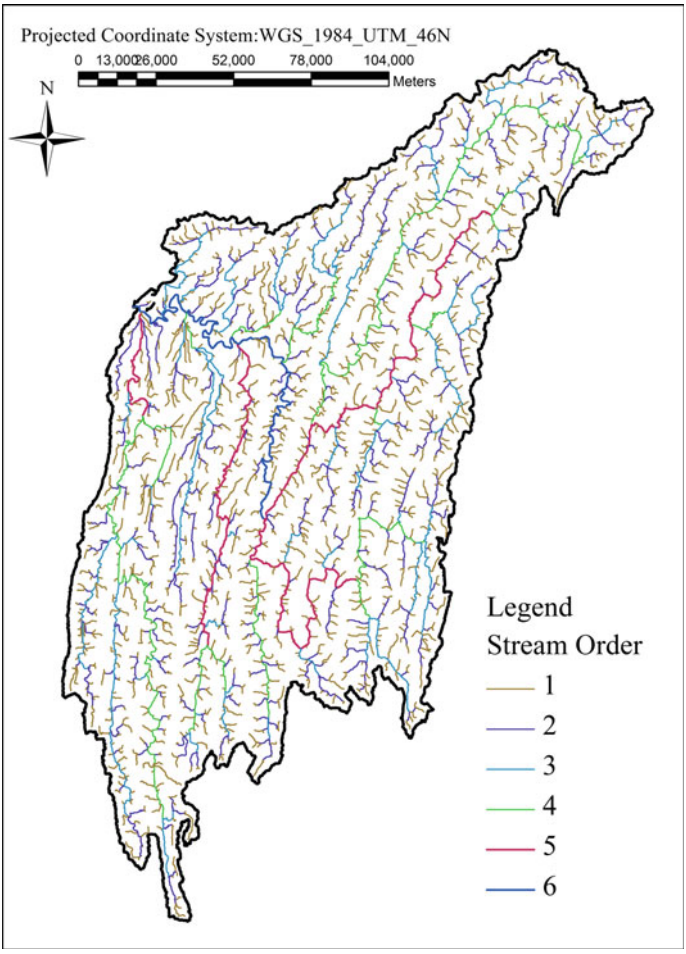

Fig. 1 Delineated basin area and its stream ordered map for the study area projected along WGS_1984_UTM_46 N

Table 1 Formulae for determining Hortons's ratios

Morphometric parameters	Formula	
Bifurcation ratio	$R_b = N_u/N_{u+1}$	N_u is number of streams, L_u is length of stream segments, and A_u is the area of the streams of given order
Stream length ratio	$R_L = L_u/L_{u-1}$	
Stream area ratio	$R_a = A_u/A_{u-1}$	

2 Methodology

2.1 Computation of Horton's Ratios

The Horton's ratios were determined using the formulae as presented in Table 1.

2.2 Derivation of IUH Using GIUH Model

The modus operandi for IUH derivation using GIUH model is as follows:

(i) Horton's ratio (bifurcation ratio, length ratio, and area ratio) was computed using GIS platform on the basis of drainage system ordered by Strahler order technique;

(ii) The dynamic velocity V corresponding to peak discharge for a given storm can be determined from the correlation between length and slope characteristic for a watershed as follows.

$$V = 0.8562L^{0.23}S^{0.385} \tag{1}$$

(iii) The time of concentration is obtained using the equation

$$t_c = 0.01947L^{0.77}S^{-0.0385} \tag{2}$$

$$t_c = 1/60(L/V) \tag{3}$$

(iv) The instantaneous unit hydrograph (IUH) was worked out using the assumption of a triangular instantaneous unit hydrograph, and the expressions for peak and time to peak of the GIUH suggested by GIUH—Rodriguez-Iturbe and Valdes (1979) are

$$q_p = 1.31R_L^{0.43}(V/L_\Omega) \tag{4}$$

$$t_p = 0.44(L_\Omega/V)(R_b/R_a)^{0.55}R_L^{-0.38} \tag{5}$$

The total duration of the IUH, i.e. base time t_b, is given by

$$t_b = 2/q_p \tag{6}$$

By multiplying, we obtain a non-dimensional expression, WR as:

$$WR = q_p t_p = 0.5764(R_b/R_a)^{0.55}R_L^{0.05} \tag{7}$$

This dimensionless term is invariable for every basin, which is independent of dynamic velocity and storm characteristics, but depends on the individuality of the respective basin and might be useful for assessment of basin homogeneity. It signifies that the IUH can be derived by means of single constraint (i.e. either q_p or t_p) where Ω = order of the basin; L_Ω = length of the highest order stream (km); q_p = peak flow (per hour); t_p = time to peak (h); t_c = time of concentration in min; t_b = base time in hours; R_b, R_L, and R_a = Horton's bifurcation ratio, length ratio, and area ratio, respectively; L = length of the mainstream to the outlet in metre (m); S = mean watershed slope (m/m); and V = peak velocity in m/s.

3 Results and Discussion

3.1 Geomorphic Resources Characterization

The basin parameters are extracted from the DEM and are presented in Table 2. The geomorphological characteristics of the catchment for various order of streams are presented in Table 3. Horton's ratios, namely bifurcation ratio (R_b) = 3.25, stream length ratio (R_L) = 1.86, and stream area ratio (R_a) = 3.56 for the whole basin, were determined (Fig. 2).

Table 2 Details of derived characteristics of the study area

Morphometric parameters	Values
Area A (km^2)	25039
Perimeter P (km)	1566.12
Max. elevation (km)	3011
Min. elevation (km)	19
Basin slope (%)	37.11

Table 3 Geomorphological characteristics of the catchment for various order of streams

Stream order (U)	Total no. of streams (N_u)	Total length of streams (L_u) (km)	Drainage area (A) (km^2)
1	1583	4072.16	15745
2	683	1903.13	19649
3	392	1165.21	21950
4	280	806.86	23635
5	170	496.26	24793
6	1	198.14	25059

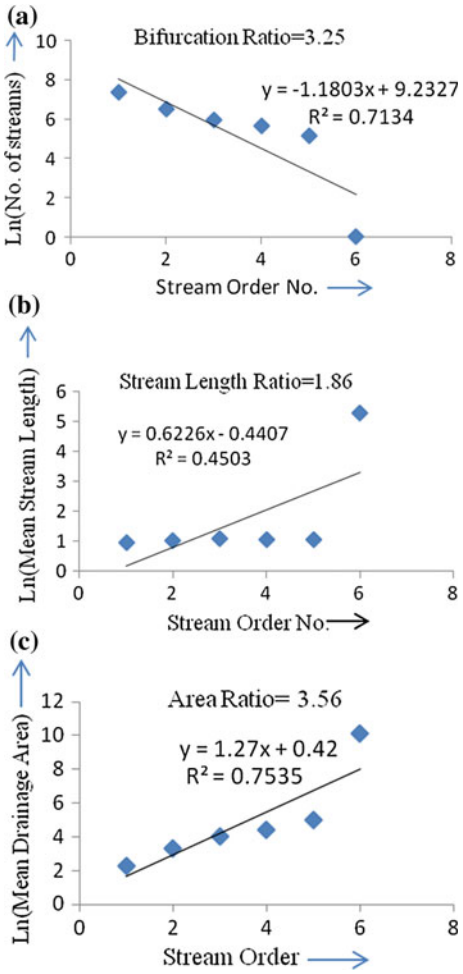

Fig. 2 *Line graph* showing the linear regression line between **a** *numbers of streams* and *stream order*, **b** *natural logarithm of mean stream length* and *stream order*, **c** *natural logarithm of mean drainage area* and *stream order*

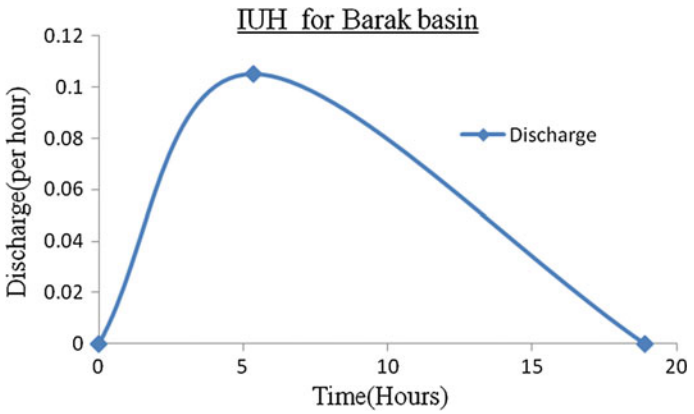

Fig. 3 Instantaneous unit hydrograph for the study area plotting graph between (*time in hours*) and (*discharge in per hours*)

3.2 *Derivation of IUH from Geomorphic Resources Characterization*

Determination of Horton's ratio: The peak velocity V for the basin for a given storm is 12.25 m/s, and the time of concentration was obtained 756.52 min. The peak (q_p), time to peak (t_p), and base time (t_b) of the GIUH were determined from the Eqs. (4)–(6) (Fig. 3).

$$q_p = 0.105/\text{h},\ t_p = 5.34\,\text{h},\ \ t_b = 19.9\,\text{h, and } WR = q_p t_p = 0.56$$

4 Conclusions

The subsequent conclusions can be attained from this study:

1. The IUH for an ungauged watersheds can be expected quite precisely through (GIUH) approach relating the dynamic velocity parameter with Horton's ratios derived from geomorphological characteristics, with no past rainfall–runoff data;
2. The complete shape of IUH of the watersheds can be attained from sufficient information and can be used for further study of required duration;
3. The fundamental constraint for employing these approach is the DEM of the basin with characteristic ordered stream network present; and
4. Evaluation of peak discharge by coupling geomorphology and Horton's ratios can be beneficial for development and supervision of watersheds of ungauged hilly regions of India.

References

1. Rodríguez-Iturbe, I., Valdez, J.B.: The geomorphologic structure of hydrology response. Water Resour. Res. **15**(6), 1409–1420 (1979)
2. Jain, S.K., Singh, R.D., Seth S.M: Design flood estimation using GIS supported GIUH approach. Water Resour. Manage. **14**, 369–376 (2000)
3. Bhabagrahi, S., Chatterjee, C., Raghuwanshi, N.S., Singh, R., Kumar, R.: Flood estimation by GIUH-based Clark and Nash models. J. Hydrol. Eng. ASCE. 515–525 (2000)
4. Horton, R.E.: Erosional development of streams and their drainage basins: hydrophysical approach to quantitative morphology. Bull. Geol. Soc. Am. **56**, 275–370 (1945)
5. Jotish, N. et al.: A geomorphological based rainfall-runoff model for ungauged watersheds. Int. J. Geomat. Geosci. **2**(2) (2011)
6. Melton, M.A.: Geometric properties of mature drainage systems and their representation in an E4 phase space. J. Geol. **66**, 35–54 (1958)
7. Strahler, A.N.: Quantitative analysis of watershed geomorphology. Trans. Am. Geophys. Union **38**, 913920 (1957)

Flow Analysis in a Meandering River Using HEC-RAS Model

Angana Borah and B.S. Sil

Abstract Flood flow studies contribute to a huge percentage of research in the field of water resource. Considering a few simplifications, an attempt has been made to create an accurate one-dimensional, unsteady, flow model for the Barak River defining upstream section at Fulertaal ghat and downstream section at Badarpur ghat of the Barak River. The flow model is analyzed with the aid of widely used modeling program, HEC-RAS. Based on the principle governing gradually varying flow, the flow model is derived from the Saint-Venant equations. The accuracy of the model depends upon the assumptions and limitations, accuracy of geometric data, flow data, boundary conditions, and numerical accuracy of the computation schemes. The study indicates that river flow can be routed through any intermediate cross section from the upstream location to downstream location for a discrete time step with the assistance of limited number of known parameters.

Keywords Unsteady flow · One dimensional · HEC-RAS · Barak River

1 Introduction

The general properties of flow in an open-channel flow condition, such as velocity and pressure gradient, varies in the longitudinal as well as normal direction and can be expected to have components in the three primary directions rendering complexity in the analysis of such three-dimensional problems. However, for the purpose of obtaining engineering solutions, a majority of open-channel flow problems are analyzed by one-dimensional analysis where only the mean or representative properties of a cross section are considered and their variations in the longitudinal directions are determined. This method, when properly used, not only simplifies the problem but also gives meaningful results. Flood routing is a technique of determining the flood hydrograph at a section of a river by utilizing the data of flood flow

A. Borah (✉) · B.S. Sil
NIT Silchar, Silchar 788010, Assam, India
e-mail: borah.angana@gmail.com

V. Garg et al. (eds.), *Development of Water Resources in India*,
Water Science and Technology Library 75, DOI 10.1007/978-3-319-55125-8_6

at one or more upstream sections. As a flood wave travels downstream, it undergoes two phenomenon, viz. peak attenuation and translation. Flood-routing techniques are utilized to estimate the stages, or rates of flow, in order to predict flood wave propagation along river reaches. Flood routing can be carried out in two distinct ways, lumped or hydrologic routing and distributed or hydraulic routing. Hydraulic routing can be further divided into diffusion wave routing and dynamic wave routing which involves the complete solution of Saint-Venant equations. The limitations of hydraulic modeling have been overcome due to the advancement of computer programs and computational schemes.

1.1 Study Area

The area selected for the current study purpose encompasses the Barak River from Fulertaal to Badarpur ghat. The whole Barak basin extends between a longitude of 89° 50′ E to 94° 0′ E and latitude of 22° 44′ N to 25° 58′ N. The major left-bank tributaries Sonai, Rukni, Katakhal, Dhaleswari, Singla, and Langai in Cachar Plain and the right bank tributaries include Labak, Madhura, Dalu, Jatinga, and Larang [1]. The basin has both subtropical and temperate climate. Rainfall occurring in the monsoon season contributes to approximately 65% of the annual rain, whereas the pre-monsoon season roughly over the period March through May accounts for 25% of the annual rain produced to different geophysical phenomena like depressions and convectional storms. There are instances of severe flooding recorded in the region (Fig. 1).

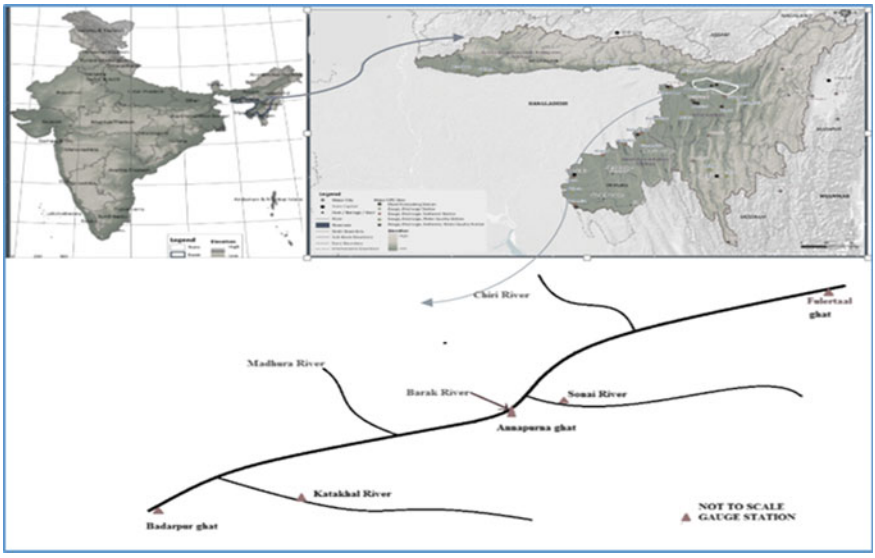

Fig. 1 Schematic representation of the study reach

2 Methodology and Model Application

In order to create a model that precisely represents the actual site conditions and is computationally efficient at the same time, robust planning is required. There are many assumptions taken into consideration while modeling the various processes that take place within the system with reference to the hydrogeological aspects of the model. In this study, the following are the assumptions of St. Venant Equations are applicable: (a) Flow is one-dimensional. (b) Inherent assumption of 1D finite difference river modeling is that flow velocities are perpendicular to the cross section. (c) Hydrostatic pressure prevails and vertical accelerations are negligible. (d) Streamline curvature is small. (e) Bottom slope of the channel is small. (f) Manning's and Chezy's equations are used to describe resistance effects. (g) The fluid is incompressible. (h) Channel boundaries are considered fixed and therefore not susceptible to erosion or deposition [2].

2.1 Methodology

The HEC-RAS model was created using standard water engineering concepts. In this study, HEC-RAS is used to estimate and understand flow occurrences throughout the river channel. Assistance has been taken HEC-RAS user manual (2010, 2015) in order to understand the theory behind computation procedure describing the solution of the equations used for each step of the results process [3]. The governing equations for unsteady flow analysis are given by the following nonlinear equations, Eqs. (1) and (2).

$$\frac{ds}{dt} = I_{(t)} - Q_{(t)} \tag{1}$$

where I_t and Q_t denote the flow rates at upstream and downstream for any instant of time (t), respectively; S is the channel storage; and $\frac{ds}{dt}$ is the change in storage during a time interval (Δt).

$$\frac{\partial Q}{\partial t} + \frac{\partial}{\partial x}\left(\frac{Q^2}{A}\right) + gA\frac{\partial h}{\partial x} + gAS_f = 0 \tag{2}$$

Here, h = elevation of the water surface measured above datum (i.e., stage).

A system of nonlinear algebraic equations can be obtained by applying the implicit finite difference scheme directly to the above mentioned equations. Finite difference approximation is a numerical method of calculation of partial differential equations. Newton–Raphson iteration technique is one of the means of solving nonlinear equations adopted by many scientists to obtain solution. The working of HEC-RAS is based on the Preissmann scheme which uses a four-point weighted

method (also known as box scheme). In subcritical flow, one boundary condition is required at the upstream end and another at the downstream end. However, in supercritical flows, both the boundary conditions are applied at the upstream end.

2.2 Model Application

For a given set of operation policies, an unsteady flow (one-dimensional) simulation model can be used to simulate the flow rates, water surface elevations, and velocities at various locations throughout a river–reservoir system for specified time steps. In this study, an attempt is being made to analyze the river/flood flow simulation in Barak River in the reach between Fulertal and Badarpur ghat with the help of hydraulic modeling software, HEC-RAS that allows one to perform one-dimensional steady and unsteady flow river hydraulics calculation.

Geometric Data Input to the Model

In order to generate the required geometric data, assistance has been taken from HEC-geoRAS which is GIS tool for support of HEC-RAS using ArcGIS in the development of the model. Figure 2 represents the modeled reach of the Barak River from Fulertaal to Badarpur Ghat as imported in HEC-RAS. Here, the geometric properties to be input into HEC-RAS, such as cross-sectional elevation along the reach, river lengths in-between the cross sections from upstream to downstream, channel profile slope, have been extracted. It is to be noted here that data obtained from the topographic survey was that for low flow period, the underwater topo has been ignored and the cross-sectional elevation data of the river bed profile has been approximated. As such, this report is not meant to validate any results. The whole reach has been further divided into two segments: (i) from Fulertaal to Annapurna Ghat and (ii) from Annapurna to Badarpur Ghat, and analyzed separately.

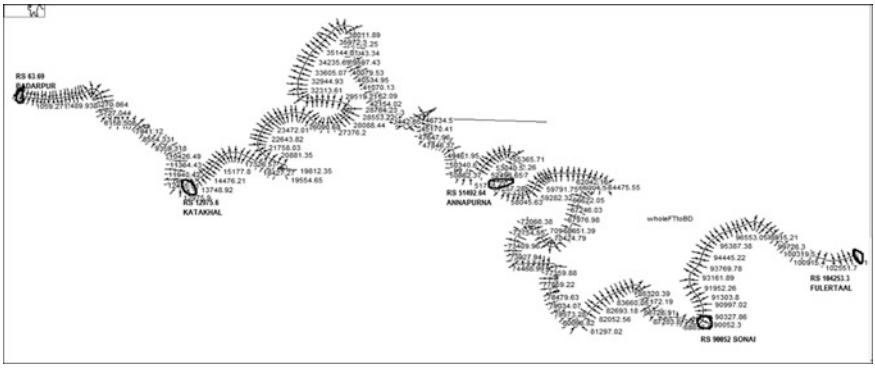

Fig. 2 Cross sections as depicted in a geo-referenced HEC-RAS model

Table 1 Factors considered in the selection of Manning's n

Material	n_0	Degree of irregularity	n_1	Variation of cross section	n_2
Earth	0.020	Smooth	0.000	Gradual	0.000
Rock	0.025	Minor	0.005	Alt. occasionally	0.005
Fine gravel	0.024	Moderate	0.010	Alt. frequently	0.010–0.015
Coarse gravel	0.028	Severe	0.020		
Channel obstructions	n_3	Vegetation	n_4	Degree of meandering	m_5
Negligible	0.000	Low	0.005–0.010	None	1.000
Minor	0.010–0.015	Medium	0.010–0.025	Minor	1.000
Appreciable	0.020–0.030	High	0.025–0.050	Appreciable	1.150
Severe	0.040–0.060	Very high	0.050–0.100	Severe	1.300

Flow Data Input to the Model

Flow data input in necessary for unsteady flow simulation at the boundary conditions in the form of discharge and stage for a particular time period. The lateral inflow hydrograph, on the other hand, acts as an internal boundary condition. In order to delimit flood plains only, steady flow simulation with your peak discharge is sufficient, whereas to estimate flood travel time, flood wave attenuation and so on, it is required to carry out an unsteady flow simulation with a hydrograph. The temporal extent of the study was selected as January 1, 2003–December 31, 2003, due to lack of availability of reliable data of a recent time.

Calibration of Model

In the selected study reach, there is a limited influence of the resistance of hydraulic structures, so Manning's n has been used as principle calibration parameter. From the equation given by Cowan in 1956, Manning's "n" has been taken as the basis for calibration of roughness coefficient (Chow, 1959) as:

$$n = (n_0 + n_1 + n_2 + n_3 + n_4) \times m_5 \tag{3}$$

where the values of n_0, n_1, n_2, n_3, n_4 and m_5 are taken from the values listed in Table 1, and m_5 is the correction factor to account for meandering of the channel.

2.3 Performance Evaluation Criteria

Table 2 illustrates the statistical performance evaluation criteria used to determine the efficacy of the present model.

Table 2 Statistical performance evaluation criteria

Sl. no.	Terminology	Formula
1	Nash Sutcliffe coefficient of efficiency (CE)	$CE = 1 - \frac{\sum_{t=1}^{T}\left((O)_o^t - (O)_m^t\right)^2}{\sum_{t=1}^{T}\left((O)_o^t - (\overline{O})_o\right)^2}$
2	Coefficient of correlation (Corr.)	$\text{Corr.} = \frac{N\sum_{t=1}^{T}\left(O_0^t O_m^t\right) - \sum_{t=1}^{T}(O)_0^t \sum_{t=1}^{T}(O)_m^t}{\sqrt{\left(N\sum_{t=1}^{T}\left((O)_0^t\right)^2 - \left(\sum_{t=1}^{T}(O)_0^t\right)^2\right)\left(N\sum_{t=1}^{T}\left((O)_m^t\right)^2 - \left(\sum_{t=1}^{T}(O)_m^t\right)^2\right)}}$
3	Sum of squared error (SSE)	$SSE = \sum_{t=1}^{N}\left((O)_o^t - (O)_m^t\right)^2$

O_0^t = observed value at time "t"; $(O)_m^t$ = modeled value at time "*t*"; N = total number of pairs of hydrograph ordinates data; $(\overline{O})_o$ = mean of observed outflow.

Table 3 Comparison of stage hydrograph for the reach Fulertaal to Annapurna ghat

At Fulertaal ghat			
Manning's n	CE	Corr.	SSE
0.07	0.91118	0.96823	0.76980
0.08	0.90646	0.96399	0.81072
0.09	0.88209	0.96024	1.02199

Table 4 Comparison of stage hydrograph for the reach Annapurna ghat to Badarpur ghat

At Annapurna ghat			
Manning's n	CE	Corr.	SSE
0.07	0.82279	0.99552	1.86273
0.08	0.86002	0.99646	1.47137
0.09	0.87581	0.99636	1.30535

3 Results and Conclusion

However, by the equation forwarded by Cowan in 1956 (Chow 1959), the Manning's n was calculated as 0.07. Hence, starting with this value as the base of the calibration model, numerous simulations were run for different values of n. Results obtained from considering the value of "n" as 0.07, 0.08, and 0.09 has been shown in tabular form listed below. The model gives best fit value of Manning's n at 0.08 when flow is simulated for the entire reach from Fulertaal to Badarpur ghat which is an average of the best fit value for both the reaches. Using this approximation of Manning's n as 0.08, hydraulic routing is carried out for the three reaches separately and its performance evaluation conducted (Tables 3, 4, and 5).

The results have been shown as hydrograph listed below showing comparison of flow hydrographs in Figs. 3, 4, and 5. And, the performance of the model is illustrated with the help of performance evaluation criteria mentioned above in

Table 5 Comparison of stage hydrograph for the reach Fulertaal ghat to Badarpur ghat

At Fulertaal ghat			
Manning's n	CE	Corr.	SSE
0.07	0.82582	0.94515	1.50964
0.08	0.85296	0.94182	1.27441
0.09	0.84093	0.93911	1.37872

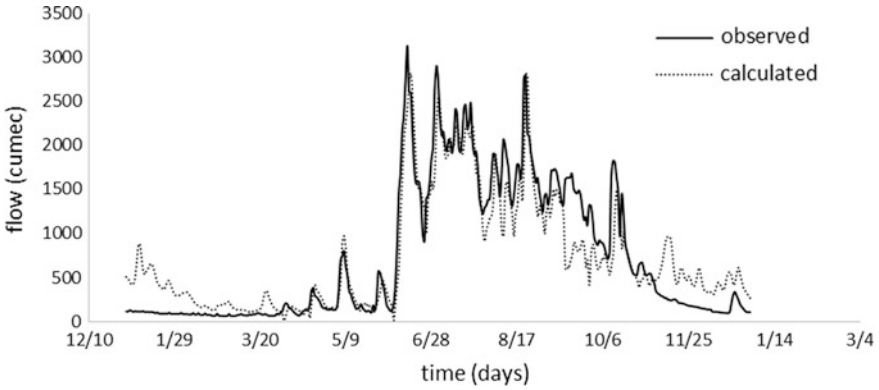

Fig. 3 Comparison of simulated and observed flow hydrograph at Annapurna ghat for the reach, Fulertaal ghat to Annapurna ghat

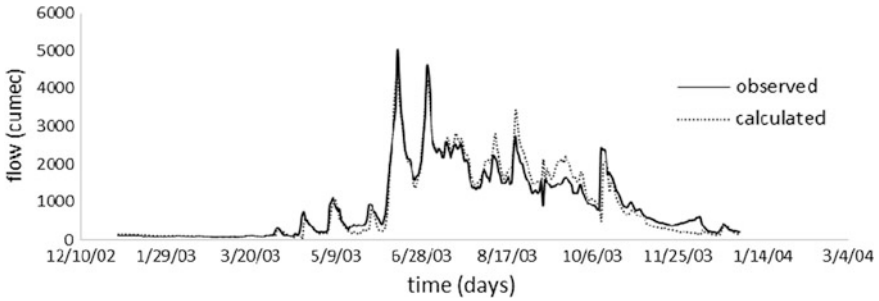

Fig. 4 Comparison of simulated and observed flow hydrograph at Badarpur ghat for the reach, Annapurna ghat to Badarpur ghat

Table 6 for Manning's n 0.08. Verification results disclose an encouraging coefficient of efficiency as 0.886137 with the observed data. It was observed from the stage and flood hydrographs depicted in the results section that stage as well as flow is comparable to the observed series for higher magnitude events while some amount of discrepancy is noticed for the events of lower magnitude. So the results obtained for the other locations within the reach can be said to be reliable [3].

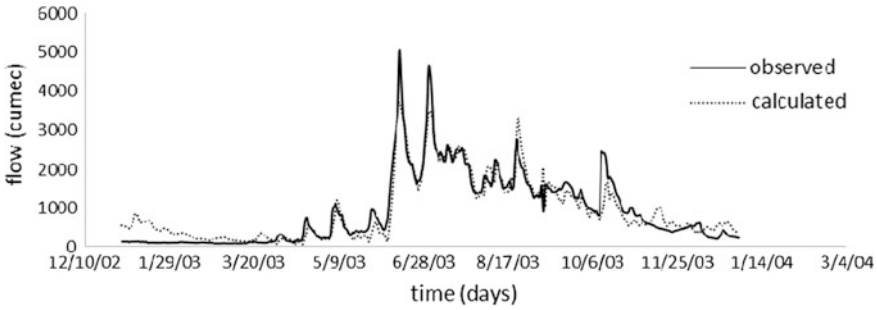

Fig. 5 Comparison of simulated and observed flow hydrograph at Badarpur ghat for the reach, Fulertaal ghat to Badarpur ghat

Table 6 Model performance evaluation

	CE	Corr.	SSE
Comparison of flow hydrograph for the reach Fulertaal ghat to Annapurna ghat at *Annpurna ghat*	0.83602	0.91965	101246.15
Comparison of flow hydrograph for the reach Annapurna ghat to Badarpur ghat at *Badarpur ghat*	0.92416	0.96804	63384.10
Comparison of flow hydrograph for the reach Fulertaal to Badarpur ghat at *Badarpur ghat*	0.87895	0.93816	10117552
Comparison of flow hydrograph for the reach Fulertaal to Badarpur ghat at *Annapurna ghat*	0.84240	0.92485	9731093

3.1 Conclusion

The aim of this study is thus to explore a methodology for utilizing advanced flood-routing tools in data-sparse settings in the developing world. Hydraulic routing using Saint-Venant equations was performed for the reach between Fulertaal and Badarpur ghat with the support of HEC-RAS which is a software developed by the US Army Corps of Engineers. Keeping other hydraulic coefficients, such a coefficient of expansion and coefficient of contraction required in the nonlinear equations as constant, the parameter for calibration of the model as chosen as Manning's roughness "n". The performance of the models has been found satisfactory by conducting statistical evaluation of the computed values. The outcome of the present study can be stated as that flow hydrograph can be figured out for any intermediate location in the river reach and subsequently the peak flow can be anticipated from the simulated flow hydrographs at the intermediate cross sections of the river channel from minimum input data.

References

1. Choudhury, P.S., Ullah, N.: Downstream flow top width prediction in a river system. S. Afr. Water Res. Comm. Water SA **40**(3), 481–490 (2014)
2. Horrit, M.S., Bates, P.D.: Evaluation of 1D and 2D numerical models for predicting river flood inundation. J. Hydrol. **268**(1–4), 87–89 (2002)
3. U.S. Army Corps of Engineers: HEC-river analysis system user's manual, Version 4.1 (2010)
4. Parhi, P.K., et al.: Calibration of channel roughness for Mahanadi river, (India) using HEC-RAS model. J. Water Resour. Prot. **4**, 847–850 (2006)

Study of Hydrodynamic and Sediment Transport in Gulf of Khambhat, Western Coast India—A Numerical Approach

Rajan Kumar Jha, A.K. Singh, L.R. Ranganath and Ajai Singh

Abstract Coastal sedimentation is a problem that needs to be addressed, more so in areas where any infrastructure development is planned. The research carried out in this article aims to develop a depth-averaged model to represent the hydrodynamics and sediment transport patterns prevalent during non-monsoon and monsoon in the entire Gulf of Khambhat along west coast of India. In this study, the spatial resolution of model is 100 m $\times$ 100 m and the freshwater discharge in monsoon and non-monsoon from the rivers (Narmada, Mahi and Sabarmati) joining the gulf had been considered. The model results were found to be in good agreement with the observed current data and it was found that the gulf is ebb dominated with a short falling period and a longer rising period. The sediment transport pattern is predicted along with expected total suspended sedimentation for non-monsoon and monsoon. The sedimentation studies indicated that there is a trend of siltation.

Keywords Hydrodynamics · Sediment distribution · Numerical modelling · Gulf of Khambhat

R.K. Jha (✉)
Water Engineering & Management, Central University of Jharkhand, Ranchi 835205, Jharkhand, India
e-mail: rajan.jha@cuj.ac.in

A.K. Singh
ARO, Central Water & Power Research Station, Pune 411024, India

L.R. Ranganath
CRO, Central Water & Power Research Station, Pune 411024, India

A. Singh
CWEM, Central University of Jharkhand, Ranchi 835205, Jharkhand, India

V. Garg et al. (eds.), *Development of Water Resources in India*,
Water Science and Technology Library 75, DOI 10.1007/978-3-319-55125-8_7

1 Introduction

India is a country having coastal length of 7517 km. As a country with such a large coastline, India experienced various problems related to beach. The issue of shore erosion and accretion in India has received special attention from the government and the world because the effect has direct impact on social life, demolition of infrastructure, settlements along the bank, navigation, tourism and other coastal environment loss. Therefore, in order to develop coastal area with infrastructure we need to have a proper idea of the accretion/erosion in the selected area so that it should have a very less effect on it in the near future. Accretion problems generally occur at places where the sediment transporting capacity of the hydraulic system is reduced due to the minimal in steady (currents) and oscillatory (waves) velocities of flow and related turbulent motions. Problems related to sedimentation are mostly associated with human interference in the physical system such as the construction of the artificial structures or the dredging of sediment from the bed to increase the flow depth or width. However, accretion or erosion also is a basic phenomenon of nature dealing with loose sediments within the transferring cycle from source to drop locations. Natural sedimentation areas are known as shoals, flats, banks, sheets, bars, etc.

These studies were carried out at Central Water & Power Research Station (CWPRS), Pune, in (MMCE) laboratory to analyses the flow field and sedimentation pattern prevalent at the site.

2 Materials and Methods

Gulf of Khambhat lies in the northern part of the Arabian Sea as shown in Fig. 1. It is triangular shaped depression on the western part of India, between the Saurashtra peninsula and the Gujarat. The length of the proposed region is approximately 130 km, while its width varies between 20 km and 65 km. The gulf enclosed an area of about 3200 km^2 and a maximum depth of 35 m. The tidal currents in the gulf are very strong and multidirectional with two prevailing directions, i.e. on the way to upstream during peak flood and downstream during peak ebb. Due to the funnel shape of the gulf, the tide height increases vastly from the entrance to the upstream end [1]. The maximum current observed during tide is around 2.5 m/s in the entire gulf with high wave energy [2]. It receives drainage from Ambika, Purna, Kim, Tapti, Narmada, Mahi, Sabarmati and Dhadhar rivers. The large volume of suspended sediments and silts is carried by the discharge of these rivers. Narmada which is one of the major rivers of this region carries a large volume of suspended load from the eastern side of the gulf which forms Deltaic islands such as Alia Bet.

Fig. 1 Location map of study area (courtesy Google Earth)

2.1 Field Data Analysis

The data required for model studies such as bathymetry, tide, currents and sediment loads were collected and analysed. The data for bathymetry are obtained from C-MAP. Gulf has an open boundary at the seaward end connecting 72°1′ E to 72° 43′ E longitude and 21°8′ N to 22°18′ N latitude. The bathymetry used in the computational model is shown of area 130 × 65 km with grid spacing of 100 m as shown in Fig. 2. The tide level for non-monsoon (October) and monsoon (July) was extracted from C-MAP tidal database at the location of 72°30′ E and 21°42′ N, and it is found that the location has tidal range of 9.38 m as shown in Figs. 3 and 4. And the gulf is characterized by mixture of fine sand and clay. The average grain size diameter at the site of interest is recorded as between 0.05 mm and 0.15 mm. From the site investigations undertaken by CWPRS, it was found that the sediment in the

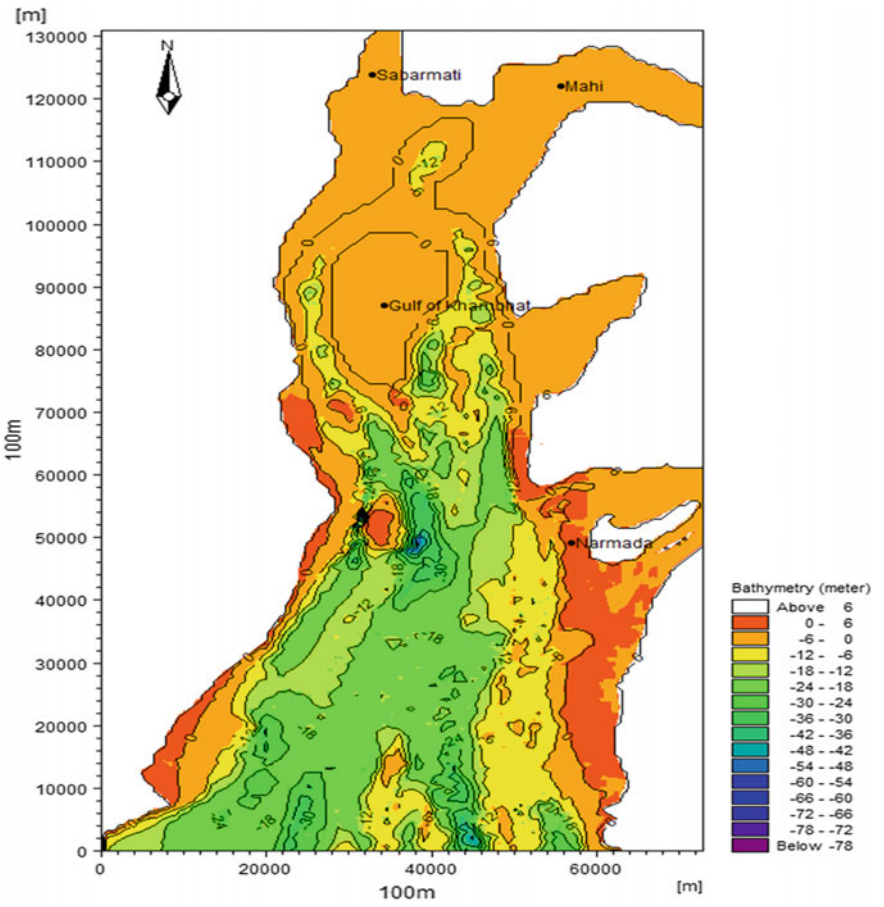

Fig. 2 Bathymetry-GoK (C-MAP)

gulf has a specific density of around 2.65 g/m^3 [3] and the average sediment concentration recorded in month of October is 50 mg/l near Narmada estuary and in month of July it is nearly 500 mg/l.

2.2 Model Description

The study was carried out using the MIKE-21 hydrodynamic (HD) and mud transport (MT) model. The hydrodynamic model in the MIKE21 flow model (MIKE HD) is a general numerical modelling system for the simulation of water

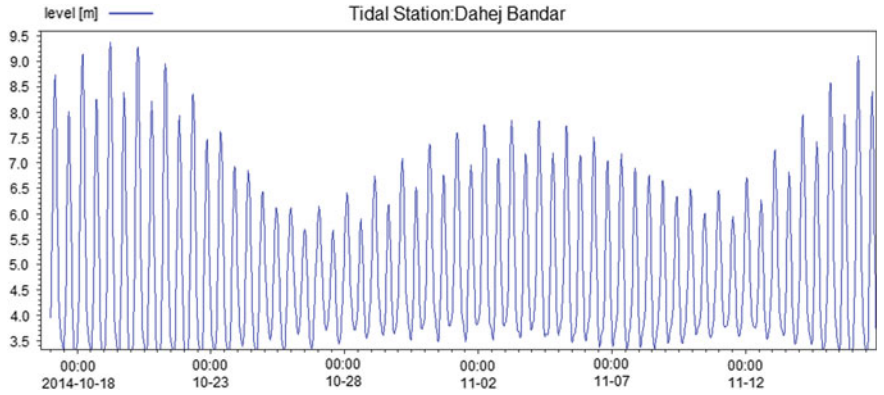

Fig. 3 Tide level in non-monsoon

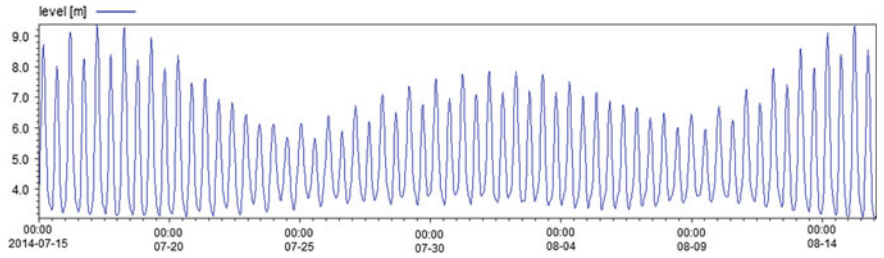

Fig. 4 Tide level in monsoon

levels and flows in estuaries, bays and coastal areas. It simulates unsteady two-dimensional flows in one layer fluids and has been applied in large number of studies. The appropriate governing equations for studying water movement in coastal areas are the two-dimensional shallow water equations. These are obtained by vertically integrating the three-dimensional Navier–Stokes equations of motion making the following simplified assumptions:

The flow is incompressible, the flow is well mixed (no variation in density) and vertical accelerations are negligible. Simulation of hydrodynamics is based on these shallow water equations given below,

$$\frac{\partial \zeta}{\partial t} + \frac{\partial p}{\partial x} + \frac{\partial q}{\partial y} = \frac{\partial d}{\partial t} \tag{1}$$

$$\frac{\partial p}{\partial t} + \frac{\partial}{\partial x}\left(\frac{p^2}{h}\right) + \frac{\partial}{\partial y}\left(\frac{pq}{h}\right) + gh\frac{\partial \zeta}{\partial x} + \frac{gp\sqrt{p^2+q^2}}{C^2h^2} - \frac{1}{\rho_w}\left[\frac{\partial}{\partial x}(h\tau_{xx}) + \frac{\partial}{\partial y}(h\tau_{xy})\right] - \Omega_q - fVV_x + \frac{h}{\rho_w}\frac{\partial}{\partial x}(p_a) = 0 \quad (2)$$

$$\frac{\partial q}{\partial t} + \frac{\partial}{\partial y}\left(\frac{q^2}{h}\right) + \frac{\partial}{\partial x}\left(\frac{pq}{h}\right) + gh\frac{\partial \zeta}{\partial y} + \frac{gq\sqrt{p^2+q^2}}{C^2h^2} - \frac{1}{\rho_w}\left[\frac{\partial}{\partial y}(h\tau_{yy}) + \frac{\partial}{\partial x}(h\tau_{xy})\right] + \Omega_p - fVV_y + \frac{h}{\rho_w}\frac{\partial}{\partial y}(p_a) = 0 \quad (3)$$

where
$h(x, y, t)$—water depth $(=\zeta - d,\ m)$; $d(x, y, t)$—time varying water depth (m); $\zeta(x, y, t)$—surface elevation (m); $p, q(x, y, t)$—flux densities in x and y direction $(m^3/s/m) = (uh, vh)$; (u, v) = depth-averaged velocities in x and y direction; $C(x, y)$—Chezy resistance $\left(m^{\frac{1}{2}}/s\right)$; g—acceleration due to gravity (m/s^2); $f(V)$—wind friction factor; $V, V_x, V_y(x, y, t)$—wind speed and components in x and y direction (m/s); $\Omega(x, y)$—Coriolis parameter, latitude dependent (s^{-1}); $p_a(x, y, t)$—atmospheric pressure $(kg/m/s^2)$; ρ_w—density of water (kg/m^3); t—time; and $\tau_{xx}\tau_{xy}\tau_{yy}$—components of effective shear stress.

The governing equations are solved using alternating directions implicit (ADI) finite difference technique based on Crank–Nicholson scheme. This entails covering the area with a mesh or grid and discretizing elevations and velocities in space and time to fit on this grid. Having discretized the variables, derivatives are approximated by simple differences divided by the distance between consecutive grid points. The space differences involve variables at the unknown time level calculated; thus, a system of equations involving the boundary conditions has to be solved before the value of the variables at the next tie step can be obtained by alternating direction implicit scheme. It implies that in one time step, there are two half time steps. In one half time step, the scheme is implicit in the east–west direction and explicit in north–south direction. In the next time step, computations are implicit in the model north–south direction and explicit in the model east–west directions. ADI scheme is computationally efficient and widely used. The solution of equation at every grid point results in simulation if flow conditions over a period of time.

The MIKE 21 flow model, mud transport (MT) module describes erosion, transport and deposition of mud or sand/mud mixtures under the action of currents and waves. The purpose of sediment transport modelling at this stage is to gain some understanding on the rate of bed level changes within the natural and man-made canals and water ways as a result of tidal flow.

3 Results and Discussion

3.1 Model Studies Conducted

Series of model experiments were conducted for the evaluation of hydrodynamic circulation and sediment distribution along gulf of Khambhat. Kumar and Kumar [4] studied hydrodynamics based on measurement of waves, currents and tides off Dahej in Gulf of Khambhat. It was concluded from the study that tide at 14 m was larger than that at 24 m water depth with an increase of 0.19 m in the mean tidal range. The maximum current speed was 3 m/s with average value of 1 m/s at 24 m water depth and 3.3 m/s with average value of 0.8 m/s at 14 m water depth. Also during peak flood, the concentrations of sediment were found to vary from 60 to 500 mg/l in the upper part and from 40 to 508 mg/l in the lower part of gulf. However, the sediment concentrations varied from 110 to 517 mg/l in the upper part and from 100 to 530 mg/l in the lower part during the ebb period [1]. The tidal amplitude in the gulf increases up to 10 m and the velocity up to 4 ms^{-1} [5].

3.2 Simulation of Flow Field for Non-monsoon

Initially the studies were conducted with non-monsoon in the Narmada, Mahi and Sabarmati estuaries and the adjoining sea portion of Gulf of Khambhat. From the computational model, it could be seen that there are four open boundaries where flow conditions are required to be defined. Initially the flow simulations were carried out by providing tide with tidal range of 9.4 m. The tidal boundaries were provided along the southern boundary with appropriate phase lag. It can be observed that the model results match well with the field data, and hence, there is good agreement indicating that the model is proved as shown in Fig. 5. The

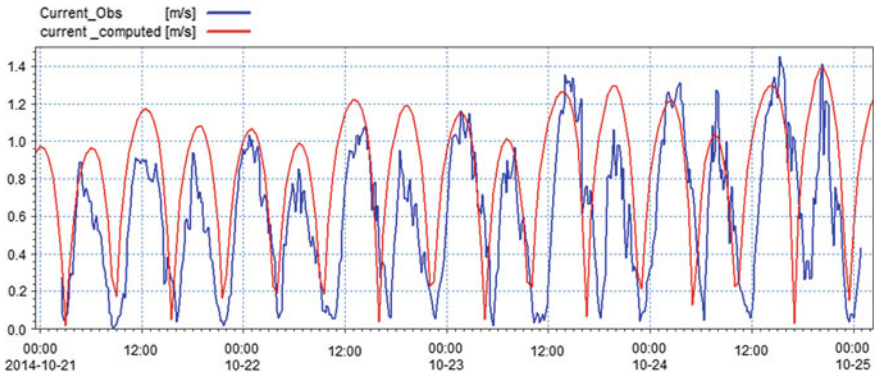

Fig. 5 Comparison of currents (computed vs. observed)

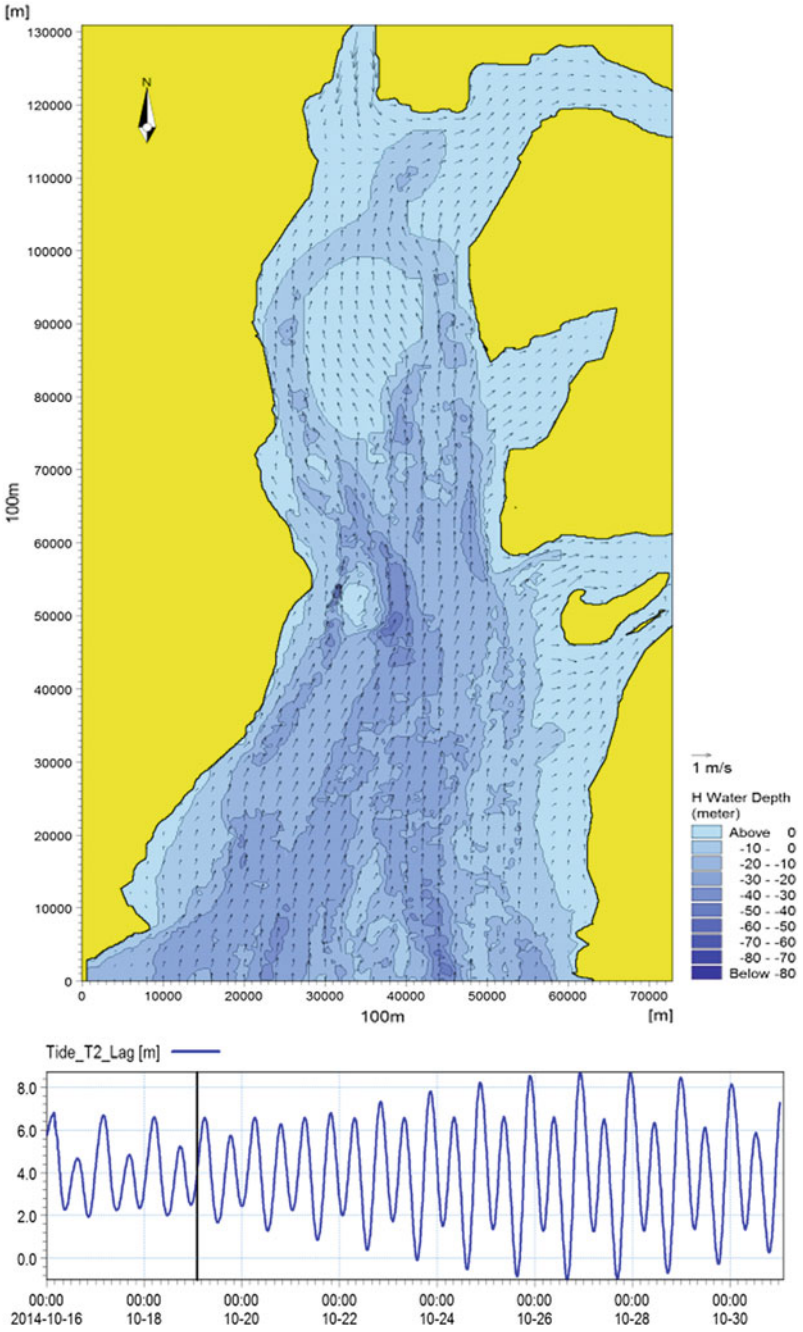

Fig. 6 Flow field during peak flood (non-monsoon)

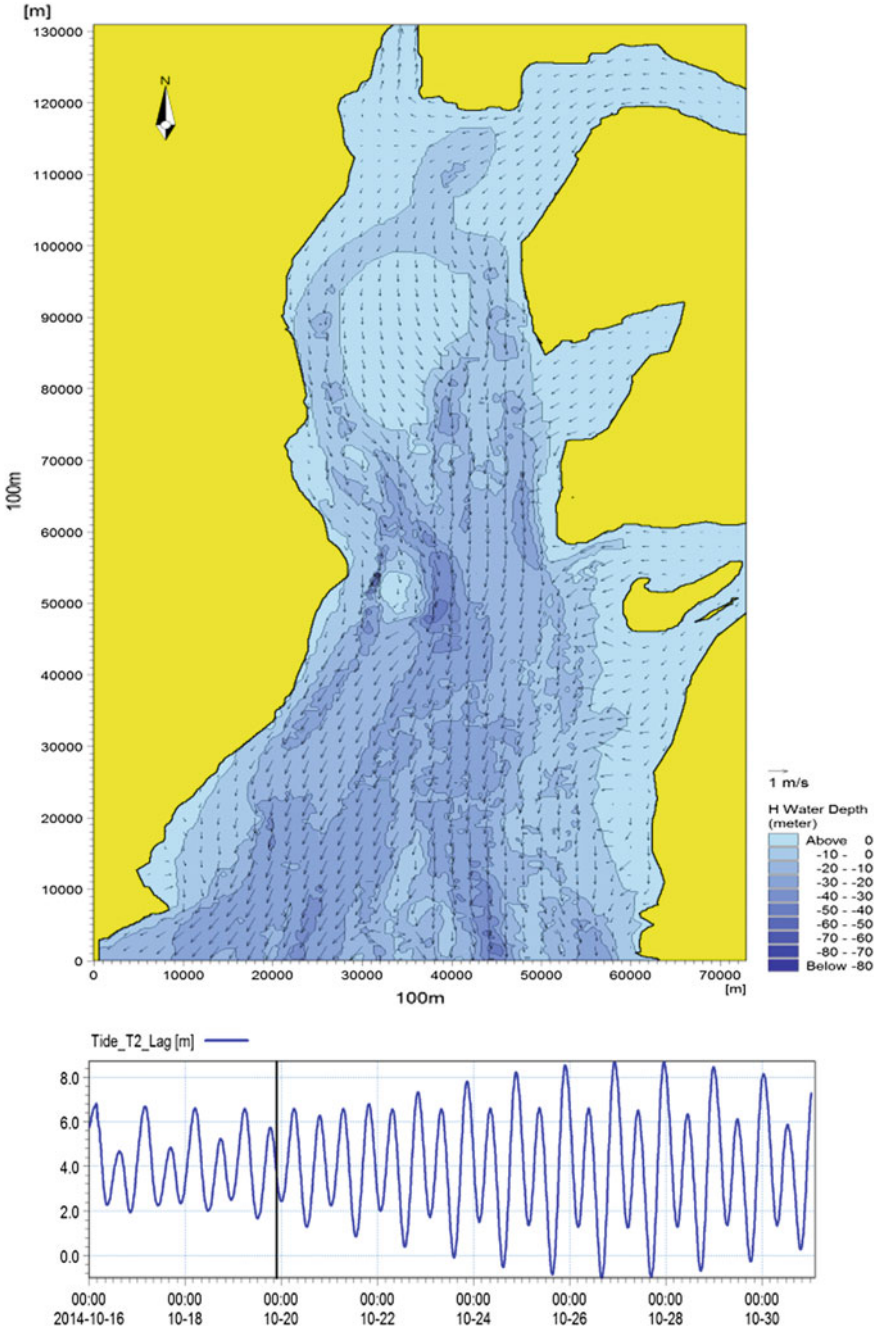

Fig. 7 Flow field during peak ebb (non-monsoon)

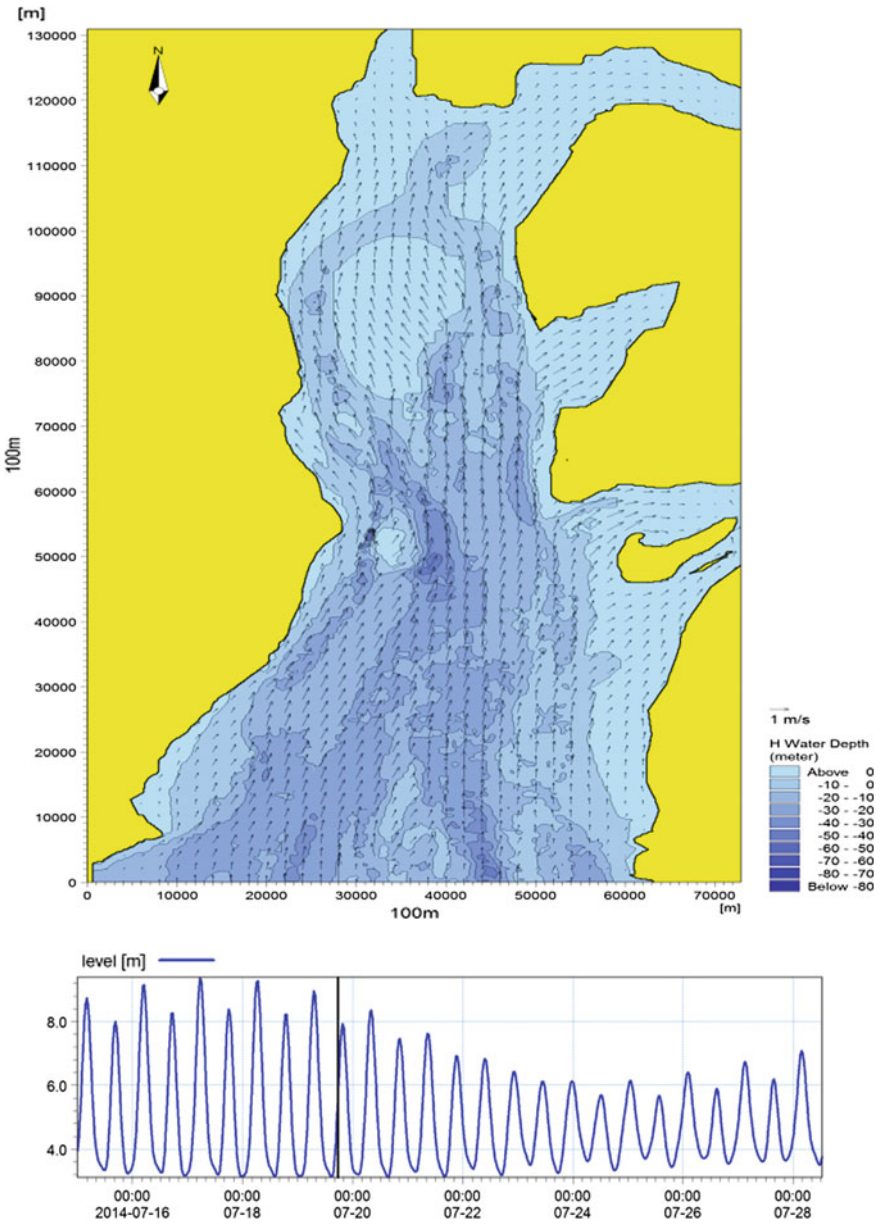

Fig. 8 Flow field during peak flood (monsoon)

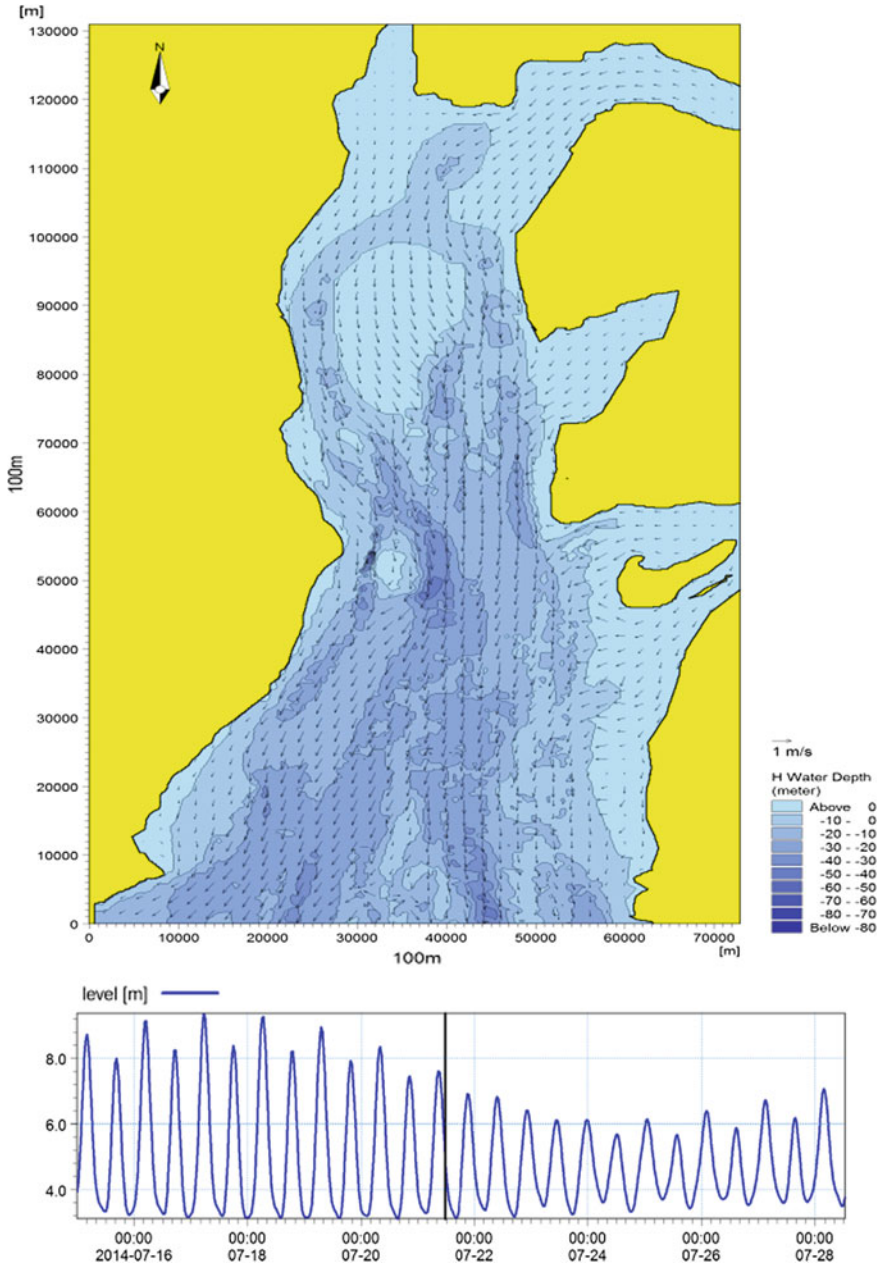

Fig. 9 Flow field during peak ebb (monsoon)

maximum current speed is about 1.45 m/s in peak flood condition which is shown in Fig. 6. The flood currents are stronger than EBB, LW and HW tide condition, and in peak ebbing, the maximum current speed is about 1.5 m/s as shown in Fig. 7.

3.3 Simulation of Flow Field for Monsoon

The same model set up of that of non-monsoon was modified by increasing the fluxes at different estuary and by incorporating the tide of monsoon that is for July month. It can be observed that the maximum current speed is about 1.5 m/s during

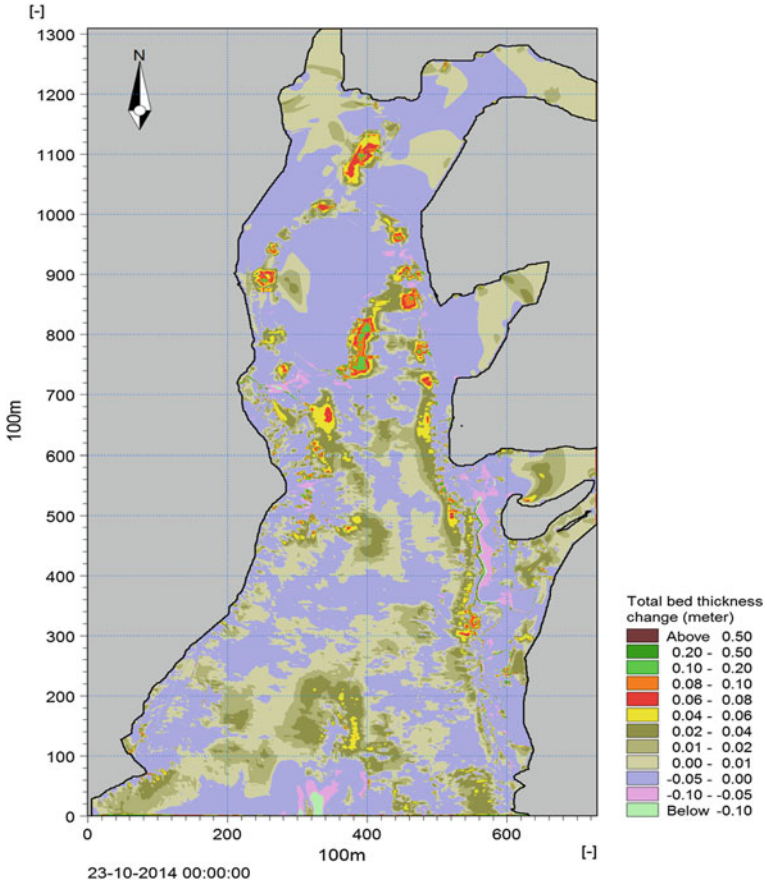

Fig. 10 Total bed thickness change (m) during non-monsoon

peak flood and the flood currents are stronger than EBB, LW and HW tide condition shown in Fig. 8. And during ebbing, it is increases up to 1.9 m/s. It is shown in Fig. 9.

3.4 Sedimentation Studies

The model was simulated for a simulation period of 15 days. The sedimentation during different phases of the tide was observed. The siltation pattern during non-monsoon is shown in Fig. 10 and SSC is shown in Fig. 11. It is found that siltation is high in the middle of gulf and there is slight erosion near the open sea and at Narmada estuary and the mud flats surrounding the mainland is prone to siltation, and during monsoon, it is found that there is slight siltation in the middle

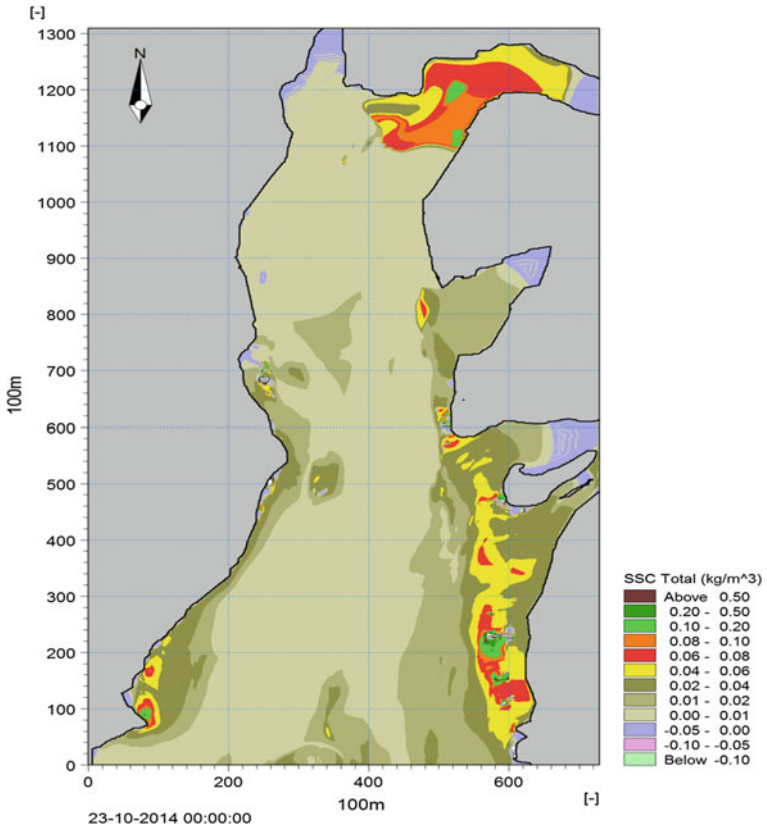

Fig. 11 Total SSC (kg/m^3) during non-monsoon

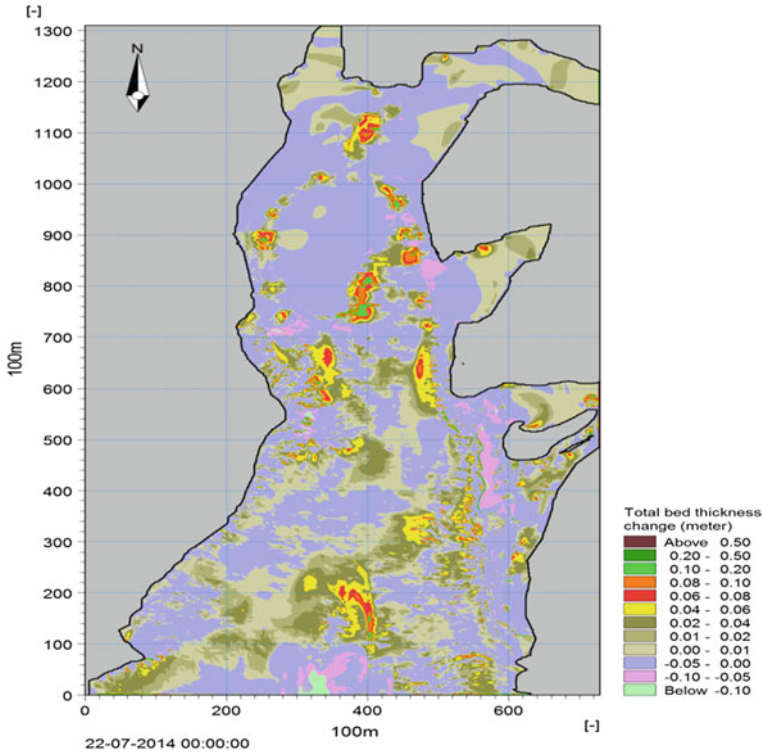

Fig. 12 Total bed thickness change (m) during monsoon

of gulf and there is slight erosion near the Narmada estuary and it is shown in Fig. 12 and SSC for monsoon is shown in Fig. 13.

4 Conclusions

An attempt to understand the hydrodynamic and sedimentation conditions prevalent in the entire gulf of Khambhat during non-monsoon and monsoon was successfully made in the present research. Two-dimensional finite difference-based mathematical models MIKE-21 HD and MIKE-21 MT were used for simulation of hydrodynamics and sedimentation in and around the area. The model was calibrated with the current data available for the location. The model showed good correlation with the observed current data. The model is considered to simulate the hydrodynamic behaviour to a good extent inside the Gulf. The important findings can be summarized as follows:

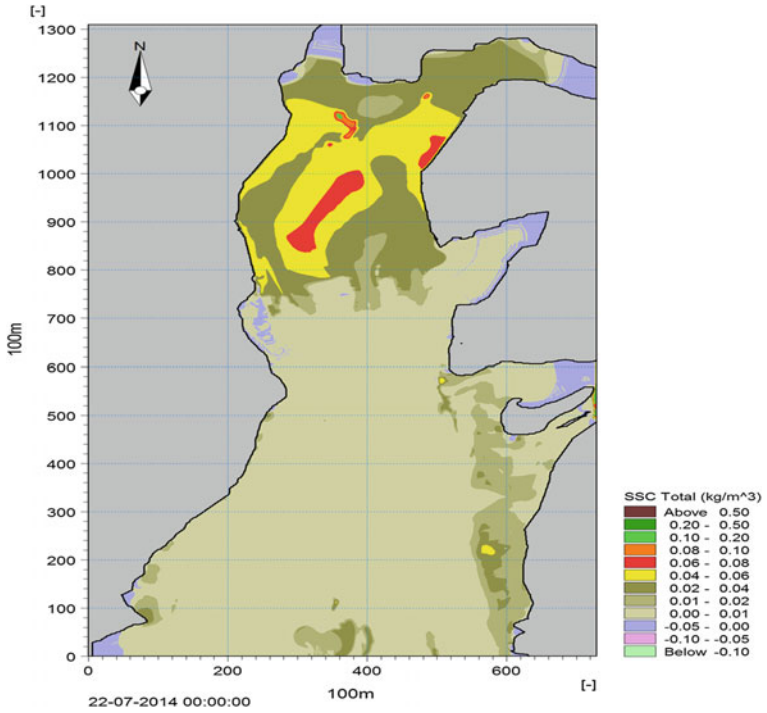

Fig. 13 Total SSC (kg/m^3) during monsoon

- Hydrodynamic simulations indicate an average current speed of 0.75 m/s inside the gulf during non-monsoon and in monsoon it is around 1 m/s and near the shore during non-monsoon it is 1.45 m/s and 1.5 m/s during monsoon.
- The gulf is found to be ebb dominated with a short falling period and a longer rising period. The currents during ebb tide are found to be stronger than during the flood tide.
- It can be concluded that during monsoon the sediment deposition at the mouth of Narmada estuary is large in comparison with non-monsoon.
- Initial hydrodynamic and sedimentation studies with the non-monsoon and monsoon indicated that flow conditions are conducive with no adverse circulations. The sedimentation studies indicated that there is a trend of siltation.
- The relation between sediment grain size and sediment transport is not linear and is interdependent on many other factors such as, bed slope and bed resistance.

4.1 Recommendation for Further Research

There is definite scope of further improvement in the model for the region. The following points should be considered for any further research to be carried out for the location:

A much better calibration could be achieved with detailed field surveys containing data regarding the surface elevation at the site, wave and wind parameters, and current speed vectors at the location of interest. A time series for a minimum of a year would improve the quality of the model predictions.

A survey showing the sediment grain size distribution at the gulf will also help in realizing a realistic bed resistance value and bottom friction parameter. Both the parameters were kept at a constant value in the model and the variations from the measured value can be attributed to this assumption.

The confidence in the results can be further improved by obtaining field data containing detailed sediment gradation and sediment diameter (D50) variation along the gulf. MIKE-21 can be utilized effectively to model the current and sediment transport occurring at the site. Further research may also include development or improvement of any existing model (CoSMOS, Telemac). This would provide a comprehensive modelling tool to understand the coastal processes active in the Arabian region.

Acknowledgements The authors wish to thank the director Central Water & Power Research Station for their invaluable inputs, guidance, cooperation and constant encouragement during this research.

References

1. Sinha, P.C., Jena, G.K., Jain, I., Rao, A.D., Husain, M.L.: Numerical modelling of tidal circulation and sediment transport in the Gulf of Khambhat and Narmada estuary, West Coast of India. J. Sci. Technol. **18**(2), 293–302 (2010)
2. Sen Gupta, R., Deshmukhe, G.: Coastal and Maritime Environment of Gujarat. Gujarat Ecological Society, Vadodara, India (2000)
3. Central Water & Power Research Station (CWPRS): Technical Report (2014)
4. Kumar, V.S., Kumar, K.A.: Waves and currents in tide dominated location off Dahej, Gulf of Khambhat. J. Mar. Geod. **33**, 218–231 (2010)
5. Kumar, S.S., Balaji, R.: Tidal hydrodynamics along Gulf of Khambhat, West Coast of India. International Conference on Water Resources, Coastal and Ocean Engineering. Aquat. Proc. **4**, 41–48 (2015)

Assessment of Sedimentation in Barak River Reach Using HEC-RAS

Bahnisikha Das and B.S. Sil

Abstract Sediment transport study is important in Barak River in the context of river bank erosion, deposition, and water quality management. The initiation of computer technologies has enabled engineers to resolve sediment transport equations through computer simulations. In this study, it is intended to carry out a sediment transport study in the Barak River reach for which the latest version of Hydrologic Engineering Centre-River Analysis System (HEC-RAS) is used. Ackers–White sediment transport equation is used to analyze characteristics of sediment transport. From the analysis of the model, total sediment erosion and deposition were obtained at different cross sections between the study reach. The model is calibrated with the observed data and a statistical performance analysis is done. The result shows that the model is performing well and can describe sediment discharge movement as well as can estimate the amount of sediment deposition and erosion at different sections in the study reach.

Keywords Erosion · Deposition · Sediment transport · HEC-RAS · Ackers–White · Barak River

1 Introduction

Rivers are the chief resources of water supply used for various purposes. The river is a dynamic system that undergoes continuous changes always. They are affected by various natural and human factors causing remarkable changes to rivers in long run leading to what is known as geomorphologic changes. Thus, the information of river situation such as the erosion and deposition conditions is the chief priorities of the various projects on river. Mismanagement and misuse of a catchment area leads to the contribution of additional sediment load to the river reaches. The high sediment discharge alters the shape and size of the channel and could be dangerous

B. Das (✉) · B.S. Sil
Civil Engineering, NIT Silchar, Silchar, India
e-mail: bahnisikha.das513@gmail.com

V. Garg et al. (eds.), *Development of Water Resources in India*,
Water Science and Technology Library 75, DOI 10.1007/978-3-319-55125-8_8

depending on where this transport takes place. Moreover, the release of effluents from industries and agricultural practices into the river channel pollutes aquatic system. High amount of sediment in the channel may be destructive for fish habitats and ecosystems. Also, sediment erosion may cause destabilization of the channel resulting in the failure of banks of the channel or the various hydraulic structures located in the channel bed [4], whereas the sediment deposition reduces the channel size thus adding stress to the channel banks and hence raising the water surface elevation level of the channel [8]. Therefore, realistic estimate of sediment transport rates in alluvial channel is essential for a number of water management issues [1].

Barak River is the major river of Barak valley used for numerous purposes. The river rises in Nagaland and passes through the Manipur Hills. It then flows from Lakhipur in the west direction via Cachar region of Assam over a distance of approximately 130 km before entering Bangladesh. The study reach extends from the Annapurna Ghat to Badarpur Ghat which is located toward the downstream end of Barak River covering a distance of approximately 51 km. The width of the river channel appears to be around 150 m and 300 m, respectively. The gradient of the river is less than 0.05 meters per kilometer which is tremendously flat even for a large river [5]. The fall in river water stage between Annapurna Ghat and Badarpur Ghat is approximately 4 m or less. The river is of highly meandering nature that has undergone considerable transformation at various channel locations in Barak valley [6]. The soil formation along the bank consists of a sequence of layers of silty clay, fine sands, and highly plastic clay. The sediment that is transported by the Barak River in considerable amount consists of fine silt and clay particles that are in suspension. The average bankfull discharge of the study area is around 3,800 cubic meters per second. The bank of the channel can resist the moderate flood flow velocities, and hence, most of the bank failures are generally linked with the formation of eddies and scour at sharp bends, or with geotechnical circumstances during falling stages or with seepage occurring into the banks from nearby ponds located along the banks. Sedimentation issues in the Barak River cause increasing pressure on the nearby societies and ecosystems as shifting river course on the one hand is displacing people from its bank and on the other raises doubts on the stability of river course in extreme flood conditions.

The developments of computer in mathematical modeling encouraged its application for analysis and prediction of the changes occurring in the geometry of rivers [7]. The application of a proper computer model to a particular region and its calibration is exclusively important which can simulate the changes in bed and bank elevation during floods in various seasons of year. Numerous mathematical models have been presented by many researchers in this topic on the basis of various assumptions and solutions including: HEC-6, CCHE1D model, CCHE2D model, MIKE11, FLUVIAL, and HEC-RAS model. Some of them became commercial and were used several times in different projects around the world.

1.1 Overview of HEC-RAS Model

HEC-RAS is a hybrid model developed by Hydrologic Engineering Centre, US Army Corps of Engineers. The model is one-dimensional which is utilized for hydraulic analysis of the river channels. The system includes four river analysis components which are steady flow water surface profile computations, unsteady flow simulation, sediment transport computations, and water quality analysis [3]. It uses an iterative method for calculation of water surface profile, and for calculating sediment transport rate, it uses number of semi-theoretical and empirical methods. The computations of sediment transport in the model allow the user to model the dynamic changes in river bed.

HEC-RAS has been present in the public realm for over 15 years and has been peer-reviewed (HEC 2010). It can be downloaded from the HEC Website which is available free of cost and is maintained by the US Army Corps of Engineers. It is also broadly used by numerous government agencies and private firms. However, the model cannot perform two-dimensional analyses for sediment transport and are not capable of predicting changes in the cross sections of river.

2 Methodology and Model Application

The sediment transport model requires a geometry file, steady flow profile, quasi-unsteady flow file, and sediment file to create the conditions similar to the river in HEC-RAS model.

For preparing the geometric data, the cross-sectional data were taken from digital elevation model (DEM) which was obtained from U.S. Geological Survey (USGS) records of satellite images taken with Shuttle Radar Topography Mission (SRTM). The dem is having a spatial resolution of 3 arc-seconds. The cross-sectional data perpendicular to the river course was drawn using HEC-GeoRAS, an extension of Arc GIS software. The geometric data are then imported into HEC-RAS, shown in Fig. 1. The entire study reach was divided into a total of 64 cross sections with an average distance of 0.75 km between each cross section.

To determine the river hydraulics, Manning's roughness coefficient is calibrated in the selected river reach with the steady flow analysis which uses the theory of stream flow energy balance with a known water surface elevation. Then, water surface elevation for each cross section is generated by standard step method which is an iterative procedure of solving the energy equation [2] stated as

$$Z_2 + Y_2 + \frac{\alpha_2 V_2^2}{2g} = Z_1 + Y_1 + \frac{\alpha_1 V_1^2}{2g} + h_e \quad (1)$$

where

Z_1, Z_2 Elevation of the main channel inverts,

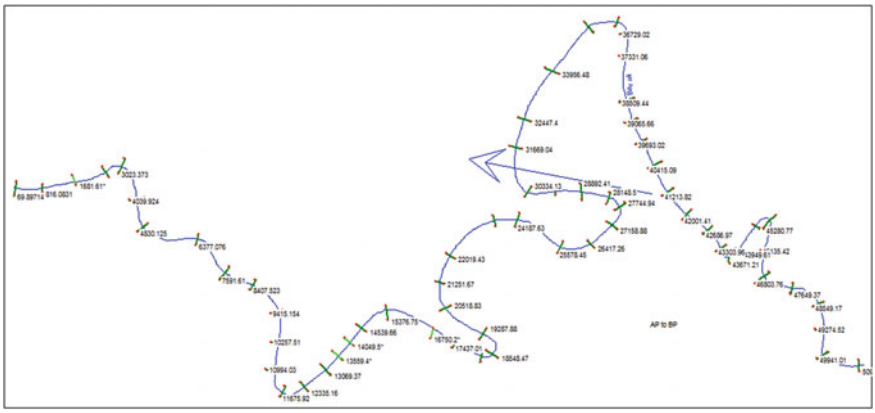

Fig. 1 Schematic plan of the study reach in HEC-RAS

Y_1, Y_2 Depth of water at cross sections,
V_1, V_2 Average velocities (total discharge/total flow area),
α_1, α_2 Velocity weighting coefficients,
g Gravitational acceleration,
h_e Energy head loss.

For sediment transport calculations, HEC-RAS uses "quasi-unsteady" flow approach which approximates a continuous hydrograph with a series of discrete steady flow profile. It should be defined in both upstream and downstream of studied boundary conditions of the river. At the upstream cross section (Annapurna Ghat), the boundary condition of *flow series* was utilized where a series of flows were defined at definite time intervals. In quasi-unsteady flow, the variable steps are considered in HEC-RAS model and a 24-h period of time has been considered in this work. The downstream boundary condition at the outlet of the study area (Badarpur Ghat station) is given the option of the *normal depth*. Sediment transport analysis in HEC-RAS model assumes a sediment control volume associated with each cross section. The Exner equation is then solved over the control volume, computing from upstream to downstream as mentioned as follows:

$$(1-\lambda_p)B\frac{\partial \eta}{\partial t} = -\frac{\partial Q_s}{\partial x} \tag{2}$$

where

η Bed elevation,
B The width of the control volume,
q Volumetric transport rate,
λ_P Bed porosity.

The equation is solved separately by computing a sediment transport capacity for each grain size in the control volume associated with each cross section. If the

capacity is greater than the sediment supply entering the control volume, there is erosion of the bed sediments. If supply surpasses capacity, there is an excess of sediment leading to the deposition of sediment. The size of sediment particles plays an important role in erosion and deposition of sediment in the river; defining the sedimentation part in HEC-RAS, each cross section should have a gradation curve in a discrete bed. For that, samples were collected from Annapurna Ghat station and gradation was done in the laboratory and the bed gradation of the remaining 63 cross sections was interpolated using HEC-RAS tool. The upstream boundary condition was given the option of *Equilibrium Load* in which the volumetric sediment discharge is assumed equal to the transport capacity everywhere in the reach.

3 Results and Discussion

3.1 Hydraulic Calibration of Model

The calibration of calculated data by the model is performed using the observed values at Annapurna Ghat station. The model was run repetitively from 1 June–30 June 2003, by altering Manning's roughness coefficient value at the various cross sections under steady flow analysis in order to get the best value of n. The initial value is obtained from equation given by Cowan

$$n = (n_0 + n_1 + n_2 + n_3 + n_4)m_5 \tag{3}$$

where

n_0 Base value for n for a straight uniform, smooth channel in natural materials,
n_1 Value added to correct for surface irregularities,
n_2 Value for variation in shape and size of channel,
n_3 Value for obstructions,
n_4 Value for vegetation and flow condition,
m_5 Correction factor to account for the meandering of the channel.

From physical interpretation of the values of the various parameters, the n value was obtained as 0.07. The Nash–Sutcliffe efficiency (CE) was used to select the best n value for estimating the water surface elevation of Annapurna Ghat station. However, the model performance was also checked through correlation coefficient (Corr).

The result of calibration is represented in Table 1.

Hence, the best result is obtained with roughness coefficient value as 0.07 same as that obtained from the equation given by Cowan. Hence, the final calibrated value of n was taken as 0.07.

Table 1 Statistical parameters showing the performance of the model with different n values

Statistical parameters	n = 0.07	n = 0.08	n = 0.06
Nash–Sutcliffe efficiency	0.915	0.914	0.856
Correlation coefficient	0.998	0.997	0.996

Table 2 Statistical parameters showing the performance of the model with different sediment transport functions

S. no.	Transport function	Fall velocity	n		Nash–Sutcliffe efficiency	Correlation coefficient	SSE
1	*Ackers–White*	*Report 12*	*0.07*	*AP*	*0.673*	*0.867*	*47387144460*
				BP	*0.595*	*0.786*	*21551471086*
2	Toffaletti	Report 12	0.07	AP	0.189	0.866	48387144460
				BP	0.591	0.776	21857577900
3	Laursen (Copeland)	Dietrich	0.07	AP	−1.050	0.863	265032006218
				BP	0.064	0.759	44315760821
4	Yang	Van Rijn	0.07	AP	−0.949	0.836	32692646283
				BP	0.207	0.745	22177374373

3.2 Selection of Sediment Transport Function

The second phase of HEC-RAS model calibration was done after calibrating the model hydraulically by running the steady flow analysis. The next step is to evaluate the model for sedimentation calculations. Here, the sediment discharge is used for calibration of the model. The model was run repetitively with different sediment transport functions, which is required for the calculation of sediment transport capacity, and the best transport function was selected which produces the value of sediment discharge close to the observed value at both upstream and downstream cross section. Table 2 displays the comparison of different transport functions and fall velocity method available in HEC-RAS 5 using Nash–Sutcliffe efficiency, correlation coefficient, and sum of square error.

The above table shows that Ackers–White transport function produces better value of the various statistical parameters at both upstream and downstream cross sections as compared to others. Therefore, this transport function is used in the present study for further calculations.

3.3 Prediction of Invert Changes

The invert of a river is an important criterion in geometry of the river cross section to define the potential of erosion or deposition. It undergoes changes during the time affected from river phenomena. The invert change in the model was produced using Ackers–White sediment transport function from Annapurna Ghat to Badarpur

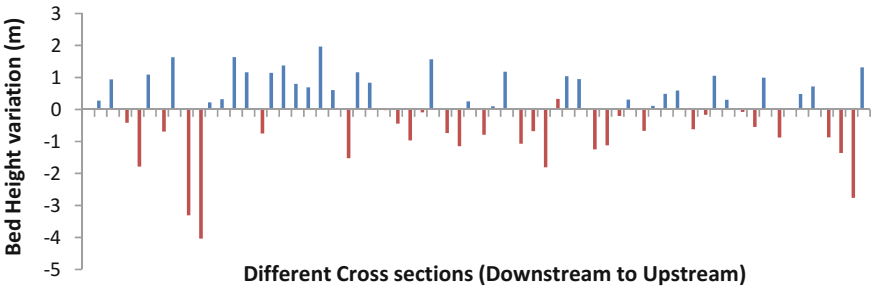

Fig. 2 Prediction of cumulative erosion and deposition of Barak River in the study reach

Ghat station having 64 cross sections from River Station (RS) 50999.31 to River Station (RS) 69.89. The difference between invert change in each cross section and initial bed level will determine the sedimentation. If the invert change is lesser than the initial bed level, then deposition takes place in that particular cross section and vice versa. Figure 2 shows the cumulative value of erosion and deposition of sediment at the various cross sections in the study reach from 1 June to 31 October 2004.

The maximum cumulative depth of erosion in the reach is about 4.04 m occurring at River Station 43949.69 (10th cross section from upstream) and the maximum cumulative depth of deposition is about 1.97 m at River Station 37331.06 (20th cross section from upstream) in wide regions of river as shown in Fig. 2. Because of meandering nature of Barak River, most of the erosion occurs on the concave side and deposition occurs on the convex side of the river bend. By field visit, it is also observed that the simulated erosion and deposition at the various cross sections are approximately same as the practical condition.

4 Conclusion

The present study deals with the simulation of sedimentation condition of the Barak River from Annapurna Ghat to Badarpur Ghat using HEC-RAS. The model was first calibrated for hydraulic conditions of the river, and the Manning's roughness coefficient of 0.07 that gives the best value of Nash–Sutcliffe efficiency (0.92) was considered which was also obtained from the equation given by Cowan. Then, the selection of sediment transport function is performed by calibrating sediment discharge. Ackers–White sediment transport function was found to provide better sedimentation result with Nash–Sutcliffe efficiency of 0.67. Then, channel invert variations were estimated for determination of erosion and deposition at various cross sections. It was found that the model is able to describe the sediment discharge movement as well as can estimate the amount of sediment deposition and erosion at different sections in the study reach. Because of meandering nature of

Barak River, most of the erosion occurs on the concave side and deposition occurs on the convex side of the river bend. It is noteworthy that the sediment transport function of this work has been proposed as more appropriate function not only because it gives better results but since each sediment transport function is based on specific geometric, hydraulic, and sedimentation conditions and it matches well with present study reach. Thus, the geometric, hydraulic, and sedimentation conditions of each sediment transport functions and also the river reach of study are of critical importance in optimized application of these methods.

References

1. Bhattacharya, B., Price, R.K., Solomatine, D.P.: A data mining approach to modeling sediment transport. In: 6th International Conference on Hydroinformatics—Liong, Phoon & Babovic. World Scientific Publishing Company (2014)
2. Brunner, G.W.: HEC-RAS, River Analysis System Hydraulic Reference Manual (2010)
3. Brunner, G.W.: HEC-RAS, River Analysis System User's Manual (2010)
4. Canfield, H.E., Wilson, C.J., Lane, L.J., Crowell, K.J., Thomas, W.A.: Modeling scour and deposition in ephemeral channels after wildfire. Catena **61**(2–3), 273–291 (2005)
5. Das, J.D., Dutta, T., Saraf, A.K.: Remote sensing and GIS application in change detection of the Barak River Channel, N.E. India. J. Indian Soc. Remote Sens. **35**(4), 301–312
6. Das, P.: Study of Barak River meander and associated hazard around Silchar Town, Assam, using remote sensing and GIS. J. Earth Sci. India **5**(2), 51–59 (2012)
7. Haghiabi, A.H., Zaredehdasht, E.: Evaluation of HEC-RAS ability in erosion and sediment transport forecasting. World Appl. Sci. J. **17**(11), 1490–1491 (2012)
8. Hummel, R., Duan, J.G., Zhang, S.: Comparison of unsteady and quasi-unsteady flow models in simulating sediment transport in an ephemeral Arizona stream. J. Am. Water Resour. Assoc. **48**(5), 987–998 (2012)

Neuro Fuzzy Application in Capacity Prediction and Forecasting Model for Ukai Reservoir

Surabhi Saxena and S.M. Yadav

Abstract A major fortress for flood and draughts is a reservoir. Capacity prediction of a reservoir is an integral part for its modelling. This paper exhibits the use of soft-computing technique ANFIS (Adaptive Neuro Fuzzy Inference System) to model behavior of Ukai reservoir. Using input/output data values, the proposed ANFIS computed balance capacity of Ukai reservoir. The input parameters include storage capacity for power generation, releases in left bank main canal, releases through gates, evaporation and inflow in to the reservoir. Out of the 14 models generated, the minimum error obtained to calculate the balance capacity of the reservoir was 0.06675. Calibration has been done for the years 2004–2010. The membership function used in this case was triangular with an epoch of 25. Model is validated for 2011–2014 and the minimum error predicted for validating the model was 0.0592, which is accurate enough to predict the capacity of the reservoir at the end of the period.

Keywords ANFIS · Balance capacity · Membership function and epoch

1 Introduction

Reservoir operation is a complex problem, particularly for multi-purpose reservoirs where joint use of storage is an objective. With the advent in engineering technology for water resources management problems, evaluation through computer based simulation and optimization is now a prominent option [10]. To maximize benefits and achieve the objectives while modelling a reservoir, water resources need to be managed in the best possible manner [4].

S. Saxena (✉) · S.M. Yadav (✉)
Civil Engineering Department, Sardar Vallabhbhai National Institute of Technology, Surat, India
e-mail: s170192@gmail.com

S.M. Yadav
e-mail: shivnam27@gmail.com

V. Garg et al. (eds.), *Development of Water Resources in India*,
Water Science and Technology Library 75, DOI 10.1007/978-3-319-55125-8_9

1.1 Literature Review

The basic architecture and learning procedure of ANFIS (Adaptive Neuro Fuzzy Inference System) was discussed by Jyh-Shing et al. [4]. For the modelling of nonlinear functions, identification of nonlinear components in the control system and for the prediction of chaotic time series, ANFIS architecture was employed by Jyh-Shing et al. [4]. Comparing the reservoir operations with various techniques like NNP (Neural Network Performance), Multiple Linear Regression procedure (MLR), Stochastic Dynamic Programming (SDP) and Standard Operating Policies (SOP), the results were obtained for deriving operating policies by Raman et al. [7]. This was due to the fact that neural network works for more complex problems than regression problems. Utilizing first-order Sugeno Fuzzy Inference System, Roy [8] predicted the surface roughness in turning operation. A fuzzy rule based model was developed for the operation of a single purpose reservoir. It was illustrated through the case study of Malaprabha irrigation reservoir in Karnataka, India [2]. To determine optimal reservoir operating rules, Kerachian et al. [6] formulated an algorithm combining ANFIS based water quality simulation and Genetic Algorithm-based optimization technique. Based on the reliability of water supply to downstream demands and water demands, utility functions for the proposed models were developed. The results also predicted the reduction in salinity of the allocated water. A conceptual model was developed to assist water resource managers in assessing impact of management on water supplies in watersheds and large river basins [1]. Kadhim [5] classified ANFIS as a system theoretic model, and is capable for creating an acceptable simulation of complex and nonlinear processes even in data scarce conditions. The soft computing techniques like ANN (Artificial Neural Network) and Fuzzy are more reliable than the conventional methods. ANN give good results for more number of inputs, and for less number of inputs, Fuzzy is a better technique. This was determined by Dinesh et al. [3].

2 Study Area

Ukai is a multipurpose project located on River Tapi near village Ukai of Fort-Songadh Taluka in Surat district. The catchment is located between longitudes 72°32′25″–78°36′30″ and latitudes 20°5′0″–22°52′30″. Ukai dam is built at about 30 km upstream of the Kakrapar weir. Ukai dam is located at a distance of 94 km from Surat City of Gujarat. Ukai Dam is built on Tapti River (Fig. 1). The dam is meant to provide irrigation. It also generates hydroelectricity for the surroundings areas. The salient features of Ukai reservoir is presented as Table 1. These data have been collected from India—WRIS website.

Headworks of Ukai dam was completed in the year 1972 after a construction period of 7 years. Yield of Tapi river at Ukai dam site is 11,350 MCM at 75% dependable yield. Out of this, 38.4% share is of Gujarat, i.e. 3,947 MCM.

Table 1 Salient features of Ukai reservoir

Attribute	Value
Name of reservoir	Ukai reservoir
State	Gujarat
River	Tapi
Maximum water level (m)	106.985
Full reservoir level (m)	105.16
Minimum draw down level (m)	78.77
Gross storage capacity (MCM)	8510
Basin	Tapi
Live storage capacity (MCM)	7097
Dead storage capacity (MCM)	684.39
Submergence area (Th. ha)	60.1
Catchment area (km^2)	62225

Fig. 1 Location of Ukai reservoir in Tapi river. *Source* Google earth as on April 20, 2016

2.1 Data Collection

The model evaluates the balance capacity of the reservoir at the end of the time stretch considered. The data collected include the storage capacity, water levels, discharge through power house, releases through Ukai left bank main canal, releases through radial gates, evaporation, average discharge, volume, inflow and the balance capacity. The data were analyzed and three input parameters were considered for further processing in ANFIS. Ten daily inflow–outflow data from 2004 to 2014 of Ukai water resources project were procured from the Narmada Water Resources, Water Supply and Kalpsar department and were processed.

3 Adaptive Neuro Fuzzy Inference System (ANFIS)

A kind of Artificial Neural Network based on Takagi-Sugeno Fuzzy Inference System is ANFIS (Adaptive Neuro Fuzzy Inference System). This technique was developed in the early 1990s. Integrating both Fuzzy logics and neural networks, it extracts the benefits of both of the techniques. The ANFIS system reflects a set of Fuzzy If-Then rules that can give results for nonlinear functions. ANFIS is thus a universal estimator. Genetic Algorithm may also be used to obtain better results for ANFIS. Figure 2 represents structure of ANFIS model.

3.1 Methodology

An ANFIS architecture based on a first-order Sugeno model with the following fuzzy if–then rules are shown as (Eqs. 1 and 2):

$$\text{Rule a: If } x = A_1 \text{ and } y = B_1; \text{ then } f_1 = p_1 \cdot x + q_1 y \cdot r_1 \tag{1}$$

$$\text{Rule b: If } x = A_2 \text{ and } y = B_2; \text{ then } f_2 = p_2 \cdot x + q_2 y \cdot r_2 \tag{2}$$

where, x and y are the inputs, A_1 and B_1 are the membership functions for inputs, p_1, q_1 and r_1 are the various parameters of the output function that are recognized during the training process. ANFIS structure is composed of five layers (Fig. 3). The first layer consists of input nodes generating the membership grades based on the appropriate fuzzy set that belong to membership functions. The second layer

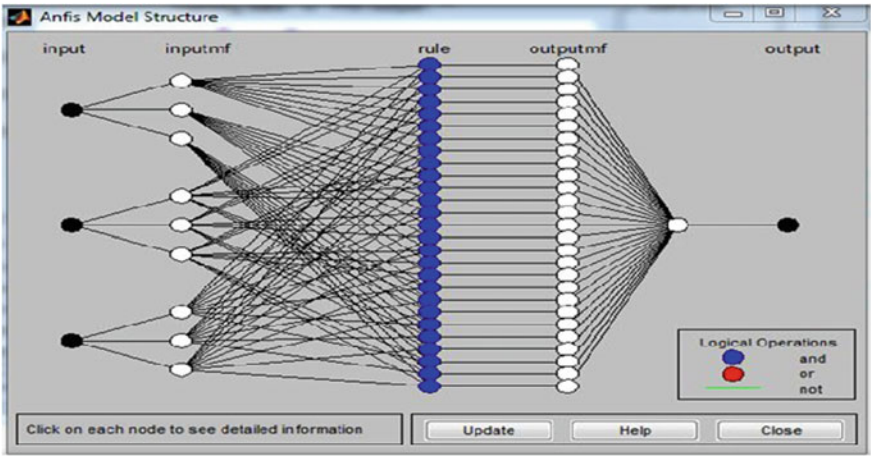

Fig. 2 Structure of ANFIS model. *Source* Model development (MATLAB screenshot) after loading input data in ANFIS command

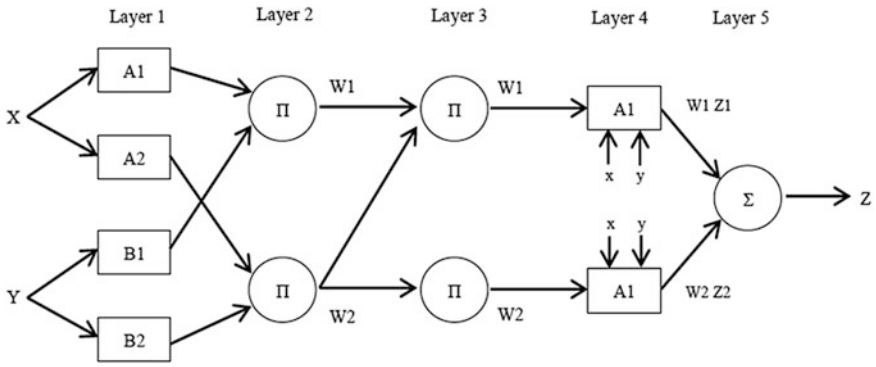

Fig. 3 A typical ANFIS architecture used in this study [9]

consists of rule nodes that generate the strengths by multiplying the incoming signals and outputs operator results. The third layer consists of consisting average nodes computes the normalized strengths. The fourth layer consists of consequent nodes that calculate the first-order Takagi-Sugeno rules for each fuzzy rule based on the output generated.

A systematic approach to generate fuzzy from given input–output dataset are the Takagi-Sugeno rules. Fifth layer includes a single output node that calculates the overall output of ANFIS as the summation of the input variables.

4 Results and Analysis

The data compiled for this study represents 10 years of ten daily data of storage capacity, discharge through power house, releases through left bank main canal, releases through radial gate, evaporation and inflow values for the Ukai reservoir system. Thirty percent data have been used for the testing of the model and 70% of the data is for the training of the ANFIS model. Based on RMSE (Root Mean Square Error) and R^2 (Coefficient of determination), the major objective of the training process was to obtain the optimal solution. Two hundred and fifty-two data sets were used to develop ANFIS model. Figure 4 includes circular data loaded for training purpose and plus sign indicates data loaded for checking the model. Total 14 models were developed with different possibilities, by trial and error, out of which few models with good results were selected. Table 2 represents the total number of membership functions (MFs) used to create the models, input parameters, output MFs and epochs. MOD12 gives better results than other models. For MOD12 model, linear triangular function with three input membership function and output membership function as constant was considered. Epochs considered were 25,

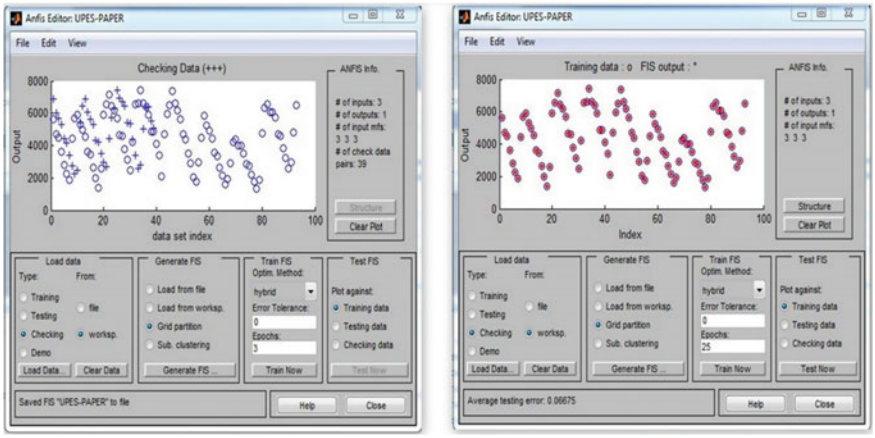

Fig. 4 Loading of training and checking data to calculate the average testing error

Table 2 Models generated to obtain the best results

Model	MF type (input)	MF type (output)	Epoch	Error	Testing error
MOD1	Trimf	Linear	25	22.0924	22.0924
MOD2	Trapmf	Constant	25	41.087	41.0845
MOD3	Gbellmf	Constant	25	19.62181	19.8705
MOD4	Gaussmf	Constant	25	11.6697	11.868
MOD5	Psigmf	Linear	25	21.273	21.74
MOD6	Pimf	Linear	30	20.1761	21.426
MOD7	Gaussmf	Linear	30	81.58	13.925
MOD8	Trapmf	Linear	30	20.2273	20.586
MOD9	Trimf	Linear	30	22.0924	23.003
MOD10	Trimf	Constant	30	0.28755	0.286
MOD11	Trimf	Constant	250	0.269	0.31
MOD12	**Trimf**	**Constant**	**25**	**0.06675**	**0.06675**
MOD13	Trimf	Constant	30	0.41891	0.512
MOD14	Pimf	Constant	30	0.35599	0.42

the error and the average testing error was 0.06675. Although results obtained from various other models were also good. Models MOD10, MOD11, MOD13 and MOD14 gave error value less than unity, which is good. The data were in such a manner that the best results obtained by it were from triangular MF and pimf (pie shaped membership function). Rest of the MFs like gbellmf, trapmf, gaussmf, psigmf could not produce good results comparatively in the present study.

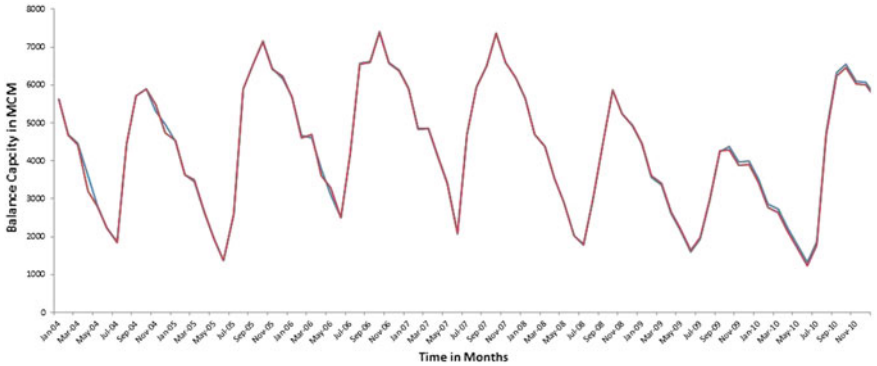

Fig. 5 Observed and predicted balance capacity calibrated for the period January 2004–December 2010

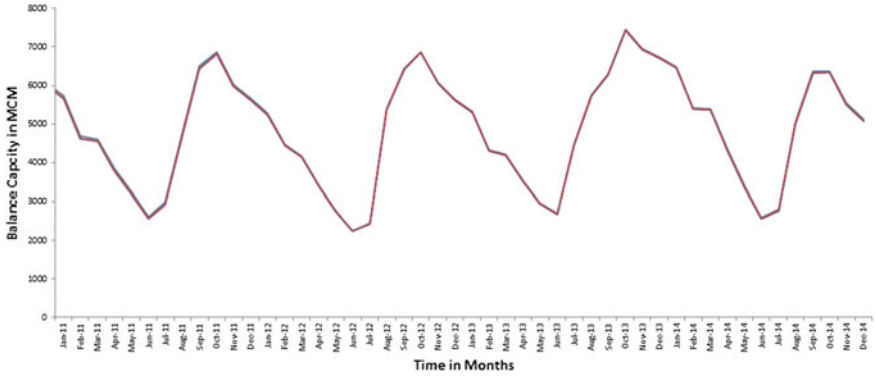

Fig. 6 Observed and predicted balance capacity validated for the period January 2011–December 2014

5 Calibration

Calibration of the ANFIS model was computed for the period January 2004–December 2010. The error predicted for this process was calculated to be 0.06675. Figure 5 depicts the balance capacity of the observed and predicted data. Both lines almost coincide predicting the minimum error by the model.

6 Validation

Figure 6 represents plot between observed capacity and predicted capacity. The R^2 predicted for the validation is 0.0592. Validation of the model has been done for the period January 2011–December 2014. The results of ANFIS model were verified by

the 252 rules generated. The output value, i.e. the balance capacity at the end of the period, was similar enough to get error as 0.06675. Input 1 here refers to the capacity of the reservoir in the beginning of the period, and input 2 includes discharge through power house, releases in the left bank main canal, releases through gates and evaporation. Input 3 refers to the total volume and inflow in MCM. Figure 6 is the validation of the data calibrated for this study.

7 Conclusions

This study was an attempt to balance storage of reservoir modeling using ANFIS models with the input parameters of the storage capacity, discharge through power house, left bank main canal, discharge through gates, evaporation and inflow.

- The results of the study confirmed the validity of this method as the output generated from the model equalizes the capacity of the reservoir at the end of the period. This paper evaluates capacity efficiently by ANFIS based learning techniques.
- Proposed ANFIS-based technique may facilitate the reservoir planning stage in making its decision regarding the evaluation of other techniques while construction.
- The model was calibrated for the year 2004–2010. The minimum error predicted for calibrating the model was 0.06675. Epochs considered were 25, and the error and the average testing error was 0.06675.
- The results obtained with linear triangular function, three input membership functions and output membership function as constant, R^2 calculated was 0.0592. This model could thus give a very low value for the error, thus making the model accurate. This validates the model.

References

1. Arnold, J.G., Srinivasan, R., Muttiah, R.S., Williams, J.R.: Large area hydrological modelling and assessment Part I. J. Am. Water Resour. Assoc. 73–89 (1998)
2. Bijaya, P., Shreshtha, L.D., Stakhiv, E.Z.: Fuzzy rule based modelling of reservoir operation. J. Water Resour. Plan. Manag. 262–269 (1996)
3. Bisht, D., Jain, S., Mohan Raju, M.: Prediction of water table elevation fluctuation through fuzzy logic and artificial neural networks. Int. J. Adv. Sci. Technol. **51** (2013)
4. Jang, J.S.R.: ANFIS (Adaptive network based fuzzy inference system). IEEE Trans. Syst. Man Cybern. **23**, 665–685 (1993)
5. Kadhim, H.H.: Self learning of ANFIS inverse control using iterative learning technique. Int. J. Comput. Appl. **21**, 24–29 (2011)
6. Kerachian, R., Karamouz, M., Soltany, F.: Optimal reservoir operation considering the water quality issues. Application of adaptive neuro fuzzy inference system. In: World Environmental and Water Resource Congress ASCE (2006)

7. Raman, H., Chandramouli, V.: Deriving a general operating policy for reservoirs using neural network. J. Water Resour. Plan. Manag. **122**(4), 262–269 (1996)
8. Roy, S.S.: Design of adaptive neuro fuzzy inference system for predicting surface roughness in turning operation. J. Sci. Ind. Res. **64** (2005)
9. Takagi, T., Sugeno, M.: Fuzzy identification systems and its application to modelling and control. IEEE Trans. Syst. Man Cybern. **15**, 116–132 (1985)
10. Talei, A., Chua, L.H., Quek, C., Jansson, P.E.: Runoff forecasting using a Takagi-Sugeno neuro fuzzy model with online learning. J. Hydrol. 17–32 (1985)

Use of Mathematical Techniques for Determining the Reliability of Springs

Ajay Kumar Vashisht

Abstract The perennial springs of the Himalayan region are fulfilling the water needs of the inhabitants from the time immemorial. At present, the discharging pattern of majority of these has become seasonal and has concentrated to monsoon months only; the foremost responsible factor for this is the change in precipitation pattern. The change in climate has altered the precipitation pattern which is further answerable for declination in recharging component of spring catchments. Consequently, the springs and the streams (which are based on their flows) are under tremendous stress. The spring water availability throughout the year is completely based on its reliability which can be quantified by analyzing spring's temporal discharge data. Therefore, in the present chapter, various mathematical techniques/methods that can be adapted for determining the reliability of existing springs are discussed by considering the realistic data.

Keywords Spring hydrology · Recession period · Time-lag · Spring water management

1 Introduction

The Greater Himalayas can also be considered as the overhead water storage structure of Asia. The complete Himalayan region is marked with great climatic variability. From the recent past, the whole region is facing the hydrological extremes such as floods and droughts. Now, it is an established fact that global warming is primarily responsible for change in weather conditions of the region [1]. Probably, the maximum impact has been noticed on the precipitation pattern which has changed from low-intensity longer-duration events to high-intensity

A.K. Vashisht (✉)
Department of Soil and Water Engineering, College of Agricultural Engineering and Post-Harvest Technology, Central Agricultural University (Imphal), Ranipool, Sikkim, India
e-mail: akvashisht74@yahoo.com

V. Garg et al. (eds.), *Development of Water Resources in India*,
Water Science and Technology Library 75, DOI 10.1007/978-3-319-55125-8_10

smaller-duration events. Specifically mentioning, this change has been noticed from the last four to five decades. The most deleterious effect of the changed precipitation pattern is the reduction in the recharging of the spring catchments. Therefore, the formations responsible for feeding the springs are not getting enough opportunity to saturate fully. A spring catchment may comprise more than one formation with different geohydrological properties [2]. The recharging and discharging time of highly permeable formations is considerably less than the formations having lower permeability. Because of this reason, the formations with lower permeability get lesser opportunity to recharge from a smaller-duration intense-rainfall event and vice versa. Therefore, the amount of rainwater that the highly permeable formation receives from monsoon showers discharges out from spring orifice within the end of monsoon or at the most up to post-monsoon season. Year by year, the average discharge rate of the perennial springs in the region is declining.

To cope up with the water-scarce scenario, there is a need to adapt spring water management practices. The feasible possibilities include the construction/installation of water storage structures, transfer of water from excess to shortage areas [3], rejuvenation of springs and/or seepage spring development [4]. However, the adaption of any water management practice requires the information on the reliability of spring a priori. The various criteria for determining the reliability of a spring are (i) time-lag from the occurrence of particular rainfall event to consequent increase in the spring discharge; (ii) the quantity of rainwater getting stored in spring catchment; (iii) maximum to minimum discharge ratio of spring in a year; and (iv) discharge rate and yield prediction of spring for the upcoming recession period. In order to assess the reliability of the springs, rainfall as well as discharge rate data of spring is required [5]. Based upon the temporal discharge data of spring, its reliability based upon above-mentioned criteria can be quantified by using various mathematical techniques/methods. Therefore, the aim of the present chapter is to explain various mathematical techniques/methods by considering the realistic data of springs.

2 Time-Lag

The time taken by the volume of rainwater which gets an opportunity to infiltrate and deep percolate to the storage of a particular spring catchment and which comes out of the spring orifice after certain delay is known as ‘time-lag.’ The time-lag factor depends upon (i) infiltration and deep percolation rates of catchment formation(s); (ii) capacity of the spring catchment; (iii) the existence of more than one formation with varied geohydrogeological characteristics in different geometrical patterns. As rainfall is received in intermittent passion, the spring discharge varies with time. The discharge rate of a spring is steered by the formation permeability, whereas its life span (perennial or seasonal) depends upon the storage capacity of catchment [2]. Other than the formations which contain water-soluble rocks, porous medium characteristics do not change frequently. Therefore, it is quite logical that

the time-lag provided by the catchment can be evaluated by analyzing the amount of rainfall received and its effect on spring discharge pattern. This method was first proposed by Vashisht and Sharma [6]. The applicability of the proposed method has been shown by using the realistic data of a perennial spring (named *Ranipool*). The discharge rate of the spring is being regularly monitored from March 2013.

The spring is located in the small town of *Ranipool* at 27° 17.684′ N latitude and 088° 35.448′ E longitude. The spring orifice is at an elevation of 915 m above mean sea level (MSL) in East District of Sikkim State. The Google Earth image and recently snapped photograph of the spring are shown in Fig. 1. The average annual rainfall of the area is 2200 mm which is usually received during the months of April to October. The catchment area of the spring is covered with forest with patches of agricultural lands.

The *Ranipool* spring is regularly monitored for its discharge rate. The users have fixed a galvanized iron pipe at the spring orifice to create clear-cut outfall of water (Fig. 1). The discharge rate of the spring is measured three times before averaging it for final reading. For reducing the human error, the averaging becomes essential particularly when spring is discharging with higher rate. For understanding of the readers, the proposed method is demonstrated by considering only one recession period data of the spring. In year 2013–2014, recession period was 197 days long which occurred from October 20, 2013, to May 05, 2014. It means that spring was discharging with maximum rate on October 20. Figure 2 shows the flowing pattern of spring during the recession period. The logarithmic function is used to create smoothness in flowing pattern. In spite of this, recession curve is showing considerable variation in discharge with time. This variation in discharge can be attributed to the intermittent showers which were received in the monsoon season of 2013 and later on in February month of 2014.

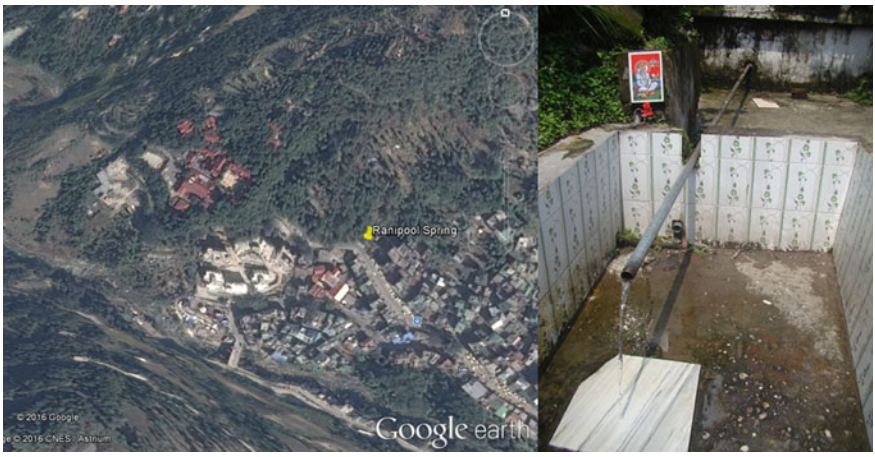

Fig. 1 Google Earth view of *Ranipool* spring and its recently snapped photograph

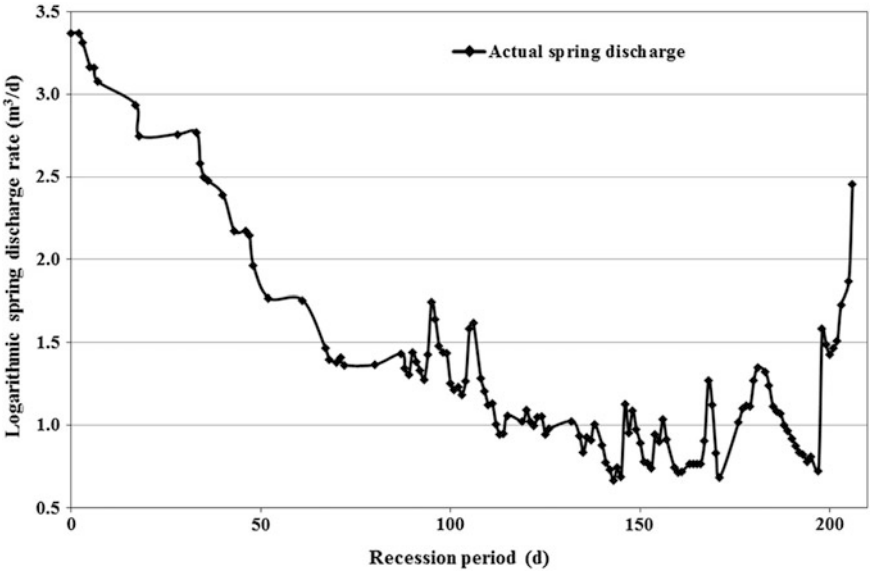

Fig. 2 Discharging pattern of *Ranipool* spring during recession period

Step 1 (No lag)			Step 2 (1-d or 1-week lag)			Step 3 (2-d or 2-week lag)		
Cumulative Rainfall (CR) column	Is placed against	Cumulative spring discharge (CSD) column	Cumulative Rainfall (CR) column	Is placed against	Cumulative spring discharge (CSD) column	Cumulative Rainfall (CR) column	Is placed against	Cumulative spring discharge (CSD) column
CR1	:	CSD1			CSD1			CSD1
CR2	:	CSD2	CR1	:	CSD2			CSD2
CR3	:	CSD3	CR2	:	CSD3	CR1	:	CSD3
CR4	:	CSD4	CR3	:	CSD4	CR2	:	CSD4
CR5	:	CSD5	CR4	:	CSD5	CR3	:	CSD5
CR6	:	CSD6	CR5	:	CSD6	CR4	:	CSD6
CR7	:	CSD7	CR6	:	CSD7	CR5	:	CSD7
Correlation coefficient - 1			Correlation coefficient - 2			Correlation coefficient - 3		

Fig. 3 Procedure for evaluating time-lag

The proposed method can be conveniently used for daily or weekly cumulative values of rainfall and spring discharge data. With increase in the number of days for evaluating cumulative values, results may alter from actuality. The only condition is to maintain the uniformity between the two (i.e., rainfall and spring discharge). Data set of any duration can be considered but longer the duration more accurate will be

the result. The complete procedure is explained in Fig. 3. In the step 1, cumulative values of rainfall in a column (for the considered period) are placed against the column containing cumulative values of spring discharge data for the same period (Fig. 3). The time-lag for this data set is equal to zero for which the value of correlation coefficient is calculated using standard statistical procedure. In the step 2, column containing cumulative values of rainfall is given one-day time-lag as shown in Fig. 3. Again, correlation coefficient value is evaluated. The said procedure is continued till a maximum value of correlation coefficient is achieved.

Following the above-mentioned procedure, correlation coefficient values for the monitored data of *Ranipool* spring are evaluated and are graphically presented in Fig. 4. Perusal of the figure shows that for 38-d time-lag, the correlation coefficient value is maximal. Hence, it is concluded that for *Ranipool* spring the rain water received by catchment from a particular event will discharge out from the spring orifice after 38 days. The investigations also show that the evaluated time-lag factor is for the first exponential component only. Obviously, the time-lag duration for the second exponential component will be higher than the first. Logically, the spring will be more reliable if time-lag period is more. Moreover, the time-lag factor can be utilized to determine the depth of rainfall required to avoid drought [7]. In other terms, the amount of water should be recharged to spring catchment to avoid dry conditions during recession period.

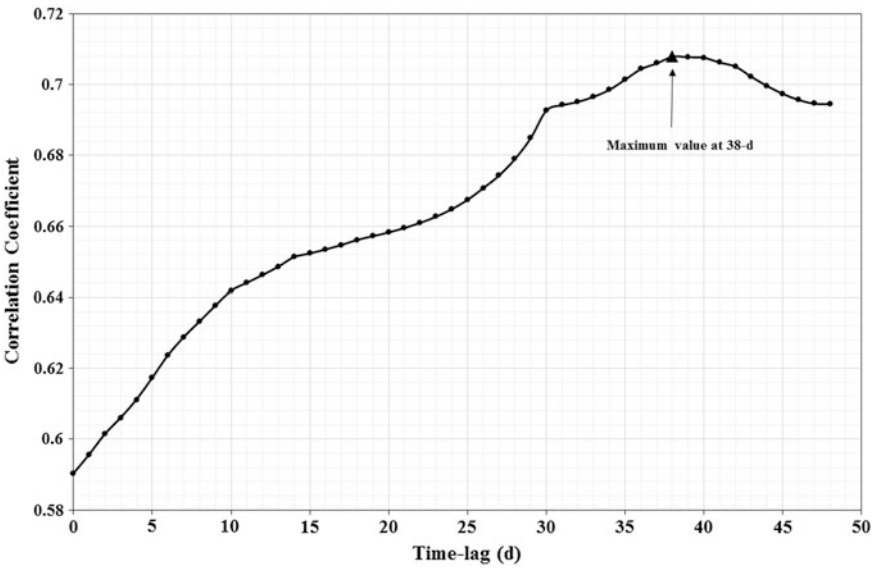

Fig. 4 Change in correlation coefficient with change in time-lag

3 Rainfall Versus Spring Yield

Rainwater has to cross the formation(s) of spring catchment before discharging through spring orifice. Therefore, the relationship between total annual rainfall and total spring discharge per year could not be considered simple [8]. Moreover, for understanding the hydrogeological conditions of the spring catchment, their relationship model is a beneficial tool [9]. The relationship between rainfall and spring discharge can be investigated using cross-correlation analyses [10], linear model [11] and by a nonlinear time-series model [12]. For showing the applicability of the technique, relevant data of a spring (named *Ranichauri*) are obtained from the project entitled 'All India Coordinated Research Project (AICRP) on Groundwater Utilization (GWU),' Irrigation and Drainage Engineering, G. B. Pant University of Agriculture and Technology, Pantnagar, Uttarakhand. Geographically, the spring is located at 30° 18′ 47.09″ N latitude and 078° 24′ 33.34″ E longitude and at an altitude of 1871 m above MSL. The annual yield of the spring along with the annual rainfall received in the region for the 8-year period is presented in Table 1.

The table also includes the maximum to minimum yield ratio of the spring for all the 8 years. Previously, Vashisht and Sharma [6] have considered this ratio as one of the reliability criterion of springs. However, it was realized later on that there is one major drawback in this criterion. According to this criterion, lesser value of ratio for a particular year means that spring has discharged more uniformly in that year. In Table 1, the minimum ratio is for the year 2001 which is equal to 1.83. Following the basis of said criterion, spring has discharged more consistently in this year. But, the comparison of spring yield in the considered year with the rest shows that it was the year during which minimum discharge was received. From the uniform discharge rate point of view, the proposed criterion is reasonably correct, but practically the spring has discharged only 42.36% of the maximum yield monitored during the data collection years. Because of this flaw, it was realized that there is a need to suggest a more reliable criterion. The portion of the rainfall which gets an opportunity to infiltrate and deep percolate to the spring catchment storage

Table 1 Yearly discharging pattern of *Ranichauri* spring

Year	Annual rainfall (mm)	Annual spring yield (m^3)	Maximum/minimum yield ratio	Yield per unit rainfall (m^3/mm)
(1)	(2)	(3)	(4)	(5)
1999	939.7	4915.25	34.834/6.912 = 5.04	5.23
2000	1334.4	6494.31	43.632/8.410 = 5.19	4.87
2001	719.1	2924.54	12.355/6.768 = 1.83	4.07
2002	1254.6	4681.84	28.800/7.862 = 3.66	3.73
2003	1173.8	3931.21	26.582/6.163 = 4.31	3.35
2004	1174.7	4590.62	31.292/3.874 = 8.08	3.91
2005	1386.9	6904.55	42.984/7.685 = 5.60	4.98
2006	897.0	3556.37	28.800/5.976 = 4.82	3.96
				Average = 4.26

is responsible for the spring yield. Neglecting the role of rainfall and spring catchment's surface characteristics, a relation can be developed between the amount of rainfall received and the yield of the spring. After arranging the rainfall and their corresponding yield data in ascending order, an exponential equation is written which is showing a correlation value of 72.41%. It can be written as

$$y = 1426.8\, e^{0.0011x} \tag{1}$$

In Eq. (1), x is the rainfall in mm and y is the spring yield in m^3. It is worth to mention here that the mathematical equation representing the relation between rainfall and yield will be unique for each spring. Proceeding in the similar manner, Agarwal et al. [13] found a polynomial relationship between rainfall and spring discharge for two watersheds. Other than Eq. (1), a more general criterion can also be evolved from the data presented in Table 1. In column (5) of Table 1, spring yields per unit mm of rainfall received in all the 8 years have been presented. From the column, an average quotient of 4.26 m^3/mm is evaluated. Though, not exact but a crude idea regarding the yield of the spring in a particular year can be evaluated by multiplying this average value with the total rainfall expected in that year. Once again, the evaluated average quotient will also be unique for each spring.

4 Discharge Rate Prediction of Spring

The graphical representation of spring discharge rate (Q) with respect to time (t) is known as spring hydrograph. Roughly, hydrograph can be divided into two portions, i.e., accession curve (or rising limb) and recession curve (or declining limb). Recharging of spring catchment due to intermittent rainfall showers is reflected by the increase in discharge rate of the spring quite nonuniformly. It is because of this reason that the recession curve of the hydrograph is usually studied.

Even during the recession period, frequent small-scale variations can be observed which can be smoothened by taking the logarithmic transformation. While drawing the recession curve, the peak discharge value of the spring (i.e., first value) is plotted against time $t = 0$ on timescale. The remaining recession period's discharge values are timed consecutively. Recession curve for the *Ranipool* spring is presented in Fig. 2. Next step is to formulate a generalized mathematical equation for the recession curve(s). For the purpose, the recession curve(s) are fitted with the one or more number of mathematical components. These mathematical components may be linear, polynomial, logarithmic, exponential or any combination of these. Purpose is to fit the recession curve with maximum possible accuracy. Maillet [14] has proposed a more general form (i.e., exponential) for fitting the recession curve of a hydrograph as

$$Q_t = Q_0 e^{-\alpha t} \tag{2}$$

Table 2 Mathematical parameters of the *Ranipool* spring

Discharge rate of first exponential component at $t_1 = 0$ (Q_{01}), (m^3/d)	29.030
Depletion coefficient (i.e., slope) of first exponential component (α_1), (d^{-1})	0.0279
Duration of first exponential component, (d)	72
Discharge rate of second exponential component at $t_2 = 0$ (Q_{02}), (m^3/d)	3.906
Depletion coefficient (i.e., slope) of second exponential component (α_2), (d^{-1})	0.0051
Duration of second exponential component (d)	125
Total duration of recession period (d)	197

where Q_t represents the discharge rate of the spring at time t, Q_0 indicates the peak discharge rate value of the spring which is considered at time $t = 0$, and α characterizes the recession coefficient whose value is influenced by the geological and morphological structure of the spring catchment. Sometimes, 'recession coefficient' is also termed as 'depletion coefficient.' A spring catchment may comprise formations with different geohydrological properties, and their existence can be judged by studying the general slope pattern of the recession curve. Depending upon the number of formations in the spring catchment, the recession curve represents these by slope(s). If recession curve is showing n number of slopes, then it is obvious that the same number of exponential components is required to write mathematical function. Therefore, Eq. (2) modifies to

$$Q_{ti} = Q_{0i}e^{-\alpha_i t_i}; \quad for\, i = 1\, to\, n; \quad t_i = 0\, to\, T_i \tag{3}$$

where Q_{0i} and Q_{ti} are the discharge rates of the spring for the ith exponential component of the recession curve at time $t = 0$ and at time $t = t_i$, respectively. Further, T_i and α_i represent the duration and recession coefficient of ith exponential component, respectively. Neglecting the shorter-duration minor variations in the slope, the recession curve of the *Ranipool* spring can be fitted with two mathematical components whose parameters are tabulated in Table 2.

With the use of Eq. (3) and parameters given in Table 2, discharge rate of the *Ranipool* spring at any instant can be evaluated. On the basis of the maximum discharge rate of the spring during monsoon season, discharge rate values for the upcoming recession period can be predicted. On the basis of these predictions, water management policy for the upcoming recession period can be decided well within time.

5 Spring Yield

The yield of a spring that is regularly monitored can be evaluated by summing up daily discharge values for the considered period. However, for predicting the yield of a spring for any upcoming recession period, a spring discharge function is required which can be formulated based on the generalized mathematical

parameters expressed in Table 2. The discharge function for the recession period of *Ranipool* spring can be conveniently written as

$$V(197\,d) = \left[\sum_{t_1=T_0=0}^{72-1} 29.030 \times e^{-0.0279\times(t_1-0)}\right] + \left[\sum_{t_2=72}^{197} 3.906 \times e^{-0.0051\times(t_2-72)}\right] \tag{4}$$

Equation (4) is representing the addition of two exponential components. Both the components are expressing the spring yield for respective durations (i.e., for 72 and 125 d). It is worth to mention here that the last value of the first exponential component will be the first for the second. It is because of this reason the end limit of the first exponential component is represented as '72–1.' On solving discharge function (4), the yield of the *Ranipool* spring is evaluated equal to 1262.19 m^3 for a recession period of 197 d. The peak discharge rate of any spring generally occurs during the period ranging between mid- and end monsoon. By knowing the peak discharge rate value, discharging pattern and yield of any spring can be predicted using Eqs. (3) and (4). On the basis of predicted behavior of spring, the users will get enough time to manage their needs during upcoming recession period.

6 Optimization of the Size of Water Storage Structure

It is already mentioned in introduction section of the paper that the changing rainfall pattern is altering the rainwater distribution ratio of runoff component to spring catchment recharging component. With the increase in the runoff and reduction in the recharging of spring catchment, springs are losing their reliability. For sustaining livelihood, people are now exploring the remote places for tapping water. Plastic pipes are generally used to convey water from spring orifice to storage tanks. Breaking of pipes, leakage from joints, blocking of pipes due to entrapped air and interference with spring orifice by crab activity are some frequently occurring problems that are faced by the inhabitants. For uninterrupted water supply, the inhabitants have appointed persons on regular basis to maintain the system. However, this might not be the only solution for every household. In the present water-scarce scenario, there is a need to give weightage to the adaption of spring water management practices. Probably, the most feasible and acceptable solution is to create reserve storage for water during the periods of its excess (i.e., monsoon season). Usually, the capacity of the overhead tanks is decided based on the 1- or 2-day requirement of the family. However, when we have to take the decision regarding the complete recession period (which may lengthen up to 200 days), it becomes a very difficult task. Reduction in the availability of spring water during recession period directly increases the size of storage structure and, consequently, its cost and space requirement. The size of the storage structure depends on spring's discharging pattern during recession period and number of users. Therefore,

it becomes essential to optimize the storage capacity of structure before its construction/installation. The optimization process is based on the correct evaluation of difference between water demand and its availability during the recession period [15]. It is very easy to evaluate the demand which is completely based on the number of persons along with the other uses. Equation (3) can be used to predict spring discharge rate, whereas Eq. (4) can be used to predict yield.

Consider that D L/d is the daily water requirement of a person. If P_N is the total number of persons, then the total daily demand T_D can be evaluated as

$$T_D = P_N \times D \tag{5}$$

Until T_D is less than daily spring discharge, there is no need of any storage structure. The period for which T_D remains higher than daily spring discharge is known as water shortage period and is termed as T_{short}. The mathematical equation for evaluating storage structure's capacity considering no wastage and excess use ($O_{sc\text{-}w}$) can be written by combining Eqs. (4) and (5) as

$$O_{sc-w} = P_N \times D \times T_{short} - \left[\sum_{t_1=T_0=0}^{72-1} 29.030 \times e^{-0.0279\times(t_1-0)}\right] + \left[\sum_{t_2=72}^{197} 3.906 \times e^{-0.0051\times(t_2-72)}\right] \tag{6}$$

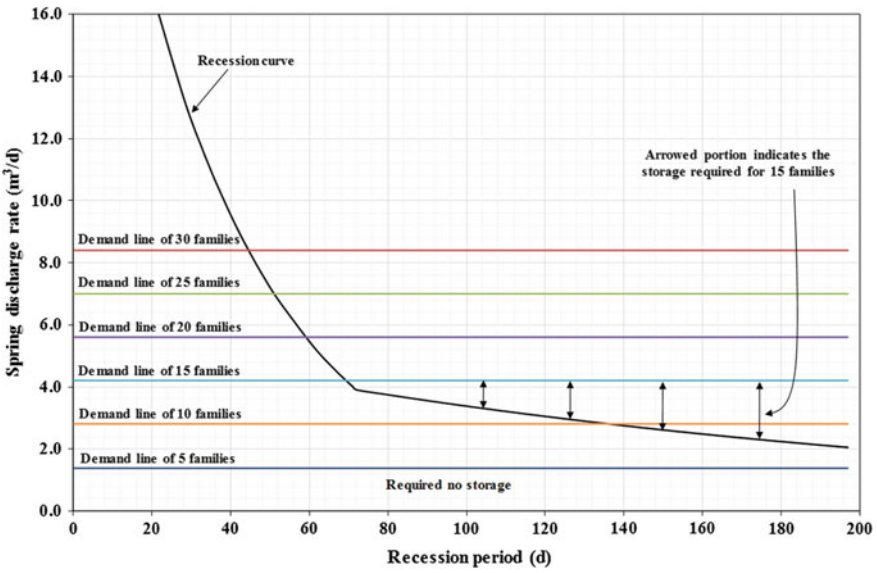

Fig. 5 Optimized capacity of a water storage structure based upon number of families

Based upon the number of families which are dependent on *Ranipool* spring, the capacity of the storage structure required is graphically presented in Fig. 5. Perusal of Fig. 5 clearly indicates that there is no need of any additional storage for 5 families. The actual demand for water from 30 families in the recession period is 1268.40 m^3. However, with the use of Eq. (6), the optimized capacity of the storage structure required comes equal to 758.94 m^3 only which is approximately 60% of the actual demand.

7 Conclusions

In the present water-scarce scenario, the livelihood sustainability in the Himalayan region is completely based on the adaption of various spring water management practices. For that, information regarding spring's reliability should be known a priori. The reliability of a spring can be determined by (i) the delay that is caused to rainwater by spring catchment formation(s) before its discharge from spring orifice; (ii) the quantity of rainwater getting stored in spring catchment; (iii) maximum to minimum discharge ratio of spring; and (iv) discharge rate and yield prediction of spring in the upcoming recession period. Based upon the temporal discharge data of a spring, various mathematical techniques/methods can be used to determine its reliability. Infiltrated and deep-percolated water come out of spring orifice after certain time-lag. It is an obvious conclusion that the spring with more time-lag will be more reliable. Neglecting the role of rainfall and spring catchment's surface characteristics, an exponential relation can be developed between the amount of rainfall received and the yield of the spring. Though not exact, but this relation (unique for every spring) can predict spring yield up to reasonable accuracy. By predicting the spring's discharge rate and yield for upcoming recession period, the users may get enough time to take appropriate decision to cope up with upcoming dry season. In the end, a method for optimizing the size of storage structure is presented. It is concluded that by adapting the proposed procedure, enough space and money can be saved while constructing/installing water storage structure of optimized capacity.

Acknowledgements The data used in this paper are taken from the author's ongoing DST-funded project entitled 'Prediction of lean season discharge of springs for efficiently managing it to fulfill water needs of the mountain inhabitants.' Some relevant data are also procured from the Indian Council of Agricultural Research, New Delhi, funded project named AICRP on GWU, Department of Irrigation and Drainage Engineering, G. B. Pant University of Agriculture and Technology, Pantnagar, Uttarakhand, India.

References

1. IPCC: Climate change 2007: climate change impacts, adaptation and vulnerability. Working Group II contribution to the Intergovernmental Panel on Climate Change Fourth Assessment Report. Summary for policymakers (2007) 23 pp
2. Vashisht, A.K., Bam, B.: Formulating the spring discharge-function for the recession period by analyzing its recession curve: a case study of the Ranichauri spring (India). J. Earth Syst. Sci. **122**(5), 1313–1323 (2013)
3. Agarwal, A., Arora, M., Gurung, R.K.N.: Springs of mid-western Himalayan (Uttarakhand) and their response. Mausam **67**(2), 509–512 (2016)
4. Vashisht, A.K.: Adaption of seepage spring development technique to manage the water scarcity in Himalayan region—a practical approach. Water Util. J. **11**, 93–98 (2015)
5. Malvicini, C.F., Steenhuis, T.S., Walter, M.T., Parlange, J.-Y., Walter, M.F.: Evaluation of spring flow in the uplands of Matalom, Leyte, Philippines. Adv. Water Resour. **28**, 1083–1090 (2005)
6. Vashisht, A.K., Sharma, H.C.: Study on hydrological behaviour of a natural spring. Curr. Sci. **93**(6), 837–840 (2007)
7. Fiorillo, F.: Spring hydrographs as indicators of droughts in karst environment. J. Hydrol. **373**, 290–301 (2009)
8. Patchick, P.F.: Springs of the Argus mountains, California and their use in a desert community. Int. Assoc. Sci. Hydrol. Bull. **9**(3), 46–55 (1964)
9. Liu, L., Shu, L., Chen, X., Wang, E., Oromo, T.: Rainfall-driven spring hydrograph modeling in a karstic water system, southwestern China. Water Resour. Manage. **24**(11), 2689–2701 (2010)
10. Fiorillo, F., Doglioni, A.: The relation between karst spring discharge and rainfall by cross-correlation analysis (Campania, southern Italy). Hydrogeol. J. **18**, 1881–1895 (2010)
11. Estrela, T., Sahuquillo, A.: Modeling the response of a karstic spring at Arteta aquifer in Spain. Groundwater **35**(1), 18–24 (1997)
12. Jian, W.-B., Yao, H., Wen, X.-H., Chen, B.-R.: A nonlinear time series model for spring flow: an example from Shanxi Province, China. Groundwater **36**(1), 147–150 (1998)
13. Agarwal, A., Agarwal, N.K., Rathi, V.K.: Water stress on springs of Lesser Himalayan region. British J. Appl. Sci. Technol. **9**(3), 243–255 (2015)
14. Maillet, E.: Essais d′Hydraulique Souterraine et Fluviale (Underground river and hydraulic tests). Herman, Paris, France (1905)
15. Vashisht, A.K.: Development of an analytical function for optimizing the capacity of spring water storage structure. Sustain. Water Resour. Manage. **2**(4), 337–352 (2016). doi:10.1007/s40899-016-0073-4

Impact of Rainwater on Bituminous Road Surfacing

Gourav Goel and S.N. Sachdeva

Abstract Accumulation of rainwater on roads due to lack of proper drainage causes loss of adhesive bond between bitumen and aggregate which results into stripping and severe damage to the pavement. Indian Standard (IS 6241-1971: method of test for determination of stripping value of road aggregate. Laboratory test, 1971) [1] prescribes the stripping test in which aggregate coated with bitumen is kept immersed in water for 24 h at 40 °C. After the test, the retained coating of bitumen should be minimum 95% for the aggregate to be suitable for road construction. Most of the time, the aggregate exhibits no stripping under laboratory conditions, whereas it fails in stripping under field conditions. To understand this problem, a laboratory investigation was conducted on the aggregate of Haryana taking into consideration some of the prevailing field conditions like acidic/alkaline nature of water and the presence of traffic on the roads. The test results indicated that the pH of water and application of external pressure affected the stripping considerably.

Keywords Rain water · Stripping · Adhesion · pH value · Traffic

1 Introduction

Moisture damage contributes significantly to pavement failures throughout the country. It weakens the resistance of pavement to failures like rutting and fatigue cracking. Its presence in bituminous pavements is a primary cause which results in weakening or eventual loss of adhesive bond of bitumen with aggregate. One of the principal fundamental properties for good performance of bituminous pavement is proper adhesion between aggregate and bitumen. This phenomenon of loss of bond between aggregate and bitumen is known as stripping. For prevention of damage, adequate drainage must be provided. Nowadays, the roads are lacking in respect of

G. Goel (✉) · S.N. Sachdeva
Department of Civil Engineering, NIT, Kurukshetra 136119, Haryana, India
e-mail: gouravgoelshinu@gmail.com

V. Garg et al. (eds.), *Development of Water Resources in India*,
Water Science and Technology Library 75, DOI 10.1007/978-3-319-55125-8_11

proper drainage facilities, which is one of the main reasons for road damage due to stripping. Aggregate surface physical characteristics such as texture and particle shapes are important factors which can be related to the occurrence of stripping. In addition, presence of salt in water, acidity–alkalinity of water and traffic are other factors which may affect stripping. Jain and Sengupta [2] in their study reported 100% stripping of aggregates in the presence of salt (1% NaCl). An increase of almost 200% in stripping value with the application of external pressure on the aggregates at the time of stripping was reported by Shakya and Sachdeva [3]. Stripping can cause rutting, ravelling, bleeding, cracking and formation of potholes and culminate with complete failure of the pavement.

In India, Bureau of Indian Standard [1] prescribes the test for stripping of coarse aggregate. The test is designed to capture the amount of stripping due to the presence of water on road surface. In general, it is found that the test has a doubtful correlation with actual field performance.

2 Mechanism of Stripping

Striping is one of the main causes due to which distresses in the bituminous layers occur. The existence of water in bituminous pavement is often one of the main factors affecting the durability of bituminous pavement. Damage due to moisture presence in pavement layers can be related to adhesion loss and cohesion loss. In adhesion loss, the bitumen film is stripped away from the aggregate by the presence of water between bitumen and aggregate [4]. This may be due to the fact that aggregate has more affinity with water than the bitumen binder. In cohesion loss, the interaction of water with bitumen results in reduction of cohesion within bitumen [5].

Five different mechanisms that may be associated with stripping of bitumen film from aggregate surface [6, 7] are described as follows.

2.1 Detachment

When the bitumen film gets separated from aggregate by the presence of thin layer of water without any break in bitumen film such that the film can be peeled off cleanly from the aggregate, it is known as detachment. This indicates complete loss of adhesion.

2.2 Displacement

When there is a break in the bitumen film, water penetrates into the aggregate resulting in stripping by displacement mechanism. Due to the movement of traffic, the breaking of bitumen film generally takes place at sharp edges and corners of angular aggregate where bitumen coating is usually thin or incomplete. Changes in the pH of the water held between aggregate and bitumen lead to the build-up of opposing, negatively charged, electrical double layers on the aggregate and bitumen surfaces, which results in separation of bitumen from the aggregate.

2.3 Spontaneous Emulsification

In spontaneous emulsification, inverted emulsion is formed due to immersion of bitumen film (continuous phase) in water (discontinuous phase). This phenomenon causes stripping that is further aggravated by the presence of mineral clays. Rate of stripping will also depend upon the type of bitumen.

2.4 Pore Pressure

In high void mixes, build-up of pore pressure by the traffic in the impermeable voids may also cause stripping.

2.5 Hydraulic Scouring

Water on a saturated pavement surface gets pressed down into pavement in front of a moving tyre and gets sucked away behind the tyre. This causes compression and tension cycles resulting into stripping by hydraulic scouring.

3 Experimental Details

The Indian Standard [1] describes the stripping test for the coarse aggregate. The experimentation has been carried out in the Highway Engineering Laboratory of National Institute of Technology, Kurukshetra.

Materials Used. In the present study, the bitumen (VG-30 grade) obtained from a nearby refinery and aggregate obtained from three different quarries of the Haryana State was used to determine the stripping value. Table 1 gives the details of the materials used in the study.

Table 1 Source/type of material

Material	Type
Coarse crushed aggregate	Type 1, source: Yamuna Nagar quarry, colour: light bluish-white Type 2, source: Dadri quarry, colour: light white-reddish Type 3, source: Narnaul quarry, colour: dark bluish
Bitumen	VG-30 grade, source: Panipat refinery, 5% of mass of aggregate
Water	Potable water
HCL acid	For making water acidic (pH values 3 and 5)
NaOH	For making water alkaline (pH values 9 and 11)

Table 2 Stripping of aggregate due to extended contact time

Sr. no.	Contact time (days)	Striping of aggregate (%) for					
		Aggregate Type 1		Aggregate Type 2		Aggregate Type 3	
		Without pressure	With pressure	Without pressure	With pressure	Without pressure	With pressure
1	1	0	1	0	1	0	1
2	2	1	1	1	1	1	1
3	3	1	2	1.5	2.5	1	1.5
4	4	2	3	2.5	3	1.5	2
5	5	2.5	4	3	5	2	2.5

4 Test Results and Discussion

Various tests were carried out under standard conditions [1] and varying conditions to determine the change in the value of stripping of aggregate. Three types of aggregate from different sources were taken for evaluating the value of stripping under various testing conditions.

4.1 Stripping of Aggregate Due to Extended Contact Time

Stripping of aggregate was tested by increasing the water immersion time from 1 day to 5 days in order to determine the effect of extended contact time of aggregate with water on the value of stripping. The effect of traffic load and tyre friction was simulated by applying external pressure manually with a small tyre. The results are shown in Table 2.

It is observed that the stripping value of all aggregate types increases with increase in immersion time of aggregate in water. Similarly, the stripping value increases with application of external pressure for all the three types of aggregate considered in the study. Type 1 and Type 2 aggregate exhibited more stripping than Type 3 aggregate under both conditions of with and without the application of external pressure.

Table 3 Stripping of aggregate under acidic condition

Sr. no.	Contact time (days)	Striping of aggregate (%) for											
		Aggregate Type 1				Aggregate Type 2				Aggregate Type 3			
		Without pressure		With pressure		Without pressure		With pressure		Without pressure		With pressure	
		pH value		pH value		pH value		pH value		pH value		pH value	
		5	3	5	3	5	3	5	3	5	3	5	3
1	1	0	0	1	1	0	0	1	1	0	1	1	1
2	2	1	1	1	1	1.5	1.5	2	2.5	1	1	1.5	2
3	3	1.5	1.5	2	2	2	2	2.5	3	1.5	3	2	4
4	4	2	2	3	3	3	3.5	3	4	2	4	2.5	5
5	5	3	3.5	4.5	11	4	4	5	17	3	5	3.5	6

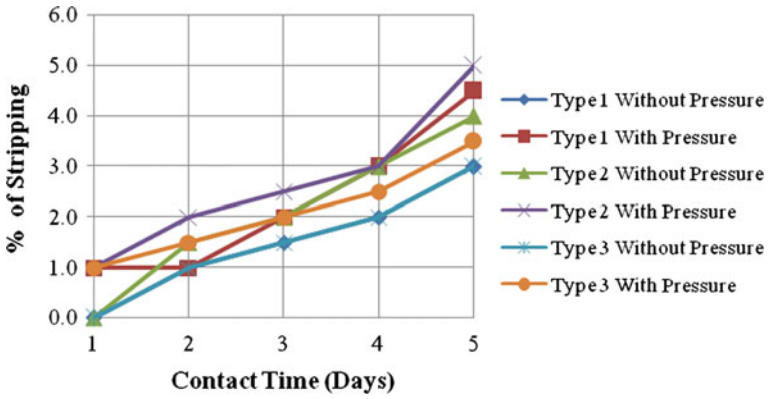

Fig. 1 Stripping of aggregate with water of pH value 5

4.2 Stripping Value of Aggregate Under Acidic/Alkaline Water Condition

pH value of water affects the value of stripping of aggregate. Indian Standard [1] recommends the use of distilled water in testing, but in field the pH value of water may vary to a great extent. Bituminous pavements near chemical industries and food processing industries or with improper drainage are prone towards inundation under acidic and/or alkaline condition.

Stripping value of coarse aggregate under acidic condition. The bitumen–aggregate mixtures were tested under acidic condition that is under pH value of 3 and 5. The mixing water was made acidic with pH value 5 by pouring requisite quantity of HCL in 250 ml of water. The results are given in Table 3 and presented in Fig. 1 for pH value 5.

It is observed from Fig. 1 that the stripping value of coarse aggregate increases with increase in immersion time and with application of external pressure. Type 2

aggregate shows more stripping than other two types of aggregate for pH value 5. The mixing water is made acidic with pH value 3 by pouring requisite quantity of HCL in 250 ml of water. The results are given in Table 3 and presented in Fig. 2 for pH value 3. It is observed from Fig. 2 that the stripping value of coarse aggregate increases with increase in immersion time and with application of external pressure. All types of aggregate for pH value 3 show more stripping with application of pressure.

Figure 3 depicts the comparison of stripping values of all types of aggregate under pH values 3, 5 and 7 after 5 days of water immersion time. It is observed that more acidic water results in more stripping with pressure as well as without pressure.

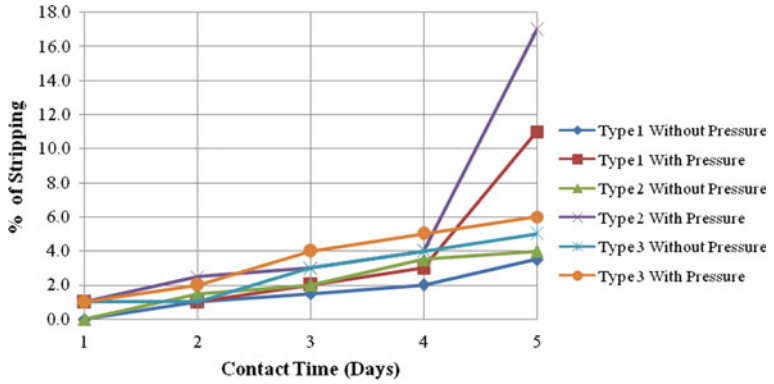

Fig. 2 Stripping of aggregate with water of pH value 3

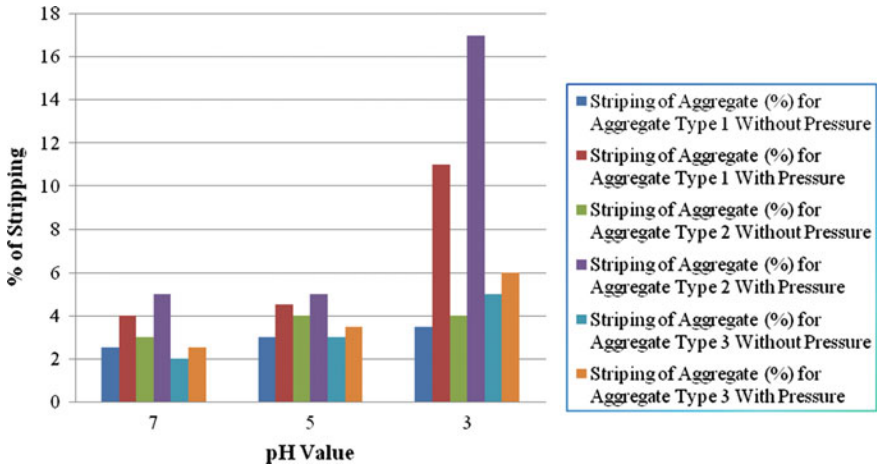

Fig. 3 Stripping of aggregate at the end of 5 days under acidic condition

Table 4 Stripping of aggregate under alkaline condition

Sr. no.	Contact time (days)	Striping of aggregate (%) for											
		Aggregate Type 1				Aggregate Type 2				Aggregate Type 3			
		Without pressure		With pressure		Without pressure		With pressure		Without pressure		With pressure	
		pH value		pH value		pH value		pH value		pH value		pH value	
		9	11	9	11	9	11	9	11	9	11	9	11
1	1	0.5	1	1	1	1	1	1	9	0.5	1	1	1
2	2	1	2	2	3	1	2	1	15	1	1	1	1
3	3	1	2.5	5	5.5	2	2.5	3	19	1	1.5	1.5	2
4	4	3	3.5	5.5	6	3	4	5	21	2	3	3.5	4.5
5	5	4	5	6	7	4	5	6	24	4	5	5	6

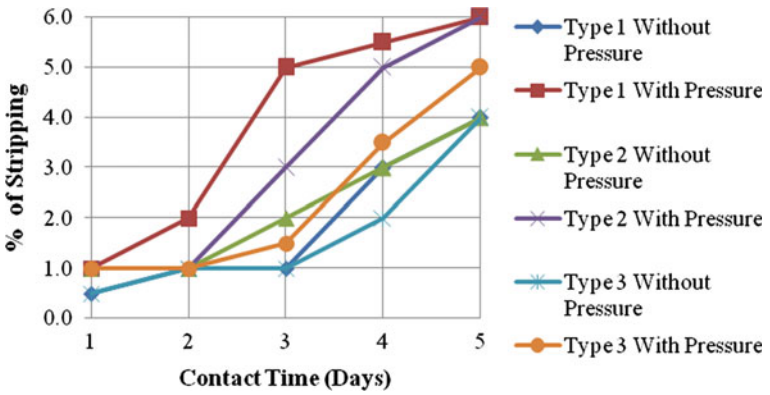

Fig. 4 Stripping of aggregate with water of pH value 9

Stripping value of coarse aggregate under alkaline condition. The bitumen–aggregate mixtures were tested under alkaline condition, that is, under pH values 9 and 11. The sample water is made alkaline with pH value 9 by pouring requisite quantity of dilute NaOH (N/5 normality) in 250 ml of water. The results are given in Table 4 and depicted in Fig. 4 for pH value 9.

It is observed from Fig. 4 that the stripping value of coarse aggregate increases with increase in immersion time and with application of external pressure. Aggregate Type 1 from Yamuna Nagar quarry shows more stripping with application of pressure for pH value 9.

The sample water is made alkaline with pH value 11 by pouring requisite quantity of dilute NaOH (N/5 normality) in 250 ml of water. The results are given in Table 4 and presented in Fig. 5 for pH value 11.

It is observed from Fig. 5 that the stripping value of coarse aggregate increases with increase in immersion time and with application of external pressure. Type 2 aggregate shows more stripping with application of pressure for pH value 11. Type 3 aggregate shows less stripping with pressure also for pH value 11.

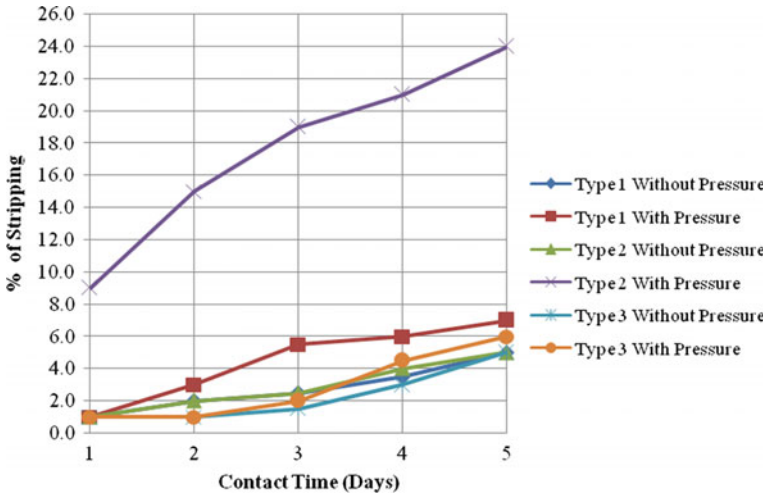

Fig. 5 Stripping of aggregate with water of pH value 11

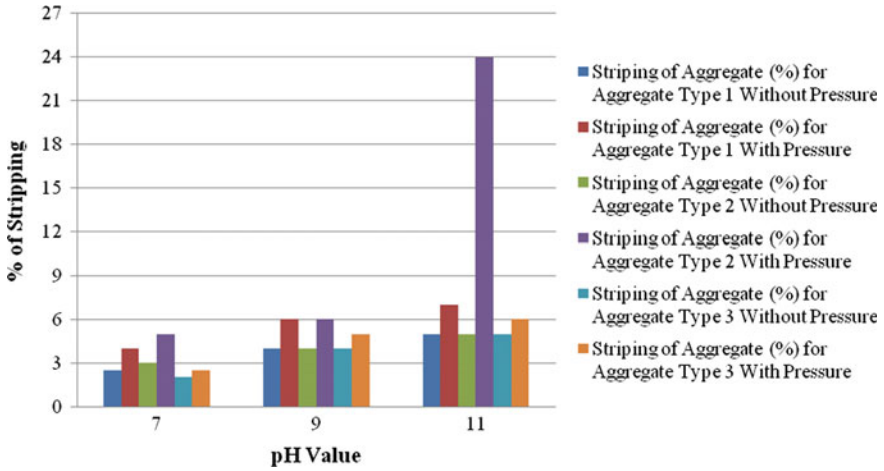

Fig. 6 Stripping of aggregate at the end of 5 days under alkaline condition

Figure 6 depicts the comparison of stripping values of all types of aggregate under pH values 7, 9 and 11 after 5 days of water immersion time. It is observed that more alkaline water results in more stripping with and without pressure.

Figure 7 shows stripping of Type 1 aggregate under acidic condition of pH 3 with external pressure.

Figure 8 shows stripping of Type 2 aggregate under alkaline condition of pH 11 with external pressure.

Fig. 7 Stripping of Type 1 aggregate under acidic condition pH 3 with pressure

Fig. 8 Stripping of Type 2 aggregate under alkaline condition pH 11 with pressure

5 Conclusions

It is observed that the stripping of aggregate gets affected due to variation in the standard conditions. The main conclusions drawn from the study are:

1. Accumulation of rain water on roads due to poor drainage conditions results in stripping of bitumen from aggregate. Stripping of aggregate increases with the increase in immersion time of rain water with coated aggregate.
2. The movement of traffic on road during and after the rain aggravates the phenomenon of stripping. The stripping increases with application of external pressure on the coated aggregate which shows that the effect of traffic needs to be properly simulated in the laboratory test conditions.

3. Accumulated rain water on the road may be acidic or alkaline depending upon the nature of industrial/sewage effluent in the side drains of the road. The more the acidic nature of water, the more is the stripping caused. Similarly, the alkalinity of water also affects the stripping adversely. The more is the alkalinity of water, the more is the stripping. Alkalinity of water is found to affect the stripping more adversely than the acidity of water.
4. The type of aggregate also affects stripping. Type 2 aggregate obtained from Dadri quarry exhibited maximum stripping, whereas the Type 3 aggregate from Narnaul quarry showed the least stripping under most of the varying conditions of test.
5. The standard conditions of test in the laboratory need to be modified to simulate the field conditions in a more realistic manner to accurately predict the stripping behaviour of aggregate.

References

1. IS 6241-1971: Method of test for determination of stripping value of road aggregate. Laboratory test, pp. 1–4 (1971)
2. Jain, P.K., Gupta, J.B.: Studies on mitigation of moisture damage in bituminous pavements. Indian J. Eng. Mater. Sci. **14**, 48–54 (2007)
3. Shakya, R., Sachdeva, S.N.: Stripping of aggregates due to unfavorable field conditions. Colloqium on Transportation System Engineering and Management, CTR, CED, NIT Calicut, India May 12–13, (2014) Paper Id-172
4. McCann, M., Sebaaly, P.: A quantitative evaluation of stripping potential in hot mix asphalt using ultrasonic energy for moisture accelerated conditioning. Transportation Research Record 1767, Washington, D.C., pp. 48–59 (2001)
5. Zhu, F.: Developing simple lab test to evaluate HMA resistance to moisture, rutting, thermal cracking distress. A Dissertation presented to The Graduate Faculty of the University of Akron, March 2008
6. Tarrer, A.R., Wagh, V.: The effect of the physical and chemical characteristics of the aggregate on bonding. SHRP-A/UIR-91–507, pp. 1–19 (1991)
7. Mehrara, A., Khodaii, A.: A review of state of the art on stripping phenomenon in asphalt concrete. Constr. Build. Mater. **38**, 423–442 (2013)

Application of Overall Index of Pollution (OIP) for the Assessment of the Surface Water Quality in the Upper Ganga River Basin, India

Anoop Kumar Shukla, C.S.P. Ojha and R.D. Garg

Abstract This study investigates effects of surface water quality of Upper Ganga river basin. The current study uses a general categorization system, viz. excellent, acceptable, slightly polluted, polluted and heavily polluted water for the quality assessment of surface water. Considering the Indian scenario, Indian Standards and CPCB have defined the concentration ranges for these classes. Further, water quality parameters, viz. hardness $CaCO_3$, biological oxygen demand (BOD), fluoride (F), dissolved oxygen% (DO%) and pH, were studied in basins for the pre-, post- and monsoon time periods. The numerical equations to convert the actual concentration values into pollution indices were used. On the basis of individual index data, an 'Overall Index of Pollution' (OIP) is calculated. The OIP is calculated at Uttarkashi and Rishikesh stations on Upper Ganga river basin using observed water quality data. Water quality degradation has occurred in the basin; consequently, the health status of the river has changed from acceptable to polluted.

Keywords Overall index of pollution · River basin · Surface water quality · Urbanization

1 Introduction

Water is a very essential and precious natural resource for sustaining life on this planet. Owing to the increase in population and indiscriminate utilization, this vital resource is now under tremendous pressure. The water quality is evaluated with

A.K. Shukla (✉) · C.S.P. Ojha · R.D. Garg
Department of Civil Engineering, Indian Institute of Technology,
Roorkee 247667, Uttarakhand, India
e-mail: anoopgeomatics@gmail.com

C.S.P. Ojha
e-mail: cspojha@gmail.com

R.D. Garg
e-mail: rdgarg@gmail.com

V. Garg et al. (eds.), *Development of Water Resources in India*,
Water Science and Technology Library 75, DOI 10.1007/978-3-319-55125-8_12

respect to its chemical, physical and biological characteristics [17]. Anthropogenic activities are potential drivers affecting the quality and quantity of available water resources on local, regional and global scale. These drivers pose a threat to the quality and quantity of water resources directly by increased anthropogenic water demands and water pollution. Uncontrolled population increase and economic hardship is forcing people to migrate to cities and thus causing rapid urbanization [5]. Anthropogenic activities in a river basin are directly correlated with the decline in water quality [8]. Population growth results in increase in food demands and agricultural/horticultural practices. During farming practices, various chemicals are introduced into the crop lands in the form of fertilizers, pesticides, herbicides, etc. Hence, runoff from the agricultural lands is the major source of non-point source pollution in rural river basins [16, 19, 22]. In urban river basins, leachates of landfill sites and storm water runoff are the major non-point sources of pollution [20], whereas direct dumping of untreated waste into the rivers, municipal discharges and industrial effluents, etc., are the major point sources of pollution. Water quality degradation has serious implications on human health and on river basin ecosystem [3, 6, 18]. Hence, water quality indicator parameters are often used in water quality assessment studies. With limited fresh water resources, water scarcity has become a global crisis throughout the world. The previous and most water scarcity evaluation studies paid attention to water quantity, but water quality was an ignored aspect. Ban et al. [3] observed that water quality monitoring programs monitor and produce large and complex datasets on parameters related to physicochemical and bacteriological properties of the river water. The analysis and interpretation of these datasets pose a challenge. Broadly, there are two methods to study the spatio-temporal variations in the water quality of a river: (i) direct methods where spatio-temporal variability in the water quality parameters are studied with the help of statistical analysis and graphs and (ii) indirect methods where different water quality/pollution indices based on environmental standards of surface water are used [14]. Hence, different regions/countries have developed their own water quality or pollution indices for different types of water uses based on their respective water quality standards/permissible pollution limits [15]. Water Quality Index (WQI) is a single numerical value that reflects the health of a water body by giving combined effects of various water quality parameters. WQI is a simplest and fastest indicator to assess water quality of a river [9].

There are several site-specific water quality/pollution indices available throughout the world for evaluating health status of river water. Few most frequently used ones are: Composite Water Quality Identification Index (CWQII) [3], River Pollution Index (RPI), Forestry Water Quality Index (FWQI) and National Sanitation Foundation Water Quality Index (NSFWQI) [9], Canadian Water Quality Index (CWQI) [7], Comprehensive water pollution index of China [12], Prati's implicit index of pollution [13], Horton's index, Nemerow and Sumitomo Pollution index, Bhargava's index, Dinius second index, Smith's index, Aquatic toxicity index, Chesapeake Bay water quality indices, Modified Oregon WQI, Li's regional water resource quality assessment index, Stoner's index, Two-tier WQI, Canadian WQI by Canadian Council of Ministers of the Environment (CCME),

Universal WQI, Overall Index of Pollution (OIP), Coastal WQI for Taiwan, etc. [1, 14]. Water Quality Indices help to analyze and interpret huge and complex water quality datasets to investigate the spatio-temporal variations in water quality of a river. Knowledge of composite effect of the water quality parameters is sometimes important to derive meaningful conclusions out of large water quality datasets. Water quality indices study the combined effects of variations in water quality parameters on river health and compare the water quality health status across different monitoring sites in a river basin. They determine the water quality parameters exceeding the permissible limits of a particular region/country and their changing trends [1]. Remote sensing and GIS are resourceful tools in preparing and analyzing spatial datasets. Remote sensing technology is often used in preparing maps of a region, whereas GIS helps in delineation of river basin boundaries, extraction of study area, etc. [10, 11, 21]. In this study, an Overall Index of Pollution (OIP) based on the Indian water quality standards is used to assess the state of the water quality across the Upper Ganga river basin for pre-monsoon, monsoon and post-monsoon.

2 Study Area

In India, the Ganges being the longest river, and also ranking among the world's top 20 rivers in regard to the quantity of water dispense, commences at the confluence of the Alaknanda and Bhagirathi rivers, which unite at Dev Prayag in Tehri Garhwal district of Uttarakhand, India, within the mountain range of the Himalayas. The river Bhagirathi is considered to be the actual source of Ganga which emerges from the base of Gangotri Glacier, Gaumukh. The River Ganga is segregated into three zones, viz. Upper Ganga basin, Middle Ganga basin and Lower Ganga basin. The area for the study, i.e., Upper Ganga river basin, is situated in the northern part of India which encompasses an area of around 22,292.1 km^2. The altitude of the study area varies from 7512 m in the Himalayan terrains to 275 m in the plains. Approximately 433 km^2 of the entire region of the basin is under glacier landscape and 288 km^2 is under fluvial landscape. The river basin of Ganga is located in the state of Uttarakhand, India, within the geographical coordinates 30° 38′–31° 24′ N latitude and 78° 29′–80° 22′ E longitude with an area of 22,292.1 km^2 up to Haridwar. About 60% of the basin is utilized for agricultural purpose (the primary harvest type being maize, wheat, sugarcane, rice, potato and bajra), whereas 20% of the basin is under the forest area, majorly in the upper mountainous region, and nearly 2% of the basin is permanently covered with snow in the mountain peaks. Most predominant soil groups found in the region are sand, clay, loam and their compositions. Due to favorable agricultural conditions, majority of the population practices agriculture and horticulture. However, a large portion of the total population lives in cities along Ganga river basin. Most of them work in urban or industrial areas. In the Upper Ganga river basin, the average annual rainfall varies from 550 to 2500 mm [4], and a major part of the rains is due to the south-westerly monsoon that prevails from July to late September. To understand the water quality of the Upper Ganga river basin,

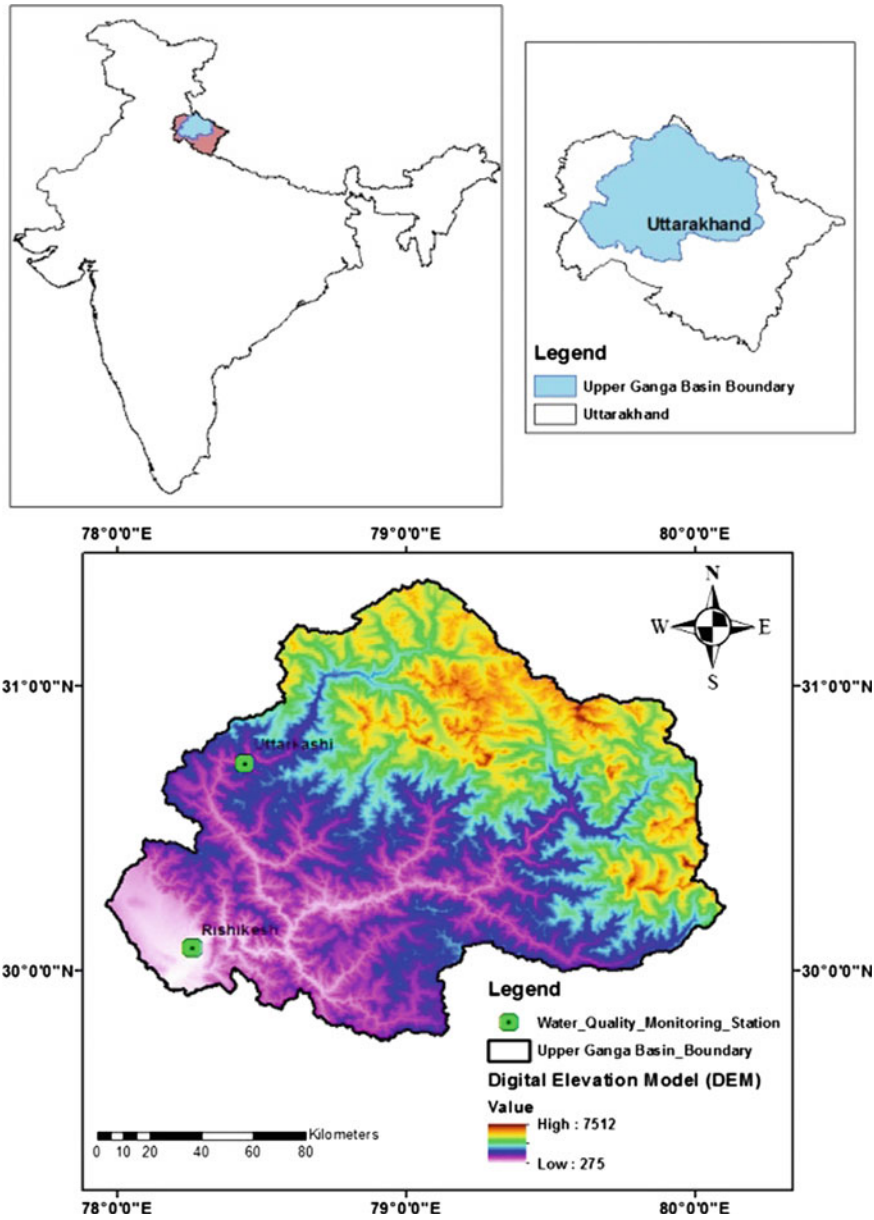

Fig. 1 Study area location and DEM of the Upper Ganga river basin with water quality monitoring stations

two water quality monitoring stations, viz. Uttarkashi and Rishikesh are chosen in the upper reach of the river basin. This part of the river basin comprises of hilly undulating terrain with moderately anthropogenic influences. Spatio-temporal changes in the water quality of these monitoring stations are examined over a period of year 2001–2012. The geographical location and other information of the study area Upper Ganga river basin are given in Fig. 1.

3 Materials and Methods

3.1 Data Collection

In this study, two types of datasets are used: (i) spatial datasets: (a) Advanced Spaceborne Thermal Emission and Reflection Radiometer (ASTER) 1 arc-second global Digital Elevation Model (DEM) of 30-m spatial resolution derived from Land Processes Distributed Active Archive Center (LP DAAC), National Aeronautics and Space Administration (NASA) (ii) Non-spatial datasets acquired from various departments of Government of India: (a) monthly water quality datasets of the year 2001–2012 from Central Water Commission (CWC) and (b) water quality reports from Central Pollution Control Board (CPCB), Uttar Pradesh Pollution Control Board (UPPCB), Uttarakhand Environment Protection and Pollution Control Board, National Institute of Hydrology (NIH) and CWC. Details of water quality monitoring stations are given in Table 1, and their locations are illustrated in Fig. 1.

3.2 Overall Index of Pollution (OIP)

A WQI called 'Overall Index of Pollution' (OIP) developed by Sargoankar and Deshpande [17] assesses the health condition of surface water, distinctively under the Indian conditions. It is a general categorization proposal based on the conception analogous to Prati et al. [13]. It takes into consideration the classification scheme of Central Pollution Control Board (CPCB), India, water quality standards of Indian Standards Institution (ISI), water quality standards of European Community (EC) and World Health Organization (WHO), etc. In this scheme, water quality status is reflected in stipulations of effects of pollution caused by specifications considered under the study. There are total five categories, viz. C_1:

Table 1 Location details of water quality monitoring stations

Sr. no.	Station name	Longitude	Latitude	River	District
1	Uttarkashi	78° 26′ 24″ E	30° 43′ 48″ N	Bhagirathi	Uttarkashi
2	Rishikesh	78° 15′ 36″ E	30° 04′ 48″ N	Ganga	Dehradun

Table 2 Water quality classification scheme. *Source* Sargoankar and Deshpande [17]

Classification	Class	Class index (score)	Concentration limit/ranges of water quality parameters				
			BOD (mg/L)	DO (%)	F (mg/L)	Hardness $CaCO_3$ (mg/L)	pH (pH unit)
Excellent	C_1	1	1.5	88–112	1.2	75	6.5–7.5
Acceptable	C_2	2	3	75–125	1.5	150	6.0–6.5 and 7.5–8.0
Slightly polluted	C_3	4	6	50–150	2.5	300	5.0–6.0 and 8.0–9.0
Polluted	C_4	8	12	20–200	6.0	500	4.5–5 and 9–9.5
Heavily polluted	C_5	16	24	<20 and >200	<6.0	>500	<4.5 and >9.5

Table 3 Mathematical expression for value function curves. *Source* Sargoankar and Deshpande [17]

S. no.	Parameter	Concentration range	Mathematical expressions
1.	BOD	<2 2–30	$x = 1$ $x = y/1.5$
2.	DO%	≤ 50 50–100 ≥ 100	$x = \exp(-(y - 98.33)/36.067)$ $x = (y - 107.58)/14.667$ $x = (y - 79.543)/19.054$
3.	F	0–1.2 1.2–10	$x = 1$ $x = ((y/1.2) - 0.3819)/0.5083$
4.	Hardness $CaCO_3$	≤ 75 75–500 >500	$x = 1$ $x = \exp(y + 42.5)/205.58$ $x = (y + 500)/125$
5.	pH	7 >7 <7	$x = 1$ $x = \exp((y - 7.0)/1.082)$ $x = \exp((7 - y)/1.082)$

excellent/pristine, C_2: acceptable/requires disinfection, C_3: slightly polluted/requires filtration and disinfection, C_4: polluted/requires special treatment and disinfection and C_5: heavily polluted/cannot be used. On the basis of water quality standards/limits of CPCB, ISI or other international agencies, the different concentration levels of the parameters are put into these classes. In favor to fetch the various water quality parameters into a common unit, an integer value (also known as class index) 1, 2, 4, 8 and 16 is assigned to each class, i.e., C_1, C_2, C_3, C_4 and C_5, respectively, in geometric progression. The class indices denote the pollution stage of water in numerical values (Table 2). Then the concentration value of the parameter is allocated to the individual mathematical equation of value function curves to obtain one number value called an Individual Parameter Index (IPI) or (P_i) (Table 3). IPI signifies the intensity of pollution for that particular factor.

Finally, the Overall Index of Pollution (OIP) is calculated as a mean of all the Individual Pollution Indices or (P_i) considered in the study and mathematically it is given by expression (1):

$$Overall\ Index\ of\ Pollution\ (OIP) = \frac{\Sigma_i P_i}{n} \quad (1)$$

where P_i is the pollution index for the ith parameter, i = 1, 2, …., n and n denotes the number of parameters.

4 Methodology

In this study, water quality datasets of three seasons/months, i.e., pre-monsoon period (May), monsoon period (July) and post-monsoon period (November), are analyzed. The water quality datasets of year 2001–2012 were used to compute OIP at each water quality monitoring station.

The study is conducted in two phases: (i) In the first phase, remote sensing and GIS techniques are used. First ASTER DEM data are used to delineate the Upper Ganga river basin boundary (ii) in the second phase, Individual Parameter Indices (IPIs) were calculated for each parameter at a given time interval. Finally, OIP is estimated for each water quality monitoring station across the Upper Ganga river basin over a period of 2001–2012. OIP method is used to comprehend the effects on the seasonal water quality of the rivers. The seasonal data were used to understand the effects of seasons on water quality of the basins.

5 Results and Discussion

Water quality data of only three seasons, i.e., pre-monsoon period (May), monsoon (July) and post-monsoon period (November), were considered in this study for a time span 2001–2012 (Table 4 (i–vi)). Three different seasons' data were used to understand the seasonal variations in water quality of the basins. All the OIP were computed for all the stations of the basins. In this study, the following seven water quality parameters were used for the basins: hardness $CaCO_3$, BOD, fluoride (F), DO% and pH. Different units of measurements are used to measure different water quality parameters. It is required to bring all these parameters to one commensurate unit to get a single integrated value of pollution. This step is called estimation of Individual Parameters Index (IPI) or (Pi). Hence, first step is to estimate the IPI of each water quality parameter. May, July and November months' water quality data of 2001–2012 were used to compute the Individual Parameter Indices (IPIs) at each station (Table 5 (i–vi)). The mathematical equations given in Table 3 were used to compute IPI of a respective water quality parameter. As discussed earlier in the

Table 4 Water quality parameters across Upper Ganga river basin for pre-monsoon, monsoon and post-monsoon seasons over periods of 2001–2012

(i) Pre-monsoon (May) season (2001)		
Parameters (Year 2001)	Water quality monitoring stations	
	Uttarkashi	Rishikesh
	May	May
BOD	1.1	1.1
DO%	**88**	**71**
F	0.19	0.23
Hardness $CaCO_3$	65	76
pH	**8.1**	**8.1**
(ii) Pre-monsoon (May) season (2012)		
Parameters (Year 2012)	Water quality monitoring stations	
	Uttarkashi	Rishikesh
	May	May
BOD	1.1	1.0
DO%	**73**	**81**
F	0.45	0.09
Hardness $CaCO_3$	45	33
pH	**7.8**	**7.8**
(iii) Monsoon (July) season (2001)		
Parameters (Year 2001)	Water quality monitoring stations	
	Uttarkashi	Rishikesh
	July	July
BOD	1.1	1.0
DO%	**77**	**60**
F	0.04	0.16
Hardness $CaCO_3$	60	67
pH	**8.1**	**8.1**
(iv) Monsoon (July) season (2012)		
Parameters (Year 2012)	Water quality monitoring stations	
	Uttarkashi	Rishikesh
	July	July
BOD	1.2	1.2
DO%	**64**	**75**
F	0.26	0.19
Hardness $CaCO_3$	24	23
pH	**7.7**	**8.0**

(continued)

Table 4 (continued)

(v) Post-monsoon (Nov) season (2001)		
Parameters (Year 2001)	Water quality monitoring stations	
	Uttarkashi	Rishikesh
	November	November
BOD	1.1	1.1
DO%	**89**	**64**
F	0.22	0.26
Hardness $CaCO_3$	68	74
pH	**8.1**	**8.1**
(vi) Post-monsoon (Nov) season (2012)		
Parameters (Year 2012)	Water quality monitoring stations	
	Uttarkashi	Rishikesh
	November	November
BOD	1.0	1.2
DO%	**73**	**77**
F	0.44	0.06
Hardness $CaCO_3$	34	56
pH	**7.6**	**7.8**

paper, the source of pollution and pollutants is different in rural and urban basins. In rural basin, the rivers are polluted mainly from non-point source of pollution, i.e., runoff from agricultural fields carrying chemical fertilizers. From the IPI results, it was observed that two water quality parameters, viz. DO% and pH, affect the water quality of the river basin. They showed high values of IPIs and significant variations than other five parameters, viz. BOD, fluoride (F) and hardness $CaCO_3$ in the river basin. All the OIP were computed for all the stations in the basin using water quality data of pre-monsoon (May), monsoon (July) and post-monsoon (November) months from 2001 to 2012. The data are given in (Table 5 (i–vi)).

The scheme of water quality categorization and the method adopted for estimating OIP was applied to assess the water quality status at Uttarkashi and Rishikesh sampling stations on the Upper Ganga river basin. The OIP was calculated by taking the average of all the pollution indices for individual water quality parameters. Figure 2a–c depicts the estimated OIP at Uttarkashi and Rishikesh stations in the pre-monsoon (May), monsoon (July) and post-monsoon (November) months from 2001 to 2012, and Fig. 3a–c location-wise. At Uttarkashi, the overall water quality was in the range class C_2 (1–2) acceptable for the pre-monsoon (May), monsoon (July) and post-monsoon (November) months from 2001 to 2012.

Table 5 Individual Parameter Indices (IPIs) and overall indices of pollution (OIP) computed at various water quality monitoring stations of Upper Ganga river basin over periods of 2001–2012 for pre-monsoon, monsoon and post-monsoon seasons

(i) Pre-monsoon (May) season (2001)		
Parameters	Water quality monitoring stations	
	Uttarkashi	Rishikesh
	May	May
BOD	1.00	1.00
DO%	1.33	2.49
F	1.00	1.00
Hardness $CaCO_3$	1.00	1.78
pH	2.76	2.76
OIP (2001)	**1.42**	**1.81**
(ii) Pre-monsoon (May) season (2012)		
Parameters	Water quality monitoring stations	
	Uttarkashi	Rishikesh
	May	May
BOD	1.00	1.00
DO%	2.36	1.81
F	1.00	1.00
Hardness $CaCO_3$	1.00	1.00
pH	2.09	2.09
OIP (2012)	**1.49**	**1.38**
(iii) Monsoon (July) season (2001)		
Parameters	Water quality monitoring stations	
	Uttarkashi	Rishikesh
	July	July
BOD	1.00	1.00
DO%	2.08	3.24
F	1.00	1.00
Hardness $CaCO_3$	1.00	1.00
pH	2.76	2.76
OIP (2001)	**1.56**	**1.80**
(iv) Monsoon (July) season (2012)		
Parameters	Water quality monitoring stations	
	Uttarkashi	Rishikesh
	July	July
BOD	1.00	1.00
DO%	2.97	2.22
F	1.00	1.00
Hardness $CaCO_3$	1.00	1.00

(continued)

Table 5 (continued)

(iv) Monsoon (July) season (2012)		
Parameters	Water quality monitoring stations	
	Uttarkashi	Rishikesh
	July	July
pH	1.91	2.52
OIP (2012)	**1.58**	**1.55**
(v) Post-monsoon (November) season (2001)		
Parameters	Water quality monitoring stations	
	Uttarkashi	Rishikesh
	November	November
BOD	1.00	1.00
DO%	1.27	2.97
F	1.00	1.00
Hardness $CaCO_3$	1.00	1.00
pH	2.76	2.76
OIP (2001)	**1.41**	**1.75**
(vi) Post-monsoon (November) season (2012)		
Parameters	Water quality monitoring stations	
	Uttarkashi	Rishikesh
	November	November
BOD	1.00	1.00
DO%	2.36	2.08
F	1.00	1.00
Hardness $CaCO_3$	1.00	1.00
pH	1.74	2.09
OIP (2012)	**1.42**	**1.44**

At Rishikesh, it was slightly polluted in 2006 in the months of monsoon (July) and post-monsoon (November) months. The slightly polluted range was class C_3 (2–4), and OIP of monsoon (July) and post-monsoon (November) months was 2.49 and 2.64, respectively. The graphs are shown in Fig. 3b, c. But it was acceptable in pre-monsoon (May) and range class is C_2 (1–2). At Uttarkashi sample station (the upper reach of river Ganga), water quality status was indicated as acceptable range class C_2 (1–2) in pre-monsoon (May), monsoon (July) and post-monsoon (November) months from 2001 to 2012. The results are shown in Fig. 2a–c. This is obvious because there are no drains meeting river Ganga upstream of this point in the stretch under consideration. Thus, based on the estimated values of OIPs, the sampling stations where pollution control measures are required can be

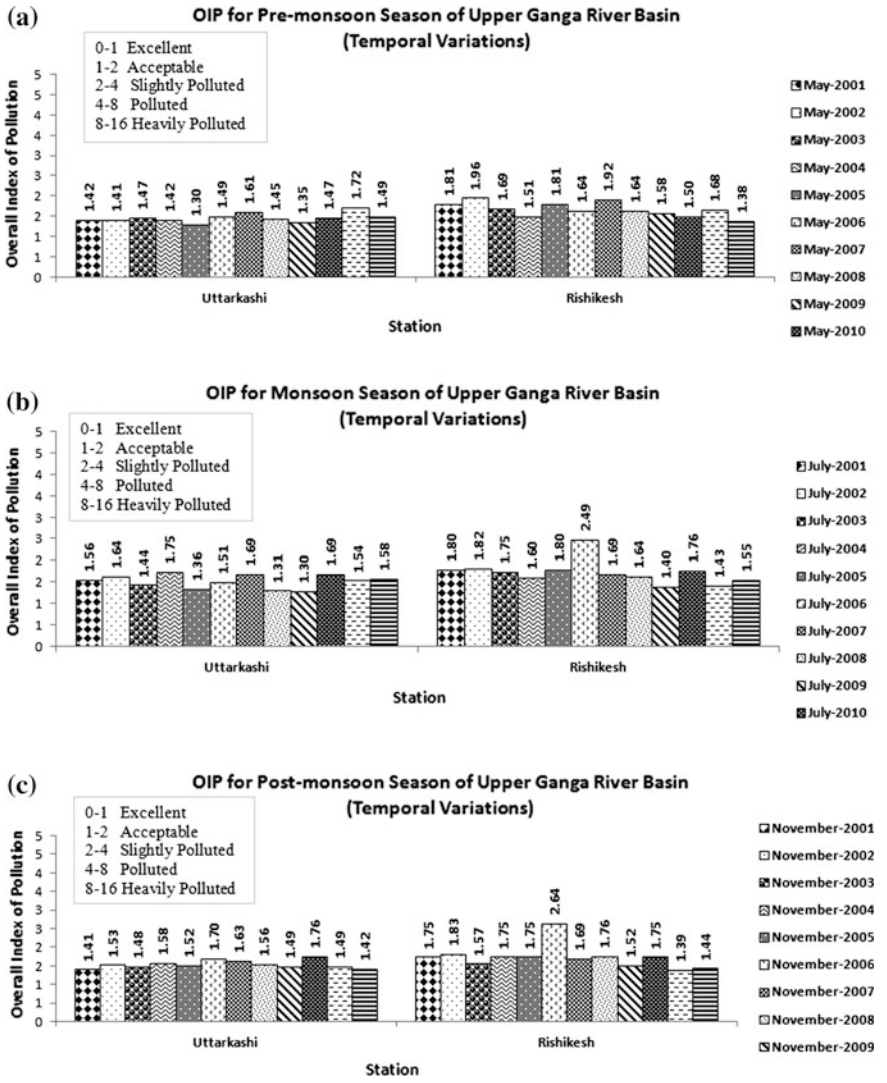

Fig. 2 **a**, **b**, **c** Overall index of pollution for Upper Ganga river basin (year-wise)

identified. The detail about the specific parameters responsible for pollution can be obtained by referring to the concentration ranges defined in Table 2, and the level of treatment required to make the water suitable for designed use at that location can be decided.

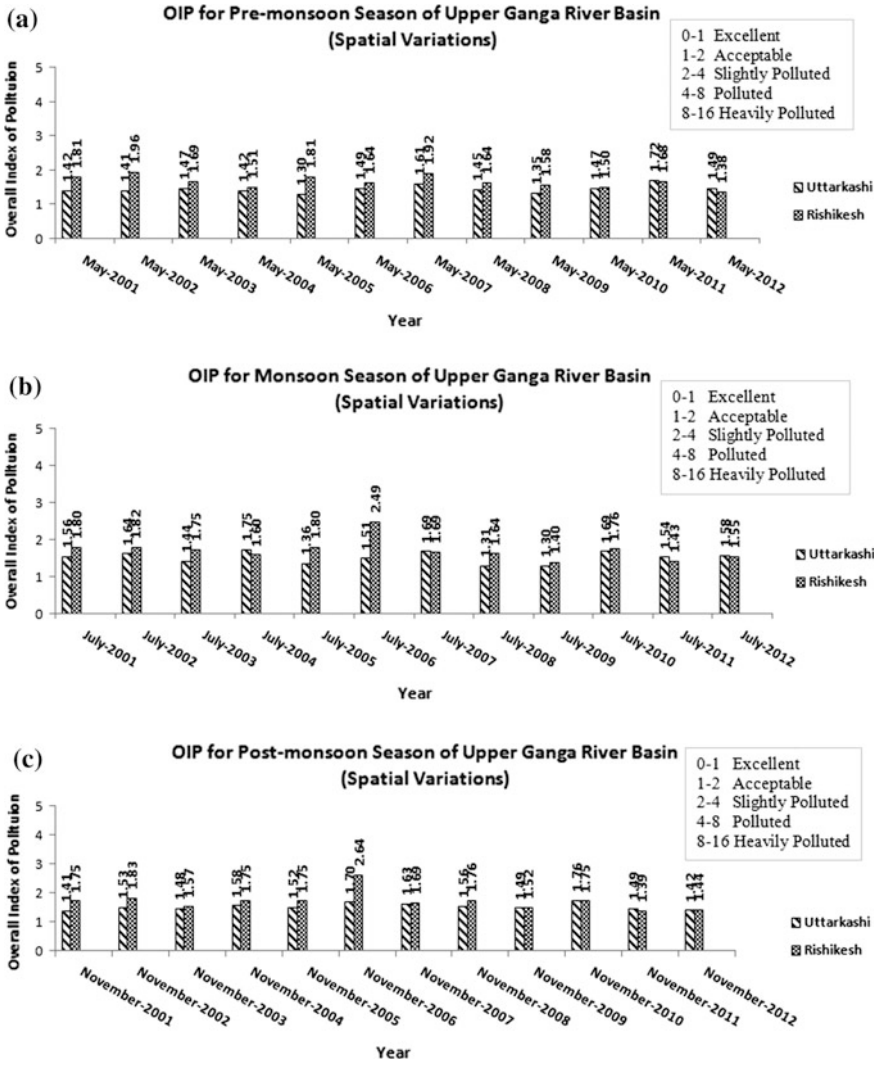

Fig. 3 **a**, **b**, **c**Overall index of pollution for Upper Ganga river basin (location-wise)

6 Conclusions

A comprehensive study is done to understand the effects of seasonal surface water quality of the Upper Ganga river basin. Water quality degradation has occurred in basins consequently affecting the health status of the river Ganga. It was observed that water quality parameters, viz. DO% and pH, showed high spatio-temporal

variations in the basin, whereas water quality parameters, viz. BOD, fluoride (F) and hardness $CaCo_3$, showed low spatio-temporal variations in basin. Almost similar trends of changes in OIP were observed for pre-monsoon, monsoon and post-monsoon seasons of Uttarkashi sample station with minor variations in the magnitude. Because Uttarkashi observation station is surrounded by hills and due to less population, they are not much influenced by human intervention. The river at these locations has high stream flow, and the waste generated in these areas is treated well before discharging it to the river. At Rishikesh, it was slightly polluted in 2006 in the months of monsoon (July) and post-monsoon (November) months. The slightly polluted range was class C_3 (2–4), and OIP of monsoon (July) and post-monsoon (November) months was 2.49 and 2.64, respectively. Water quality of Rishikesh station changed from acceptable to slightly polluted class due to pollutants load around this station.

OIP is a promising tool to study the effect of water quality changes across a river basin. Therefore, water quality assessment using OIP tool could help to assess and solve local and regional water quality-related problems over a river basin. This could help the policy makers and planners to understand the status of water pollution so that suitable strategies could be made for sustainable development in a river basin.

References

1. Abbasi, T., Abbasi, S.A.: Water Quality Indices. Elsevier (2012)
2. Ballester, M.V.R., de C. Victoria, D., Krusche, A.V., Coburn, R., Victoria, R.L., Richey, J.E., Logsdon, M.G., Mayorga, E., Matricardi, E.: A Remote sensing/GIS-based physical template to understand the biogeochemistry of the Ji-Parana River Basin (Western Amazonia). Remote Sensing of Environment, vol. 87(4), pp. 429–445 (2003)
3. Ban, X., Wu, Q., Pan, B., Du, Y., Feng, Q.: Application of composite water quality identification index on the water quality evaluation in spatial and temporal variations: a case study in Honghu Lake, China. Environ. Monit. Assess. **186**(7), 4237–4247 (2014)
4. Bharati, L., Jayakody, P.: A report on hydrology of the Upper Ganga River Basin. International Water-Management Institute. Project Report No: H043412 (2010). http://publications.iwmi.org/pdf/H043412.pdf (2010). Accessed 01 June 2014
5. Bjorklund, G., Connor, R., Goujon, A., Hellmuth, M., Moriarty, P., Rast, W., Warner K., Winpenny, J.: Demographic, economic and social drivers: Chapter 2. World Water Development Report 3 (2011). United Nations Educational, Scientific and Cultural Organization (UNESCO). http://webworld.unesco.org/ (2015). Accessed 05 Aug 2015
6. Chalmers, A.T., Van Metre, P.C., Callender, E.: The chemical response of particle-associated contaminants in aquatic sediments to urbanization in New England, USA. J. Contam. Hydrol. **91**(1), 4–25 (2007)
7. Farzadkia, M., Djahed, B., Shahsavani, E., Poureshg, Y.: Spatio-temporal evaluation of Yamchi Dam basin water quality using canadian water quality index. Environ. Monit. Assess. **187**(4), 1–15 (2015)
8. Haldar, S., Mandal, S.K., Thorat, R.B., Goel, S., Baxi, K.D., Parmer, N.P., Patel, V., Basha, S., Mody, K.H.: Water pollution of Sabarmati River—a Harbinger to potential disaster. Environ. Monit. Assess. **186**(4), 2231–2242 (2014)

9. Hoseinzadeh, E., Khorsandi, H., Wei, C., Alipour, M.: Evaluation of Aydughmush river water quality using the national sanitation foundation water quality index (NSFWQI), river pollution index (RPI), and forestry water quality index (FWQI). Desalin. Water Treat. **54**, 2994–3002 (2014)
10. Kindu, M., Schneider, T., Teketay, D., Knoke, T.: Drivers of land use/land cover changes in Munessa-Shashemene landscape of the south-central highlands of Ethiopia. Environ. Monit. Assess. **187**(7), 1–17 (2015)
11. Kumar, T., Jhariya, D.C.: Land quality index assessment for agricultural purpose using multi-criteria decision analysis (MCDA). Geocarto Int. **30**(7), 822–841 (2015)
12. Li, J., Meng, X., Zhang, Y., Li, J., Xia, L., Zheng, H.: Analysis of the temporal and spatial distribution of water quality in China's Major River Basins, and trends between 2005 and 2010. Front. Earth Sci. **9**(3), 463–472 (2015)
13. Prati, L., Pavanello, R., Pesarin, F.: Assessment of surface water quality by a single index of pollution. Water Res. **5**(9), 741–751 (1971)
14. Rai, R.K., Upadhyay, A., Ojha, C.S.P., Singh, V.P.: The Yamuna River Basin: Water Resources And Environment, vol. 66. Springer Science & Business Media (2011)
15. Rangeti, I., Dzwairo, B., Barratt, G.J., Otieno, F.A.O.: Ecosystem-specific water quality indices. Afr. J. Aquat. Sci. **40**(3), 227–234 (2015)
16. Rashid, I., Romshoo, S.A.: Impact of anthropogenic activities on water quality of Lidder River in Kashmir Himalayas. Environ. Monit. Assess. **185**(6), 4705–4719 (2013)
17. Sargaonkar, A., Deshpande, V.: development of an overall index of pollution for surface water based on a general classification scheme in indian context. Environ. Monit. Assess. **89**(1), 43–67 (2003)
18. Smith, V.H., Tilman, G.D., Nekola, J.C.: Eutrophication: impacts of excess nutrient inputs on freshwater, marine, and terrestrial ecosystems. Environ. Pollut. **100**(1), 179–196 (1999)
19. Tong, S.T., Naramngam, S.: Modeling the impacts of farming practices on water quality in the little miami river basin. Environ. Manage. **39**(6), 853–866 (2007)
20. Tsihrintzis, V.A., Hamid, R.: Modeling and management of urban stormwater runoff quality: a review. Water Resour. Manag. **11**(2), 136–164 (1997)
21. Wilson, C.O.: Land use/land cover water quality nexus: quantifying anthropogenic influences on surface water quality. Environ. Monit. Assess. **187**(7), 1–23 (2015)
22. Yang, F., Xu, Z., Zhu, Y., He, C., Wu, G., Qiu, J.R., Fu, Q., Liu, Q.: Evaluation of agricultural nonpoint source pollution potential risk over china with a transformed-agricultural nonpoint pollution potential index method. Environ. Technol. **34**(21), 2951–2963 (2013)

Part II
Climate Change & Global Warming

Transport of Contaminants During Groundwater Surface water Interaction

Jyoti Chaubey and Himanshu Arora

Abstract Groundwater–surface water (GW–SW) interaction plays an important role in alluvial aquifer-related studies because of the possible exchange of solutes along with water. Thus, the contamination of surface water may affect the groundwater quality as well. The present study provides a review of contaminant transport in groundwater due to GW–SW interaction. Various factors affecting the transport of contaminants during this interaction like flow of groundwater from surface water, contaminant characteristics and transport mechanisms have been studied. These transport mechanisms are formulated into a set of mathematical equations known as governing equations of groundwater flow and solute transport. The different numerical methods adopted for solving those equations have also been reviewed. The methods discussed are finite difference method, finite element method and meshfree methods.

Keywords Groundwater–surface water interaction · Contaminant transport · Numerical methods

1 Introduction

Increasing demand for groundwater as public water supply has made the susceptibility of groundwater contamination an important point of concern. There are various reasons of groundwater contamination, and interflow from surface water bodies is one of them (especially in alluvial aquifers). Various studies show the existence of interrelationship between surface water and groundwater [1].

J. Chaubey (✉) · H. Arora
Civil Engineering Department, IIT Roorkee, Roorkee 247667, India
e-mail: jyotidce@iitr.ac.in

H. Arora
e-mail: hiitrdce@iitr.ac.in

V. Garg et al. (eds.), *Development of Water Resources in India*,
Water Science and Technology Library 75, DOI 10.1007/978-3-319-55125-8_13

Contamination of any one of them will lead to the contamination of the other. Therefore, studying the transport processes of contaminant during the GW–SW interaction is of primary concern.

Factors involved in GW–SW interaction plays an important role in determining the direction of hydrologic exchange of water and contaminants. The transport of contaminants in GW–SW infiltration system can be determined by processes like advection, diffusion, dispersion, (ad)sorption/desorption and certain reactions including redox reactions, hydrolysis and biological transformations [2].

The solutions to the problems related to groundwater flow and solute transport are generally accomplished by solving the governing equations either by analytical methods or by using numerical methods. In general, the analytical methods provide an exact solution of the equations, but they are based on several assumptions (simplifying the inhomogeneity of the problem) which may not represent the actual complex field scenario. On the other hand, numerical methods account for the inhomogeneity of the nature and hence do not have such assumptions which might be severely violated in practice. Numerical methods can be broadly categorized into finite difference method (FDM), finite element method (FEM), finite volume method (FVM), method of characteristics (MOC), boundary element method and meshfree method (MM). A few of the above methods have been discussed briefly in the present study.

2 Contaminant Transport During GW–SW Interaction

The transport of contaminants during GW–SW interaction will primarily depend upon the direction of flow of water (interflow) which in turn will affect the exchange of contaminants. In the present study, the movement of contaminants from the surface water to groundwater has been studied. Hence, the contaminants from here onward will mean the contaminants present in groundwater due to the GW–SW interaction. Once the direction and amount of exchange is known, then the transport mechanisms of contaminants in groundwater need to be studied. In general, the factors responsible for the transport of contaminant during GW–SW interaction could be broadly categorized as:

- Direction of hydrologic exchange (water and contaminant) between groundwater and surface water
- Contaminants characteristics (conservative and non-conservative)
- Transport mechanisms (advection, diffusion and dispersion)
- Reactions (destructive and nondestructive)

These processes are elaborated in the proceeding sections.

2.1 Factors Affecting the Direction of Hydrologic Exchange Between GW and SW

The rate of interflow between hydraulically connected groundwater and surface water depends upon the relative levels of stream stage and the adjacent groundwater gradients, the position and geometry of the stream within the alluvial plain, groundwater aquifer geometry and parameters (such as hydraulic conductivity distribution, porosity) and boundary conditions [3].

Direction of the interflow depends upon the relative levels of water table and the free surface of the stream. If the water table level is lower than the free surface of the stream, then there will be effluent seepage from the stream, i.e., stream tends to lose surface water to the groundwater. On the other hand, stream gains water from groundwater when the adjacent water table is higher than the free surface of the stream. Flow-through streams gain groundwater through the upgradient bank and a portion of the stream bed and lose water through the downgradient bank [4] (Fig. 1).

Sophocleus [5] and Winter [6] performed analysis to investigate the groundwater coupling with the surface water and concluded that velocity, quantity and direction of exchange processes along with the spatial direction are controlled by gradient between surface water and groundwater table, leakage through riverbed material and hydraulic conductivity of soil.

Another important factor is the variable density-driven flow, where the density varies as a function of fluid pressure, suspended solid content in the fluid and

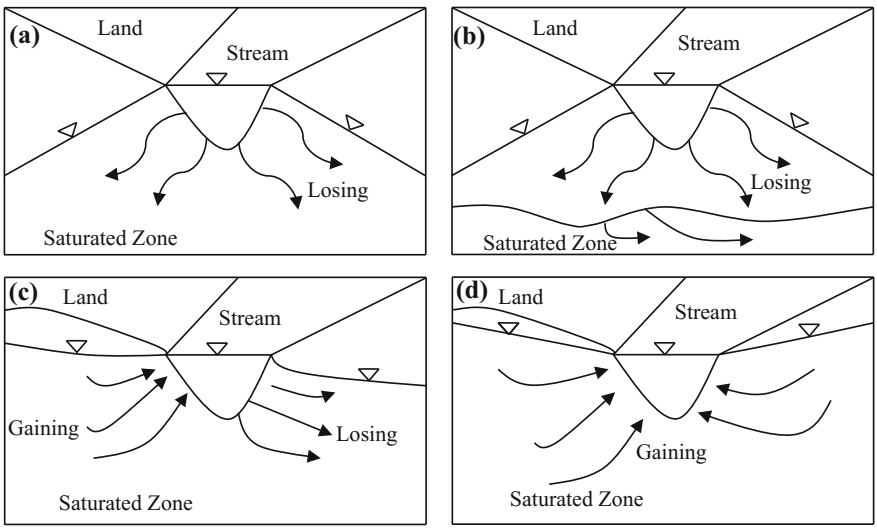

Fig. 1 Modes of exchange between surface and subsurface waters: (**a**) and (**b**) losing channel; (**c**) flow-through situation; (**d**) gaining channel

temperature of the fluid. Accounting for this flow is important in upconing below wells [7, 8], seawater intrusion in coastal regions, unstable flow phenomena where a denser fluid (seawater) overlies a less dense fluid (groundwater) [9] or wastewater disposal in deep salt formations [10].

Thus, the above studies show that the groundwater does interact with the surface water and the direction of flow depends upon the topography of terrain, the relative position of surface water bodies and groundwater flow systems, spatial distribution of flow system, i.e., hydraulic gradient and geomorphology of the region. Flow direction also depends upon the type of stream, that is whether it is ephemeral, intermittent or perennial, groundwater pumping (induced influent condition) and transpiration from groundwater by near-shore vegetation (which causes depression which in turn leads surface water to seep into the groundwater).

2.2 Contaminant Characteristics

Contaminants in groundwater are usually present as miscible solids/liquids or immiscible solids/liquids. Depending upon physicochemical properties, pollutants can broadly be classified as conservative pollutants and non-conservative pollutants. Conservative pollutants are the pollutants which do not transform physically or chemically to non-toxic substances under normal conditions (e.g., salts and metals). Pollutants which transform to non-toxic substances through physical, chemical or biological processes (e.g., organic pollutants, ammonia) are non-conservative pollutants. Conservative pollutants are long-lived and stable compounds which persist in the groundwater. Non-conservative pollutants degrade or transform into other compounds, and the transformation rate depends on the physical, chemical and biological conditions occurring within the groundwater.

2.3 Transport Mechanisms

Once contaminant (dissolved solute) enters the groundwater regime, the spreading of the contaminant is aided by several transport mechanisms which include advection, diffusion and hydrodynamic dispersion. A brief description of these mechanisms is given in the following sections.

2.3.1 Advection

The movement of the contaminant taking place due to groundwater flow is termed as advection. The amount of contaminant being transported is proportional to the contaminants concentration in flowing water and also the amount of groundwater flowing. Considering that the contaminant having an average concentration c is

occupying some part of void space of porous media (let volumetric fraction = n) and groundwater is flowing with an average velocity q, then the *advective flux*, J_{adv}, of the contaminant is given as (Bear and Cheng [11])

$$J_{adv} = nqc \tag{1}$$

Thus, advection is the mass flux of the contaminant passing through a unit area of porous flow domain, normal to the flow velocity, per unit time.

2.3.2 Diffusion

The process in which the contaminant movement in groundwater is due to the concentration gradient, i.e., contaminant will move from a region of larger concentration toward a region of lesser concentration, is known as diffusion. It is independent of groundwater flow, i.e., it will occur even if the fluid is at rest. Hence, diffusion process is irreversible with time. It may occur horizontally or vertically along the layers of the aquifer medium provided the concentration gradient exists along the layers [12]. Flux due to molecular diffusion (J) is based on Fick's law and is given as

$$J = -\left(D_d^*\right)_{ij}\frac{\partial c}{\partial x_j} \tag{2}$$

where $\left(D_d^*\right)_{ij}$ = coefficient of molecular diffusion and c = concentration of contaminant.

2.3.3 Hydrodynamic Dispersion

Dispersion refers to the spreading of the contaminants along the flow path (average groundwater flow velocity direction). This happens because groundwater flow velocity is not uniform at particle level. In the void space between the particles of porous media, the magnitude of flow velocity varies from zero at the surface of the particles to the maximum value at some intermediate point in the pore space (Fig. 2a). Also the direction of the flow velocity changes due to the irregular arrangement of particles in the media (Fig. 2b). This change in magnitude and direction of the groundwater flow velocity results in mixing along the flow path. This mixing is termed as mechanical dispersion which results in a dilution of the contaminant as the flow advances [12]. Molecular diffusion and mechanical dispersion together are termed as hydrodynamic dispersion (Fig. 2) [11].

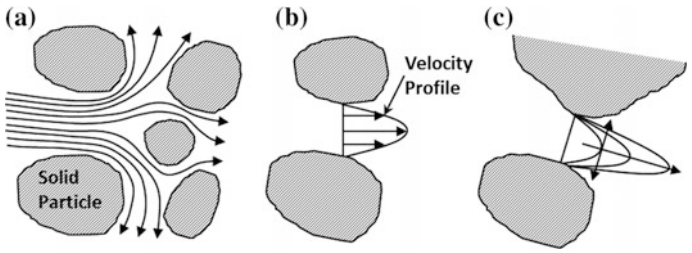

Fig. 2 Mechanical dispersion (**a**), (**b**), and molecular diffusion (**c**)

Coefficient of hydrodynamic dispersion (D_h) is given by

$$D_h = D + D_d^* \tag{3}$$

where D = coefficient of mechanical dispersion and D_d^* = coefficient of diffusion.

2.3.4 Adsorption

When contaminant enters the porous medium domain, there is a possibility that some of the contaminants may get adsorbed onto the particles (solids) of the porous medium. This adsorption results in the reduction of the contaminant concentration and retardation of the velocity of contaminant migration. Usually, the organic contaminants are more prone to adsorption and the presence of organic carbon in the aquifer material further enhances the process.

In earlier studies, contaminant transport was based on equilibrium adsorption models with two phases: sorbed immobile phase and dissolved phase. The sorbed immobile phase consisted of the solid phase and the sorbed contaminants onto it. Later on, it was concluded that this two-phase adsorption models of contaminant transport are applicable when the porous medium does not contain the mobile colloidal fines [13]. If mobile colloidal fines are present in the porous medium, then the contaminant transport models are based on equilibrium adsorption models with three phases: mobile colloidal phase, mobile liquid phase and the immobile solid phase [14].

2.4 Reactions

Reactions occurring in the saturated porous medium domain can be classified into two—destructive and nondestructive. Destructive reactions irreversibly transform or destroy the contaminant into other compounds. These reactions include abiotic reactions, biodegradation and radioactive decay. Nondestructive reactions are reversible processes which do not transform or destroy the compound, but may result in change in contaminant concentration. These reactions include precipitation and dissolution, adsorption and ion exchange.

3 Numerical Methods for Contaminant Transport Modelling

Contaminant transport during GW–SW interaction is usually studied either by field experiments or by modelling approach. Field experiments involve injecting tracers into the stream area of interest, and the quantity of the tracer in the groundwater is monitored near the reach. This tracer breakthrough curve is used to infer quantitatively the GW–SW exchange along the reach. Modelling approach involves the development of conceptual model and solving them by numerical methods to assess the GW–SW exchange during interaction. This approach is discussed in detail in the following section.

3.1 Modelling Approach

The modelling of groundwater flow and contaminant transport can be broadly categorized into following steps: (1) Representing the real physical study domain with a mathematical model, i.e., the governing equations of flow and transport. (2) Defining the problem in terms of the variables to be identified (estimated). (3) Obtaining the hydrogeological parameters of the study area and source and sink terms. (4) Prescribing the boundary conditions and initial conditions and obtaining the solution (estimating the variable) by applying the suitable solution method [15].

The three-dimensional contaminant transport equation is given by [16]

$$\frac{\partial c}{\partial t} + \frac{v_i}{R}\frac{\partial c}{\partial x_i} - \frac{\partial}{\partial x_i}\left(\frac{D_{ij}}{R}\frac{\partial}{\partial x_j}\right) + \lambda c = 0 \tag{4}$$

where i, j = 1, 2, 3 for the flow in three directions; c = concentration of contaminant; D_{ij} = dispersion coefficient along i direction due to flow in j direction; v_i = velocity of flow of water along i direction; λ = radioactive decay constant of the contaminant; and R = retardation factor related to adsorption and/or chemical reaction.

The velocity in Eq. 4 is given by,

$$v_i = \frac{\partial h}{\partial x_i}\frac{K_{ii}}{\phi} \tag{5}$$

where K_{ii} = hydraulic conductivity along i direction; h = potentiometric head; and ϕ = aquifer porosity.

The head field (h) of Eq. 5 is estimated from the three-dimensional groundwater flow equation given as [16]

$$\frac{\partial}{\partial x_i}\left(K_{ii}\frac{\partial h}{\partial x_j}\right) - W = S_s\frac{\partial h}{\partial t} \tag{6}$$

where K_{ii} = hydraulic conductivity along i coordinate axes assumed to be parallel to the principal permeability directions; W = volumetric flux per unit volume (for any abstraction from the aquifer, W = sink term, and for recharge into the aquifer, W is source term); t = time; and S_s = specific storage.

Solution of Eqs. 4 and 6 is the spatiotemporal distribution of c and h which satisfy the above equations for a given set of initial and boundary conditions, source/sink terms and flow and transport parameters. Modeling of groundwater contaminant transport involves the solution of both the equations which are either solved independently or simultaneously. Solution can be obtained by analytical method or by numerical method. Though the solutions obtained by analytical methods are exact solutions, they are based on numerous assumptions which do not hold good in complex real field scenarios. On the other hand, numerical methods, though provide approximate solution, involve lesser assumptions.

3.2 Solution Methods for Numerical Model

Among many, the three classical choices for the numerical solution of governing equations of groundwater flow and solute transport are FDM, FEM and FVM.

3.2.1 Finite Difference Method (FDM)

FDM is the one of the oldest numerical methods for solving the partial differential equations and is based upon the application of Taylor series expansion to approximate the differential equations. In this method, the continuous system described by Eqs. 4 and 6 is replaced by a finite set of discrete spatial and temporal points. Partial derivatives in equations are replaced by difference equation obtained from the truncated Taylor series expansion. This substitution leads to the formation of systems of simultaneous linear algebraic difference equations, the solution of which yields spatiotemporal distribution of concentration and head. A discretized flow and solute transport domain is shown in Fig. 3.

Let u be the variable, then derivative of c can be expressed as

$$\frac{\partial c}{\partial x} \approx \frac{c_i - c_{i-1}}{\Delta x} \tag{7}$$

$$\frac{\partial c}{\partial x} \approx \frac{c_{i+1} - c_i}{\Delta x} \tag{8}$$

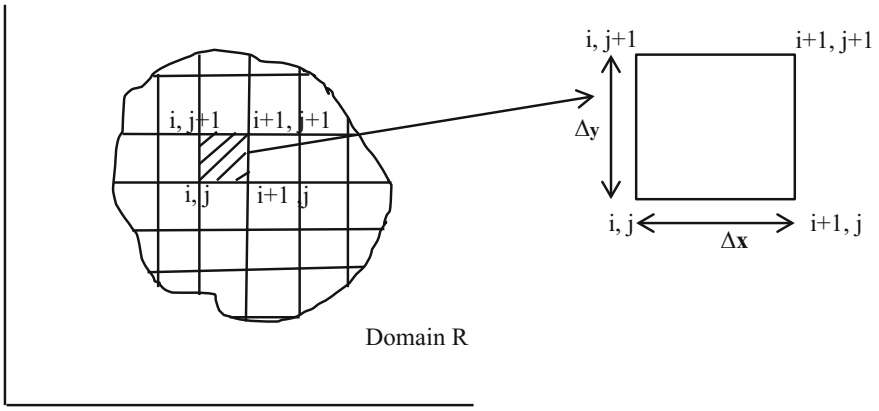

Fig. 3 Flow and solute transport domain divided into cells by a mesh of grid lines

$$\frac{\partial c}{\partial x} \approx \frac{c_{i+1} - c_{i-1}}{2\Delta x} \tag{9}$$

Equations (7)–(9) are referred to as backward, forward and centered finite difference approximations of $\partial c/\partial x$, respectively.

For example, taking a case of horizontal flow, with no induced abstraction, the governing differential equation for a confined aquifer reduces to

$$\frac{\partial^2 h}{\partial x^2} + \frac{\partial^2 h}{\partial y^2} = \frac{S}{T}\frac{\partial h}{\partial t} \tag{10}$$

Forward difference simulation for time derivative of above equation, for i, j, $t = (k + 1)\Delta t$,

$$\frac{h_{i,j-1}^{k} - 2h_{ij}^{k} + h_{i,j+1}^{k}}{(\Delta x)^2} + \frac{h_{i-1,j}^{k} - 2h_{ij}^{k} + h_{i+1,j}^{k}}{(\Delta y)^2} = \frac{S}{T}\frac{h_{ij}^{k+1} - h_{ij}^{k}}{\Delta t} \tag{11}$$

In above equation, there is one unknown and the equation is known as explicit scheme. Backward difference simulation for time derivative of Eq. 10, for i, j, $t = (k + 1)\Delta t$,

$$\frac{h_{i,j-1}^{k+1} - 2h_{ij}^{k+1} + h_{i,j+1}^{k+1}}{(\Delta x)^2} + \frac{h_{i-1,j}^{k+1} - 2h_{ij}^{k+1} + h_{i+1,j}^{k+1}}{(\Delta y)^2} = \frac{S}{T}\frac{h_{ij}^{k+1} - h_{ij}^{k}}{\Delta t} \tag{12}$$

In above equation, there are five unknowns and the equation is known as implicit scheme because the equation will have to be solved as a system of simultaneous equations for the unknowns. Although explicit scheme involves less computational time, implicit scheme is used for numerical methods because of the unconditional stability of implicit equation.

In FDM, the governing flow and transport partial differential equation (PDE) is discretized into rectangular grids, which may become cumbersome for the larger study domain with complex geometries. This led to the application of an integral form of the PDEs and subsequently led to the development of FEM.

3.2.2 Finite Element Method (FEM)

In FEM discretization process is started with the equation's integral form. Partial differential equation is transformed into an integral equation which includes derivatives of first order only. Then integration is performed numerically over elements into which considered domain is divided.

$$I = \iint F\left(x, y, U_1, U_2, \frac{\partial U_1}{\partial x}, \frac{\partial U_2}{\partial x}, \frac{\partial U_1}{\partial y}, \frac{\partial U_2}{\partial y}\right) dxdy \tag{13}$$

where x, y, U_1(x, y) and U_2(x, y) are independent variables. Objective is to minimize I or ∂I = 0.

For example, integral function for 2D steady-state flow equation in domain R can be written as

$$\text{Minimize } I = 0.5 \iint \left[K_{xx} \left(\frac{\partial h}{\partial x}\right)^2 + K_{yy} \left(\frac{\partial h}{\partial y}\right)^2 \right] dxdy \tag{14}$$

Objective equation becomes

$$[S]\{h\} = 0 \tag{15}$$

where [S] = global matrix of coefficients which incorporates properties of porous medium and geometry and {h} = vector of unknown heads at the nodes of the element into which the entire domain is divided.

3.2.3 Meshfree Method (MM)

Above-mentioned methods are the classical methods which use the temporal and spatial discretization of domain. Latest development in the field of solving the governing groundwater flow and solute transport differential equation is the meshfree algebraic methods. In MM, predefined meshes are not required; instead, just the set of scattered nodes within the problem domain including boundaries is used. Since mesh is not created in this method, it is saves substantial time in modeling and simulation [17].

There are a number of meshfree approximation methods like moving least-squares (MLS), natural element method (NEM), reproducing kernel particle method (RKPM), smoothed particle hydrodynamics (SPH), radial basis function

method (RBF), point collocation method (PCM). Features of MM include the absence of mesh, computationally inexpensive, shape functions of any desired order of continuity can be constructed, and the convergence results of MM are considerably better than the results obtained by other mesh-based shape functions [17].

The use of the type of method depends upon the requirement of the problem posed. Suppose if discontinuity has to be addressed in the solution of the governing PDE, then MM can be applied. The imposition of essential boundary conditions requires certain attention in MM and may degrade the convergence of the method. In that case, FDM or FEM can be used.

3.3 Contaminant Transport Models

Once a numerical model with a suitable solution method has been constructed, to solve the large number of set of simultaneous algebraic equations, algorithms with

Table 1 Software used for groundwater flow and solute transport modeling

S. no.	Model	Authors	Description
1	**MODFLOW** (modular finite difference groundwater flow model)	McDonald and Harbough [18]	Simulates 3D groundwater flow using cell-centered FDM
2	**MOC3D** (three-dimensional method-of-characteristics groundwater flow and transport model)	Konikow et al. [19]	Simulates 3D flow using cell-centered FDM and MOC for solute transport
3	**MT3DMS** (modular 3D multi-species transport model for simulation of advection, dispersion and chemical reactions of contaminants in groundwater systems)	Zheng et al. [20]	Simulates 3D groundwater flow using MODFLOW and solute transport by modified MOC
4	**FEMWATER** (three-dimensional finite element model of water flow through saturated–unsaturated media)	Lin et al. [21]	Simulates 3D density-dependent flow through variably saturated porous media and three-dimensional Eulerian–Lagrangian model of solute transport
5	**Random-Walk** (random-walk solute transport model for selected groundwater quality evaluations)	Prickett et al. [22]	Simulates groundwater flow using FDM and solute transport by particle-in-a-cell method (for advection) and random-walk method (for dispersion)
6	**FEFLOW** (finite element subsurface flow and transport simulation system)	Diersch [23]	Simulates 3D density-dependent saturated and unsaturated flow and solute transport using FEM
7	**STOMP** (subsurface transport over multiple phases)	Nichols et al. [24]	Coupled solution of groundwater flow and solute transport using finite difference volume approach
8	**PHAST** (program for simulating groundwater flow, solute transport and multicomponent geochemical reactions)	Parkhurst et al. [25]	Simulates multicomponent, reactive solute transport in 3D saturated groundwater flow systems using FDM

iterative procedures are required which are usually executed with the help of computer codes (or softwares) [11]. Some of the widely used computer codes are listed in Table 1.

4 Conclusion

The increasing use of groundwater for consumptive purposes has increased the risks of its vulnerability toward contamination. Among various causes of groundwater contamination, contamination from surface water sources is a major threat to the groundwater. For the effective management of groundwater sources, the understanding of transport of contaminants during GW–SW interaction is needed. For modelling the contaminant transport, along with the mechanism of transport of contaminant in porous media, a proper understanding of groundwater surface water interaction is also needed.

References

1. Sophocleous, M.A.: Interactions between groundwater and surface water: the state of the science. Hydrogeol. J. **10**, 52–67 (2002)
2. Schwarzenbach, R.P., Giger, W., Hoehn, E., Schnelder, J.K.: Behavior of organic compounds during infiltration of river water to groundwater. Field Stud. Environ. Sci. Technol. **17**, 472–479 (1983)
3. Woessner, W.W.: Stream and fluvial plain groundwater interaction—rescaling hydrologic thought. Ground Water **38**(3), 423–429 (2000)
4. Jackli, J.: Exchange of groundwaters and surface waters. J. Hydrol. **56**, 125–143 (1974)
5. Sophocleous, M.A.: Managing water resources system: why safe yield is not sustainable. Ground Water **35**(4), 561–567 (1997)
6. Winter, T.C.: Relation of streams, lakes, and wetlands to groundwater flow systems. Hydrog. J. **7**, 28–45 (1999)
7. Diersch, J.G., Prochnow, D., Thiele, M.: Finite-element analysis of dispersion-affected saltwater upconing below a pumping well. Appl. Math. Model. **8**, 305–312 (1984)
8. Reilly, T.E., Goodmann, A.S.: Analysis of saltwater upconing beneath a pumping well. J. Hydrol. **9**, 169–204 (1987)
9. Liu, H.H., Dane, J.H.: A criterion for gravitational instability in miscible dense plumes. J. Contam. Hydrol. **23**(3), 233–243 (1996)
10. Oldenburg, C.M., Pruess, K.: Dispersive transport dynamics in a strongly coupled groundwater-brine flow system. Water Resour. Res. **31**, 289–302 (1995)
11. Bear, J., Cheng, A.H.D.: Modeling Groundwater Flow and Contaminant Transport, vol. **23**. Springer, New York (2010)
12. Fetter, C.W.: Contaminant Hydrogeology. Macmillan Publishing Company (1993)
13. Sen, T.K., Khilar, K.C.: Review on subsurface colloids and colloid-associated contaminant transport in saturated porous media. Adv. Colloid Interface **119**, 71–96 (2006)
14. Sen, T.K., Nalwaya, N., Khillar, K.C.: Colloid-associated contaminant transport in porous media: 2. Math. Model. AIChE J. **48**(10), 2375–2385 (2002)

15. Blessent, D., Therrien, R., MacQuarrie, K.: Coupling geological and numerical models to simulate groundwater flow and contaminant transport in fractured media. Comput. Geosci. **35**, 1897–1906 (2009)
16. Bear, J.: Hydraulics of Groundwater. McGraw-Hill Series (1979)
17. Mategaonkar, M., Eldho, T.I.: Two-dimensional contaminant transport modeling using meshfree point collocation method (PCM). Eng. Anal. Bound. Elem. **36**, 551–561 (2012)
18. McDonald, M.G., Harbaugh, A.W.: A modular Three-Dimensional Finite-Difference Ground-Water Flow Model. U.S. Geological Survey Open-File Report 83–875 (1984)
19. Konikow, L.F., Goode D.J., Hornberger, G.Z.: A Three-Dimensional Method-of-Characteristics Solute-Transport Model (MOC3D). U.S. Geological Survey Water-Resources Investigations Report 96–4267. http://pubs.usgs.gov/wri/1996/4267/report.pdf (1996). Accessed 06 Jun 2016
20. Zheng, C., Wang, P.P.: MT3DMS, A Modular Three-Dimensional Multi-Species Transport Model for Simulation of Advection, Dispersion and Chemical Reactions of Contaminants in Groundwater Systems. Documentation and User's Guide. http://www.geology.wisc.edu/courses/g727/mt3dmanual.pdf (1999). Accessed 06 Jun 2016
21. Lin, H.C., Richards, D.R., Yeh, G.T., Cheng, J.R., Chang, H.P., Jones, N.L.: FEMWATER: A Three-Dimensional Finite Element Computer Model for Simulating Density Dependent Flow and Transport. U.S. Army Engineer Waterways Experiment Station Technical Report. http://homepage.usask.ca/~mjr347/gwres/femwref.pdf (1996). Accessed 06 Jun 2016
22. Prickett, T.A., Naymik, T.G., Lonnquist, C.G.: A random-walk solute transport model for selected groundwater quality evaluations. Bulletin 65 Illinois State Water Survey. http://www.isws.illinois.edu/pubdoc/b/iswsb-65.pdf. Accessed 06 Jun 2016
23. Hans-Jörg, G.D.: FEFLOW–Finite Element Modeling of Flow, Mass and Heat Transport in Porous and Fractured Media. Springer, Berlin (2014)
24. Nichols, W.E., Aimo, N.J., Oostrom, M., White, M.D.: STOMP Subsurface Transport Over Multiple Phases: Application Guide. PNNL-11216 (UC-2010), Pacific Northwest National Laboratory, Richland, Washington. http://www.pnl.gov/main/publications/external/technical_reports/PNNL-15782.pdf (1997). Accessed 06 Jun 2016
25. Parkhurst, D.L., Kipp, K.L., Engesgaard, P., Charlton, S.R.: PHASTA Program for Simulating Ground-Water Flow, Solute Transport, and Multicomponent Geochemical Reactions. U.S. Geological Survey Techniques and Methods 6-A8. http://pubs.usgs.gov/tm/2005/tm6A8/ (2004). Accessed 06 Jun 2016

Spatiotemporal Variations in the Precipitation Deficit and Groundwater Recharge Deficit of Mula–Mutha Watershed, Maharashtra, India

Satyavati Shukla, M.V. Khire and S.S. Gedam

Abstract The Mula–Mutha watershed of Maharashtra, India, is under chronic water shortage since past few decades. Due to uneven distribution of rainfall across the watershed, majority of its population are reliant on groundwater resources for its domestic and agricultural demands. In this study, an attempt is made to investigate the spatiotemporal variations in the precipitation deficit and groundwater recharge deficit of Mula–Mutha watershed using the Standardized Precipitation Index (SPI) and Standardized Water-Level Index (SWI), respectively. These variations are studied by generating SPI and SWI maps in geographic information system (GIS) environment for two seasons, viz. pre-monsoon (May) and post-monsoon (October), of the years 2001–2010. This paper helps to identify the groundwater stress zones across the study area where proper management of groundwater resources is required. Results reveal that in the Mula–Mutha watershed hydrologic stress varies highly in time and space. Few zones are identified where groundwater stress is more frequent. There are no regular spatiotemporal patterns observed in the precipitation deficit and groundwater recharge deficit across the region.

Keywords GIS · Groundwater · Precipitation · Spatialtemporal · Watershed

1 Introduction

In a region, severe water scarcity results due to various factors such as inadequate precipitation, high evapotranspiration, Land Use/Land Cover (LULC) transformations and over-exploitation of water resources. As these factors are not linearly correlated with each other, they vary in time and space [4]. There is always

S. Shukla (✉) · M.V. Khire · S.S. Gedam
Centre of Studies in Resources Engineering, Indian Institute of Technology Bombay, Mumbai 400076, Maharashtra, India
e-mail: satyashukla@iitb.ac.in

V. Garg et al. (eds.), *Development of Water Resources in India*,
Water Science and Technology Library 75, DOI 10.1007/978-3-319-55125-8_14

uncertainty and variability in the occurrence of rainfall and groundwater in space and time [10]. In India, the national groundwater abstraction rate is one of the highest in the world along with USA [8]. In semiarid regions of India, groundwater recharge is mainly dependent on rainfall occurred during monsoon season. Therefore, variations in the rainfall directly affect its water resources [3]. Groundwater is the primary source of water supply to fulfill domestic, agricultural, industrial and ecological water demands in these regions. During water stress situations, it provides the resilience to water supplies. Yet groundwater depletion has accelerated in the past few decades [6]. Assessment of stress in groundwater resources helps in planning the groundwater stress-coping measures. Mula–Mutha watershed of Maharashtra state, India, falls under semiarid climatic zone. Due to dissimilarities in the geological, topographical, climatological and hydro-chemical conditions across the watershed, the groundwater behavior in this region is highly complex. The majority of the region is a part of Deccan Trap where the occurrence of groundwater is controlled by geological structures, soil, lithology, LULC, rainfall and recharge conditions [13]. This region is facing a chronic water shortage for the last few decades. With an uneven distribution of rainfall across the watershed, majority of its population are dependent on groundwater resources for its domestic and agricultural demands [7, 11]. If the abstraction of groundwater is not controlled, soon the groundwater in the region may exceed safe exploitation levels. With uncertainties in future climatic changes, achieving developmental targets along with sustainable groundwater management is extremely challenging. Hence, groundwater management is an important factor in conserving sustainable conditions in semiarid regions [1, 15]. GIS aids in preparing and analyzing spatial datasets such as satellite data and digital elevation model (DEM) data. It helps in delineation of watershed boundaries, extraction of study area and pictorial presentation of spatial analysis results, etc. Hence, spatiotemporal changes occurring in a watershed are often studied using GIS [5]. The groundwater level (GWL) data obtained from Piezometers/groundwater observation wells are often used to understand the GWL fluctuations in a region [2, 9]. GWL varies with different seasons; hence, GWL data of pre-monsoon and post-monsoon seasons of the years 2001–2010 are analyzed for the study area. The aim of this study is to investigate the spatiotemporal variations in the precipitation deficit and groundwater recharge deficit of the Mula–Mutha watershed using the SPI and SWI, respectively. These variations are studied by generating SPI and SWI maps in GIS environment for both pre-monsoon and post-monsoon seasons over the period of 2001–2010. This paper helps to identify the groundwater stress zones across the study area where proper management of groundwater resources is required. The results obtained are analyzed, compared and correlated to understand spatiotemporal variations in the precipitation deficit and groundwater recharge deficit in the study area.

2 Study Area

Mula–Mutha watershed of Maharashtra state, India, extends from Western Ghats in the west to Deccan plateau in the east as shown in Fig. 1. It falls under semiarid climatic zone of India and covers a total area of 2,918.20 km^2. The study area has longitudinal extent of 73° 20′ to 74° 20′ and latitudinal extent of 18° 17′ to 18° 44′. Mula, Mutha, Pauna, Ambi, Ram, Mose and Walki are the major rivers contributing this watershed. Mula and Mutha rivers meet in the heart of the Pune city. Mega city Pune falls in the study area along with Pimpri-Chinchwad industrial zone. The altitude in the watershed ranges from 495 to 1327 m as shown in Fig. 2. Slope in the watershed varies from 0 to 68.05° as shown in Fig. 3. Geology mainly comprises of basaltic lava flows of depth 100–300 m. The major soil group in the region is medium black soil. Due to high water demands from urban and agricultural

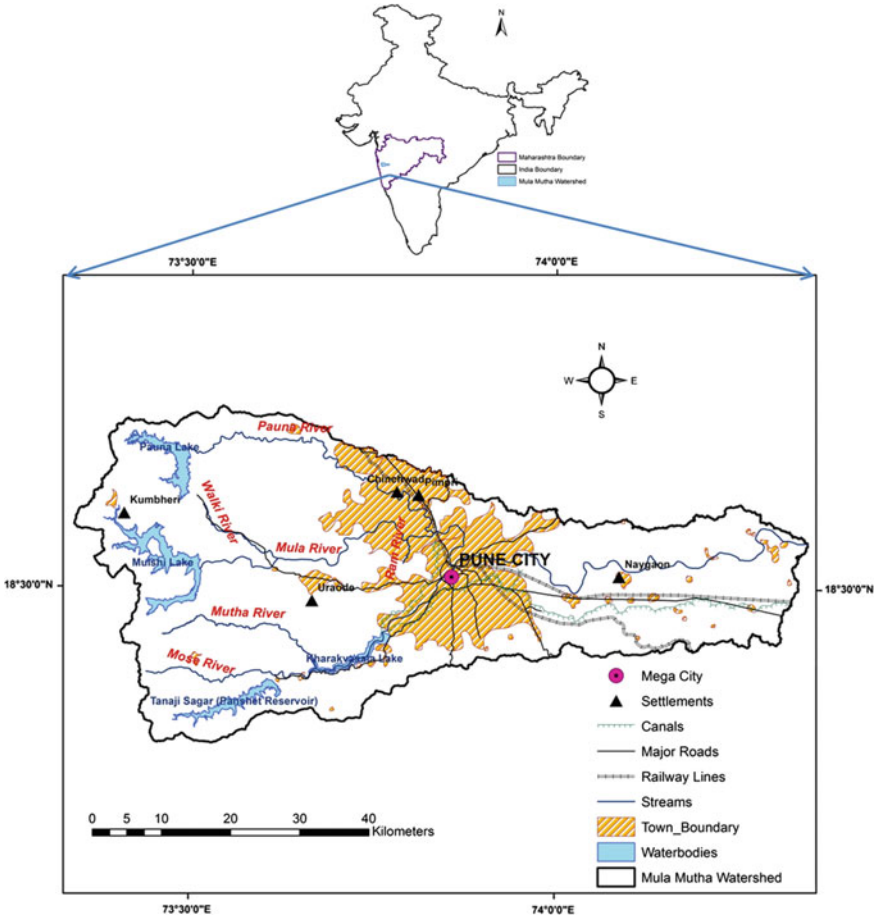

Fig. 1 Location map of the Mula–Mutha watershed

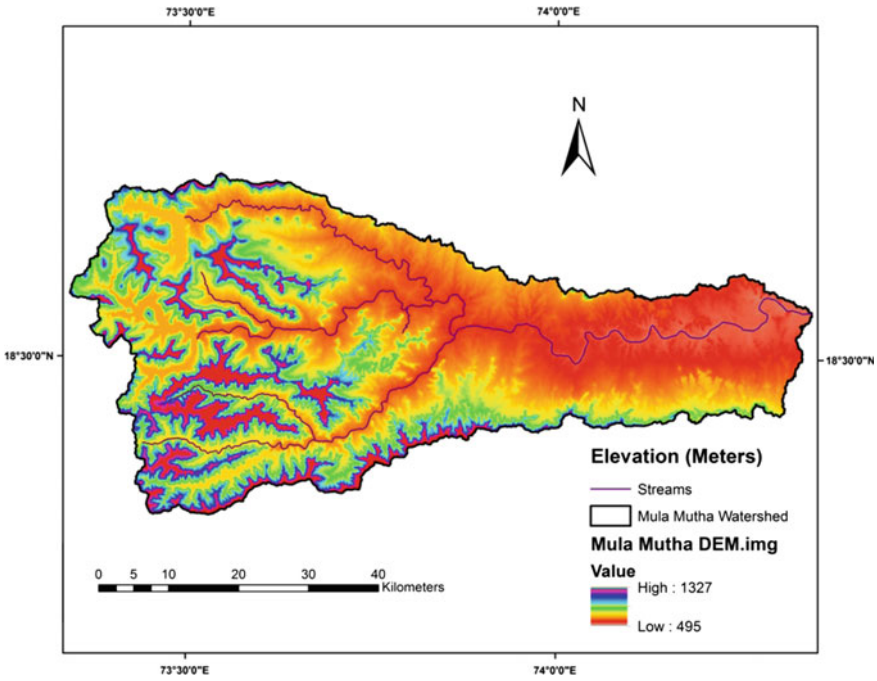

Fig. 2 DEM with major stream network in the study area

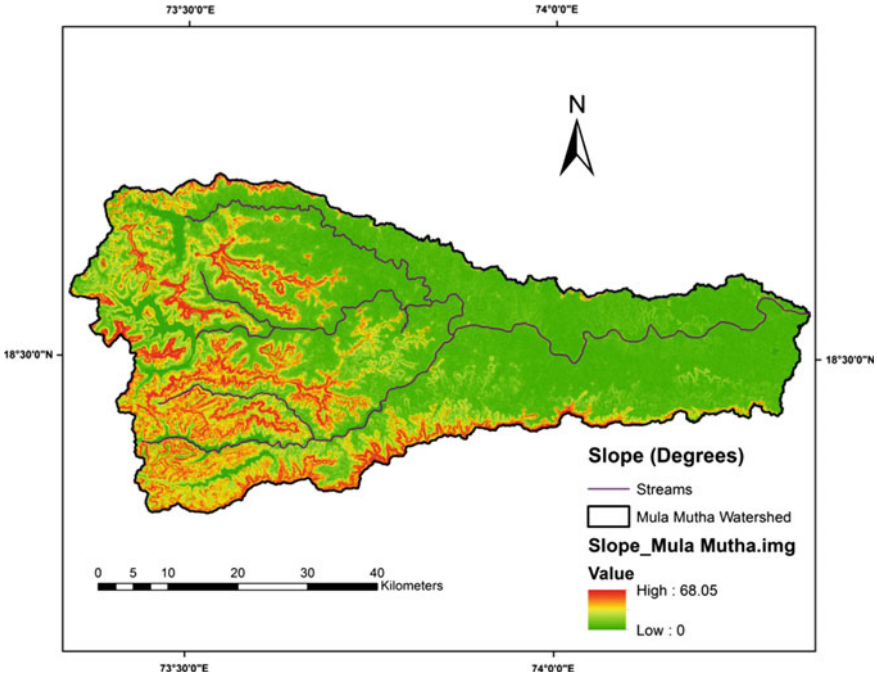

Fig. 3 Slope map with major stream network in the study area

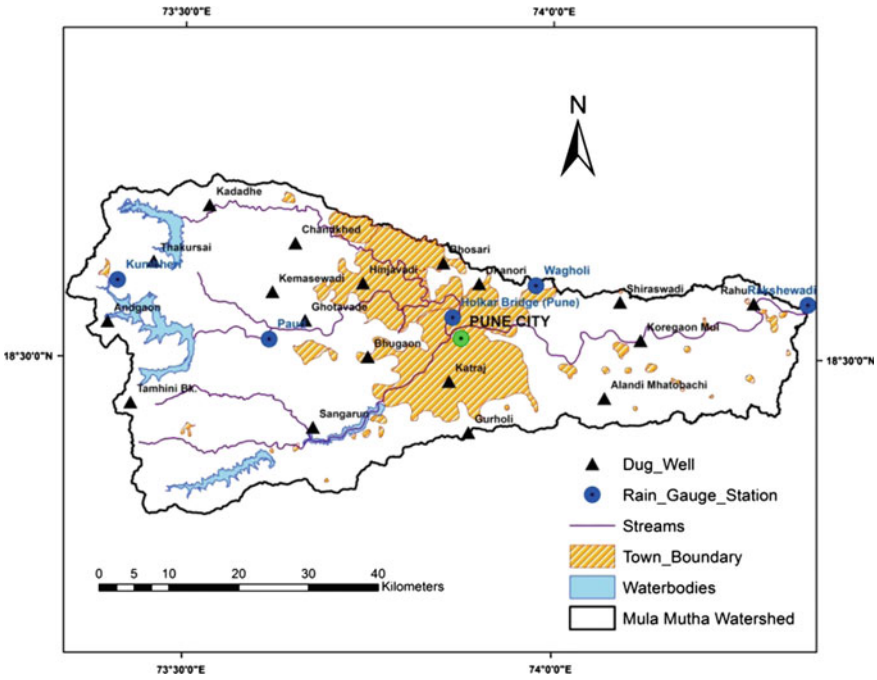

Fig. 4 Map showing rainfall gauge stations and dug wells in the study region

regions, the watershed is suffering from the water scarcity since past few decades (Fig. 4).

This study area has primarily three agricultural seasons, viz. Kharif (monsoon), Rabi (post-monsoon) and Zaid (summer). Bajra, groundnut, cotton, sugarcane, gram and wheat are the main crops grown in the region. Horticulture is also practiced in the region at various places. This region experiences most of its precipitation ($\sim$85%) during June to mid-October which occurs due to southwest monsoon. The rainfall is highly uneven in the study area. Western part of it experiences much higher rainfall than the eastern parts. Heavy storms often cause runoff and soil erosion in the region. The uneven precipitation across the region coupled with basaltic rock structure leaves about $\sim$60% of the study area drought prone. The hottest months in the region are April and May, whereas December and January are the coolest months. The mean annual temperature in the region is $\sim$24.88 °C. The mean minimum and maximum temperatures are about 17.76 °C and 31.59 °C, respectively. Extensive LULC changes are observed in the watershed in the past four decades due to increasing urbanization, industrialization and agricultural activities [12].

3 Materials and Methods

3.1 Data Used

The main aim of the study is to comprehend the spatiotemporal variations in the precipitation deficit and groundwater recharge deficit of the study region. First of all, Shuttle Radar Topography Mission (SRTM) DEM data and Landsat Operational Land Imager (OLI) satellite image (October 14, 2014) of 30-m spatial resolution are derived from United States Geological Survey (USGS) Web site. Further, monthly GWL dataset of 10 years, i.e., from 2001 to 2010 is acquired from Groundwater Survey and Development Agency (GSDA), Government of Maharashtra, Pune, India. Daily rainfall dataset from 2001 to 2010 is acquired from Hydrology Project (H. P.) office, Nasik, Pune, Government of Maharashtra, India. In this study, the indices such as SPI and SWI are used to evaluate precipitation deficit and groundwater recharge deficit in the study area, respectively. All the GIS analysis is performed on ArcGIS 10.1.

3.2 Standardized Precipitation Index (SPI)

Topographic variations across the study area have resulted in a very uneven distribution of rainfall. Hence to evaluate the rainfall deficit anomalies in the region, SPI is estimated using the seasonal precipitation datasets over a period of 2001–2010. The mathematical Eq. (1) is used for calculating SPI:

$$SPI = \left(X_{ij} - X_{im}\right)/\sigma. \tag{1}$$

where X_{ij} = seasonal rainfall of 'i'th and 'j'th observations, X_{im} = seasonal mean and σ = standard deviation [4, 14].

3.3 Standardized Water-Level Index (SWI)

For majority of the population in the study region, the groundwater resources are the primary source of water to fulfill their increasing water demands. Therefore, it is crucial to monitor its groundwater resources. To evaluate the spatiotemporal variations in the seasonal GWL of the study area, SWI is estimated using the seasonal GWL datasets over a period of 2001–2010. The mathematical Eq. (2) is used for calculating SWI:

$$SWI = \left(W_{ij} - W_{im}\right)/\sigma. \tag{2}$$

Table 1 Classification schemes for SPI and SWI. *Source* [14]

S. no.	SPI	SWI	Rainfall/groundwater deficit category
1	<−2.0	>2.0	Extreme deficit
2	<−1.5	>1.5	Severe deficit
3	<−1.0	>1.0	Moderate deficit
4	<0.0	>0.0	Mild deficit
5	>0.0	<0.0	No deficit

where W_{ij} = seasonal groundwater level of 'i'th and 'j'th observations, W_{im} = seasonal mean and σ = standard deviation. These equations are used to generate SPI and SWI maps on GIS platform for comprehending the spatiotemporal variations in the precipitation deficit and groundwater recharge deficit of the study area. Table 1 illustrates the classification scheme of SPI and SWI to interpret the type of precipitation/groundwater deficit in a region at a given time and space [4, 14].

4 Methodology

First of all, the SRTM DEM dataset is processed on GIS platform to delineate the Mula–Mutha watershed and to estimate the slope in the region. False Colour Composite (FCC) of the study area is generated using Landsat OLI satellite image of October 14, 2014, to comprehend the existing landforms in the study region as shown in Fig. 5.

The following base layers, viz. rivers, waterbodies, mega city, settlements, major railway lines, major roads and canals, are manually digitized from geo-referenced Survey of India (SoI) toposheets. They are further updated with Landsat OLI FCC image to prepare the updated base map of the study area. For rainfall analysis, a total five rainfall stations and, for groundwater analysis, 18 groundwater monitoring wells (dug wells) are chosen across the study area as shown in Fig. 4. Rainfall dataset of both the seasons, viz., pre-monsoon (May) and post-monsoon (October) seasons, over the period of 2001–2010 is analyzed using SPI. It helped to understand the rainfall deficit anomalies in the region. Similarly, GWL dataset of both seasons over the period of 2001–2010 is analyzed using the SWI to understand the groundwater recharge deficit anomalies in the region. Rainfall and groundwater data are point data; hence, spline spatial interpolation method is used to create SPI and SWI maps. These maps are analyzed, compared and correlated to understand the spatiotemporal variations in the precipitation deficit and groundwater recharge deficit in the study area.

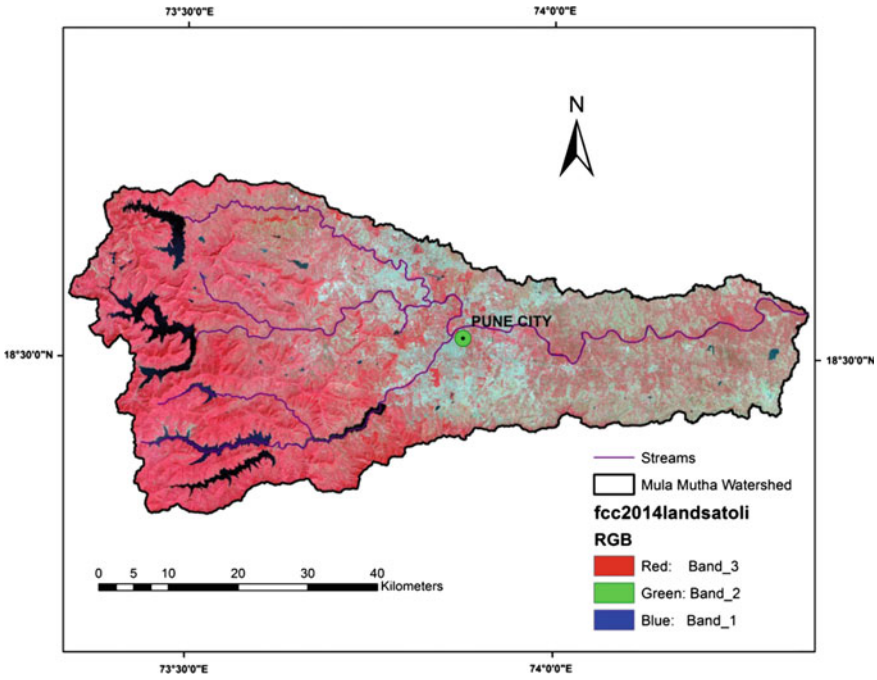

Fig. 5 FCC of the study region (Landsat OLI Image of October 14, 2014)

5 Results and Discussion

5.1 Patterns of Rainfall in the Study Area

The study area received about 1407 mm of annual average rainfall during the period of 2001–2010. The maximum and minimum rainfall were recorded in the year 2005 (2242 mm) and 2001 (990 mm), respectively. In most of the years, the annual rainfall is below mean line as shown in Fig. 6. The annual rainfall in the study region results from southwest monsoon, and it is dominated by five months, i.e., June to October. The high topographic variations in the study area result in a highly uneven distribution of rainfall in space and time. Higher elevation zones in western part of the watershed experience a very high rainfall, whereas comparatively flat eastern part remains dry with low rainfall. The highest rainfall is recorded at Kumbheri rainfall station which lies in the hilly Western Ghat region. The lowest rainfall is recorded at Rakshewadi which lies in the eastern part of the study region as shown in Fig. 7.

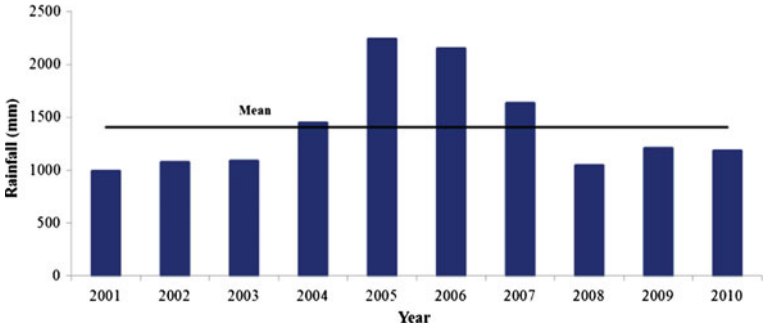

Fig. 6 Average annual rainfall in the study area between 2001–2010

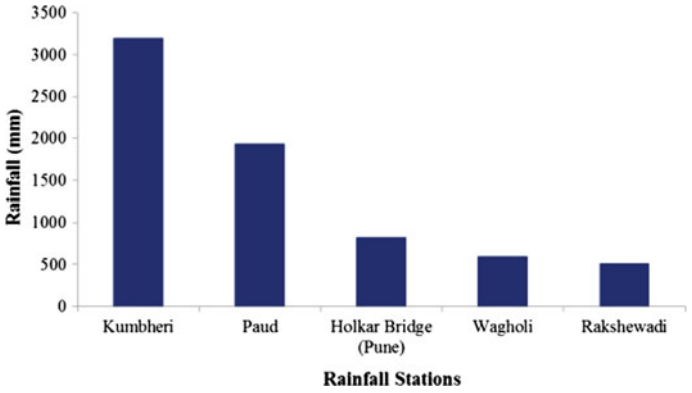

Fig. 7 Rainfall variation in the study area from west to east

5.2 Variations in the Precipitation Deficit

The study area experienced mild to moderate precipitation deficit in the pre-monsoon season of the period 2001–2010. The precipitation deficit is observed over the years 2001, 2002, 2003, 2008 and 2010 in pre-monsoon season. However, the study region experienced no deficit to mild precipitation deficit in the post-monsoon season. It is observed over the years 2004, 2007 and 2008.

Due to the poor rainfall in the year 2008, the entire region suffered from drought. Visual interpretation of the SPI maps of both pre-monsoon and post-monsoon seasons revealed a very random spatiotemporal distribution of precipitation deficit zones in the study region. There are some pockets of southwestern and southeastern region where precipitation deficit is more frequent as shown in Fig. 8. The rainfall occurrence is a very uncertain natural phenomenon. Hence, during precipitation deficit, groundwater resources can be explored to meet the water demands in a region.

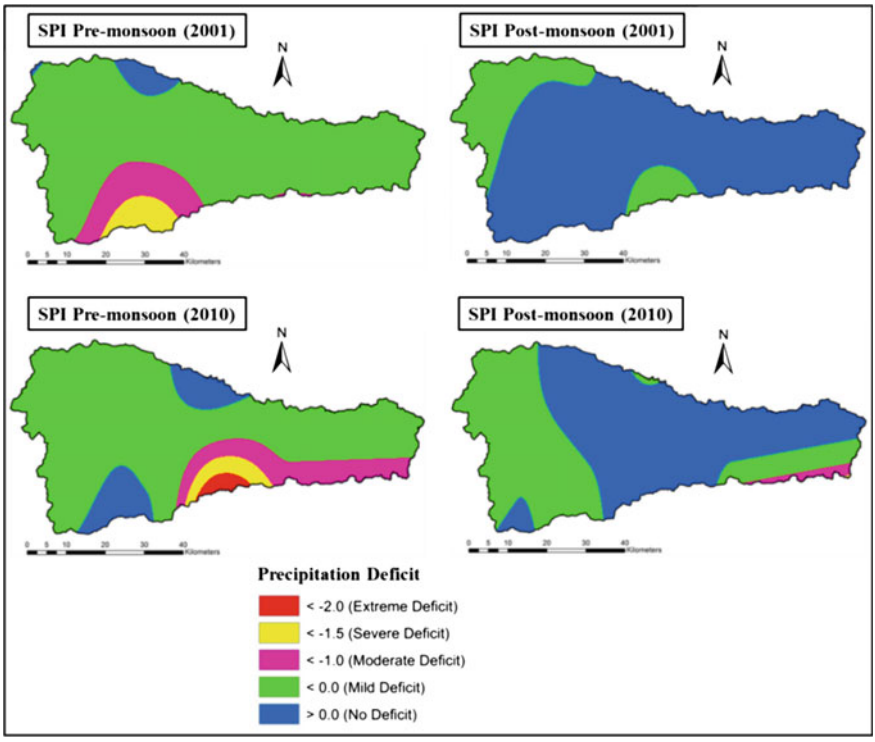

Fig. 8 Spatial distribution of precipitation deficit zones in the study region

5.3 Variations in the Groundwater Recharge Deficit

SWI maps of both the seasons, viz. pre-monsoon and post-monsoon, revealed a very random spatial distribution of groundwater depletion zones in the study area. Dug wells such as Dhanori, Hinjavadi and Gurholi are located in and around urban areas. It is observed that these wells are under groundwater recharge deficit. Dug wells, viz., Rahu, Alandi Mahatobachi, Shiraswadi and Koregaon Mul are located in the eastern part of the study region which experiences low rainfall. It is a highly intense agricultural zone using well water for irrigation as shown in Fig. 5. These wells are also under groundwater recharge deficit. In the urban areas, groundwater level is actually affected mainly due to reduced infiltration from impervious land surfaces and draining of rain water through storm water drains. In rural areas, groundwater is affected due to over abstraction of groundwater mainly for irrigation. Hence, groundwater recharge deficit is more frequent in eastern and south-western part of the region as shown in Fig. 9. On comparing SPI and SWI values over the study area, it is observed that SPI values not always correlate and

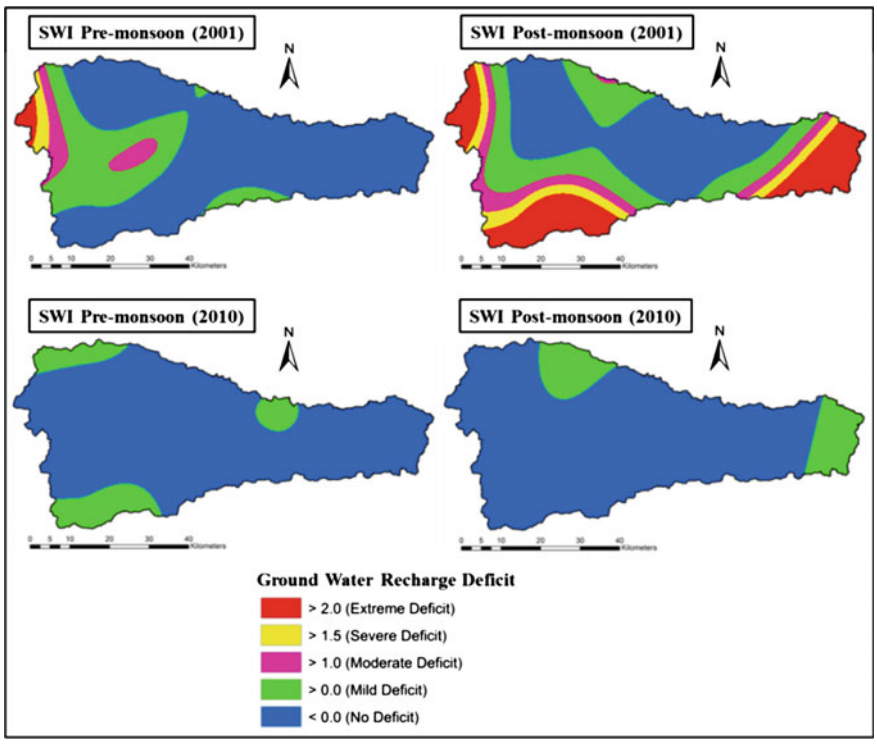

Fig. 9 Spatial distribution of groundwater depletion zones in the study region

correspond to SWI values. There is no direct relationship between the two parameters. Negative SPI and positive SWI values not always represent water deficit in the area. Rainfall and groundwater both are highly dynamic in nature.

6 Conclusions

From SPI and SWI analysis, it is concluded that there are random occurrences of precipitation deficit and groundwater recharge deficit across the study area. The study area has a very uneven distribution of rainfall in space and time. Availability of groundwater in a region is affected by various local parameters, viz., rainfall, elevation, slope and LULC at individual well locations. A high variability is observed in these parameters across the study area. Therefore, the GWL also varies highly in time and space in both the seasons, viz. pre-monsoon and post-monsoon. No regular trend is observed in the GWL of the region. SPI and SWI indices facilitate the study of spatiotemporal variations in the precipitation and groundwater

recharge deficit in a region. GWL in post-monsoon season is higher in comparison with the pre-monsoon season due to groundwater recharge during monsoon season. Therefore, this region has good scope for groundwater development.

References

1. Ahmadi, S.H., Sedghamiz, A.: Geostatistical analysis of spatial and temporal variations of groundwater level. Environ. Monit. Assess. **129**(1–3), 277–294 (2007)
2. Anuraga, T.S., Ruiz, L., Kumar, M.M., Sekhar, M., Leijnse, A.: Estimating groundwater recharge using land use and soil data: a case study in South India. Agric. Water Manag. **84**(1), 65–76 (2006)
3. Bhuiyan, C.: Various drought indices for monitoring drought condition in Aravalli terrain of India. In: Proceedings of XXth ISPRS Congress, pp. 12–23 (2004)
4. Bhuiyan, C., Singh, R.P., Kogan, F.N.: Monitoring drought dynamics in the Aravalli region (India) using different indices based on ground and remote sensing data. Int. J. Appl. Earth Obs. Geoinf. **8**(4), 289–302 (2006)
5. Daniel, E.B., Camp, J.V., LeBoeuf, E.J., Penrod, J.R., Dobbins, J.P., Abkowitz, M.D.: Watershed modeling and its applications: a state-of-the-art review. Open Hydrol. J. **5**, 26–50 (2011)
6. Ganapuram, S., Nagarajan, R., Chandra Sekhar, G.: Identification of groundwater drought prone zones in pedda vagu and ookachetti vagu watersheds, tributaries of the Krishna River, India. Geocarto Int. **31**(4), 385–407 (2016)
7. Garg, K.K., Bharati, L., Gaur, A., George, B., Acharya, S., Jella, K., Narasimhan, B.: Spatial mapping of agricultural water productivity using the SWAT Model in Upper Bhima Catchment. India Irrig. Drain. **61**, 60–79 (2012)
8. Gleeson, T., Wada, Y.: Assessing regional groundwater stress for nations using multiple data sources with the groundwater footprint. Environ. Res. Lett. **8**(4), 044010 (2013)
9. Healy, R.W., Cook, P.G.: Using groundwater levels to estimate recharge. Hydrogeol. J. **10**(1), 91–109 (2002)
10. Machiwal, D., Jha, M.L.: Trend and homogeneity in subsurface hydrologic variables: case study in a hard-rock aquifer of Western India. In: Hydrologic Time Series Analysis: Theory and Practice. Capital Publishing Company (2012). ISBN: 81-85589-68-2
11. Nandargi, S., Patekar, T.A., Mulye, S.S.: Rainfall and groundwater level variation in Pune District. India Stud. Atmos. Sci. **1**, 24–40 (2014)
12. National Informatics Center (NIC)-District Pune: District Gazetteer Information Government Report. Collectorate Pune District, Government of Maharashtra, India. http://pune.nic.in/puneCollectorate/Gazette/gaz.aspx (2009). Accessed 12 Jan 2015
13. Patki, N., Ghodke, V.R., Sathe, N.J.: Delineation of recharging zones for groundwater in Bhima River Basin, Pandharpur, Maharashtra. In: Proceeding of International Conference SWRDM-2012 (Red), vol. 5(9), p. 8 (2012)
14. Shukla, S., Khire, M.V., Gedam, S.S.: Remote sensing and GIS based impact assessment of land transformations on groundwater level of a Rapidly Urbanizing Watershed of India. In: Proceedings of 2016 IEEE International Symposium held on Geoscience and Remote Sensing Symposium (IGARSS), 10–15 July 2016, at Beijing, China, pp. 787–790. (2016)
15. Surinaidu, L., Bacon, C.G.D., Pavelic, P.: Agricultural groundwater management in the upper Bhima Basin, India: current status and future scenarios. Hydrol. Earth Syst. Sci. **17**(2), 507–517 (2013)

Drawdown Minimization by EMPSO in a Heterogenous Aquifer System

A.K. Rashida

Abstract Groundwater is an important reliable source of potable water, and in many regions, the industrial, agricultural and municipal water demands are met with the available ground water resources. Groundwater depletion is a vital issue experienced worldwide. Lift-dominated agricultural and industrial water consumption is one of the primary causes for the groundwater depletion in many areas, and over-pumping has largely depleted the shallow aquifers. This has forced the well drillers to go for the deeper aquifer regions, which is occasionally not replenishable and nor economical. Thus, it becomes necessary to address this critical issue of rapid decline of the water table. This work presents an elitist-mutation particle swarm optimization (EMPSO) approach for minimization of drawdown from heterogeneous confined aquifer system. First optimal solutions are obtained by particle swarm optimization (PSO), and these subsequently correlated with EMPSO results. The optimization problem consists in minimizing the drawdown for a period of time. Considering realistic parameters of aquifer, finite element simulation model was developed to find collective drawdown minimization by coupling with EMPSO.

Keywords Finite element method · Particle swarm optimization · Elitist-mutated PSO formulation

1 Introduction

Numerical simulation–optimization groundwater modelling can help to predict the actual aquifer system behaviour. The confined heterogeneous aquifer considered for the present study is similar to the Blue Lake aquifer (BLA) of Northern California in Humboldt County. BLA is actually a sloping unconfined aquifer with an

A.K. Rashida (✉)
Department of Physical Oceanography, Cochin University of Science and Technology, Cochin 682016, Kerala, India
e-mail: rashidaak91@gmail.com

V. Garg et al. (eds.), *Development of Water Resources in India*,
Water Science and Technology Library 75, DOI 10.1007/978-3-319-55125-8_15

enormous slope of 0.21% towards the west of Pacific Ocean. About 20 km^2 area is surrounded by it. This sloping aquifer consists of a Mad River flowing to the eastern margin of the aquifer. Presently for simulation convenience, BLA unconfined aquifer is treated as confined aquifer without considering slope. The present study has been first conducted to estimate the groundwater head distribution in the confined BLA. The groundwater head distribution in the confined BLA is simulated for 1-year planning period (June–May) and influence of pumping can be seen. Further, groundwater flow balance is computed for the entire domain. Later optimal solutions are obtained at the proposed wells by an improved particle swarm technique. Earlier Chu and Willis [1] worked out the explicit finite difference solution for the BLA aquifer. Later Rastogi and Sulekha (1997) developed numerical models based on certain schemes in finite difference method involving successive over relaxation (SOR), iterative alternating direction implicit (IADI), strongly implicit procedure (SIP) and finite element technique for the Blue Lake Aquifer (BLA) system. An annual discharge of 440,004 m^3 of water per year from 16 wells (six existing wells and 10 proposed wells) was taken by earlier workers for this aquifer which is also considered by the present authors for simulation purpose. Variable monthly surface recharge and river seepage from the Mad River are contributing to the aquifer over the study period of 1 year. The aquifer is subjected to a net recharge or discharge by the river depending on the relative river and aquifer head variations. The storativity value for present problem is taken as 0.3 in the flow domain. Presently simulation–optimization model is developed to minimize drawdown for ten wells which were mentioned in Rastogi [6] and were minimized by him using finite difference coupled with Modular Incore Nonlinear Optimization System (MINOS) developed by the Stanford University, USA. Therefore, basic data are same except that finite element and EMPSO are adopted presently for the optimal solutions.

2 Methodology

2.1 Governing Equations

The two-dimensional time variant groundwater flow in a confined and non-homogeneous aquifer has been represented in the governing equation as

$$\frac{\partial}{\partial x}\left[T_x \frac{\partial h}{\partial x}\right] + \frac{\partial}{\partial y}\left[T_y \frac{\partial h}{\partial y}\right] = S\frac{\partial h}{\partial t} + Q_w \delta(x - x_i)(y - y_i) - q \tag{1}$$

Initial condition is given as

$$h(x, y, 0) = h_0(x, y) \quad \text{for all } x, y \in \Omega \tag{2}$$

Boundary conditions used are:

$$h(x, y, t) = h_1(x, y, t) \qquad x, y \in \partial\Omega_1 \tag{3}$$

$$T\frac{\partial h}{\partial n} = q(x, y, t) \qquad x, y \in \partial\Omega_2 \tag{4}$$

where $h(x, y, t)$ = piezometric head (m), $T(x, y)$ = transmissivity (m^2/d), S = storage coefficient, x, y = horizontal space variables (m), Q_w = source or sink function ($-Q_w$ source, Q_w = sink (m^3/d/m^2), t = time in days, Ω = the flow region, $\partial\Omega$ = the boundary region ($\partial\Omega_1 \cup \partial\Omega_2 = \partial\Omega$), $\frac{\partial}{\partial n}$ = normal derivative, $h_0(x, y)$ = initial head in the aquifer flow domain (m), $h_1(x, y, t)$ = known value of the boundary head (m), $q(x, y, t)$ = known inflow rate (m^3/d/m), δ is Dirac delta function = 1 if $x = x_i, y = y_i; = 0$ if $x \neq x_i, y \neq y_i$ [7].

2.2 Finite Element Formulation

The Galerkin finite element formulation with implicit time scheme is applied to Eq. (1), and the system of equations generated is as follows [5]:

$$[G]\left\{h_I^{t+\Delta t}\right\} + \frac{1}{\Delta t}[P]\left\{\left(h_I^{t+\Delta t}\right) - \left(h_I^{t}\right)\right\} = \{F\} \tag{5}$$

$[G]$ = conductance matrix, $[P]$ = storativity matrix, $\{F\}$ = flux vector.

The initial condition, i.e. groundwater head in the entire aquifer, is assumed to be known. By solving the above equations, the head at each new time step is calculated. Solution of (Eq. 5) gives head distribution in the aquifer for a simulation period of 1 year.

2.3 Particle Swarm Optimization

The PSO is an optimization technique first proposed by Kennedy and Eberhart in 1995 based on simplified social behaviour of swarm of birds. The PSO's evolutionary computational framework was further innovated by incorporating an adaptive culture model [9]. In the D-Dimensional space, the PSO algorithm optimizes each particle's velocity and position through a corporative behaviour. In this method, each particle is depicted as a solution to the optimization problem. In PSO, each particle represents a solution to the optimization problem and the swarm being population of the set of vectors notated by the position and velocity vector, i.e. (X, V), respectively. The best previously visited position of the ith particle and the present global best position in the swarm are stored as pbesti = ($p_{i1}, p_{i2}, \ldots, p_{id}$) and

gbest = (p_{g1}, p_{g2}, …, p_{gd}), respectively, where g is the index of the best particle in the swarm. Each of the initially assumed solutions is improved upon in each iteration process through the following equations [2].

$$v_{id}^{m+1} = v_{id}^{m} + c_1 \text{rand1}\left(p_{id} - x_{id}^{m}\right) + c_2 \text{rand2}\left(p_{gd} - x_{id}^{m}\right) \tag{6}$$

$$x_{id}^{m+1} = x_{id}^{m} + v_{id}^{m+1} \tag{7}$$

Equations 6 and 7 represent a learning facilitation process, by which an individual learns both from their neighbours and from their own intuition, and apply the learned experience gathered through local and global search cognitively. The advancement in solution is denoted by v_{id} (velocity), where the index for the decision variables (d = 1, …, D); i = 1, …, pop and pop = number of particles in the swarm; m = iteration number; rand1 and rand2 = uniformly generated random numbers in [0, 1]; $c1$ and $c2$ = cognitive and social parameters, respectively, also known as acceleration constants. The new iteration best with better fitness solution leads the swarm as global best to find further better solution [2].

2.4 Elitist-Mutated PSO Formulation

EMPSO algorithm is an enhanced technique for multi-objective optimization problems. Elite particle swarm optimization with mutation replaces the worst solution of the new population with the best solution of the current population. Mutation operator is put forward to increase the diversity of the particle swarm optimization problem. Kumar and Reddy [4] incorporated the elitist PSO approach for solving complex reservoir system problems. Compared to PSO, the EMPSO approach prevents the algorithm being stuck at the local optima and produces best global optimal solutions. The elitist-mutation operator suggested by Kumar and Reddy [4] is given below.

Let NMmax = number of particles to be elitist-mutated, g = index of global best particle, pem = probability of mutation, ASF = index of sorted population, rand = uniformly distributed random number U[0, 1], randn = Gaussian random number N[0, 1], and VR[d] = range of decision variable d

For i = 1 to NMmax l = ASF[i]_For d = 1 to dim if (rand < pem)
X[l][d] = P[g][d] + 0.1 * VR[d] * randn else
X[l][d] = P[g][d]

If the mutated value surpasses the limits, then it is constrained to the upper or lower margins. During this elitist-mutation step, the velocity vector of the particle is unaltered.

3 Simulation–Optimization Model Formulation

Presently the entire Blue Lake Aquifer domain was discretized into 471 triangular elements involving 316 nodes with 15 zones of different zonal hydraulic conductivity (Fig. 1). The elements chosen are triangular. A computer code for Galerkin finite element simulation modelling was developed in MATLAB for steady- and transient-state conditions. A mass balance check was made after 1, 30, 180 and 365 days and was found satisfactory. It is found that inflow–outflow was reflected in the change in storage in the BLA aquifer; hence, the correctness of the solution was established. Later it was coupled with optimization model to minimize drawdown for 10 proposed wells. The simulation model calculates the groundwater head in the aquifer. The objective function is estimated subject to the related constraints by using these simulated head values. The optimization model calls the simulation model in every iteration till optimal solution is achieved.

3.1 Minimization of Drawdown for 10 Proposed Wells at Given Location

The decision variables considered for optimization are well pumping discharges. The lower and upper limits on the permissible values of pumping discharges from the wells are fixed at 4000 and 13,500 m^3/d. The total demand is assigned (Q_{demand}) as 87049.46 m^3/d, which is normally decided by groundwater authority. In each iteration, the cumulative drawdown from the proposed 10 wells is calculated by the PSO model by calling upon the FEM model. If the total well discharge is less than the demand, a penalty function $P(Q)$ (Eq. 9) is imposed. After trying out different values for β viz. 2.5, 2 and 1 reported in the literature, a value of $\beta = 2$ was observed to give the best results. The equations used for minimization of drawdown can be given as [8].

Minimize

$$\sum_k h'_k - h_k + \beta P(Q) \tag{8}$$

Under the constraints

$Q_{min} < Q_k < Q_{max}$

$\sum Q_k \geq Q_{demand}$

where k = nodal location of wells k = 76, 81, 90, 163, 180, 198, 212, 221, 231 and 242, h'_k = groundwater head at each well after t days of pumping, h_k = initial groundwater head at each well, β = a scaling constant.

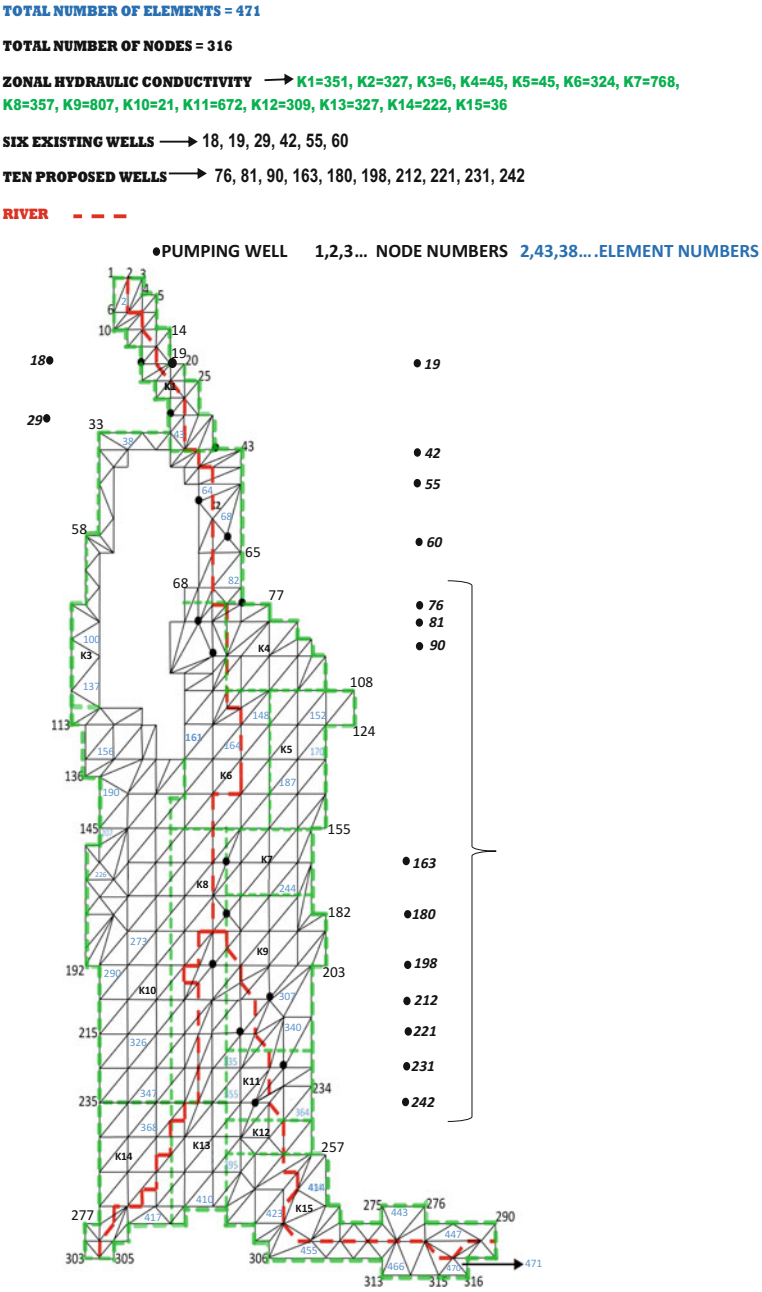

Fig. 1 Discretized BLA domain

P is a penalty function defined as:

$$P(Q) = \begin{cases} Q_{\text{demand}} - \sum_k Q_k & \sum_k Q_k < Q_{\text{demand}} \\ 0 & \sum_k Q_k \geq Q_{\text{demand}} \end{cases} \quad (9)$$

$Q_{\min}$ minimum permissible value of discharge from wells
$Q_{\max}$ maximum permissible value of discharge from wells
Q_{demand} total water demand.

4 Tuning of PSO Parameters

PSO has a set of user-defined and problem-specific parameters—population size, inertia weight, acceleration constants. These parameters include population size, inertia weight and acceleration constants and are problem specific. The tuning of PSO parameters has been carried out by conducting sensitivity analysis to review the influence of behavioural parameters on the optimal values. In PSO, there are a swarm or population of potential solutions, which are called particles, which move through the search field with a mentioned velocity to obtain the optimal solution. A memory is also maintained so that previous best position is in track. Particles are distinguished as personally best and globally best based on their position. Here, the maximum permissible value of PSO velocity update in every iteration was kept equivalent to the range of the decision variable ($v_{\max}$ = 13,500). From the experimentation, it was found that a population size of 25 gave the best solution after trying out of 8, 9, 10, 13, 15, 20 and 25 initially assumed solutions in the population set (Fig. 3). A particular number of iterations were selected as the stopping criteria such that improvement in the solution beyond this number should give very small value or almost zero improvement in the solution. It was noted that an increment in the number of iterations beyond 40 does very small improvement in solution and increases the computational time of the programme. It was found that inertia weight plays an important role. However, no specific values could be adopted from the literature which was stated as problem specific. Therefore, different values of inertia weight were tried before choosing the best suitable values to the present problem. From these trial observations, the linearly dropping inertia weight value from 1.2 to 0.4 was observed to produce ideal results as compared to those obtained using a constant value of inertia weight (w = 0.729), inertia weight deviating between 0.9–0.4 and arbitrary adopted values of inertia weight between 0 and 1, 0.4 and 0.9, and 1.2 and 0.4, respectively. Different sets of acceleration constants namely, $c1$ = $c2$ = 1.496, 1.5, 2.05; $c1$ = 2, $c2$ = 1.5; $c1$ = 1.5, $c2$ = 2 are tested to examine their effect on the optimal values. Among all the sets, $c1$ = $c2$ = 1.5 gave the best result (Fig. 2).

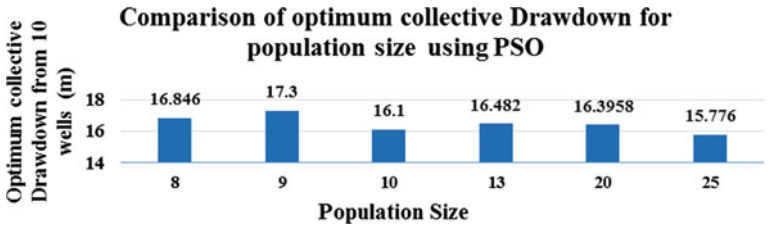

Fig. 2 Influence of population size on optimum collective drawdown from 10 wells

5 Elitist-Mutated PSO Formulation

Elitist-mutated particle swarm optimization is an efficient heuristic algorithm characterized by faster and optimal convergence rate than standard PSO algorithm. The important behavioural parameters (to be adjusted) in an EMPSO algorithm are the iteration at which elitist mutation should begin and the number (percentage of elitism) of particles to be mutated. Appropriate values for inertia weight, acceleration constants and population size are required to be selected. It was found that a population size of 20 yielded best results with earlier convergence for EMPSO. It was observed that linearly varying inertia weight of 1.8–0.4 gives best results compared to the rest. The inertia weight was chosen to vary between 1.8–0.4 and acceleration constants $c1 = c2 = 1.5$ up to the iteration where the mutation is applied. After this, a value of $c1 = 0.2$ and $c2 = 0.5$ was considered. In order to restrict the magnitude of the improvement in solutions (velocity) from nullifying the effect of the mutation, lesser values (as compared to those used in standard PSO) for $c1$ and $c2$ were chosen. Different numbers of trials were performed to ascertain the iteration number at which elitist mutation should begin. It was found that starting the elitist mutation at the 15th iteration yielded the best results and better convergence. The percentage of solutions to be mutated was selected to be 20% after trying out several trials with 30, 40 and 50% mutation of the swarm. It was seen that EMPSO showed an earlier convergence with better solution compared to standard PSO. The objective function value obtained through drawdown minimization is 14.8332 m (Fig. 4).

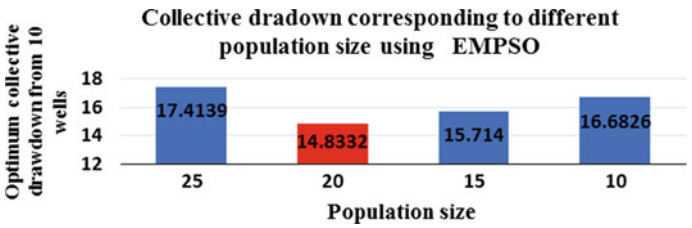

Fig. 3 Comparison of population size with respect to optimum collective drawdown from 10 wells using EMPSO

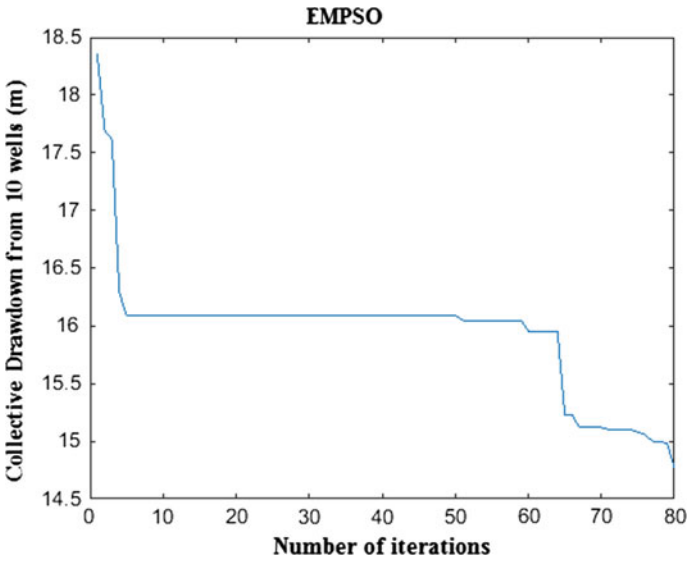

Fig. 4 Optimum collective drawdown (14.77 m) from 10 proposed wells using EMPSO with 20% of elitism for 80 iterations

Table 1 Comparison of optimal discharge associated with minimum drawdown from 10 proposed wells by standard PSO and EMPSO [Iteration number = 40]

Optimizer used	Collective drawdown (m)	Total discharge (m^3/d)	Simulation time (s)
Standard PSO	15.776	89,143	9433.870911
EMPSO	14.999	87,188	6002.291577

A comparison of the results obtained through both the methods viz. standard PSO and EMPSO for the drawdown minimization is presented in Table 1.

6 Conclusions

This study dealt with the minimization of drawdown in a heterogeneous confined aquifer using elitism concept combined with mutation in the basic PSO algorithm. The performance of the standard PSO can be enhanced by tuning its parameters to give better solution. From observations of PSO, the value of inertia weight (w) linearly dropping from 1.2 to 0.4 was observed to produce ideal results as compared to those obtained using constant value $w = 0.729$, w deviating between 0.9–0.4 and arbitrary adopted values of w between 0 and 1, 0.4 and 0.9, and 0.4, respectively. The observations implied the improvement in the individual swarm quality and the accelerated convergence on applying EMPSO concept. The computational convergence time for proposed EMPSO method was observed

approximately 36.4% faster than the original PSO method. EMPSO solutions are also better than PSO as the collective drawdown from ten proposed wells is marginally smaller by EMPSO than PSO. Therefore, the author recommends EMPSO for groundwater system planning and management problems.

Acknowledgements The author wish to thank Dr. A.K. Rastogi, Professor, Water Resources Engineering, Department of Civil Engineering, IIT, Bombay, for his valuable and esteemed guidance, constant encouragement and constructive criticisms and the Department of Civil Engineering, Indian Institute of Technology, Bombay, for providing the computational facilities.

References

1. Chu, W.S., Willis, R.: An explicit finite difference model for unconfined aquifers. Ground Water **22**(6), 728–734 (1984)
2. Eberhart, R.C., Shi, Y.: Particle swarm optimization: developments, applications and resources. In: Proceedings of the Congress on Evolutionary Computation 2001, Seoul, Korea. IEEE Service Centre, Piscataway, NJ (2001)
3. Gray, W.G., Pinder, G.F., Brebbia, C.A.: Finite Elements in Water Resources. Pentech Press, London (1977)
4. Kumar, D.N., Reddy, M.J.: Multipurpose reservoir operation using particle swarm optimization. J. Water Resour. Plan. Manag. **133**(3), 192–201 (2007)
5. Pinder, G.F., Gray, W.G.: Finite Element Simulation in Surface and Subsurface Hydrology. Academic Press, New York, NY (1977)
6. Rastogi, A.K.: Optimal pumping policy and groundwater balance for the blue lake aquifer, California, involving nonlinear groundwater. Hydraul. J. Hydrol. **111**, 177–194 (1989)
7. Rastogi, A.K.: Numerical Groundwater Hydrology. Penram International Publication, Mumbai (2012)
8. Cyriac, R., Rastogi, A.K.: Optimization of pumping policy using coupled finite element-particle swarm optimization modelling. ISH J. Hydraul. Eng. 91–95 (2015)
9. Kennedy, J.: Thinking is social: experiments with the adaptive culture model. J. Conflict Resolut. **42**(1), 56–76 (1998)

Downscaling Precipitation in Hemavathy River Basin by Three Different Approaches

A.N. Rohith and K.V. Jayakumar

Abstract Hydrologic risk assessment studies in the context of changing climate scenario require quality information at regional scale. Commonly used general circulation models (GCMs), simulating climate impacts, have low spatial resolution. A number of statistical and dynamical downscaling approaches are available to overcome the mismatch between site resolution at which information is required and the GCM spatial resolutions. Three such statistical downscaling approaches, viz. Long Ashton Research Station-Weather Generator (LARS-WG), linear scaling (LS) and quantile mapping (QM), are used to downscale daily precipitation data from EC-EARTH model simulations under Representative Concentration Pathway (RCP) 4.5 scenario in Hemavathy River basin. It is observed that an increase in precipitation intensities and magnitudes is expected.

Keywords Climate change · GCM · Downscaling · LARS-WG · Linear scaling · Quantile mapping

1 Introduction

Hydrologic risk assessment always demands quality and quantity information like observed precipitation temperature and streamflow within a study area. The knowledge about possible changes in occurrences of hydrologic variables in future is also necessary in both risk assessment and implementing structural and non-structural adaptation measures. General circulation models are used to simulate the future climate response. Most of the researchers [1–3], based on GCM simulations, suggest an increasing trend in both magnitude and frequency of future precipitation events over India. The GCM outputs are available at a resolution of

A.N. Rohith (✉) · K.V. Jayakumar
National Institute of Technology Warangal, Hanamkonda, India
e-mail: rohithan.ns@gmail.com

K.V. Jayakumar
e-mail: kvj@nitw.ac.in

V. Garg et al. (eds.), *Development of Water Resources in India*,
Water Science and Technology Library 75, DOI 10.1007/978-3-319-55125-8_16

100–200 km, but the hydrologic assessment needs the data at much smaller scale generally less than 100 km; this spatial gap can be overcome using downscaling techniques [4].

A number of downscaling techniques (ARCC, 2014) are available in the literature to address the bias in GCM simulations due to mismatch between spatial resolutions. Statistical downscaling techniques are widely used due to less computational demands where predictors and predictand are related to empirical relationships. Statistical downscaling model (SDSM) is an effective tool to downscale temperature, but it shows poor performance [3] in downscaling precipitation. Support vector machine (SVM) has got wide range of applications [1, 5, 6], due to its ability to capture nonlinear relationships. Other similar types of methods include artificial neural networks (ANN) and canonical correlation. Regression-based models are generally sensitive to predictor selection. K-nearest neighbour (KNN) is a nonparametric pattern recognition approach used widely due to less computational efforts. Devak and Dhanya [7] observed that SVM fails to capture peak events compared to KNN method. Weather generator methods [8–10] are simple, effective, commonly used and less time-consuming methods. Bias correction methods [11, 12] include linear scaling, quantile mapping, power transformation and delta change approach. LS method is used to adjust bias in the model simulations by means of adjusting monthly means. A nonparametric approach, viz. quantile mapping, is one of the approaches where extreme events can be well simulated, where bias in quantiles, monthly means and variances due to differential spatial resolution can be corrected. This study aims to compare three downscaling methods, viz. Long Ashton Research Station-Weather Generator (LARS-WG), linear scaling and quantile mapping, to downscale daily precipitation data to river basin scale.

2 Study Area and Data

The area taken up for the study is a part of the Hemavathy river, which is a tributary of River Cauvery in Karnataka State in the southern part of India. There is a major irrigation project constructed across the dam with a culturable command area of 283581 ha. The Hemavathy dam is constructed downstream of the confluence of River Hemavathy and Yaguchi stream. The area lies on the western part on the upstream of the Hemavathy dam and enclosed between latitude 12.1°–12.7° N and longitudes 75.4°–76.4° E, covering an area of 3237 km^2 and stream length of 94 km. The catchment of this river basin receives an average rainfall of 4300 mm per year; wettest month is July with 1200 mm of average rainfall. The digital elevation model (DEM) of the study area is shown in Fig. 1.

1° gridded precipitation data are procured from Indian Meteorological Department, and the grid point used in this study is 12.5° N latitude and 75.5° E longitude. 1.11209° × 1.125° resolution GCM simulations for EC-EARTH are downloaded from Data Distribution Centre, Intergovernmental Panel for Climate

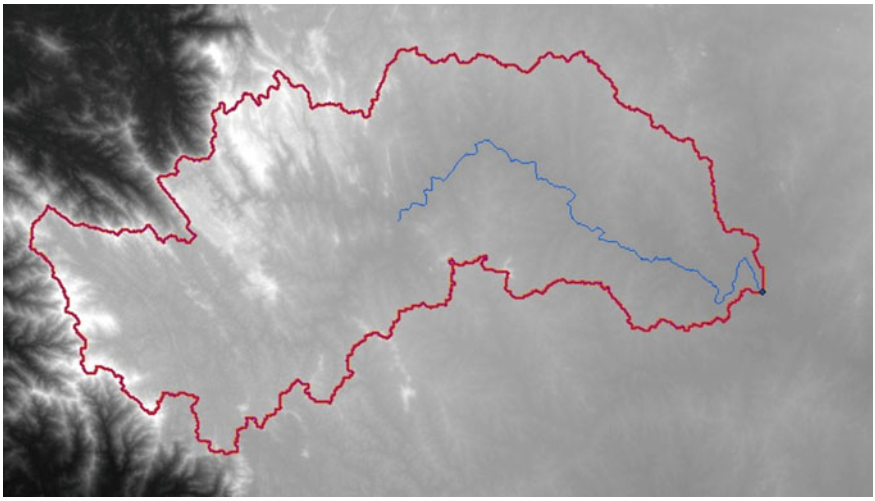

Fig. 1 DEM showing the catchment boundary of study area

Change (http://www.ipcc-data.org/sim/gcm_monthly/AR5/Reference-Archive.html) for RCP4.5 scenario. Precipitation data from GCM grid points 12.89713° N and 75.375° E are used to downscale all three methods.

3 Methodology

For the purpose of downscaling the observed data, the period from 1975 to 2005 is considered as the control period. The EC-EARTH's RCP4.5 scenarios precipitation output from 2010 to 2100 is downscaled using three methods mentioned earlier. The three flow charts for the downscaling approaches used in this study are presented in Fig. 2a–c.

3.1 Downscaling Using LARS Weather Generator

A semi-parametric weather generator is used to generate series of wet and dry spells, based on semi-empirical distributions of observed time series. Change factors in terms of changes in monthly mean of future GCM simulations compared to control period GCM simulations given in Eq. (1) are multiplied to generated time series so that future changes in the climate scenarios are accounted. This method is a simple delta approach with a weather generator. A day with rainfall less than 1 mm is considered as insignificant and assumed as a dry day.

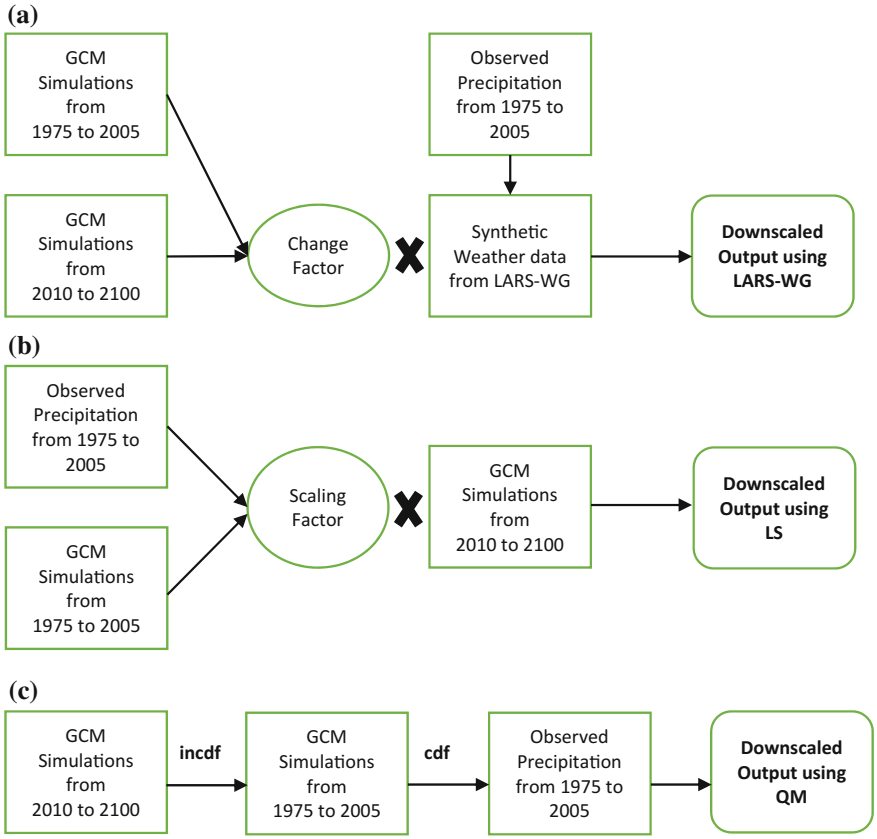

Fig. 2 Flow chart of downscaling using **a** LARS-WG. **b** Linear scaling. **c** Quantile mapping

$$\Delta P_i = \frac{\mu_{i\,\mathrm{FGCM}}}{\mu_{i\,\mathrm{CGCM}}} \tag{1}$$

where ΔP_i is the change factor corresponding to ith month, $\mu_{i\mathrm{FGCM}}$ is mean precipitation of ith month simulated by GCM for future period and $\mu_{i\mathrm{CGCM}}$ is mean precipitation of ith month of GCM in control period. Changes in wet and dry spell lengths are not considered since these affect the monthly means. The future weather data corresponding to these change factors are generated using weather generator separately for three time periods (2011–2040, 2041–2070 and 2071–2100) for RCP4.5 scenario.

3.2 Linear Scaling

In this approach, the bias in the monthly means is corrected using a correction factor. Changes in monthly means between observed station precipitation and GCM simulations for same the time period (1975–2005) are calculated for all the months using Eq. (2). The calculated changes are used as multiplicative factors to GCM-simulated future time series to downscale precipitation to local scale.

$$P_{i\,\text{future}} = P_{i\,\text{FGCM}} * \frac{\mu_{i\,\text{obs}}}{\mu_{i\text{CGCM}}} \tag{2}$$

where $P_{i\text{future}}$ is the future downscaled daily precipitation, $P_{i\text{FGCM}}$ is future GCM-simulated precipitation, $\mu_{i\text{obs}}$ is mean of observed precipitation and $\mu_{i\text{CGCM}}$ is mean of GCM-simulated precipitation over control period for ith month.

3.3 Quantile Mapping

QM is an effective approach to apply daily scaling. Here, the quantiles of observed and GCM-simulated values of control period are mapped, and the corresponding bias is corrected as given in Eq. (3). Quantile mapping is a nonparametric method, and empirical cumulative distributions are fitted to data irrespective of distribution it follows.

$$P_{i\,\text{future}} = \text{ECDF}^{-1}_{i\,\text{obs}}(\text{ECDF}_{i\,\text{CGCM}}(P_{i\,\text{FGCM}}) \tag{3}$$

where $P_{i\text{future}}$ is the downscaled daily precipitation of ith month, $\text{ECDF}_i^{-1}{}_{\text{obs}}$ is inverse cumulative distribution of observed data for ith month, $\text{ECDF}_{i\text{CGCM}}$ is the ith month cumulative distribution function of GCM simulations for control period and $P_{i\text{FGCM}}$ is the future ith month GCM simulations.

4 Results and Discussion

4.1 Model Calibration

Calibration of LARS-WG: The daily precipitation data from control period are used for calibration of the model. Synthetic time series of 30 years from the calibrated site is generated from different random seeds, and the performance of the LARS-WG is evaluated by performing the Kolmogorov–Smirnov (KS) test, checking the monthly means and determining the coefficient of determination and the root-mean-square error (RMSE) between observed data and generated data from all the random seeds for baseline period. After all the tests are performed,

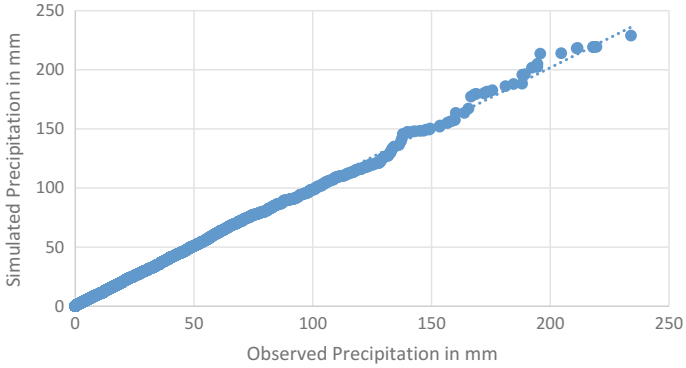

Fig. 3 Quantile plot between observed and LARS-WG-simulated daily precipitation values

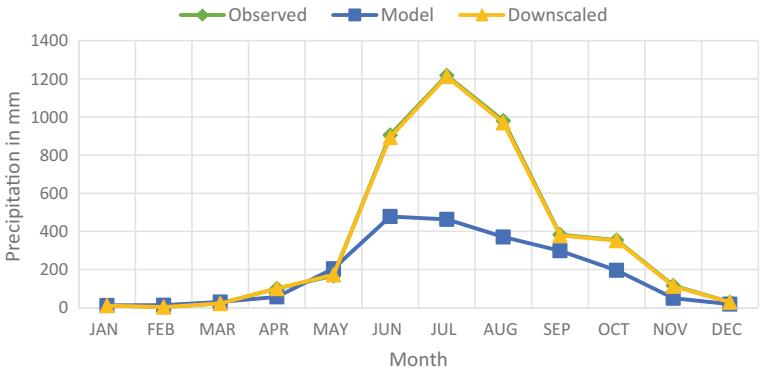

Fig. 4 Monthly means of observed, GCM-simulated and corrected precipitation after quantile mapping

the random seed, which is best in resampling the observed data, is chosen for downscaling. KS test is performed at 5% significance level; the null hypothesis is rejected, which signifies that both observed and simulated belong to the same type of distribution. Figure 3 shows the Quantile–Quantile (Q–Q) plot between simulated values from LARS-WG and observed data, with coefficient of determination of 0.99 and root-mean-square error of 0.72.

Quantile Mapping: The variations in the quantiles of observed and GCM simulations are corrected using quantile mapping as given by Eq. (3); the process is carried out separately for all the months so that the monthly mean and variance are also corrected with quantiles. The KS test performed signifies that both observed and corrected samples belong to similar distribution with 95% confidence level. Figure 4 shows the monthly means of observed, corrected and GCM-simulated precipitations, and it can observed that even after quantiles are mapped, monthly means are also corrected.

4.2 Downscaling

After the calibration of weather generator, scenario files are created with change factors for all the months as given by Eq. (1) for three time periods (2011–2040, 2041–2070 and 2071–2100) with respect to control period (1975–2005). The change factors obtained for future time periods are given in Table 1, which are used as perturbation factors in LARS-WG to obtain downscaled future precipitation separately for each period.

Linear scaling is performed by multiplying the future GCM simulations with scaling factors obtained using Eq. (2) based on control period, and the obtained scaling factors are given in Table 1, which are then applied to GCM precipitation from 2011 to 2100 to obtain downscaled precipitation.

Quantile mapping is done for GCM simulations from 2011 to 2100 by using Eq. (3), and the downscaled outputs from all the three models are shown in Fig. 5 as total annual precipitations. It can be observed that an increasing trend is seen in the total annual precipitation in future under RCP4.5 scenario. Peaks of high magnitudes are observed in QM method compared to LARS-WG and LS methods. This is because that in both LARS-WG and LS methods, the downscaling is done based on changes in monthly mean but in case of QM method downscaling is done on a daily basis, every quantile will have its own change factor. More number of low-magnitude precipitations years is simulated in LARS-WG; this may be due to the assumption that same precipitation pattern as observed will follow in future.

Monthly mean precipitations are plotted over a 3-year time span for the QM output and for observed rainfalls in the control period, as shown in Fig. 6. Though there is no shift in starting of monsoon (June), and the wettest month being restricted to July, there is an increase in the average rainfall in both July and

Table 1 Change factors for LARS-WG in different time periods and scaling factors for linear scaling

Month	Change factors for LARS-WG			Scaling factor for linear scaling
	2011–2040	2041–2070	2071–2100	
January	1.27	1.18	0.99	0.930778
February	1.25	1.34	0.90	0.297269
March	0.91	0.86	0.74	0.748469
April	1.14	1.16	1.11	1.763976
May	1.06	1.12	0.92	0.814356
June	1.07	0.97	1.05	1.893137
July	1.07	1.07	1.15	2.628097
August	1.27	1.22	1.35	2.641336
September	0.93	1.07	1.02	1.284861
October	1.06	0.97	1.02	1.806429
November	1.17	1.00	1.55	2.330202
December	0.95	1.29	0.90	1.572319

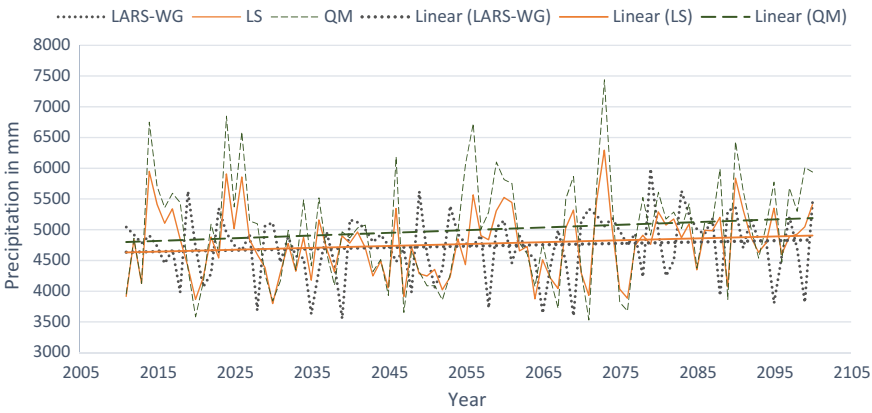

Fig. 5 Downscaled total annual precipitation from LARS-WG, LS and QM

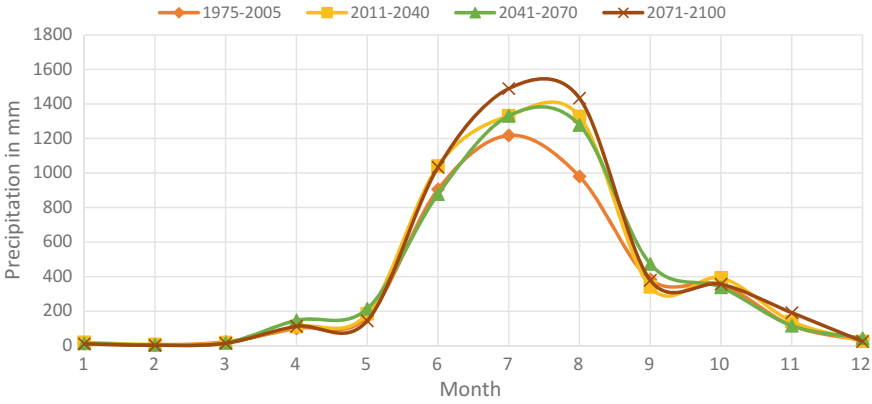

Fig. 6 Thirty-year monthly mean precipitation for observed and downscaled output from QM method

August, from 1217 mm in control period to 1332 mm in the near future and 1488 mm in the far future for the month of July, and 980 mm in control period to 1328 mm in the near future and 1433 mm in the far future for the month of August.

The annual maximums of QM method outputs are fitted with generalised extreme value (GEV) distribution, and the intensities corresponding to return periods 10, 20, 40, 60, 80 and 100 years are shown in Fig. 7. An increase in both intensities and frequency is observed in future.

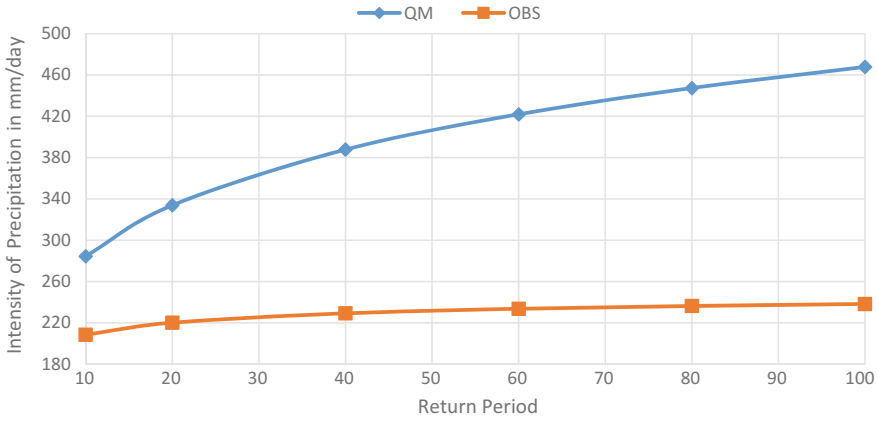

Fig. 7 Twenty-four-hour return levels for the QM method outputs under RCP4.5 scenario and in observed period

5 Conclusions

The effectiveness of the future climate impact studies depends on the ability of the GCM models to simulate climate response and the approach used to bridge the mismatch between spatial resolutions. Among the three approaches used to downscale precipitation, QM method is observed to simulate higher peaks than LARS-WG and LS methods. Total annual precipitation simulated by LARS-WG is comparatively less. This is due to the assumption that same type of distribution as observed will follow in future and the perturbation factors that are applied as changes in monthly means which will not account the changes in quantiles. The simulations from all the three models show an increasing trend in total annual precipitations. Considering QM method as superior when compared to LARS-WG and LS methods, the future downscaled precipitation data are analysed, and it was found that July will remain as the wettest month and precipitations during both July and August are expected to increase in magnitude in future under RCP4.5 scenario. The annual maximums from 2011 to 2100 and observed precipitations from 1975 to 2005 are fitted with GEV distribution, and an increase in extreme precipitation intensity and frequency is observed.

References

1. Anandhi, A., Srinivas, V.V., Nanjundiah, R.S., Nagesh Kumar, D.: Downscaling precipitation to river basin in India for IPCC SRES scenarios using support vector machine. Int. J. Climatol. **28**, 401–420 (2008). doi:10.1002/joc.1529

2. Kannan, S., Ghosh, S.: Prediction of daily rainfall state in a river basin using statistical downscaling from GCM output. Stoch. Environ. Res. Risk Assess. (Springer) (2010). doi:10.1007/s00477-010-0415-y
3. Meenu, R., Rehana, S., Majumdar, P.P.: Assessment of hydrologic impacts of climate change in Tunga-Bhadra river basin, India with HEC-HMS and SDSM. Hydrol. Process. (2012). doi:10.1002/hyp.9220
4. ARCC: A Review of downscaling methods for climate change projections. African and Latin American Resilience to Climate Change, under USAID (2014)
5. Devak, M., Dhanya, C.T., Gosain, A.K.: Dynamic coupling of support vector machine and K-nearest neighbour for downscaling daily rainfall. J. Hydrol. **525**, 286–301 (2015). doi:10.1016/j.jhydrol.2015.03.051
6. Raje, D., Mujumdar, P.P.: A comparison of three methods for downscaling daily precipitation in the Punjab region. Hydrol. Process. (2011). doi:10.1002/hyp.8083
7. Devak, M., Dhanya, C.T.: Downscaling of precipitation in Mahanadi Basin, India. Int. J. Civil Eng. Res. **5**, 111–120 (2014)
8. Furrer, E.M., Katz, R.W.: Improving the simulation of extreme precipitation events by stochastic weather generators. Water Resour. Res. **44**, W12439 (2008). doi:10.1029/2008WR007316
9. Hashmi, M.Z., Shamseldin, A.Y., Melville, B.W.: Comparison of SDSM and LARS-WG for simulation and downscaling of extreme precipitation events in a watershed. Stoch. Environ. Res. Risk Assess. **25**, 475–484 (2011). doi:10.1007/s00477-010-0416-x
10. Lu, Y., Qin, X.S., Mandapaka, P.V.: A combined weather generator and K-nearest-neighbour approach for assessing climate change impact on regional rainfall extremes. Int. J. Climatol. (2015). doi:10.1002/joc.4301
11. Claudia, T., Seiberth, J.: Bias correction of regional climate model simulations for hydrological climate-change impact studies: review and evaluation of different methods. J. Hydrol. **456–457**, 12–29 (2012)
12. Fang, G.H., Yang, J., Chen, Y.N., Zammit, C.: Comparing bias correction methods in downscaling meteorological variables for a hydrologic impact study in an arid area in China. Hydrol. Earth Syst. Sci. **19**, 2547–2559 (2015)

Quality of Rooftop Harvested Rainwater Stored in Polyethylene Terephthalate Container

Sakshi Gupta and Deepak Khare

Abstract Quality of rainwater is gaining awareness day by day in today's era looking over to the current crisis of freshwater sources and even scarcity of water. Due to the hasty increase in levels of pollution, urbanization, industrialization and climate change the quality of available water sources is depreciating day by day and we are left with the only option to look for some other reliable sources of water which can be potable enough and can be stored and used round the year specially during the dry spells of the year. This current study stresses on the harvested rainwater quality from the rooftops to look for the different aspects during storage which alters the quality of water and to find out the different methodologies which can be implemented for storing harvested rainwater so that the quality of the harvested water can be preserved during storage and is intact till the point it reaches its consumers. The outcome of this study can provide some firm rules for efficient rooftop rainwater harvesting. In the current work, polyethylene terephthalate material has been used as a storage material under different temperature conditions to analyze the quality of rainwater. The similar experimentation can be carried out with different materials for more diversity and analysis in the results.

Keywords Rooftop · Rainwater quality · Polyethylene container · Potable water · Urbanization

1 Introduction

Rainwater is usually treated as an invulnerable and relevant source of drinking water and is widely used in urban and rural areas in major parts of the world. The areas with acute shortage of water and other reliable sources are indulged into

S. Gupta (✉) · D. Khare
Department of Water Resources Development and Management,
Indian Institute of Technology, Roorkee 247667, Uttarakhand, India
e-mail: sakshilibran@gmail.com

D. Khare
e-mail: kharefwt@gmail.com

V. Garg et al. (eds.), *Development of Water Resources in India*,
Water Science and Technology Library 75, DOI 10.1007/978-3-319-55125-8_17

practice of rainwater harvesting since ages and rainwater is usually collected and stored for use round the year mainly during dry spells. But the main issue arising is with the quality of stored rainwater with time, if it is healthy to consume and if the required drinking water parameters are obtained from it with time after facing the long storage in different materials or mediums and random temperatures. Therefore, this experimentation was taken up to scrutinize the quality of rainwater after storage in polyethylene terephthalate storage container so as to successfully implement this practice in all the places facing crisis for drinking water and to involve more masses into this healthy practice for a better society. Increased awareness for the use of safe water has generated more demand for fresh water [1, 2]. More than half the world's population is living with the dearth of water for suitable sanitation, and about 20% population is living with crisis for potable water. River, lakes and groundwater are all considered as inferior water sources in correlation with rain which is the first course of water in the natural hydrologic cycle. But with time this fact has been scorned that it is the one furnishing the other inferior water sources. Harvesting of rainwater emphasizes on knowing the precious value of rain and to make best possible use of it at the place of its occurrence.

Due to the diminishing open land and increasing covered area, only a very less amount of precipitation is able to reach the ground and rest is wasted through the drains as storm water. The best way for managing harvesting of rainwater is by doing it through rooftops. It is emanating at a fast rate due to ease in collection. But the quality of the harvested water differs to a huge extent compared to the standards as specified in drinking water specifications regardless of the actuality that it is the purest form of water. Past studies show that the water collected is contaminated feebly due to the presence of various pathogenic organisms, heavy metals, various site conditions, roof materials and if the area is near heavy vehicular exhaust.

The main emphasis has been laid on the actuality that the suitability and quality of the harvested rainwater from the rooftops lean on the practice by which it is collected, stored and much upon the material of the storage and even microbiological quality should be given due consideration [3–5]. For using the stored harvested water for a longer duration, it becomes imperative to scrutinize the alterations which may appear in the water quality after or during longer storage durations.

2 Area of Study

The area for study chosen here is renowned Indian Institute of Technology, Roorkee, present in Uttarakhand state of India. This institute happens to be one of the best technical institutes in the world playing an important role in furnishing all the divisions of technological development. Roorkee is a part of Uttarakhand state situated in Haridwar district giving Himalayan view with ranges brimming in both east and northeast. The city of Roorkee is along the edges of Ganga canal flowing on the way amidst Dehradun and Delhi on the National Highway 58. Roorkee is

acknowledged for having one of the primeval cantonments of the country, i.e., Roorkee Cantonment and for having Bengal Sappers headquarters since 1853. The city has a mediocre elevation of about 268 m with location at 29.87° N and 77.88° E and can be reached at a distance of 172 km from New Delhi near foothills of Himalayas amidst Ganga and Yamuna rivers.

3 Locations for Sample Collection

The locations for collection of samples were preferred depending on their ambience which included overhanging trees, proximity to the areas with varying intensities of pollution owing to the traffic loads in the concerned area. Following these criteria, two sampling locations were chosen within the premises of the institute Sarojini Bhawan, a girls hostel surrounded by the overhanging tress and another sampling location was on the outer periphery of the institute Ghananand Pandey hostel which is in the close proximity to the highway and there by having high loads of vehicles and pollution. The rainwater was hoarded from rooftops through downpipes and in the containers placed under them in a single event of rainfall; the rainwater was initially hoarded in another containers due to complication in direct collection of rainwater [6].

4 Methodology and Data Presentation

The rainwater collected was stored under two different temperature conditions at room temperature (LOW) and in sunlight (HIGH) and in polyethylene terephthalate bottles. The experimentation has been done at a time lapse of about one month between September and March to analyze its quality with respect to the specifications given by Indian Standards of Drinking Water as given in [7] for resolving the parameters such as acidity, turbidity, hardness, pH, chlorides, alkalinity, specific conductivity, dissolved oxygen and total dissolved solids. It was also considered essential to collect all the samples in sole event of the rainfall itself. The pH and specific conductivity have been analyzed by using digital measuring devices. The very first testing after collection and storage was done within an hour at around 11 a.m. The varying parameters for scrutinizing the quality of the harvested rainwater was done by using simplified chemical analysis products which usually comes with a trade name of Pack tests for water quality. Total dissolved solids were calculated by the multiplication of constant 65 with specific conductivity. Coliform bacteria were also determined at a gap of one month only. The foremost consideration was not to add any water during complete storage duration to the stored water. The varying range of water quality parameters during experimentation is given in Tables 1 and 2.

Table 1 G.P. Hostel polyethylene terephthalate

Parameters	25/9/2015		1/11/2015		1/12/2015		2/1/2016		2/2/2016		3/3/2016	
	L	H	L	H	L	H	L	H	L	H	L	H
Turbidity	1	1	0	0	0	0	0	0	0	0	0	0
Acidity	10	10	10	10	10	10	10	10	10	10	10	10
pH	6.5	6.5	5.5	5.5	5.5	5.5	5.5	7	5.5	7	5.5	7
Hardness	30	30	16	28	24	32	20	24	20	22	20	22
Alkalinity	50	50	20	20	20	20	20	40	30	40	30	30
Chloride	30	30	10	10	10	10	10	10	20	10	20	10
Dissolved oxygen	7.15	7.15	6.15	6.5	1.95	1.3	3.9	1.95	8.45	7.8	9.1	7.8
Specific conductivity	5	5	4	6	4	6	4	6	4	6	4	7
TDS	32.5	32.5	26	39	26	39	26	39	26	39	26	45.5
Microbiological quality	P	P	P	P	P	P	N	N	N	N	N	N

Table 2 Sarojini Bhawan polyethylene terephthalate

Parameters	25/9/2015		1/11/2015		1/12/2015		2/1/2016		2/2/2016		3/3/2016	
	L	H	L	H	L	H	L	H	L	H	L	H
Turbidity	5	5	0	0	0	0	0	0	0	0	0	0
Acidity	10	10	10	10	10	10	10	10	10	10	10	10
pH	6	6	5.5	5.5	5.5	5.5	5.5	5.5	5.5	5.5	5.5	9
Hardness	40	40	30	40	24	50	16	50	20	50	20	50
Alkalinity	40	40	30	200	30	200	30	200	30	40	30	40
Chloride	20	20	20	20	20	20	20	20	10	20	10	20
Dissolved oxygen	5.2	5.2	4.5	6.55	9.1	5.85	7.8	8.45	8.45	7.8	9.1	7.15
Specific conductivity	5	5	4	7	4	4	5	3	4	4	4	5
TDS	32.5	32.5	26	45.5	26	26	32.5	19.5	26	39	26	32.5
Microbiological quality	P	P	P	P	P	P	N	N	N	N	N	N

5 Results and Discussion

Initially little turbidity is found in all the samples at both low and high temperature owing to the remaining undesirable particles in the harvested rainwater even after keeping the provision for first flush but with time during storage were found settling down, hence reducing to zero in the following tests of turbidity which is within the permissible limits as per Indian standard.

Acidity comes out to be nearly constant during entire storage and is also found to be proportional directly to the pH value of the water sample which is under the acceptable limits. This current analysis also concludes that the water quality in

relation to pH is somewhere better at high temperature in correlation to the low temperature. Hardness is found to be varying in the range 20–75 mg/l which is in the permissible limits as well as per the standards and in general has no conflicting effect on human health. Alkalinity has shown variation during entire experimentation between 20 and 200 mg/l and for potable use the higher permissible limit is 400 mg/l. Chloride is also found to be within the acceptable limits. Dissolved oxygen has changed in all the settings of storage indicating that it is dependent on temperature and therefore affects quality of water. In the current study, the containers placed in sunlight have been found with algae; therefore, direct sunlight should be avoided during storage. From health point of view, dissolved oxygen has no adverse effect on human health.

Specific conductivity for rainwater usually varies between 10 and 20 micro-Siemens/cm, and below 200 micro-Siemens/cm, it is taken to be of good quality, also total dissolved solids are proportional to the specific conductivity directly and a value up to 500 mg/l for drinking purpose is considered good. Result analysis of the entire experimentation in the present study points out that all the water quality parameters have their values within the acceptable limits of basic guidelines and standards. Microbiological quality has also shown improvement with time if care is taken not to add any water in the stored samples; initially, the tests came positive implying the unsuitability of the harvested rainwater for drinking but with the passing time the water quality improved and tests done further came negative as well.

6 Conclusion

Water to be used as potable water should be free from organic substances, minerals and organisms causing paradoxical physiological effects on regular consumption of such waters for longer durations. The current experimentation also concludes that the quality of water improves during storage with time if no additional water is reckoned to the harvested water and if appropriate storage and collection methodologies such as initiating proper first flush and other cleanliness are properly followed. From the results achieved, we can conclude that a polyethylene terephthalate container is good for storage under high temperature or sunlight compared to room temperature as quality is coming more acceptable in case of high temperature for both drinking water parameters and microbiological quality, also the storage should be done away from direct sunlight to avoid any algae formation to maintain the water quality of the harvested rainwater from the rooftops for a longer time. Rather partial sunlight is far better than room temperature and direct sunlight in case of polyethylene terephthalate material to have a better quality and to avoid algae production as well.

References

1. Meera, V., Ahammed, M.: Water quality of rooftop rainwater harvesting systems: a review. Aqua **55**, 257–268 (2006)
2. Nzewi, E.U., Srujana, S., Lee, E.J.: Monitoring of roof-harvested rainwater quality. In: Reston, VA: ASCE copyright Proceedings of the 2011 World Environmental and Water Resources Congress, May 22, 26, 2011, American Society of Civil Engineers: Palm Springs, California| d 20110000 (2011)
3. Kurukulasuriya, M.: Effective application of first flush device to improve rainwater quality. In: 9th International Rainwater Catchment Systems Conference. Rainwater Catchment: An Answer to the Water Scarcity of the Next Millennium Petrolina, Brazil, July (1999)
4. Lye, D.J.: Rooftop runoff as a source of contamination: a review. Sci. Total Environ. **407**(21), 5429–5434 (2009)
5. Michaelides, G., Young, R.: Provisions in design and maintenance to protect water quality from roof catchments. Int. J. Environ. Stud. **25**(1–2), 1–11 (1985)
6. Kitamura, K., Kita, I., Takeuchi, A.: The effect of storage location on collected rainwater quality
7. IS 10500: 2012

Comparison of Turbulent Hydrodynamics with and without Emergent and Sparse Vegetation Patch in Free Surface Flow

Debasish Pal, Bapon Halder and Prashanth R. Hanmaiahgari

Abstract In the present study, we have compared the turbulent hydrodynamics in open turbulent flow with and without an emergent and sparse vegetation patch. The rigid patch, located at the middle cross-sectional region, was made by acrylic cylindrical rods with regular spacing between them along streamwise and transverse directions. The measurements of flow velocity components were taken by a Nortek Vectrino Plus acoustic Doppler velocimeter, and experimental data were collected along cross section for vegetation-free fully developed flow and along the cross section which is located at the middle of the streamwise length of the vegetation patch. Inside the vegetation patch, we have observed decreased value of time-averaged streamwise velocity in comparison with those of the vegetation-free fully developed flow. The time-averaged values of transverse and vertical velocities show increased magnitude with respect to the corresponding values in the vegetation-free fully developed flow. Inside the vegetation patch, with increasing transverse length from right-hand sidewall to left-hand sidewall, the magnitudes of normal stresses gradually increase and exceed the corresponding magnitudes of normal stresses in the vegetation-free fully developed flow. Along the cross section inside the patch, the magnitudes of governing Reynolds shear stress are smaller than the corresponding values of Reynolds shear stress without the vegetation. Along the cross section inside the patch, the vectors of secondary current follow are directed towards the left-hand sidewall together with zigzag pattern in vertical direction. In the interior of the vegetation, the strength of anticlockwise vortex in terms of the magnitude of moment of momentum is greater than that of the vegetation-free fully developed flow.

D. Pal (✉) · B. Halder · P.R. Hanmaiahgari
Department of Civil Engineering, IIT Kharagpur, Kharagpur 721302, India
e-mail: bestdebasish@gmail.com

B. Halder
e-mail: bapon.india18@gmail.com

P.R. Hanmaiahgari
e-mail: hpr@civil.iitkgp.ernet.in

V. Garg et al. (eds.), *Development of Water Resources in India*,
Water Science and Technology Library 75, DOI 10.1007/978-3-319-55125-8_18

Keywords Turbulence · Emergent vegetation · Sparse vegetation · Free surface flow · Energy spectrum · Secondary current

1 Introduction

Vegetation of trees is often observed on the floodplain edge of natural rivers. The intensity of flow is highly influenced by the induced drag force of the vegetation. Due to the importance of vegetation in ecology and environment, the investigation of the hydrodynamic properties and the turbulence structure together with the effect of vegetation is a significant topic of research in the river engineering. A large number of investigations have been done in open-channel turbulent flow with emergent vegetation where researchers [3, 7–9, 15] predicted the flow resistance with different values of discharge, density of vegetation, stem diameter and several other factors. The experimental study of White and Nepf [13] revealed that at the edge of the vegetation patch, a shear region with two layers is found where the inner layer is related to the momentum penetration into vegetation and the outer layer contains the structure of the vortices generated in the shear region. Stoesser et al. [10] followed a formation of shear layer between inside and outside the vegetation patch owing to the presence of steep velocity gradients along streamwise, transverse and vertical directions. The experimental study of Zhang et al. [14] revealed that an emergent vegetation patch has an ability in forcing water from the vegetated area to the vegetation-free space and the force increases with an increase in the vegetation density. Investigators [1, 11] found that the emergent vegetation patch increases the hydraulic roughness in the flow region, and the eddies generated in the entire flow depth are responsible for intense turbulent mixing in the patch.

The sparse nature of emergent vegetation has several applications which are jute plantation, mangroves, wetland flow and several others. It is worth mentioning that till now, no comprehensive experimental comparison of turbulent features along cross section has been done between an emergent and sparsely vegetated open-channel flow and the vegetation-free fully developed flow. The overlooked research topic has been addresses in this study, and its organization has been done as follows. The methodology of experiment is in Sect. 2. The results obtained and the corresponding detailed discussions are given in Sect. 3. The study is ended by a summary of conclusions.

2 Experimental Methodology

We have performed the experiments in a flume located in Hydraulic and Water Resources Engineering Laboratory of Indian Institute of Technology Kharagpur, India. The flume with a longitudinal slope of 0.0002 had dimensions of 1200 cm long, 91 cm width and 61 cm deep, and it was located on a fixed steel frame

structure with hollow sections. To ensure the structural rigidity of the water pressure during flow, the flume was strengthened with two glass sidewalls with dimensions of 800 cm long and 1.5 cm thickness, and the sidewalls were used in obtaining a clear view of the flow. Standing in the middle of the flume and looking in the flow direction, the two glass sidewalls were treated as right-hand side (RHS) wall and left-hand side (LHS) wall according to our right and left hands, respectively, and it can be understood well from the top view of the experimental set-up shown in Fig. 1. A honeycomb baffle wall was attached at the inlet of the flume, and the baffle wall broke large eddies into small eddies in the flow so that it can achieve a fully developed nature after a certain downstream length from the inlet. The channel bed was made rough by coating sand particles of size D_{50} = 0.25 cm. We have considered the test section as 300 cm long, and its initial point was started from 700 cm downstream from the inlet where the flow was fully developed.

At the middle region of the cross-sectional area of the flume, we fixed the vegetation patch at 100 cm downstream from the starting of the test section. We have used seventy uniform cylindrical rods with dimensions of 30 cm long and 0.64 cm diameter for the preparation of the rigid vegetation patch. Those rods were set-up perpendicularly on a perspex sheet which was attached in the channel bed. We have arranged the rods by a 7 × 10 array where seven rows and ten columns followed the streamwise and transverse directions, respectively. The sparse nature of the vegetation patch was achieved by maintaining regular spacings of 9 and 4 cm between the centres of two consecutive cylinders along streamwise and transverse directions, respectively. The dimensions of the vegetation patch were 81 cm long and 24 cm width. The arrangement of the sparse vegetation patch in the flume can be clarified from the top view of not to scale diagram of the experimental set-up in Fig. 1.

Two centrifugal pumps were used for the recirculation of the water in the underground sump and the flume. We have measured the flow rate by a calibrated V-notch and the average flow velocity was 29 cm/s. Providing a tailgate at the downstream end of the flume, an emergent vegetated flow was obtained by maintaining the flow depth h as 15 cm which is smaller than the length (30 cm) of the cylindrical rod used as a plant in the vegetation patch. The flow depth and a

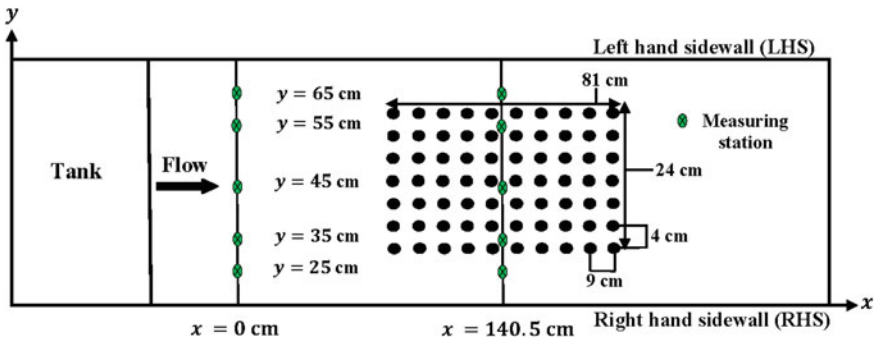

Fig. 1 Schematic diagram of the top view of the flow with sparse vegetation

vertical position from the channel bed were measured using a pointer gauge with an accuracy ±0.01 cm. A Nortek Vectrino Plus ADV with a fixed probe and four side looking beams was used for the measurement of instantaneous streamwise, transverse and vertical components of flow velocity. For easy positioning of ADV and pointer gauge, we have provided carriages on rails on the sidewalls of the flume. For the measurement of flow velocity, we waited 30 min to allow the stabilization of the flow field. Along the cross section located at the starting point of the test section, a three-dimensional coordinate system was considered where the intersection point of the channel bed and the RHS wall represented the origin, and the axes x, y and z represented the streamwise, transverse and vertical directions, respectively. We collected data along two cross-sectional regions at $x = 0$ and 140.5 cm in which the second location represented the middle point of the length of vegetation patch. For each streamwise point, measurements were taken at five transverse points expressed by $y = 25$, 35, 45, 55 and 65 cm. The top view of the measurement locations together with the coordinate system can be understood clearly from Fig. 1. The ADV measured the velocity at fifteen vertical locations from the channel bed given by $z = 0.3$, 0.5, 0.7, 0.9, 1.5, 2, 2.5, 3, 4, 5, 6, 7, 8, 9 and 10 cm.

We recorded velocity at each vertical point with time of 120 s, sampling frequency of 100 Hz and sampling volume of 2.5 cm^3. To avoid erroneous result, we removed the random spikes from the recorded data by the spike filtering technique given in the literature [4, 6, 12]. The cubic interpolation was used in replacing the values of removed spikes. After that, signal-to-noise ratio test as proposed by Chanson et al. [2] was applied in obtaining good quality of data and the ratio value was maintained as 15. At the end, we considered the data with correlation value greater than 75% and was used in comparing the turbulent hydrodynamic along cross section in open-channel flow with and without sparse vegetation.

3 Results and Discussion

We have computed turbulent features from the processed data in Sect. 2 and have compared the turbulent hydrodynamics along the cross section for vegetation-free fully developed flow ($x = 0$ cm) and the cross section located at the midpoint of the streamiwse length of the vegetation patch ($x = 140.5$ cm). The comparison analysis has been done by explaining the detailed physics of the observed characteristics of three-dimensional time-averaged velocity components, normal stresses, Reynolds shear stresses, turbulent kinetic energy spectrum, secondary current and vortex structure. We have denoted the time-averaged components of streamwise, transverse and vertical as u, v and w, respectively, and the corresponding fluctuation components are represented by u', v' and w', respectively. The vertical height z from the channel bed is normalized by the flow depth h and normalized vertical height is represented by $\xi = z/h$.

3.1 Time-Averaged Velocity of Flow

The time-averaged three-dimensional components of flow velocity provides an apparent idea of the turbulent fluctuations. Figure 2 shows the comparison of time-averaged streamwise velocity u along the cross sections for $x = 0$ and 140.5 cm where the ranges of u magnitude are 25–50 cm/s and 15–35 cm/s, respectively. It is observed that along the cross section located interior of the vegetation patch ($x = 140.5$ cm), the magnitudes of u shows decreasing value in comparison with the corresponding values of vegetation-free fully developed flow ($x = 0$ cm). We have observed no significant magnitude difference in the cross-sectional profiles of u at $x = 0$ cm. However, at $x = 140.5$ cm, the values of u are decreasing with increasing transverse length from the RHS wall to the LHS wall inside the vegetation patch ($y = 35$, 45 and 55 cm) and the decreased rate of depth-averaged u value is in the order of 4 cm/s. In comparison with the components of u at $y = 55$ cm, the components of u increase at $y = 65$ cm as the flow is free from the vegetation patch near the LHS wall. Inside the vegetation patch at $x = 140.5$ cm, the flow faces the obstruction of cylinders which are fixed in the first half downstream length of the vegetation patch. Therefore, the flow losses its intensity and results in decreasing magnitude of u in comparison with that of the vegetation-free fully developed flow. Inside the vegetation patch, eddies are generated due to the interaction between flow and cylinders and it is worth mentioning that the strength of anticlockwise rotating eddies is greater than the strength of clockwise rotating eddies in the patch. The anticlockwise rotating eddies decrease the magnitude of u along the transverse length inside the patch ($y = 35$, 45 and 55 cm). Due to the blockage of cylinders, the flow separations from the vegetation patch to the RHS and LHS sidewalls are responsible for the smaller magnitude of u between the sidewalls and the patch ($x = 140.5$ cm, $y = 25$ and 65 cm) in comparison with the corresponding u magnitude in the vegetation-free fully developed flow. An observed important phenomenon is that the magnitudes of u at $y = 65$ cm adjacent to the LHS wall are smaller than the magnitudes of u at $y = 25$ cm adjacent the RHS wall.

The comparison of time-averaged transverse velocity v along the cross sections for $x = 0$ and 140.5 cm is shown in Fig. 3. We have observed that v shows positive

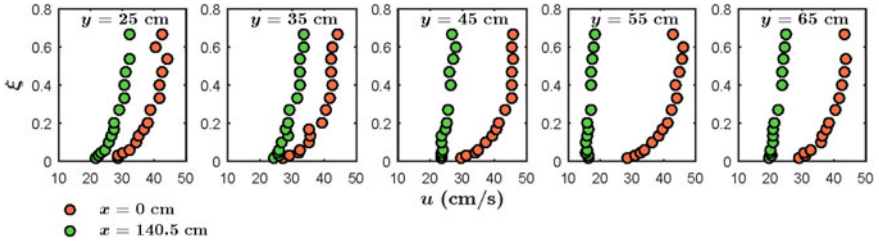

Fig. 2 Comparison of time-averaged streamwise velocity profiles u in two cross sections represented by $x = 0$ cm (vegetation-free fully developed flow) and $x = 140.5$ cm (midpoint of the length of the vegetation patch length)

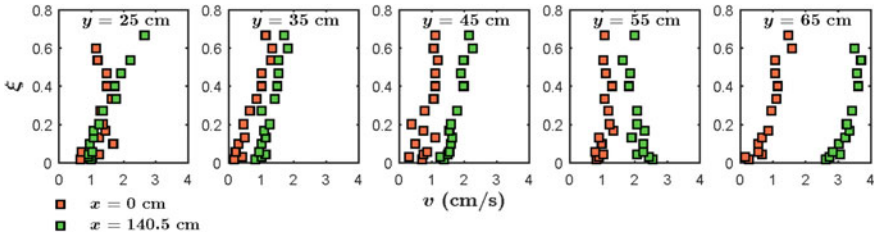

Fig. 3 Comparison of time-averaged transverse velocity profiles v in two cross sections represented by $x = 0$ cm (vegetation-free fully developed flow) and $x = 140.5$ cm (midpoint of the length of the vegetation patch length)

values throughout the cross section and the ranges of v magnitudes are obtained as 0–2 and 0.8–4 cm/s at $x = 0$ and 140.5 cm, respectively. The positive value implies that the flow turns towards the LHS wall. At $y = 25$ cm where the flow was not obstructed by the vegetation, we have observed no significant difference in transverse velocities at $x = 0$ and 140.5 cm except far from the channel bed. Eddies which are generated around the cylinders in the separation region of the patch move towards the free surface through swirling motion and influence the flow field which is located far from the channel bed at $y = 25$ cm; therefore, a difference in magnitude of v component is observed in the region. With increasing transverse length from the RHS wall to the LHS wall inside the patch ($y = 35$, 45 and 55 cm), the magnitude of v increases and the phenomenon is continued after crossing the vegetation patch at $y = 65$ cm adjacent to the LHS wall. The increased rate of depth-averaged v value is in the order of 0.4 cm/s. The large number of anti-clockwise rotating eddies along the cross section increases the magnitude of v with increasing transverse length. Apart from this, the magnitudes of v at $y = 35$, 45, 55 and 65 cm along the cross section inside the vegetation patch ($x = 140.5$ cm) are greater than the vegetation-free fully developed flow ($x = 0$ cm) and the difference in magnitude increases with increasing transverse length. The increase in inertial force in transverse direction inside the vegetation patch is responsible for the increased magnitude difference. For $y = 25$ and 65 cm at $y = 140.5$ cm, an interesting phenomena is observed that the magnitude of v at $y = 25$ cm is smaller than the magnitude of v at $y = 65$ cm. The released vortices adjacent to LHS wall are stronger than the released vortices adjacent to the RHS wall; therefore, the magnitudes of v at $y = 65$ cm are greater than the magnitude of v at $y = 25$ cm.

Figure 4 shows the comparison of time-averaged vertical velocity w along the cross sections for $x = 0$ and 140.5 cm. For vegetation-free fully developed flow ($x = 0$ cm), the values of w along the cross section are negative which imply downward vertical velocity. Along the cross section inside the patch ($x = 140.5$ cm), the values of w are greater than the corresponding values of w for $x = 0$ cm. At $x = 140.5$ cm, the profiles of w along cross section show both positive and negative values throughout the flow depth except at $y = 45$ cm where negative values of w are observed throughout the flow depth. The intricate turbulent mixing inside the vegetation patch and the complicated dynamics of flow separations due to the blockage

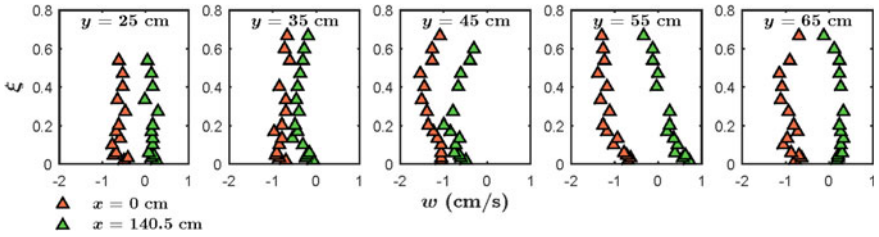

Fig. 4 Comparison of time-averaged vertical velocity profiles w in two cross sections represented by $x = 0$ cm (vegetation-free fully developed flow) and $x = 140.5$ cm (midpoint of the length of the vegetation patch length)

of the cylinders are responsible for the irregular behaviour of v profiles along the cross section inside the vegetation patch ($y = 25$, 35, 55 and 65 cm). Besides this, we have envisaged that due to the symmetrical position of the vegetation patch along cross section, the separation of flow is very less at $x = 45$ cm for the vegetation-free fully developed flow and the flow moves inside the vegetation patch with greater value, in other words smaller negative value. We can notice that from the midregion of the cross section inside the vegetation patch ($y = 45$ cm), w has a tendency in converging from negative to positive value with increasing transverse length towards the RHS wall and LHS wall. The observed characteristic implies that the flow has a high potential of erosion in the midregion of the cross section in the interior of the patch; however, the ability of erosion decreases with increasing transverse length towards the sidewalls.

Overall, we can say that though the position of the vegetation is symmetric along the cross section; nevertheless, no symmetry of u, v and w along the cross section inside the patch is observed with respect to the midpoint of the channel width.

3.2 Normal Stresses

In open-channel turbulent flow, the three normal stresses $\overline{u'^2}, \overline{v'^2}$ and $\overline{w'^2}$ along streamwise, transverse and vertical directions, respectively, have important role in characterizing the fluctuations of flow velocity. The profiles of $\overline{u'^2}, \overline{v'^2}$ and $\overline{w'^2}$ at $x = 0$ and 140.5 cm are shown in Figs. 5, 6 and 7, respectively. We have observed that the ranges of the magnitudes of $\overline{u'^2}, \overline{v'^2}$ and $\overline{w'^2}$ are 0–40, 0–30 and 0–10 cm^2/s^2, respectively. For vegetation-free fully developed flow ($x = 0$ cm), we have observed that the profiles of $\overline{u'^2}$ and $\overline{v'^2}$ have a decreasing phenomenon with increasing vertical height from the channel bed together with the existence of corresponding maximum values near the channel bed; however, the nature of $\overline{v'^2}$ is not conclusive. Apart from this along the cross section inside the vegetation patch at $x = 140.5$ cm, the magnitudes of $\overline{u'^2}, \overline{v'^2}$ and $\overline{w'^2}$ increase with increasing transverse length from the RHS wall to the LHS wall before crossing the edge of the vegetation patch ($y = 25$, 35, 45

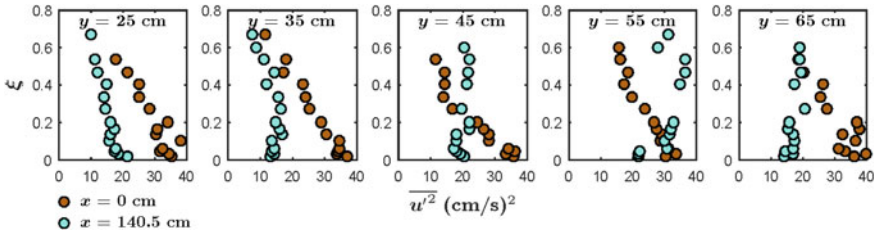

Fig. 5 Comparison of streamwise normal stress $\overline{u'^2}$ in two cross sections represented by $x = 0$ cm (vegetation-free fully developed flow) and $x = 140.5$ cm (midpoint of the length of the vegetation patch length)

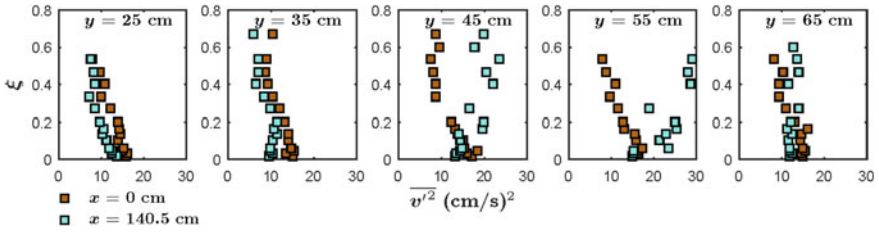

Fig. 6 Comparison of transverse normal stress $\overline{v'^2}$ in two cross sections represented by $x = 0$ cm (vegetation-free fully developed flow) and $x = 140.5$ cm (midpoint of the length of the vegetation patch length)

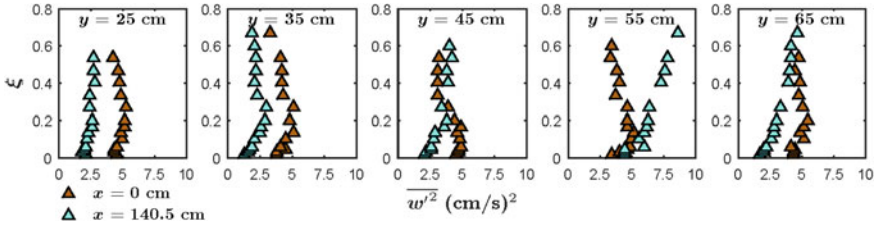

Fig. 7 Comparison of vertical normal stress $\overline{w'^2}$ in two cross sections represented by $x = 0$ cm (vegetation-free fully developed flow) and $x = 140.5$ cm (midpoint of the length of the vegetation patch length)

and 55 cm). Inside the vegetation patch, the rate of increasing magnitude of depth-averaged $\overline{u'^2}$, $\overline{v'^2}$ and $\overline{w'^2}$ are in the order of 6, 7 and 1 cm^2/s^2, respectively. The vortices generated due to the interaction between flow and cylinders of the vegetation create higher fluctuations in the components of flow velocity which result in the increased values of normal stress inside the vegetation patch. After crossing the vegetation patch along transverse direction ($y = 65$ cm), the values of $\overline{u'^2}$, $\overline{v'^2}$ and $\overline{w'^2}$ further decrease in comparison with the corresponding values at $y = 55$ cm. The fluctuations in velocity components seem to be decreased after crossing the

vegetation patch along transverse direction and result in decreasing magnitude of $\overline{u'^2}$, $\overline{v'^2}$ and $\overline{w'^2}$. Moreover, at $x = 140.5$ cm, the peak values of $\overline{u'^2}$, $\overline{v'^2}$ and $\overline{w'^2}$ profiles have a tendency in shifting gradually from near the channel bed to far from the bed with increasing transverse length from the RHS wall to the LHS wall. Inside the patch, slowly moving fluid parcel near the bed ejected towards the free surface through swirling motion and results in increased velocity fluctuations far from the channel bed in comparison with the region near the channel bed; therefore, the peak values of $\overline{u'^2}$, $\overline{v'^2}$ and $\overline{w'^2}$ occur far from the channel bed.

From Figs. 5, 6 and 7, we can state that at $y = 25$ and 65 cm where the flow is not obstructed by the vegetation, the magnitude of $\overline{u'^2}$, $\overline{v'^2}$ and $\overline{w'^2}$ at $x = 140.5$ cm is smaller than the corresponding values of normal stresses at $x = 0$ cm. The interesting phenomenon states that beside the patch where the flow is free from the vegetation, the fluctuations of velocity components are smaller than those of the vegetation-free fully developed flow. Besides this, after entering into the vegetation patch from the side of RHS wall ($y = 35$ cm), the values of normal stresses show smaller magnitude with respect to the corresponding magnitude at $x = 0$ cm; however, with increasing transverse length ($y = 45$ and 55 cm), the profiles of $\overline{u'^2}$, $\overline{v'^2}$ and $\overline{w'^2}$ exhibit scatter in the data inside the patch due to higher velocity fluctuations and the magnitudes increase gradually in comparison with those values at $x = 0$ cm. Similar to the profiles of time-averaged velocity of flow, no symmetric nature of $\overline{u'^2}$, $\overline{v'^2}$ and $\overline{w'^2}$ is observed along the cross section inside the patch with respect to the midpoint of the channel width.

3.3 Reynolds Shear Stresses

The three Reynolds shear stresses $-\overline{u'w'}$, $-\overline{u'v'}$ and $-\overline{v'w'}$ play the most important role in the spatial distribution of flow velocity in open-channel turbulent flow. The flow field is highly influenced by $-\overline{u'w'}$, and its variation at $x = 0$ and 140.5 cm are shown in Fig. 8. We have observed that along the cross section inside the patch

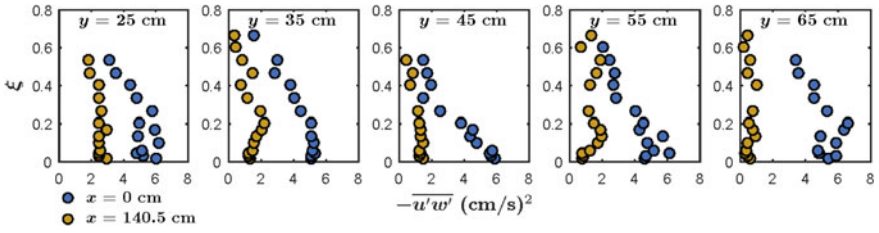

Fig. 8 Comparison of Reynolds shear stress $-\overline{u'w'}$ in two cross sections represented by $x = 0$ cm (vegetation-free fully developed flow) and $x = 140.5$ cm (midpoint of the length of the vegetation patch length)

($x = 140.5$ cm), the magnitudes of $-\overline{u'w'}$ are smaller than the corresponding values of vegetation-free fully developed flow at $x = 0$ cm. The prevalence of outward and inward events at $x = 140.5$ cm is responsible for the decreasing magnitude of $-\overline{u'w'}$. For vegetation-free space ($y = 25$ and 65 cm) along the cross section at $x = 104.5$ cm, we have followed that the magnitudes of $-\overline{u'w'}$ at $y = 25$ cm adjacent to the RHS wall are greater than the values of $-\overline{u'w'}$ at $y = 65$ cm adjacent to the LHS wall. Inside the vegetation patch, the irregular detachment of wake vortices is responsible for the scatter in the profile of $-\overline{u'w'}$ at $y = 35$ and 55 cm; however, at the midregion ($y = 45$ cm) of the cross section, $-\overline{u'w'}$ is developing a consistent profile.

Figure 9 shows the comparison of $-\overline{u'v'}$ at $x = 0$ and 140.5 cm and scattered trend in the profiles is observed. Moreover, at both streamwise positions, the profiles exhibit both positive and negative values. Interestingly, it is observed that with increasing transverse length from the RHS wall to the LHS wall ($y = 35$, 45 and 55 cm), the deviation between the corresponding profiles ($x = 0$ and 140.5 cm) of $-\overline{u'v'}$ is gradually decreased and after crossing the vegetation patch along transverse direction (y = 65 cm), the values of $-\overline{u'v'}$ at $x = 140.5$ cm are greater than the values of $-\overline{u'v'}$ at $x = 0$ cm. The comparison of Reynolds shear stress $-\overline{v'w'}$ for $x = 0$ and 140.5 cm is shown in Fig. 10. We have observed highly scattered profile of $-\overline{v'w'}$ at both cross-sectional regions and their values are similar for a given

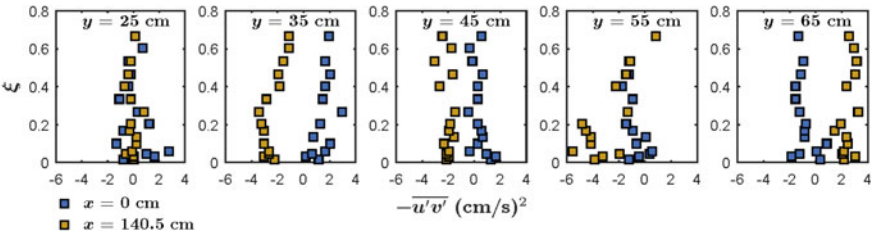

Fig. 9 Comparison of Reynolds shear stress $-\overline{u'v'}$ in two cross sections represented by $x = 0$ cm (vegetation-free fully developed flow) and $x = 140.5$ cm (midpoint of the length of the vegetation patch length)

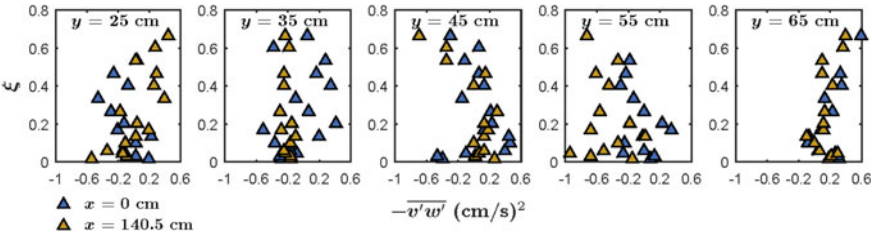

Fig. 10 Comparison of Reynolds shear stress $-\overline{v'w'}$ in two cross sections represented by $x = 0$ cm (vegetation-free fully developed flow) and $x = 140.5$ cm (midpoint of the length of the vegetation patch length)

y location. For the profiles of Reynolds shear stresses $-\overline{u'w'}$, $-\overline{u'v'}$ and $-\overline{v'w'}$, we have noticed no symmetrical characteristic with respect to the midpoint of the channel width though the position of the vegetation is symmetric along the cross-sectional area.

3.4 Turbulent Kinetic Energy Spectrum

The turbulent kinetic energy spectrum is analysed through the power spectral density (PSD) of the velocity signals. We have computed PSD using fast Fourier transform based on the Welch period gram spectrum estimator method in which a 2048-point Hamming window is used with 50% overlap. The signals each composed of 90,000 samples are measured at middepth (z = 7.7 cm) for two cross-sectional regions given by x = 0 and 140.5 cm. The spectral content of the velocity signal represents the energy spectrum of each frequency range and provides information about the flow features. In turbulent flows, each frequency is related to turbulent eddies of corresponding time and length scales. We have computed PDS of streamwise, transverse and normal velocity signals at x = 0 and 140.5 cm and have presented in Fig. 11. The spectral model tracks the dissipation of turbulent kinetic energy through the wavenumber space. Figure 11a represents the PSD at x = 0 cm and exhibits that in the inertial subregion where energy cascading takes place, the dissipation of the energy follows Kolmogorov −5/3 laws. However, at x = 140.5 cm, the slope of the energy spectrum is approximately equal to −1 as shown in Fig. 11b, i.e. slower decay of turbulent kinetic energy is observed in the interior of vegetation. Figure 11b also demonstrates that the concentration of turbulent kinetic energy is found to be in the inertial subrange of frequency between 1 and 20. Moreover, the energy spectrum deviates from the Kolmogorov −5/3 law which implies the prevalence of strong non-homogeneity of the flow field in the interior of the vegetation patch.

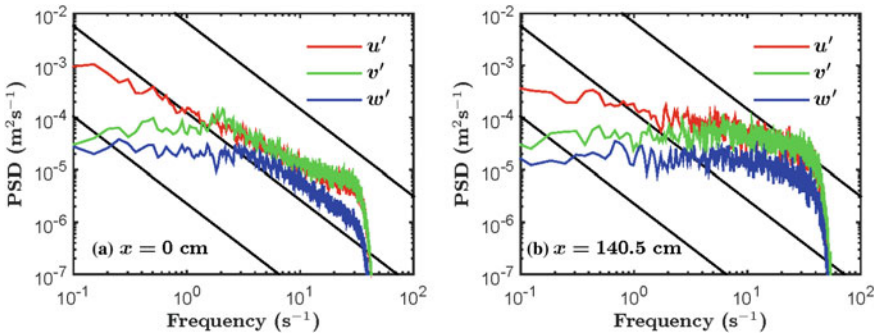

Fig. 11 Comparison of power spectral density (PSD) in two cross sections represented by x = 0 cm (vegetation-free fully developed flow) and x = 140.5 cm (midpoint of the length of the vegetation patch length)

3.5 Secondary Current

Secondary current is an important feature in the turbulent flow to characterize the transverse and vertical velocities of the flow. For the comparison of the secondary current at $x = 0$ and 140.5 cm, the vector plot of (v, w) at those regions is shown in Fig. 12. We can notice from Fig. 12 that strong secondary current is present in the flow region with and without vegetation represented by $x = 0$ and 140.5 cm, respectively. The secondary current at $x = 0$ cm is directed towards the LHS wall with downward vertical direction. Besides this, at $x = 140.5$ cm, the secondary current is also directed towards the LHS wall; however, a zigzag pattern is followed along the cross-sectional region due to the upward and downward directions of vertical velocity. At $x = 140.5$ cm where the flow faces no blockage of the vegetation ($y = 25$ and 65 cm), the secondary current turns vertically upward direction compared to the vertically downward direction in the vegetation-free fully developed flow ($x = 0$ cm).

The characteristic implies that over an erodible sediment bed, deposition would occur in the vegetation-free space along the cross section inside the vegetation patch. Inside the vegetation patch at $y = 35$, 45 and 55 cm, the secondary current converges gradually and changes its direction from downward to upward with increasing transverse length which indicates the reduction in erosion ability of the flow with an increase in transverse length inside the vegetation patch.

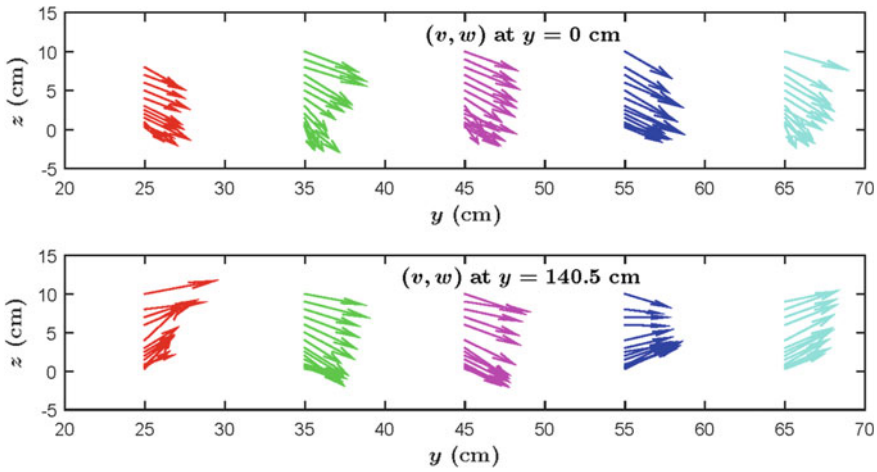

Fig. 12 Comparison of secondary current vectors (v, w) in two cross sections represented by $x = 0$ cm (vegetation-free fully developed flow) and $x = 140.5$ cm (midpoint of the length of the vegetation patch length)

3.6 Strength of Vortex

The three-dimensional velocity measurements are used in calculating the strength of vortex in terms of the magnitude of moment of momentum (MOM). Strictly speaking, due to the highly irregular nature of the turbulent flow inside the vegetation patch, it is very difficult to get a clear vortex structure along the cross-sectional area using ADV measurement. For a rough estimation, we have assumed (y_c, z_c) as the coordinate of the centre C of the vortex where y_c is the midpoint of the vegetation width and z_c is the middle point of the flow depth along vertical direction. For a unit weight of water, the MOM at a point P is calculated as

$$H_P = \frac{\gamma}{\rho}\left(\vec{R} \times \vec{V}\right) \tag{1}$$

where the position vector of P is $\vec{R}$ and $\vec{V}$ is the local velocity vector given by $V_{Py}\vec{j} + V_{Pz}\vec{k}$ where $\vec{j}$ and $\vec{k}$ express the unit vectors along y and z directions, respectively, the weight of the water is represented by γ and the mass density of the water is denoted by ρ. The coordinate of the P is assumed as (y_P, z_P) therefore $\vec{R} = \overrightarrow{OP} - \overrightarrow{OC} = (y_P - y_C)\vec{j} + (z_P - z_C)\vec{k}$ where O is the origin. We have computed MOM at P from Eq. (1) as

$$H_P = \frac{\gamma}{\rho}\left[(y_P - y_C)V_{Pz} \times (z_P - z_C)V_{Py}\right]\vec{i} \tag{2}$$

where $\vec{i}$ indicates the unit vector along x direction. For a cross section, the summation of MOM is obtained as

$$H_{cs} = \sum_{i=1}^{n} H_{Pi} \tag{3}$$

where n is total number of measurement points at the cross section. The detailed explanation about the advantage of the calculation of the strength of vortex in terms of MOM is given in Marelius and Sinha [5]. From Eqs. (1) to (3), the magnitudes of MOM are calculated for x = 0 and 140.5 cm as 139.8 and 572.9 cm^2/s^2, respectively. The positive values of MOM imply the anticlockwise rotation of vortex, and its strength inside the vegetation patch is greater than that in the vegetation-free fully developed flow.

4 Conclusions

The present study compares the phenomenological features along cross section in an emergent and sparsely vegetated open-channel flow and fully developed flow without the vegetation. Along the cross section inside the vegetation patch,

the magnitudes of time-averaged streamwise velocity are smaller in comparison with those of the vegetation-free fully developed flow. The values of time-averaged transverse and vertical velocities along the cross section in vegetation-free fully developed flow are smaller than the corresponding values along the cross section inside the vegetation patch. In the interior of the vegetation patch, the magnitudes of three normal stresses increase with increasing transverse length from the RHS wall to the LHS wall and exceed the corresponding values of the vegetation-free fully developed flow. At the cross-sectional locations where the flow faces no obstruction of vegetation, the magnitudes of normal stresses along the cross section inside the vegetation patch are smaller than the corresponding magnitudes of the vegetation-free fully developed flow. Among the three Reynolds shear stresses, the magnitudes of $-\overline{u'w'}$ along the cross section inside the vegetation are smaller than those of the vegetation-free fully developed flow; however, the remaining two Reynolds shear stresses $-\overline{u'v'}$ and $-\overline{v'w'}$ show poor correlation and their characteristics are not conclusive. In the vegetation-free fully developed flow, the power spectral density follows the Kolmogorov −5/3 law; however, a deviation from the law in the interior of the patch is followed due to the prevalence of non-homogeneity of the flow field. The secondary current follows a zigzag pattern towards the LHS wall along the cross section inside the vegetation patch; however, in the vegetation-free fully developed flow, the secondary current is directly towards the LHS wall with downward vertical direction. Inside the vegetation patch, the strength of anticlockwise vortex is greater than that in the vegetation-free fully developed flow. Finally, it can be concluded that the results obtained from this study would be useful for mathematical modelling of turbulent hydrodynamics in an emergent and sparsely vegetated open-channel flow and the model could be verified with the presented experimental data.

Acknowledgements IIT Kharagpur has given financial assistance to the first author Debasish Pal through a SRIC project (code: FVP).

References

1. Bennett, S.J., Wu, W., Alonso, C.V., Wang, S.S.: Modeling fluvial response to in-stream woody vegetation: implications for stream corridor restoration. Earth Surf. Proc. Land. **33**(6), 890–909 (2008)
2. Chanson, H., Trevethan, M., Aoki, S.I.: Acoustic doppler velocimetry (ADV) in small estuary: field experience and signal post-processing. Flow Meas. Instrum. **19**(5), 307–313 (2008)
3. Cheng, N.S.: Calculation of drag coefficient for arrays of emergent circular cylinders with pseudofluid model. J. Hydraul. Eng. **139**(6), 602–611 (2012)
4. Goring, D.G., Nikora, V.I.: Despiking acoustic doppler velocimeter data. J. Hydraul. Eng. **128**(1), 117–126 (2002)
5. Marelius, F., Sinha, S.K.: Experimental investigation of flow past submerged vanes. J. Hydraul. Eng. **124**(5), 542–545 (1998)

6. Mori, N., Suzuki, T., Kakuno, S.: Noise of acoustic doppler velocimeter data in bubbly flows. J. Eng. Mech. **133**(1), 122–125 (2007)
7. Musleh, F.A., Cruise, J.F.: Functional relationships of resistance in wide flood plains with rigid unsubmerged vegetation. J. Hydraul. Eng. **132**(2), 163–171 (2006)
8. Nepf, H.M.: Flow and transport in regions with aquatic vegetation. Annu. Rev. Fluid Mech. **44**, 123–142 (2012)
9. Ortiz, A.C., Ashton, A., Nepf, H.: Mean and turbulent velocity fields near rigid and flexible plants and the implications for deposition. J. Geophys. Res.: Earth Surf. **118**(4), 2585–2599 (2013)
10. Stoesser, T., Kim, S.J., Diplas, P.: Turbulent flow through idealized emergent vegetation. J. Hydraul. Eng. **136**(12), 1003–1017 (2010)
11. Vargas-Luna, A., Crosato, A., Uijttewaal, W.S.J.: Effects of vegetation on flow and sediment transport: comparative analyses and validation of predicting models. Earth Surf. Proc. Land. **40**(2), 157–176 (2015)
12. Wahl, T.L.: Discussion of despiking acoustic doppler velocimeter data by Derek G. Goring and Vladimir I. Nikora. J. Hydraul. Eng. **129**(6), 484–487 (2003)
13. White, B.L., Nepf, H.M.: Shear instability and coherent structures in shallow flow adjacent to porous layer. J. Fluid Mech. **593**, 1–32 (2007)
14. Zhang, H., Wang, Z., Dai, L., Xu, W.: Influence of vegetation on turbulence characteristics and reynolds shear stress in partly vegetated channel. J. Fluids Eng. **137**(6), 061,201 (8 pages) (2015)
15. Zhao, K., Cheng, N.S., Wang, X., Tan, S.K.: Measurements of fluctuation in drag acting on rigid cylinder array in open channel flow. J. Hydraul. Eng. **140**(1), 48–55 (2013)

Evaluation of Pan Evaporation Model Developed Using ANN

Shreenivas Londhe and Shalaka Shah

Abstract Estimation of evaporation is of vital importance in all walks of life. Traditionally, evaporation is estimated using several direct and indirect methods. Most of these methods have disadvantages like extensive data requirement, due to which they are difficult to apply. Chaudhari et al. (Int J Hydrol Sci Technol 2 (4):373–390, 2012) [2] successfully developed evaporation models for Nashik climatic centre, located in Maharashtra, India, using the soft computing tool of Artificial Neural Networks. In their work, they showed that ANN models work reasonably well in terms of estimation accuracy for pan evaporation modelling. Among the various parameters used by Chaudhari et al. (Int J Hydrol Sci Technol 2 (4):373–390, 2012) [2], two of them were the minimum and maximum daily temperatures as two separate inputs for calibration of the ANN models. This study proposes a novel approach of using average daily temperature as a single input instead of using the minimum and maximum temperature. The models were developed for both average and minimum and maximum temperature, and a detailed analysis was performed for evaluating both the sets. For this purpose, various objective and subjective assessments were carried out, most of which showed that the models trained using average temperature were giving better results. Additionally, the authors were also able to portray the importance of using the correct error measures as per the physical process being modelled and the error measures to be used while judging evaporation models.

S. Londhe (✉)
Department of Civil Engineering, Vishwakarma Institute of Information Technology, Pune, India
e-mail: shreenivas.londhe@viit.ac.in

S. Shah
Vishwakarma Institute of Information Technology, Pune, India
e-mail: shalaka18@hotmail.com

V. Garg et al. (eds.), *Development of Water Resources in India*,
Water Science and Technology Library 75, DOI 10.1007/978-3-319-55125-8_19

1 Introduction

An accurate estimation of evaporation is crucial for the management of agricultural irrigation, water balance, water supply and land resources planning. The amount of evaporation may be influenced by several meteorological factors, such as temperature, atmospheric pressure, wind speed, solar radiation and atmospheric humidity. Owing to the complexity involved in estimation of evaporation, researches have presented several direct and indirect methods, including experimental determination, empirical formulas, semiempirical formulas, mass transfer and water budget, in past decades [1]. Although it is possible to measure evaporation using evaporimeters, it is hard to place evaporation pans at every place where there is a planned or existing reservoir and irrigation project. Also, empirical methods are data intensive, they require measurement of many meteorological variables. It was thus thought of to try alterative techniques to estimate potential evaporation with reasonable accuracy and avoiding excessive data measurement. Chaudhari et al. [2] successfully developed evaporation models for Nashik climatic centre, located in Maharashtra, India, using the soft computing tool of Artificial Neural Networks. In their work, they showed that ANN models work reasonably well in terms of estimation accuracy for pan evaporation modelling. This was due to the ability of ANNs to represent nonlinear relationships that are difficult to model by means of other computational methods. Thus, for the present work the evaporation models were formed for Nashik.

In India, daily pan evaporation along with maximum and minimum humidity, maximum and minimum temperature, sunshine duration, wind speed, rainfall, etc., is measured at full climatic stations in different regions of the state and the data are collected and supplied to the user by agencies like Hydrology Project (HP), Indian meteorological department (IMD) and agricultural research institutes in every state. The question thus arises as to which parameters, when used as inputs, would give reasonably accurate results for modelling of evaporation. To gain insight on the importance of inputs, separate models were formed, by varying the inputs in each model. All these models were trained and tested using the neural network toolbox in MATLAB. To judge the accuracy of the models formed various error measures were taken into consideration.

To assess the performance of any hydrological model, both subjective and objective estimates should be made, as to how close the simulated behaviour of a particular model can get to its observed behaviour. The most fundamental method of evaluating the performance of a model is through a visual inspection of the differences between simulated and observed time series or scatter plots. With the help of these plots, subjective assessments can be formulated, of the model behaviour with respect to systematic (overprediction or underprediction) behaviour of the model. For objective assessment, however, one or more mathematical estimates of the error that occurs between the simulated and observed time series are required [3]. For the present work, various error measures were used to evaluate the accuracy of the ANN models developed and to judge the best model out of them. Also, a

critic was made as to which error measures would be sufficient for measuring the accuracy of the evaporation models developed using ANN.

The paper is organized as follows: succeeding sections discuss, study area and data followed by soft computing tools followed by the methodology, model formulation and their assessment. Later section discusses results followed by conclusions with references in the last section.

2 Study Area and Data

In the present study, the evaporation model at Nashik was developed. Nashik is located in northern Maharashtra at 600 m from the mean sea level. Nashik lies on western edge of the Deccan Plateau which is a volcanic formation. The total land area of the city is about 259.13 km^2 which makes it the fifth largest urban area of Maharashtra. A map showing the location of Nashik can be seen in Fig. 1. The data used for this work were measured by the Hydrology Project, Nashik. It was available for a span of 7 years, from 2002 to 2008. The various parameters used for forming the ANN models were maximum humidity (MHS), sunshine duration (MSD), maximum temperature (MTX), minimum temperature (MTN), wind speed (MWS) and pan evaporation (MEP).

3 Artificial Neural Networks

Artificial Neural Network is a systematic arrangement of system's causative variable (input neurones) and the output variables (output neurones) mostly connected by one or more hidden layers with neurones which works similar to the biological

Fig. 1 Location of Nashik on the map of India

neural network in the human brain. The mapping of input and output for the required accuracy is done by using an iterative procedure for minimizing the error between the observed and network predicted variables (outputs). The calibration ('training' as per ANN terminology) is done on a set of data using a training algorithm which minimizes the error and makes the network ready to face the unseen data kept aside for testing the model. The ANN was first introduced and applied in last decade of the twentieth century and is now an established technique in modelling water flows. The readers referred to books like Bose and Liang [4], Wassarman [5] and research papers by the ASCE Task Committee [6] and [7] for understanding the preliminary concepts and working of ANN.

4 Methodology

4.1 Input Selection

Five climatic variables, namely maximum humidity (MHS), sunshine duration (MSD), maximum temperature (MTX), minimum temperature (MTN) and wind speed (MWS), were used as input with pan evaporation (mm/day) as the output in the present study. The selection of inputs was done by calculating average mutual information (AMI) of every input with the output. AMI is one of the many quantities that measures how much one random variable tells us about the other. High mutual information indicates a large reduction in uncertainty; low mutual information indicates a small reduction; and zero mutual information between two random variables means the variables are independent.

With the help of AMI between the output and each of the inputs, five models were initially prepared. The first model had only one input, that is, MTX as it had the maximum value of AMI with the output. The second highest value of AMI was of MHS with the output, and thus for model 2 MTX and MHS were used as inputs. Similarly, by adding one input for each model, a total of five models were prepared.

A second set of data was also prepared, in which, instead of using daily minimum and maximum temperature, the mean daily temperature was used by taking the average of MTX and MTN. This was done as most of the empirical equations, given in FAO 56 (Crop evapotranspiration) [8], use daily average temperature for modelling of evaporation. This set of data had only four inputs, namely MSD, MHS, MWS and Daily average temperature (AVGTEMP). The same methodology as explained above was followed for input selection for these variables and four separate models were formed. Details of AMI between inputs and output are presented in Table 1. The models developed as per procedure mentioned above are presented in Table 2.

Table 1 AMI of each input with output

Output/Input	MWS	MTX	MTN	MHS	MSD	AVGTEMP
MEP	0.1973	0.5428	0.2537	0.3448	0.2787	0.5001

Table 2 Formation of models for both sets

Set A		Set B		Output
Model no.	Input	Model no.	Input	
1A	MTX	1B	AVGTEMP	MEP
2A	MTX MHS	2B	AVGTEMP MHS	MEP
3A	MTX MHS MSD	3B	AVGTEMP MHS MSD	MEP
4A	MTX MHS MSD MTN	4B	AVGTEMP MHS MSD MWS	MEP
5A	MTX MHS MSD MTN MWS			MEP

4.2 Model Formulation

Once the input output datasets were formed they were trained and tested using MATLAB Neural Network toolbox. Three-layered feed-forward networks were developed with inputs varying from 1 to 5 in case of Set A and 1–4 in case of Set B, according to the number of inputs for that particular model. For every model, such a network was developed making in all five networks in Set A and four networks in Set B. The output neurone was always the MEP. The hidden neurones were fixed by trial and error. The transfer functions used were 'log-sigmoid' and 'linear' for all cases between first (input) and second (hidden) layer and second (hidden) and third (output) layer, respectively. The algorithm used was LM. Testing was done with remaining 30% of data. The fitness criterion was the mean squared error (mse). The MATLAB and Neural Network Toolbox versions for the current work are 7.10.0.499 (R2010a) and 6.0.4 (R2010a), respectively.

As mentioned above, for the subjective analysis of the models under study, scatter plots were obtained for the 30% data used for testing. Figures 2, 3, 4 and 5 show the scatter plots comparing the results of Set A and Set B, of all the models under study.

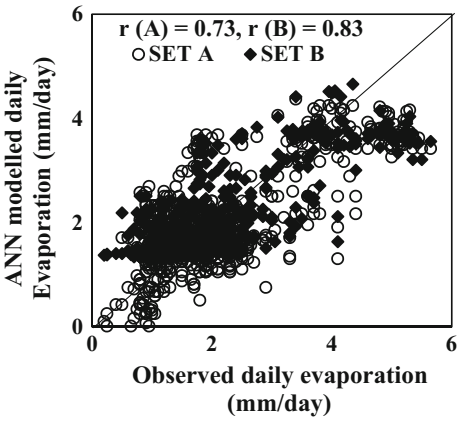

Fig. 2 Scatter plot for models 1A and 1B

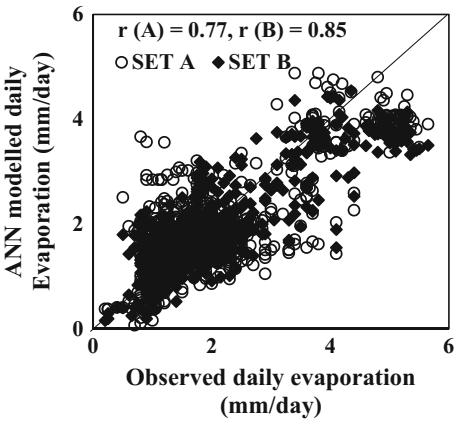

Fig. 3 Scatter plot for models 2A and 2B

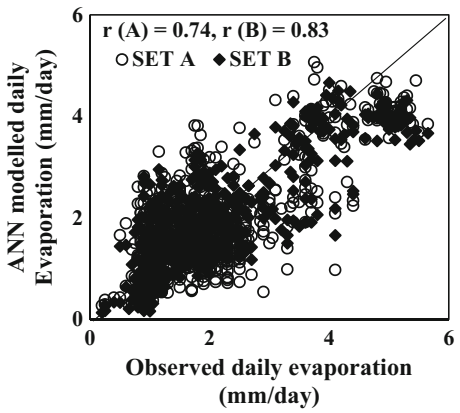

Fig. 4 Scatter plot for models 3A and 3B

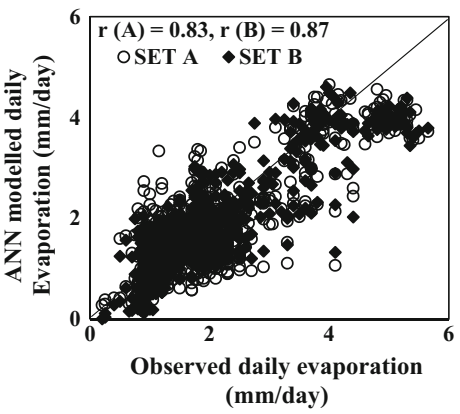

Fig. 5 Scatter plot for models 4A and 4B

Table 3 Statistical parameters of observed and modelled time series

Statistical parameters		Model 1	Model 2	Model 3	Model 4	Model 5
Average	Observed	2.09	2.09	2.09	2.09	2.09
	Set A	2.0	2.00	2.01	1.9	1.94
	Set B	2.1	1.97	1.95	1.9	–
Minima	Observed	0.2	0.2	0.2	0.2	0.2
	Set A	0.01	0.07	0.26	0.26	0.13
	Set B	1.34	0.16	0.13	0.007	–
Maxima	Observed	5.65	5.65	5.65	5.65	5.65
	Set A	4.37	4.88	5.07	4.65	4.82
	Set B	4.66	4.55	4.66	4.61	–
Standard deviation	Observed	1.2	1.2	1.2	1.2	1.2
	Set A	0.96	1.00	1.05	1.06	1.12
	Set B	0.86	0.95	1.04	1.04	–

Various error measures, for the 30% data used for testing, between the observed and output values for each model of both sets were calculated to judge the accuracy of developed models as given in Tables 3 and 4. The readers are referred to [3] for the formulae and further understanding of the statistical parameters and error measures stated in Tables 3 and 4.

5 Results and Discussion

Figures 2, 3, 4 and 5 show the scatter plots for models 1–4 (Sets A and B), respectively. It can be seen from Fig. 2 that both the sets of results have overpredicted values. From Figs. 3 and 4 for models 2 and 3, respectively, it can be observed that the number of overpredicted values has decreased, but the scatter for model 4, in Fig. 5, shows a better distribution of values along the best-fit line. Further, Fig. 5 also shows that Set B (having average temperature as input) is showing results a shed better than Set A (having minimum and maximum temperate as inputs) in terms of both under and over prediction of values. Thus, as per the subjective assessment of the models developed, model 4B is the one having best performance.

The objective assessment of hydrological models can be split into two distinct categories: those for evaluating continuous hydrographs and those that should be applied to single-event models. In the present work, the error measures falling under the latter category are of importance. As per [3], the evaluation metrics can be divided into three categories:

Table 4 Error analysis for both sets of results

Error measures		Model 1		Model 2		Model 3		Model 4		Model 5
		Set A	Set B	Set A	Set B	Set A	Set B	Set A	Set B	Set A
AME	Absolute parameters	2.79	2.46	2.67	0.55	3.12	2.44	3.03	2.77	2.56
ME		0.09	−0.007	0.1	0.16	0.08	0.14	0.20	0.17	0.15
MAE		0.66	0.53	0.6	0.49	0.66	0.53	0.54	0.47	0.30
RMSE		0.83	0.69	0.77	0.65	0.82	0.68	0.70	0.62	0.65
RMSE4E		1.08	0.95	1.06	0.92	1.07	0.93	0.97	0.87	0.87
RAE	Relative parameters	0.68	0.55	0.62	0.51	0.68	0.55	0.56	0.49	0.54
MARE		0.42	0.35	0.38	0.27	0.42	0.31	0.31	0.28	0.31
MRE		−0.08	−0.17	−0.07	−0.004	−0.08	0.009	0.03	0.04	0.04
MSRE		0.27	0.33	0.28	0.13	0.27	0.17	0.17	0.12	0.16
RVE		0.04	−0.003	0.05	0.07	0.04	0.07	0.09	0.08	0.07
r	Dimensionless coefficients	0.73	0.83	0.77	0.85	0.74	0.83	0.83	0.87	0.85
RSqr		0.53	0.68	0.60	0.73	0.55	0.69	0.69	0.76	0.72
CE		0.52	0.67	0.59	0.71	0.54	0.68	0.66	0.74	0.71
IoAd		0.16	0.12	0.13	0.09	0.14	0.10	0.1	0.08	0.08
PI		−3.78	−2.27	−3.1	−1.92	−3.63	−2.22	−2.34	−1.63	−1.95

Note Full forms of error measures serially—absolute maximum error, mean error, mean absolute error, root mean square error, fourth root mean quadrupled error, relative absolute error, mean absolute relative error, mean relative error, mean squared relative error, relative volume error, coefficient of correlation, coefficient of determination, coefficient of error, index of agreement, persistence index

1. Statistical parameters of observed and modelled time series datasets.
2. Statistical parameters of the residual error between observed and modelled time series datasets.
3. Dimensionless coefficients that contrast model performance with accepted norms or recognized standards.

The various parameters falling into these categories are given in Tables 3 and 4.

Table 3 shows the statistical analysis of the observed and modelled daily evaporation (for both sets) separately. From the table it can be seen that in case of the daily average, maxima and minima values, there is no distinction in the results as to which model out of the 5 or which set out of the two is working better. Though the values for standard deviation mildly point at Set A giving better results than Set B for all the four models. Again, while comparing the performance of the models, model 4 seems to be giving results slightly better than the others.

Table 4 gives the absolute and relative parameters as well as the dimensionless coefficients which would help in the judging the accuracy of the ANN models developed. Absolute errors provide a quantitative assessment of model error expressed in terms of the units of the variables of interest and that can thereafter be interpreted in a meaningful manner. Relative errors provide a quantitative assessment of model error expressed in terms of unbiased unit-free metrics that can thereafter be used to support interpretation in a purposeful context. The use of relative error measurements is intended to compensate the limitations of absolute error measurements which, although useful, do not necessarily give an indication of the importance of an error.

For the present study, all the absolute errors point towards the Set B models working a shed better, except ME (mean error). This may be because positive and negative errors tend to cancel each other out. Thus, for a better evaluation of the model MAE (mean absolute error) is often preferred to ME. Furthermore, these errors are consistent with the observation made from the scatter plots and show that model 4B is working the best out of all the models. The relative errors also show results that are in line with the absolute errors.

From the analysis of the results shown by the dimensionless parameters it can be seen that r (coefficient of correlation), RSqr (coefficient of determination) and CE (coefficient of error) are showing results consistent with the previous two types of errors. On the other hand, IoAd (index of agreement) seems to point towards Set A having better results. Also, the remaining error, PI (persistence index) shows that none of the models are performing even satisfactorily. The reason behind this is that these dimensionless parameters, though they are being widely used for judging hydrological models, are based on a consideration of linear relationships. They are insensitive to additive and proportional differences between the observed and modelled datasets, such that high scores can be obtained, even if the simulated values are considerably different from the observed values in terms of magnitude and variability. They are also oversensitive to outliers and thus biased towards a consideration of extreme events such that the true overall relationship is obscured [3]. Also, PI is a measure that is to be used to judge the accuracy of models that deal

with forecasting a parameter a particular lead time ahead. Hence, it is of no use when it comes to estimation of evaporation.

With the help of both the subjective and objective assessments of the ANN models developed for estimation of daily pan evaporation, it is proved that evaporation models would give better results when the average daily temperature is used as an input instead of using the maximum and minimum temperature as two different inputs. Additionally, it also can be concluded that out of all the models trained at Nashik, the performance of model 4B, having inputs—AVGTEMP, MHS, MSD and MWS, is superior to rest of the models.

6 Conclusion

Evaporation plays a vital role for design and maintenance of various water resources projects. The present work deals with the estimation of pan evaporation at Nashik by varying the input parameters based on the value of average mutual information of each of the inputs with the outputs. Till date, researchers have been using the minimum and maximum daily temperatures as two separate inputs for calibration of the ANN models. This study proposes a novel approach of using average daily temperature as a single input instead of using the minimum and maximum temperature. Furthermore, a subjective and objective assessment of the models was done to determine the best set of results.

It was observed that majority of the error measures showed that the evaporation models were giving better results when the average daily temperature was used as an input instead of using the maximum and minimum temperature as two different inputs. It could also be concluded that the absolute and relative error measures should be used for judging the performance of the evaporation models. The dimensionless parameters may at times be misleading as they are based on a consideration of linear relationship between input and output, which is not applicable to the nonlinear process of evaporation. It might also be noted that the error measures chosen to judge the accuracy of the models should be determined only after a thorough study of the measure. For the present work, the dimensionless parameter PI was used to judge the models and the results obtained showed that the models were performing worse than a ‘no knowledge’ model. This was because the error measure is to be used when the models are formulated to predict any parameter at a particular lead time, and not for models that are estimating a parameter at the current time step. Thus, the study also showed the importance of using the correct evaluation measures during the modelling of any hydrological parameter.

References

1. Chang, F.J., Sun, W., Chung, C.H.: Dynamic factor analysis and artificial neural network for estimating pan evaporation at multiple stations in northern Taiwan. Hydrol. Sci. J. **58**(4), 1–13 (2013)
2. Chaudhari, N., Londhe, S.N., Khare, K.: Estimation of pan evaporation using soft computing tools. Int. J. Hydrol. Sci. Technol. **2**(4), 373–390 (2012)
3. Dawson, C.W., Abrahart, R.J., See, L.M.: Hydrotest: a web-based toolbox of evaluation metrics for the standardised assessment of hydrological forecasts. Environ. Model Softw. **22**, 1034–1052 (2006)
4. Bose, N.K., Liang, P.: Neural Network Fundamentals with Graphs, Algorithms and Applications. Tata McGraw-Hill Publication (1998)
5. Wasserman, P.D.: Advanced Methods in Neural Computing. Van Nostrand Reinhold, New York, 255 (1993)
6. The ASCE Task Committee: Artificial neural networks in hydrology I: preliminary concepts. J. Hydrol. Eng. **5**(2), 115–123 (2000)
7. Maier, H.R., Dandy, G.C.: Neural networks for prediction and forecasting of water resources variables: a review of modelling issues and applications. Elsevier Environ. Model. Softw **15**, 101–124 (2000)
8. FAO Irrigation and Drainage Paper, No. 56, Crop Evapotranspiration, (guidelines for computing crop water requirements) (1998)

Estimation of Pan Evaporation and Actual Evapotranspiration Using GIS and Remote Sensing

Praveen Rathod and V.L. Manekar

Abstract This study demonstrates the estimation of actual evapotranspiration and pan evaporation based on the satellite images. LISS III and Landsat images are used in this study. LISS III and Landsat images are available in different bands. All bands are composited and mosaicked to form single image of the study area. Composited image is classified into five different classes namely Forestland, Agricultural Land, Fallow Land, Water Bodies and Built-up Area. Separate methodology for the estimation of actual evapotranspiration and pan evaporation has been proposed. To determine actual evapotranspiration, Normalized Difference Vegetation Index (NDVI) map is generated using ARCGIS. For the different years, average NDVI values and corresponding Kc values are obtained. Reference evapotranspiration (Eto) is obtained by Penman–Monteith model. Actual evapotranspiration is obtained by multiplying reference evapotranspiration to a crop coefficient (Kc). RMSE and NRMSE between observed and predicted evapotranspiration are found to be 0.27 mm and 0.7 mm, respectively. To determine pan evaporation, Normalized Difference Water Index (NDWI) map is generated using ARCGIS. Total 24 Landsat satellite images are used to obtain NDWI values on the Water Bodies. NDWI is correlated with the relative humidity-dependent Pan coefficient. Correlation coefficient between pan coefficient and NDWI was found to be 0.92. A new model is proposed relating to modified pan coefficient (Kwp) and NDWI. Pan evaporation is obtained by dividing Eto by NDWI-dependent modified pan coefficient (Kwp). Coefficient of correlation and RMSE between observed and predicted pan evaporation is found to be 0.70 and 0.5 mm, respectively.

Keywords Evapotranspiration · Crop coefficient · NDVI · ARCGIS

P. Rathod (✉) · V.L. Manekar
Civil Engineering Department, SVNIT, Surat 395007, India
e-mail: praveenrathodsh03@gmail.com

V.L. Manekar
e-mail: vivek_manekar@yahoo.co.in

V. Garg et al. (eds.), *Development of Water Resources in India*,
Water Science and Technology Library 75, DOI 10.1007/978-3-319-55125-8_20

1 Introduction

In today's scenario, water conservation is very important. Globally climate is changing, and at most of the places temperature trend indicates increasing. Everything on this planet needs more water than usual usage if the temperature increases. Crop water differs from crop to crop. Evapotranspiration is also an important factor for irrigation management. Therefore, determination of evapotranspiration is an essential part of irrigation supply. One of the widely accepted methods to determine the evaporation is by multiplying the reference evapotranspiration (Eto) to the crop coefficient (Kc) [8]. Food and Agricultural Organization has given crop coefficient values for different crops at different stages. Determination of crop coefficient is given in FAO-56, [2]. In FAO-56, crop coefficients are intended to use with reference grass [3]. FAO-56 is also a mentioned method for predicting Eto from Penman–Monteith equation which is based on a hypothetical grass reference of height 0.12 m having an albedo of 0.23 and surface resistance of 70 s m^{-1} for 24-h time steps [2]. Standardized equations for computing parameters in the FAO-56 Penman–Monteith equation are given in Allen et al. [3]. Crop coefficient represents total effects of major characteristics that distinguish the crop from the reference ETo [1], these characteristics are crop height, albedo of the crop–soil, crop–soil surface. Detail explanation of each parameter can be found in [1]. During the period of crop growing, Kc value increases from minimum to fully develop canopy. Usually Kc value is time-dependent smooth curve. Once the full canopy is developed, Kc value starts declining and it depends on growth characteristics of the crop and irrigation management [11]. Crop coefficients primarily depend on leaf age, the dynamics of canopies, canopy roughness, light absorption by the canopy, crop physiology and surface wetness [9], and detail explanation for all the factors can be found in Kamble et al. [10, 11].

The Normalized Difference Vegetation Index (NDVI) is extensively used for the irrigation scheduling, change detection, land cover characterization, vegetation monitoring, drought detection and crop yield assessment [9, 11]. NDVI calculated for the red and near-infrared reflectance. Between wavelength of 0.7 and 1.3 μm, green vegetation reflectance will be more so NDVI value varies between −1 and −1, +1 value of NDVI indicates the high vegetation, and −1 value indicates the zero vegetation. Many researchers (e.g. Kamble et al. [11] and many other authors) have shown that there is strong correlation between crop coefficient (Kc) and NDVI. The Normalized Difference Vegetation Index can be easily obtained by processing satellite images of at least two bands of red and NIR bands in ARCGIS. Once the NDVI value obtained from the satellite images, it can be correlated with Kc. Once the Kc obtained indirectly from the NDVI value, actual evapotranspiration can be obtained.

Determination of actual evapotranspiration from the NDVI-dependent Kc value is effective within the crop, vegetative or forest area. But determination of evaporation from no vegetative places like Water Bodies or barren land above-mentioned

method won't be more effective because reflectance in the red and near-infrared range will be almost zero for the Water Bodies. So to identify Water Bodies, new index is introduced by Gao [6], i.e. Normalized Difference Water Index (NDWI). It is computed using the near-infrared (NIR) reflectance and the short wave infrared (SWIR) reflectance. NDWI is almost insensitive to atmospheric effects than NDVI, and NDWI does not remove reflectance from the soil, like NDVI does [6]. Many researchers (e.g. [4, 7]) have shown its usefulness in drought warning (e.g. [4, 7]). So NDWI can be used to extract the information about Water Bodies and can be related to evaporation.

Main objective of this study is to determine actual evapotranspiration from the green vegetation by using NDVI and Kc models and pan evaporation from the Water Bodies using NDWI.

2 Area Description

Tapti River/Tapi River is a river of central India. Tapati, Tapti, Tapee, Taapi are the various names used to denote Tapti River. Also known as, the daughter of Sun God, its basin extends over an area of 65,145 km^2. In India, Tapti River originates at Multani of Betul District. The Basin of Tapti River lies in three Indian States, namely Gujarat, Madhya Pradesh and Maharashtra, which covers an area about

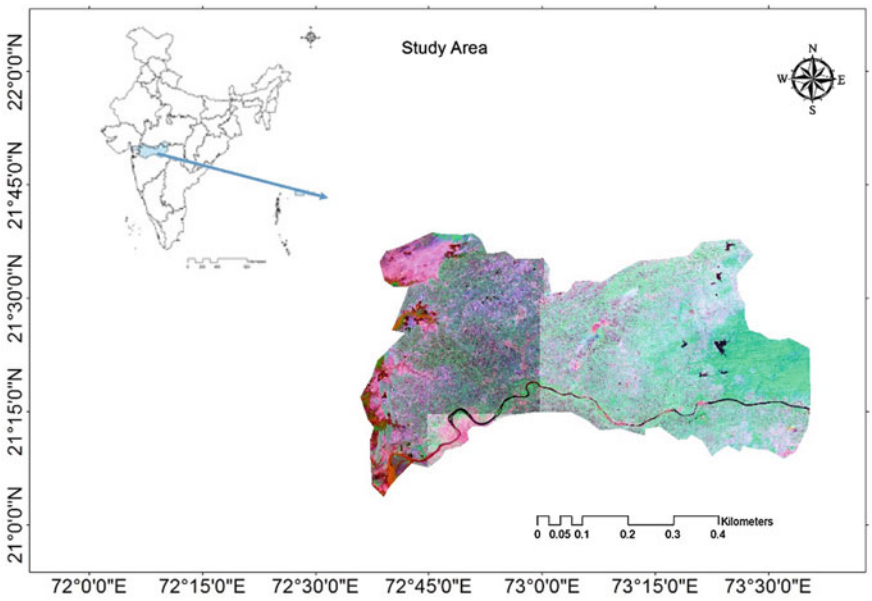

Fig. 1 Lower Tapi Basin

3,837 km^2, 9,804 km^2 and 51,504 km^2, respectively. This study is limited to the Lower Tapi Basin as shown in Fig. 1 (most of the area comes in Gujarat State of India), and it lies between east longitudes of 72067′–73041′ and north latitudes of 21°21′–21°66′.

3 Data Collection

For the present study, climatical data (e.g. minimum temperature, maximum temperature, wind velocity, relative humidity, sun shine hour precipitation and pan evaporation) are procured from the State Water Data Centre (SWDC), Gujarat. For the period of 1999–2014, rainfall data were collected for daily frequency and all other parameters were computed for twice daily frequency. Total seven stations are used which are uniformly distributed over entire study area. Average climatical data are given in Table 1. For the generation of NDVI map and NDWI map Resource Sat 1: LISS III and Landsat images are used and resolution of these image is 23.5 and 30 m, respectively.

4 Research Method

In the present study, it is mainly focused on the determination of evaporation and evapotranspiration from satellite images and climatic parameters because these data are easily available and these data are more reliable. Detail methodology in the form of algorithm is shown in Fig. 2. Research methodology is mainly divided into two parts: in the first part, one part evapotranspiration is determined from NDVI and Kc values and on the other hand, evaporation is determined using NDWI.

Table 1 Average climatical data for the period 1999–2014

Station	Min temperature (°C)	Max temperature (°C)	Relative humidity (%)	Wind speed (km/h)	Sunshine (min)	Pan evaporation (mm)	Rainfall (mm)
Amli	20.74	33.2	65	4.78	30	2	8.96
Chopadvav	22.35	32.45	62.5	9.16	30	3.14	6.37
Godsamba	23.22	32.5	69.8	2.35	30	2.36	5.6
Kakrapar	22.9	33.2	69.65	0.52	30	2.18	6.35
Olpad	22.93	32	69.62	3.98	30	3.13	2.92
Rander	23.48	32.28	71	4.5	30	3.1	
Ukai	23.19	31.85	65.32	3.1	30	2.2	10.04

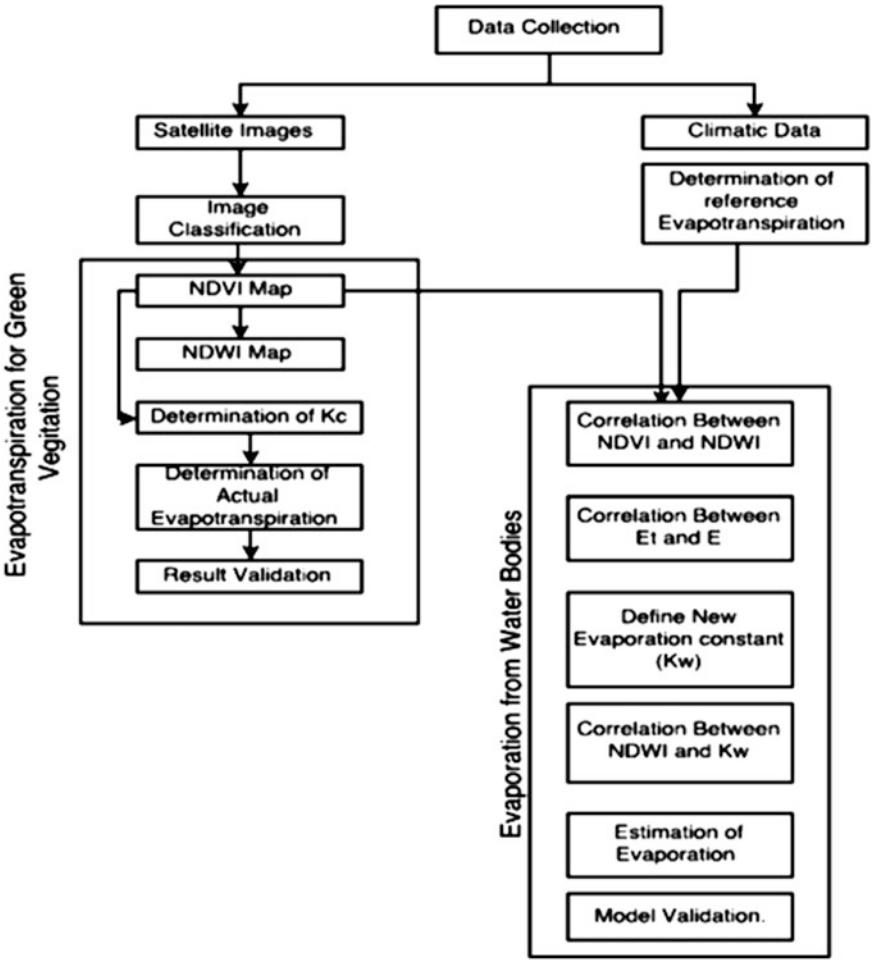

Fig. 2 Evaporation and evapotranspiration algorithm

4.1 Estimation of Actual Evapotranspiration

Radiance of the reflectance for the crops is good between 0.86 and 1.24 μm, so NDVI is calculated between these two bands from the remote sensing data but at the same time Water Bodies have no reflectance in this range that is why evapotranspiration is determined by the NDVI. Before obtaining the NDVI values from the composite raster of LISS III satellite, image has to be classified. In the present study area, image is classified into five different classes, namely Forestland, Agricultural Land, Water Bodies, Built-up area and Barren Land. Different classes and their contribution of area are given in Table 2. Once the image is classified, NDVI raster can be generated in ARCGIS by image analysis tool. Many researchers (e.g. [11, 13])

Table 2 Image classification

Class	Pixel count	Area
Water	104443	93.9987
Forest land	604743	544.2687
Barren land	2335882	2102.294
Agriculture land	594646	535.1814
Built-up land	645586	581.0274

have given the relationship between NDVI and Kc. In the present study, regression equation (Eq. 1) given by Baburao et al. [11] is being used.

$$\mathrm{Kc} = 1.457\mathrm{NDVI} - 0.1725 \tag{1}$$

Once the Kc values are obtained for the different NDVI values, reference evapotranspiration is determined from the climatic parameters and using Etc/Eto relationship with the Kc value actual evapotranspiration (Etc) is calculated. To convert observed pan evaporation into evapotranspiration relation given by Trezza [16] is being used.

$$\mathrm{E(t)} = \mathrm{EP(t)} \times \tanh[\mathrm{P(t)}/\mathrm{EP(t)}] \tag{2}$$

where E(t) represents the actual evapotranspiration, EP(t) is the pan evaporation value, P(t) is the rainfall and tanh is the hyperbolic tangent function. Thus, obtained evapotranspiration is compared with the predicted evapotranspiration. Root mean square error (RMSE) validates proposed methodology and normalized root mean square error, which should be near or equal to zero for the good prediction.

4.2 Estimation of Evaporation from Water Bodies

There is good correlation between Kc and evapotranspiration as shown in Fig. 3. But Kc = Etc/Eto relationship cannot be used for the estimation of evaporation because Kc accounts evaporation and transpiration and it is related to NDVI values and NDVI values for the Water Bodies will be in negative. There will be potential evaporation in case of Water Bodies. Reflectance of water between 0.4 and 0.75 μm is good so to identify the Water Bodies using remote sensing data Normalized Difference Water Index (NDWI) is used [6]. NDWI is calculated using the following relationship.

$$NDWI = \frac{NIR_{0.86\mu m} - SWIR_{1.24\mu m}}{NIR_{0.86\mu m} + SWIR_{1.24\mu m}} \tag{3}$$

NDWI should be same everywhere on the water but it is not, because it is very much sensitive towards the water vapours. If relative humidity is high in the air, there can be high scattering that is one of the reasons for showing different NDWI.

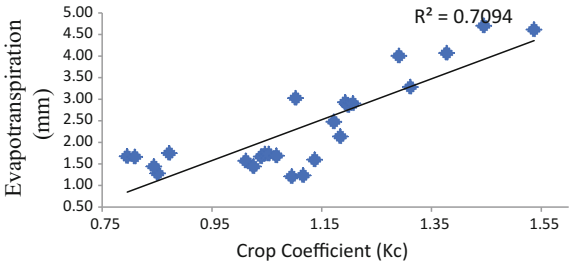

Fig. 3 Correlation between Kc and evapotranspiration

And the another reason for the variation for NDWI is if there is shallow depth Water Bodies, soil can also reflect to some extent and this reflectance may affect to the NDWI. To estimate evaporation, a pan coefficient (ratio of reference evapotranspiration to pan evaporation) is correlated with NDWI. Eagleman [5] has shown that pan coefficient is the function of relative humidity. Synder [15] also given the pan coefficient as the function of relative humidity and upwind distance fetch of low-growing vegetation. So taking pan coefficient constant everywhere may not be correct. To the certain extent, NDWI also depends on amount of moisture present near the vicinity of Water Bodies. To avoid confusion between actual pan coefficient and pan coefficient, which is related to NDWI, notation Kmp (modified pan coefficient) is being used. So in this study, Kmp is defined as the ratio of reference evapotranspiration to the pan evaporation and it is correlated with the NDWI. NDWI values for October 2008, November 2011, January 2012 and November 2013 are collected from the NDWI raster near the Water Bodies. Using the Joe (1997) equation, pan coefficients are computed using the relative humidity for all the stations and for all the period mentioned above. Thus, obtained NDWI and Kmp values are correlated and regression model is formed by using least square technique.

5 Results and Discussion

5.1 Image Classification

LISS III images of study area are freely available on the Bhuvan website (http://bhuvan.nrsc.gov.in/data/download/index.php#). LISS III satellite image is in the four different bands, and all these bands are composited and made single image by mosaic tool in the ARCGIS. Study area is classified into five different classes, namely Forest area, Agricultural Land, Water Bodies, Barren land and Built-up area. Image classification is performed by maximum likelihood algorithm in the ARCGIS by collecting at least 100 samples in each of the classes. Result obtained after classification is shown in Table 2. From the table, it can be seen that there is more barren land followed by Forest land. Purpose of doing classification is while collecting the pixel values for the NDVI and NDWI very helpful.

5.2 *Estimating Evapotranspiration for Vegetation from the NDVI and Kc Model*

There is good correlation between Kc with NDVI and evapotranspiration [14]. Correlation between Kc and evapotranspiration is shown in Fig. 3. There are different values of crop coefficient for different crops given by FAO-56; on the other hand, leaf reflectance is also different for different crops. Using reflectance between red and NIR, NDVI map is generated in ARCGIS as shown in Fig. 4. From the NDVI values, Kc values are computed using the regression model given by Baburao et al. [11] (Eq. 1). Using Etc/Eto = Kc, the actual evapotranspiration (Etc) can be calculated by multiplying Kc to Eto. Eto values are computed using Penman–Monteith method. However, using satellite images, which is having 23.5-m resolution, it will be quiet difficult to obtain crop coefficient for a particular crops. So in this study average value of NDVI for particular class is obtained from the satellite image. Figure 5 shows predicted and observed evapotranspiration. RMSE and NRMSE are found to be 0.27 and 0.7, respectively.

Since reference evapotranspiration can be estimated from the climatic data more precisely, pan evaporation data have to be maintained very well and sometimes it will become more laborious to do so. Estimation of pan evaporation is very important for irrigation scheduling, Hydrologic Modelling, Ground Water Modelling, etc. Evaporation from the Water Bodies estimated using NDWI and Kmp model. NIR and SWIR bands in LISS III and Landsat satellite images are used for the NDWI map generation in ARCGIS as shown in Fig. 6. Correlation between

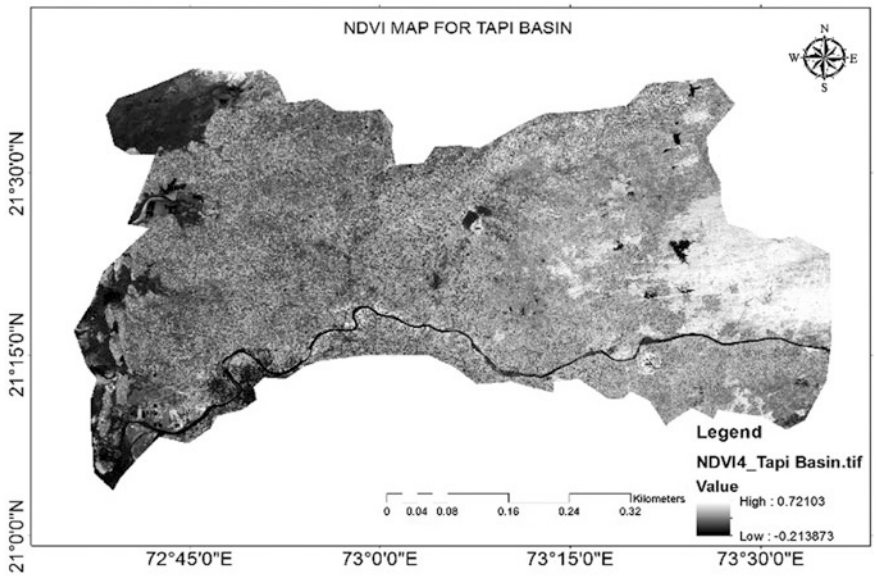

Fig. 4 NDVI Map for Tapi Basin

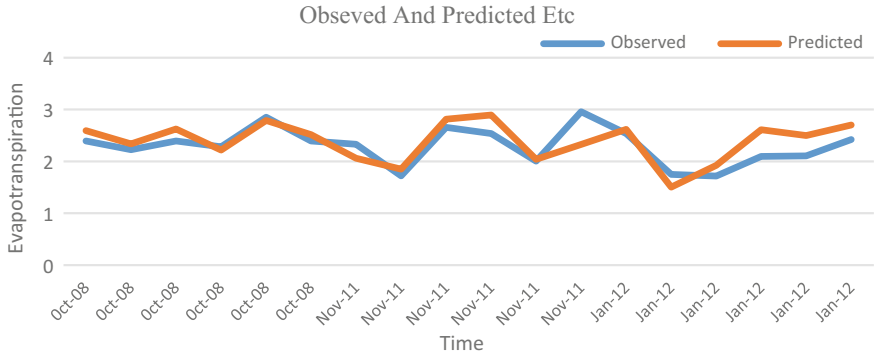

Fig. 5 Estimating evaporation from Water Bodies at different stations

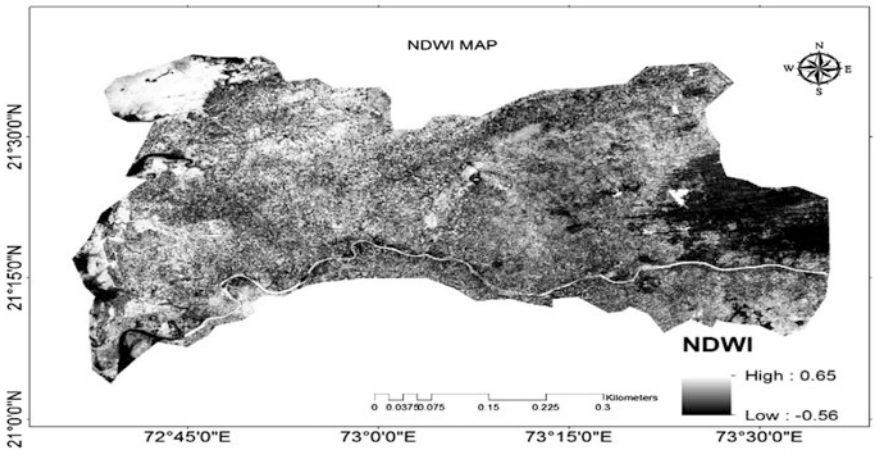

Fig. 6 NDWI map for lower Tapi Basin

NDWI and Kmp values is shown in Fig. 7. By least square method, obtained Kmp and NDWI model is shown in Eq. 4. Eto values are computed using Penman-Monteith method. Using the relationship Eto/Epan = Kp. Evaporation from the pan is computed by dividing Eto by Kp (Eto/Kp). Station, which is very near to water body, is Rander. 24 Landsat images are used to obtain NDWI value for 2 years starting from November 2011 to December 2012. NDWI values vary between minimum value of 0.13 to the maximum value of 0.36. Results obtained by this methodology are shown in Fig. 8. Coefficient of correlation between observed and predicted pan evaporation is found to be 0.70, and RMSE is 0.5 mm.

$$\text{Kmp} = 0.3814\,\text{NDWI} + 0.5989 \tag{4}$$

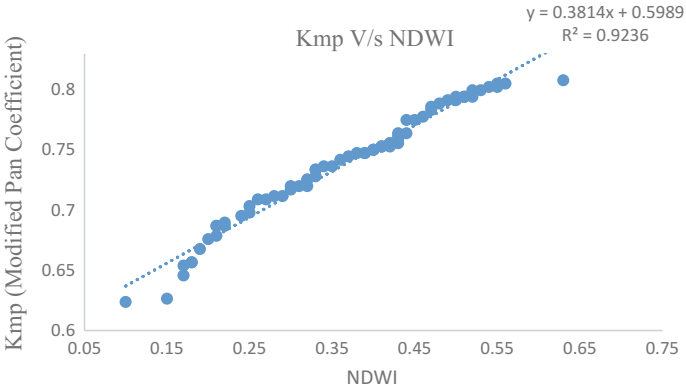

Fig. 7 Correlation between Kmp and NDWI

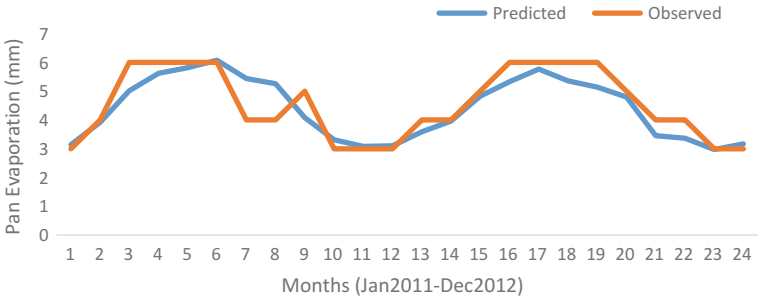

Fig. 8 Pan evaporation at Rander station from January 2011 to December 2012

Least value of NDWI observed is 0.1, and corresponding Kmp is 0.6. Maximum value of NDWI observed from the map is 0.63 and corresponding Kmp is found to be 0.8, so in the present study area Kmp can vary between 0.6 and 0.8. NDWI can be 1 for the ideal reflectance from the Water Bodies; in that case, Kmp can be 0.9803. That means pan evaporation is almost equal to evaporation from the Water Bodies. NDWI and Kmp model is only applicable for the estimation of evaporation from the Water Bodies. NDWI map is not applicable on Forestland, Agricultural Land, Fallow Land and Built-up Land because reflectance from the soil becomes more from these classes.

6 Conclusion

The present study demonstrates the estimation of actual evapotranspiration and pan evaporation considering reference evapotranspiration can be accurately determined by the climatic data. Based on NDVI values obtained by the satellite image, crop

coefficient is determined. Using the crop coefficient and Etc/Eto relationship, actual evapotranspiration (Etc) is determined. RMSE and NRMSE are found to be 0.27 and 0.7, respectively. Pan evaporation is determined by correlating NDWI and pan coefficient. Correlation between NDWI and pan coefficient is found to be 0.92. Coefficient of correlation between observed and predicted pan evaporation is found to be 0.70, and RMSE is 0.5 mm.

References

1. Allen, R.G.: Using the FAO-56 dual crop coefficient method over an irrigated region as part of an evapotranspiration intercomparison study. J Hydrol. **229**(1), 27–41 (2000)
2. Allen, R.G., Pereira, L.S., Smith, M., Raes, D, Wright J.LL.: FAO-56 dual crop coefficient method for estimating evaporation from soil and application extensions. J. Irrig. Drain. Eng. **131**(1), 2–13 (2005)
3. Allen, R.G., Pereira, L.S, Raes, D, and Smith, M.: ETc-single crop coefficient (kc). Crop evapotranspiration (guidelines for computing crop water requirements). FAO Irrigation and Drainage Paper, pp. 103–134. FAO, Rome (1998)
4. Ceccato, P.N., Jaya, I.N.S., Qian J., Tippett, M.K., Robertson, A.W., Someshwar, S.: Early warning and response to fires in Kalimantan, Indonesia (2002)
5. Eagleman, J.R.: Pan evaporation, potential and actual evapotranspiration. J. Appl. Meteorol. **6** (3), 482–488 (1997)
6. Gao, B.C.: NDWI—A normalized difference water index for remote sensing of vegetation liquid water from space. Remote Sens. Environ. **58**(3), 257–266 (1996)
7. Gu, Y., Brown, JF., Verdin, JP., Wardlow, B.: A five-year analysis of MODIS NDVI and NDWI for grassland drought assessment over the central great plains of the United States. Geophys. Res. Lett. **34**(6) (2007)
8. Hunsaker, D.J., Pinter Jr, P.J., Barnes E.M., Kimball, B.A.: Estimating cotton evapotranspiration crop coefficients with a multispectral vegetation index. Irrig. Sci. **22**(2): 95–104 (2003)
9. Justice, C.O., Townshend, J.R.G.: Special issue on the moderate resolution imaging spectroradiometer (MODIS): A new generation of land surface monitoring. Remote Sens. Environ. **83**, 1–2 (2002)
10. Kamble, B., Irmak, A.: Assimilating remote sensing-based ET into SWAP model for improved estimation of hydrological predictions. In: Proceeding of the 2008 IEEE International Geoscience and Remote Sensing Symposium, vol. 3, Boston, MA, USA, 7–11 July 2008 doi:10.1109/IGARSS.2008.4779530
11. Kamble, B., Kilic, A., Hubbard, K.: Estimating crop coefficients using remote sensing-based vegetation index. Remote Sens. **5**(4): 1588–1602 (2013)
12. Pereira, L.S., Perrier, A., Allen, R.G., Alves, I.: Evapotranspiration: Review of Concepts and Future Trends. ASCE, J. Irrig. Drain. Engrg. **25** (1996)
13. Rafn, E.B., Contor, B., Ames, D.P.: Evaluation of a method for estimating irrigated crop-evapotranspiration coefficients from remotely sensed data in Idaho. J. Irrig. Drain. Eng. **134**(6), 722–729 (2008)
14. Rafn, E., Contor, B., Ames, D.: Evaluation of a method for estimating irrigated crop-evapotranspiration coefficients from remotely sensed data in Idaho. J. Irrig. Drain. Eng. **134**(6): 722–729 (2008). doi:10.1061/(ASCE)0733-9437

15. Snyder, R.L.: Equation for evaporation pan to evapotranspiration conversions. J. Irrig. Drain. Eng. **118**(6), 977–980 (1992)
16. Trezza, R.: Evapotranspiration using a satellite-based surface energy balance with standardized ground control. Ph.D. dissertation, Uta State University, Logan, Utah, USA (2002)

Assessment of Reference Evapotranspiration in the Context of Climate Change for Central India (Madhya Pradesh)

Brij Kishor Pandey and Deepak Khare

Abstract In this article, trend detection of reference evapotranspiration (RET_o) was investigated for Madhya Pradesh State, Central India. There were 45 stations selected for the study, and analysis was carried out for 102-year duration (1900–2002). Trend of the RET_o was detected based on the monthly, seasonally and annually applying nonparametric Mann–Kendall (MK) tests at the 5% and 1% significant level. The same tool was also applied on the other climatic variables (T_{max}, T_{min}, cloud cover and vapor pressure) to observe the reason of existence of such trend in RET_o.

Keywords Reference evapotranspiration · Trend · Mann–Kendall · Climate change

1 Introduction

Reference evapotranspiration (RET_o) is one of the most key components of hydrologic, environment and climatic system. It is responsible for water planning for agriculture, design and management of irrigation system [2, 9, 11]. There are many researchers worked on the trend analysis in the other climate variables and reference evapotranspiration. Parametric and nonparametric tests are tools to analyze the data for analysis [4, 18]. Tabari et al. [15] detected the trend considering 20 meteorological stations of West Iran using Mann–Kendall and regression method. Analysis was carried out on the basis of monthly, seasonal and annually for about 40 years. In the results, it has been found that 70% station showing the positive trend using Mann–Kendall, whereas 75% stations showing the positive trend using

B.K. Pandey (✉) · D. Khare
Department of Water Resources Development and Management, Indian Institute of Technology (IIT) Roorkee, Roorkee, India
e-mail: brijk.iit@gmail.com

D. Khare
e-mail: kharefwt@gmail.com

V. Garg et al. (eds.), *Development of Water Resources in India*,
Water Science and Technology Library 75, DOI 10.1007/978-3-319-55125-8_21

the regression method. Bandyopadhyay et al. [1] carried out the trend detection of RET_o using Mann–Kendall over India. In total, 133 stations were selected from the different agro-ecological regions from India and the study was carried out for the duration of 32 years. In the results, ET_o is rising for the whole India during the selected 32 years of the study period. Authors observed that the main reason of this raising trend is due to variation in relative humidity (increased) and wind speed (decreased). Shadmani et al. [13] investigated the temporal trend of arid region of Iran using Mann–Kendall (MK) and Spearman's rho tests. For the study purpose, 13 meteorological stations were selected for the ET and the analysis has been carried out for the 41-year period. Trend was detected on the basis of monthly, seasonal and annually for the duration. In the result, rising (positive) as well as decreasing (negative) trend has been found for some regions, but in most of the regions, no trend was found under the verified significance level. Tebakari et al. [16] analyzed the pan evaporation for Kingdom of Thailand. The analysis has been carried out for the 19 years (1982–2000) for considering 27 observation stations. In the result, 19 stations found decreasing trend and 8 stations found increasing trend and no station found no-rise, no-fall trend within significant level. Gong et al. [5] evaluated the climatic variables which affect the ET_o in the sensitivity analysis for Changjiang basin, China. Climatic variables such as air temperature (T), solar radiation (Rn), wind speed (U), relative humidity (RH), of 41-year historical data have been used for the study from 150 observation stations. Results implied that relative humidity and solar radiation are sensitive parameters and are quite predictable with the help of sensitivity coefficient.

The aim of the study is to detect the temporal trend of RET_o for central India applying Mann–Kendall (MK) test and Sen's slope under 95% and 99% confidence level value and, therefore to identify the sensitive climatic parameters which are the main cause for the rising/decreasing trend.

2 Study Area

In total, 45 districts of central region of India (Madhya Pradesh) have been considered for this study. In each district, meteorological station has been established by Indian Meterological Data (IMD) selected for the study. The central region of India is located between about latitude 21°′N–27°′N and longitude 74°′E–82°′E. One of the west flowing river of India, Narmada flows through the center of the state. There are three types of climatic season found in the central region: summer season (April–June), monsoon season (July–September) and winter season (December–February). The eastern part (hilly area) of the study area receive high rainfall, whereas northern and western part receive the minimum rainfall comparatively (Fig. 1). In general, average annual precipitation over the study area is about 1350 mm.

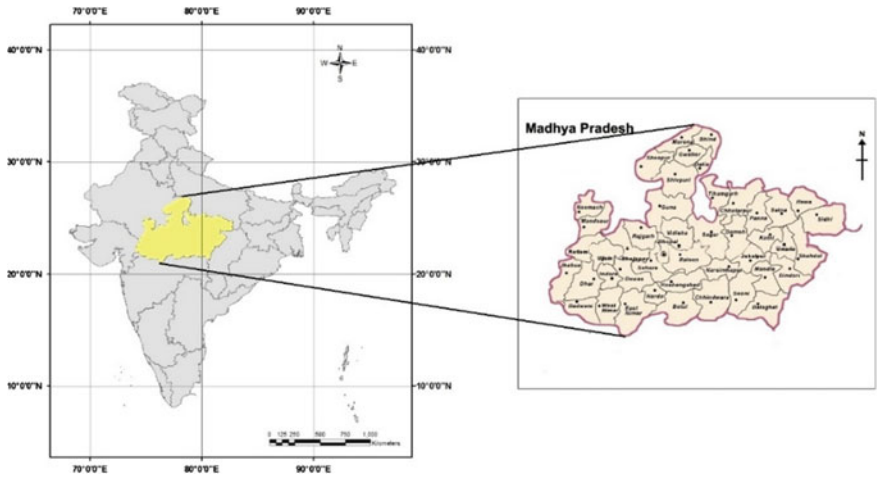

Fig. 1 Central India and selected meteorological stations

3 Materials and Methodology

There are 45 stations selected for the study purpose of central India (Madhya Pradesh). In this study, RET_o and others meteorological series for all the stations were obtained from the India Water Portal website (http://www.indiawaterportal.org). Mann–Kendall test was used for the trend detection. This method is not able to estimate the slope or magnitude of the trend. In order to quantify the slope and magnitude, Sen's slope method has been used [11, 12]. Before using the non-parametric test, data were used for pre-whitening test for the purpose of serial independency check, as required for the Mann–Kendall test [2, 7, 10].

3.1 Mann–Kendall (MK) Test

Mann–Kendall is the nonparametric test for trend analysis [12, 14, 17]. It is based on null hypothesis testing for check the existence of trend in the terms of yes or no. It is the simple and strong method. In addition to this, it also works with the missing values and outliers.

$$X = \sum_{i=1}^{n-1} \sum_{j=i+1}^{n} \operatorname{sgn}\left(P_j - P_i\right) \tag{1}$$

$$\operatorname{sgn}(P_j - P_i) = \begin{cases} +1 & if \quad (P_j - P_i) > 0 \\ 0 & if \quad (P_j - P_i) = 0 \\ -1 & if \quad (P_j - P_i) < 0 \end{cases} \tag{2}$$

for a RET_o series, P_i, i = 1, 2, 3, …, n.

$$(\sigma_s)^2 = \frac{1}{18}\left[n(n-1)(2n+5) - \sum_{p=1}^{q} t_p(t_p - 1)(2t_p + 5)\right] \tag{3}$$

$$Z_{MK} = \begin{cases} \frac{(X-1)}{\sigma_s} & if \quad X > 0 \\ 0, & if \quad X = 0 \\ \frac{(X+1)}{\sigma_s} & if \quad X < 0 \end{cases} \tag{4}$$

where Z = standard normal variate, and α = significance level for the test. If $|Z| > Z_{1\text{-}\alpha/2,}$ there is no trend rejected, according to the null hypothesis.

3.2 *Sen's Slope Estimation Test*

Sen's slope is the tool to estimate the monotone trend of the equally spaced time series data. In this study, it is used to quantify the slope of the series [3, 6, 8].

$$\beta = \text{Median}\left(\frac{P_i - P_j}{i - j}\right) \text{for all } i < j \tag{5}$$

where β is the slope between data points P_i and P_j.

4 Results

Trend analysis was performed by applying the MK test on long-term reference evapotranspiration (RET_o) data. The study was carried out for the long-term data of 102 years (1901–2002) based on long-term monthly, seasonal and annual series.

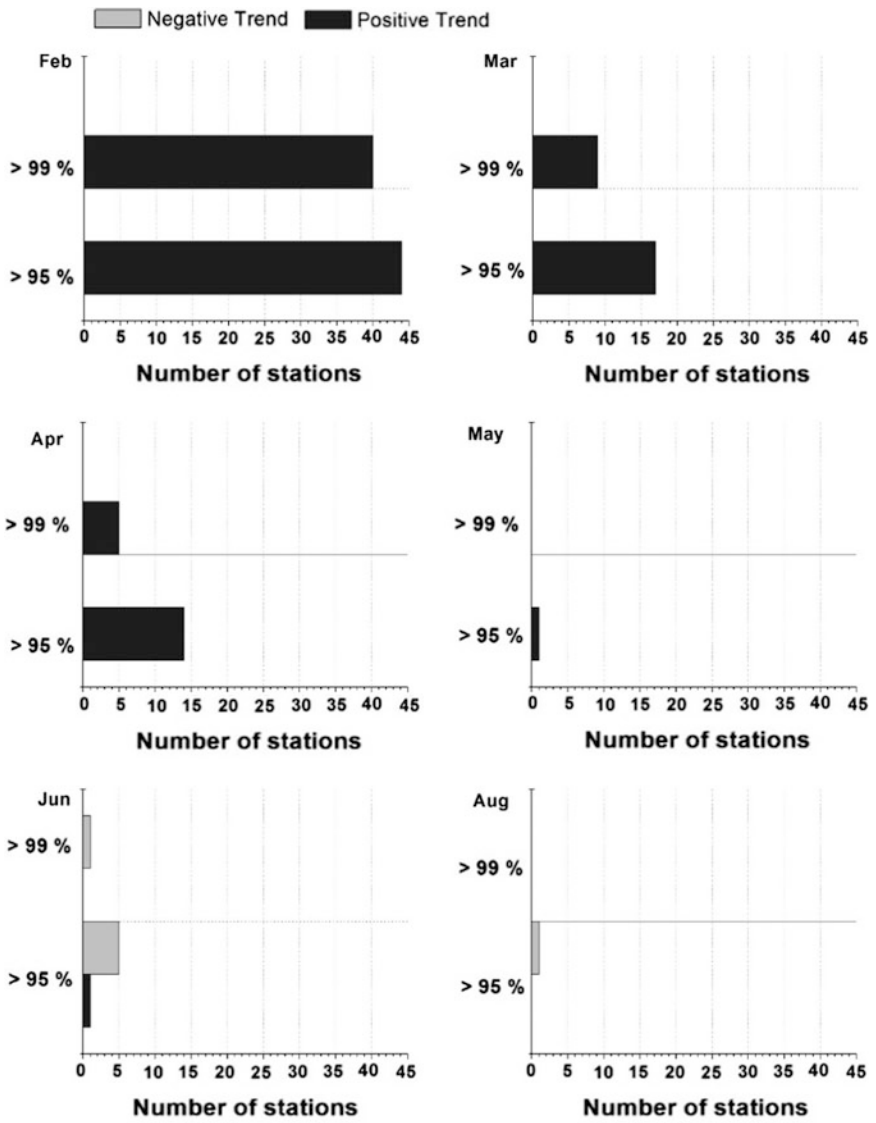

Fig. 2 The number of stations in monthly series of RET_o series by MK test at the 95% and 99% of confidence level

Monthly based study indicated that there is no trend in the month of January and July for the region. Figure 2 indicates that there are more stations with positive trend in the month of November and December as compared to rest of the month. Seasonal and annual results are shown in Fig. 3.

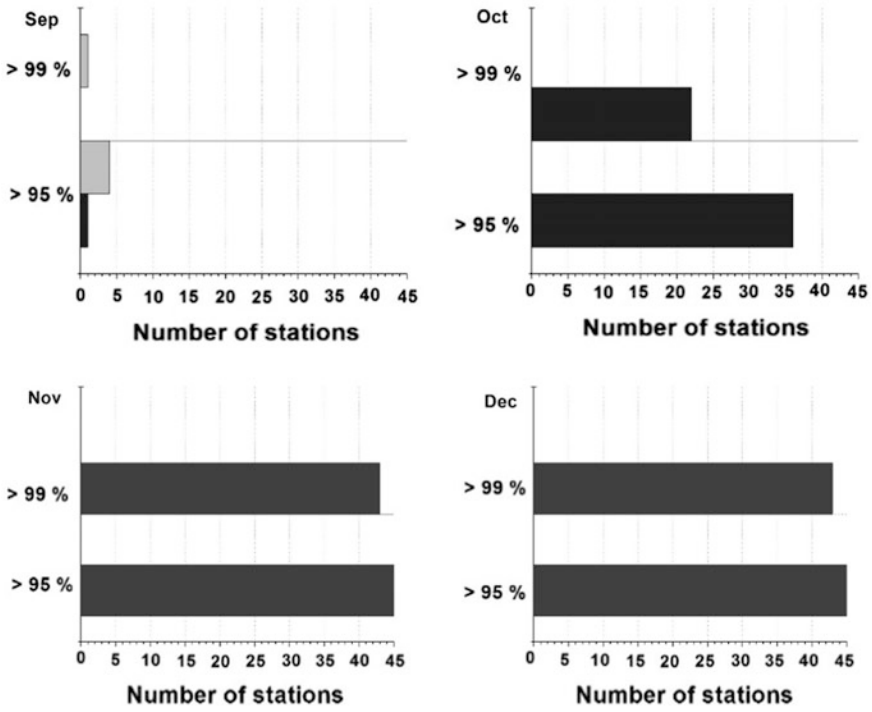

Fig. 2 (continued)

Many factors controlled reference evapotranspiration, mainly temperature (T), solar radiation (R_n), relative humidity (Rh) and wind speed (U) [1, 5]. Only 12 stations were selected for the sensitivity analysis and trend detection evaluated for five meteorological parameters including: precipitation (PCP), maximum temperature (T_{max}), minimum temperature (T_{min}), cloud cover (CC) and vapor pressure (VP) for the period of 1901–2002. Table 1 indicates the Z value of meteorological parameters obtained by using MK test.

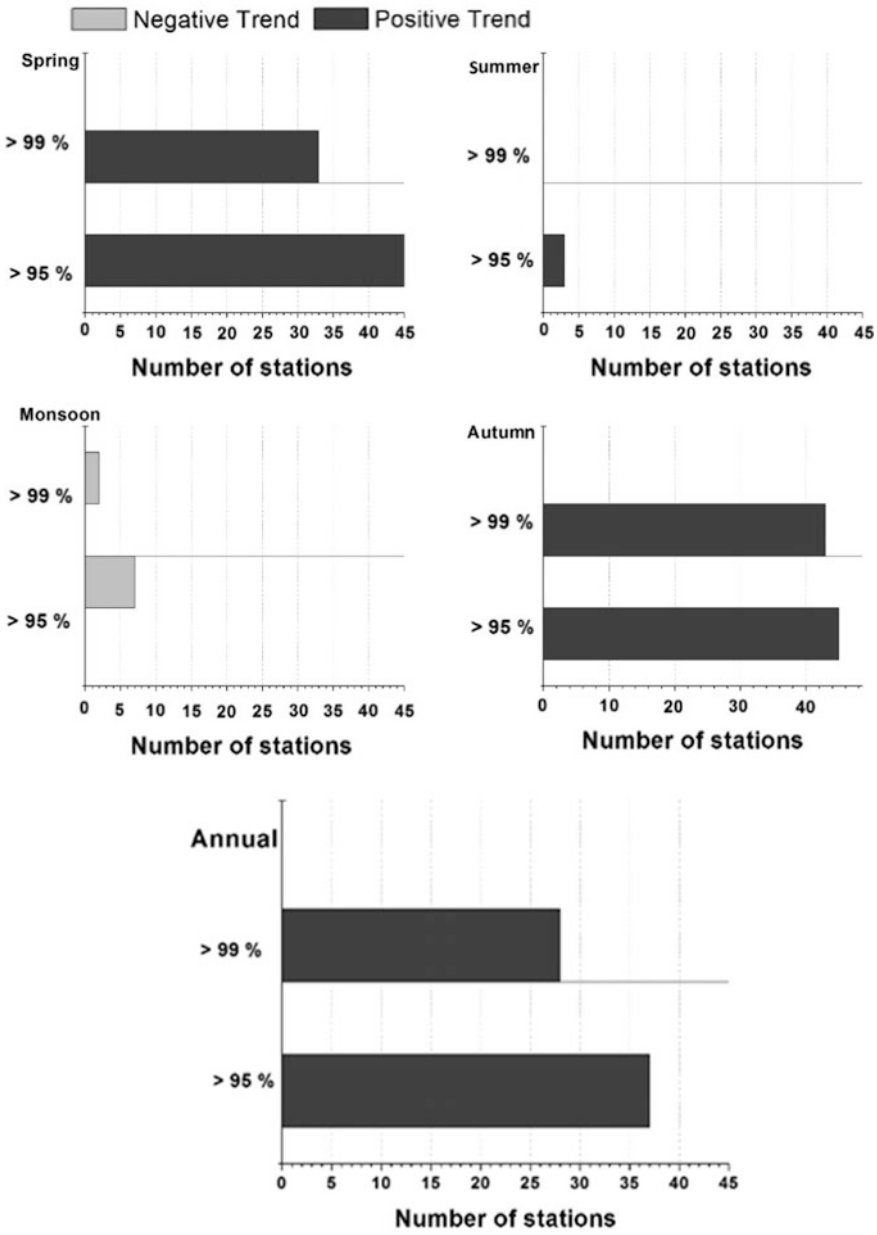

Fig. 3 The number of stations for seasonal and annual RET_o series of trend by MK test at the 95% and 99% of confidence level

Table 1 Z-value of meteorological parameters for selected stations of Madhya Pradesh (critical value at 1% and 5% significance level are (+, −) 2.58 and (+, −) 1.96, respectively for two tailed test)

Stations	RET	PCP	T_{max}	T_{min}	CC	VP
Barwani	−5.91	−1.04	−5.86	−5.84	−1.48	−5.22
Betul	−4.18	0.92	−4.71	−4.74	−1.73	−4.73
Dhar	−5.67	−0.53	−5.77	−5.77	−1.97	−4.44
Dindori	−2.31	1.88	−4.40	−5.33	−0.51	−3.99
East Nimar	−5.14	0.49	−5.44	−5.43	−1.95	−4.73
Harda	−4.71	−4.71	−4.71	−4.71	−4.71	−4.71
Hoshangabad	−4.20	−4.20	−4.20	−4.20	−4.20	−4.20
Jabalpur	−2.96	−2.96	−2.96	−2.96	−2.96	−2.96
Mandla	−2.63	1.47	−4.50	−5.29	−0.95	−4.05
Narmada	−5.69	0.39	−5.66	−5.60	−2.04	−5.29
Narsimhapur	−3.33	−3.33	−3.33	−3.33	−3.33	−3.33
West Nimar	−5.63	−0.78	−5.78	−5.73	−1.92	−4.59

5 Conclusion

In this analysis, 45 meteorological stations were considered for the temporal trend analysis in the central region of India (Madhya Pradesh). Applying the Mann–Kendall test, Z value for RET_o has been evaluated for the stations. Results imply the positive trend in the autumn and spring season, whereas negative trend has been found at very few stations in the monsoon season. Sensitivity of the trend was analyzed with other climatic parameters such as precipitation, temperature, temperature, cloud cover and vapor pressure.

Acknowledgements The authors would like to acknowledge the Indian Water Portal Web site for sharing the data archive. In addition, authors wish to thank the Department of Water Resources Development & Managment, Indian Institute of Technology (IIT) Roorkee and Ministry of Human Resources and Development, New Delhi.

References

1. Bandyopadhyay, A., Bhadra, A., Raghuwanshi, N., Singh, R.: Temporal trends in estimates of reference evapotranspiration over India. J. Hydrol. Eng. **14**(5), 508–515 (2009)
2. Camici, S., Brocca, L., Melone, F., Moramarco, T.: Impact of climate change on flood frequency using different climate models and downscaling approaches. J. Hydrol. Eng. **19**(8), 04014002 (2014)
3. Dinpashoh, Y., Jhajharia, D., Fakheri-Fard, A., Singh, V.P., Kahya, E.: Trends in reference crop evapotranspiration over Iran. J. Hydrol. **399**(3), 422–433 (2011)
4. Gao, G., Chen, D., Xu, C.-Y., Simelton, E.: Trend of estimated actual evapotranspiration over China during 1960–2002. J. Geophys. Res: Atmos. **112**(D11), n/a–n/a (2007)

5. Gong, L., Xu, C.-Y., Chen, D., Halldin, S., Chen, Y.D.: Sensitivity of the Penman-Monteith reference evapotranspiration to key climatic variables in the Changjiang (Yangtze River) basin. J. Hydrol. **329**(3), 620–629 (2006)
6. Goyal, M.K.: Statistical analysis of long term trends of rainfall during 1901–2002 at Assam, India. Water Resour. Manage. **28**(6), 1501–1515 (2014)
7. Hossain, F.: Paradox of peak flows in a changing climate. J. Hydrol. Eng. **19**(9), 02514001 (2014)
8. Jain, S., Kumar, V., Saharia, M.: Analysis of rainfall and temperature trends in northeast India. Int. J. Climatol. **33**(4), 968–978 (2013)
9. Liu, G.H., Luan, Z.Q., Yan, B.X., Guo, Y.D., Wang, Z.X.: Response of hydrological processes to land use change and climate variability in the upper Naoli River watershed, northeast China. Water Resour. **42**(4), 438–447 (2015)
10. Neupane, R.P., Kumar, S.: Estimating the effects of potential climate and land use changes on hydrologic processes of a large agriculture dominated watershed. J. Hydrol. Part 1, **529**, 418–429 (2015)
11. Pandey, B.K., Gosain, A.K., Paul, G., Khare, D.: Climate change impact assessment on hydrology of a small watershed using semi-distributed model. Appl. Water Sci. 1–13 (2016)
12. Sethi, R., Pandey, B., Krishan, R., Khare, D., Nayak, P.C.: Performance evaluation and hydrological trend detection of a reservoir under climate change condition. Model. Earth Syst. Environ. **1**(4), 1–10 (2015)
13. Shadmani, M., Marofi, S., Roknian, M.: Trend analysis in reference evapotranspiration using Mann-Kendall and Spearman's Rho tests in arid regions of Iran. Water Resour. Manage. **26** (1), 211–224 (2012)
14. Tabari, H., Marofi, S., Aeini, A., Talaee, P.H., Mohammadi, K.: Trend analysis of reference evapotranspiration in the western half of Iran. Agric. For. Meteorol. **151**(2), 128–136 (2011)
15. Tabari, H., Somee, B.S., Zadeh, M.R.: Testing for long-term trends in climatic variables in Iran. Atmos. Res. **100**(1), 132–140 (2011)
16. Tebakari, T., Yoshitani, J., Suvanpimol, C.: Time-space trend analysis in pan evaporation over kingdom of Thailand. J. Hydrol. Eng. **10**(3), 205–215 (2005)
17. Xu, K., Milliman, J.D., Xu, H.: Temporal trend of precipitation and runoff in major Chinese rivers since 1951. Global Planet. Change **73**(3), 219–232 (2010)
18. Xu, Z.-X., Zhang, N.: Long-term trend of precipitation in the Yellow river basin during the past 50 years. Geogr. Res. **1**, 003 (2006)

Runoff Curve Number for 36 Small Agricultural Plots at Two Different Climatic Conditions in India

Mohan Lal, S.K. Mishra, Ashish Pandey and Yogendra Kumar

Abstract The performance of eight different curve number (CN) estimation methods, viz. storm event mean and median, rank-order mean and median, log-normal frequency, S-probability (SP), geometric mean and least square fit, was evaluated using rainfall–runoff data measured on 36 small agricultural plots located at two different climatic conditions in India. The least square fit method was observed to estimate significantly lower CN than other methods except log-normal frequency method. Based on the overall score, the method performance in runoff estimation was as follows: S-probability > geometric mean > storm event mean > rank-order median > rank-order mean > least square fit > storm event median > log-normal frequency. The runoff (or CN) production in the study plots was mainly dependent on soil type as compared to land uses and slope. An inverse relationship between CN and infiltration capacity was found to observe which support the applicability of National Engineering Handbook (Chap. 4) tables where CNs decline with soil type (or infiltration capacity).

Keywords Agricultural plot · Curve number · Climatic · India · Runoff

1 Introduction

The Soil Conservation Service curve number (SCS-CN) method [1] also known as Natural Resources Conservation Service curve number (NRCS-CN) is an empirical method predicting runoff from the given rainfall event using a parameter S (or CN)

M. Lal (✉) · S.K. Mishra · A. Pandey
Department of Water Resources Development and Management,
Indian Institute of Technology, Roorkee 247667, Uttarakhand, India
e-mail: mohan841987@gmail.com

M. Lal · Y. Kumar
Irrigation and Drainage Engineering Department, Govind Ballabh Pant University
of Agriculture and Technology, Pantnagar 263145, Uttarakhand, India

V. Garg et al. (eds.), *Development of Water Resources in India*,
Water Science and Technology Library 75, DOI 10.1007/978-3-319-55125-8_22

based on the major hydrologic characteristics such as prior soil moisture, land use/land cover and soil type. Since its inception, the method has undergone a various amendment including extension from agricultural to forest and urban watersheds [2]. There are number of hydrologic, water quality and erosion models such as Soil and Water Assessment Tool (SWAT) [3], Agricultural Non-Point Source (AGNPS) [4], Chemical Runoff and Erosion from Agricultural Management Systems (CREAMS) [5], and Erosion Productivity Impact Calculator (EPIC) [6] available in the literature which have used SCS-CN method for runoff estimation due its simplicity and low input data requirement. In addition, it has been also used in some other application including coupling with Universal Soil Loss Equation (USLE), sediment yield or soil moisture modeling [7–9].

The SCS-CN method combines catchment climatic and hydrologic parameters in one entity called the curve number (CN) [10, 11]. It has been found that the CN is a variable identity which varies with rainfall and changes from watershed to watershed [12]. For ungauged watershed, the values of CN generally estimated from well-known National Engineering Handbook chapter four (NEH-4) tables using watershed hydrologic characteristics. But the use of observed P–Q data-based CN over NEH-4 tables CN is recommended because later found to over-designs the hydrologic system [13]. In SCS method, the selection of correct value of CN is very essential because the estimated runoff is highly sensitive to the CN used in runoff analysis [14]. A number of methods exist in the literature for determining the CN based on measured P–Q data. The NEH-4 method also known as storm event method in which mean or median considered as watershed representative CN; traditionally recommended by SCS [1, 15], geometric mean method [15, 16], least squares method (LSM) [17], asymptotic fitting method (AFM) [15, 18], Log-normal frequency method [13], Rank-order method [17], S-probability method [19] are most common and widely used among the hydrologic community. Besides estimation of CNs, few researchers analyzed the relative accuracy of all such methods [13, 16, 20–24] utilizing data from the various parts of the globe.

Despite the widespread use of all methods, there is not an single agreed method to determine the CN values based on observed P–Q dataset [25] because each method is as good as another [26]. Therefore, there is a need of regional studies for analyzing the accuracy of each method in runoff prediction using locally measured rainfall–runoff data. The accuracy of curve number method for Indian watersheds is rarely been examined due to lack of observed P–Q data from agricultural watershed [20]. In view of the above, the present study has been conducted for analyzing the relative accuracy of various method used for CN determination using data from agricultural plots in Indian condition.

2 Materials and Methods

2.1 Site Description

The present study uses the rainfall and runoff dataset measured on 36 small agricultural plots of the various characteristics situated at two different locations in India. The salient characteristics of the study regions are shown in Table 1. The natural rainfall (P)–runoff (Q) events were captured on 35 plots of different slope, land use, and hydrologic soil group (HSG) during August 2012–April 2015 (or three crop growing seasons in study area) for the experimentation work carried out at Roorkee, India (site 1). Similarly, at site two, 40 natural P–Q events were captured on one plot of Sorghum land use during 2005–2009 [27].

Table 1 Characteristics of study sites

Description	Site 1	Site 2
River	Solani river catchment (tributary of Ganga river basin)	Musi river catchment (tributary of Krishna river basin)
State	Indian Institute of Technology, Roorkee, Uttarakhand	Central Research Institute for Dryland Agriculture, Hyderabad
Latitude and Longitude	29° 50′ 9″ N; 77° 55′ 21″ E	17° 20′ N; 78° 35′ E
Area (m^2)	Size 22 m × 5 m per plot	765
No. of plots	35 (rainfall events varying from 5 to 18 per plot)	1 (40 rainfall events)
Slope (%)	1, 3 and 5	3.27
Soil	Soil of various HSGs	Light textured red soil representing Alfisols
Land use	Sugarcane, maize, blackgram and fallow	Sorghum
Average annual rainfall (mm)	1200–1500 (mostly (70–80%) received during the monsoon season (June–September))	746.2 mm (mostly (about 70%) received during the monsoon season (June–September))
Elevation (m) above MSL	226	515
Climate	Semi-humid and subtropical	Semiarid tropical
Data recorded period	2012–2015	2005–2009
Mean monthly temperature	Summer: 35.6–38.6 °C Winter: 13.5–16.8 °C	Summer: 35.6–38.6 °C Winter: 13.5–16.8 °C

2.2 SCS-CN Method

The SCS-CN method consists of the following equations:

$$Q = \frac{(P - \lambda S)^2}{(P + S - \lambda S)} \text{ for } P > \lambda S; \text{otherwise } Q = 0 \quad (1)$$

where P (mm) is the rainfall, Q (mm) is the direct surface runoff, S (mm) is the potential maximum retention, and λ is the initial abstraction ratio (λ = 0.2, a standard value recommended by SCS).

S can be calculated where observed P–Q data are available as follows (for λ = 0.2) [28]

$$S = 5\left[(P + 2Q) - \left(4Q^2 + 5PQ\right)^{1/2}\right] \quad (2)$$

S can be transformed into CN using the following equation:

$$CN = \frac{25400}{(S + 254)} \quad (3)$$

In Eq. (3), S is in mm.

2.3 Estimation of CN from Observed P–Q Data

In the present study, eight different CN estimation methods from available P–Q data have been used for comparison. The details of each one are as follows:

Storm Event Method. In this method, natural P–Q dataset is used to derive event-wise CN using standard Eqs. (2) and (3). The mean of all events CN was considered as representative CN corresponding to the average antecedent moisture condition (AMC-II) of the plot [16, 29]. In the present paper, representative mean CN method is designated as M1.

Least Square Fit Method. Based on the observed rainfall (P) and runoff (Q) data, the only parameter S (or CN) was estimated using least square fit minimizing the sum of squares of residuals (Eq. 4) [16, 21, 22, 30] employing Microsoft Excel (solver) tool:

$$\sum_{i}^{n} (Q_i - Q_{ci})^2 = \sum \left\{ Q_i - \left[\frac{(P - 0.2S)^2}{(P + 0.8S)} \right] \right\}^2 \Rightarrow \text{Minimum} \quad (4)$$

where Q_{ci} (mm) and Q_i (mm) are, respectively, the predicted and observed runoff for rainfall event i, and n is the total number of rainfall events. Here, the least square fit CN method is designated as M2.

Geometric Mean Method. The step-wise procedure for deriving the CN (AMC-II) using geometric mean method is given below [16]

i. Derive the event-wise S using standard Eq. (2).
ii. Take the logarithm of the events S (i.e., log S).
iii. Find the arithmetic mean of the log S series.
iv. Estimate the geometric mean (GM) of the S (S_{GM}) by taking the antilogarithm of the mean of log S (i.e., $S_{GM} = 10^{\log S}$).
v. Calculate the geometric mean CN using $CN_{GM} = 25{,}400/(254 + 10^{\log S})$.

The geometric mean CN method is designated as M3.

Log-normal Frequency Method. In this method, the logarithms of each set of natural P and Q pair were computed individually. The value of S was then calculated by employing Eq. (2) using mean log P and log Q values [13, 20]. Finally, the representative CN (AMC-II) value for plot was computed using Eq. (3). Here, this method is designated as M4.

NEH-4 Median Method. This method is traditionally recommended by SCS [1, 15], in which the median of event-wise CN derived using standard Eqs. (2) and (3) was considered as representative CN of plot. Here, the median CN method is designated as M5.

Rank-Order Method. This method requires ordered series of P–Q pairs [15, 21]. The naturally measured P and Q values were sorted separately and then realigned by common rank-order basis to form a new set of P–Q pairs of the equal return period, in which runoff Q is not necessarily matched with the original rainfall P [11, 15, 18, 21, 23, 25]. For each ordered P–Q pair, S and CN were determined employing Eqs. (2) and (3), respectively. The representative CN (AMC-II) of the plot is mean or median of the event-wise CNs series computed with the ranked P–Q pairs. Here, mean and median are designated as method M6 and M7, respectively.

In method M1–M7, the antecedent moisture condition (AMC) was decided based on the previous 5-day rainfall (P_5). The details of choosing the criteria for AMC-I, AMC-II and AMC-III can be found elsewhere [11, 31]. For wet (AMC-III) and dry (AMC-I) conditions, the CN (AMC-II) values were adjusted using Eqs. (5) and (6), respectively, as follows [32]:

$$CN_{III} = \frac{CN_{II}}{0.427 + 0.00573\,CN_{II}} \tag{5}$$

$$CN_{I} = \frac{CN_{II}}{2.281 - 0.01281\,CN_{II}} \tag{6}$$

S-probability Method. For each set of natural P–Q pair, the value of S (or CN) is determined using Eqs. (2) and (3). The Weibull plotting position was used to derive the log-normal probability distribution for the calculated values of S. The S values corresponding to 90, 50 and 10% probability levels were used to estimate the representative CN values for AMC-III, II and I, respectively [19, 20, 33, 34]. Here, this method is designated as M8.

The comprehensive detail of the all methods used in the present paper can be found elsewhere [1, 12, 13, 15–23, 26, 29, 33, 34].

The estimated CN by various methods (i.e., M1–M8) along with the plot characteristics is shown in Table 2.

2.4 Goodness of Fit

The performance of all the methods was evaluated based on the root-mean-square error (RMSE), Bias, Nash–Sutcliffe Efficiency (NSE) [35] and Index of agreement (D) [36].

$$\mathrm{RMSE} = \left(\frac{1}{n}\sum_{i}^{n}\left(Q_i - Q_{ci}\right)^2\right)^{1/2} \tag{7}$$

$$\mathrm{NSE} = \left(1 - \frac{\sum_{i=1}^{n}\left(Q_i - Q_{ci}\right)^2}{\sum_{i=1}^{n}\left(Q_i - \overline{Q}\right)^2}\right) \tag{8}$$

$$e = \frac{\sum_{i=1}^{n}\left(Q_{ci} - Q_i\right)}{n} \tag{9}$$

$$D = \left(1 - \frac{\sum_{i}^{n}\left(Q_i - Q_{ci}\right)^2}{\sum_{i}^{n}\left(\left|Q_i - \overline{Q}\right| + \left|Q_{ci} - \overline{Q}\right|\right)^2}\right) \tag{10}$$

where $\overline{Q}$(mm) is the average of observed runoff for all storm events.

In this study, the arithmetic means of NSE, Bias, D and RMSE values are used as a yardstick for overall performance evaluation. Kolmogorov–Smirnov test was used to assess the normality of data. The nonparametric Kruskal–Wallis test was used to test significance level. The statistical analyses were carried out using SPSS20.0, and least square fitting by using Microsoft Excel (Solver).

Table 2 Estimated curve numbers using the eight different methods for the 36 agricultural plots of various characteristics

Plot no.	Land use	Slope (%)	Infiltration capacity[a] (mm/h)	HSG[b]	No. of events	Curve number (AMC-II) estimation method							
						M1	M2	M3	M4	M5	M6	M7	M8
1	Sugarcane	5	7.36	B	15	80.61	79.93	81.42	77.77	81.24	80.79	81.24	81.24
2	Sugarcane	3	8.77	A	15	79.47	80.09	80.75	76.00	79.88	79.74	79.71	79.88
3	Sugarcane	1	6.51	B	15	81.27	81.51	82.69	76.39	81.09	81.60	81.37	81.09
4	Fallow	5	12.1	A	10	78.49	75.05	79.15	75.97	78.08	78.58	79.06	78.08
5	Fallow	3	6.15	B	10	80.10	75.52	81.13	75.24	79.21	80.19	79.07	79.21
6	Fallow	1	10.28	A	10	74.64	70.87	75.22	72.24	77.75	74.64	73.60	77.75
7	Maize	5	4.24	B	10	82.10	82.19	82.73	76.10	80.88	82.18	81.86	80.88
8	Maize	3	5.52	B	10	80.31	80.24	80.61	75.62	79.77	80.33	79.22	79.77
9	Maize	1	2.82	C	10	83.46	84.81	84.14	77.95	81.49	82.44	84.13	81.49
10	Blackgram	5	15.22	A	10	81.12	82.06	81.92	76.65	79.77	81.30	81.65	79.77
11	Blackgram	3	13.82	A	10	78.87	78.38	79.59	75.23	79.16	79.02	79.72	79.16
12	Blackgram	1	5.66	B	10	79.26	78.95	80.49	75.36	80.28	79.47	80.28	80.28
13	Sugarcane	5	25.5	A	13	79.38	74.49	80.18	79.05	79.83	79.46	80.10	79.83
14	Sugarcane	3	10.18	A	13	82.71	78.50	84.27	82.13	83.65	82.96	83.76	83.65
15	Sugarcane	1	14.9	A	13	81.10	76.05	82.21	80.88	84.48	81.25	80.88	84.48
16	Maize	5	10.25	A	11	80.17	77.97	81.14	78.01	81.52	80.21	79.88	81.52
17	Maize	3	26.9	A	11	78.79	75.49	79.53	76.35	80.02	78.87	78.47	80.02
18	Maize	1	22.05	A	11	81.92	82.26	83.34	79.00	82.47	82.04	81.50	82.47
19	Blackgram	5	21.5	A	11	76.53	64.73	77.59	76.15	79.44	80.98	79.65	79.44
20	Blackgram	3	19.4	A	11	80.06	73.07	81.17	79.44	81.72	80.20	80.94	81.72
21	Blackgram	1	18.5	A	11	80.78	77.88	82.41	78.76	79.65	80.98	79.65	79.65
22	Fallow	5	22.92	A	13	77.89	69.61	79.15	77.76	83.07	78.01	80.01	83.07
23	Fallow	3	7.9	A	11	77.94	68.90	79.64	74.19	81.66	73.81	72.75	81.66

(continued)

Table 2 (continued)

Plot no.	Land use	Slope (%)	Infiltration capacity[a] (mm/h)	HSG[b]	No. of events	Curve number (AMC-II) estimation method							
						M1	M2	M3	M4	M5	M6	M7	M8
24	Fallow	1	19.8	A	13	78.34	70.59	79.62	78.10	81.42	78.45	78.64	81.42
25	Sugarcane	5	2.68	C	10	91.36	90.33	92.60	91.92	92.35	91.55	91.02	92.35
26	Sugarcane	3	3.5	C	10	87.99	86.84	88.75	88.11	88.10	88.17	87.97	88.10
27	Sugarcane	1	3.1	C	10	85.95	84.62	86.83	85.97	86.29	86.20	86.00	86.29
28	Maize	5	2.67	C	4	95.55	95.30	95.81	95.76	95.95	95.55	95.96	95.95
29	Maize	3	3.96	C	4	93.60	93.49	93.81	93.56	93.95	93.59	93.95	93.95
30	Maize	1	3.45	C	4	88.63	88.89	89.01	88.23	87.44	88.63	87.44	87.44
31	Lentil	5	4.24	B	5	77.96	66.70	79.11	76.61	79.80	78.12	77.22	79.80
32	Lentil	3	5.52	B	5	74.25	73.57	75.37	69.62	75.28	74.38	73.82	75.28
33	Chana	5	15.22	A	5	74.44	47.61	75.41	74.05	75.00	74.48	75.00	75.00
34	Chana	3	13.82	A	5	69.79	54.35	70.70	67.58	72.26	69.46	69.91	72.26
35	Chana	1	5.66	B	5	73.68	45.13	75.04	70.11	80.55	73.55	72.23	80.55
36	Sorghum	3.27	–	B	40	74.05	72.87	75.09	72.23	73.69	74.15	73.90	73.90

[a]Infiltration capacity was calculated using double ring infiltrometer test; [b]HSGs were determined based on soil infiltration capacity [1]

3 Results and Discussion

3.1 Curve Number Estimation

The curve number (AMC-II) estimated using eight different methods is presented in Table 2. As seen, the CNs estimated by least squares fit (M2) method range from 45.12 (plot 35) to 95.30 (plot 28). The CNs estimated by traditionally recommended NEH-4 median (M5) method range from 72.26 (plot 34) to 95.55 (plot 28). In general, the CNs estimated by geometric mean (M3) method are usually larger (17 of 36 plots) followed by S-probability (M8) (15 of 36 plots). Based on overall mean (mean of representative CNs of 36 plot), M2 was found to estimate the lowest CNs among all methods. In contract, M8 method found to estimate the larger CNs. The multiple comparison result of CNs estimated by all the eight methods is shown in Table 3. Based on the Kruskal–Wallis test analysis, mixed results were obtained. There was no single method which has produced significantly higher (or lower) CNs than other. Method M3 produced significantly ($p < 0.05$) higher CNs than M2 and M4, but it was statistically insignificant with others (i.e., M1, M5, M6, M7, M8). Similarly, M2 produced significantly lower CNs than other methods except M4. The CNs estimated by M1, M3, M5, M6, M7, and M8 were statistically insignificant among each other.

3.2 Effect of Land Use, Soil Type and Plot Slope on Runoff Coefficient (Rc) and Curve Number (CN)

The effect of land use, soil type, and slope on runoff coefficient (Rc) was tested individually for their significance. To this end, plots located in the same land use, HSG, and slope were grouped separately for checking the significances among studied variables. Since the data distribution fails to pass the normality test for the three individual groups (i.e., land use, HSG, and slope), the nonparametric Kruskal–Wallis test was used to test significance level. The results of nonparametric Kruskal–Wallis test are shown in Table 3. The test revealed that land use did not show any significant difference in runoff coefficient (Rc) except the sugarcane which has produced significantly ($p < 0.05$) higher Rc than blackgram and fallow land use. In case of HSGs, soil type C has produced significantly higher runoff coefficient (Rc) than did B and A, but the last ones did not differ from each other. In addition, slope did not show any effect on Rc as all three groups of slope were insignificantly different from each other.

As seen from Table 3, land uses did not show any significant difference in CNs (estimated by M5) except sugarcane which has produced significantly ($p < 0.05$) higher CNs than blackgram and fallow land uses. Furthermore, slope also did not show any effect on CNs as all the three groups (i.e., 5, 3 and 1%) of slope were statistically insignificant. In the present study, CN was mainly found to influence by

Table 3 Table showing the multiple comparison results of CN determination for different groups

CN determination group			Land uses group				HSG group				Slope group			
Method	CN	n	Land use	Rc	CN	n	HSG	Rc	CN	n	Slope (%)	Rc	CN	n
M1	80.63 a	36	Sugarcane	0.245 a	83.66 a	126	A	0.176 a	79.89 a	220	5	0.209 a	81.97 a	129
M2	76.08 b	36	Blackgram	0.170 bc	80.99 bc	72	B	0.168 a	76.65 b	142	3	0.196 a	81.47 a	127
M3	81.60 a	36	Maize	0.200 bca	82.40 bca	72	C	0.363 b	88.95 c	58	1	0.205 a	81.96 a	124
M4	78.45 cb	36	Fallow	0.151c	79.67 c	73								
M5	81.62 a	36												
M6	80.70 a	36												
M7	80.60 a	36												
M8	81.62 a	36												

Within one group, variables with no letter (alphabet a, b, c) in common have significantly different Rc or CN at the 0.05 significance level (based on the Kruskal–Wallis test) (n is the number of rainfall events)

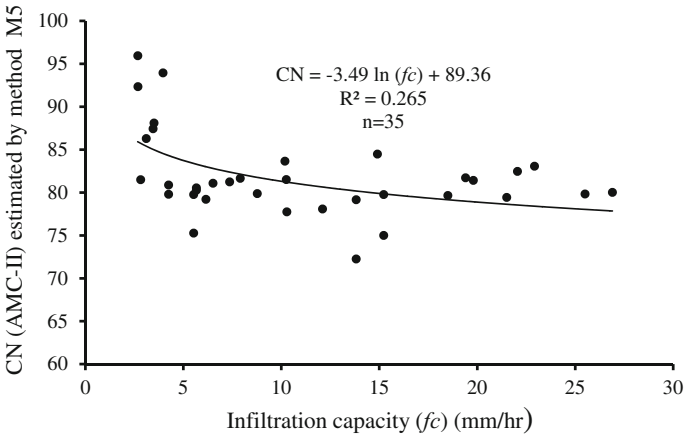

Fig. 1 Relationship between estimated CN and infiltration capacity for 35 plot data

soil type because all the three group of soil type (i.e., A, B, and C) have significantly different CNs.

Since the runoff (or CN) production in study plots was mainly influenced by the soil type (i.e., infiltration capacity) as compared to land uses and slope. A negative relationship between CNs (estimated by M5) and infiltration capacities (*fc*) was also detected with significant correlation ($R^2 = 0.265$; $p < 0.01$). The results from this analysis (Fig. 1) support the applicability of NEH-4 tables where CNs decline with soil type (i.e., *fc*).

3.3 Performance Evaluation

In order to judge the runoff estimation accuracy of CNs estimated by various methods used in this study, the runoff was estimated for the 1–24 plots datasets. The plots 25–36 were excluded from the analysis due unavailability of P_5 data. Table 4 shows the mean values of NSE, RMSE, Bias, and D for the runoff estimation using the CNs estimated by eight different methods. Considering the cumulative mean value of RMSE as an yardstick of evaluation, the performance of eight method was as follows: M8 > M3 > M1 > M7 > M6 > M2 > M5 > M4.

For further analyses based on the mean values of D, the M3 was found to perform superior followed by M8. Similarly, based on mean values of NSE, M8 performance was good, whereas M5 performed poorest. The model performance based on NSE was as follows: M8 > M2 > M1 > M3 > M7 > M6 > M4 > M5. As shown in Table 4, the variation in the mean Bias values by different methods

Table 4 Comparison of runoff estimation using eight different curve number determination methods for 24 plots datasets

	M1	M2	M3	M4	M5	M6	M7	M8
RMSE (mm)								
Maximum	10.303	10.211	9.746	13.429	11.106	10.189	10.200	10.631
Mean	7.834	7.915	7.716	8.953	8.247	7.909	7.895	7.307
Minimum	5.545	5.377	4.911	6.269	5.276	5.483	5.759	2.880
Index of agreement (D)								
Maximum	0.923	0.929	0.944	0.860	0.932	0.925	0.916	0.986
Mean	0.764	0.703	0.784	0.667	0.761	0.762	0.761	0.779
Minimum	0.626	0.387	0.623	0.512	0.606	0.582	0.603	0.635
Bias (mm)								
Maximum	5.186	4.733	4.713	7.727	6.333	5.813	4.897	5.130
Mean	1.896	3.043	1.041	2.873	1.328	1.856	1.783	1.617
Minimum	−1.162	0.666	−3.674	−1.021	−4.643	−3.387	−2.606	−0.779
NSE								
Maximum	0.724	0.741	0.784	0.545	0.750	0.730	0.703	0.950
Mean	−0.068	−0.024	−0.111	−0.195	−0.324	−0.159	−0.158	0.052
Minimum	−2.705	−1.791	−3.094	−2.671	−5.319	−4.628	−3.726	−1.791

was varied from 1.041 mm (for M3) to 3.043 (for M2). The performance of different methods based on Bias criteria can be described as M3 > M5 > M8 > M7 > M6 > M1 > M4 > M2.

The results from present analysis show that there are no single methods which do have performed good based on all the four goodness-of-fit criteria. However, either M3 or M8 can be considered as good among all based on individual goodness-of-fit criteria.

For evaluating the overall performance, the methods were ranked based on the mean statistics, viz. D, RMSE, Bias, and NSE. To this end, a rank of 1–8 was assigned to show the RMSE, Bias from lowest to highest, and D and NSE from highest to lowest. After assigning of ranks, corresponding marks of 8 to 1 are given to each index. For example, a method having the minimum RMSE, Bias, and maximum D, NSE will be ranked 1. The method corresponding to rank 1 will be achieved to score 8 marks. The overall performance of method was judged based on the total marks gained by method using all four statistics. The first rank will be given to the method scoring highest marks, whereas last rank (i.e., eight) will be given to method scoring lowest marks. Table 5 shows the ranks and marks achieved by all methods for their respective performance indices. As seen from this table, M8 performed best followed by M3. Based on overall score (Table 5), the methods performance can be described as follows: M8 > M3 > M1 > M7 > M6 > M2 > M5 > M4.

Table 5 Performance evaluation of models based on ranks (scores)

Performance indices and their ranks (scores)										
Method	RMSE (mm)	Rank (score)	D	Rank (score)	Bias (mm)	Rank (score)	NSE	Rank (score)	Total score	Overall rank
M1	7.834	3 (6)	0.764	3 (6)	1.896	6 (3)	−0.068	3 (6)	21	3
M2	7.915	6 (3)	0.702	7 (2)	3.043	8 (1)	−0.024	2 (7)	13	6
M3	7.716	2 (7)	0.784	1 (8)	1.041	1 (8)	−0.111	4 (5)	28	2
M4	8.953	8 (1)	0.667	8 (1)	2.873	7 (2)	−0.195	7 (2)	6	8
M5	8.247	7 (2)	0.761	6 (3)	1.328	2 (7)	−0.324	8 (1)	13	7
M6	7.909	5 (4)	0.761	4 (5)	1.856	5 (4)	−0.159	6 (3)	16	5
M7	7.895	4 (5)	0.761	5 (4)	1.783	4 (5)	−0.158	5 (4)	18	4
M8	7.307	1 (8)	0.779	2 (7)	1.617	3 (6)	0.052	1 (8)	**29**	**1**

4 Conclusions

The following conclusions can be drawn from the present study:

1. Soil type (as compared to land uses or slopes) was found to be main explanatory variable for runoff (or CN) production in the study plots.
2. An inverse relationship between CN and infiltration capacity was detected which support the applicability of NEH-4 tables where CN decline with soil type (i.e., infiltration capacity).
3. The least square fit (M2) method found to estimate significantly low CNs as compared to other methods except log-normal (M4) method.
4. The S-probability (M8) method proves to be best among all methods followed by geometric mean (M3) method.

Acknowledgements This research (site 1) was supported by a grant from the Indian National Committee on Surface Water (INCSW) and Ministry of Water Resources, Govt. of India, New Delhi under the Research and Development project (MOW-627-WRD) on "Experimental Verification of SCS Runoff Curve Numbers for Selected Soils and Land Uses." Special thanks to the Mondal et al. [27] for providing the 40 rainfall–runoff data.

References

1. SCS: 'Hydrology' National Engineering Handbook, Supplement A, Section 4, Soil Conservation Service, USDA, Washington, DC (1972)
2. Rallison, R.E.: Origin and evaluation of the SCS runoff equation. In: Proceedings of Irrigation and Drainage Symposia on Watershed Management, vol. 2, pp. 912–924. ASCE, New York (1980)
3. Arnold, J.G., Williams, J.R., Srinivasan, R., King, K.W.: SWAT: soil and water assessment tool. USDA-ARS, Grassland, Soil and Water Research Laboratory, Temple, TX (1996)

4. Young, R.A., Onstad, C.A., Bosch, D.D., Anderson, W.P.: AGNPS: a nonpoint-source pollution model for evaluating agricultural watersheds. J. Soil Water Conserv. **44**(2), 168–173 (1989)
5. Knisel, W.G.: CREAMS: a field-scale model for chemical, runoff and erosion from agricultural management systems. Conservation Research Report No. 26, South East Area, US Department of Agriculture, Washington, DC (1980)
6. Sharpley, A.N., Williams, J.R.: EPIC-Erosion/productivity impact calculator: 1. Model determination. US Department of Agriculture. Tech. Bull., No. 1768 (1990)
7. Gao, G.Y., Fu, B.J., Lu, Y.H., Liu, Y., Wang, S., Zhou, J.: Coupling the modified SCS-CN and RUSLE models to simulate hydrological effects of restoring vegetation in the Loess Plateau of China. Hydrol. Earth Syst. Sci. **16**, 2347–2364 (2012)
8. Mishra, S.K., Tyagi, J.V., Singh, V.P., Singh, R.: SCS-CN based modelling of sediment yield. J. Hydrol. **324**, 301–322 (2006)
9. Tyagi, J.V., Mishra, S.K., Singh, R., Singh, V.P.: SCS-CN based time-distributed sediment yield model. J. Hydrol. **352**, 388–403 (2008)
10. Ebrahimian, M., Nuruddin, A.A.B., Soom, M.A.B.M., Sood, A.M., Neng, L.J.: Runoff estimation in steep slope watershed with standard and slope-adjusted curve number methods. Pol. J. Environ. Stud. **21**(5), 1191–1202 (2012)
11. Ajmal, M., Moon, G., Ahn, J.: Kim T Quantifying excess storm water using SCS-CN–based rainfall runoff models and different curve number determination methods. J. Irrig. Drain. Eng. **141**(3), 04014058 (2015)
12. McCuen, R.H.: Approach to confidence interval estimation for curve numbers. J. Hydrol. Eng. **7:1**(43), 43–48 (2002). doi:10.1061/(ASCE)1084-0699(2002
13. Schneider, L.E., McCuen, R.H.: Statistical guidelines for curve number generation. J. Irrig. Drain. Eng. **131**(3), 282–290 (2005)
14. Hawkins, R.H.: The importance of accurate curve numbers in the estimation of storm runoff. Water Resour. Bull. **11**(5), 887–891 (1975)
15. Hawkins, R.H., Ward, T.J., Woodward, D.E., Van Mullen, J.A. (eds.): Curve Number Hydrology: State of the Practice. ASCE, Reston, VA (2009)
16. Tedela, N.H., McCutcheon, S.C., Rasmussen, T.C., Hawkins, R.H., Swank, W.T., Campbell, J.L., Adams, M.B., Jackson, C.R., Tollner, E.W.: Runoff curve number for 10 small forested watersheds in the mountains of the Eastern United States. J. Hydrol. Eng. **17**, 1188–1198 (2012)
17. Hawkins, R.H., Jiang, R., Woodward, D.E., Hjelmfelt, A.T., Van Mullem, J.A., Quan, Q.D.: Runoff curve number method: examination of the initial abstraction ratio. In: Proceedings of the Second Federal Interagency Hydrologic Modeling Conference. ASCE Publications, Las Vegas (2002)
18. Hawkins, R.H.: Asymptotic determination of runoff curve numbers from data. J. Irrig. Drain. Eng. **119**(2), 334–345 (1993)
19. Hjelmfelt Jr., A.T.: Investigation of curve number procedure. J. Hydraul. Eng. **117**, 725–737 (1991)
20. Ali, S., Sharda, V.N.: A comparison of curve number based methods for runoff estimation for small watersheds in semi arid region of India. Int. J. Hydrol. Res. **39**(3), 191–200 (2008)
21. D'Asaro, F., Grillone, G.: Empirical investigation of curve number method parameters in the Mediterranean area. J. Hydrol. Eng. **17**, 1141–1152 (2012)
22. D'Asaro, F., Grillone, G., Hawkins, R.H.: Curve number: empirical evaluation and comparison with curve number handbook tables in sicily. J. Hydrol. Eng. **19**(12), 04014035 (2014)
23. Lal, M., Mishra, S.K., Pandey, A.: Physical verification of the effect of land features and antecedent moisture on runoff curve number. Catena **133**, 318–327 (2015)
24. Stewart, D., Canfield, E., Hawkins, R.H.: Curve number determination methods and uncertainty in hydrologic soil groups from semiarid watershed data. J. Hydrol. Eng. **17**, 1180–1187 (2012)

25. Soulis, K.X., Valiantzas, J.D.: SCS-CN parameter determination using rainfall-runoff data in heterogeneous watersheds—the two-CN system approach. J. Hydrol. Earth Sys. Sci. **16**, 1001–1015 (2012)
26. Tedela, N.H., McCutcheon, S.C., Rasmussen, T.C., Tollner, E.W.: Evaluation and improvement of the curve number method of hydrological analysis on selected forested watersheds of Georgia. Project report submitted to Georgia Water Resources Institute, Supported by the U.S. Geological Survey, p. 40 (2008)
27. Mandal, U.K., Sharma, K.L., Prasad, J.V.N.S., Reddy, B.S., Narsimlu, B., Saikia, U.S., Adake, R.V., Yadaiah, P., Masane, R.N., Venkanna, K., Venkatravamma, K., Satyam, B., Raju, B., Srivastava, N.N.: Nutrient losses by runoff and sediment from an agricultural field in semi-arid tropical India, Indian. J. Dryland Agric. Res. Dev. **27**(1), 01–09 (2012)
28. Hawkins, R.H.: Improved prediction of storm runoff in mountain watershed. Irrig. Drain. Div. ASCE **99**, 519–523 (1973)
29. Bonta, J.V.: Determination of watershed curve number using derived distributions. J. Irrig. Drain. Div. **123**(1), 28–36 (1997)
30. NRCS: 'Hydrology' National Engineering Handbook, Supplement A, Section 4, Soil Conservation Service, USDA, Washington, DC (1997)
31. Mays, L.W.: Water Resources Engineering, 2nd edn. Willey, Arizona. ISBN: 978-0-470-46064-1 (2005)
32. Hawkins, R.H., Hjelmfelt, A.T., Zevenbergen, A.W.: Runoff probability, storm depth, and curve numbers. J. Irrig. Drain. Eng. **111**(4), 330–340 (1985)
33. Hjelmfelt, A.T.: Empirical-investigation of curve number techniques. J. Hydraul. Eng. Div. **106**(9), 1471–1476 (1980)
34. Hjelmfelt, A.T., Kramer, K.A., Burwell, R.E.: Curve numbers as random variables. In: Proceedings of International Symposium (1982)
35. Nash, J.E., Sutcliffe, J.E.: Modeling infiltration during steady rain. Water Resour. Res. **9**, 384–394 (1970)
36. Legates, D.R., McCabe, G.J.: Evaluating the use of "goodness-of-fit" measures in hydrologic and hydro climatic model validation. Water Resour. Res. **35**(1), 233–241 (1999)

Comparison of Various Functional Forms for Wheat Crop Yield in Kanpur Nagar (Uttar Pradesh)

Alok Gupta, C.S.P. Ojha and Anuj Kumar

Abstract The present study aims at finding functional forms for wheat crop yield in an area located in Kanpur Nagar, in terms of monthly NDVI, rainfall and mean temperature. To verify wheat NDVI with the ground truth, a plot of 5 acres is chosen. It has been assumed that yield for this plot is same as that of whole study area. Functional form with all three variables performed the best. Whenever temperature is included as one of the variables, mean absolute percent error is about 7% and 15% in training and testing, respectively. Functional forms are ranked based on their performance. It is concluded that if NDVI data are not complete for the study period, modeled yield has very poor correlation with NDVI. Also, temperature of the first cropping month has the highest sensitivity when temperature is taken as a variable for wheat crop yield modeling.

Keywords NDVI · Wheat crop yield · Multilinear regression · ArcGIS

1 Introduction

Kanpur Nagar (Uttar Pradesh), the area of this study, lies in the Ganga basin. Total area of Kanpur Nagar district is 3155 km^2. Wheat is the largest grown Rabi crop here. As per the crop yield data, wheat is grown in about 67% and 32% of the total area during 1999–2003 and 2004–2013, respectively. Earlier workers [1, 2] have found that Normalized Difference Vegetation Index (NDVI) is key variable for modeling wheat crop yield. Here reassessment of this kind of approaches will be done. NDVI, soil moisture, surface temperature and rainfall is considered to fit a multilinear regression model for the crop yield by some researchers [3]. They took corn and soybean crops and obtained the crop yield models. They took growth season average of NDVI. An effort will be made to assess whether yield of wheat

A. Gupta (✉) · C.S.P. Ojha · A. Kumar
Department of Civil Engineering, Indian Institute of Technology,
Roorkee 247667, Uttarakhand, India
e-mail: alokrax@gmail.com

V. Garg et al. (eds.), *Development of Water Resources in India*,
Water Science and Technology Library 75, DOI 10.1007/978-3-319-55125-8_23

crop at Kanpur Nagar depends more on meteorological conditions (rainfall and mean temperature) or not. If this happens, satisfactory early predictions of yield can be made just by knowing the temperature and rainfall of 1st and/or 2nd months and with the help of simple tools such as MS Excel. This will be helpful in food security policy making before crop is actually harvested.

Wheat crop yield is modeled in six different functional forms using monthly NDVI, monthly rainfall and monthly mean temperature for four cropping months. Functional forms for yield are proposed as linear combinations of monthly NDVI (N_1, N_2, N_3, N_4), monthly precipitations (P_1, P_2, P_3, P_4) and monthly mean temperature (T_1, T_2, T_3, T_4) as follows:

(i) Yield in terms of NDVI only (Y-NDVI)

$$Y = \sum_{i=1}^{4} n_i N_i \tag{1}$$

(ii) Yield in terms of NDVI and Rainfall (Y-NDVI-RF)

$$Y = \sum_{i=1}^{4} n_i N_i + \sum_{i=1}^{4} p_i P_i. \tag{2}$$

(iii) Yield in terms of NDVI, Rainfall and mean Temperature (Y-NDVI-RF-T)

$$Y = \sum_{i=1}^{4} n_i N_i + \sum_{i=1}^{4} p_i P_i + \sum_{i=1}^{4} t_i T_i. \tag{3}$$

(iv) Yield in terms of NDVI and temperature (Y-NDVI-T)

$$Y = \sum_{i=1}^{4} n_i N_i + \sum_{i=1}^{4} t_i T_i, \tag{4}$$

(v) Yield in terms of Rainfall and Temperature (Y-RF-T)

$$Y = \sum_{i=1}^{4} p_i P_i + \sum_{i=1}^{4} t_i T_i \tag{5}$$

(vi) Yield in terms of only Temperature (Y-T)

$$Y = \sum_{i=1}^{4} n_i T_i. \tag{6}$$

Here n_i, p_i and t_i (for i = 1, 2, 3 and 4) are parameters for these proposed functional forms.

Annual observed yield in tonnes/hectare (T/ha) for the wheat crop is given. Annual modeled yield is obtained by Eqs. (1)–(6). Input variables are changed and performance of these models is reported in terms of absolute percent error (APE) with respect to observed yield. Using 'Solver' tool in MS Excel, parameters are optimized in such a way that mean absolute percent error (MAPE) is minimized for each model.

2 Study Area

Kanpur Nagar is selected as one of the various locations in the Ganga basin. Figure 1 shows the study area which lies in Kanpur, one of the districts of Uttar Pradesh. To ensure the mapping of NDVI with wheat crop, a ground-truth location plot is selected at Tatiyaganj in Kanpur Nagar (shown in Google Earth image, Fig. 2). This plot lies in IMD temperature grid (latitude 27.5° and longitude 80.5°) and precipitation grid (latitude 26.5° and longitude 80.25°). It has been assumed that behavior of ground-truth plot is same as whole Kanpur Nagar.

3 Data Used

NDVIs for 1999–2013 are obtained from Landsat Archive L7 ETM+SLC-on (1999–2003) and L7ETM+SLC-off (2003–2013) imageries, downloaded from the Web site of the US Geological Survey [4]. These are of 30-m resolution and multiband images in which band 3 and 4 corresponding to red and near infrared (NIR), respectively. These two bands are used to calculate NDVI using raster calculator in ArcGIS 10.3.1. District Kanpur falls in Path-144 and Row-42 in these imageries. Dates of the images along with NDVIs are given in Table 1. In L7 ETM +SLC-off images during 2003–2013, scan line corrector was off. Landsat_gapfill extension (with single file gap fill) was used for correcting the lines in these images. NDVI layers were extracted using shape file of Kanpur Nagar as the mask. 5 ha field ground-truth plot (Figs. 1 and 2) was used for verification that wheat is grown during December–March. NDVI of Kanpur Nagar is extracted using this plot as a mask. It is assumed that annual wheat crop yield for this field is same as that of annual crop yield of Kanpur Nagar. Since this plot is very small and it was informed that wheat is grown in approximately whole plot, NDVI for a date is taken to be mean of NDVI of all pixels. But, Fig. 2 shows that this plot (area enclosed by red lines) does not have uniform vegetation (wheat as reported). Similarly, whole area may not have same crop intensity for other years too. Hence, average NDVI for February (month of maximum NDVI) is lesser than that of reported average February NDVI for Agra, Bharatpur, Bhiwani, etc., in earlier researches [5].

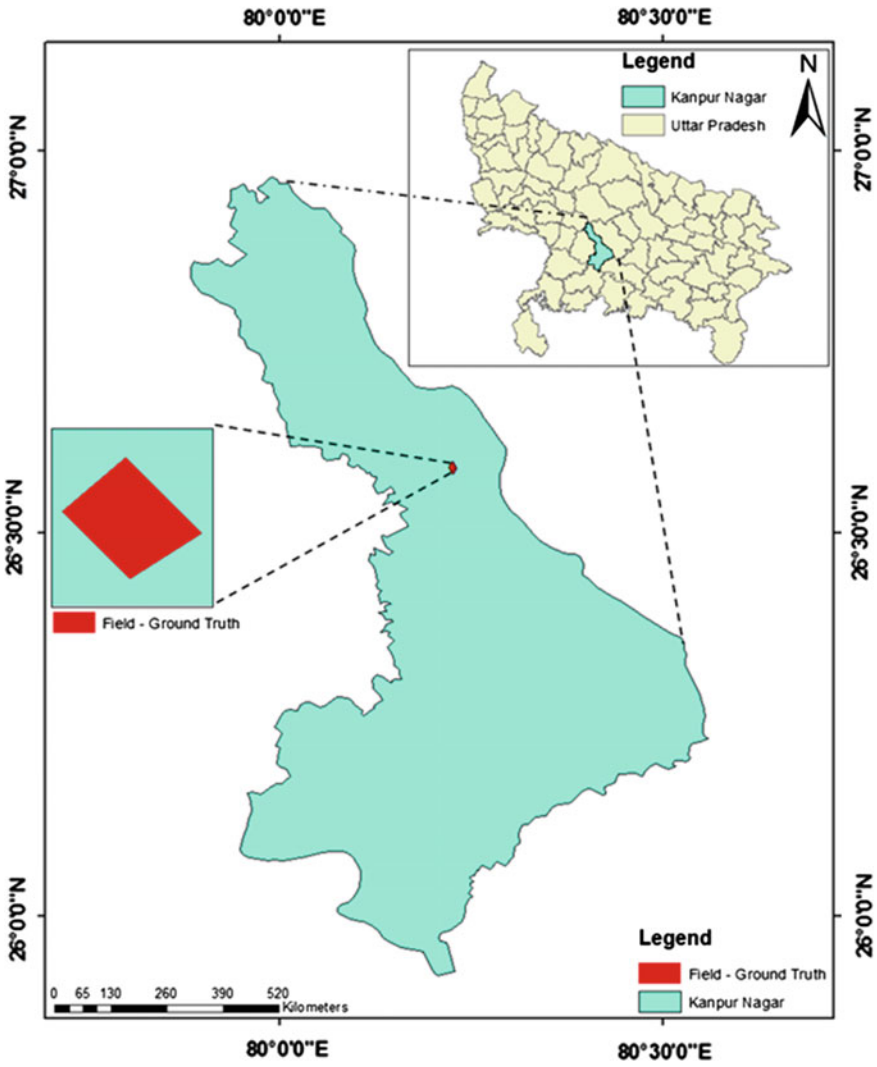

Fig. 1 Study area: Kanpur Nagar in the map of Uttar Pradesh

Available images used for computing NDVI do not correspond to the same date of various months. Hence, average of monthly NDVI is computed. For any year, NDVI for the months with no images is computed by proportioning NDVI of the months with available images using ratio of mean monthly NDVIs. No images were available for 2003–2004 and 2006–2007 to calculate NDVI. Observed yield for wheat crop is taken from the Web site of Ministry of Agriculture and Farmers Welfare [6].

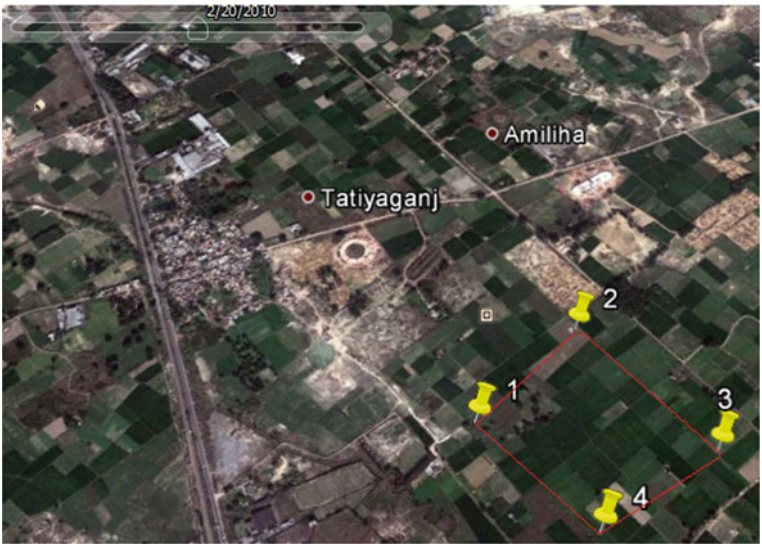

Fig. 2 Ground-truth plot (shown as *red* quadrilateral) at Tatiyaganj, Kanpur Nagar

Table 1 NDVI for different dates in the period of study

Date in Dec	NDVI	Date in Jan	NDVI	Date in Feb	NDVI	Date in Mar	NDVI
11 December 1999	0.0745	09 January 2005	0.3591	2 February 2002	0.3178	3 March 2001	0.2807
29 December 2000	0.0690	13 January 2012	0.3412	5 February 2003	0.4067	14 March 2005	0.2592
19 December 2002	0.1066	29 January 2012	0.3578	21 February 2003	0.5612	12 March 2010	0.3574
1 December 2005	0.2349	15 January 2013	0.0419	10 February 2005	0.3662	15 March 2011	0.3647
17 December 2007	0.1097			26 February 2005	0.3995	1 March 2012	0.2845
06 December 2009	0.0056			19 February 2008	0.2890	17 March 2012	0.2581
12 December 2011	0.0349			5 February 2009	0.3621	4 March 2013	0.4766
28 December 2011	0.3020			11 February 2011	0.2974	20 March 2013	0.2967
Avg. NDVI for December	0.1172	Avg. NDVI for January	0.2750	Avg. NDVI for February	0.3750	Avg. NDVI for March	0.3222

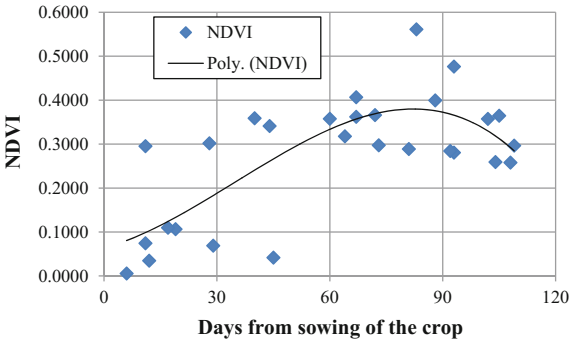

Fig. 3 Variation in NDVI in four cropping months

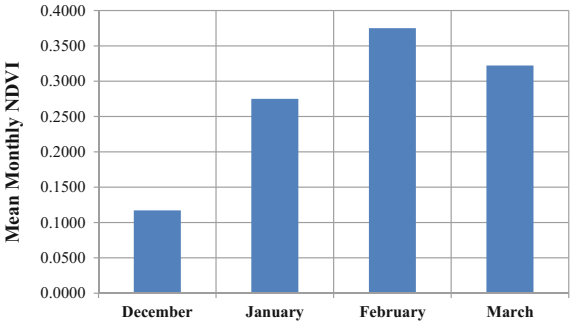

Fig. 4 Mean monthly NDVI in four cropping months

NDVI values and third-order polynomial trend line for the four cropping months of wheat (December–March) is shown in Fig. 3. Average monthly NDVI is plotted for 1st to 4th cropping month. It may be noted that NDVI is maximum for the 3rd month in both Figs. 3 and 4. Similar nature of monthly variation in NDVI is reported in earlier research [5] for Agra, a district of Uttar Pradesh less than 300 km from Kanpur Nagar [7].

India Meteorological Department (IMD) grid data of rainfall (resolution of $0.25° \times 0.25°$) and mean temperature (resolution of $1° \times 1°$) are used to find monthly rainfall and monthly mean temperature for the study area. Ground-truth location plot (of area about 5 acres) at Tatiyaganj, Kanpur Nagar, is chosen to assess wheat NDVI. Thiessen polygon method is used here for finding rainfall and mean temperature at ground-truth plot. Summary of the data used for training and testing periods is given in Tables 2 and 3, respectively.

4 Methodology

Flowchart (Fig. 5) shows the methodology used in this study. As discussed earlier, NDVIs are obtained from Landsat Archive L7ETM+SLC-on (1999–2003) and L7ETM+SLC-off (2003–2013) imageries. For L7ETM+SLC-off, scan line corrector

Table 2 Data used for training

Year	Observed yield (T/ha)	Month	NDVI	Rainfall (mm)	Temperature (°C)
1999–00	3.27	Month-1	0.0745	0.4	17.1
		Month-2	0.1748	0	15.3
		Month-3	0.2383	0	17.1
		Month-4	0.2048	0	23.1
2000–01	3.1	Month-1	0.069	0	16.8
		Month-2	0.2395	0.1	14.5
		Month-3	0.3266	0	18.9
		Month-4	0.2807	2.7	24.2
2001–02	3.29	Month-1	0.0993	0	17
		Month-2	0.233	2.2	15.6
		Month-3	0.3178	18.3	18.7
		Month-4	0.2731	0	24.4
2002–03	2.95	Month-1	0.1066	2.7	17.7
		Month-2	0.3549	9.4	12.1
		Month-3	0.4839	23.4	18.7
		Month-4	0.4158	0	23.7
2004–05	2.58	Month-1	0.1196	0	16.9
		Month-2	0.3591	8	15.9
		Month-3	0.3829	0	19.1
		Month-4	0.2592	5.3	25.2
2005–06	2.8	Month-1	0.1172	2.7	15.9
		Month-2	0.275	0	16.4
		Month-3	0.375	0	22.5
		Month-4	0.3222	11.7	24.2
2007–08	2.67	Month-1	0.1097	0.1	16.9
		Month-2	0.2119	0	15.6
		Month-3	0.289	0	17.4
		Month-4	0.2484	0.5	25.9
2008–09	2.94	Month-1	0.1131	0	18.3
		Month-2	0.2655	0	16.7
		Month-3	0.3621	0.9	19.9
		Month-4	0.3112	0.7	25

was off, and hence, the lines in the images had to be removed using 'landsat_gapfil' tool in ENVI 5.1 for the bands B3 and B4. These two bands were used to calculate NDVI using raster calculator in ArcMap 10.3.1 to apply formula for NDVI in terms of NIR and Red [8] for each pixel. Meteorological data, namely rainfall and mean temperature, are taken as other input. Thiessen polygons are prepared to obtain the influence area for each grid of rainfall and mean temperature. It was observed that

Table 3 Data used for testing

Year	Observed yield (T/ha)	Month	NDVI	Rainfall (mm)	Temperature (°C)
2009–10	2.95	Month-1	0.0056	9.8	17.7
		Month-2	0.2621	5.1	13.6
		Month-3	0.3574	16	19.6
		Month-4	0.3071	0	26.8
2010–11	3.48	Month-1	0.0929	1.1	17
		Month-2	0.2181	0.3	13.8
		Month-3	0.2974	8	19.1
		Month-4	0.3647	0.4	24.8
2011–12	3.46	Month-1	0.1684	0	16.4
		Month-2	0.3495	49.3	14.7
		Month-3	0.4766	12	18.1
		Month-4	0.2581	0.1	23.9
2012–13	3.56	Month-1	0.0179	0	16.4
		Month-2	0.0419	3.1	13.6
		Month-3	0.45	132.9	18.1
		Month-4	0.3867	1.1	24.1

ground-truth plot lies in single grid of both rainfall and temperature. Monthly rainfall and mean temperature are obtained from the daily data.

Six functional forms with three variables, namely NDVI, rainfall and mean temperature, are considered as Eqs. (1)–(6) and model parameters are obtained by minimizing MAPE for the training period (8 years). Now these six functional forms are used to estimate yield for the testing period (4 years). Then a ranking is prepared to compare performance of all the models in terms of MAPE for training and testing periods. Training and testing period are taken as 67 and 33% of whole period of the data. This segmentation of data is followed by earlier researchers [9] in machine learning techniques.

5 Results

Using 'Solver' tool in MS Excel for minimizing the MAPE, the parameters for all the models are obtained and are listed in Table 8. Modeled crop yield and MAPE for training and testing periods are given in Tables 4 (for Eqs. 1–3), 5 (for Eqs. 4–6), 6 (for Eqs. 1–3) and 7 (for Eqs. 4–6). Six models are ranked by comparing the performance using MAPE for training and testing periods (Table 9).

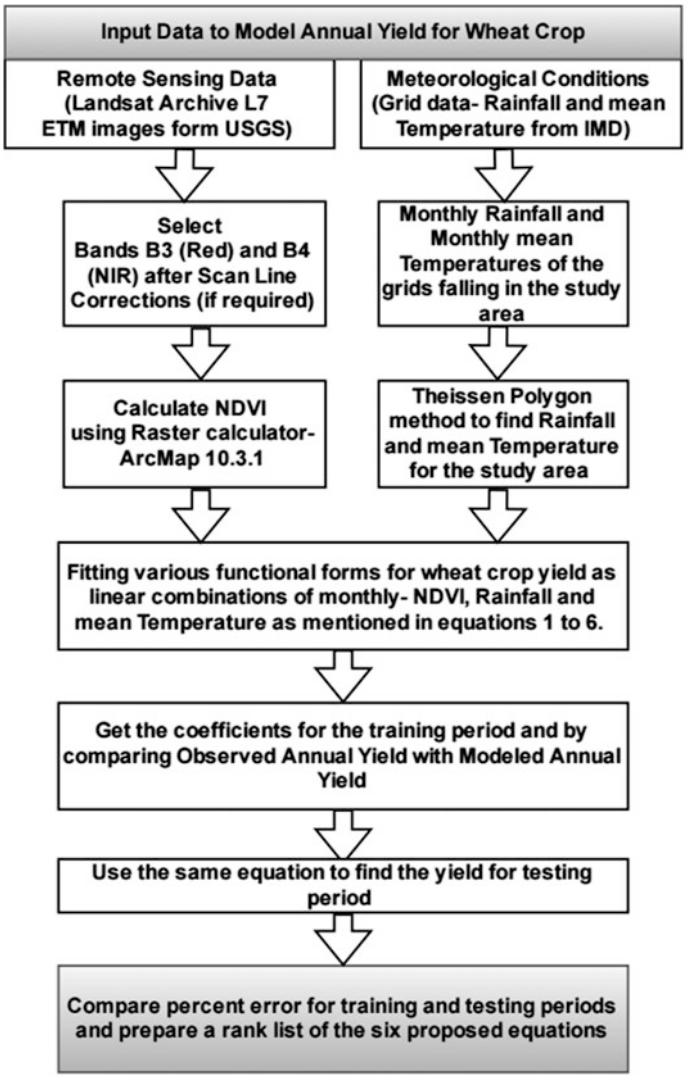

Fig. 5 Flow diagram for modeling wheat crop yield

Values of the parameters are used for commenting on the performance of functional forms. Performance of the six functional forms is as follows:

Y-NDVI (Eq. 1): For this model, MAPE varies from 18.34% (for training period) to 59.6% (for testing period). This model, though performs poorly, has highest sensitivity toward NDVI of 1st month ($n_1 = 25.898$).

Table 4 Modeled yield and error estimates for Eqs. (1)–(3)—training

Year	Obs. yield (T/ha)	Equation 1: Y-NDVI		Equation 2: Y-NDVI-RF		Equation 3: Y-NDVI-RF-T	
		Modeled yield (T/ha)	APE	Modeled yield (T/ha)	APE	Modeled yield (T/ha)	APE
1999–00	3.27	1.93	41	0.57	82.5	2.76	15.8
2000–01	3.10	1.79	42.1	1.17	62.2	2.7	12.8
2001–02	3.29	2.58	21.7	1.22	62.9	2.89	12.1
2002–03	2.95	2.77	6.1	2.95	0.0	2.95	0.0
2004–05	2.58	3.1	20.4	3.66	42.0	2.76	7.0
2005–06	2.80	3.04	8.7	3.93	40.7	2.67	4.7
2007–08	2.67	2.85	6.7	0.91	65.9	2.73	2.4
2008–09	2.94	2.94	0	0.98	66.6	2.97	1.3
		MAPE	18.3	MAPE	52.9	MAPE	7.0

Table 5 Modeled yield and error estimates for Eqs. (4)–(6)—training

Year	Obs. yield (T/ha)	Equation 4: Y-NDVI-T		Equation 5: Y-RF-T		Equation 6: Y-T	
		Modeled yield (T/ha)	APE	Modeled yield (T/ha)	APE	Modeled yield (T/ha)	APE
1999–00	3.27	2.94	10.3	2.57	21.4	2.94	10.2
2000–01	3.10	2.87	7.1	2.64	14.8	2.88	7.0
2001–02	3.29	2.93	11.0	2.97	9.9	2.93	10.8
2002–03	2.95	2.95	0.0	2.95	0.1	2.95	0.0
2004–05	2.58	2.92	13.4	2.73	5.8	2.93	13.6
2005–06	2.80	2.79	0.2	2.8	0.0	2.8	0.0
2007–08	2.67	2.91	9.0	2.7	1.1	2.91	9.2
2008–09	2.94	3.16	7.6	2.84	3.2	3.16	7.8
		MAPE	7.3	MAPE	7.0	MAPE	7.3

Table 6 Modeled yield and error estimates for Eqs. (1)–(3)—testing

Year	Obs. yield (T/ha)	Equation 1: Y-NDVI		Equation 2: Y-NDVI-RF		Equation 3: Y-NDVI-RF-T	
		Modeled yield (T/ha)	APE	Modeled yield (T/ha)	APE	Modeled yield (T/ha)	APE
2009–10	2.95	0.15	94.9	2.09	29.2	2.96	0.6
2010–11	3.48	2.41	30.7	0.97	72.1	2.77	20.4
2011–12	3.46	4.37	26	10.69	208.5	2.74	20.9
2012–13	3.56	0.47	86.8	1.67	53.2	3.66	2.9
		MAPE	59.6	MAPE	90.7	MAPE	11.2

Y-NDVI-RF (Eq. 2): This model performs poorest with MAPEs 52.85% (for training period) and 90.73% (for testing period). This model too, though performs poor, has highest sensitivity toward NDVI of 1st month ($n_1 = 6.9469$).

Y-NDVI-RF-T (Eq. 3): This model performs the best with MAPEs 6.99% (for training period) and 11.19% (for testing period). This model has highest sensitivity toward temperature of the 1st month ($t_1 = 1.352$). Second highest sensitive parameter is temperature of 2nd month ($t_2 = 0.0285$). So, by knowing temperature of 1st month, one can predict the yield with about 7% error. But the fact is that yield depends on several other conditions which are stochastic in nature. NDVI of 3rd and 4th months comes next in order of sensitivity with parameter values $n_3 = 0.0025$ and $n_4 = 0.0023$.

Table 7 Modeled yield and error estimates for Eqs. (4)–(6)—testing

Year	Obs. yield (T/ha)	Equation 4: Y-NDVI-T		Equation 5: Y-RF-T		Equation 6: Y-T	
		Modeled yield (T/ha)	APE	Modeled yield (T/ha)	APE	Modeled yield (T/ha)	APE
2009–10	2.95	2.98	1	3.09	4.88	2.98	1.1
2010–11	3.48	2.88	17.2	2.78	20.1	2.89	17.1
2011–12	3.46	2.82	18.5	2.78	19.9	2.83	18.4
2012–13	3.56	2.8	21.4	4.63	30.3	2.8	21.4
		MAPE	14.5	MAPE	18.8	MAPE	14.5

Table 8 Parameter for various models

Equation for the functional form	Functional form code	Value of the parameters
Equation 1 ($Y = \sum_{i=1}^{4} n_i N_i$)	Y-NDVI	$n_1 = 25.898$, $n_2 = 0.000$, $n_3 = 0.003$, $n_4 = 0.013$
Equation 2 ($Y = \sum_{i=1}^{4} n_i N_i + \sum_{i=1}^{4} p_i P_i$)	Y-NDVI-RF	$n_1 = 6.9469$, $n_2 = 0.0004$, $n_3 = 0.0375$, $n_4 = 0.0273$, $p_1 = 0.0994$, $p_2 = 0.1908$, $p_3 = 0.0049$, $p_4 = 0.2418$
Equation 3 ($Y = \sum_{i=1}^{4} n_i N_i + \sum_{i=1}^{4} p_i P_i + \sum_{i=1}^{4} t_i T_i$)	Y-NDVI-RF-T	$n_1 = 0.0000$, $n_2 = 0.0002$, $n_3 = 0.0025$, $n_4 = 0.0023$, $p_1 = 0.0056$, $p_2 = 0.0000$, $p_3 = 0.0078$, $p_4 = 0.0020$, $t_1 = 0.1352$, $t_2 = 0.0285$, $t_3 = 0.0004$, $t_4 = 0.0000$
Equation 4 ($Y = \sum_{i=1}^{4} n_i N_i + \sum_{i=1}^{4} t_i T_i$)	Y-NDVI-T	$n_1 = 0.0000$, $n_2 = 0.0002$, $n_3 = 0.0025$, $n_4 = 0.0023$, $t_1 = 0.1483$, $t_2 = 0.0256$, $t_3 = 0.0004$, $t_4 = 0.0000$
Equation 5 ($Y = \sum_{i=1}^{4} p_i P_i + \sum_{i=1}^{4} t_i T_i$)	Y-RF-T	$p_1 = 0.0079$, $p_2 = 0.0000$, $p_3 = 0.0156$, $p_4 = 0.0000$, $t_1 = 0.0352$, $t_2 = 0.0324$, $t_3 = 0.031_3$, $t_4 = 0.0406$
Equation 6 ($Y = \sum_{i=1}^{4} t_i T_i$)	Y-T	$t_1 = 0.1476$, $t_2 = 0.0267$, $t_3 = 0.0004$, $t_4 = 0.0000$

Table 9 Ranking of performances of six functional forms

Rank	Functional form	Equation no.	MAPE in training	MAPE in testing
1	Y-NDVI-RF-T	Equation 3	6.99	11.19
2	Y-RF-T	Equation 5	7.04	18.76
3	Y-T	Equation 6	7.33	14.49
4	Y-NDVI-T	Equation 4	7.33	14.53
5	Y-NDVI	Equation 1	18.34	59.60
6	Y-NDVI-RF	Equation 2	52.85	90.73

Y-NDVI-T (Eq. 4): This model too has highest sensitivity toward temperature of the 1st month (t_1 = 1.483). Second highest sensitive parameter is temperature of the 2nd month (t_2 = 0.0256).

Y-RF-T (Eq. 5): This model too has highest sensitivity toward temperature 1st month (t_1 = 0.0352). Here also, second highest sensitive parameter is temperature of 2nd month (t_2 = 0.0324).

Y-T (Eq. 6): This model too has highest sensitivity toward temperature of 1st month (t_1 = 0.0352). Here also, second highest sensitive parameter is temperature of 2nd month (t_2 = 0.0324).

6 Discussion

Images used to calculate NDVI were of high resolution (30 m). But since images for all four cropping months for period of study were not available, an approximation was made to estimate NDVI of each gap. This might have introduced some error, and hence, dependence of yield on NDVI could not be captured. So, high resolution images could not be useful due to lack of images for several months in cropping period. Also, there could have been some error introduced due to SLC-off correction method used in this study.

Model Y-NDVI-RF-T (with all variables) comes first in the rank list. Model Y-T has only four parameters, yet performs very well with 7.3% and 14.5% of errors in training and testing, respectively. Eight years of observed data is used to fit all the six models so the model which has lesser number of parameters and yet has lesser MAPE will be considered better.

Functional forms Y-NDVI and Y-NDVI-RF do not perform well, but as soon as mean temperature is included in the models (Y-NDVI-RF-T, Y-RF-T, Y-T and Y-NDVI-T), the performance of the models improves significantly. Hence, starting from Y-NDVI-RF-T, variables are dropped one by one. Error increases by less than 0–0.7% if we drop NDVI from the analysis (Y-NDVI-RF-T vs. Y-RF-T and Y-T vs. Y-NDVI-T). Error increases by 4–5% if we drop rainfall from the analysis (Y-NDVI-RF-T vs. Y-NDVI-T). But there is significant increase (188%) in the error by inclusion of rainfall and functional form is changed from Y-NDVI to Y-NDVI-RF.

7 Conclusion

In this study, six functional forms for wheat crop yield in Kanpur Nagar were proposed as linear combination of monthly NDVI (derived from 30 m resolution Landsat 7 ETM images), monthly rainfall and monthly mean temperature. Against our expectation, functional form with NDVI (30 m resolution) and/or rainfall did not perform well. Reason for this was the absence of complete NDVI data. Functional form with temperature only performed much better than those of with rainfall and NDVI only. But functional form with all the variables performed the best. It was found that whenever temperature was included as one of the variables, MAPE was about 7% in the training and about 15% in the testing.

References

1. Lopresti, M.F., Di Bella, C.M., Degioanni, A.J.: Relationship between MODIS-NDVI data and wheat yield: a case study in Northern Buenos Aires province, Argentina. Inf. Process. Agric. **2** (2), 73–84 (2015)
2. Zhang, H., Chena, H., Zhou, G.: The model of wheat yield forecast based on MODIS-NDVI—a case study of Xinxiang. ISPRS Ann. Photogram. Remote Sens. Spatial Inf. Sci. **I-7**, 25–28 (2012)
3. Prasad, A.K., Chai, L., Singh, R.P., Kafatos, M.: Crop yield estimation model for Iowa using remote sensing and surface parameters. Int. J. Appl. Earth Obs. Geoinf. **8**, 26–33 (2006)
4. United States Geological Survey. http://earthexplorer.usgs.gov. Accessed 10 July 2016
5. Sahay, B., Ramana, K.V., Chandrasekar, K., Biswal, A., Sai, M.V.R.S., Rao, S.V.C.K.: In-season assessment of rabi crop progression and condition from multi source data. In: The International Archives of the Photogrammetry, Remote Sensing and Spatial Information Sciences, vol. XL-8, pp. 929–926 (2014)
6. Ministry of Agriculture and farmers Welfare. http://aps.dac.gov.in/APY/Public_Report1.aspx. Accessed 15 July 2016
7. MapsofIndia.com. http://www.mapsofindia.com/distance/kanpur-to-agra.html. Accessed 25 Aug 2016
8. Wikipedia. https://en.wikipedia.org/wiki/Normalized_Difference_Vegetation_Index. Accessed 15 Aug 2016
9. Solomatine, D.P., Shrestha, D.L.: A novel method to estimate model uncertainty using machine learning techniques. Water Resour. Res. **45**(12) (2009)

Agrometeorological Wheat Yield Prediction Models

Nitin Bharadiya and Vivek Manekar

Abstract This study aims at the development of agrometeorological wheat yield prediction models for Surat district of Gujarat state, India. Three yield models such as agrometeorological yield, agrometeorological spectral yield and agrometeorological spectral trend yield were developed and compared with actual yield. The multiple linear regression analysis was used to develop agrometeorological wheat yield prediction models. The coefficient of determination (R^2) values was analyzed, and the perfect agrometeorological group was elected as T_{min} (minimum temperature), T_{max} (maximum temperature) and HTU (heliothermal units), NDVI (normalized difference vegetation index) and TPY (trend predicted yield).

Keywords Agrometeorological yield · Agrometeorological spectral yield · Agrometeorological spectral trend yield · Wheat yield prediction

1 Introduction

Crop production is a complex process which is regulated by several factors. One of them is weather variables which affect crop production. Weather is used as an indicator of variation in crop yield modeling and also plays important role in crop growth and development. Climatic and agrometeorological variables are used for development and prediction of crop yield model. Temperature, evapotranspiration, sunshine hour, rainfall, relative humidity, base period of crop and wind speed are variables which influence the crop productivity [1–3]. Parameterization of various factors such as soil, weather and technology and the study of their relationship with crop productivity is vital for crop yield modeling [4–7]. Variables like climatic

N. Bharadiya (✉) · V. Manekar
Department of Civil Engineering, S.V. National Institute of Technology, Surat, India
e-mail: bharadiya.nitin@gmail.com

V. Manekar
e-mail: vivek_manekar@yahoo.co.in

V. Garg et al. (eds.), *Development of Water Resources in India*,
Water Science and Technology Library 75, DOI 10.1007/978-3-319-55125-8_24

parameters which define the agricultural productivity of any place have always been a topic of detailed investigation [8].

Agriculture yield is benefited when there is a rise in rainfall, but rising temperatures (warming) are harmful [9]. Weather-based yield models are used in several countries like India, Canada, USA and Russia on an experimental or operational basis [10]. Also, wheat yield forecasted with a weighted rainfall index [11]. The study of agrometeorological forecasting models for wheat yield was carried out in India and other countries also [12–21].

Models available in the literature for prediction of crop yield such as Thornthwaite Memorial model [22, 23], Miami model [22, 23], Chikugo model [24] etc., incorporates a few climatic variables in the model. While comparing the results of these models with each other and with actual yield, it is found that out of these models, Thornthwaite Memorial model gives better result. It is also observed that Thornthwaite Memorial model is over-predicting the yield values up to 25%. Hence, it is felt that this over prediction may be because of the inclusion of limited parameters in the model.

Therefore, climatic and agrometeorological variables are used to develop agrometeorological yield models such as agrometeorological yield, agrometeorological spectral yield and agrometeorological spectral trend. This study has been carried out to establish relationship between wheat yield and climatic and agrometeorological variables using multiple linear regression to predict wheat yield of Surat district of Gujarat state, India.

2 Methodology

Study Area

Study area is Surat district of Gujarat state which is located at 20° 55′ N, 73° 03′ E. Data are collected from India Meteorological Department (IMD), State Water Data Center (SWDC), Department of Agriculture and Cooperation, Gandhinagar, Gujarat, and Surat Irrigation Circle (SIC) for the period from 1998–1999 to 2010–2011.

Growing Degree Days (GDD)

It is used to find relationship between crop growth and temperature [25]. GDD predicts different phenophase of wheat and gives good result [26]. It is represented as:

$$\mathrm{GDD} = \sum_{a}^{b} \left\{ \left[\frac{T_{max} + T_{min}}{2} \right] - T_b \right\} \tag{1}$$

GDD Growing degree days (°C)
T_{max} Maximum temperature (daily) (°C)
T_{min} Minimum temperature (daily) (°C)

T_b Base temperature (°C), i.e., minimum temperature below which the growth is not expected. In this case, 5 °C was selected as a base temperature for various stages of wheat growth [7]
If $T_{Mean} < T_b$, GDD = 0
a Phenophase date of starting
b Phenophase date of ending

Index of Spectral

The derivational product of satellite which expresses the area of green vegetation is recognized as normalized difference vegetation index (NDVI). In visible area, growing green plants are absorbing radiations and emitting infrared radiation. NDVI data were downloaded from the website http://bhuvan.nrsc.gov.in. NDVI was computed using the equation given below:

$$\text{NDVI} = \frac{\text{NIR} - \text{R}}{\text{NIR} + \text{R}} \tag{2}$$

where

NIR Near-infrared reflectance band
R Red reflectance band

Value of spectral pattern is ranging from −1 (water) to +1 (growth of vegetation)

Temperature Difference (T_D)

Temperature difference was expressed by using the following equation:

$$T_D = \sum_{a}^{b} (T_{max} - T_{min}) \tag{3}$$

where

T_D Temperature difference in °C

Photothermal Units (PTU)

Photothermal units (PTU) are used because of the influence of photoperiod and temperature which causes changes in plant phases. Length of the night is taken for short-day plants, and length of the day is taken for long-day plants while calculating photothermal units (PTU) [3]. Photothermal units are calculated by using the following formula.

$$\text{PTU} = \sum_{a}^{b} (\text{GDD} \times \text{N}) \tag{4}$$

where

PTU Photothermal units (°C day hours)
GDD Growing degree days (°C day)
N Maximum possible sunshine hours collected from [27]

Heliothermal Units (HTU)
Similarly, HTU is calculated by using the following equation.

$$\mathrm{HTU} = \sum_{a}^{b} (\mathrm{GDD} \times \mathrm{n}) \tag{5}$$

where

HTU Heliothermal units (°C day hours)
n Actual sunshine hours

Trend Predicted Yield (TPY)
Simple regression analysis was carried out for two variables (year and yield). Time (year) was taken as a dummy parameter [28], and trend predicted yield was calculated using below expression.

$$Y = \mathrm{a} + \mathrm{bT} \tag{6}$$

where

Y Yield (kg/ha)
a Intercept
b Regression coefficient
T Time (years) (1998 = 1)

3 Results and Discussion

Wheat yield modeling is carried out by using the different agrometeorological indices. The simple, multiple linear regression analysis was used to develop agrometeorological wheat yield prediction models. The coefficient of determination (R^2) values was analyzed, and the perfect agrometeorological group was selected as T_{min}, T_{max} and HTU (heliothermal units), NDVI (normalized difference vegetation index) and TPY (trend predicted yield).

(a) **Agrometeorological Yield**

$$Y = 404.411 + 27.019\mathrm{T}_{\min} + 15.58\mathrm{T}_{\max} + 0.0102\mathrm{HTU} \quad (7)$$

(b) **Agrometeorological spectral yield**

$$Y = 636.08 + 20.264\mathrm{T}_{\min} + 11.68\mathrm{T}_{\max} + 0.00765\mathrm{HTU} + 210.95\mathrm{NDVI} \quad (8)$$

(c) **Agrometeorological spectral trend yield**

$$Y = 617.22 + 16.21\mathrm{T}_{\min} + 9.34\mathrm{T}_{\max} + 0.0061\mathrm{HTU} + 168.762\mathrm{NDVI} + 0.108\mathrm{TPY} \quad (9)$$

Calculated yield using these agrometeorological crop yield models is compared with the actual yield for its validation (Fig. 1).

Statistical Performance

Models were tested for their statistical analysis. The ratio of calculated crop yield and actual crop yield is known as discrepancy ratio (r). It is calculated for all models taken in this study. It is considered as perfect model if value of discrepancy ratio (r) is 1. For all models, standard deviation of discrepancy ratio is obtained. The ratio of difference of computed crop yield and actual crop yield divided by actual crop

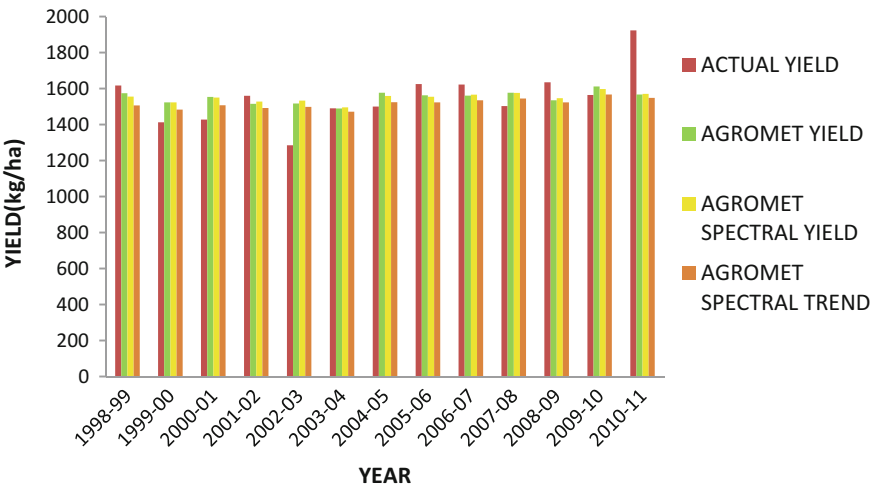

Fig. 1 Validation plot of developed Agrometeorological Wheat Yield Models

Table 1 Statistical performance of agrometeorological yield, agrometeorological spectral yield, agrometeorological spectral trend yield, Thornthwaite Memorial model and Miami model

Sr no.	Statistical performance criteria	Agrometeorological yield (Eq. 7)	Agrometeorological spectral yield (Eq. 8)	Agrometeorological spectral trend yield (Eq. 9)	Thornthwaite Memorial model	Miami model
01	Discrepancy ratio	1.0076	1.0074	0.9956	0.0830	0.0830
02	Standard deviation of discrepancy ratio	0.0880	0.0895	0.0856	0.0430	0.0320
03	Mean percentage error	0.0005	0.0000	0.0000	−0.0010	−0.0010
04	Standard deviation of mean percentage error	0.0000	0.0000	0.0000	0.0000	0.0000

yield in percentage is taken as mean percentage error. Therefore, standard deviation of mean percentage error is obtained for given models in this study. The results of obtained statistical performances of the models are given in Table 1.

4 Conclusions

Prediction of wheat yield carried out for Surat district of Gujarat state, India, using agrometeorological yield models such as agrometeorological yield, agrometeorological spectral yield and agrometeorological spectral trend yield. T_{min}, T_{max} and HTU (heliothermal units), NDVI (normalized difference vegetation index) and TPY (trend predicted yield) were selected as perfect agrometeorological subset to develop agrometeorological spectral trend yield model which predicts wheat yield better when compared with actual yield due to strong correlation with wheat yield.

References

1. Abbate, P.E., Dardanelli, J.L., Cantarero, M.G., Maturano, M., Melchiori, R.J.M., Suero, E. E.: Climatic and water availability effects on water-use efficiency in wheat. Crop Sci. **44**(2), 474–483 (2004)
2. Meena, R.P., Dahama, A.K.: Crop weather relationship of groundnut (Arachishypogaea L.) during different phenophases under irrigated condition of Western Rajasthan. J. Agromet. **6**, 25–32 (2004)
3. Reddy, T.Y., Reddi, C.H., Reddy, T.Y., Reddi, C.H.: Principles of Agronomy. Kalyani Publishing (2001)
4. Baier, W.: Crop-weather models and their use in yield assessments (1977)
5. Dadhwal, V.K.: Crop growth and productivity monitoring and simulation using remote sensing and GIS. In: Satellite Remote Sensing and GIS Applications in Agricultural Meteorology, pp. 263–289 (2003)
6. Koocheki, A., Kamali, G.H., Banaian, M.: Simulation of primary production. The center of Agrobiological Research and Department of Theoretical Production Ecology, Wageningen, Netherlands. Published by World Meteorological Organization. Geneva, July (Translated in Persian, Tehran) (1993)
7. Sharma, A., Sood, R.K., Kalubarme, M.H.: Agrometeorological wheat yield forecast in Himachal Pradesh. J. Agromet. **6**, 153–160 (2004)
8. Verma, U., Dabas, D.S., Hooda, R.S., Kalubarme, M.H., Manoj, Y., Grewal, M.S., Sharma, M.P., Prawasi, R.: Remote sensing based wheat acreage and spectral-trend agrometeorological yield forecasting: factor analysis approach. Stat. Appl. **9**(1&2), 1–13 (2011)
9. Seo, S.N.N., Mendelsohn, R., Munasinghe, M.: Climate change and agriculture in Sri Lanka: a Ricardian valuation. Environ. Dev. Econ. **10**(05), 581–596 (2005)
10. Merritt, E.S.: Space observations in agricultural information systems: a review of today's systems with requirements for tomorrow. In: International Astronautical Federation, International Astronautical Congress, 35th, Lausanne, Switzerland (1984)
11. Stephens, D.J., Walker, G.K., Lyons, T.J.: Forecasting Australian wheat yields with a weighted rainfall index. Agric. Forest Meteorol. **71**(3–4), 247–263 (1994)
12. Bal, S.K., Mukherjee, J., Mallick, K., Hundal, S.S.: Wheat yield forecasting models for Ludhiana district of Punjab state. J. Agromet. **6**, 161–165 (2004)

13. Bazgeer, S.: Land use change analysis in the sub mountainous region of Punjab using remote sensing, GIS, and agrometeorological parameters. Doctoral dissertation, Punjab Agricultural University; Ludhiana (2005)
14. Bazgeer, S., Mahey, R.K., Sharma, P.K., Sood, A., Sidhu, S.S.: Pre-harvest wheat yield prediction using agromet-spectral-trend-yield models for Hoshiarpur and Rupnagar districts of Punjab. J. Ind. Soc. Remote Sens. **34**(3), 269–277 (2006)
15. Bazgeer, S., Kamali, G., Mortazavi, A.: Wheat yield prediction through agrometeorological indices for Hamedan, Iran. Desert **12**(1), 33–38 (2007)
16. Bazgeer, S., Mahey, R.K., Sidhu, S.S., Sharma, P.K., Sood, A., Noorian, A.M., Kamali, G.H.: Wheat yield prediction using remotely sensed agromet trend-based models for Hoshiarpur district of Punjab, India. J. Appl. Sci. **8**, 510–515 (2008)
17. Esfandiary, F., Aghaie, G., Mehr, A.D.: Wheat yield prediction through agro meteorological indices for Ardebil District. World Acad. Sci. Eng. Technol. **49**, 32–35 (2009)
18. Iqbal, M.J., Ali, Z.U., Ali, S.S.: Agroclimatic modelling for estimation of wheat production in the Punjab Province, Pakistan. Proc. Pak. Acad. Sci. **49**, 241–249 (2012)
19. Kalubarme, M.H., Mahey, R.K., Dhaliwal, S.S., Sidhu, S.S., Singh, R., Mahajan, A., Sharma, P.K.: Agromet-spectral wheat yield modeling in Punjab. In: Proceedings of National Symposium on Remote Sensing of Environment with special. Emphasis on Green Revolution, pp. 11–17 (1995)
20. Sarma, A.A.L.N., Kumar, T.L., Koteswararao, K.: Development of an agroclimatic model for the estimation of rice yield. J. Ind. Geophys. Union **12**(2), 89–96 (2008)
21. Verma, U., Ruhal, D.S., Hoodal, R.S., Yadav, M., Khera, A.P., Singh, C.P., Kalubarme, M. H., Hooda, L.S.: Wheat yield modelling using remote sensing and agrometeorological data in Haryana state. J. Ind. Soc. Agric. Stat. **56**(2), 190–198 (2003)
22. Lieth, H.: Modelling the primary productivity of the world. Nat. Resour. UNESCO **VIII-2**, 5–10 (1972)
23. Lieth, H., Box, E.: Evapotranspiration and primary productivity: C.W. Thornthwaite memorial model. Pub. Climatol. **25**, 37–46 (1972)
24. Uchijima, Z., Seino, H.: Agroclimatic evaluation of net primary productivity of natural vegetations: (1) Chikugo model for evaluating net primary productivity. J. Agric. Meteorol. **40**(4), 343–352 (1985)
25. Nuttonson, M.Y.: Wheat-climate relationships and the use of phenology in ascertaining the thermal and photo-thermal requirements of wheat. Based on data of North America and of some thermally analogous areas of North America in the Soviet Union and in Finland. American Institute of Crop Ecology (1955)
26. Hundal, S.S., Singh, R., Dhaliwal, L.K.: Agro-climatic indices for predicting phenology of wheat (Triticumaestivum) in Punjab. Indian J. Agric. Sci. **67**(6) (1997)
27. Doorenbos, J., Pruitt, W.O.: Guidelines for predicting crop water requirements. Tech Note 24. Food and Agriculture Organization of United Nations, Rome (1975)
28. Draper, N.R., Smith, H.: Applied Regression Analysis, pp. 299–368. Wiley, New York (2003)

Developing a Real-Time Decision Support System in the Wake of Climate Change

Ayushi Vyas and Siby John

Abstract This paper presents a real-time decision support system (DSS) which is a comprehensive computerized information system for water resource management in the wake of climate change. With the integration of geographical information system (GIS), remote sensing and hydrological modeling, a comprehensive and efficient tool which can improve the quality of decisions taken in river water management is presented and demonstrated. The basic concepts and data processing adopted in developing the DSS are outlined, and the hydrological model working is described. It is demonstrated that the DSS developed provides an efficient and effective tool for decision-making purposes in river water systems management and dealing with hydrological dynamics in the event of climate change.

Keywords Hydrological modeling · DSS · Climate change · River systems · GIS

1 Introduction

In the current scenario, the main problem for the decision makers in the water management authorities is to understand the impacts of climate change and global warming. Climate change and associated issues necessitate an integrated and holistic approach in river water systems management. Real-time decision support system (DSS) is reported as a potential tool to assist water resources management decision makers [1, 2]. Hydrological model integrated with a real-time data acquisition, i.e., a real-time DSS, can prove very beneficial in the continuous monitoring of water resources and hence to handle the disasters caused by climate change [3, 4]. The climate change effect on the river system is directly from the changing precipitation and temperature [5]. The major limitations of the faced by

A. Vyas (✉) · S. John
Civil Engineering Department, PEC University of Technology, Chandigarh, India
e-mail: ayushi.vyas4@gmail.com

S. John
e-mail: johnsiby1@gmail.com

V. Garg et al. (eds.), *Development of Water Resources in India*,
Water Science and Technology Library 75, DOI 10.1007/978-3-319-55125-8_25

majority of the water management bodies are out of date transmission systems, not proper coverage of basin, changes in forecasts, in-efficient tools and manpower dependability. However, the bulk data which need to be handled as part the decision-making process in river water management cannot be met with such primitive systems. The geographical information systems (GIS) technology can prove beneficial for water resource managers and decision makers by providing tools for useful storage and handling of remotely sensed data. This is because of the GIS's capability to compile various bulk data sources that it is efficient and accurate to aid in calculating hydro-meteorological parameters [6, 7].

This study deals with study of hydrological dynamics of river Satluj and Beas in the wake of global warming and climate change. The real-time DSS developed as part of the study comprises real-time data acquisition, analyzing, modeling and visualization of the decision operations which covers all the requirements for the decision making in water resources management. In context of the climate change and consequent changing hydrodynamics of the river system, a hydrological model and decision support system (DSS) are presented and demonstrated.

2 The Study Area

The study area for this study is the Satluj–Beas River catchment shown in Fig. 1, having total geographical area of 56,860 km^2 and 12,560 km^2, respectively. Around 19,827 km^2 area of Satluj basin lies in the Indian boundary, while the rest lies in the Tibet. Satluj basin in India is elongated in shape and lies majorly in the Himalayas. Beas rises from the Kullu district and meets the Satluj River at Harike after flowing over a 150 kms. The altitude of the study area ranges majorly from about 400–8000 m above msl, but small portion lies around 6500 m. The great

Fig. 1 Satluj–Beas River catchment

contrast in the topographical relief in the Himalayas causes variations in climate in the Satluj–Beas basin. Major components responsible for such variations are those altitudes, topography and barrier effect. Most significant factors responsible for regulating the climatic conditions of Himalayas are the elevation and aspect. Because of the variation in altitudes, the climate distinguishes from humid tropical climate in low-lying regions to cold temperature at around 2,100 m due to heavy snowfall in winters and proceeds to polar climate as the altitude increases beyond 2,100 m.

3 Real-Time Data Acquisition and Processing

In this study, several hydro-meteorological remotely sensed data sets have been used, which are discussed below.

3.1 Hydro-meteorological Data

The hydro-meteorological real-time and forecasted data of Satluj–Beas basin are downloaded from various servers. Fifteen days quantitative and ensemble precipitation and instantaneous temperature forecast with 0.25° resolution can be downloaded from NCAR-FTP server after every 24 h. The quantitative precipitation and temperature forecast for 10 days in grib file format revised after every 6 h can be downloaded from NOAA (National Oceanic and Atmospheric Administration) for GFS model. The short-term precipitation and temperature forecast for next 72 h with 9 km × 9 km grid can be downloaded from IMD-server. The near-real-time TRMM (Tropical Rainfall Measuring Mission) precipitation data with 0.25° for every 3 h are downloaded and converted into HEC-DSS grid files. The hourly real-time precipitation and temperature data from IMD and outflow–inflow ground data from BBMB sites can be downloaded and converted into HEC-DSS time series and can be tracked. GPM (Global Precipitation Measurement Mission) provides near-real-time precipitation data with 0.1° resolution and half an hour interval. Reverb Echo NASA can be used to retrieve 500 m MODIS snow cover imageries and other satellite data. GLDAS can be used for downloading 0.125° 3-h temperature and remotely sensed SWE grid.

3.2 Data Processing

After downloading of the real-time and forecasted remotely sensed data, the sensitivity analysis of the data is performed for maintaining consistency, removal of faulty data and interpolation technique can be applied for missing data. The Model

Builder tools in ArcGIS software convert these data downloaded files into a format being read by the model selected. Hence, all the data downloaded are converted and saved into HEC-DSS time series files. Then an hourly time series of the precipitation and temperature data obtained is constructed in HEC-DSS which can be imported to the hydrological model used. By using temperature and precipitation data grid files, snow water equivalent can also be obtained which can be verified for Satluj–Beas basin using MODIS imageries [8].

4 Description of the Model

Hydrological modeling is effectively used for the calculation of the catchment's runoff volumes as a result of rainfall [9]. The objective of hydrological modeling is to understand the hydrological dynamics related to the basin and the different factors which may lead to an alteration in these phenomena. They are also efficient for monitoring the climate change effects [10]. A selection methodology can be defined for the preference of models for a hydrological project from among all choices available. The objective is to select the model satisfying the requirements like flexibility with different scales, easy to handle, efficient user interface etc. [11]. HEC-RTS is the selected model which has an integration of different modeling systems representing various hydrological as well as hydrodynamic feature of the catchment. Main HEC-RTS analysis softwares are HEC-MetVue, HEC-MFP, etc. HEC-MetVue processes observed meteorological data for input to HMS. Inputs are either point or gridded estimates of meteorological data such as precipitation and temperature. Outputs are observed meteorological time series formatted for compatibility with HEC-HMS (Hydrologic Modeling System). HEC-MFP (Meteorologic Forecast Processor) processes meteorological forecasts for input to HEC-HMS. Inputs are forecasted meteorological data such as precipitation and temperature. The forecasts can be entered manually or can be obtained from external sources such as ECMWF, GFS and IMD. Outputs are forecasted meteorological time series formatted for compatibility with HEC-HMS. HEC-HMS [12, 13] simulates watershed response to precipitation. Inputs may include observed or forecasted precipitation, temperature, snowpack and other environmental conditions. Outputs include flows throughout the watershed, including inflows to reservoirs and local flows below the reservoirs. HEC-ResSim is Reservoir System Simulation program which simulates behavior of reservoirs and linking channels, following user-specified operations for reservoir release decision making. Inputs include flows into reservoirs and unregulated flows downstream of reservoirs (from HEC-HMS). Outputs include reservoir releases, downstream regulated flows, and reservoir storage conditions.

5 Methodology

The layout of the Beas and Satluj River and its catchment area can be downloaded from ASTER global DEM from Reverb echo NASA website [14] and mosaicing them obtained DEM in ArcGIS. Re-project the DEM in ArcGIS in wgs 1984 43N for raster format and in NAD 1927 for grid format. Open the HEC GeoHMS toolbar in ArcGIS and do the preprocessing of the DEM. Hence basin model delineation will take place [15]. Then HEC-RTS model is used to link the hydro-meteorological data with the catchment using the time series files generated by HEC-DSS. So the real-time data are linked with hydrological models. The daily runoff volumes were calculated using the model, and resulted data are calibrated and validated.

The HEC-HMS model computed runoff volumes by subtracting water volume that is suspected to losses like interception, infiltration, evaporation or transpiration from the total precipitation. It depends on the results of differential equations to calculate the catchment's surface runoff. It also includes the alternative models to compute the losses. Moreover, it has separate components to represent the parameters involved in the runoff process. Initial and constant loss model is a runoff volume calculating model which considers the losses while calculating the runoff volumes. ModClark model calculates the direct runoff that mainly composed of the overland flow and interflow. Selection of the loss model for estimating the model parameters are important steps in the inputting of data into the hydrological model. Since grid files are created with the time series data in HEC-DSS so gridded transform model for computation of direct runoff, i.e., ModClark transform is used [16]. By varying parameter involved in Mod Clark transform and initial and constant loss method model can calibrated. Moreover, historical data of gauged catchments are also helpful in fine-tuning the observed results [17].

At the calibration point, model compares the observed hydrograph with the computed hydrograph. The initial loss rate can be estimated between the ranges of 0–500 m, while constant loss rate between the ranges of 0–300 mm/h for calibration purposes depending on the abundant soil type in the study area.

The model validation is performed by using current year (2014–2015) data. Model simulation is performed for the whole catchment using the data parameters obtained by calibration and validation.

6 Results

HEC-RTS model is very helpful in displaying real-time hydro-meteorological data along with the catchment. Precipitation and temperature grid files are helpful to predict the snow water equivalent (SWE) as shown in Fig. 2. It is helpful parameter to predict the snowmelt runoff.

The historic surface runoff trend of Bhakra reservoir having Satluj river inflow values is computed using data from fifty hydro-meteorological stations located at

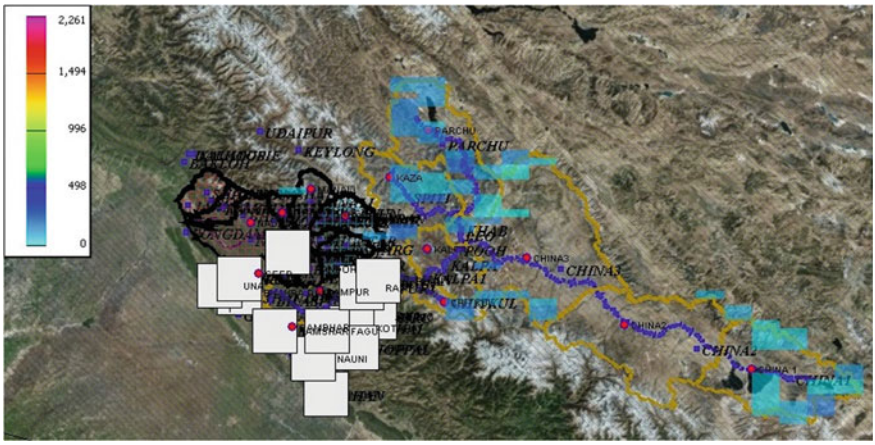

Fig. 2 SWE generated by the model

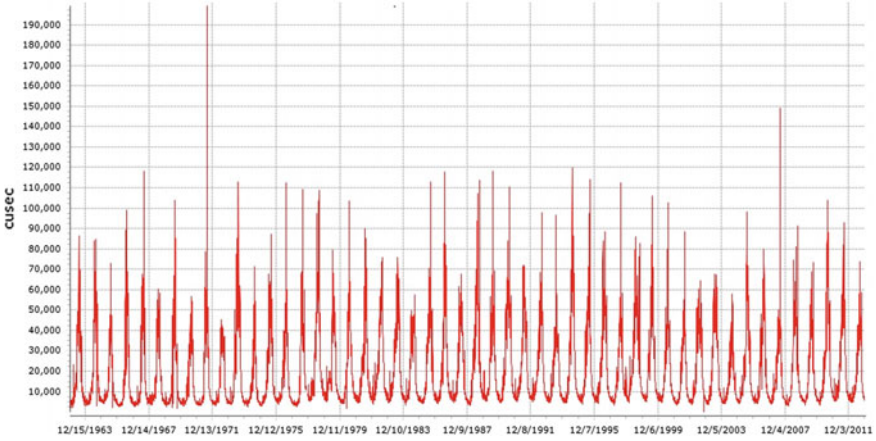

Fig. 3 Trend of inflow data values for Bhakra reservoir from 1965 to 2011 used for calibration of model

different locations across the Satluj catchment. Historical data of Satluj and Beas river runoff are used for calibrating the model and for validating the simulated results. The yearly data from 1965 to 2011 year data for the Bhakra inflow values as shown in Fig. 3 were collected and used for finding the current performance of model.

Moreover, the surface runoff data for Bhakra reservoir in year 1965–2011 is used to plot the variability in the inflow values during these periods. The graph in Fig. 4 shows the wet and dry period for the Bhakra inflows depicting the maximum and minimum runoff in the Bhakra reservoir in the year 1965–2011. The considerable runoff change especially during the pre-monsoon period in Satluj–Beas basin

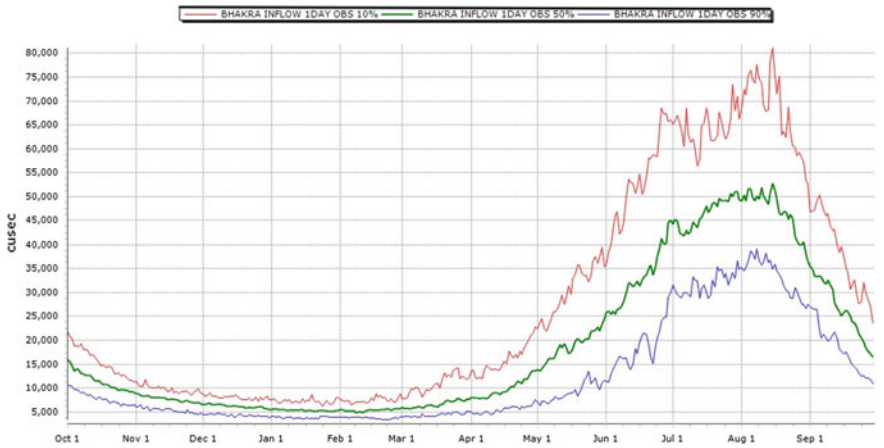

Fig. 4 Seasonal variation in the inflow values of Bhakra reservoir along with its minimum, mean and maximum values in year 1965–2011

provokes a growingly tough task in regulating future water resources year-round. If precipitation is fixed in a particular time period, this will surely make water resource management difficult. Moreover, large variability in values is depicting the possible climate change effects on water resources.

The maximum mean inflow values vary in the winter, summer, monsoon and autumn seasons of India. Maximum mean annual flow of around 60,000 cusec is observed in the monsoon months phase due to water availability from precipitation as well as from snowmelt runoff. Moreover, Satluj basin sub-catchments situated above the elevation of Bhakra reservoir receives a greater proportion of the snowmelt runoff in the monsoon season.

Similar data can also be obtained for the precipitation, temperature, snow water equivalent and surface runoff data for the sub-catchments of Satluj and Beas basin. Higher values of snow water equivalent in higher altitudes implies high snowmelt runoff values, whereas low-lying altitude areas also supplement with the precipitation.

Further, validation of model with the help of historical data is presented in Fig. 5 for the Bhakra reservoir for Satluj river inflow values in the year 1986–2003.

Similar verification and validation of model performance is performed for inflows to Pong dam reservoirs using 47 hydro-meteorological stations data in Beas basin (Fig. 6).

Subsequently, with the help of HEC-RTS, the current model performance in the year 2014–2015 Bhakra reservoir is obtained and plotted in Fig. 7.

To predict the current scenarios created by climate change due to increase in temperature and for continuous monitoring of snowmelt runoff, the plot is obtained for year 2015 and to create a next 10-day forecasts by simulating model as shown in Fig. 8.

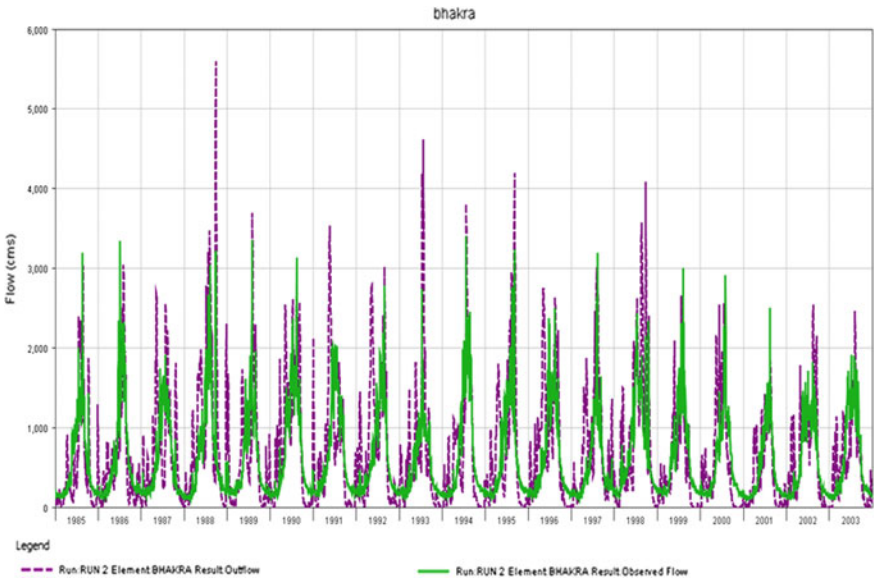

Fig. 5 Observed versus simulated Bhakra runoff values for model validation

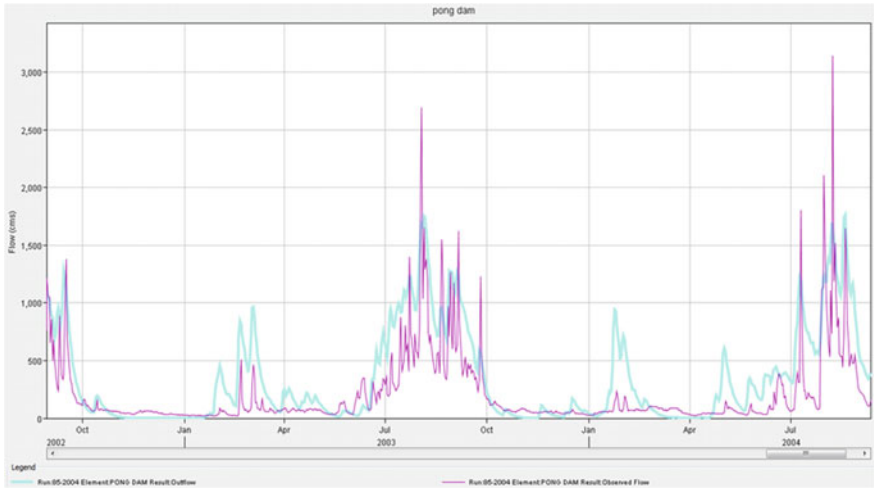

Fig. 6 Observed versus simulated Pong dam runoff values for model validation

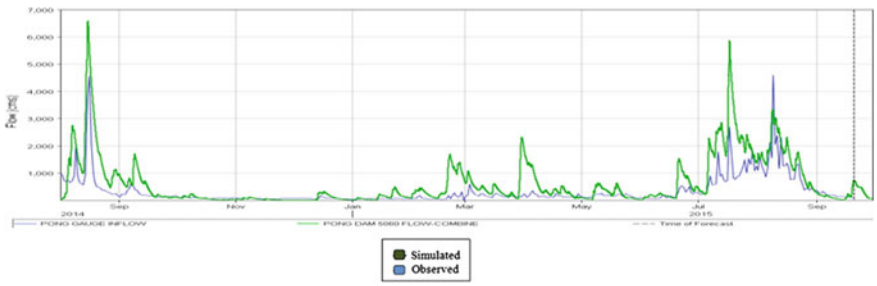

Fig. 7 Current model performance for Pong dam reservoir

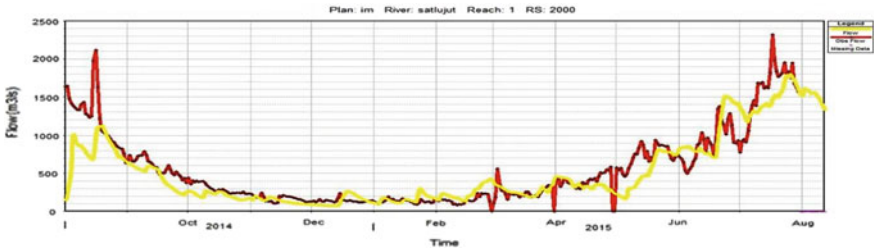

Fig. 8 Observed versus simulated plots for Bhakra Dam during snowmelt runoff monsoon 2015 for Bhakra dam on river Satluj

7 Discussion and Conclusions

Modeling precisely, a very large catchment like Satluj–Beas basin is very difficult due to complex hydrologic, hydraulic, topographic, climatic and other natural factors. Moreover, most of the area of Satluj basin lies outside the India boundary in China borders so to predict the inflow values, the simulated values have to rely on the remotely sensed data. The calibration of model has to be performed on the basis of the gauged sub-catchments of the Satluj basin which lie in Indian boundary so there are chances of variability in observed and simulated runoff values. But from the comparison of these resulted values, it can be seen that they are quite similar. An accurate precision can be obtained by further fine-tuning by varying model parameters.

A proper understanding of rainfall variations in India is mandatory to recognize the effects of climate change and valuable for water management [18], so a real-time decision support system developed in Satluj–Beas basin can prove beneficial in the forecasting of the variability so that any disaster can be avoided. Continuous monitoring of water resources is need of the hour in the wake of climate change, and necessary steps are need to be taken to tackle the disasters probabilities due to negligence of management in water resources. Moreover, hydrological

studies prove helpful for the prediction of future runoff values such as the model used here can forecast efficiently for the next 10 days.

To conclude from the discussion above, it is clear that there is need of integrated system using real-time remotely sensed data reliable for hydrological studies. Water resources planning for future is difficult as the future is unsure, unforeseeable and complex. Subsequently, steps like real-time monitoring and development of a DSS are required to be established for water management. Various types of simulation models for hydrological modeling have been tried, and still there is a need to try for the Indian River basins. And then we can really estimate the effects of global warming as well as climate change on the Indian basins as state of fresh water resources, at global as well as national level, is a great matter of concern. Furthermore, due to global warming, temperature of earth is increasing day by day effecting snowmelt runoff and the other processes associated with the river basins, so it is highly recommendable to analyze the water reservoir and inflow levels in the river system on a daily basis and to forecast accurately as well as efficiently.

References

1. Haberlandt, U.: From hydrological modeling to decision support. Adv. Geosci. **27**, 11–19 (2010)
2. Huang, C., Nan, Z., Ge, Y., Li, X.: A decision support system for irrigation water allocation along the middle reaches of the Heihe River Basin, Northwest China. Environ. Model. Softw. **47**, 182–192 (2013)
3. Nepal, S.: Impacts of climate change on the hydrological regime of the Koshi river basin in the Himalayan region. J. Hydro-environ. Res. **10**, 76–89 (2016)
4. Ragab, R., Prudhomme, C.: Climate change and water resources management in arid and semi-arid regions: prospective and challenges for the 21st century. Biosyst. Eng. **81**, 3–34 (2002)
5. Liu, T., Tung, C.P., Ke, K.Y., Chuang, L.H., Lin, C.Y.: Application and development of a decision-support system for assessing water shortage and allocation with climate change. Paddy Water Environ **7**, 301–311 (2009)
6. Al-Abed, N., Abdulla, F., Khyarah, A.: Abu: GIS-hydrological models for managing water resources in the Zarqa River basin. Environ. Geol. **47**, 405–411 (2005)
7. Singh, P., Thakur, J.K., Singh, U.C.: Morphometric analysis of Morar River Basin, Madhya Pradesh, India, using remote sensing and GIS techniques. Environ. Earth Sci. **68**, 1967–1977 (2013)
8. Giardino, C., Bresciani, M., Villa, P., Martinelli, A.: Application of remote sensing in water resource management: the case study of Lake Trasimeno, Italy. Water Resour. Manag. **24**, 3885–3899 (2010)
9. Choudhari, K., Panigrahi, B., Paul, J.C.: Simulation of rainfall-runoff process using HEC-HMS model for Balijore Nala watershed, Odisha, India. Int. J. Geomat. Geosci. **5**, 253–265 (2014)
10. Bhatt, D., Mall, R.K.: Surface water resources, climate change and simulation modeling. Aquatic Procedia **4**, 730–738 (2015)
11. Dolcine, L., Prévil, C., Brham, A., Ahluwalia, H., Menaoui, El.: Inflow modeling and reservoir management in Souss-Massa application of satellite remote sensing to support water resources management in Africa, vol. 7, pp. 43–55. Technical Documents in Hydrology, UNESCO, Paris TIGER Initiative (2010)

12. Rao, K.H.V.D., Bhanumurthy, V., Roy, P.S.: Application of satellite—based rainfall products and SRTM DEM in hydrological modelling of Brahmaputra Basin. J. Indian Soc. Remote Sens. **37**, 587–600 (2009)
13. Yener, M.K., Şorman, A.Ü., Şorman, A.A., Şensoy, A, Gezgin, T.: Modeling studies with HEC-HMS and runoff scenarios in Yuvacik Basin, Turkiye. International Congress on River Basin Management, pp. 621–634 (2009)
14. Jain, S.K., Goswami, A., Saraf, A.K: Assessment of snowmelt runoff using remote sensing and effect of climate change on runoff. Water Resour. Manag. **24**, 1763–1777 (2010)
15. Gupta, A., Singh, P., Singh, M.: Hydrological inferences from watershed analysis for water resource management using remote sensing and GIS techniques. Egypt. J. Remote Sens. Space Sci. **17**, 111–121 (2014)
16. Hydrologic Engineering Center. http://www.hec.usace.army.mil
17. Zhang, X., Srinivasan, R., Zhao, K., Liew, M.V.: Evaluation of global optimization algorithms for parameter calibration of a computationally intensive hydrologic model. J. Hydrol. Eng. **19**, 1374–1384 (2014)
18. Jain, S.K., Kumar, V.: Trend analysis of rainfall and temperature data for India. Curr. Sci. **102**, 37–49 (2012)

Experimental Study on Mining Pit Migration

Bandita Barman, Bimlesh Kumar and Arup Kumar Sarma

Abstract Mining of both coarse aggregate and sand from river bed or floodplain can cause changes in the river system. Unrestricted dredging of such materials creates large pits on the river bed. In this present study, experimental work has been performed to understand the behaviour of mining pit under different flow conditions. Four experiments with rectangular mining pit were conducted to investigate the channel bed deformation near mining pit region. Bed profiles at different time intervals are plotted from the data obtained from ultrasonic ranging system. From experimental analysis, it has been observed that migration of mining pit happens towards downstream of the pit, whereas there is no such evidence of migration towards upstream. The migration speed is observed to be different with different flow conditions.

Keywords Mining · Ultrasonic ranging system · Degradation

1 Introduction

River beds and floodplains are mined to supply fine and coarse aggregates for construction work. Its adverse impacts on river system have been studied by many researchers. Mining can induce erosion of channel bank and bed [1, 4, 5, 11–13]; it leads to lowering of groundwater table [10] and also impacts on ecology [7]. Mining of aggregates upstream of dam or bridge can cause serious damage to the river bed which may result in the failure of existing structures in rivers [9, 15]. Migration of mining pit was studied by both experimental and numerical approaches [2, 3, 6, 8, 14]. Experimental work on mining pit migration is necessary to understand the channel bed response to such activities. The main aim of this paper is to analyse the migration of mining pit under different flow conditions by conducting experiment on laboratory flume.

B. Barman (✉) · B. Kumar · A.K. Sarma
Indian Institute of Technology Guwahati, Guwahati 781039, Assam, India
e-mail: ditabarman@gmail.com

V. Garg et al. (eds.), *Development of Water Resources in India*,
Water Science and Technology Library 75, DOI 10.1007/978-3-319-55125-8_26

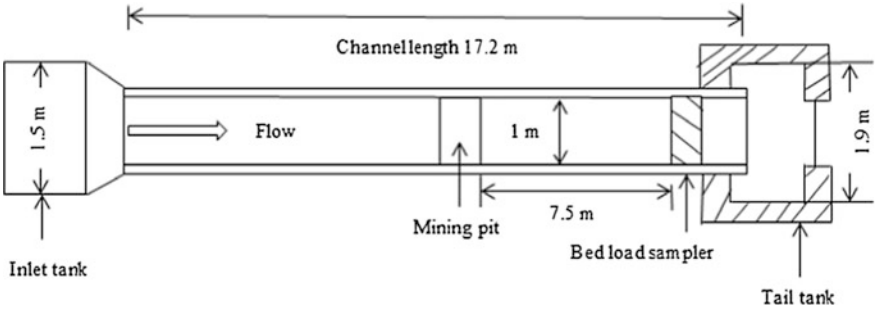

Fig. 1 Plan view of experiment set-up

Table 1 Different flow conditions

	Velocity, v (m/s)	Depth of flow, y (m)	Froude no.
Run1	0.277	0.128	0.25
Run2	0.299	0.102	0.299
Run3	0.3527	0.1005	0.355
Run4	0.396	0.096	0.408

2 Experimental Set-up

A rectangular flume 17.2 m long and 1 m wide was used for these series of experiments, and its plan view is shown in Fig. 1. Channel bed was covered with 21-cm-thick uniform sand layer of particle size (d_{50}) 0.418 mm and standard deviation 1.17. Before constructing the mining pit, channel bed was flooded with water to compact the sand layer. A pit of 50 cm length and 10 cm depth in the whole width of the channel was made at 7.5 m from a downstream point.

Discharge was kept constant for the whole set of experiments. Different flow conditions were used for different set of experiments under the constraints that flow conditions are subcritical and sediment movement occurs only as bed load. No sediment overloading was done at the upstream of the flume. Channel bed was adjusted to a bed slope of 0.001. Depth of water from bed level was measured at different time intervals by using ultrasonic ranging system. This instrument facilitates to take measurement of bed profile of the channel at any time interval without draining the water. Different flow conditions are summarized in Table 1.

3 Results and Discussion

Ultrasonic ranging system gives us channel bed profile at any user-specific time interval along the length and width of the channel. This instrument (SeaTek®) is used to measure the geometry reading of the channel bed. The assembled automatic

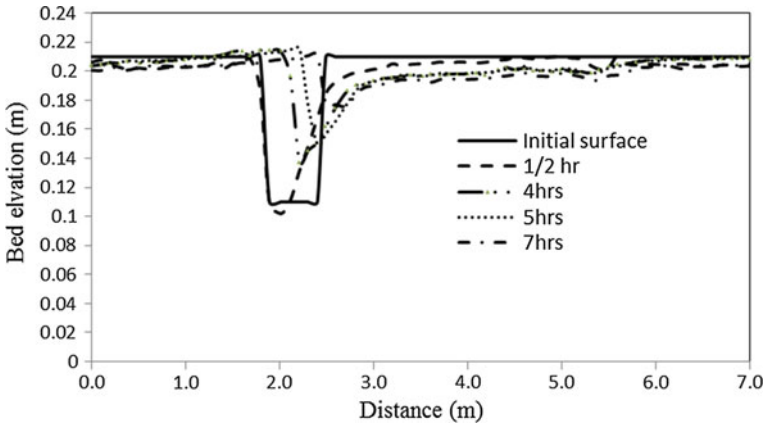

Fig. 2 Longitudinal channel bed profiles at 50-cm section

trolley system with four pairs of transducers resting on the rail of the laboratory flume moves with constant speed. The SeaTek instrument uses 5-MHz ultrasound to measure the distance to a target of wavelength 0.3 mm in water. This system is having 0.1 mm resolution. Channel bed profile at different time intervals for Run4 is shown in Fig. 2.

The transport/migration of the sediment material from upstream depends on the magnitude of the bed shear stress. It is well known that sediment transport happens when bed shear stress is greater than threshold shear stress. As 0.418 mm (d_{50}) sand has been used, the critical or threshold shear stress is 0.236 N/m^2 as per Shields criterion. Sediment migration has been observed in all the four runs. It is observed from Fig. 2 that the upstream end of the mining pit is moving towards downstream with time. Degradation of channel bed is more prominent in downstream of the mining pit and propagating towards downstream. Similar type of profiles is also observed for other flow condition, but the migration time of upstream end depends on the flow conditions. Calculation of bed shear stress for all the runs has been shown in Fig. 3. It can be seen that they are in transport condition.

A comparison of Run3 and Run4 after 4 h is presented in Fig. 4. It is observed from Fig. 4 that upstream end migration and downstream propagation of degradation are more prominent with increase in flow velocity and Froude number, keeping other parameters such as channel geometry and sediment property constant.

One important observation can be made from Figs. 2 and 4 that removal of bed material in excess of replacement by transport from upstream causes the bed to lower upstream and downstream of pit. These lowering may have several effects on river morphology. These bed lowering can undermine any support structure near the pit site if present results in principle can have validity for field condition. Degradation may change the morphology of the river bed, which comprises one aspect of the aquatic habitat. Thus, there is a need for more experimentation on these aspects.

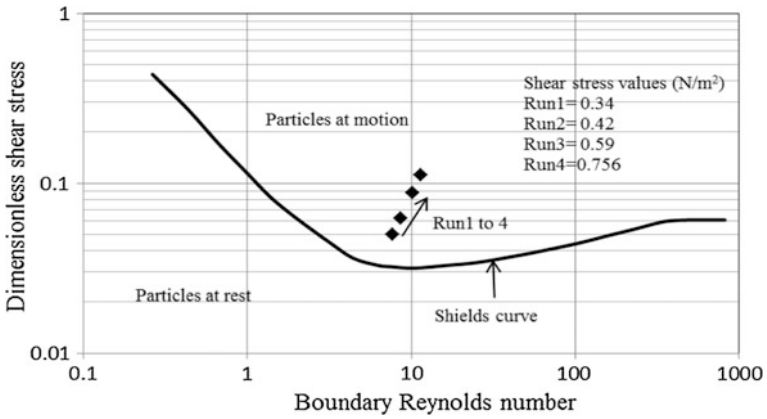

Fig. 3 Shields diagram and bed shear stress

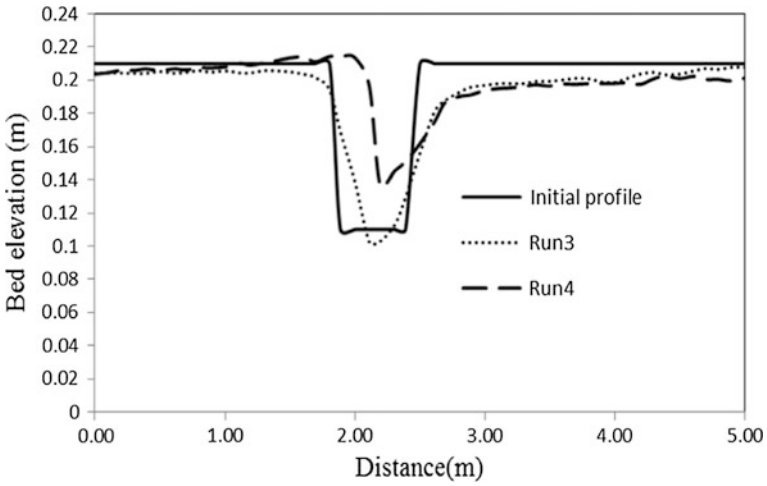

Fig. 4 Longitudinal channel bed profiles at 50-cm section for Run3 and Run4

4 Conclusions

Four experiments were conducted to study mining-induced channel bed deformation in a laboratory flume. Channel bed degradation in both upstream and downstream of pit occurs in all the four runs as shear stress values are above the threshold of bed load movement. It has been observed that mining pit on the channel bed interrupts the degradation process by expanding degradation towards downstream. However, there are possibilities to investigate more in this case with more variation of flow conditions and pit geometry.

References

1. Brestolani, F., Solari, L., Rinaldi, M., Lollino G.: On morphological impacts of gravel mining: the case of the Orco River. Engineering Geology for Society and Teritory, vol. 3, pp. 319–322. Springer, Switzerland
2. Cao, Z., Pender, G.: Numerical modelling of alluvial rivers subjected to interactive sediment mining and feeding. Adv. Water Resour. **27**, 533–546 (2004) (Elsevier)
3. Chen, D., Liu, M.: One and two dimensional modelling of deep gravel mining in the Rio Salado. Worlds Environmental and Water Resources Congress, pp. 3462–3470. ASCE (2009)
4. Collins, B.D., Dunne, T.: Gravel transport, gravel harvesting, and channel bed degradation in rivers draining the southern olympic mountains, Washington, USA. Environ. Geol. **13**, 213–224 (1989) (New York)
5. Collins, B.D., Dunne, T.: Fluvial geomorphology and river gravel mining: a guide for planners, vol. 98. California Division of Mines and Geology, Special Publication (1990)
6. Gill, M.A.: Hydrodynamics of mining pits in erodible bed under steady flow. J. Hydraul. Eng. **120**, 1337–1348 (1994) (ASCE)
7. Kim, C.: Impact analysis of river aggregate mining on river environment. KSCE J. Civil Eng. **9**, 45–48 (2005)
8. Lee, H.Y., Fu, D.T., Song, M.H.: Migration of rectangular mining pit composed of uniform sediment. J. Hydraul. Eng. **119**, 64–80 (1993) (ASCE)
9. Lu, J., Liu, C., Guan, J., Liu, L., Liu, H.: Sand and gravel mining in upstream of Yangtze river and its effects on three gorges reservoir. Worlds Environmental and Water Resources Congress, pp. 1821–1830. ASCE (2015)
10. MasPla, J., Montaner, J., Sola, J.: Ground water resources and quality variations caused by gravel mining in coastal stream. J. Hydraul. Eng. **216**, 197–213 (1999) (Elsevier)
11. Rinaldi, M., Wyzga, B., Surian, N.: Sediment mining in alluvial channels: physical effects and management perspective. River Res. Appl. **21**, 805–828 (2005)
12. Rovira, A., Batalla, R.J., Sala, M.: Response of a river sediment budget after historical gravel mining (The Lower Tordera, NE Spain). River Res. Appl. **21**, 829–847 (2005)
13. Vade, J.P.M, Boix, C.F., Ollero, A.: Incision due to gravel mining: modeling a case study from the Gallego River, Spain. Geomorphology, **117**, 261–271 (2010) (Elsevier)
14. Wu, W., Wang, S.S.Y.: Simulation of morphological evolution near sediment mining pits using a 1-D mixed-regime flow and sediment transport model. Worlds Environmental and Water Resources Congress. ASCE (2008)
15. Yanmaz, A.M., Cicekdag, O.: Channel mining induced streambed instability around bridges. Watershed Management and Operations Management. ASCE (2000)

Orogeny as a Controller of Climate Change and Monsoon

Sugandha Panwar, Manas Mishra and Govind Joseph Chakrapani

Abstract Climate on earth had varied throughout the geological past and so do the plate motions. Movement of tectonic plates itself leads to the collision of plates and at the same time the process of mountain building or orogeny. Recent data and climate modeling have related the Cenozoic climate change to the upliftment of the Tibetan plateau. The Himalayan–Tibetan plateau system controls the heat flow and atmospheric circulation and thereby influences the monsoon systems of South and East Asia. Orogeny also influences many natural processes which lead to a change in climate, such as regression, transgression, subduction, volcanism, chemical weathering and vegetation shift. At present, the rate of climate change is unprecedented and attributed many times to the human interventions. However, we need to determine the natural factors that control the climate on earth. In the present paper, we reviewed the fundamental role of orogeny in controlling the climate.

Keywords Orogeny · Climate change · Plate tectonics · Chemical weathering · Leaf area index (LAI)

1 Introduction

Understanding the climate change and its likely impacts on living beings is one of the important challenges toward the scientific community. But climate change is not a new phenomenon for our planet; since the development of primitive atmosphere on the earth, global climate has varied continuously. On the geological timescales, variation in temperature has been continuous with intense climatic oscillations between icehouse and greenhouse periods [1, 2]. The climate of the earth depends on the radiative balance, in particular, the amount of energy the earth receives from the sun and the amount of energy it releases back [3]. Climate forcing is the term

S. Panwar (✉) · M. Mishra · G.J. Chakrapani
Department of Earth Sciences, Indian Institute of Technology Roorkee, Roorkee, India
e-mail: sugandha.panwar@gmail.com

V. Garg et al. (eds.), *Development of Water Resources in India*,
Water Science and Technology Library 75, DOI 10.1007/978-3-319-55125-8_27

cited in the literature, for any process that alters this energy balance and can be separated into internal and external type [4, 5] (refer Table 1).

Since the last century, researchers have reconstructed the paleoclimate by exploring the wide array of records such as sedimentary rocks, lake sediments, pollen cores, volcanic ash, ice sheets, tree rings, nest of animals, geomorphic and paleomagnetic data. By affecting the atmospheric pattern, the orography seems to influence the global climate. Since Cenozoic, the Himalayas and the Tibetan plateau have affected the intensity of the Asian monsoon [6–11]. Figure 1 shows the location and extent of the Himalaya and the Tibetan plateau. The Tibetan plateau is the largest and highest mountain plateau on the earth surface covering an area of 4×10^6 km^2 with a mean elevation of 5 km [11]. Here, in this paper, we discuss

Table 1 Factors influencing global climate (compiled from Refs. [3, 4])

Climate forcing factors	
Internal (processes relating to atmosphere, hydrosphere and lithosphere of the earth)	Continental drift, orogeny, volcanism, atmospheric/ocean heat exchange, atmospheric composition, atmospheric and surface reflectivity
External (relating to the changes in the influx of solar energy)	Solar output, earth's axis and orbit, interstellar dust
Others	Asteroid collision

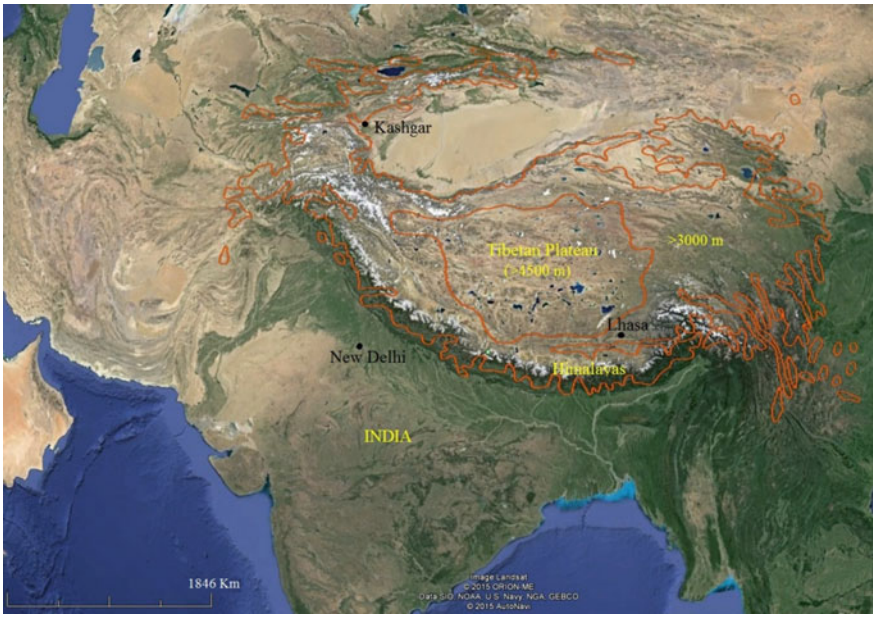

Fig. 1 Extent of Himalayas and Tibetan plateau on Google imagery (boundaries of the Himalayas and Tibetan plateau obtained from Ref. [12])

the effect of the Himalayan–Tibetan orogeny on the progressive development of Asian monsoon and the role of orogeny in controlling the global climate.

2 Boundary Conditions for Relating Orogeny and Climate

Since the plate tectonic theory got ground in geology, many of the scientists became interested in determining the relationship between plate tectonics and climate change. Researchers have developed various models from 0D to 3D to determine how changes in the position of continents were associated with earth's radiative balance and the global climate. Donn and Shaw (1977) were among the first climatic modelers who used drift of continents as a boundary condition to study glaciation at high latitudes [13]. Berner and his colleagues in 1983 cited BLAG hypothesis stating that the rate of sea floor spreading controls the rate of CO_2 delivered into the atmosphere and that the chemical weathering process through the negative feedback mechanism controls the temperature on earth [14]. In the 1980s, Raymo et al. argued that chemical weathering is not just the negative feedback, but it is the main controller of temperature on earth through silicate weathering of rocks that is highly affected by the physical weathering processes [15]. Figure 2 displays the mechanism of global carbon cycle involving silicate weathering and subduction.

The most widely used 3D model such as atmospheric general circulation models (AGCMs) stimulate global paleoclimate and helps in the understanding of different forcing factors [16]. As orogeny is a slow process in comparison with the atmospheric changes, in the numerical experiments and models, it is represented by considering land–sea distribution and topography as boundary conditions [16]. The

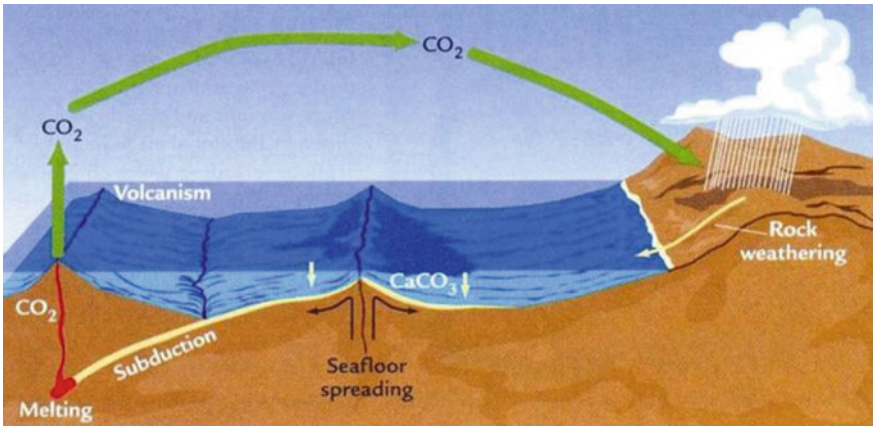

Fig. 2 Global carbon cycle and CO_2 pool (adapted from Ref. [15])

Cenozoic climate change was correlated with the upliftment of the Himalayas and enhanced weathering rates. Several numerical models have been stimulated to investigate the changes in the height of the Tibetan plateau as a sensitive parameter controlling the global climate.

3 History of Upliftment of the Tibetan Plateau and the Development of Monsoon

The continent–continent (India–Asia) collision which began in the Eocene resulted in the creation of the ever largest structures on earth, the Himalayas and the Tibetan plateau. Zhao and Morgan (1985) proposed that crustal thickening has built the Tibetan plateau [17]. Later, crustal thickening was predicted to be largely from the continuous lateral widespread and thickening of viscous flow of crust and mantle, and the isostatic response to this event resulted in the rapid uplift of the plateau [10, 18–20]. At present, this theory of crustal flow is considered to explain the origin of a plateau in a factual way and is supported by many researchers. As the period of magmatism is related to the tectonics, researchers have argued that basaltic volcanism in Tibet is caused by the melting of the middle lithosphere [18]. Late Miocene was estimated to be the age of upliftment by assuming the development of east–west extensional faults in parts of the southern plateau [21]. Various researchers see this event as a continuous process [10, 21–23], but others consider it as more complex, which have gained more weight comparatively. Tapponnier et al. (2001) suggested the upliftment of the Tibetan plateau as three time-dependent blocks; southern part was elevated during the Eocene period preceded by the central and northern parts during the Oligo-Miocene and Plio-Quaternary period respectively [11]. Chung et al. (1998) and Wang et al. (2008) also suggested that the southeastern margin of the Tibetan plateau was uplifted 30–40 Ma before the upliftment of the rest of the plateau [24, 25]. Some studies suggest that the Tethyan Himalayas were at or near modern elevation by the mid-Miocene [26, 27].

Different approaches were applied by different researchers to unravel the timing of activation of monsoon and its strengthening along with the upliftment of the Tibetan Plateau. Kroon et al. (1991) related the appearance of cold water foraminifer *Globigerina bulloides* (recovered from the core samples collected from the Arabian Sea) with the period of upwelling at 8.5 Ma [28]. Quade et al. (1989) observed a major shift in the vegetation cover from forest to grassland at 7.4 Ma and related the dramatic change in the vegetation with the commencement of the monsoon [29]. This vegetation change was found to precede the appearance of *Globigerina bulloides* at approximately 1 million year gap which was due to delayed response of vegetation to the intensification of upwelling [28]. A $\delta^{18}O$ study conducted on the carbonate rocks present in the NE margin of the Tibetan plateau suggests that $\sim$12 Ma sufficient area of the plateau was at an adequate height to block humid airflow from the Indian Ocean and affect the atmospheric

circulation pattern [30]. But due to differential upliftment rates, the mid-Miocene period was reported to mark changes in the monsoon system [31, 32]. An et al. (2001) suggested the commencement of East Asian monsoon at 7.2 Ma and it was during 3.4–2.6 Ma that renewed strengthening of the East Asian monsoon took place due to the accelerating uplift of the Tibetan plateau [8]. Guo et al. (2002) used the paleomagnetic approach for dating the loess deposits in North China and considered early Miocene as a period for the strengthening of the winter monsoon [33]. Through these different studies, it can be assumed that the drastic change in the intensity of the monsoon took place at $\sim$6–8 Ma and tectonic upliftment of the Tibetan plateau influenced the atmospheric circulation pattern.

However, still a lot of disagreements remain regarding the timing of the onset and subsequent variations of the monsoon. There are many studies that do not see Tibetan plateau as the forcing factor for the climate change during Miocene. For example, Gupta et al. (2004) argued that the late Miocene increase in the intensity of monsoon was due to increased ice volume in the Antarctic ice sheets and global cooling [34]. Chakrobarty et al. (2006) considering the role of Tibetan plateau in determining the strength of the monsoon point that atmospheric instability due to sea surface temperature forcing is the first necessary condition for the onset of Indian summer monsoon [35].

4 Auxiliary Factors Affecting Climate Due to Orogeny

The factors that affect the climate due to orogeny are a result of complex interaction between the climatically driven forces and the vertical crustal movements. Following are the main factors that can cause changes in the climate.

4.1 Sea Level Fluctuation

Sea level fluctuation is a dominant factor that influences climate by affecting the seasonal cycle of temperature on land, land–sea distribution and precipitation. The rate of seafloor spreading has control over the rate of magma generation and release of CO_2 into the atmosphere [36, 37] (Sect. 2, Fig. 2).

The sea level change may affect the geometry of the ocean basins and the global volume of oceans. Plate tectonic reconstruction provides a sincere way to assess the location of landmasses through geologic time and aids to reproject the thermohaline circulation system. Through plate tectonic reconstructions, it can be stated, that the presence of near-equatorial currents alms the greenhouse episodes, but when landmasses exist at the equator, near-equatorial currents are not developed leading to large-scale glaciations [38]. Figure 3 shows the changes in thermohaline circulation pattern before and after the dismissal of the Tethys Ocean gateway time transferring thermal energy in the world oceans. These changes in the ocean current

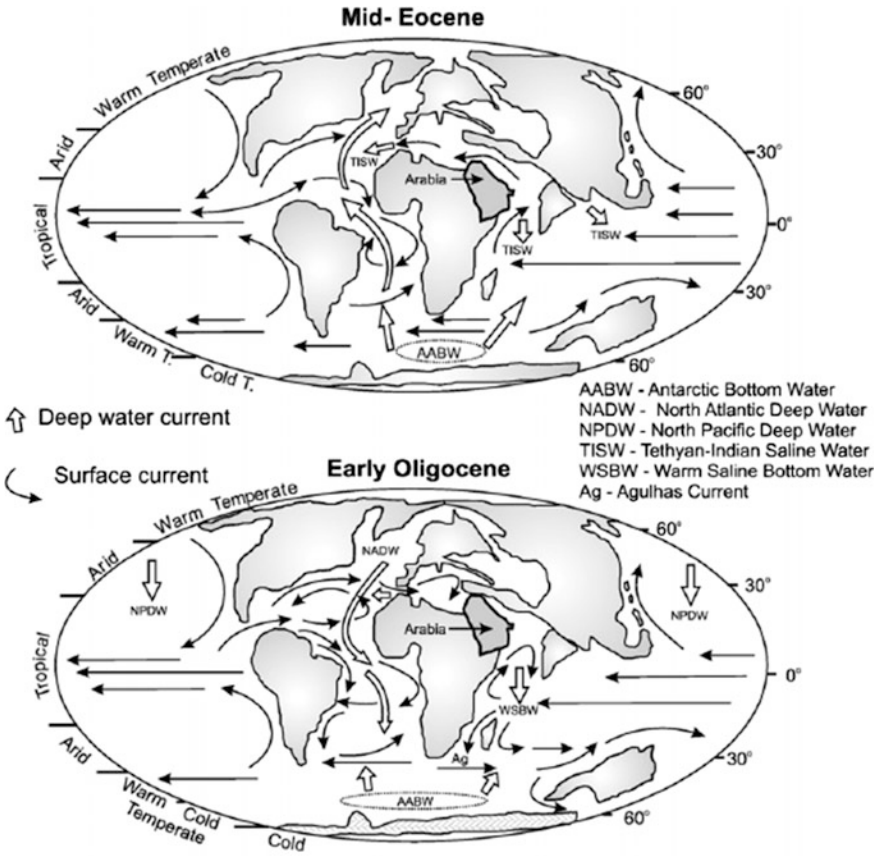

Fig. 3 Changes in thermohaline circulation pattern during the mid-Eocene and early Oligocene (adapted from Ref. [43])

caused global cooling and growth of glaciers at Eocene/Oligocene boundary at ~34 Ma (Oi-1 glaciation). Oceanic gateways such as the Central American isthmus, Australia–Antarctic passage, the Tethys, and the Indonesian straits seem to affect the salinity, convection currents between the oceans and the process of sedimentation [39, 40]. Scotese and Golonka (1993) and Crowley and Baum (1995) simulated the climatic models for paleogeographic reconstruction of the Late Ordovician time (440 Ma) that features high CO_2 level and land area half than that at present, their results displayed a large increase in average runoff for individual land grid points [41, 42]. Climate change can regulate the volume of water by controlling thermal dilation of oceans and ice sheet formations. The only difference is that the mechanism associated with climate change shows abrupt changes, whereas tectonic processes act on a longer timescale.

4.2 Tectonics and Earthquakes

Landscape dynamics can be related to both the tectonics and erosion processes. Upliftment of Himalayas is uniform or steady for millions of years, but climatic factors are highly variable [44]. Based on the laboratory experiments, it was revealed that tectonic supported upliftment leads to progressive increase in denudation rate more than the climatic factors [45, 46]. However, some studies confirm high exhumation rates in the areas of high precipitation [47, 48]. The only way to study the role of tectonics is the regions that have very low rainfall. The Shillong plateau in the Eastern Himalayas acts as an orographic barrier and since Miocene–Pliocene transition reduces the mean annual precipitation downwind in the east Bhutan. The apatite fission track ages calculated by Grujic et al. (2006) show that recent changes in the geomorphology and erosion pattern of the Bhutan Himalayas are climatic induced with tectonic upliftment having a minor effect [44]. The Himalayas shows the highest upliftment and erosion rates in the world, resulting in a high frequency of earthquakes and landslides. The study of Shukla et al. (2014) in the Western Himalayas interpreted earthquakes data of $\sim$100 years and observed that most of the earthquakes and landslides are concentrated around highly active tectonic zones [49]. The tectonic activities in the mountainous belts can trigger the landslides, rockfall, earthquakes and avalanches that can affect the geomorphology of the area. Tectonic activities can affect the river system; globally, 25–75% of all streams in non-glaciated areas are tectonically influenced [50]. Change in the river course can influence the landscape and climatic pattern of the region by affecting the erosion and deposition processes.

Earthquakes not only influence the topography but can also affect the atmospheric composition. Some studies show that prior to the earthquake, high electric fields are generated that are believed to penetrate into the ionosphere and affect the ozone concentration [51–53]. This behavior of ozone concentration proves the existence of a relation between climate and tectonics. The study of Obzhirov et al. (2004) relates increased methane flux during periods of seismo-tectonic activity (due to creation or reactivation of faults resulting in leakage of underground methane deposits) to the enhanced global warming [54].

4.3 Volcanism

During a volcanic eruption, the major gases evolved are carbon dioxide (CO_2), sulfur dioxide (SO_2), water vapor (H_2O), hydrogen sulfide (H_2S), methane (CH_4), carbon monoxide (CO), etc., of which SO_2 and CO_2 can alter the net radiation budget of the earth. The oxidation of SO_2 produced a thick horizontal layer of H_2SO_4 aerosol in the stratosphere, which scatters and absorbs the incoming solar radiation. This phenomenon can modify the earth's temperature for years. Rampino

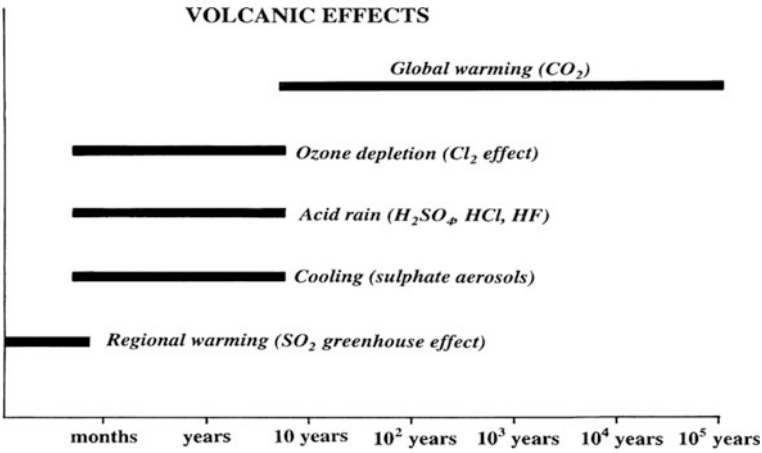

Fig. 4 Volcanic gases and the time interval over which they affect the earth's climate (adapted from Ref. [56])

and Self (1987) stated that volcanic activity and formation of aerosol cloud in the stratosphere can cool the earth's surface by ~0.3 °C annually and warm the stratosphere by 6 °C following the eruption [55]. The effect of volcanism and the radiation effect over the past 10 K years were studied from the Greenland ice cores and dust anomalies. The core samples revealed that most of the cold events were followed by the volcanic activities and the amount of SO_2 emitted into the atmosphere. The amount of SO_2 ejected depends on the volume of magma and the tectonic context.

The small eruption does not spoil the compositional ratio of the atmosphere to a greater extent. The annual input of CO_2 ejected from volcanoes is $\sim 10^{11}$ kg; it is noticeably lesser than the annual anthropogenic release of 10^{13} kg [56]. Yet successive large eruptions and the long residence time of CO_2 in the atmosphere can affect the climatic regime of the earth (Fig. 4). However, in comparison with the flood basalts, all volcanic eruptions in the past were small. The Deccan volcanic activity at the Cretaceous–Tertiary boundary had injected 10^{17} g of sulfate aerosols once every 10–100 ka over a period of 1 Myr, leading to acid rain and cooling the world temperature by 1 °C.

4.4 Chemical Weathering

In spite of the fact that the Tibetan plateau covers only 5% of the global land area, due to high erosion activities, Tibetan rivers carry one-fourth of the global total dissolved matter [57, 58]. Out of 20×10^9 tonnes year^{-1} of global suspended

sediments transported by the rivers, the Himalayan Rivers, viz. the Ganga and the Brahmaputra, constitute ~25% of the flux [59]. Transportation of sediment by rivers is an important aspect that influences directly the climate, pedogenesis, landscape evolution, aquatic life, river water quality and dams and reservoirs on the channel [43]. The deposition of organic carbon exerts a negative feedback on the global climate change [60, 61]. Thus, chemical weathering of silicate rocks in the Himalayan–Tibetan region plateau is a significant sink for atmospheric CO_2 drawdown since the Cenozoic time [36, 62, 63]. Recall Fig. 2 explaining the mechanism of CO_2 burial by the process of tectonics and chemical weathering. Bickle (2002) and Harris (2006) mention that in the world without Tibetan plateau, the average global temperature would probably be higher by ~1–6 °C [10, 64].

4.5 Vegetation Change

Vegetation depends on the availability of sunlight, water, temperature, slope, altitude, soil type, etc. All these factors are affected in response to the orogenic processes causing variation in plant distribution which directly or indirectly creates an impact on climate and climate change. Sewall et al. (2000) carried out the sensitivity study investigating the change in vegetation and surface topography on the climate using the Genesis Global Climate Model version 2.0 [65]. The control case was termed as OLDVT, and the model produced climate as NEWVOLDT. OLDVT was stimulated on Eocene topography, shorelines and vegetation distribution. Boundary conditions for NEWVOLDT were identical to those of OLDVT, except the distribution of new vegetation. Figure 5 shows that vegetation distribution is quite different in both the scenarios. The results showed that with a change in the vegetation in NEWVOLDT case, the global mean temperature decreased by 0.52 °C and 0.93 °C during December–January–February (DJF) and June–July–August (JJA) periods, respectively.

The above climatic changes can be explained by concerning the increases in the leaf area index (LAI) that influences the evapotranspiration. The new vegetation distribution (NEWVOLDT) had 1.18×10^8 and 1.49×10^8 km^2 times greater LAI in both DJF and JJA, respectively (refer Table 2). The increased evapotranspiration may have cooled the surface temperature by 2–6 °C. The changes in temperature and evapotranspiration pattern have a great impact on the total cloud formation and latent heat. In NEWVOLDT scenario, total cloudiness formation during JJA increased by 20–40% over Central Asia and ~25% over Europe and North Central South America (Fig. 5), whereas latent heating increases up to 55 W/m^2 over the Central Asia and Central Africa. For further detail on the change in climatic parameters due to vegetation, refer to Sewall et al. [65].

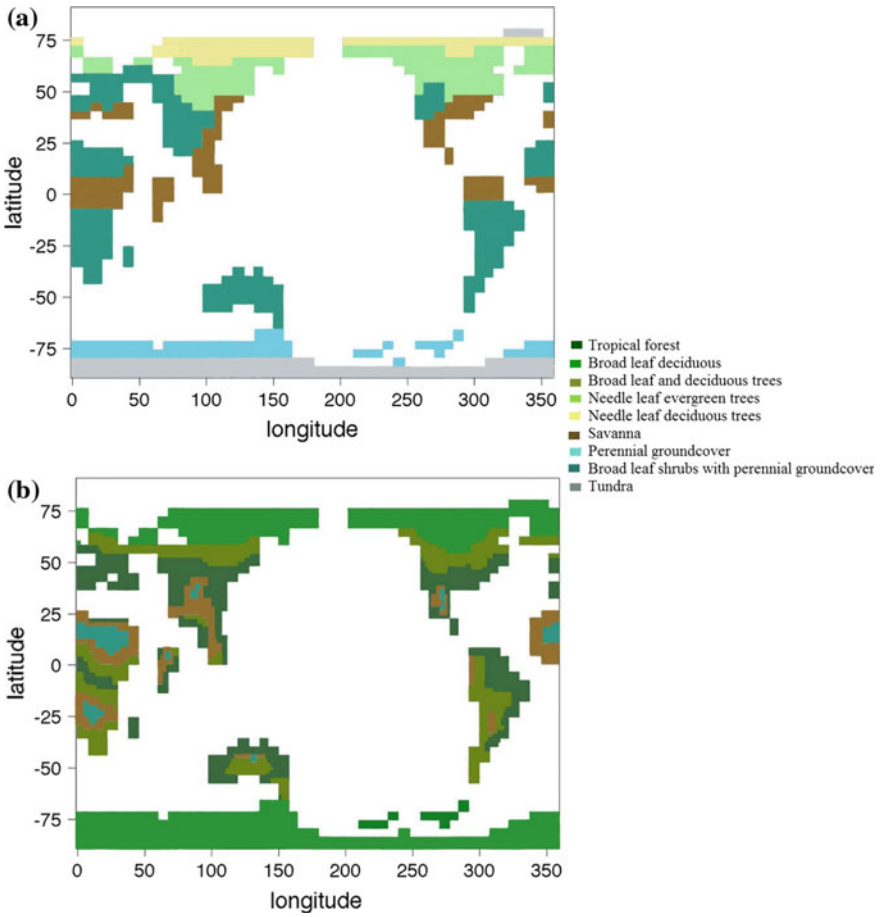

Fig. 5 Change in global vegetation distribution **a** old Eocene global vegetation distribution. **b** New Eocene global vegetation distribution (adapted and modified from Ref. [65])

On the other hand, some researchers prospect that the culminating of the C_4 plants during the Miocene was the major factor that has affected the hydrologic cycle, atmospheric circulation and weathering and erosion processes. The studies of Hay et al. (2002) and Burbank et al. (1993) mentioned that the transition from C_3 to C_4 plants was not regionally associated with the Himalayas, but was the worldwide trend [66, 67].

Table 2 Change in leaf area index (LAI) during climate change scenario (adapted from Ref. [65])

Vegetation type	LAI × areal extent in old vegetation distribution	LAI × areal extent in new vegetation distribution	Difference in coverage (new–old) (km^2)
June–July–August (JJA)			
Tropical forest	0	2.16×10^8	2.16×10^8
Broadleaf deciduous trees	0	7.90×10^7	7.90×10^7
Broadleaf and needle leaf trees	0	1.41×10^8	1.41×10^8
Needle leaf evergreen trees	1.58×10^8	0	-1.58×10^8
Needle leaf deciduous trees	1.72×10^7	0	-1.72×10^7
Savanna	1.10×10^8	6.76×10^7	-4.24×10^7
Perennial groundwater	2.64×10^6	0	-2.64×10^6
Broadleaf shrubs with perennial groundcover	7.13×10^7	6.83×10^6	-6.45×10^7
Broadleaf shrubs with bare soil	0	0	0
Tundra	1.63×10^6	0	-1.63×10^6
Total	3.61×10^8	5.10×10^8	1.49×10^8
December–January–February (DJF)			
Tropical forest	0	2.16×10^8	2.16×10^8
Broadleaf deciduous trees	0	3.85×10^7	3.85×10^7
Broadleaf and needle leaf trees	0	1.01×10^8	1.01×10^8
Needle leaf evergreen trees	1.34×10^8	0	-1.34×10^8
Needle leaf deciduous trees	0	0	0
Savanna	7.13×10^7	4.6×10^7	-2.5×10^7
Perennial groundwater	1.66×10^7	0	-1.66×10^7
Broadleaf shrubs with perennial groundcover	6.78×10^7	1.08×10^7	-5.70×10^7
Broadleaf shrubs with bare soil	0	0	0
Tundra	4.31×10^6	0	-4.31×10^6
Total	2.94×10^8	4.12×10^8	1.18×10^8

5 Summary

Climate change is not a new phenomenon for the planet Earth. Climate forcing factors are many, but the orogeny controlling the climate is a strong view that supports Cenozoic climate change. Subduction of Indian and Eurasian plates that started at 55 Myr resulted in the elevation of Tibetan plateau ($\sim$5 km). The lower crustal flow is a widely accepted concept for the upliftment. Several of the geodynamic models, exhumation and diachronous upliftment studies have reconstructed the upliftment past of the Tibetan plateau. The process of the upliftment took place in succession. The Southern Tibet was elevated earlier and later due to compression, Central and Northern parts were elevated. Since the late Miocene, the southern part of the plateau was stabilized near present elevation and has affected the global climate by influencing the pressure gradient and patterns of atmospheric circulation. Though there is still a controversy regarding the exact timing of the strengthening of monsoon, most of the studies imply $\sim$6–8 Ma was the time when there was a drastic change in the pattern of the monsoon system. The tectonic processes such as sea level fluctuation, volcanism, earthquakes, chemical weathering and change in vegetation can also influence global climate significantly.

Acknowledgements SP thanks University Grant Commission, New Delhi, for providing Research Fellowship. Special thanks to Ms. Stephy Thomas (IDT student, IIT Roorkee) for helping in the compilation of the manuscript.

References

1. Crowley, T.J., North, G.R.: Paleoclimatology, p. 339. Oxford University Press (1991)
2. Zachos, J., Pagani, M., Sloan, L., Thomas, E., Billups, K.: Trends, rhythms and aberrations in global climate 65 Ma to present. Science **292**, 686–693 (2001)
3. Houghton, J.T., Jenkins, G.J., Ephraums, J.J.: Climate Change: the IPCC scientific assessment. In: Intergovernmental Panel on Climate Change, p. 365. Cambridge University Press (1990)
4. Mitra, A.: Sensitivity of Mangrove Ecosystem to Changing Climate, p. 322. Springer (2013)
5. Panwar, S., Chakrapani, G.J.: Climate change and its influence on groundwater resources. Curr. Sci. **105**, 37–46 (2013)
6. Yanai, M., Li, C., Song, Z.: Seasonal heating of the Tibetan plateau and its effects on the evolution of the Asian summer monsoon. J. Meteorol. Soc. Jpn **70**, 319–351 (1992)
7. Harrison, T.M., Copeland, P., Kidd, W.S.F., Lovera, O.M.: Activation of the Nyainqentanghla shear zone: implications for uplift of the southern Tibetan Plateau. Tectonics **14**, 658–676 (1995)
8. An, Z., Kutzbach, J.E., Prell, W.L., Porter, S.C.: Evolution of Asian monsoons and phased uplift of the Himalayan-Tibetan plateau since Late Miocene times. Nature **411**, 62–66 (2001)
9. Liu, X., Yin, Z.Y.: Sensitivity of East Asian monsoon climate to the uplift of the Tibetan Plateau. Palaeogeogr. Palaeoclimatol. Palaeoecol. **183**, 223–225 (2002)
10. Harris, N.: The elevation history of the Tibetan plateau and its implications for the Asian monsoon. Palaeogeogr. Palaeoclimatol. Palaeoecol. **241**, 4–15 (2006)

11. Tapponnier, P., Zhiqin, X., Roger, F., Meyer, B., Arnaud, N., Wittlinger, G., Jingsui, Y.: Oblique stepwise rise and growth of the Tibetan Plateau. Science **294**, 1671–1677 (2001)
12. Fielding, E.J.: Tibet uplift and erosion. Tectonophysics **260**, 55–84 (1996)
13. Donn, W.L., Shaw, D.M.: Model of climate evolution based on continental drift and polar wandering. Geol. Soc. Am. Bull. **102**, 1499–1516 (1977)
14. Berner, R.A.: A new look at the long term carbon cycle. Geol. Soc. Am. Today **9**, 1–6 (1999)
15. Ruddiman, W.F.: Earth's Climate: Past and Future, 2nd edn, p. 388. W.H. Freeman and Company, New York (2008)
16. Fluteau, F.: Earth dynamics and climate changes. C.R. Geosci. **335**, 157–174 (2003)
17. Zhao, W.L., Morgan, W.J.: Uplift of Tibetan Plateau. Tectonics **4**, 359–369 (1985)
18. Molnar, P., England, P., Martinod, J.: Mantle dynamics, uplift of the Tibetan plateau and the Indian monsoon. Rev. Geophys. **31**, 357–396 (1993)
19. Platt, J.P., England, P.C.: Convective removal of lithosphere beneath mountain belts: thermal and mechanical consequences. Am. J. Sci. **294**, 307–336 (1994)
20. Zheng, H., Powell, C.M., An, Z., Zhou, J., Dong, G.: Pliocene uplift of the Northern Tibetan Plateau. Geology **28**, 715–718 (2000)
21. Williams, H.M., Turner, S.P., Pearce, J.A., Kelley, S.P., Harris, N.B.W.: Nature of the source regions for post-collisional, potassic magmatism in Southern and Northern Tibet from geochemical variations and inverse trace element modelling. J. Petrol. **45**, 555–607 (2003)
22. Harrison, T.M., Copeland, P., Kidd, W.S.F., Yin, A.: Raising Tibet. Science **255**, 1663–1670 (1992)
23. Clark, M.K., Royden, L.H.: Topographic ooze: building the eastern margin of Tibet by lower crustal flow. Geology **28**, 703–706 (2000)
24. Chung, S.L., Lo, C.H., Lee, T.Y., Zhang, Y., Xie, Y., Li, X., Wang, K.L., Wang, P.L.: Diachronous uplift of the Tibetan plateau starting 40 Myr ago. Nature **394**, 769–773 (1998)
25. Wang, C.S., Zhao, X.X., Liu, Z.F., Lippert, P.C., Graham, S.A., Coe, R.S., Yi, H.S., Zhu, L. D., Liu, S., Li, Y.L.: Constraints on the early uplift history of the Tibetan Plateau. Proc. Natl. Acad. Sci. USA **105**, 4987–4992 (2008)
26. Garizone, C.N., Dettman, D.L., Quade, J., DeCelles, P.G., Butler, R.F.: High times on the Tibetan Plateau: Paleoelevation of the Thakkhola graben. Nepal. Geology **28**, 339–342 (2000)
27. Xia, L., Li, X., Ma, Z., Xu, X., Xia, Z.: Cenozoic volcanism and tectonic evolution of the Tibetan plateau. Gondwana Res. **19**, 850–866 (2011)
28. Kroon, D., Steens, T., Troelstra, S.R.: Onset of monsoonal related upwelling in the western Arabian Sea as revealed by planktonic foraminifers. In: Proceedings of the Ocean Drilling Program-Scientific Results, vol. 117, pp. 257–263 (1991)
29. Quade, J., Cerling, T.E., Bowman, J.R.: Development of Asian monsoon revealed by marked ecological shift during the latest Miocene in northern Pakistan. Nature **342**, 163–166 (1989)
30. Dettman, D.L., Kohn, M.J., Quade, J., Ryerson, F.J., Ojha, T.P., Hamidullah, S.: Seasonal stable isotope evidence for a strong Asian monsoon throughout the past 10.7 m.y. Geology **29**, 31–34 (2001)
31. Clift, P.D., Hodges, K.V., Heslop, D., Hannigan, R., Van Long, H., Calves, G.: Correlation of Himalayan exhumation rates and Asian monsoon intensity. Nat. Geosci. **1**, 875–880 (2008)
32. Xu, Q., Ding, L., Zhang, L., Cai, F., Lai, L., Yang, D., Liu-Zeng, J.: Paleogene high elevations in the Qiangtang Terrane, central Tibetan Plateau. Earth Planet. Sci. Lett. **362**, 31–42 (2013)
33. Guo, Z.T., Ruddiman, W.F., Hao, Q.Z., Wu, H.B., Qiao, Y.S., Zhu, R.X., Peng, S.Z., Wei, J. J., Yuan, B.Y., Liu, T.S.: Onset of Asian desertification by 22 Myr ago inferred from loess deposits in China. Nature **416**, 159–163 (2002)
34. Gupta, A.K., Singh, R.K., Joseph, S., Thomas, E.: Indian Ocean high-productivity event 10–8 Ma: linked to global cooling or to the initiation of the Indian monsoons? Geology **32**, 753–756 (2004)
35. Chakraborty, A., Nanjundiah, R.S., Srinivasan, J.: Theoretical aspects of the onset of Indian summer monsoon from perturbed orography simulations in a GCM. Ann. Geophys. **24**, 2075–2089 (2006)

36. Raymo, M.E., Ruddiman, W.F.: Tectonic forcing of late Cenozoic climate. Nature **359**, 117–122 (1992)
37. Berner, R.A.: GEOCARB II: a revised model of atmospheric CO_2 over Phanerozoic time. Am. J. Sci. **294**, 56–91 (1994)
38. Gerhard, L.C., Harrison, W.E.: Distribution of oceans and continents: a geological constraint on global climate variability. In: Gerhard, L.C., Harrison, W.E., Hanson, B.M. (eds.) Geological Perspectives on Global Climate Change, vol. 47, pp. 35–50. AAPG Studies in Geology, American Association of Petroleum Geologists, Tulsa, OK (2001)
39. Haq, B.U.: Paleogene paleoceanography: early Cenozoic oceans revisited. In: Proceedings 26th International Geologic Congress, Geology of Oceans Symposium (Abstract), Paris, Oceanologica Acta (1981) pp. 71–82
40. Maier-Reimer, E., Mikolajewicz, U., Crowley, T.J.: Ocean general circulation model sensitivity experiment with an open Central American isthumus. Paleoceanography **5**, 349–366 (1990)
41. Scotese, C.R., Golonka, J.: Paleogeographic Atlas: Paleomap Project. University of Texas-Arlington, Arlington, TX (1993)
42. Crowley, T.J., Baum, S.K.: Reconciling Late Ordovician 440 Ma glaciations with very high 14X CO_2 levels. J. Geophys. Res. **100**, 1093–1101 (1995)
43. Allen, M.B., Armstrong, H.A.: Arabia-Eurasia collision and the forcing of mid-Cenozoic global cooling. Palaeogeogr. Palaeoclimatol. Palaeoecol. **265**, 52–58 (2008)
44. Grujic, D., Coutand, I., Bookhagen, B., Bonnet, S., Blythe, A., Duncan, C.: Climatic forcing of erosion, landscape, and tectonics in the Bhutan Himalayas. Geology **3410**, 801–804 (2006)
45. Burbank, D.W., Blythe, A.E., Putkonen, J., Pratt-Sitaula, B., Gabet, E., Oskin, M., Barros, A., Ojha, T.P.: Decoupling of erosion and precipitation in the Himalayas. Nature **426**, 652–655 (2003)
46. Bonnet, S., Crave, A.: Landscape response to climate change: insights from experimental modeling and implications for tectonic versus climate uplift of topography. Geology **31**, 123–126 (2003)
47. Thiede, R.C., Bookhagen, B., Arrowsmith, J.R., Sobel, E., Strecker, M.: Climatic control on rapid exhumation along the Southern Himalayan Front. Earth Planet. Sci. Lett. **222**, 791–806 (2004)
48. Reiners, P.W., Ehlers, T.A., Mitchell, S.G., Montgomery, D.R.: Coupled spatial variations in precipitation and long-term erosion rates across the Washington Cascades. Nature **426**, 645–647 (2003)
49. Shukla, D.P., Dubey, C.S., Ningreichon, A.S., Singh, R.P., Mishra, B.K., Singh, S.K.: GIS-based morpho-tectonic studies of Alaknanda river basin: a precursor for hazard zonation. Nat. Hazards **71**, 1433–1452 (2014)
50. Melton, F.A.: Aerial photographs and structural geology. J. Geol. **67**, 351–370 (1959)
51. Artru, J., Lognonne, P., Blanc, E.: Normal modes modeling of post seismic ionospheric oscillations. Geophys. Res. Lett. **28**, 697–700 (2001)
52. Singh, R.P., Cervone, G., Singh, V.P., Kafatos, M.: Generic precursors to coastal Earthquakes: inferences from Denali fault Earthquake. Tectonophysics **431**, 231–240 (2007)
53. Ganguly, N.D.: Variation in atmospheric ozone concentration following strong Earthquakes. Int. J. Remote Sens. **30**(2), 349–356 (2009)
54. Obzhirov, A., Shakirov, R., Salyuk, A., Suess, E., Biebow, N., Salomatin, A.: Relations between methane venting, geological structure and seismo-tectonics in the Okhotsk Sea. Geo-Mar. Lett. **24**, 135–139 (2004)
55. Rampino, M.R., Self, S.: Sulfur-rich volcanic eruptions and stratospheric aerosols. Nature **310**, 677–679 (1987)
56. Wignall, P.B.: Large igneous provinces and mass extinctions. Earth Sci. Rev. **53**, 1–33 (2001)
57. Palmer, M.R., Edmond, J.M.: Controls over the strontium isotope composition of river water. Geochim. Cosmochim. Acta **56**, 2099–2111 (1992)

58. Alama, M., Alama, M.M., Curray, J.R., Chowdhury, M.L.R., Gania, M.R.: An overview of the sedimentary geology of the Bengal Basin in relation to the regional tectonic framework and basin-fill history. Sed. Geol. **155**, 179–208 (2003)
59. Berner, E.K., Berner, R.A.: The Global Water Cycle: Geochemistry and Environment, p. 397. Prentice-Hall, Englewood Cliffs, N.J. (1987)
60. France-Lanord, C., Derry, L.A.: Organic carbon burial forcing of the carbon cycle from Himalayan erosion. Nature **390**, 65–67 (1997)
61. Galy, V., France-Lanord, C., Beyssac, O., Faure, P., Kudrass, H., Palhol, F.: Efficient organic carbon burial in the Bengal fan sustained by the Himalayan erosional system. Nature **450**, 407–410 (2007)
62. Gaillardet, J., Dupre, B., Louvat, P., Allegre, C.J.: Global silicate weathering and CO_2 consumption rates deduced from the chemistry of large rivers. Chem. Geol. **159**, 3–30 (1999)
63. Galy, A., France-Lanord, C., Derry, L.A.: The strontium isotope budget of Himalayan rivers in Nepal and Bangladesh. Geochim. Cosmochim. Acta **63**, 1905–1925 (1999)
64. Bickle, M.J.: Impact of the Himalayan orogeny on global climate. EOS Trans. Am.Geophys. Union 83 (2002) (Fall Meeting Supplement GC61A-04)
65. Sewall, J.O., Sloan, L.C., Huber, M., Wing, S.L.: Climate sensitivity to changes in land surface characteristics. Glob. Planet. Change **26**, 445–465 (2000)
66. Hay, W.W., Soeding, E., DeConto, R.M., Wold, C.N.: The late Cenozoic uplift-Climate change paradox. Int. J. Earth Sci. **91**, 746–774 (2002)
67. Burbank, D.W., Derry, L.A., France-Lanord, C.: Reduced Himalayan sediment production 8 Myr ago despite an intensified monsoon. Nature **364**, 48–50 (1993)

Trend Analysis of Climatic Parameters at Kurukshetra (Haryana), India and Its Influence on Reference Evapotranspiration

Deepak Kumar Soni and K.K. Singh

Abstract This study has been undertaken to estimate the change in climatic parameters of Kurukshetra region, viz. annual average minimum and maximum air temperatures, annual morning and evening relative humidity, sunshine hours, wind speed, and rainfall, from 2000 to 2013 and hence its influence on reference evapotranspiration (ET_0) as obtained by Penman–Monteith method. An Excel-embedded software MAKESENS (Mann–Kendall test for trend and Sen's slope estimates) has been used for observing and estimating trends in the time series of reference evapotranspiration and climatic parameters. Sen's slope analysis indicates that average annual maximum air temperature, wind velocity, and reference evapotranspiration show increasing trends with 0.08%, 0.12%, and 3.28% slopes, respectively, whereas decreasing trend is observed in average rainfall, relative humidity (morning), and sunshine hours with −12.0, −0.08, and −0.04%, slopes. The trends of minimum air temperature and relative humidity (evening) show no change. The positive trend in reference crop evapotranspiration indicates that the water demand required for different crops in various seasons will increase. This will warrant developing less water-intensive crops as water availability is already under stress.

Keywords Climate change · Global warming · Reference evapotranspiration · Penman–Monteith method

D.K. Soni (✉) · K.K. Singh
Department of Civil Engineering, National Institute of Technology, Kurukshetra 136119, Haryana, India
e-mail: deepak_6120054@nitkkr.ac.in

K.K. Singh
e-mail: k_k_singh_2000@yahoo.com

V. Garg et al. (eds.), *Development of Water Resources in India*,
Water Science and Technology Library 75, DOI 10.1007/978-3-319-55125-8_28

1 Introduction

Haryana is a major agriculture state in northwestern India. A large part of Haryana is located on the Indo-Gangetic alluvial plain. Irrigation in the state is mainly facilitated by canal networks originating from rivers of Punjab and Uttarakhand states and also local groundwater. Two of the most common crops in the state are rice in Kharif season and wheat in Ravi season. The crop yield is mainly influenced by the adequate and timely availability of water. However, the last century (1906–2005) has witnessed a significant positive change in the earth temperature (0.74 °C) caused by large-scale emission of greenhouse gases which is largely attributed to the anthropogenic activities and that has provoked the change in climate [1]. The adverse effect of climate change is on agriculture productivity because of decrease in rainfall and increase in temperature. Demand of irrigation water is closely related to climate change as increased dryness leads to increase demand (IPCC 2001). Evapotranspiration is a necessary parameter in irrigation system design [2]. In the past decades, various researchers have examined the possible impact of climate change on reference evapotranspiration (ET_0). According to these studies, results show that the trends in ET_0 vary with climatic conditions and region [3]. A study has been conducted to assess the sensitivity of evapotranspiration in respect of global warming in the arid zone of Rajasthan, India [4]. The study suggested an increase of 14.8% of total ET_0 demand to increase in temperature by 20%. The study also concluded that the sensitivity of ET_0 is less with increase in net solar radiation, followed by wind speed as compared to temperature. An increase of 10% of temperature, along with a 10% decrease in net solar radiation and wind speed, could be a marginal decrease in total ET (0.36%). Further, spatiotemporal characteristics of potential evapotranspiration (PET) trends are studied in China using time series from 65 stations and found a decreasing trend at all stations [5]. Furthermore, the study of Ojeda-Bustamante [6] found that by the end of century, the annual increase in reference evapotranspiration will be 10% higher compared to current value due to climate change under moderate–medium emission scenario. The present paper investigates the influence on reference evapotranspiration (ET_0) due to change in climatic factors as a result of climate change in Kurukshetra district of Haryana state.

2 Study Area and Methodology

2.1 Climatic Characteristics of Kurukshetra

The study site is located in the rice—wheat production zone of Haryana state. It lies between 29°11′–30°16′N latitude and 76°11′–77°17′W longitude, which is about 240 m above mean sea level. The location map of the area is shown in Fig. 1. The climatic conditions of the state are classified as semiarid tropical to subtropical.

Fig. 1 Location of the study area

Annual rainfall of state ranges from less than 300 mm to over 1000 mm (mean 704 mm). About 75–80% of the rain falls during June September. Major crop cultivated in this area includes rice, maize, wheat, mustard, and fodder crops.

2.2 Collection of Meteorological Data

Daily meteorological data have been collected from ICAR meteorological center, Karnal, Haryana. Daily data constitute maximum temperature, minimum temperature, morning and evening relative humidity, wind speed and sunshine hours from the year 2000 to 2013. The data set is used for trend analysis using Mann Kendall test.

2.3 Mann–Kendall Test

The Mann–Kendall test used for identifying the trends variation in climatic variables and ET_0 from time series data is one of the widely accepted nonparametric tests [7–9]. Hence, in this study, M–K test has been used to study the trends of climatic variables and ET_0. Detailed information related to the Mann–Kendall test can be found in studies published by Hamed [7–9].

2.4 Sen's Slope Estimator

The existing trend (change/year) slope can be identified using the Sen's nonparametric method. If it is assumed that the case under study has a liner trend then, $F(t)$, is defined as:

$$F(t) = Q \cdot t + B \tag{1}$$

where Q represents the trend slope and B is a constant value.

The slope Q (Eq. 1) can be estimated only after the calculation of all paired data values slopes. The slope of all data pairs can be estimated as:

$$Q_j = \frac{x_j - x_k}{j - k}, j > k$$

If the number of values of x_j in a time series is n, then the slope estimates of Q_j are $N = n(n-1)/2$. The median of the slope estimates (N) represents the Sen's estimator of slope for Q_j. The N values of Q_j are arranged in ascending order, and the Sen's estimator is defined as:

If the slope estimate N is odd, then

$$Q = Q_{[(N+1)/2]} \tag{2}$$

If the slope estimate N is even, then

$$Q = \frac{1}{2}\left(Q_{\frac{N}{2}} + Q_{\left(\frac{N+2}{2}\right)}\right) \tag{3}$$

A normal distribution-based nonparametric method is used to calculate a 100 $(1 - \alpha)$ % two-sided confidence interval. The applicability of the method is limited up to a minimum value of n which is 10, unless there are many ties.

The calculations for meteorological variables and ET_0 values using Mann–Kendall tests and Sen's slope estimator were performed using MAKESENS 1.0 which is an Excel-based software.

2.5 Penman–Monteith Equation

The Penman–Monteith equation is given by the United Nations Food and Agriculture Organization (**FAO**) for modeling evapotranspiration. Recently, a study conducted by Ngongondo et al. suggested that the Penman–Monteith method is most suited for modeling the evapotranspiration phenomenon (Ngongondo et al. in

press). The definition of Penman–Monteith method for the estimation of daily reference crop is given as [10]:

$$ET_0 = \frac{0.408\Delta(R_n - G) + \gamma \frac{900}{T+273} U_2(e_s - e_a)}{\Delta + \gamma(1 + 0.34U_2)} \tag{4}$$

where ET_0 is climatic parameter representing the reference crop evapotranspiration [mm day^{-1}], G is the soil heat flux density [MJ m^{-2} day^{-1}], U_2 is the wind speed at 2 m height [m s^{-1}], R_n is denotes the net radiation at the crop surface [MJ m^{-2} day^{-1}], T represents the mean daily air temperature at 2 m height [°C], e_s and e_a are the saturation and actual vapor pressure [kPa], $e_s - e_a$ is the saturation vapor pressure deficit [kPa], Δ shows the curve of slope vapor pressure [kPa °C^{-1}] and γ psychometric constant [kPa °C^{-1}]. ET_0 has two components: the radiative component ET_{0R} and the aerodynamic component ET_{0a}, expressed as the first and second parts. ET_0 represents the evapotranspiration from standardized vegetated surface and is a combination of two terms that include energy term and aerodynamic (wind and humidity) term, respectively. The definition of ET_0, ET_{0R}, and ET_{0a} is given as:

$$ET_0 = ET_{0R} + ET_{0a} \tag{5}$$

$$ET_{0R} = \frac{0.408\Delta(R_n - G)}{\Delta + \gamma(1 + 0.34U_2)} \tag{6}$$

$$ET_{0a} = \frac{\gamma \frac{900}{T+273} U_2(e_s - e_a)}{\Delta + \gamma(1 + 0.34U_2)} \tag{7}$$

ET_{0R} represents the reference evapotranspiration that would be obtained if the heat budget of surface were determined by radiation alone. ET_{0a} is the reference evapotranspiration imposed by the environment when the surface is fully coupled with the prevailing weather.

3 Estimation of Crop Evapotranspiration

The crop-specific evapotranspiration rate is obtained by multiplying by proper crop coefficient (K_c) to the calculated reference evapotranspiration which ultimately gives the actual crop evapotranspiration (ET_C).

$$ET_C = ET_0 \times K_c \tag{8}$$

where ET_0 represents the reference crop evapotranspiration, K_c is the crop coefficient, and ET_C is the crop evapotranspiration.

Due to different growth patterns of the same crop, different evapotranspiration demand is obtained. Crop water demand is directly related to the crop planting time or season as the evapotranspiration varies in every season due to differential energy pattern. Further, the plant factors like leaf area (evaporative surface) and stomatal closure behavior also influence evapotranspiration.

4 Results and Discussion

4.1 Study of Climate Parameter

Trend variations of different climatic parameters, viz., temperatures (maximum, average, and minimum), relative humidity (morning, average, and evening), wind velocity, sunshine hours, and rainfall, over the period of 14 years, 2000–2013, at Kurukshetra are presented in Figs. 2, 3, and 4, respectively, using MAKESENS. Figure 5 shows trend variation in reference evapotranspiration as obtained from Eq. (4).

In Fig. 2, it is seen that overall positive trend has been found with the rate of increase in maximum temperature as 0.08%. The graph also shows variation in trend with confidence interval of 99 and 95%. The residual value of maximum temperature is maximum in the year 2009 as compared to normal annual maximum temperature as shown in Fig. 6. Variation in average temperature and minimum temperature shows that there is no change in trend over the 14 years. There is rise and fall every four years. Variation in trend with confidence interval of 99 and 95% has also been plotted. The positive trend in maximum temperature indicates rise in temperature with time.

From Fig. 3, it is observed that overall negative trend has been found with the rate of decrease in relative humidity (morning) as −0.08%. The graph also shows variation in trend with confidence interval of 99 and 95%. The residual value is more or less negligible as shown in Fig. 6. Variation in relative humidity (evening) and relative humidity (average) shows that there is no change in trend over the 14 years. Variation in trend with confidence interval of 99 and 95% is also negligible.

Figure 4 corresponds to trend variations in sunshine hours, wind velocity, and rainfall from 2000 to 2013, and it is seen that there are negative, positive, and negative trends, respectively, with slope values as −0.04%, +0.12%, and −12.00%. There was also significant change in rainfall from 691 to 479 mm and 479 to 288 mm during 2004–2005 and 2005–2006, respectively. Negative trend in rainfall shows that rainfall magnitude is decreasing with time.

Using the above climatic parameters, the reference evapotranspiration was obtained using Eq. (4) and plotted in Fig. 5. During the interval from 2002 to 2006, ET_0 was below the normal value except in 2002 and 2004, but it was found above the normal value during 2008–2012, and it was above the normal value in last 5 years. It is found that the trend is positive and its slope is increasing by 3.28%.

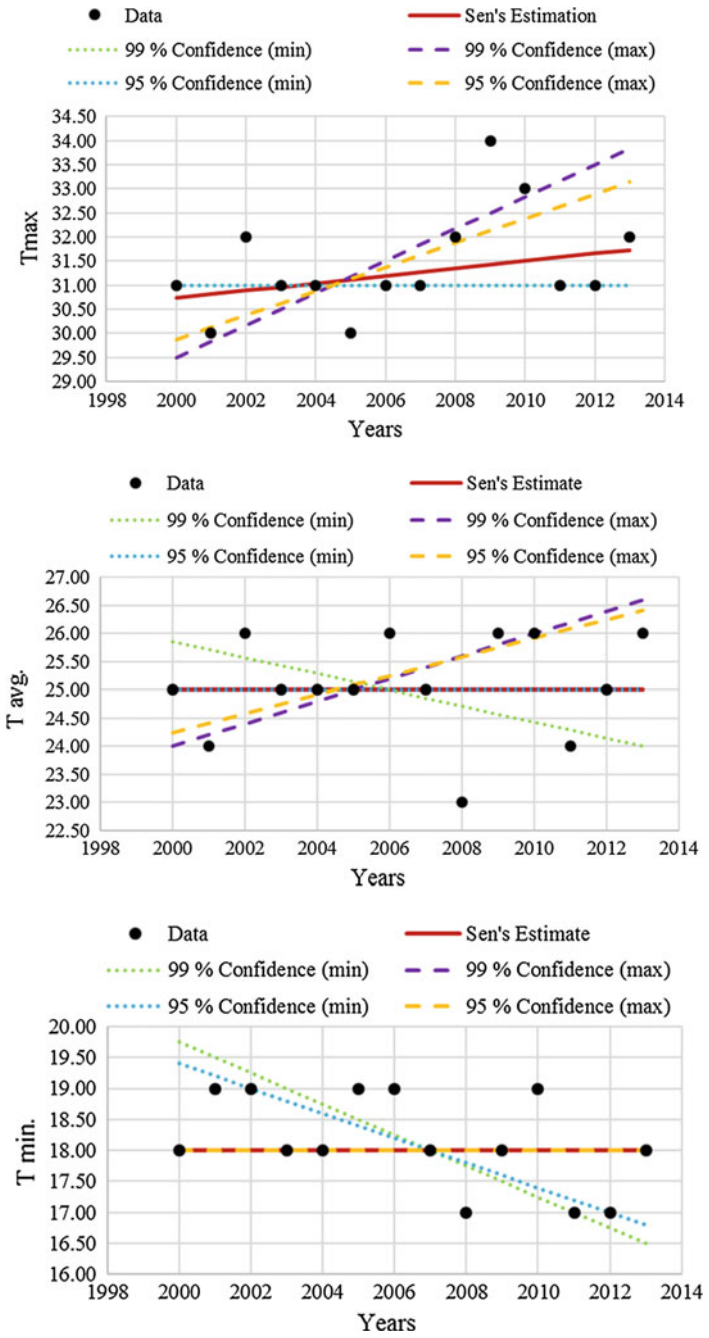

Fig. 2 Trend variations in maximum, average, and minimum temperatures from year 2000 to 2013

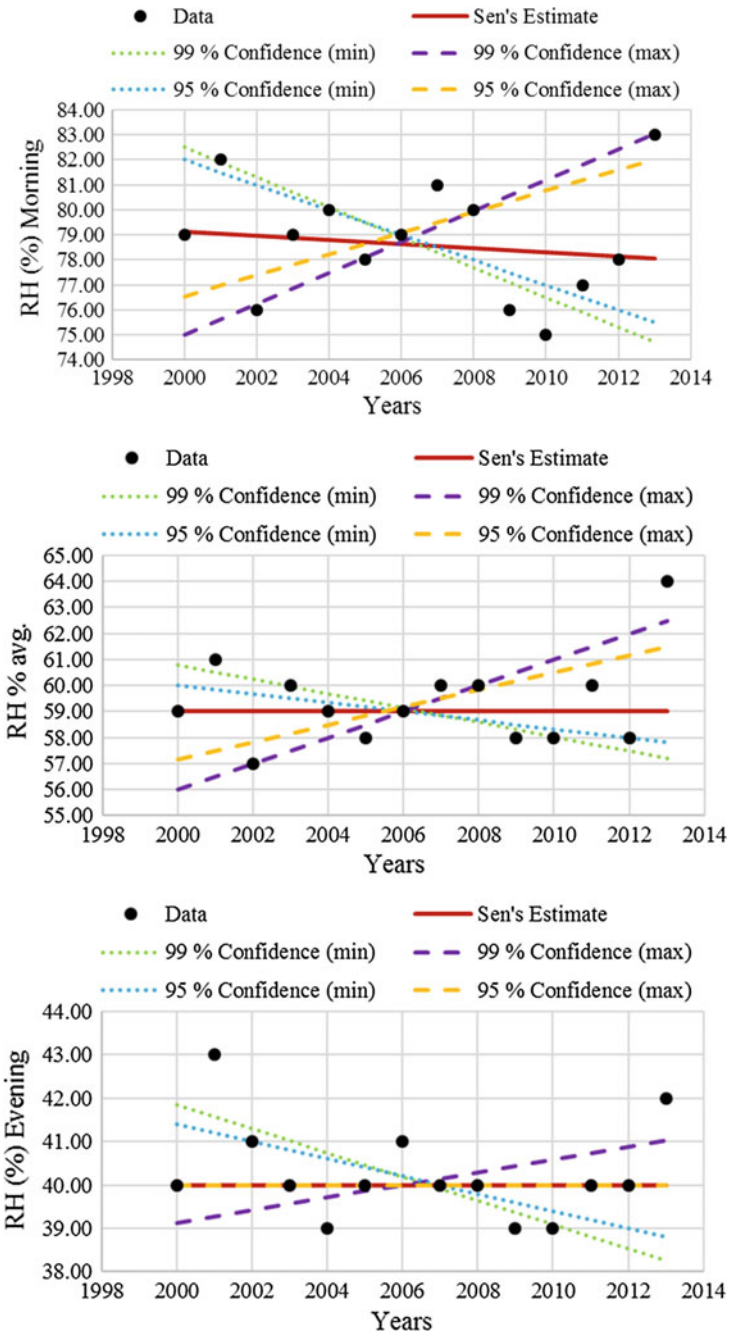

Fig. 3 Trend variations in morning, average, and evening relative humidity from year 2000 to 2013

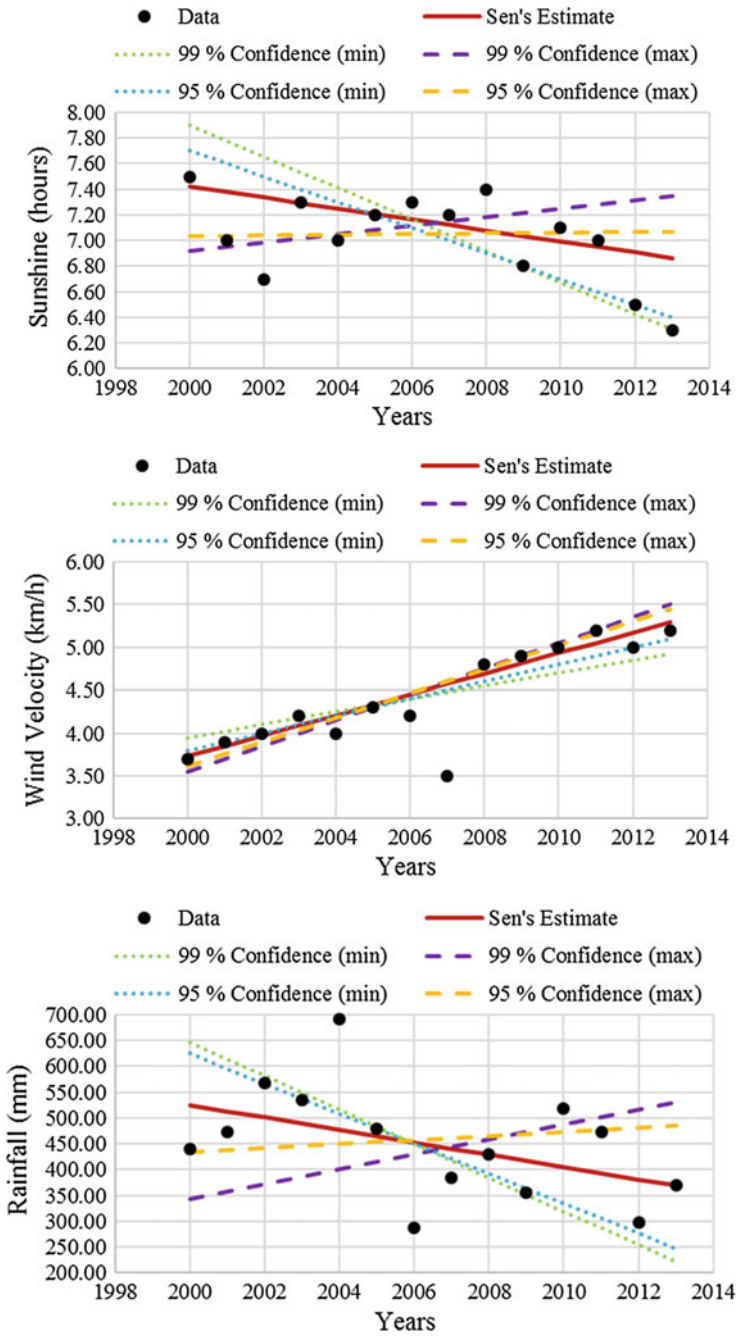

Fig. 4 Trend variations in sunshine hours, wind velocity, and rainfall from 2000 to 2013

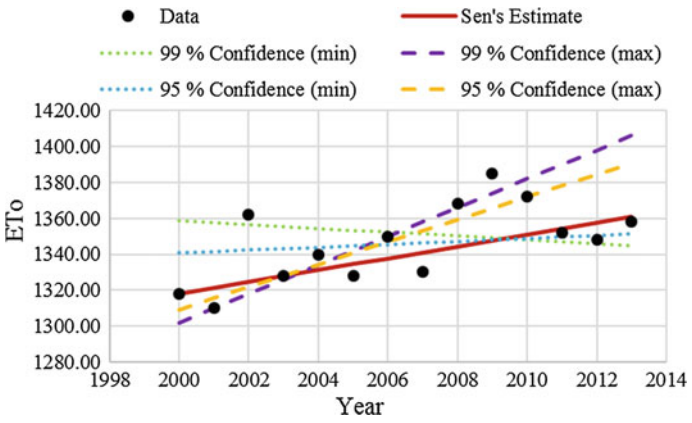

Fig. 5 Trend variations of reference crop evapotranspiration

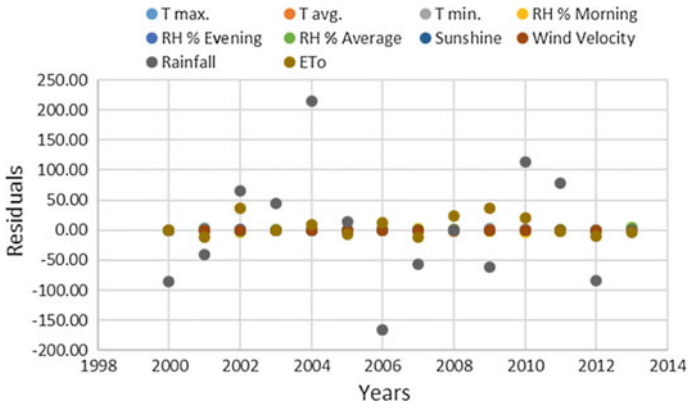

Fig. 6 Residuals for various climatic parameters

There were major dips for ET_0 in years 2005 and 2007 with the values of 1328 mm and 1330 mm, respectively. As we go toward the proceeding years, from 2007 up to 2009, ET_0 was found continuously increasing from 1330 mm to 1385 mm as wind velocity increases from 3.6 to 4.4 km/h and maximum temperature increases from 31.2 °C to 32.8 °C. During the period 2010–2013, it is observed that there are significant drops in seasonal ET_0 and maximum temperature i.e. from 1372 mm to 1348 mm and 31.3 °C to 28.7 °C, respectively. However, in the same period, there are increases in average relative humidity and wind velocity with their values increasing from 60.0 to 62.4% and 4.3 km/h to 4.7 km/h, respectively. This reflects that water demand of crop is increasing with every year. The negative rainfall trend and positive reference evapotranspiration warrant developing less water-intensive crops as water availability is already under stress.

5 Conclusions

The following conclusions are drawn from the analysis of data of climatic parameters from 2000 to 2013:

1. Maximum temperature and wind velocity show positive trends with the rate of increment of about 0.08% and 0.12%, respectively, while negative trend is observed in relative humidity (morning), sunshine hours, and rainfall with rate of reduction as −0.08, −0.04, and −12.00%.
2. Reference crop evapotranspiration shows positive trend with the rate increase as 3.28%. This reflects that water demand of crop is increasing with every year.

References

1. Sankaranarayanan, K., Praharaj, C.S., Nalayini, P., Bandyopadhyay, K.K., Gopalakrishnan, N.: Change and its impact on cotton (gossypium sp). Indian J Agric. Sci. **80**(7), 561–75 (2010)
2. Zhang, X.Y., Chen, S.Y., Sun, H.Y., Shao, L.W., Wang, Y.Z.: Change in evapotranspiration over irrigated winter wheat and maize in north China Plain over three decades. Agric. Water Manag. **98**(6), 1097–1104 (2011)
3. Rim, C.: The effect of urbanization geographical and topographical condition on reference evapotranspiration. Clim. Change **97**(3–4), 483–514 (2009)
4. Goyal, R.K.: Sensitivity of evapotranspiration to global warming: a case study of arid zone of Rajasthan (India). Agric. Water Manag. **69**(1), 1–11 (2004)
5. Thomas, A.: Spatial and temporal characteristics of potential evapotranspiration trends over China. Int. J. Climatol. **20**, 381–396 (2000)
6. Ojeda-Bustamante, W., Sifuenten-lbarra, E., Iniguez-Covarrubias, M., Montero-Martinez, M.J.: Impact of Climate Change on crop development and water requirements. Mex. Agrocienc. **45**(1) (2010). ISSN 1405-3195
7. Hamed, K.H.: Trend detection in hydrologic data: the Mann-Kendall trend test under the scaling hypothesis. J. Hydrol. **349**(3–4), 350–363 (2008). doi:10.1016/j.jhydrol.2007.11.009
8. Liang, L.Q., Li, L.J., Liu, Q.: Temporal variation of reference evapotranspiration during 1961–2005 in the Taoer river basin of Northeast China. Agric. For. Meteorol. **150**(2), 298–306 (2010). doi:10.1016/j.agrformet.2009.11.014
9. Liu, H.J., Li, Y., Tanny, J., Zhang, R.H., Huang, G.H.: Quantitative estimation of climate change effects on potential evapotranspiration in Beijing during 1951–2010. J. Geog. Sci. **24** (1), 93–112 (2014). doi:10.1007/s11442-014-1075-5
10. Allen, R.G., Pereira, L.S., Raes, D., Smith, M.: Crop Evapotranspiration—Guidelines for Computing Crop Water Requirements—FAO Irrigation and Drainage Paper 56. Food and Agriculture Organization of United Nations (FAO), Rome (1998)

Part III
Hydraulics Structures

Empirical and Mathematical Modeling of Head and Discharge Over Piano Key Weir

Harinarayan Tiwari and Nayan Sharma

Abstract Increasing demand of energy and limited conventional energy sources (coal, petroleum, natural gas, etc.) initiated the alternative thinking of hydropower projects. Due to easy and high head availability in mountainous regions, India has immense potential of hydropower. Spillways are the one of the important elements of hydropower projects. Spillways are generally used in the hydropower to spill the excess amount of water. Piano Key Weir is the ungated spillway structure generally used to get high discharge intensity under limited width. This study formulates the empirical relationship between the head and discharge over Piano Key Weir. This study also evaluates the weir coefficient values of Piano Key Weir through HEC-RAS modeling.

1 Introduction

The timely and appropriate usage of water resources continues one of the fundamental assistances produced to human society by the water resource engineer. Hydraulic structures are the important infrastructure which is used for water resources management. Hydraulic structures can be applied to deflect, interrupt, or totally prevent the flow in open channel. Main hydraulic structures are differentiated as water retaining structures, water conveying structures, and special-purpose structures. Dams are the important water retaining structures used very frequently across the globe. At present, there are 4862 completed large dams and 312 large dams are under construction in India [1]. India lies on the third position after China and USA with respect to number of dams. Irrespective of dimension and nature, structures exhibit great complexity in their hydraulic response. Reservoir dams are generally encountered with two primary issues, the first is flood control and the second is storage capacity loss due to high sedimentation rate. Flood control is assured using spillways. All dams should be constructed with a safety device,

H. Tiwari (✉) · N. Sharma
Department of WRDM, IIT, Roorkee, India
e-mail: haribit31@outlook.com

V. Garg et al. (eds.), *Development of Water Resources in India*,
Water Science and Technology Library 75, DOI 10.1007/978-3-319-55125-8_29

in the form of a spillway, against overtopping. A spillway is a structure constructed to provide limited and controlled release of flows to the downstream. Spillways are mainly classified according to its controlling nature. Spillway constitutes fraction of total dam cost. The available information indicates a large variation, ranging from 4% (unlined rock spillways) to 22% (spillways for earth and rockfill dams) [2]. There is large amount of investment for the spillways, in terms of cost. Weirs are also the barrier in the channel to divert the flow to the desired location. It is generally small in size with compare to large conventional dams.

Issue of submergence is directly associated with the placement of any type of transverse hydraulic structures in the open channel. Placement of transverse hydraulic structure across the open channel alters flow conditions in the upstream and downstream. In the upstream of hydraulic structure, there is magnitude of submergence and it must be considered before the design. Piano Key Weir is one of the alternative transverse hydraulic structures applied at several places around the world [3–7]. The study on Piano Key Weir includes its naming conventions [8], numerical and physical modeling [9], coefficient of discharge examination [4], hydraulic capacity [10], flow characteristics [5], vertical velocity profile [7], turbulent kinetic energy [11], entropic velocity distribution [12], and many more. Three-dimensional numerical model was also attempted in the vicinity of Piano Key Weir [3, 9, 13, 14]. Scope of the study is very high to standardize the features of Piano Key Weir, because it is relatively new hydraulic structure. In general, any weir has specific head discharge relationship. Estimation of coefficient of discharge facilitates us to calculate the discharge passing through weir via head measurement. Complexity of relationship is increased with the types of the hydraulic structures used for the discharge measurement and control. Study of head discharge relationship for Piano Key Weir is especially significant due to involvement of its multiple structural elements in the design. Several authors have attempted to estimate the discharge coefficient to establish the head discharge relationship over Piano Key Weir. Up to the author's knowledge, no attempt has been made so far for the nonlinear empirical relationship between discharge and head. This paper explains the research findings of the nonlinear head discharge relationship from the experimental study.

2 Piano Key Weir

Recently, the idea of Labyrinth weirs has been evolved by introducing a new shape with ramp, called Piano Key Weir. This substitute of Labyrinth weir allows for an increase in the firmness of the hydraulic structure, and it can be positioned on the top of existing or new diversion or storage dam structures [5, 15]. Due to the absence of any gates, Piano Key Weir involves very little operation and maintenance. It is also much cheaper than formal gated dam spillways [16, 17].

At constant width, A Piano Key Weir has a considerably higher discharging capacity than conventional spillways (2–4 times at low head). Piano Key Weir can

considerably enhance dam safety and the storage and/or the flood control efficiency by better handling sudden cloud burst flood than conventional dam spillways. Piano Key Weir can be designed to increase the storage by raising the crest while maintaining spillway capacity. Turbulence mechanism in the upstream PKW is still an area of vital concern for researchers due to its unknown behavior regarding sediment transport [7, 18, 19]. As noise in the signal data acquired from acoustic Doppler velocimeter and its characteristics have high impacts on turbulence and their measurements [20–22], the experimental study has been carried out using ADV. Mathematical modeling was also done in coherence with experimental study to make the results useful in the field.

Application of PK Weir for some Algerian dams allows recovering global storage volume about 250×10^6 m^3. The PK Weir can be feasible for earth and concrete dams, equipped with a free flow spillway [23]. The PKW is a new type of weir, first designed in 2001 and constructed first time in 2006 [24]. Influences of the relative width of the inlets and outlets on the hydrodynamic characteristics of the structure are presented. A process oriented analytical formulation for the evaluation of the discharge coefficient of the PKW [25].

Piano Key Weir consists of 23 or may be more geometric parameters. Every parameter has its own role to define the hydraulic characteristics of Piano Key Weir [8]. The variation effects of Piano Key Weir geometric parameters on the discharge coefficient were evaluated [4]. The role of total developed length along the overflowing crest axis (L) has been emphasized by many authors [4, 6]. For the low heads ($H/P < 0.2$), free surface flow is linear over Piano Key Weir [24, 26]. Model test was performed to understand the flow features over Piano Key Weir depending on the upstream head. All the empirical relationship for discharge coefficient established in the past is very complex in nature, so authors attempted to derive the simple empirical derivation via nonlinear optimization. The complexity mentioned in the above statement means, in the previous attempts they have estimated the relationship using multiple-dimensional parameters [4, 5]. In authors point of view, combination total developed crest length, width of channel, head over crest, and discharge over PKW have a capability to estimate the general nonlinear relationship.

3 Field Applications

The Piano Key (PK) Weir concept was developed and employed relatively recently. Several courtiers like France, Algeria, India, Vietnam, South Africa, and Sri Lanka have been directly involved in the research and development of Piano Key Weir. This alternative of Labyrinth weir provides an increase in the steadiness of the structure which can be positioned on the top of most existing or new diversion or storage dam structures [23, 27]. Hardly any manpower is required to operate the structure. Piano Key Weir can be designed to increase the storage by raising the crest while maintaining spillway capacity. Due to its cantilevered apex geometry, Piano Key Weir is more practical alternative for applications where the footprint is

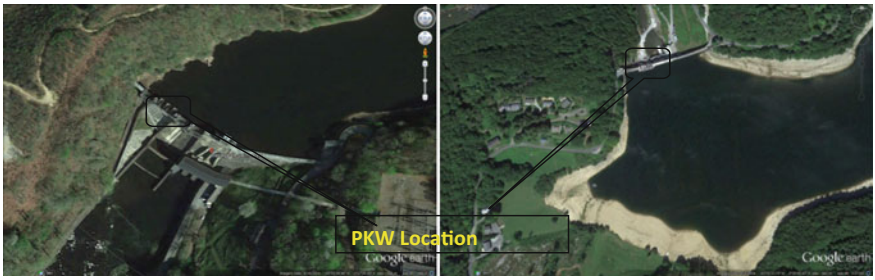

Fig. 1 Spatial location of Saint Marc and Raviege Dam PKW (In France)

Fig. 2 Google map of PKW (Sawra Kuddu HEP) and on site map of PKW (Sawra Kuddu HEP) (*Ref* HPPCL)

limited [8, 9]. The construction of Piano Key Weir has been implemented at Sawara Kuddu hydroelectric project of India with advice and consultant of IIT Roorkee [26, 28]. Some of the field implementations of Piano Key Weir with their brief details are discussed below.

3.1 Piano Key Weir in France

France is the leading countries to use Piano Key Weir in the field. Saint Marc Dam, Raviege Dam (Fig. 1), Goulours Dam, Etroit Dam, Gloriettes Dam, etc., are some examples. Design discharge of the weirs varies from 90 to 400 m^3/s.

3.2 Sawra Kuddu Hydroproject (India)

A new technology in the form of Piano Key Weir (PK Weir) type of barrage has been designed and developed by IIT Roorkee, India, for the project and will be installed for the first time in India (Fig. 2). This entails changes in size of the

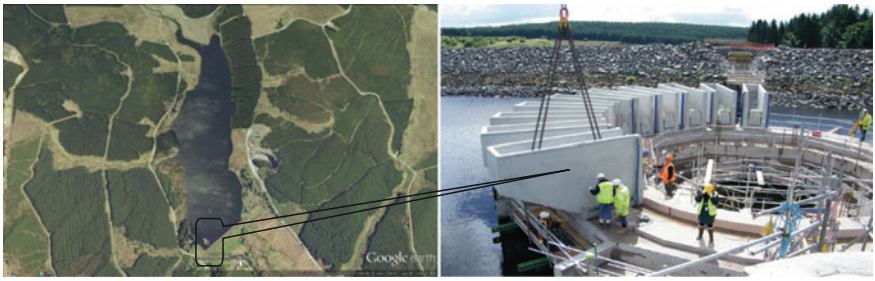

Fig. 3 Elevated view of the weir from the valve tower and spatial location of PKW (Courtesy of Scottish water and Google earth)

barrage while implementing a new technology in the field Sawra Kuddu HEP has been contemplated as a power generation development on the Pabbar River in Shimla District (HP). The project comprises of a Piano Key Weir of design discharge of 5240 m^3/s.

3.3 Black Esk Reservoir Dam

The new Piano Key Weirs were designed on Black Esk reservoir to pass the design flood (the PMF) of 183 m^3/s with a flood surcharge of 0.97 m, saving about 0.7 m from the amount of dam raising that would have been required for the alternative scheme (Fig. 3).

3.4 Tzaneen Dam PKW

The PKW alternative is favoured because it only requires a 2.8 m removal of the current ogee crest in comparison with 7.5 m removal of the current ogee crest for Labyrinth weir. The hydraulic capacity of the modified PKW allows a safe passing of the SEF (4120 m^3/s) in conjunction with a 1 m raising of the earth-fill embankments (Fig. 4).

3.5 Loombah Dam, Australia

Alternate option of Piano Key Weir was preferred based on limited geotechnical data. Due to availability of extremely hard rock and dam adjacent area blasting was not allowed. Excavation of hard rock was found very slow and expensive (Fig. 5). Piano Key Weir designed for a 1 in 10,000 (years) average recurrence interval.

Fig. 4 Spatial location of Tzaneen Dam PKW (*Ref* Google Earth)

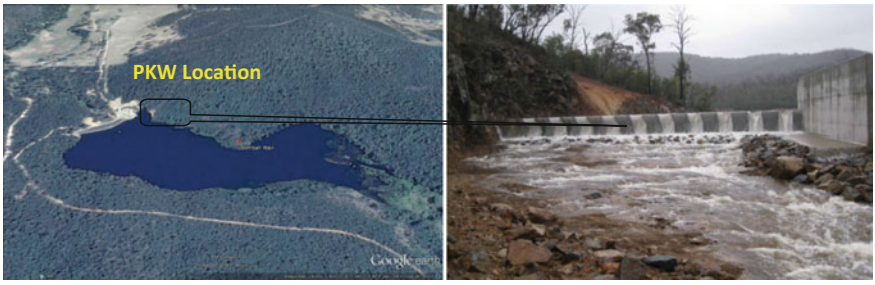

Fig. 5 Spatial location of Loombah Dam (Australia) PKW (*Ref* Google earth) and view of PKW from downstream

Fig. 6 Under construction and constructed PKW at Van Phong Dam (Vietnam)

3.6 Van Phong Dam PKW

The PK Weirs was selected to minimize the submergence issue. In Van Phong Dam, relatively safer and cheaper solution of PKW was implemented discharge intensity of 28.9 $m^3/s/m$. Site constraint was also overcome due to design of Piano Key Weir (Fig. 6) [29–31].

Fig. 7 PKW at Giritale reservoir

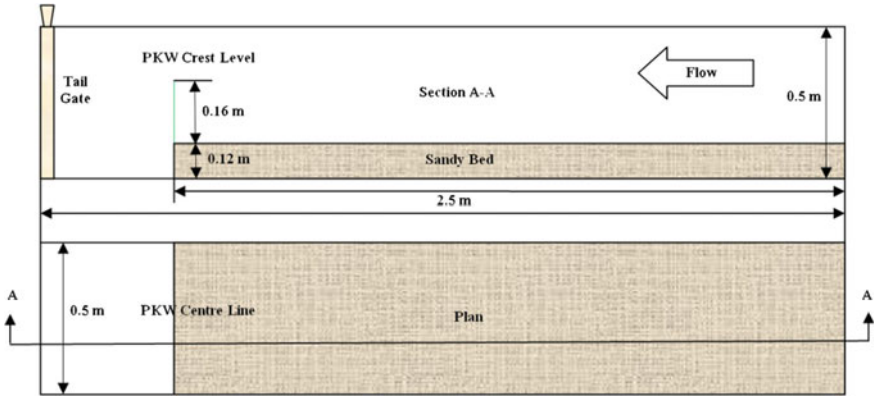

Fig. 8 Flume assembly

3.7 Giritale Reservoir PKW (Sri Lanka)

Piano Key Weir was constructed on Giritale reservoir of Sri Lanka in 2013. This alternative scheme was implemented to reduce the water shortage frequency. Capacity of Giritale reservoir was improved at relatively low cost and satisfactory efficiency was also achieved (Fig. 7) [27, 32].

4 Experimental Setup and Methodology

Head and discharge measurement over Piano Key Weir has been taken in the controlled laboratory experiments. The experiments were conducted in River Engineering Laboratory, Water Resources Development and Management Department, Indian Institute of Technology Roorkee, India. Authors attempted for nonlinear empirical relationship between head over crest and discharge. The flume width and length are 0.5 m and 3 m, respectively (Figs. 8, 9, and 10). Specification of Piano Key Weir is given in Table 1 as per standard naming convention [8].

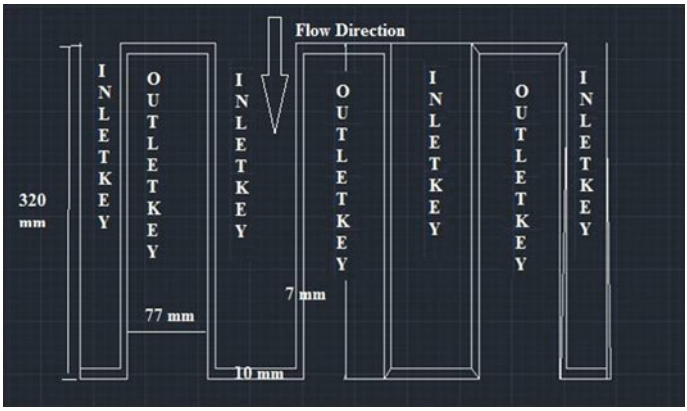

Fig. 9 Plan of PKW

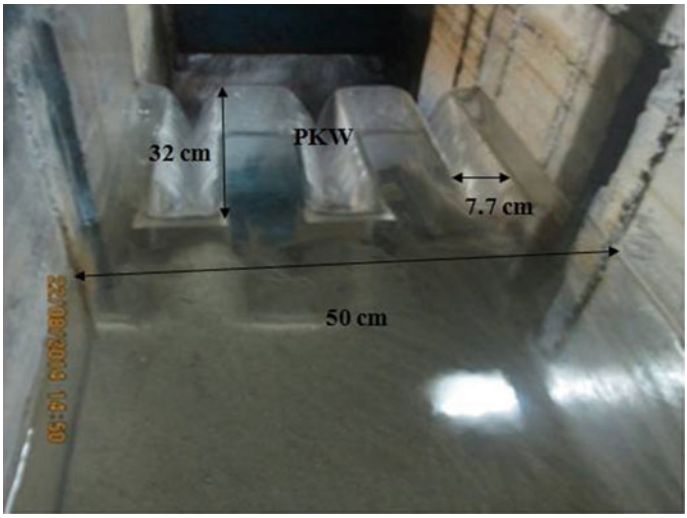

Fig. 10 Experimental setup of PKW

5 Head Discharge Relationship

Discharge over any weir is function of total head and head over crest. In addition to head over crest, total cycle length and width of the channel is the directly related with the discharge over weir. Total cycle length is defined as total developed length along the overflowing crest axis. Due to abovementioned fact, discharge (cm^3/s) can be written as the function of head over crest, total cycle length and width of the channel (Eq. 1). In this specific study, total cycle length and width were kept constant against varying discharge.

Table 1 Specification of PKW (A)

PKW components	Dimension (mm)
Inlet key width (sidewall to sidewall) (W_i)	77
Outlet key width (sidewall to sidewall) (W_o)	77
Sidewall thickness	6.5
Slope of the inlet key apron	3H: 2 V
Slope of the outlet key apron	3H: 2 V
Height of the inlet entrance measured from the PKW crest (P)	160
Upstream–downstream length of the PKW (B)	320
Downstream (inlet key) overhang crest length (B_i)	80
Upstream (outlet key) overhang crest length (B_o)	80
Base length	160
Total developed length along the overflowing crest axis (L)	2382
Total width of the PKW (W)	500
Developed length ratio of the PKW	4.76
Number of inlet key	3
Number of outlet key	3

$$\frac{Q}{LW} = f(h_c) \tag{1}$$

where L is the total cycle length and W is width of channel (in cm). Measurement has been taken here in cm. Nonlinear empirical optimization has been carried out with the help of power function with first six datasets. Exponent was taken 0.75 based on the several iterations. Using the first six datasets, value of C was computed 0.715. During calibration, coefficient of determination (R^2 = 0.965) was sufficiently high. Utilizing the value of C (0.715) and h_c, Q has been calculated for next six datasets and compared with measured discharge.

$$\frac{Q}{LW} = Ch_c^{3/4} \tag{2}$$

where C is established as 0.715. The established relationship has sufficiently positive agreement (R^2 = 0.98) with validated data.

5.1 Comparison with Kabiri-Samani and Javaheri Formula

Kabiri-Samani and Javaheri have established the empirical relationship between coefficient of discharge and Piano Key Weir components (Eq. 3). With the

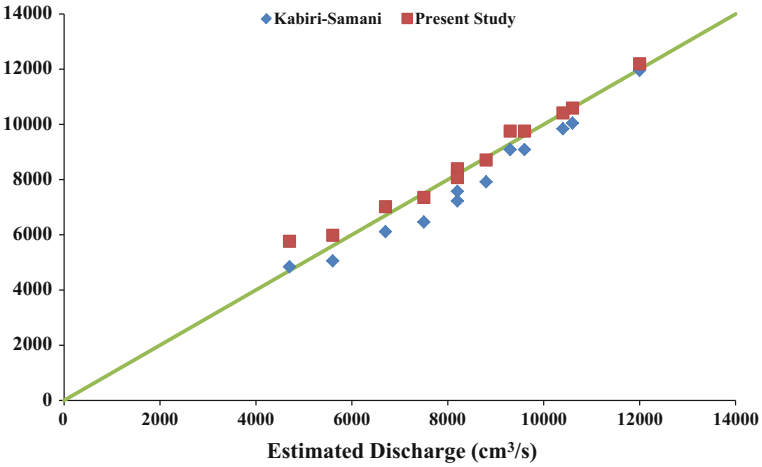

Fig. 11 Comparison of observed discharge and estimated discharge

estimated coefficient using proposed empirical relationship, the standard relationship of sharp rectangular weir (Eq. 4) can be used to estimate the discharge over Piano Key Weir.

$$C_d = 0.212\left(\frac{H}{P}\right)^{-0.675}\left(\frac{L}{W}\right)^{0.377}\left(\frac{W_i}{W_o}\right)^{0.426}\left(\frac{B}{P}\right)^{0.306}\exp\left(1.504\times\frac{B_0}{B}+0.093\times\frac{B_i}{B}\right)+0.606 \tag{3}$$

$$Q = 2/3C_d\sqrt{2g}H^{3/2} \tag{4}$$

The coefficient of determination was found almost similar (>0.96) for both the cases (Kabiri-Samani and present case) (Fig. 11). In the present case, simplicity of the formula has increased manifold.

6 Mathematical Modeling Using HEC-RAS

The problem of head and discharge is modeled using HEC-RAS. In HEC-RAS, there is no such direct option to put Piano Key Weir in open channel for the mathematical modeling. Assumption before this modeling is that Piano Key Weir can act as broad-crested weir with different weir coefficient. Authors utilized the option of broad-crested weir to calibrate and then validate weir coefficient under HEC-RAS environment. Estimation of average weir coefficient will be very helpful for the preliminary design of Piano Key Weir.

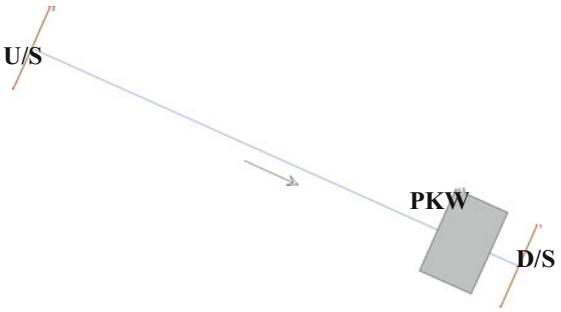

Fig. 12 Channel setup in HEC-RAS model

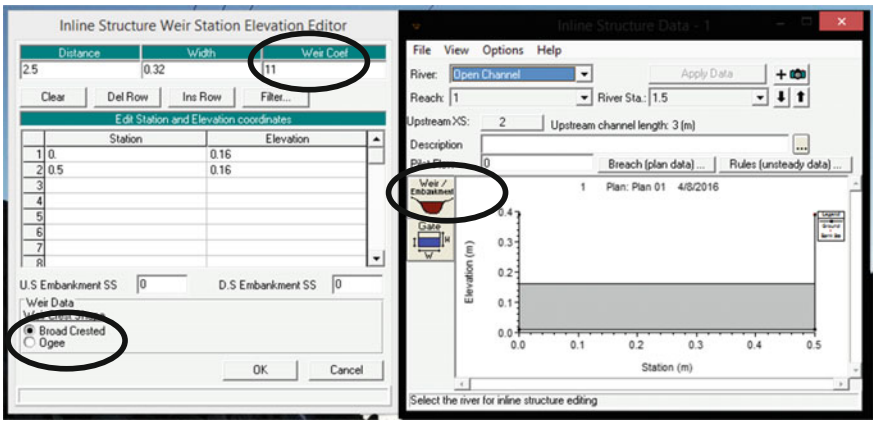

Fig. 13 Estimation of head through HEC-RAS model using different weir coefficient

6.1 Model Setup

The model has been setup in the HEC-RAS using cross-sectional data, Piano Key Weir center line position, and slope of flume (Fig. 12). A material characteristic (manning roughness) is calibrated for the flume using velocity in the upstream and head over crest.

6.2 Weir Coefficient

It is the coefficient which is used for weir flow under weir flow condition. In HEC-RAS program, the range of weir coefficient for broad-crested weir is 2.5–3.1 and for ogee weir is 3.1–4.0 (Fig. 13). Since the Piano Key Weir is high coefficient weir, its discharge passing capacity has been estimated as 2–4 times for low head condition. All the experimental conditions have low head ($H/P < 0.1$); hence,

Table 2 Correlation matrix of weir coefficient with observed head and discharge

	HWC10	HWC11	HWC12	HWC13	HWC14	HWC15	OH	Q
HWC10	1.00							
HWC11	0.70	1.00						
HWC12	0.51	0.94	1.00					
HWC13	0.55	0.96	0.99	1.00				
HWC14	0.45	0.77	0.59	0.67	1.00			
HWC15	0.90	0.62	0.35	0.43	0.66	1.00		
OH	0.89	0.77	0.53	0.61	0.79	0.96	1.00	
Q	0.87	0.84	0.63	0.70	0.81	0.92	0.99	1.00

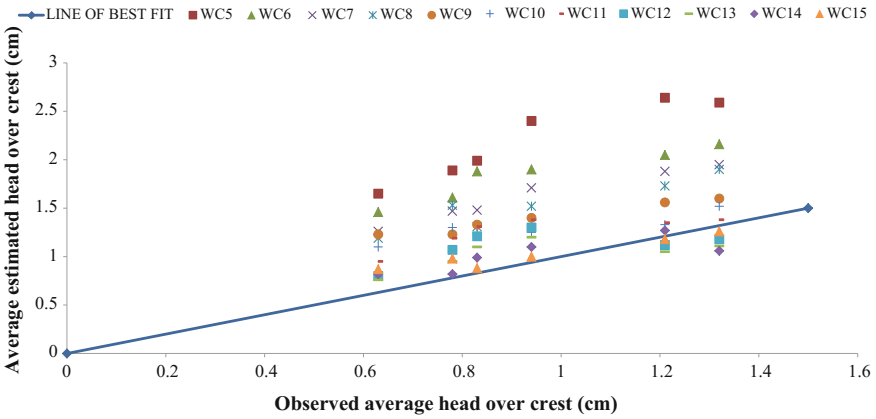

Fig. 14 HEC-RAS model run results over different weir coefficient (WC = weir coefficient in HEC-RAS model)

the experimental condition can be modeled using HEC-RAS. Discharge passing capacity is higher for PKW at specified bed width, hence the weir coefficient is expected to higher than 4. For approximation purpose, authors have considered weir coefficient (WC) in the range of 5–15. After each approximated weir coefficient, every experimental head has been compared with observed one. Using trial-and-error method, authors approximated that weir coefficient is best fitted in the range of 12–15. Where the lower weir coefficient for low H/P ratio (<0.07) and when H/P ratio is near 0.1 than weir coefficient can be approximated as 15. In between the value may be taken as average.

Table 2 represents the efficiency of head estimation under different weir coefficient (under HEC-RAS Environment) with the observed head. Table 2 also shows that the observed discharges and heads have higher efficiency with weir coefficient 10 and 15. Weir coefficient 10 is best fitted for low H/P ratio, and weir coefficient 15 is best fitted for relatively higher H/P ratio. Estimated head over crest through different weir coefficient is presented in Fig. 14.

7 Conclusions

Piano Key Weir technology has enhanced discharge capacity (of same width weir) due to its increased crest length and it has been investigated for their head over crest for different discharge conditions. As head over crest has an important consideration from upstream submergence point of view. Simple empirical equation has been established between average head over crest and discharge, which can be applied to estimate the discharge if total cycle length and width of the channel is known. This empirical study is limited to the lower head conditions ($H/P < 0.1$) only and may be further generalized using high head conditions ($H/P > 0.1$). Further, mathematical model is created using HEC-RAS and discharge coefficient has been calibrated and then validated for PKW. For the design discharge, average head over crest can be easily estimated using HEC-RAS. This discharge coefficient is also helpful to optimize width and height of weir. Discharge coefficient has been estimated in the range of 10–15 and maximum efficiency of the coefficient in between 14 and 15.

Acknowledgements Authors acknowledge IIT Roorkee, MHRD and concerned authority who provided the continuous support for the study. Authors also acknowledge the anonyms reviewers for their inputs.

References

1. GoI, National Register of Large Dams C. W. Commission, Ed., New Delhi, 2015
2. Khatsuria, R.M.: Hydraulics of Spillways and Energy Dissipators, CRC Press (2004)
3. Anderson, R.M.: Piano Key Weir Head Discharge Relationships (2011)
4. Kabiri-Samani, A., Javaheri, A.: Discharge coefficients for free and submerged flow over Piano Key weirs. J. Hydraul. Res. **50**, 114–120 (2012)
5. Machiels, O., Erpicum, S., Dewals, B.J., Archambeau, P., Pirotton, M.: Experimental observation of flow characteristics over a Piano Key Weir. J. Hydraul. Res. **49**, 359–366 (2011)
6. Ribeiro, M.L., Pfister, M., Schleiss, A.J., Boillat, J.-L.: Hydraulic design of A-type piano key weirs. J. Hydraul. Res. **50**, 400–408 (2012)
7. Sharma, N., Tiwari, H.: Experimental study on vertical velocity and submergence depth near Piano Key Weir. In: Labyrinth and Piano Key Weirs II-PKW, pp. 93–100 (2013)
8. Pralong, J., Vermeulen, J., Blancher, B., Laugier, F., Erpicum, S., Machiels, O., et al.: A naming convention for the Piano Key Weirs geometrical parameters. In: Labyrinth and Piano Key Weirs-PKW 2011, pp. 271–278 (2011)
9. Erpicum, S., Machiels, O., Dewals, B., Pirotton, M., Archambeau, P.: Numerical and physical hydraulic modelling of Piano Key Weirs. In: Proceedings of the 4th International Conferonce on Water Resources and Renewable Energy Development in Asia, (2012)
10. Leite Ribeiro, M., Bieri, M., Boillat, J.-L., Schleiss, A., Delorme, F., Laugier, F.: Hydraulic capacity improvement of existing spillways–design of a piano key weirs. In: Proceedings (on CD) of the 23rd Congress of the International Commission on Large Dams CIGB-ICOLD, pp. 100–118 (2009)
11. Tiwari, H., Sharma, N.: Turbulent kinetic energy in the upstream of Piano Key Weir. Arab. J. Sci. Eng. 1–6 (2016)

12. Tiwari, H., Sharma, N.: Nonlinear and entropic velocity distribution in open channel. ISH J. Hydraul. Eng. **22**, 163–172 (2016)
13. Abrari, L., Talebbeydokhti, N., Sahraei, S.: Investigation of hydraulic performance of piano shaped weirs using three dimensional numerical modeling. Iran. J.Sci. Technol. Trans Civ. Eng. **39**, 539–558 (2015)
14. Cicero, G., Delisle, J., Lefebvre, V., Vermeulen, J.: Experimental and numerical study of the hydraulic performance of a trapezoidal Piano Key weir. In: Labyrinth and Piano Key Weirs II, p. 265 (2013)
15. Erpicum, S., Nagel, V., Laugier, F.: Piano Key Weir design study at Raviege dam. In: Proceedings of 1st International Workshop on Labyrinth and Piano Key Weirs, (2011)
16. Tullis, J.P., Amanian, N., Waldron, D.: Design of labyrinth spillways. J. Hydraul. Eng. **121**, 247–255 (1995)
17. Anderson, R., Tullis, B.: Piano key weir hydraulics and labyrinth weir comparison. J. Irrig. Drain. Eng. **139**, 246–253 (2012)
18. Tiwari, H., Sharma, N.: Statistical Study of turbulence near piano key weir: a review. J. Exp. Appl. Mech. **5**, 16–28 (2014)
19. Tiwari, H., Sharma, N.: Turbulence study in the vicinity of piano key weir: relevance, instrumentation, parameters and methods. Appl. Water Sci. 1–10 (2015)
20. Wright, J.D., Baas, J.H.: Despiking ultrasonic doppler velocity-profiling data. J. Sediment. Res. **83**, 955–962 (2013)
21. Mori, N., Suzuki, T., Kakuno, S.: Experimental study of air bubbles and turbulence characteristics in the surf zone. J. Geophys. Res. Oceans **112** (2007)
22. Latosinski, F.G., Szupiany, R.N., García, C.M., Guerrero, M., Amsler, M.L.: Estimation of concentration and load of suspended bed sediment in a large river by means of acoustic Doppler technology. J. Hydraul. Eng. **140**, 04014023 (2014)
23. Ouamane, A., Lempérière, F.: Design of a new economic shape of weir. In: Proceedings of the International Symposium on Dams in the Societies of the 21st Century, pp. 463–470 (2006)
24. Machiels, O., Erpicum, S., Archambeau, P., Dewals, B., Pirotton, M.: Piano Key Weirs, experimental study of an efficient solution for rehabilitation. In: Proceedings of FRIAR 2010, (2010)
25. Machiels, O., Erpicum, S., Archambeau, P., Dewals, B., Pirotton, M.: Experimental study of the alveoli widths influence on the release capacity of Piano Key Weirs. In: Houille Blanche-Revue Internationale de l eau, pp. 22–28 (2010)
26. Machiels, O., Erpicum, S., Pirotton, M., Dewals, B., Archambeau, P.: Experimental analysis of PKW hydraulic performance and geometric parameters optimum. In: Proceedings of International Workshop on Piano Key Weir for In-stream Storage and Dam Safety-PKWISD-2012, pp. 97–114 (2012)
27. Jayatillake, H., Perera, K.: Design of a Piano-Key Weir for Giritale Dam spillway in Sri Lanka. In: Labyrinth and Piano Key Weirs II, p. 151 (2013)
28. Leite Ribeiro, M., Bieri, M., Boillat, J.-L., Schleiss, A., Singhal, G., Sharma, N.: Discharge capacity of piano key weirs. J. Hydraul. Eng. **138**, 199–203 (2011)
29. Khanh, M.H.T.: Utilization of Piano Key Weirs for low barrages. In: Proceeding of Hydro 2012, (2012)
30. Chi Hien, T., Thanh Son, H., Ho Ta Khanh, M.: Results of some 'piano keys' weir hydraulic model tests in Vietnam. In: Proceeding of 22nd International Congress of Large Dams, Question 87, Response 39, pp. 581–595 (2006)
31. Khanh, H.T.M., Hien, T.C., Quat, D,S.: (2012) Research and development of PK Weirs in Vietnam since, pp. 91–96 (2004)
32. Badr, K., Mowla, D.: Development of rectangular broad-crested weirs for flow characteristics and discharge measurement. KSCE J. Civ. Eng. **19**, 136–141 (2015)

Identification of Causes of Failure of Downstream Block Protection for Singanpore Weir-Cum-Causeway, Surat

Priyank J. Sharma, S.V. Chethan, P.V. Timbadiya and P.L. Patel

Abstract The Singanpore weir was constructed across the Tapi River in the year 1995 which connects Singanpore village and Rander area of Surat (Gujarat). Ever since its construction, recurring damages were observed in the first span (Ch. 40–310 m) of the weir. Further, significant damages were reported during recent floods in the years 2013 and 2014, wherein substantial scouring and settlement of the concrete blocks were observed, which eventually posed a threat to the main structure of the weir. It is important to ascertain the causes of failure of the first span of the weir as it serves as the only source of freshwater for citizens of Surat city. The hydraulics of flow during high and low discharges over the weir has been analyzed and reported in detail in this paper. It is found that repelled hydraulic jump conditions prevailed at lower discharges (<4000 m^3/s), due to deficient tail water conditions, which was the major cause of failure of downstream block protection in the first span of the weir. The present study is important for the rehabilitation of block protection of the first span and to carry out suitable remedial measures in the future.

Keywords Flood damages · Block protection failure · Hydraulic jump · Singanpore weir-cum-causeway

1 Introduction

The Singanpore weir was constructed across the Tapi River in 1995 between Singanpore village and Rander, Surat (Gujarat), that serves a causeway and created a freshwater reservoir of 31.0 MCM at +5.00 m above mean sea level (http://www.suratmunicipal.gov.in). The weir was constructed by Surat Municipal Corporation (SMC) to serve two purposes, namely (a) to provide a standing pool of water over

P.J. Sharma (✉) · S.V. Chethan · P.V. Timbadiya · P.L. Patel
Centre of Excellence on Water Resources and Flood Management, Department of Civil Engineering, Sardar Vallabhbhai National Institute of Technology Surat, Surat 395007, India
e-mail: pjs230688@gmail.com

V. Garg et al. (eds.), *Development of Water Resources in India*,
Water Science and Technology Library 75, DOI 10.1007/978-3-319-55125-8_30

Photo 1 Damaged portion of the first span (Ch. 40–310 m) at downstream of Singanpore weir, Surat

infiltration wells of Varachha water works and (b) to provide a surface and sub-surface barrier to prevent tidal water from entering into infiltration well areas. The Singanpore weir-cum-causeway was designed for a design discharge of 50-year return period of 24,000 m^3/s (≈8.47 lakh cusecs) as recommended by Central Design Organization (CDO), Gandhinagar [3]. The weir is divided into three spans, viz. (i) ungated weir first span from Ch. 40 to 310 m, (ii) ungated weir second span from Ch. 310 to 522 m, and (iii) gated under sluice third span from Ch. 522 to 620 m. It was also inferred from model studies that a concentration factor of 10% has to be accounted in calculations of hydraulic jump of the first span of the weir (Ch. 40–310 m). The severe nature of settlement was reported in the first span (Ch. 40–310 m) of the cement concrete blocks, and failure of toe wall resulted in gully or channel formation, see Photos 1 and 2. It is clearly evident that there is significant scouring downstream, and the heavy concrete blocks were dislodged from their mean position on account of enormous disturbance (velocity) in the flow. The present study investigates the likely causes of the failure/disturbance of downstream block protection of the first span (Ch. 40–310 m) of the weir through detailed hydraulic analyses.

2 Data Collection and Methodology

The data required for conducting hydraulic jump analysis at different discharges were collected from the Hydraulic Department, Surat Municipal Corporation (SMC), Surat (Gujarat). The data include the salient features of the weir, upstream (u/s) and downstream (d/s) water level at different discharges, existing weir geometry, bathymetry upstream and downstream of weir, and soil survey. The

Photo 2 Displacement of concrete blocks from its mean position of the first span (Ch. 40–310 m) at downstream of Singanpore weir, Surat

details provided by SMC reflect the fact that since the construction of weir in 1995, on several occasions, minor or major weir restoration works have been undertaken. The methodology adopted in the present study to identify the failure of concrete blocks and loose stone protection of the first span (Ch. 40–310 m) of the weir is described in Fig. 1.

3 Hydraulic Jump Analyses and Results

The detailed hydraulic analyses for existing weir portion for the first span (Ch. 40–310 m) have been carried out at different discharge conditions and investigated the likely causes of damage to the downstream concrete block and launching apron. In the present study, the tidal effect in tail water level is not considered (i.e., the critical condition) for hydraulic jump computations [1]. The first span of the weir ranges from Ch. 40 to 310 m and has a total length of 270 m. Both upstream and downstream concrete floors are at RL + 3.0 m.

From the detailed hydraulic jump analyses, as shown in Table 1, it is observed that for discharges greater than 4000 m^3/s, the hydraulic jump formation takes place within the concrete floor due to sufficiency of tail water depth. However, at lower discharges (<4000 m^3/s), the available tail water depth is not enough for the formation of the jump within the concrete floor. The jump is formed at a point where the flow depth meets the criteria of conjugate with available tail water depth, and before that, there will be the formation of a GVF profile. The Manning's roughness

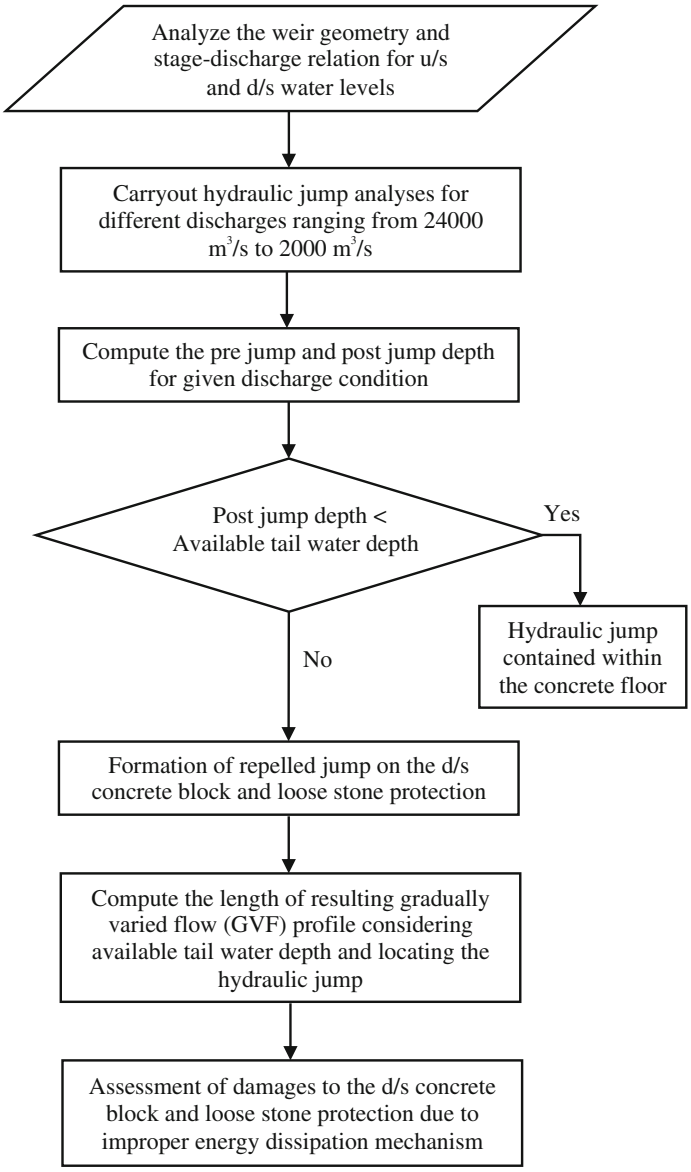

Fig. 1 Methodology adopted in the present study

coefficient (n) for the calculation of length of GVF profile using Chow's method was taken as 0.015; as the concrete surface is expected to be not very smooth due to deposition of sediments undertidal actions. Figure 2 shows that as discharge reduces, the hydraulic jump formation does not take place at the toe of weir and gets shifted further downstream, i.e., for discharges less than 4000 m^3/s, it is found that

Table 1 Summary for hydraulic jump computations at different discharges for the first span of weir (Ch. 40–310 m)

Description	Symbol	Unit	Different discharge conditions					
Total discharge	Q	m^3/s	24000	6000	5000	4000	3000	2000
HFL (U/s—computed)	H_u	m	14.25	9.15	8.66	8.31	7.82	7.22
D/s TWL without retrogression	H_{d1}	m	12.65	7.38	6.65	5.98	5.01	3.84
D/s TWL with retrogression	H_{d2}	m	12.45	7.18	6.55	5.88	4.91	3.74
Head over the crest	H_0	m	7.9	2.8	2.31	1.96	1.47	0.87
Discharge through under sluices	Q_{sluice}	m^3/s	2022	1472	1408	1361	1291	1200
Discharge through weir portion	Q_{weir}	m^3/s	21978	4528	3592	2639	1709	800
Discharge intensity	q	$m^3/s/m$	41.68	8.59	6.81	5.01	3.24	1.52
Critical depth	y_c	m	5.62	1.96	1.68	1.37	1.02	0.62
Depth of flow at u/s section	D_1	m	11.25	6.15	5.66	5.31	4.82	4.22
Depth of flow at d/s section	D_2	m	9.65	4.38	3.65	2.98	2.01	0.84
Head loss	E_L or H_L	m	1.35	1.67	1.91	2.23	2.70	3.22
Pre-jump depth	y_1	m	3.36	0.89	0.71	0.54	0.37	0.19
Post-jump depth	y_2	m	**8.72**	**3.69**	**3.30**	**2.81**	**2.23**	**1.47**
Tail water depth available	*TWD*	m	**9.45**	**4.18**	**3.55**	**2.88**	**1.91**	**0.74**
Whether repelled hydraulic jump forms on concrete block and launching apron?	–	–	**No**	**No**	**No**	**No**	**Yes**	**Yes**
Pre-jump Froude number	F_1	–	2.16	3.26	3.60	3.99	–	–
Post-jump Froude number	F_2	–	0.52	0.39	0.36	0.34	–	–
Height of jump	H_j	m	5.36	2.80	2.58	2.26	–	–
Length of jump	L_j	m	26.82	13.99	12.91	11.31	–	–
Energy dissipation	E_L/E_{f1}	%	12.00	29.78	35.16	42.92	–	–
Level of jump = d/s TEL − Ef_2	–	m	3.71	3.62	3.31	3.16	–	–
Location of beginning of jump from the toe	–	m	2.14	1.86	0.94	0.47	–	–
Back-computations								
Taking TWL as y_2'	y_2'	m	–	–	–	–	1.91	0.74
Post-jump Froude number	F_2'	–	–	–	–	–	0.39	0.76

(continued)

Table 1 (continued)

Description	Symbol	Unit	Different discharge conditions					
Total discharge	Q	m^3/s	24000	6000	5000	4000	3000	2000
Corresponding conjugate depth	y_1'	m	–	–	–	–	0.47	0.51
Pre-jump Froude number	F_1'	–	–	–	–	–	3.20	1.34
Height of jump	H_j	m	–	–	–	–	1.44	0.23
Length of jump	L_j	m	–	–	–	–	7.20	1.16
Length of GVF profile—Chow's method [2]								
Manning's coefficient	n	–	–	–	–	–	0.015	0.015
Critical slope	S_c	–	–	–	–	–	0.0022	0.0026
Hydraulic exponent for critical flow	M	–	–	–	–	–	3.00	3.00
Hydraulic exponent for uniform flow	N	–	–	–	–	–	3.33	3.33
p at y_1	p_1	–	–	–	–	–	0.26	0.21
p at y_1'	p_2	–	–	–	–	–	0.46	0.82
Length for y_1	x_1	m	–	–	–	–	57.81	21.86
Length for y_1'	x_2	m	–	–	–	–	120.77	114.08
Length of surface profile	Δx	m	–	–	–	–	62.96	92.22
Actual length of concrete floor provided	L_{act}	m	–	–	–	–	27.00	27.00

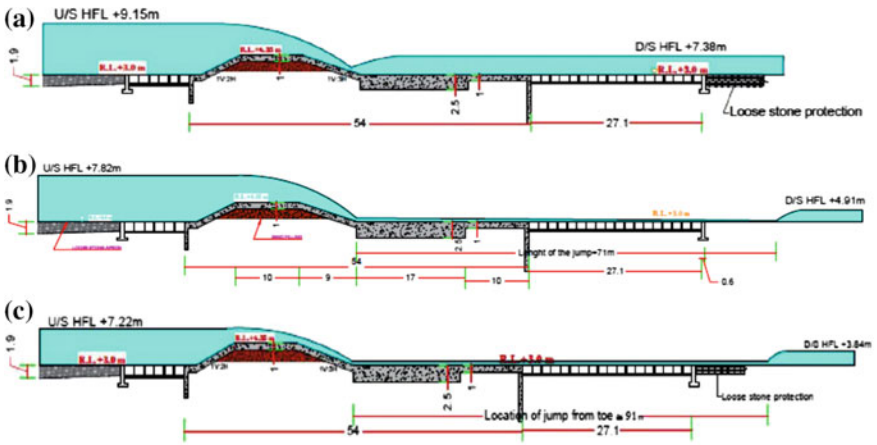

Fig. 2 Hydraulic jump formation for the first span of weir (Ch. 40–310 m) for discharges **a** 6000 m^3/s, **b** 3000 m^3/s, and **c** 2000 m^3/s

the jump gets shifted from concrete floor to the block protection and further downstream in the river bed. Due to this, the energy dissipation does not take place on the concrete floor, and thus, there is scouring of the soil underneath the concrete blocks.

Further, the toe wall was found broken due to flow concentration in the gully or channel (as shown in Photo 1). Also the loose stone protection exhibited substantial settlement due to scouring of soil under the protection work. If the foregoing condition persists for a longer duration, it would result in severe degradation immediately downstream of the weir. It is also found that 60% of time the discharge was observed to be less than 4000 m^3/s during the flood of 2013, wherein significant damage was reported to the weir. Thus, the analysis of hydraulic jumps on existing geometry of weir for Ch. 40–310 m indicated the persistence of repelled hydraulic jump condition at lower discharges (deficient tail water condition) which was the major reason for dislodging and settlement of downstream concrete block and loose stone protection of the weir.

4 Conclusions

The following key conclusions can be summarized on the basis of study undertaken in the present paper:

(i) The analysis of hydraulic jump for the first span of Singanpore weir (Ch. 40–310 m) revealed that, for lower discharges, i.e., less than 4000 m^3/s, there was shifting of hydraulic jump in the downstream of concrete floor. At discharge 2000 m^3/s, there is a significant shifting of jump, even beyond the loose stone protection. The shifting of hydraulic jump for lower discharges is due to deficient tail water condition in the river under these discharges. The formation of hydraulic jump on launching apron/concrete block at lower discharges is the prime reason for failure of protection works.

(ii) The observation of previous flow data for the year 2013 corroborates the findings in the present investigation. The observed data statistics revealed that 60% of time the discharge was observed to be less than 4000 m^3/s (which is the critical limit for the formation of hydraulic jump within the concrete floor). Hence, the persistence of low discharges over the weir for a longer time would be the possible cause of maximum damage of downstream concrete blocks and protection works.

Acknowledgements The first author wishes to acknowledge the financial support received from Department of Science and Technology (DST), Ministry of Science and Technology, Government of India, vide their letter no. DST/INSPIRE Fellowship/2015/IF150634 dated January 11, 2016. The authors are also thankful to Centre of Excellence (CoE) on "Water Resources and Flood Management," TEQIP-II, Ministry of Human Resources Development (MHRD), Government of India, for providing necessary infrastructural support for conducting the study reported in the paper. The authors are also thankful to Surat Municipal Corporation (SMC) for providing necessary data for conducting the study.

References

1. Asawa, G.L.: Irrigation and Water Resources Engineering. New Age International Ltd. Publishers, New Delhi (2005)
2. Chow, V.T.: Open Channel Hydraulics. McGraw-Hill, New Delhi (1959)
3. SMC: Project Report-Singanpore Weir Project, Surat (1993)
4. http://www.suratmunicipal.gov.in. Accessed 15 May 2016

Flow over Sharp-Crested Trapezoidal Planform Weirs

Keerat Kumar Gupta and Sanjeev Kumar

Abstract The most common structure for discharge measurement in streams is a weir. Generally, they are used as normal weirs which allow water to pass gradually over their crest, causing submergence due to afflux at upstream. For passing more discharge with low head, the weirs of different planforms were recommended to improve their discharge capability with minimum head and to limit the afflux. The present study has been carried out to investigate the discharge characteristics of trapezoidal planform weirs. The weirs efficiency is found better than the normal weir. A discharge equation has been proposed and found that it is calculating the discharge within ±5% as compared with observed discharge. The weir sensitivity which is discharge variation because of change in per unit head over the crest is also analyzed and found that the sensitivity is more at the low head over the weir and higher length-to-width ratio.

Keywords Trapezoidal planform weir · Flow measurement · Discharge coefficient · Open channel

1 Introduction

A weir is constructed across a watercourse to raise the upstream water level and hence to permit the surplus water to flow over its full crest length to the downstream side. Conventional weirs cause afflux and result in the submergence of upstream area. A lot of different planform weirs such as slanting, Duckwill, diagonal and Labyrinth weirs were recommended in the past to improve their discharging capability and to control the afflux.

K.K. Gupta (✉) · S. Kumar
Civil Engineering Department, Graphic Era University, Dehradun 248002, India
e-mail: guptak.k@rediffmail.com

S. Kumar
e-mail: er.sanjeevkr@gmail.com

V. Garg et al. (eds.), *Development of Water Resources in India*,
Water Science and Technology Library 75, DOI 10.1007/978-3-319-55125-8_31

Labyrinth weirs are zigzag in plan and hence offer a longer crest compared to a conventional weir having the same width for enhancing the flow with given working head. Since labyrinth weirs passes large flood at a comparatively low head, therefore, they are widely used to minimize inundation.

Discharge (Q) over a weir having sharp crest in a rectangular channel can be written as

$$Q = \frac{2}{3} C_d \sqrt{2g} L H^{\frac{3}{2}} \tag{1}$$

where C_d = discharge coefficient, L = length of the crest, g = gravitational acceleration, H = head over the weir. The discharge characteristics as well as channel and the weir geometry affect C_d.

A lot of planforms of labyrinth weirs are used nowadays. According to the requirement, these weirs may be sharp or broad-crested and of one or many folds in plan. Taylor [1] did an extensive study about the performance of the labyrinth weirs and produced his results in terms of a magnification ratio, i.e., ratio between discharges over labyrinth and conventional weirs for the identical head over the weir. Hay and Taylor [2, 3] tested a variety of shapes of labyrinth weirs and presented the outcomes in graphical form between the ratio of discharge (Q) over labyrinth to consequent conventional weir (Q_n) and H/P, where P = weir height. They established that the triangular labyrinth weir is more effective than the trapezoidal labyrinth weir.

Tullis et al. [4] investigated trapezoidal-shaped labyrinth weirs and proposed a relationship for design of that weir. Their finding shows that the discharge over a labyrinth weir depends on the total head, the length of the crest and the discharge coefficient. The discharge coefficient is function of height of the weir, total head, wall thickness, shape of the crest, configuration of vertex and the side walls angle. Tullis et al. [5] did experimental study on three labyrinth weirs having submerged condition and on various configurations with half-round crest. Using the dimensionless submerged head parameters, they studied the submerged labyrinth weir head–discharge relationship and found that it is not dependent on sidewall angles of the weir. Francesco et al. [6] studied the outflow procedure for a triangular labyrinth weir having sharp crest and concluded that the flow magnification is affected by either the length magnification ratio or head-to-one cycle width ratio.

Using dimensional analysis, Ghodsian [7] proposed an equation for discharge over a triangular planform weir as:

$$Q = \left[0.703 \left(\frac{H}{P} \right)^{0.928} \left(\frac{l}{w} \right)^{-0.383} P \right]^{\frac{3}{2}} g^{\frac{1}{2}} L \tag{2}$$

where l is one cycle length of labyrinth weir and w is width of a cycle. Gupta et al. [8–10] did experimental studies of various planforms labyrinth weirs.

Under free flow conditions, Kumar et al. [11, 12] conducted experimental study in a rectangular channel to explore the discharging capability of triangular and curved plan form weirs having sharp crest. They found that the effectiveness of these weirs is better than the conventional weir. A generalized equation of C_d for the triangular planform weir was proposed by Kumar et al. [11] as

$$C_d = \left(-0.065\theta^3 + 0.318\theta^2 - 0.537\theta + 1.190\right) + \left[\left(0.09\theta^3 - 0.57\theta^2 + 1.46\theta - 1.67\right)\left(\frac{H}{P}\right)\right] \quad (3)$$

This paper deals with the results of the experimental study in a rectangular flume about the characteristics of discharge for a trapezoidal planform weir having sharp crest with free flow condition. It is aimed that while keeping the head of water same, the trapezoidal planform weir shall pass more discharge compared to conventional weir.

2 Materials and Methods

2.1 Experimental Setup and Procedure

The experiments have been performed in a rectangular tilting flume of length 5.360 m, width (B) 0.245 m and depth 0.450 m in the hydraulics laboratory of Graphic Era University, Dehradun, India. The sharp-crested trapezoidal planform weirs were made by mild steel plates and were installed at 5.150 m downside from the entrance of the flume. Head of water has been measured using the point gauge of accuracy ±0.1 mm and discharge by means of an orifice meter provided in the supply pipe. Regulating gate and wave suppressors were located at the starting of the flume to control the discharge and to disperse the instability at the surface, respectively.

The experimentation was carried out for weirs of L/B ratios = 1.000, 1.023, 1.069, 1.140, 1.245, 1.397, 1.623 and 1.976 and for each L/B ratio for different discharges. Figure 1 shows the descriptive diagram of a sharp-crested trapezoidal planform weir, while Fig. 2 shows the outline of the setup for experiment. For every run, head was measured at a distance of about 4–5 times the head in the upstream side of the weir using pointer gage to avoid the curvature effect. Table 1 presents the ranges of the collected data in the present investigation.

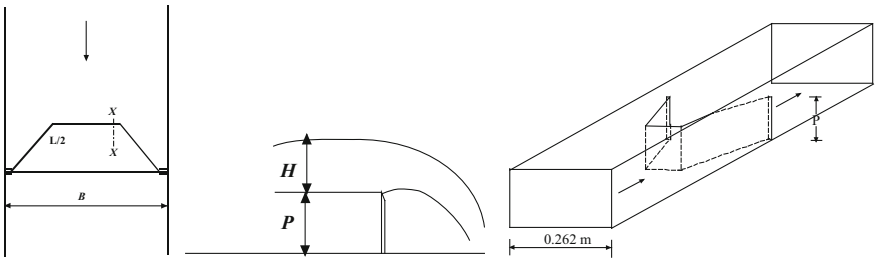

Fig. 1 Definition sketch of sharp-crested trapezoidal planform weir

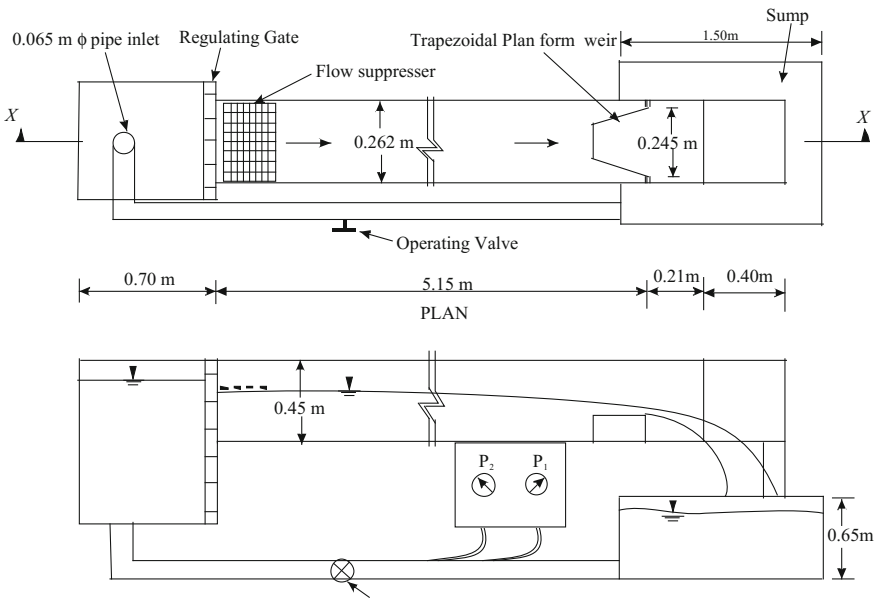

Fig. 2 Layout of the setup for experiment

Table 1 Range of parameters for trapezoidal planform weirs

S. no.	*L*/*B*	*P* (m)	*H* (m)	$Q_{observed}$ (m^3/s)	No. of runs
1	1.000	0.10	0.0319–0.0761	0.0022–0.0091	10
2	1.023	0.10	0.0416–0.0862	0.0038–0.0108	12
3	1.069	0.10	0.0345–0.0864	0.0031–0.0108	13
4	1.140	0.10	0.0327–0.0857	0.0031–0.0110	14
5	1.245	0.10	0.0356–0.0757	0.0038–0.0101	12
6	1.397	0.10	0.0327–0.0717	0.0038–0.0101	12
7	1.623	0.10	0.0250–0.0690	0.0031–0.0108	12
8	1.976	0.10	0.0255–0.0636	0.0038–0.0110	13

3 Results and Analysis

The collected data in the present investigation are analyzed to find the functional equation of discharge coefficient for every used trapezoidal planform weirs in a free flow situation in terms of Rehbock's [13] equation, i.e.,

$$C_d = a + b\left(\frac{H}{P}\right) \tag{4}$$

Here, a and b are the coefficients to be found using experimental data. The most general values for these coefficients are proposed by Rehbock as $a = 0.611$ and $b = 0.075$ for sharp-crested normal weir.

Figure 3 shows the graph between observed discharge and head for the trapezoidal planform weirs of different L/B ratios. Every plot is found curvilinear and co-focal. Figure 3 signifies that for the identical value of H, Q increases with the increase in L/B ratio because of increased crest length of the weir. For every data set, the C_d was calculated using Eq. (1) for known value of Q, H and L for weirs of different L/B ratios.

Figure 4 presents the graph of C_d versus H/P for the weirs of various L/B ratios. It was found that C_d reduces with higher range of L/B ratio because of intervention of nappe for larger range of H/P. For the less value of H/P, the intervention of nappe is not much, causing high value of C_d. The value of C_d reduces with the increase in H/P for different L/B ratios, and for $L/B = 1.0$, i.e., the conventional weir, the C_d increases with H/P, which shows the similarity as per the Rehbock's [13] equation.

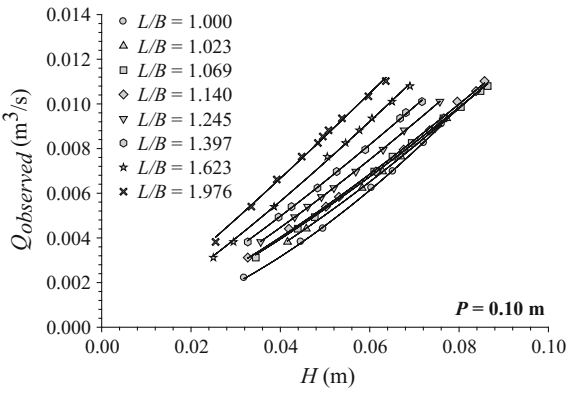

Fig. 3 Variation of $Q_{observed}$ with H for weirs of different L/B ratios

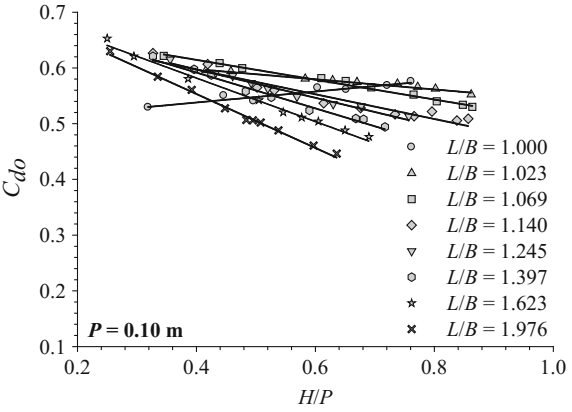

Fig. 4 Variation of C_d with H/P for weirs of different L/B ratios

3.1 Generalized Equation of Discharge for Trapezoidal Planform Weir

As per Rehbock [13], the relation of C_d with H/P followed the linear equations as follows:

$$C_d = 0.50 + 0.10(H/P) \quad \text{For } L/B = 1.000 \quad R^2 = 0.90 \tag{5a}$$

$$C_d = 0.64 - 0.10\,(H/P) \quad \text{For } L/B = 1.023 \quad R^2 = 0.97 \tag{5b}$$

$$C_d = 0.69 - 0.18(H/P) \quad \text{For } L/B = 1.069 \quad R^2 = 0.98 \tag{5c}$$

$$C_d = 0.69 - 0.22(H/P) \quad \text{For } L/B = 1.140 \quad R^2 = 0.93 \tag{5d}$$

$$C_d = 0.70 - 0.26(H/P) \quad \text{For } L/B = 1.245 \quad R^2 = 0.97 \tag{5e}$$

$$C_d = 0.72 - 0.32(H/P) \quad \text{For } L/B = 1.397 \quad R^2 = 0.98 \tag{5f}$$

$$C_d = 0.74 - 0.39(H/P) \quad \text{For } L/B = 1.623 \quad R^2 = 0.99 \tag{5g}$$

$$C_d = 0.75 - 0.49(H/P) \quad \text{For } L/B = 1.976 \quad R^2 = 0.97 \tag{5h}$$

A strong correlation between C_d and H/P was found for entire weirs. The graph of 'a' and 'b' with L/B ratios is plotted and presented in Fig. 5. A fourth-order polynomial was found suitable for 'a' and 'b' as follows:

$$a = -06.96\left(\frac{L}{B}\right)^4 + 41.64\left(\frac{L}{B}\right)^3 - 92.04\left(\frac{L}{B}\right)^2 + 89.15\left(\frac{L}{B}\right) - 31.25, \quad R^2 = 0.86 \tag{6a}$$

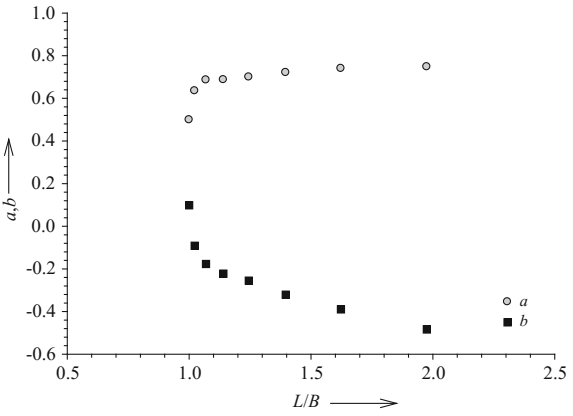

Fig. 5 Variation of '*a*' and '*b*' with *L/B*

$$b = 09.83\left(\frac{L}{B}\right)^4 - 59.07\left(\frac{L}{B}\right)^3 + 131.20\left(\frac{L}{B}\right)^2 - 127.97\left(\frac{L}{B}\right) + 46.05, \quad R^2 = 0.95 \tag{6b}$$

From total 98 data sets for trapezoidal planform weirs, 74 data sets have been utilized to generate the equation for discharge coefficient. The generated equation of C_d may be written as:

$$C_d = \left(-06.96\left(\frac{L}{B}\right)^4 + 41.64\left(\frac{L}{B}\right)^3 - 92.04\left(\frac{L}{B}\right)^2 + 89.15\left(\frac{L}{B}\right) - 31.25\right) + \left(09.83\left(\frac{L}{B}\right)^4 - 59.07\left(\frac{L}{B}\right)^3 + 131.20\left(\frac{L}{B}\right)^2 - 127.97\left(\frac{L}{B}\right) + 46.05\right)\left(\frac{H}{P}\right) \tag{7}$$

The above equation is applicable for the range $0 < H/P < 0.86$ and $1.000 \leq L/B \leq 1.976$.

3.2 *Verification for the Equation of Discharge*

The unused 24 data sets have been utilized to verify the proposed equation for C_d, i.e., Eq. (7). The discharge calculated using proposed equation has been compared with the consequent observed discharge as shown in Fig. 6, which indicates that the $Q_{calculated}$ varies between ±5% of the $Q_{observed}$ for the all the weirs studied herein.

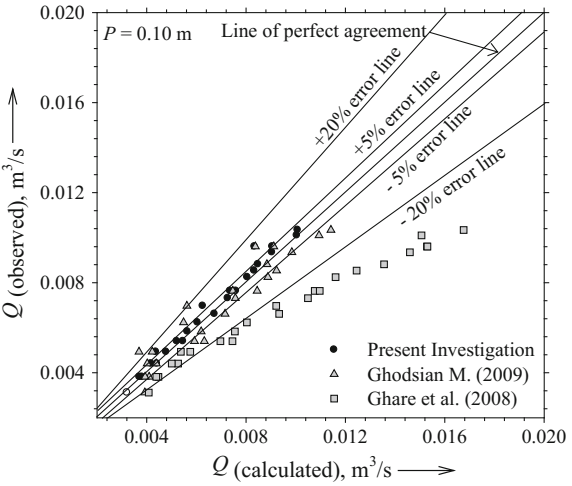

Fig. 6 Verification of $Q_{calculated}$ using Eqs. (2, 6a, 6b, 8 and 9) with $Q_{observed}$

An average percentage error (e) between observed and calculated discharge is given by Ghodsian [14] as:

$$e = \frac{100}{N}\sum_{i=1}^{N}\left[\frac{Q_{computed} - Q_{observed}}{Q_{observed}}\right] \tag{8}$$

The average % error in the discharge computation using Eqs. (1) and (7) has been found within 0–0.5% for weirs of various L/B ratios.

3.3 *Effectiveness of the Weir*

Keeping the head and weir length constant, more discharge can flow over an effective weir as compared to the other. To study the effectiveness of the trapezoidal planform weir for various L/B ratios, ratio of discharges over the trapezoidal planform weir and conventional weir, i.e., Q/Q_n, is plotted with H/P in Fig. 7.

The effectiveness of trapezoidal planform weir is more for higher L/B ratio and reduces with the increase in H/P because of intervention of the nappe downside of weir. For $H/P = 0.05$, the weirs of L/B ratio 1.023, 1.069, 1.140, 1.245, 1.397, 1.623 and 1.976 are, respectively, 1.64, 2.14, 2.44, 2.82, 3.45, 3.90 and 5.28 times more effective than the conventional weir. But, for $H/P = 1.0$, the effectiveness of trapezoidal planform weir is less, and even for $L/B = 1.976$, the effectiveness is only 1.33 times the conventional weir.

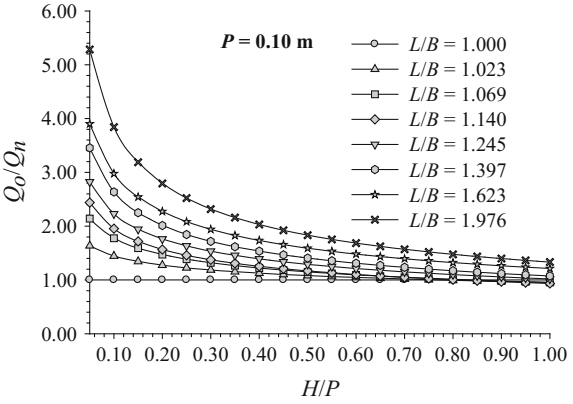

Fig. 7 Variation of Q/Q_n with H/P for the weirs of different L/B ratios

3.4 Sensitivity Analysis of the Trapezoidal Planform Weir

The weir sensitivity which is discharge variation because of change in per unit head over the crest is also analyzed for the recommend discharge equation of the trapezoidal planform weirs, which can be presented as:

$$Q = \frac{2}{3}\left[a + b\left(\frac{H}{P}\right)\right]\sqrt{2g}\,\frac{B}{\sin\frac{\theta}{2}}(H)^{\frac{3}{2}} \tag{9}$$

'a' and 'b' can be calculated from Eqs. (6a) and (6b), respectively. The first derivative of Q with H reduces to:

$$\frac{dQ}{dH} = \frac{3}{2}\frac{Q}{H} + \frac{Qb}{P\left[a + b\left(\frac{H}{P}\right)\right]} \tag{10}$$

The higher value of dQ/dH denotes higher sensitivity. The collected data were utilized to calculate dQ/dH for entire L/B ratio. The graph between dQ/dH and H is presented in Fig. 8 which indicates that the discharge over trapezoidal planform weir is more sensitive for less head over the crest. Moreover, the sensitivity reduces, as the head rises, because of intervention of the nappe downside of the weir. Moreover, sensitivity is more for the higher L/B ratio of the trapezoidal planform weir because of more length of the crest of the weir.

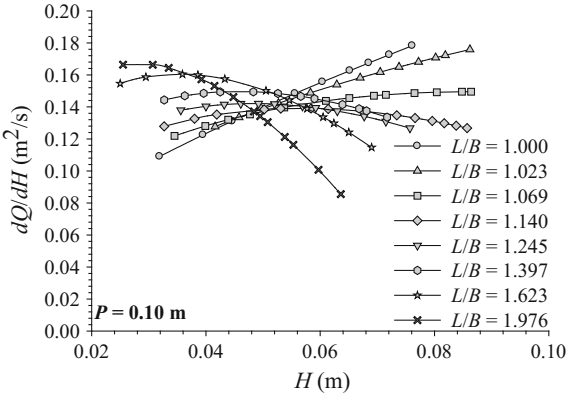

Fig. 8 Sensitivity of the trapezoidal planform weirs as function of head

4 Conclusions

An experimental investigation was performed in a rectangular flume to study the characteristics of discharge of trapezoidal planform weirs having sharp crest with free flow situations. The coefficient of discharge of the trapezoidal planform weir reduces with the increase in *L*/*B* ratio due to intervention of nappe for large value of *H*/*P*. Further, for less values of *H*/*P* and lower values of *L*/*B* ratio, the C_d is high. The calculated *Q* by using Eq. (7) is found within ±5% as compared to observed discharge. The effectiveness of the trapezoidal planform weir is more for higher *L*/*B* ratio and reduces with the increase in *H*/*P* because of intervention of the nappe in the downside of the weir. For *H*/*P* = 0.05, the weirs of *L*/*B* ratio 1.023, 1.069, 1.140, 1.245, 1.397, 1.623 and 1.976 are, respectively, 1.64, 2.14, 2.44, 2.82, 3.45, 3.90 and 5.28 times more effective than the conventional weir. But, for *H*/*P* = 1.0, the effectiveness of trapezoidal planform weir is less for all *L*/*B* ratio. It is found that the discharge over trapezoidal planform weir is much sensitive to the less head and higher *L*/*B* ratio. The sensitivity reduces, as the head rises, because of intervention of the nappe downside of weir.

References

1. Taylor, G.: The performance of labyrinth weir. Ph.D. thesis, University of Nottingham, Nottingham, England (1968)
2. Hay, N., Taylor, G.: A computer model for the determination of the performance of labyrinth weirs. In: 13th Congress of IAHR, Koyoto, Japan, pp. 361–378 (1969)
3. Hay, N., Taylor, G.: Performance of labyrinth weirs. ASCE J. Hydraul. Eng. **96**(11), 2337–2357 (1970)
4. Tullis, B.P., Amanian, N., Waldron, D.: Design of labyrinth spillways. ASCE J. Hydraul. Eng. **121**(3), 247–255 (1995)

5. Tullis, B.P., Young, J.C., Chandler, M.A.: Head-discharge relationships for submerged labyrinth weirs. ASCE J. Hydraul. Eng. **133**(3), 248–253 (2007)
6. Francesco, G.C., Vito, F., Vincenzo, P.: Experimental investigation of the outflow process over a triangular labyrinth weir. ASCE J. Irrig. Drainage **138**(1), 73–79 (2012)
7. Ghodsian, M.: Stage discharge relationship for a triangular labyrinth spillway. Proc. Inst. Civil Eng. Water Manage. **162**(3), 173–178 (2009)
8. Gupta, K.K., Kumar, S., Ahmad, Z.: An approach to analyze the flow characteristics of sharp-crested triangular planform contracted weirs. World Appl. Sci. J. **32**(7), 1311–1317 (2014)
9. Gupta, K.K., Kumar, S., Ahmad, Z.: Discharge characteristics of sharp crested W—planform weir. Dam Eng. J. **26**(1), 1–14 (2015)
10. Gupta, K.K., Kumar, S., Ahmad, Z.: Effect of weir height on flow performance of sharp crested rectangular—planform weir. World Appl. Sci. J. **33**(1), 168–175 (2015)
11. Kumar, S., Ahmad, Z., Mansoor, T.: A new approach to improve the discharging capacity of sharp-crested triangular plan form weirs. J. Meas. Instrum. Elsevier **22**, 175–180 (2011)
12. Kumar, S., Ahmad, Z., Mansoor, T., Himanshu, S.K.: A new approach to analyze the flow over sharp-crested curved plan form weirs. Int. J. Recent Technol. Eng. **2**(1), 24–28 (2013)
13. Rehbock, T.: Discussion of precise weir measurement. In: Schoder, E.W., Turner, K.B. (eds.) ASCE Trans., vol. 93, pp. 1143–1162 (1929)
14. Ghodsian, M.: Flow through side sluice gate. ASCE J. Irrig. Drainage Eng. **129**(6), 458–462 (2003)

Prediction of Local Scour Depth Downstream of an Apron Under Wall Jets

Mohammad Aamir and Zulfequar Ahmad

Abstract An experimental analysis on the development of scour hole downstream of a rigid apron under wall jets coming out from the opening of a sluice gate has been performed, and the results have been presented thereof. The similarity in the scour profiles with time has been shown by plotting the scour profile at different times. Equilibrium/asymptotic scour depth is achieved after 6–8 h for fine sediment, whereas time taken to achieve equilibrium depth of scour is lesser for coarser sediments. Equilibrium depth of scour is observed to decrease with increasing sluice opening and sediment size, whereas a rise in densimetric Froude number increases the maximum depth of scour. Effect of tailwater level on equilibrium scour depth is such that initially there is a decrease in the maximum depth of scour with rising tailwater level, but after a critical level of tailwater, the asymptotic depth of scour increases with increase in tailwater level. A new empirical equation is proposed for prediction of scour downstream of a rigid apron under wall jets.

Keywords Scour · Wall jets · Apron · Sediment transport · Hydraulics

Notation

The following symbols are used in this paper:

a	Sluice opening
D_{50}	Median sediment size
D_{90}	90% finer sediment size
D_{95}	95% finer sediment size
d_s	Depth of maximum scour at equilibrium
d_t	Tailwater depth
F	Jet Froude number
F_d	Particle densimetric Froude number

M. Aamir (✉) · Z. Ahmad
Department of Civil Engineering, Indian Institute of Technology Roorkee, Roorkee 247667, India
e-mail: mohdaamir.amu@gmail.com

V. Garg et al. (eds.), *Development of Water Resources in India*,
Water Science and Technology Library 75, DOI 10.1007/978-3-319-55125-8_32

$F_{d(95)}$ Particle densimetric Froude number based on D_{95}
g Gravitational acceleration
K_L' Factor
L Length of apron downstream of sluice gate
N Number of data
s Specific gravity of sediment particles
V Issuing jet velocity
x_s Distance of maximum scour depth from apron
Y Observed value
Y' Predicted value
Δ $(s - 1)$
σ_g Geometric standard deviation of bed material size
ϕ Angle of repose

1 Introduction

Hydraulic structures cause local scour to occur downstream of them, which is a subject of concern for many researchers due to its importance in defining the safety of such structures. Continuous scouring exposes the foundations of these structures, leading to the threatening of their stability, and hence failure of the hydraulic structure. The phenomenon of scouring downstream of a rigid apron under wall jets starts when the erosive capacity of the jet surpasses the threshold value of bed shear stress for the instigation of motion of sediment. Issuing jet from under the opening of a sluice gate develops into a wall jet as it moves over the rigid apron. It is also known as a two-dimensional (2D) jet since the ratio of its width to thickness is high. As soon as it encounters the erodible bed, the process of scouring is initiated. The erosive capacity of the jet is reduced as it moves further downstream of the erodible bed. Hence, a dune formation takes place at the end of the scour profile. Figure 1 illustrates a definition sketch of the scour hole developed under a wall jet. In this figure, d_s = maximum equilibrium scour depth, x_s = distance to asymptotic depth of scour from the end of rigid apron, x_o = longitudinal extension of scour hole, d_d = height of dune, x_d = distance to maximum height of dune crest from the end of rigid apron, a = sluice opening, V = issuing jet velocity, d_t = tailwater depth, L = length of the rigid apron. Maximum scour depth depends on various parameters, viz. sluice opening, sediment size, jet Froude number and tailwater depth. Since the jet is two dimensional, profile of the scour hole under wall jet is also two dimensional across the width of the flume. Therefore, the figure represents any longitudinal section of the profile of the scour hole.

Many investigators have studied the phenomenon of scour under wall jets, like Valentin [10], Altinbilek and Basmaci [3], Rajaratnam [8], Rajaratnam and Macdougall [9], Chatterjee et al. [4], Lee [6], Aderibigbe and Rajaratnam [2], Lim and Yu [7], Verma and Goel [11], and Dey and Sarkar [5]. Aamir and Ahmad [1]

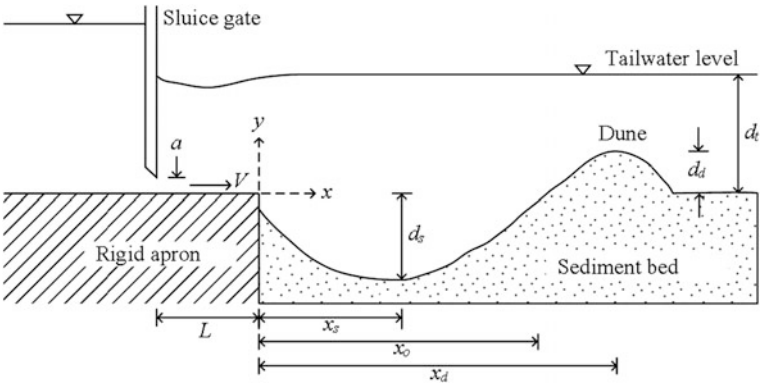

Fig. 1 Definition sketch of developed scour hole under wall jet

have presented an analysis of the existing equations for prediction of maximum scour depth using available laboratory data. In this paper, similarity of profiles of scour at different time intervals has been described. The influence of different parameters like tailwater level, sediment size and densimetric Froude number on maximum scour depth has also been studied. A new empirical equation is proposed for prediction of asymptotic depth of scour downstream of a rigid apron under wall jets.

2 Experimentation

The experimental runs were performed in the Hydraulics Laboratory of the Department of Civil Engineering, Indian Institute of Technology Roorkee, in a flume having glass side walls. The length of the flume was 10 m and its width was 0.6 m, having a depth of 0.54 m. Sluice gate was fixed at a distance of 2 m from the upstream end of the flume. A 0.2-m high rigid concrete apron was constructed with a sediment recess having a thickness of 0.2 and 2 m length. Length of the rigid apron was 0.5 m from the sluice opening. Vertical movement of the sluice gate enabled different sluice openings (a = 5, 10 and 15 mm). Discharge flowing into the flume was measured by an ultrasonic flow meter which was connected to the upstream pipe which discharged water into the flume at the upstream end. A point gauge having a least count of 0.1 mm was deployed to take measurements of the tailwater level. Tailwater level was maintained by a regulating tail gate fixed at the downstream end of the flume. The minimum tailwater level used in the present analysis was so taken that the hydraulic jump is completely submerged, i.e. the minimum tailwater level was kept more than the conjugate depth of hydraulic jump. Scour profiles were measured by pasting a piece of tracing graph paper on the side wall of the flume and marking the temporal variation of the scour profiles with pencil. Minimum grid size on the tracing graph was 1 mm × 1 mm. Since the wall

jet is two dimensional, the scour hole formed under it was also two dimensional, i.e. the profile of the scour hole was uniform across the width of the flume.

The sediment bed was initially covered with waterproof ply board, so as to avoid any undesirable scour before the tailwater level was maintained. Weights were placed over the ply board to prevent its movement due to the intensity of flow over it. When the required tailwater level was reached and maintained, the ply board was gradually removed and the process of scouring started at this point of time. Three different sediment samples were used having a median particle diameter of 0.27, 2.67 and 6.68 mm. Table 1 presents the data for all the experimental runs.

Table 1 Experimental data used in the present analysis

Run	a	V	d_t	D_{50}	F	F_d	d_s
	(mm)	(m/s)	(m)	(mm)			(m)
1A	5	1.67	0.1	0.27	7.53	25.21	0.101
2A	5	1.67	0.125	0.27	7.53	25.21	0.095
3A	5	1.67	0.15	0.27	7.53	25.21	0.101
4A	10	0.83	0.1	0.27	2.66	12.61	0.055
5A	10	0.83	0.125	0.27	2.66	12.61	0.048
6A	10	0.83	0.15	0.27	2.66	12.61	0.049
7A	15	0.56	0.1	0.27	1.45	8.40	0.040
8A	15	0.56	0.125	0.27	1.45	8.40	0.038
9A	15	0.56	0.15	0.27	1.45	8.40	0.039
10B	5	2.67	0.1	6.68	12.04	8.11	0.045
11B	5	2.67	0.125	6.68	12.04	8.11	0.046
12B	5	2.67	0.15	6.68	12.04	8.11	0.049
13B	10	1.33	0.1	6.68	4.26	4.05	0.038
14B	10	1.33	0.125	6.68	4.26	4.05	0.039
15B	10	1.33	0.15	6.68	4.26	4.05	0.042
16B	15	0.89	0.1	6.68	2.32	2.70	0.011
17B	15	0.89	0.125	6.68	2.32	2.70	0.013
18B	15	0.89	0.15	6.68	2.32	2.70	0.016
10C	5	2.67	0.1	2.67	12.04	12.83	0.053
11C	5	2.67	0.125	2.67	12.04	12.83	0.055
12C	5	2.67	0.15	2.67	12.04	12.83	0.060
13C	10	1.33	0.1	2.67	4.26	6.41	0.042
14C	10	1.33	0.125	2.67	4.26	6.41	0.045
15C	10	1.33	0.15	2.67	4.26	6.41	0.047
16C	15	0.89	0.1	2.67	2.32	4.28	0.025
17C	15	0.89	0.125	2.67	2.32	4.28	0.026
18C	15	0.89	0.15	2.67	2.32	4.28	0.029

3 Scour Profiles

The scour hole follows a specific profile at any instant of time as shown in Fig. 2. The sediment removed from the scour hole is deposited in the form of a dune just at the end of the scour hole. The height of the dune is perceived to be slightly less than the maximum depth of scour, which indicates that some amount of sediment is washed away with the flow. The scour profile keeps on changing with time as the dimension of the scour hole increases. Initially, volume of the scour hole increases rapidly with time, but as the scour hole approaches equilibrium state, the rate of change of the profile gets reduced. Also, horizontal advancement of the scour hole is slightly faster than the vertical. It can be further observed in the figure that the maximum scour depth is reached after 5–6 h, but the longitudinal extension of the scour hole keeps on growing with time and the crest of the dune keeps on shifting downstream. However, full equilibrium of the complete scour profile is reached after 7–8 h, and there is hardly any observable change in the scour hole geometry after this. Therefore, each run for finer sediment was carried out for a minimum of 8 h. In case of coarser sediment, time to reach asymptotic scour profile was lesser (about 5–6 h).

The scour profiles may be plotted in non-dimensional form to establish similarity in the scour profiles of different time intervals, as shown in Fig. 3. In these figures, x = streamwise distance from the end of the rigid apron and y = vertical distance from the top surface of the apron, and d_{st} = maximum depth of scour at any time t. A small amount of scour is also observed just at the edge of the rigid apron ($x = 0$), which is the reason for the scour profile not starting at $y = 0$. This small scour could be attributed to the high scouring capacity of the jet at the beginning of the erodible sediment bed. The sediment bed at the end of the scour profile (downstream of the dune) is not disturbed at all as the jet exhausts all of its erosive capacity.

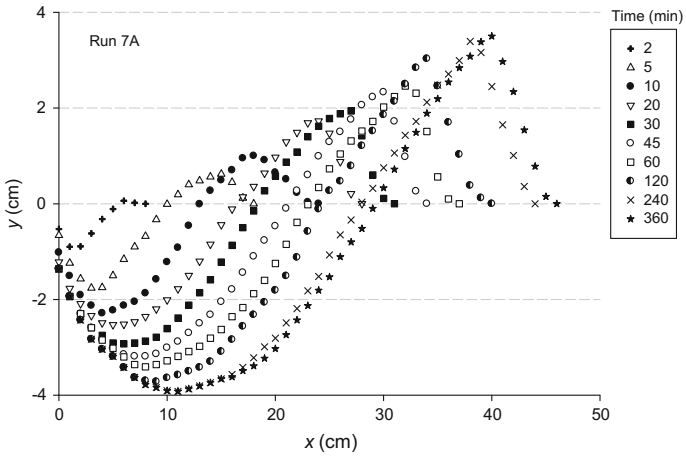

Fig. 2 Scour profiles of Run 7A at different times

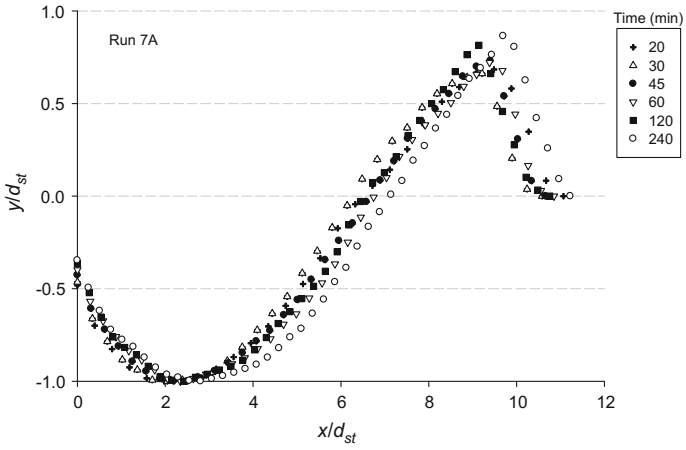

Fig. 3 Scour profiles of Run 7A at different times in non-dimensional form

4 Effects of Different Parameters on Maximum Depth of Scour

Experimental data given in Table 1 are used to examine the effect of several parameters on maximum scour depth. Figure 4 shows the effect of tailwater level/sluice opening ratio on non-dimensional equilibrium scour depth. Close examination of this figure shows that in case of finer sediment, there is a decrease in the scour depth with increasing tailwater level up to a critical tailwater level, after which the scour depth again increases. However, in case of coarser sediment, a continuous increase in the scour depth is observed with increasing tailwater level for the range of values of tailwater level used in the present analysis. For smaller size of sediment, the scour depth is more for the same sluice opening than for larger sediment sizes. Further, the scour depth is more for smaller opening of sluice gate and reduces with rise in sluice opening.

Variation of non-dimensional maximum scour depth with densimetric Froude number F_d for different sediment sizes and sluice openings is shown in Fig. 5. There is an increase in the asymptotic depth of scour with increasing densimetric Froude number. Since F_d is directly proportional to V and inversely proportional to the square root of D_{50}, d_s/a increases with decrease in D_{50} and increase in V. Figure 6 shows the variation of non-dimensional asymptotic depth of scour with D_{50}/a for different tailwater levels and sluice openings. It is evident that d_s/a decreases with increase in D_{50}/a, which means that d_s/a is less for larger sluice opening and relatively coarser sediment since comparatively more critical bed shear stress is required to start motion of the coarser sediment. Again, a decrease in d_s/a is observed with increasing sluice opening.

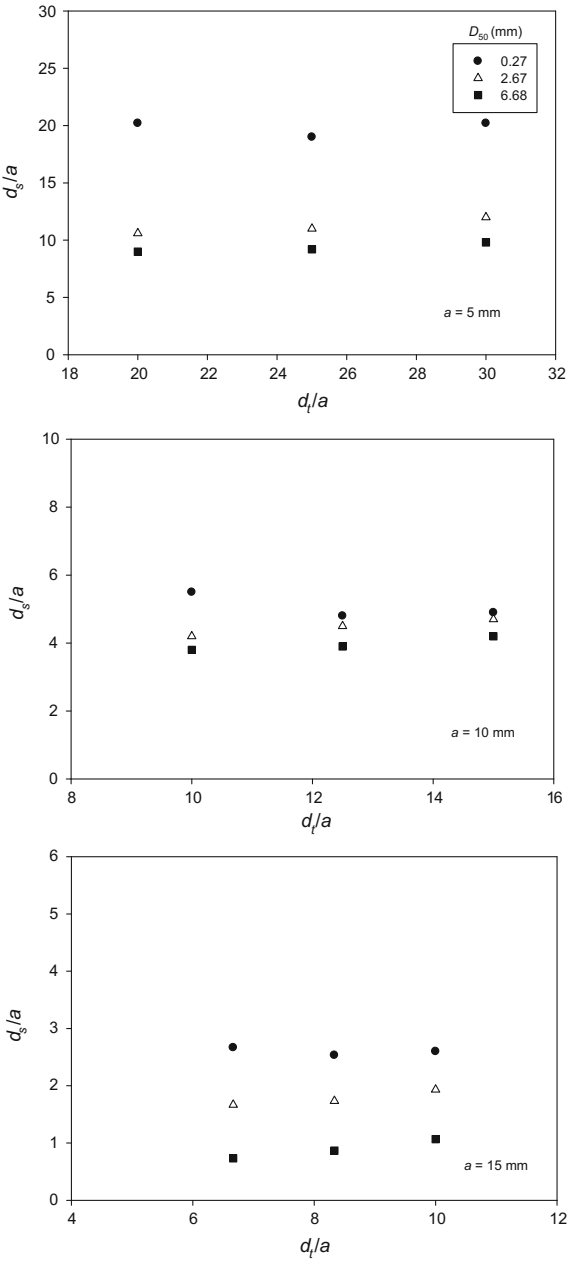

Fig. 4 Variation of d_s/a with d_t/a for different D_{50} and a

A regression analysis is carried out of the experimental data collected in the present study, which yields Eq. (1) for the prediction of asymptotic/maximum depth of scour downstream of a rigid apron under wall jets. This equation addresses

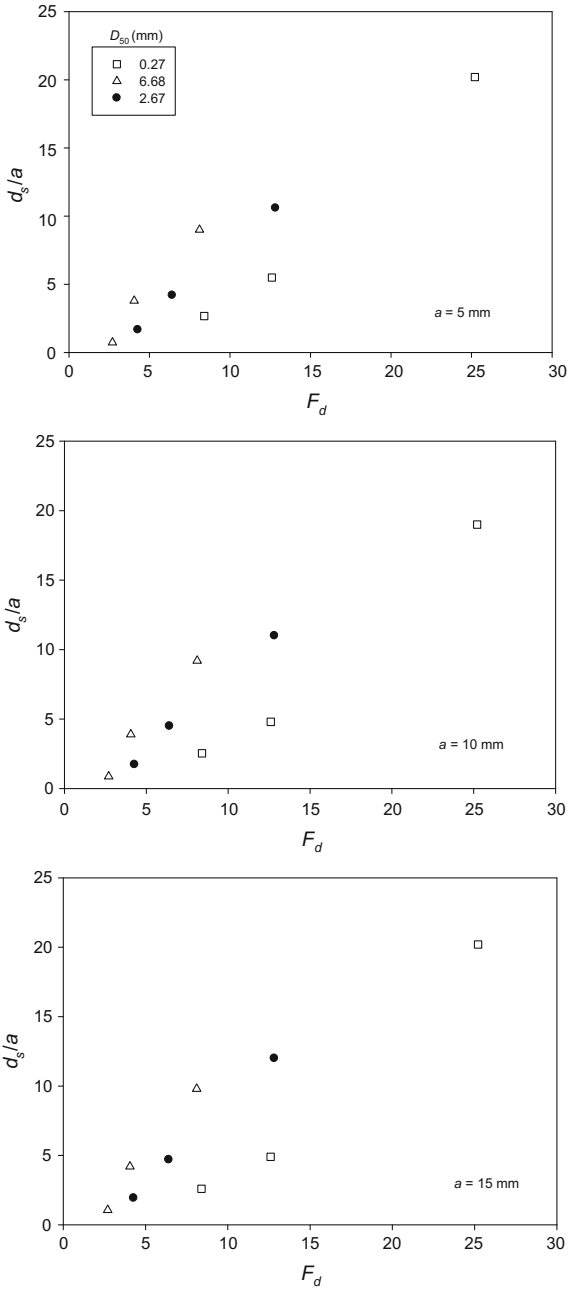

Fig. 5 Variation of d_s/a with F_d for different D_{50} and a

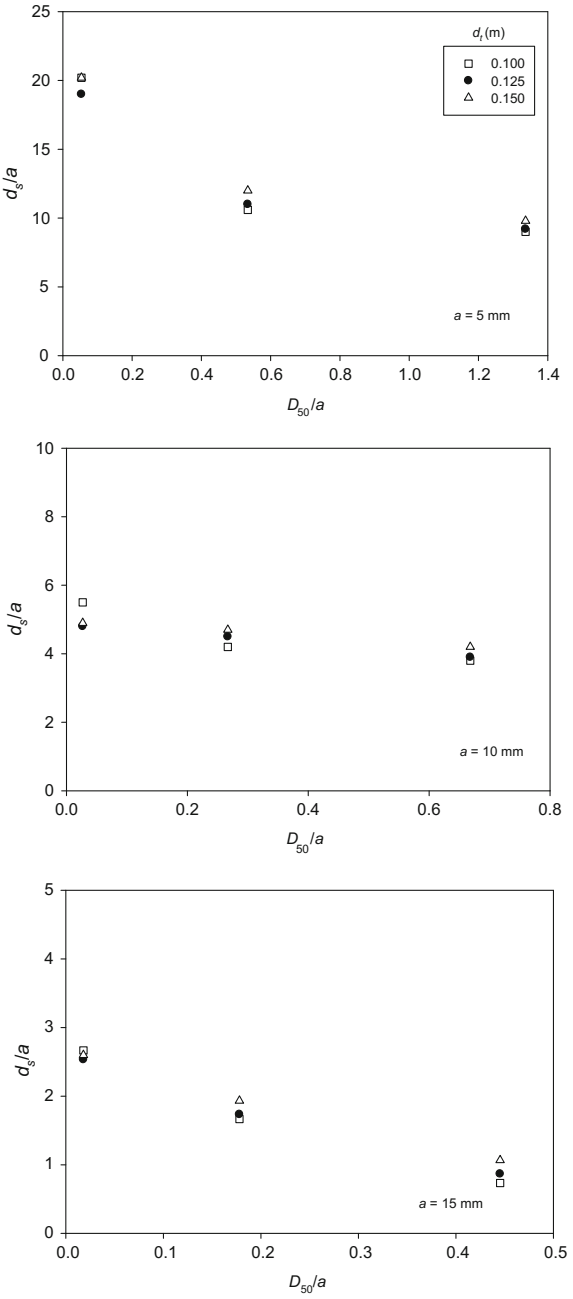

Fig. 6 Variation of d_s/a with D_{50}/a for different d_t and a

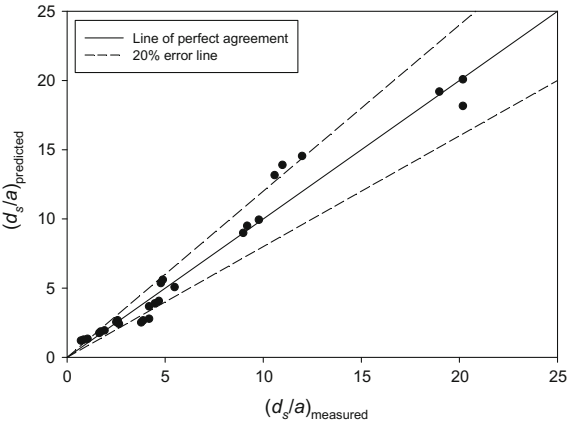

Fig. 7 Comparison of equilibrium scour depth computed using Eq. (1) with experimental data

the effect of densimetric Froude number, sediment size/sluice opening ratio and tailwater level/sluice opening ratio on non-dimensional asymptotic depth of scour.

$$\frac{d_s}{a} = 0.238F_d^{1.343}\left(\frac{D_{50}}{a}\right)^{0.255}\left(\frac{d_t}{a}\right)^{0.248} \tag{1}$$

Figure 7 demonstrates the comparison of measured d_s/a with the calculated or predicted value of d_s/a using Eq. (1). Most of the data points lie within an error line of ±20%, which states good applicability of the proposed equation. The regression coefficient between the observed and computed is 0.95, which establishes that the predicted scour is well in conformity with the observed scour. It is to be noted that the above equation is valid only in the range of $6.67 \leq d_s/a \leq 30$ and $1.45 \leq F \leq 12.04$.

5 Conclusions

The following conclusions are drawn from the present study:

- A similarity exists in the non-dimensional profiles of scour at different time intervals under wall jets.
- Time to reach equilibrium scour depth is observed to be 6–8 h for finer sediment, whereas coarser sediment takes lesser time to arrive at the asymptotic depth of scour.
- Asymptotic depth of scour is observed to reduce with rise in sluice opening and sediment size, whereas it advances with rise in densimetric Froude number.
- Effect of tailwater level on asymptotic depth of scour is such that initially there is a decrease in the depth of scour with rising level of tailwater, but after a critical tailwater level, the asymptotic depth of scour increases with increase in tailwater level.

- A new empirical equation is proposed to predict the equilibrium/asymptotic depth of scour downstream of a rigid apron under wall jets, which is well in conformity with the experimental data.

References

1. Aamir, M., Ahmad, Z.: Estimation of scour depth downstream of an apron under 2D horizontal jets. In: Proceedings of HYDRO 2015 International, 20th International Conference on Hydraulics, Water Resources and River Engineering. Indian Institute of Technology Roorkee, India (2015)
2. Aderibigbe, O., Rajaratnam, N.: Effect of sediment gradation on erosion by plane turbulent wall jets. J. Hydraul. Eng. **124**(10), 1034–1042 (1998)
3. Altinbilek, H.D., Basmaci, Y.: Localized scour at the downstream of outlet structures. In: Proceedings of the 11th Congress on Large Dams, pp. 105–121. International Commission of Large Dams, Madrid, Spain (1973)
4. Chatterjee, S.S., Ghosh, S.N., Chatterjee, M.: Local scour due to submerged horizontal jet. J. Hydraul. Eng. **120**(8), 973–992 (1994)
5. Dey, S., Sarkar, A.: Scour downstream of an apron due to submerged horizontal jets. J. Hydraul. Eng. **132**(3), 246–257 (2006)
6. Lee, W.W.L.: Erosion Downstream of a Sluice Gate. Nanyang Technological University, Singapore (1995)
7. Lim, S.Y., Yu, G.: Scouring downstream of sluice gate. In: Proceedings of the 1st International Conference on Scour of Foundations. Texas Transportation Institute, College Station, TX, vol. 1, pp. 395–409 (2002)
8. Rajaratnam, N.: Erosion by plane turbulent jets. J. Hydraul. Res. **19**(4), 339–358 (1981)
9. Rajaratnam, N., Macdougall, R.K.: Erosion by plane wall jets with minimum tail water. J. Hydraul. Eng. **109**(7), 1061–1064 (1983)
10. Valentin, F.: Considerations concerning scour in the case of flow under gates. In: Proceedings of the 12th IAHR Congress, Madrid, Spain, vol. 3, pp. 92–96 (1967)
11. Verma, D.V.S., Goel, A.: Scour downstream of a sluice gate. ISH J. Hydraul. Eng. **11**(3), 57–65 (2005)

Application of Collars Around Bevel-Nosed Rectangular Pier

Salman Beg and Mubeen Beg

Abstract An experimental investigation of scour depth variation is presented herein with an objective to examine efficacy of application of collars to a bevel-nosed rectangular pier in reducing the scour depth. Bevel-nosed rectangular pier aligned with the flow direction at low angles of attack with flow was tested without collar, with one collar and two collars under steady-state clear-water scour uniform flow condition. 76.7% and 81.54% reduction in scour depth is achieved with the application of one collar at 0° and 15° angles of attack, while 43.8% and 45.2% reduction in scour depth is achieved with the application of two collars at 0° and 15° angles of attack. This research causes considerable reduction in construction cost of bridge piers.

Keywords Bridge · Pier · Scour depth · Reduction · Device

1 Introduction

Bridges are the lifelines of a transportation system. They are required wherever waterways are crossed by roads and railways. Piers on which the superstructure of the bridges rest, play an important role in their stability and safety. These piers founded in the stream bed are subjected to scour as they are obstruction against the flow.

The bridge failures result in excessive repairs, loss of accessibility or even death [4]. The potential cost including human toll and monetary cost of bridge failure due to scour damage has highlighted the need for scour protection/reduction methods.

S. Beg (✉)
Civil Engineering Department, Vivekananda College of Technology & Management, Aligarh 202002, India
e-mail: salmanbeg1988@gmail.com

M. Beg
Civil Engineering Department, Z.H. College of Engineering & Technology, AMU, Aligarh 202002, India
e-mail: raisbeg2013@gmail.com

V. Garg et al. (eds.), *Development of Water Resources in India*,
Water Science and Technology Library 75, DOI 10.1007/978-3-319-55125-8_33

A large depth of foundation is required for bridge piers to overcome the effect of scour which is a costly proportion. Therefore, for safe and economical design, scour around the bridge piers is required to be controlled.

The bridge piers require deep and expensive pier embedment in rivers. To reduce this depth of embedment, efforts have been made by armoring devices like the riprap around the pier [1, 6, 8, 14–17, 21, 27, 28] and by flow altering devices like an array of piles in front of the pier [2, 19], a collar around the pier [3, 10, 13, 22–24, 29, 30], submerged vanes [20], a delta-wing-like fin in front of the pier [11], a slot through the pier [3, 13] and partial pier-groups [25]. The principal objective of this study is to examine experimentally the reduction efficiency of collar applied to bevel-nosed rectangular bridge pier.

2 Mechanics of Local Scour Around a Pier

2.1 Flow Pattern and Mechanism of Scouring

The vortex system and down flow are the principal causes of local scour. At the front of the pier, the velocity of flow approaching goes to zero. This causes an increase in pressure. Due to this phenomenon, the water surface level in front of pier increases. As the flow velocity decreases from the surface to the bed, the dynamic pressure on the pier face also decreases downwards. The down flow digs a hole in front of the base of the pier, rolls up and by interaction with the coming flow forms a complex vortex system (Fig. 1).

In spite of significant amount of research on pier scour, failure of bridges has been reported by many investigators including Hoffmans and Verheij [12], Chiew and Lim [7], Chiew [5], Dey and Barbhuiya [9] and Wardhana and Hadipriono [26].

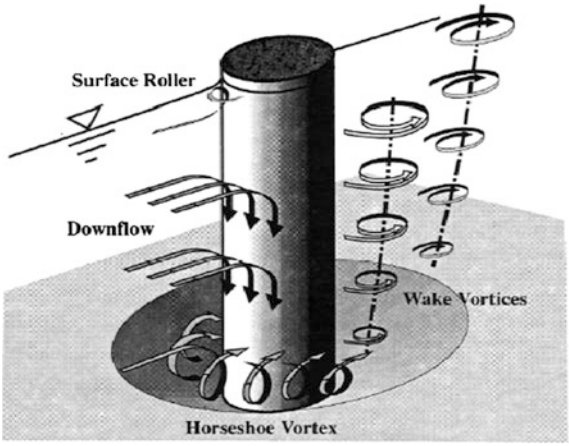

Fig. 1 Vortex system at the pier given by Melville and Cooleman [18]

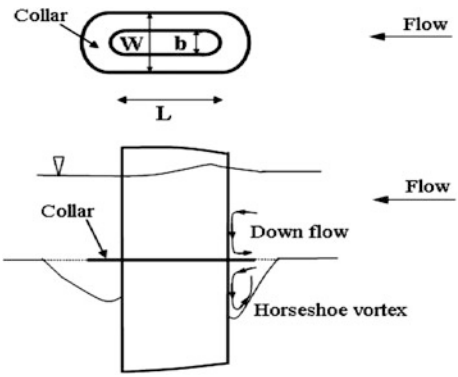

Fig. 2 Collar around round-nosed rectangular pier

Flow altering devices can be more economical, especially when the riprap material in required amount is not available near the bridge site or is expensive. However, there are certain limitations on the use of these flow altering devices to reduce the scour depth at piers. A slot may be blocked by floating debris. In addition to this, its construction is difficult. Sacrificial piles may become ineffective when the flow approaching the piers changes its direction. A thin collar plate skirting around bridge piers (Fig. 2) at or below the bed level which diverts the down flow and shields the stream bed from its direct impact is therefore a very effective mean of protection against scour.

3 Experimental Program

In the present study, 41.5-mm-wide wooden bevel-nosed rectangular piers having an aspect ratio 4 were used. Figure 3a, b shows the beveled nose rectangular pier (aspect ratio = 4) with and without collar. Collars (w/b = 2.5, where w and b are collar width and pier width, respectively) are used herein.

A series of experiments was conducted at bevel-nosed rectangular bridge pier models aligned with the flow and at 15° angle of attack with and without collar plate skirted around the pier in uniform cohesionless sediment in steady-state uniform clear-water scour conditions at 0.95 flow intensity.

Experiments were conducted in a glass sided rectangular re-circulating tilting flume, 11.0 m long, 0.756 m wide and 0.55 m deep. Water was supplied to the flume from an overhead tank, which got its supply from the laboratory water supply system. The scour depth at the piers was measured with a 3-mm-diameter point gauge mounted on the mobile carriage that traversed the flume. The scour depths could be measured to within 0.1 mm using point gauge.

All experiments started when the water in the flume was at rest at desired flow depth over a sediment bed. Temporal scour depth measurements were made and recorded during the experiment. At the end of experiment, the supply of water to the flume was carefully stopped and the flume was drained off such that there was no

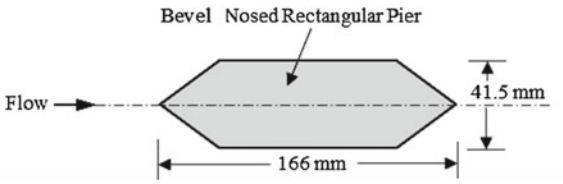

(a) Bevel nose rectangular pier (aspect ratio 4) without collar

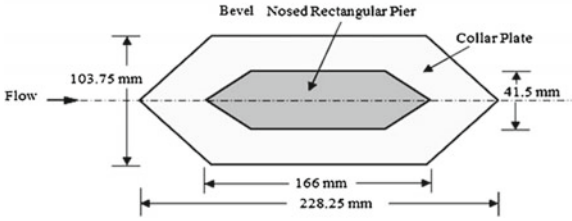

(b) Bevel nose rectangular pier (aspect ratio 4) with collar

Fig. 3 **a**, **b** Beveled nose pier without and with collars

Table 1 Mean flow, pier and sediment parameters considered in experiments

The flow properties used in present experiments	Properties of sediment used
Depth of flow, Y_0 (m) = 0.14	$d_{84.1}$ (mm) = 1.03
Mean velocity, U_0 (m/s) = 0.391	$d_{15.9}$ (mm) = 0.73
Threshold velocity, U_c (m/s) = 0.4127	Median size, d_{50} (mm) = 0.95
Critical shear velocity, U_{*c} (m/s) = 0.029	Geometric mean size, d_g (mm) = 0.867
Froude number, F_r = 0.3328	Geometric standard deviation, σ_g (mm) = 1.187
Average energy slope, S_0 = 0.001	Specific gravity, S_s = 2.65
	Fall velocity of sediment, W_0 (m/s) = 0.1
	Angle of repose, ϕ = 32°

disturbance to scour holes and scour patterns developed by the flow on the sediment bed. The flow, pier and sediment parameters used in this study are given in Table 1.

Since the experiments were performed in clear-water condition, time of experimental run of 7 h was fixed. However, in experiments with collar, test duration was more.

4 Collection of Data

The dynamic scour depths at bevel-nosed rectangular pier with and without collars were noted during the tests at reasonable interval of periods.

Photographs of the features developed on the sediment bed were taken as shown in Figs. 4 and 5.

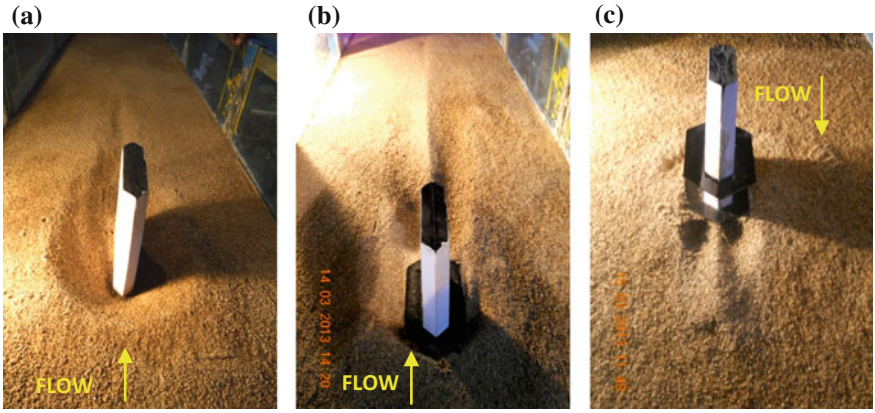

Fig. 4 Scour and deposition patterns around bevel-nosed rectangular pier at **a** $\alpha = 0°$ without collars, **b** $\alpha = 0°$ with one collar, **c** $\alpha = 0°$ with two collars

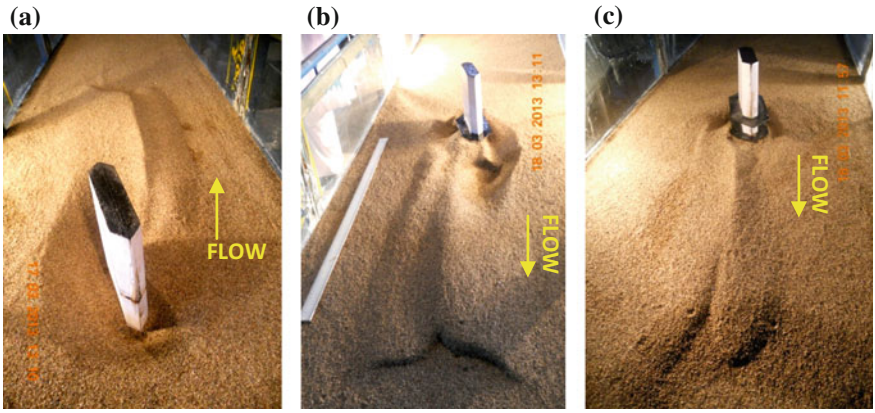

Fig. 5 Scour and deposition patterns around bevel-nosed rectangular pier at **a** $\alpha = 15°$ without collars, **b** $\alpha = 15°$ with one collar, **c** $\alpha = 15°$ with two collars

5 Results and Analysis

The data collected from experimental analysis are processed and analyzed in order to examine significance of application of collar to beveled nose rectangular pier aligned with the flow and at an angle of attack with the flow. The observed scour profiles along flow direction at 0° and 15° angles of attack, without collar, with one collar and with two collars are shown in Figs. 6, 7 and 8, respectively.

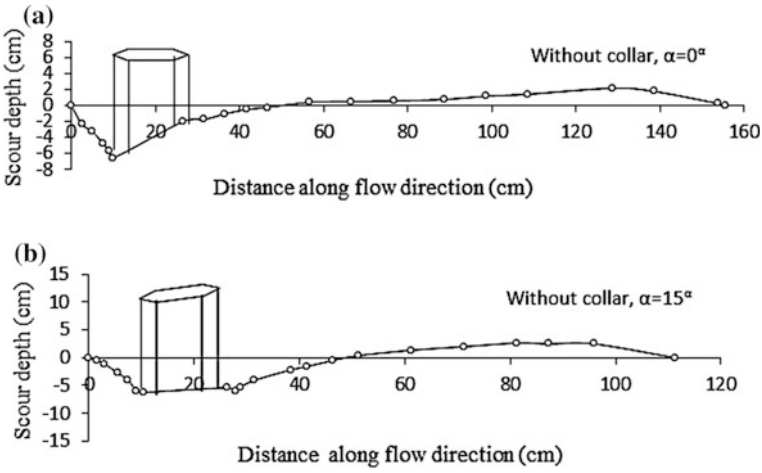

Fig. 6 Longitudinal profiles of scour for bevel-nosed rectangular pier at low angle of attack **a** without collar at $\alpha = 0°$, **b** without collar at $\alpha = 15°$

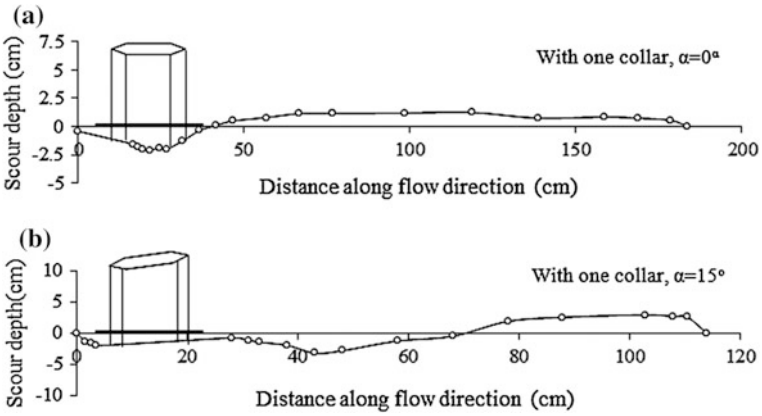

Fig. 7 Longitudinal profiles of scour for bevel-nosed rectangular pier at low angle of attack **a** with one collar at $\alpha = 0°$, **b** with one collar at $\alpha = 15°$

In Fig. 9, reduction of 76.7% and 81.54 in scour depth is observed by applying one collar and two collars, respectively, at 0° angle of attack. A reduction of 43.8% and 45.2% in scour depth is observed by applying one collar and two collars, respectively, at 15° angle of attack.

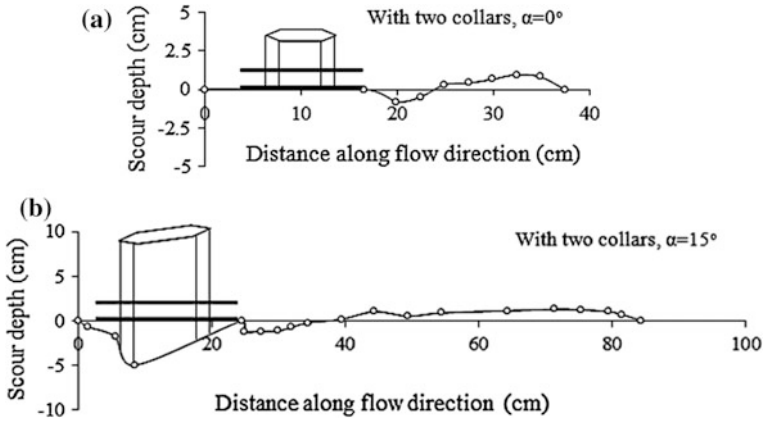

Fig. 8 Longitudinal profiles of scour for bevel-nosed rectangular pier at low angle of attack **a** with two collars at $\alpha = 0°$, **b** with two collars at $\alpha = 15°$

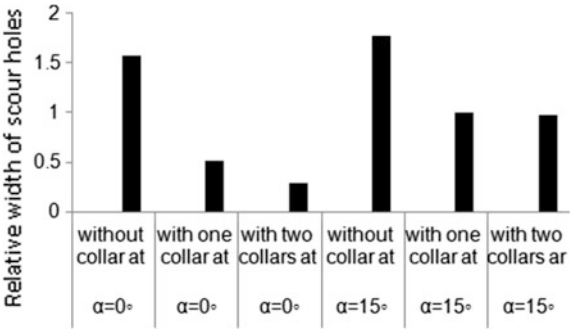

Fig. 9 Scour depth observed at beveled nose rectangular pier with and without collars at 0° and 15° angle of attack

6 Conclusions

With respect to a bevel-nosed rectangular pier without collar, 76.7% and 81.54% reduction in scour depth is observed with one collar and two collars at 0° angle of attack, respectively, whereas at 15° angle of attack, the corresponding reduction in scour depth is 43.8% and 45.2%, respectively.

At 0° and 15° angle of attack, a reduction of 32.43% and 34.51% in length of scour holes is observed with one collar, while with two collars the corresponding reduction of 42.83% and 40% in length of scour hole is observed with respect to pier without collar.

References

1. Brice, J.C., Blodgett, J.C.: Countermeasures for Hydraulic Problems at Bridges, vols. 1 & 2, pp. 10–23. Federal Highway Administration, U.S. Department of Transportation (1978)
2. Chabert, J., Engeldinger, P.: Etude des Affouillement autour des Piles des ponts (Study on Scour around Bridge Piers). Laboratoire National d'Hydraulique, Chatou, France (1956)
3. Chiew, Y.M.: Scour protection at bridge piers. J. Hydraul. Eng. ASCE **118**(9), 1260–1269 (1992)
4. Chiew, Y.M.: Mechanics of riprap failure at bridge piers. J. Hydraul. Eng. ASCE **121**(9), 635–643 (1995)
5. Chiew, Y.M.: Local scour and riprap stability at bridge piers in a degrading channel. J. Hydraul. Eng. ASCE **130**(3), 218–226 (2004)
6. Chiew, Y.M., Lim, F.H.: Failure behavior of riprap layers at bridge piers under live-bed conditions. J. Hydraul. Eng. ASCE **126**(1), 43–55 (2000)
7. Chiew, Y.M., Lim, S.Y.: Protection of bridge piers using a sacrificial sill, issue 1, pp. 53–62. Proc. of the Institution of Civil Engineers, Water and Maritime Engineering 156 (2003)
8. Croad, R.N.: Bridge pier scour protection using riprap. Central Laboratories Report No. PR3-0071, Works Consultancy Services, NZ (1993)
9. Dey, S., Barbhuiya, A.K.: Clear water scour at abutments in thinly Armored beds. J. Hydraul. Eng. ASCE **130**(7), 622–634 (2004)
10. Ettema, R.: Scour at bridge piers. Report No. 216, School of Engineering, University of Auckland, Auckland, New Zealand (1980)
11. Gupta, A.K., Gangadharaiah, T.: Local scour reduction by a delta wing-lick passive device. In: Proceedings of 8th Congress of Asia and Pacific Regional Division, 2, CWPRS, Pune, India, pp. B471–B481 (1992)
12. Hoffmans, G.J.C.M., Verheij, H.J.: Scour manual. A.A. Balkema, Rotterdam/Brookfield (1997)
13. Kumar, V., Ranga Raju, K.G., Vittal, N.: Reduction of local scour around bridge piers using slot and collar, technical note. J. Hydraul. Eng. ASCE **125**(12), 1302–1305 (1999)
14. Lim, F.H.: Riprap protection and its failure mechanisms, a thesis submitted to the School of Civil and Structural Engineering, Nanyang Technological University, Singapore in fulfillment of the requirements for the degree of doctor of philosophy (1998)
15. Lim, F.H., Chiew, Y.M.: Stability of riprap layer under live-bed conditions. In: Proceedings of Ist International Conference on New/Emerging Concepts For Rivers, RiverTech'96, vol. 2, pp. 830–837 (1996)
16. Lim, F.H., Chiew, Y.M.: Parametric study of riprap failure around bridge piers. J. Hydraul. Res. **30**(1), 61–72 (2001)
17. Lim, S.Y.: Equilibrium clear-water scour around and abutments. J. Hydraul. Eng. ASCE **123** (3), 237–243 (1997)
18. Melville, B.W., Coleman, S.E.: Bridge scour: 550p, Water Resources Publications, LLC, Colorado, USA (2000)
19. Melville, B.W., Hadfield, A.C.: Use of sacrificial piles as pier scour countermeasures. J. Hydraul. Eng. ASCE **125**(11), 1221–1224 (1999)
20. Odgaard, A.J., Wang, Y.: Scour prevention at bridge piers. In: Ragan, R.M. (ed.) Hydraulic Engineering 87, National Conference, Virginia, pp. 523–527 (1987)
21. Parola, A.C.: Stability of riprap at bridge piers. J. Hydraul. Eng. ASCE **119**, 1080–1093 (1993)
22. Schneible, D.E.: An investigation of the effect of bridge pier shape on the relative depth of scour. M.Sc. thesis, Graduate College of the State, University of Iowa, Iowa City, Iowa (1951)
23. Tanaka, S., Yano, M.: Local scour around a circular cylinder. In: Proceedings of 12th Congress I.A.H.R., Ft. Collins, Colorado, vol. 3, pp. 193–201(1967)

24. Thomas, Z.: An interesting hydraulic effect occurring at local scour. In: Proceedings of 12th Congress, I.A.H.R., Ft. Collins, Colorado, vol. 3, pp. 125–134 (1967)
25. Vittal, N., Kothyari, U.C., Haghighat, M.: Clear water scour around bridge piers group. J. Hydraul. Eng. ASCE **120**(11), 1309–1318 (1994)
26. Wardhana, K., Hadipriono, F.C.: Analysis of recent bridge failures in the United States. J. Perform. Constr. Fac **17**(3), 144–150 (2003)
27. Worman, A.: Riprap protection without filter layers. J. Hydraul. Eng. ASCE **115**(12), 1615–1630 (1989)
28. Yoon, T.H., Yoon, S.B., Yoon, K.S.: Design of riprap for scour protection around bridge piers. In: 26th IAHR Congress, UK, vol. 1, pp. 105–110 (1995)
29. Zarrati, A.M., Gholami, H., Mashahir, M.B.: Application of collar to control scouring around rectangular bridge piers. J. Hydraul. Res. IAHR **42**(1), 97–103 (2004)
30. Zarrati, A.M., Nazariah, M., Mashahir, M.B.: Reduction of local scour in the vicinity of bridge pier group using collars and riprap. J. Hydraul. Eng. ASCE **132**(2), 154–162 (2006)

Three-Dimensional Flow Measurements at Circular Pier

Ashish Kumar

Abstract This paper presents the experimental observations on flow measurement at the circular pier taken by an acoustic Doppler velocimeter. Two experimental runs (*RB* and *UPSH*) were conducted in the laboratory under clear-water condition. In one experiment, scour hole was developed, while in the second experiment scour hole was not allowed to develop by making the bed rigid. Measurements of components of time-averaged velocity around the pier in both experimental series were taken at two vertical planes: in front of pier ($\alpha = 0°$) and behind the pier ($\alpha = 180°$). Here, $\alpha = 0°$ corresponds to upstream central line in front of pier. In upstream plane close to pier at bed level, magnitude of *longitudinal* component (u) is high for the *UPSH* run on account of development of scour hole. Within the scour area region and close to pier, magnitude of w component was high for *UPSH* run. In the downstream plane at 180° behind the pier, the u component for *RB* run shows the negative value which indicates that flow is in reverse direction, i.e. towards the pier. In the *UPSH* run, u component is negative close to pier and its value is positive away from the pier, although its values decrease towards the water surface.

Keywords Circular bridge pier · Rigid bed · Scour hole · Three-dimensional flow · Flow characteristics · Acoustic Doppler velocimeter (ADV)

1 Introduction

Bridges are the essential component of land transport system. Whenever there is requirement to cross the waterways, bridges comes into pictures. Thus, these structures play important part. A main reason of bridge failure is scour activity by flow around its piers and abutments [26]. Thus, one of the main concerns about the safety of bridges is correct estimation of scour depth at bridge piers. As a result,

A. Kumar (✉)
Department of Civil Engineering, Jaypee University of Information Technology, Waknaghat, Solan, HP, India
e-mail: ashish.fce@juit.ac.in

V. Garg et al. (eds.), *Development of Water Resources in India*,
Water Science and Technology Library 75, DOI 10.1007/978-3-319-55125-8_34

number of equations and methods are available in literature. A description on pier scour relationships can be found in Melville [24], Ettema [6], Kothyari [11], Johnson [10], Kumar [21], Garde and Ranga Raju [7], Kumar et al. [20], Sheppard et al. [32], etc. A number of researches have been conducted on time variation of scour depth at circular piers and finally to achieve equilibrium scour depth [2, 3, 12–16, 22, 23, 25, 28, 31, 34, etc.]. The scour process at bridge pier is a complex phenomenon due to three-dimensional flow structure, turbulence and sediment transport phenomenon. Due to these complexities, many times these equations do not give accurate result for scour depth. Deficiency in the knowledge of flow structure close to and nearby area of bridge piers is one of the main reasons of this problem [19]. Either there will be chances of exposure of pier foundation or design of too shallow foundation due to incorrect estimation of scour depth. A number of investigations have been conducted on the flow patterns and turbulence parameters around the bridge piers that includes studies conducted by Melville [24], Dargahi [4], Ahmed and Rajaratnam [1], Graf and Istiarto [8], Muzzammil and Gangadhariah [27], Rao et al. [30], Kumar and Kothyari [18], Unger and Hager [33], Dey and Raikar [5], Radice and Tran [29], Kumar and Kothyari [19], etc. A few studies on flow structure have been conducted around the uniform piers placed on rigid bed [1, 9, 17, 24, etc.]. However, no study has been reported on the comparison of flow characteristic at circular bridge piers placed on rigid bed and in scour hole condition.

The present study was therefore taken up to fulfil the above-mentioned gaps in the knowledge of the flow structure around the piers. Broad objective of this investigation was to conduct carefully controlled set of experiments for achieving a better knowledge of flow conditions and turbulence characteristics around the cylindrical pier while these are placed in rigid bed and also when scour hole developed. A comparative study of the flow structure in front of pier and downstream of pier while scour hole was allowed to develop and in rigid bed condition has been conducted and results are reported herein.

2 Experimental Set-up and Procedure

The experiments were carried in a rectangular flume having dimensions of 30 m long, 1 m wide and 0.6 m deep. The channel was located in the laboratory of Hydraulic Engg. section of Civil Engg. Department, IIT Roorkee. Working section of channel was prepared 12 m downstream from the entrance of flume, and it had dimensions of 3 m long, 0.6 m deep and 1 m wide. The working channel section was filled with sand having sediment size d_{50} (median size) equal to 0.4 mm. Two series of experiments were conducted in clear-water condition, and ratio of shear velocity of flow to critical shear velocity was nearly equal to one. In both the

experiments, a circular pier having 11.4 cm diameter was used. In the first series named as *RB*, the bed was made rigid and scour hole did not develop. In second series (*UPSH*), scour hole around the pier developed due to flow. Both experiments were conducted for a discharge = 45 l/s, flow depth h = 16 cm and average approach flow velocity U_∞ of flow = 28 cm/s measured in the test section.

In the first experiment, circular pier model having 11.4 cm diameter was fixed vertically in the centre of the test section. Bed of test section was made rigid by spraying the cement solution over it [19]. This made the surface of the bed hard enough, and scour around the pier did not occur. This run is referred here as the rigid bed (*RB*) run. In the second experiment (*UPSH* run), scour hole developed in the aforesaid flow conditions. Variation of scour depth with time was measured at the nose of the pier. It is well established that scour hole develops very fast in the starting phase of scour process and the process becomes slow as time passes after few hours of scour activity; in the present case, the scour activity was allowed to take place for 7 h. The total depth of scour recorded at the front of pier was equal to 13.9 cm. Figure 1 shows the contours of scour depth for this run.

After the scour activity, scoured area was made hard as a rock as was done in *RB* run. This run is referred here as *UPSH* run. The measurement for the flow characteristics around the piers was taken using acoustic Doppler velocimeter (ADV) for both runs. An ADV can instantaneously measure all the three components of velocity at a given point in the flow domain. Measurements of flow velocity components and turbulence intensities were taken at any point for long durations so that observations taken become stationary. The measurements were taken at 25 Hz frequency over a duration of 4 min at each location. Each data series was revised so that data having correlation coefficient less than 70% and SNR (signal-to-noise ratio) less than 17 are filtered.

The measurement for the flow velocity components and turbulence intensities were taken in a vertical plane of symmetry ahead of pier at $\alpha = 0°$ and 180° using an ADV. Here, $\alpha = 0°$ angle corresponds to upstream central line in front of pier. Velocity distributions were measured along vertical planes at distances (r) = 10, 14, 17, 20, 25, 30, 35 and 40 cm. The coordinates of each point are defined by (r, α, z) with z being vertical distance above bed level in the text section and r the horizontal

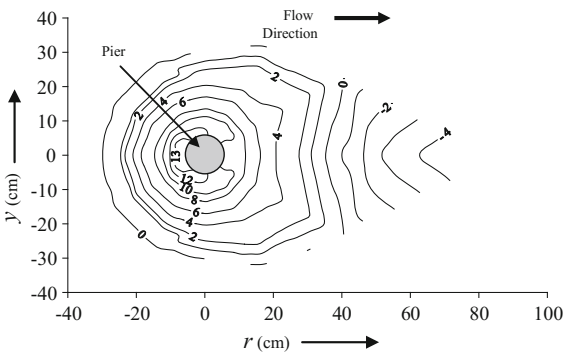

Fig. 1 Contours of scour depths (cm) around the pier for *UPSH* run [19]

distance from the centre of pier in vertical plane. The measurement of velocity and other parameters were taken at a vertical distance interval of 1 cm. The nearest reading was taken at distance of 4 mm from the bed surface.

3 Results and Discussion

Comparison of variation of time-averaged u (longitudinal) and w (vertical) components of velocities in the plane at $\alpha = 0°$ for two runs is shown in Fig. 2. The components of velocity were normalized using upstream flow velocity U_∞ while the z (vertical distance) is normalized using depth of flow h.

For the *UPSH* run near to pier at location $r = 10$ cm and below the initial level of bed in the scour hole region, the u component shows negative values, which indicates that flow is moving in the reverse direction in front of pier. For the *RB* runs where scour hole is not possible, u component is observed only above bed level of the text section. At the bed level, magnitude of longitudinal component of velocity u was observed to be high in *UPSH* run in comparison with velocity in *RB* run. The main reason behind this is evolution of scour hole ahead of pier. The v component of the velocity is mostly negligibly small in this plane. Approaching to the pier, the w component of velocity has larger negative values which means that there is a strong downward flow for the *UPSH* run. For the *RB* run, the scour hole did not develop as the w component of velocity did not show significant magnitude. Far away from the pier, the profile of w component is similar.

Figure 3a–c shows the comparison of variation of time-averaged components of velocities (longitudinal u; transverse v and vertical w) in downstream plane at $\alpha = 180°$ for *UPSH* and *RB* runs. In downstream plane behind the pier, the u component for *RB* run shows the negative value which indicates that flow is moving towards the pier, opposite to the direction of normal flow, whereas in *UPSH* run u component is negative close to pier and its value is positive away from the pier, although its values decrease towards the water surface. w component of velocity is always positive for the *UPSH* run over the entire depth of flow. For *RB* run, close to pier the w component has its value fluctuating close to zero, but as flow moves away from the pier, w component is also positive but its magnitude is less than that obtained in run *UPSH*. The normalized value of v component is seen to vary between −0.2 and 0.2 over this plane for both runs.

The turbulence characteristics are represented by intensities of turbulence ($\sqrt{\overline{u'^2}}$, $\sqrt{\overline{v'^2}}$, $\sqrt{\overline{w'^2}}$) and Reynolds' stresses ($\overline{u'w'}$, $\overline{v'w'}$). The effect of these components of turbulence intensity is presented by the term turbulent kinetic energy (k).

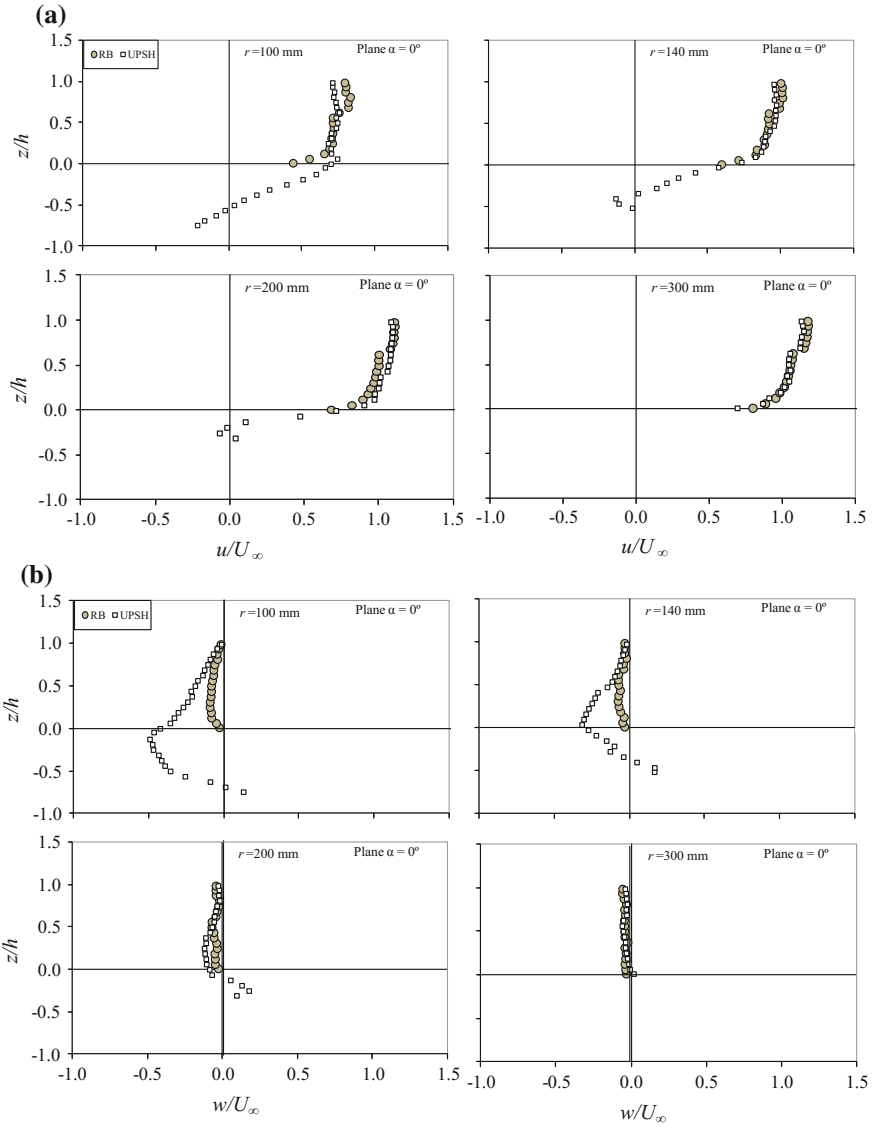

Fig. 2 **a** Comparison of longitudinal component of velocity u at rigid bed condition (*RB*) and scour hole condition (*UPSH*) runs at upstream central line of pier ($\alpha = 0°$). **b** Comparison of vertical component of velocity w at rigid bed condition (*RB*) and scour hole condition (*UPSH*) runs at upstream central line of pier ($\alpha = 0°$)

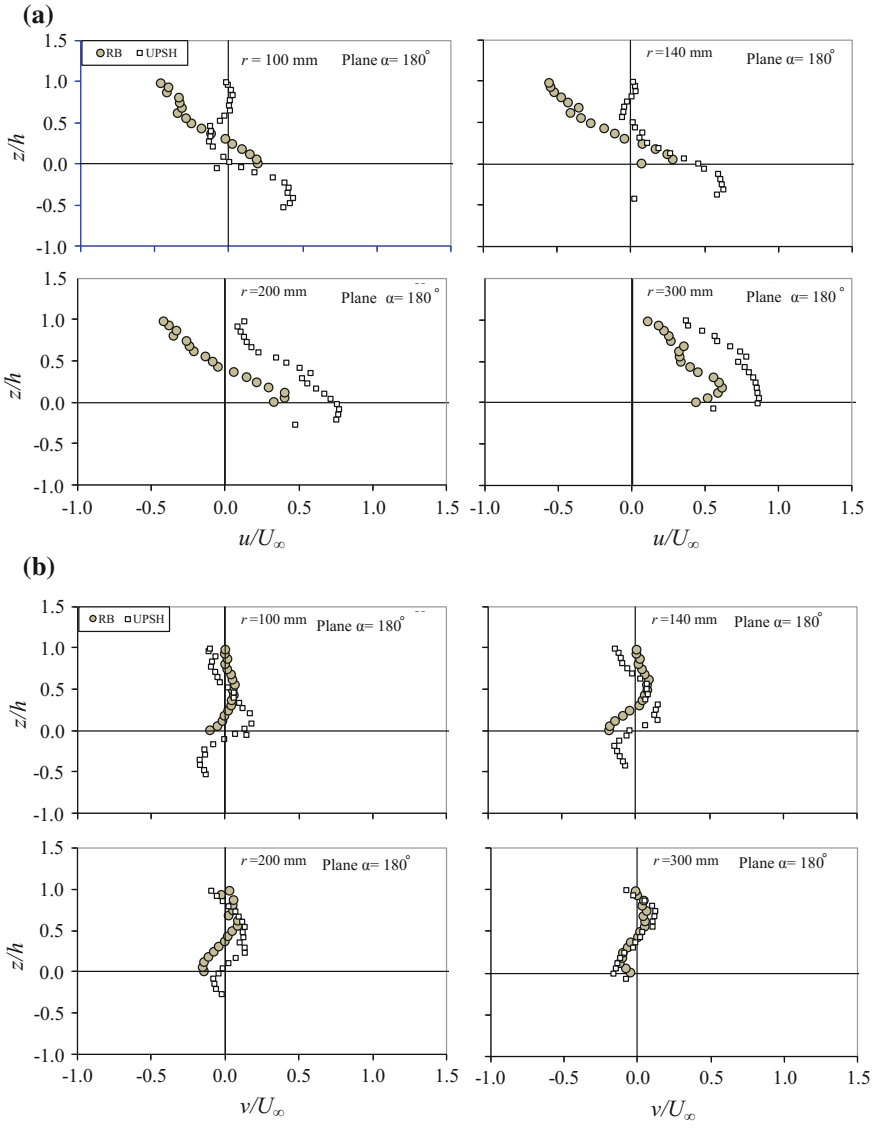

Fig. 3 **a** Comparison of longitudinal component of velocity u at rigid bed condition (*RB*) and scour hole condition (*UPSH*) runs at downstream central line of pier ($\alpha = 180°$). **b** Comparison of transverse component of velocity v at rigid bed condition (*RB*) and scour hole condition (*UPSH*) runs at downstream central line of pier ($\alpha = 180°$). **c** Comparison of vertical component of velocity w at rigid bed condition (*RB*) and scour hole condition (*UPSH*) runs at downstream central line of pier ($\alpha = 180°$)

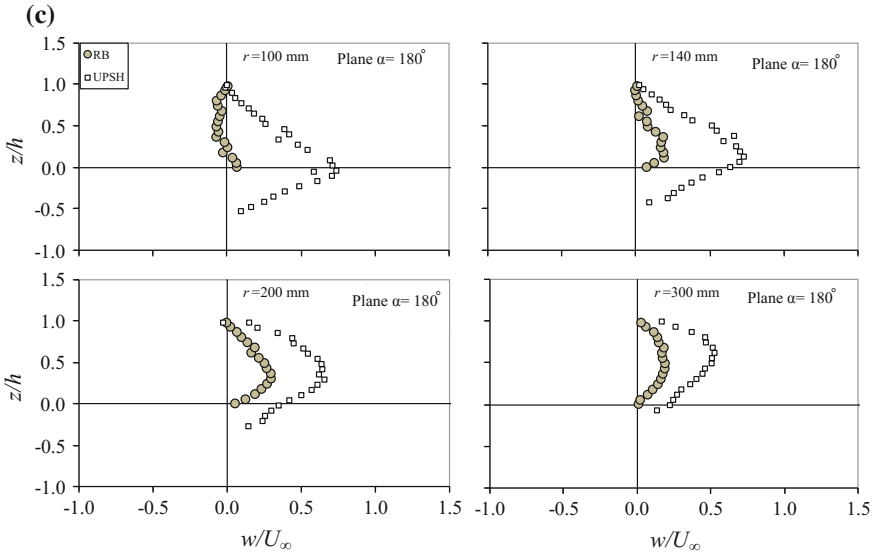

Fig. 3 (continued)

$$k = 1/2\left(\overline{u'^2} + \overline{v'^2} + \overline{w'^2}\right) \tag{1}$$

Figure 4a, b shows the variation of k values in vertical plane for experimental runs *UPSH* and *RB* at $\alpha = 0°$ and 180°. Here, u', v' and w' are fluctuation of u, v and w, respectively. The data of turbulent kinetic energy are normalized with shear velocity (u_*). In the plane at $\alpha = 0°$, in the upper region, the magnitude of turbulent kinetic energy is less in comparison with k values for RB runs. At the general level of bed ($z = 0$), k values are almost 3 times for *RB* run. Away from the pier in the upstream direction, the k profiles have the similar trend and magnitude is also more or less same for the two experimental runs.

Just behind the pier ($\alpha = 180°$), flow is highly turbulent when compared to upstream plane. For the *RB* run, it was noticed that as the flow moves towards the downstream side of pier value of turbulent kinetic energy k increases on account of turbulent mixing. The peak of k was noticed at $r = 300$ mm, and afterwards its values decreases. For *UPSH* run, peak of k was noticed just behind the pier and at the general level of bed. For the flow away from pier, magnitude of k decreases and also its peak reaches towards the water surface.

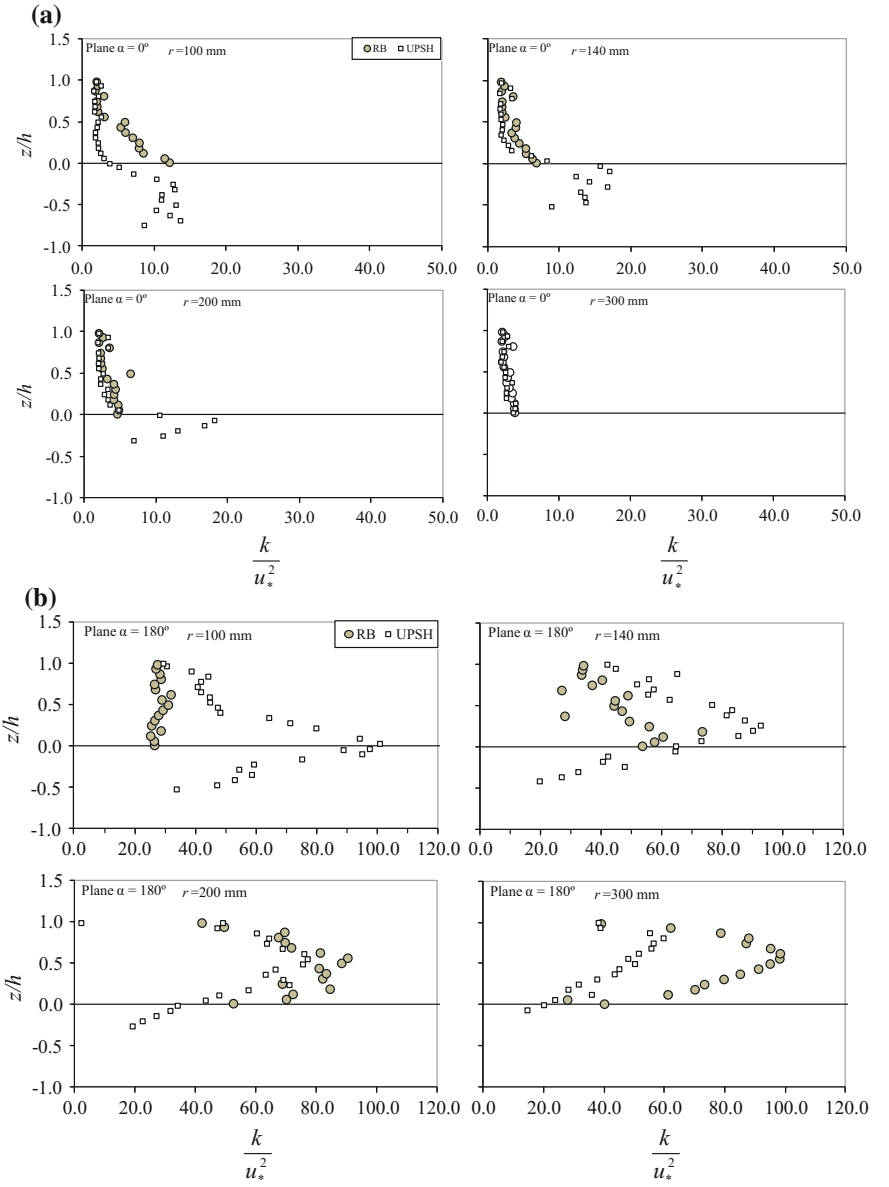

Fig. 4 **a** Comparison of normalized turbulent kinetic energy (k) of circular pier run at rigid bed condition (*RB*) and scour hole condition (*UPSH*) at upstream central line of pier ($\alpha = 0°$), **b** Comparison of normalized turbulent kinetic energy (k) of circular pier run at rigid bed condition (*RB*) and scour hole condition (*UPSH*) at downstream central line of pier ($\alpha = 180°$)

4 Conclusions

In the present investigation, flow characteristics around circular pier in two conditions, in scour hole and without scour hole, have been compared. Instantaneous data of three components of velocity and turbulence parameters at upstream and downstream of pier at different locations in vertical planes were captured by ADV. In the plane at $\alpha = 0°$, no significant change was noticed in the values of u components of the velocity between these two runs over the entire flow depth and over the entire region of measurement. However, the magnitude of w component increased significantly up stream of pier for the *UPSH* run due to development of scour hole. Flow accelerated due to evolution of scour hole ahead of pier. In the downstream plane ($\alpha = 180°$) behind the pier, the u component for *RB* run exhibited reversal of flow towards the pier for both the runs, its values decreased towards the water surface and it is negative close to pier. w component of velocity is always positive for the *UPSH* run over the entire flow depth, i.e. w component is in upward direction. For *RB* run, w component is also positive but its magnitude is less than that obtained in run *UPSH*.

The combined effect of turbulence intensity in both planes is represented by turbulent kinetic energy (k). At $\alpha = 0°$, in upper region, magnitude of turbulent kinetic energy is high for *RB* run and about 3 times in comparison with k values for *UPSH* run. Just behind the pier, flow is highly turbulent for the *UPSH* runs due to development of scour hole. As flow moves away, magnitude of turbulence decreases. For the *RB* run, as flow moves towards the downstream side of pier value of turbulent kinetic energy k increases on account of turbulent mixing. The peak of k was noticed at $r = 300$ mm, and afterwards its values decrease.

References

1. Ahmed, F., Rajaratnam, N.: Flow around bridge piers. J. Hydraul. Eng. ASCE **124**(3), 288–300 (1998)
2. Barkdoll, B.B.: Time scale for local scour at bridge piers. J. Hydraul. Eng. ASCE **126**(10), 793–794 (2000)
3. Chreties, C., Simarro, G., Teixeir, L.: New experimental method to find equilibrium scour at bridge piers. J. Hydraul. Eng. ASCE **134**(10), 1491–1495 (2008)
4. Dargahi, B.: The turbulent flow field around a circular cylinder. Exp. Fluids **8**, 1–12 (1989)
5. Dey, S., Raikar, R.V.: Characteristics of horseshoe vortex in developing scour holes at piers. J. Hydraul. Eng. ASCE **133**(4), 399–413 (2007)
6. Ettema, R.: Scour at bridge piers. Report No. 216, Department of Civil Engineering, University of Auckland, Auckland, New Zealand (1980)
7. Garde, R.J., Ranga Raju, K.G.: Mechanics of Sediment Transportation and Alluvial Stream Problem. New Age International, New Delhi (2000)
8. Graf, W.H., Istiarto, I.: Flow pattern in the scour hole around a cylinder. J. Hydraul. Res. IAHR **40**(1), 13–20 (2002)
9. Graf, W.H., Yulistiyanto, B.: Experiments on flow around a cylinder; the velocity and vorticity fields. J. Hydraul. Res. IAHR **36**(4), 637–653 (1998)

10. Johnson, P.A.: Comparison of pier scour equations using field data. J. Hydraul. Engg. ASCE **121**(8), 626–629 (1995)
11. Kothyari, U.C.: Scour around bridge piers. Ph.D. thesis, Indian Institute of Technology Roorkee (Formerly: University of Roorkee, Roorkee), India (1989)
12. Kothyari, U.C., Garde, R.J., Ranga Raju, K.G.: Temporal variation of scour around circular bridge piers. J. Hydraul. Eng. ASCE **118**(8), 1091–1106 (1992)
13. Kothyari, U.C., Garde, R.J., Ranga Raju, K.G.: Live-bed scour around cylindrical bridge piers. J. Hydraul. Res. IAHR **30**(5), 701–715 (1992)
14. Kothyari, U.C., Hagar, W.H., Oliveto, G.: Generalized approach for clear-water scour at bridge foundation elements. J. Hydraul. Eng. ASCE **133**(11), 1229–1239 (2007)
15. Kothyari, U.C., Kumar, A.: Temporal variation of scour around circular bridge piers. ISH J. Hydraul. Eng. **16**(3 SP-1), 35–48 (2010)
16. Kothyari, U.C., Kumar, A.: Temporal variation of scour around circular compound piers. J. Hydraul. Eng. ASCE **138**(11), 945–957 (2012)
17. Kumar, A.: Scour around circular compound bridge piers. Ph.D. thesis, Indian Institute of Technology, Roorkee, India (2007)
18. Kumar, A., Kothyari, U.C.: Flow characteristics within scour hole around a circular bridge pier. In: Proceedings of Conference on Hydraulics and Water Resources-HYDRO 2005, pp. 599–608. Tumkur, India (2005)
19. Kumar, A., Kothyari, U.C.: Three-dimensional flow characteristics within the scour hole around circular uniform and compound piers. J. Hydraul. Eng. ASCE **138**(5), 420–429 (2012)
20. Kumar, A., Kothyari, U.C., Ranga Raju, K.G.: Flow structure and scour around circular compound bridge piers—a review. J. Hydro-environ. Res. **6**(4), 251–265 (2012)
21. Kumar, V.: Reduction of scour around bridge piers using protective devices. Ph.D. thesis, Indian Institute of Technology, Roorkee (Formerly: University of Roorkee, Roorkee), India (1996)
22. Lança, R., Fael, C., Maia, R., Pêgo, J., Cardoso, A.: Clear-water scour at comparatively large cylindrical piers. J. Hydraul. Eng. ASCE **139**(11), 1117–1125 (2013)
23. Lee, S.O., Sturm, T.W.: Effect of sediment size scaling on physical modeling of bridge pier scour. J. Hydraul. Eng. ASCE **135**(10), 793–802 (2009)
24. Melville, B.W.: Local scour at bridge sites. Report No. 117, University of Auckland, Auckland, New Zealand (1975)
25. Melville, B.W., Chiew, Y.M.: Time scale for local scour at bridge piers. J. Hydraul. Eng. ASCE **123**(2), 125–136 (1999)
26. Melville, B.W., Coleman, S.E.: Bridge Scour. Water Resources Publications, Highlands Ranch, Colo (2000)
27. Muzzammil, M., Gangadhariah, T.: The mean characteristics of horseshoe vortex at a cylinder pier. J. Hydraul. Res. IAHR **41**(3), 285–297 (2003)
28. Oliveto, G., Hager, W.H.: Temporal variation of clear-water pier and abutment scour. J. Hydraul. Eng. ASCE **128**(9), 811–820 (2002)
29. Radice, A., Tran, C.K.: Study of sediment motion in scour hole of a circular pier. J. Hydraul. Res. **50**(1), 44–51 (2012)
30. Rao, S.K., Sumner, D., Balachandar, R.: A visualization study of fluid-structure interaction between a circular cylinder and a channel bed. J. Vis. **7**(3), 187–199 (2004)
31. Richardson, E.V., Davis, S.R.: Evaluating scour at bridges. Hydraulic Engineering, Circular No. 18 (HEC-18), 4th Ed., Report No. FHWA NHI 01-001, Federal Highway Administration, Washington, D.C. (2001)
32. Sheppard, D.M., Melville, B., Demir, H.: Evaluation of existing equations for local scour at bridge piers. J. Hydraul Eng. ASCE **140**(1), 14–23 (2014)
33. Unger, J., Hager, W.H.: Down-flow and horseshoe vortex characteristics of sediment embedded bridge piers. Exp. Fluids **42**, 1–19 (2007)
34. Yanmaz, A.M.: Temporal variation of clear-water scour at cylindrical bridge piers. Can. J. Civil. Eng. ASCE **33**, 1098–1102 (2006)

Testing and Calibration of Contact-Free Radar Type Discharge Sensor

R.P. Gupta, K.G. Bhonde and H.R. Khandagale

Abstract There are numerous techniques for measuring flow rates in open channels and closed conduits. The exact and real-time knowledge of the discharge is an important task in the fields of hydrology, water storage management and irrigation. Periodical calibration of the current meter is therefore necessary as per ISO 3455/IS 13371 [1, 2] to ascertain its performance and to account for possible wear and tear of its parts. Installation, performance, reliability and safety for rotating and non-rotating type current meters in flood plain are challenging tasks due to turbulent flow and the presence of debris, etc. To overcome this, water contact-free device is need of time, which can sense flow from distant place. Tehri Hydro Development Corporation has acquired such sensors from Sommer Messtechnik, GmbH, Austria, to measure the continuous river flow and entrusted the calibration to CWPRS, using current meter rating trolley (CMRT) facility. Equipment is based on the principle of the Doppler effect. The instrument is mounted on the CMRT above the tank. The radar sensor transmits a signal with a constant frequency in a specific angle to the water surface. The signal is reflected and received back with a shift in frequency due to Doppler effect by movements of the water surface. In order to simulate river-like flow conditions, three cup type current meters at a specific depth by rigid rod suspension were immersed at front, middle and rear sides of the trolley to propagate surface water currents. The contact-free water level measurement by sensor uses the principle of transit time measurements of reflected signals and transmits a short microwave impulse in the direction of the water surface. This impulse is reflected at the water surface and is recorded by sensor. Calibration of

R.P. Gupta (✉)
Scientist 'D', Central Water and Power Research Station (CWPRS),
Khadakwasala, Pune 411024, Maharashtra, India
e-mail: gupta_rp30@yahoo.co.in

K.G. Bhonde · H.R. Khandagale
Scientist 'B', Central Water and Power Research Station (CWPRS),
Khadakwasala, Pune 411024, Maharashtra, India
e-mail: kalindi_63@yahoo.com

H.R. Khandagale
e-mail: anuharsh2005@gmail.com

V. Garg et al. (eds.), *Development of Water Resources in India*,
Water Science and Technology Library 75, DOI 10.1007/978-3-319-55125-8_35

contact-free radar discharge sensors type RQ-30A [3] has been carried out. The result of calibration indicates close agreement between the speed of rating trolley and corresponding water velocity indicated by the sensor, which are well within the specified accuracy of ±0.02 m/s for most of values. The water level measured by the metric gauge and indicated by sensor is also within specified accuracy of ±0.002 m. Periodical calibration of the sensor is very much necessary to check its accuracy and performance.

Keywords Rotating and non-rotating type current meters · Contact-free radar type discharge sensor · Current meter rating trolley (CMRT) · Calibration of sensor

Subject Classification Codes Water resources planning and management

1 Introduction

There are numerous techniques for measuring flow rates in open channels and closed conduits. Conventional cup/propeller rotating type current meters are in use for flow measurements in rivers, open channels, penstocks and closed conduits. Non-rotating element type (stationery type) current meters like electromagnetic, acoustic Doppler current profiler (ADCP), self-recording type and contact-free radar type current meters are also used for the flow measurements in rivers, open channel and oceanography. The exact and real-time knowledge of the discharge is an important task in the fields of hydrology, water storage management strategies, irrigation and prevention of natural hazards.

In order to determine the velocity of flow from the observed values of rate of revolutions of current meter rotor, it is essential to know the relationship between these two parameters. The process of experimental determination of the relationship between velocity of flow and the rate of revolutions of its rotor is known as calibration. Periodical calibration of the current meter in use is therefore necessary to ascertain its performance and to account for possible wear and tear of its parts. The International Standards on acceptance tests of hydroturbines and pumps using current meters for discharge measurement recommend that the current meters be calibrated before and after each series of measurement so as to ensure stipulated accuracies in these standards. Even for non-rotating element types (stationery type), periodical calibration is essential to check its performance.

Installation, performance, reliability and safety for rotating and non-rotating type current meters in flood plains having high flow velocity are challenging tasks due to turbulent flow condition and the presence of debris, drifting logs and stumps. To overcome this problem, water contact-free device is utmost required which can sense flow from distant place. Tehri Hydro Development Corporation (THDC) has acquired sophisticated and advanced contact-free radar type discharge sensors from Sommer Messtechnik, GmbH, Austria, to measure the continuous river flow velocity and real-time discharge data. However, these sensors need testing and

calibration before installation at site for its accuracy and performance. The testing and calibration of four number of discharge sensors using current meter rating trolley (CMRT) facility was carried out at CWPRS, Pune.

2 Calibration of Current Meters in Straight Open Tank

Accuracy of discharge measurements using current meters depends largely on precision of calibration. The ideal way of calibration of a current meter is to tow the current meter in still water at known velocities. Calibration of current meters in straight open tank (called as rating tank) is an internationally accepted practice. The International Standards ISO 3455 [1] and Indian Bureau of Standards IS 13371 [2] specify the procedure of calibration of current meters in rating tank. During calibration, the current meter is suspended from the trolley and drawn through still water contained in the tank at a number of steady speeds of the trolley. The rotating element of a current meter is driven by the fluid at an angular velocity which is proportional to the local velocity of the fluid at the point of immersion when that velocity exceeds a critical value. Simultaneous measurements of the speed of the trolley and the rate of revolution of the rotor or the velocity indicated on the display unit of the meter are taken. In the case of rotating element current meter, the two parameters are related by one or more equations in its operating zone. The velocity of fluid is determined by counting the number of revolutions of the rotor during a specified time interval by observing the time required by the rotor to turn a given number of revolutions and constitute the calibration table or rating equation.

Non-rotating (stationary) sensor type current meter is also suspended from the trolley and drawn through still water contained in the tank at a number of steady speeds of the trolley. The velocity indicated on its display unit is compared with the corresponding trolley speed to know the deviation in measurement. However, in the case of contact-free radar type discharge sensor is usually mounted on rigid towing system of CMRT to sense the water flow from a distant place. As the still water contained in the rating tank and discharge sensor senses only flowing water, flow condition is simulated by immersing cup type current meter at different locations to propagate surface water currents. The velocity indicated on its display unit is compared with the corresponding trolley speed to know the error in measurement.

3 Current Meter Calibration Facility at CWPRS

CWPRS has a rating tank facility, which was established in 1955 for testing of ship models as well as calibration of current meters. The tank is 228 m long, 3.66 m wide and 2.13 m deep. The rating trolley is self-propelled type which runs on two parallel straight steel rails 4.267 m apart, accurately aligned with the length of the tank. The trolley incorporates precise electronic drive and speed control system and

on board computerized data acquisition and processing system so as to achieve wider speed range of 0.01 m/s (10 mm/s) to 6 m/s and uncertainties in measurement of calibration parameters within 0.1% at 95% confidence level. Figure 1 shows current meter rating trolley (CMRT) facility at CWPRS.

4 Principle of Measurement for Contact-Free Radar Type Discharge Sensor

The RQ-30 contact-free radar type discharge sensor measures [3] the flow velocity and water level at the water surface. Figure 2 shows the schematic view for discharge measurement principal of RQ-30 radar sensor.

Fig. 1 Current meter rating trolley (CMRT) at CWPRS

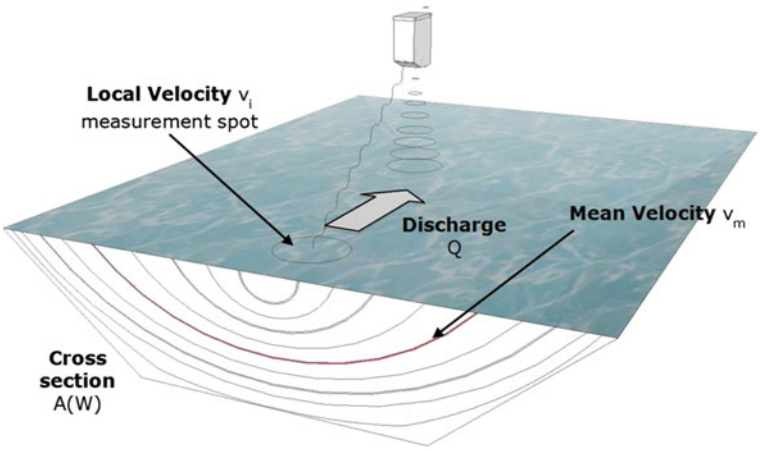

Fig. 2 Principle of radar sensor

4.1 Principle of Flow Velocity Measurement

The contact-free measurement of the flow velocity is based on the principle of the Doppler effect [4–6]. The radar sensor transmits a signal with a constant frequency in a specific angle to the water surface. Then, the signal is reflected back. Due to fluid movement, a shift in frequency is observed. This shift in frequency is linearly proportional to the velocity of fluid. The reflected signal is received by the antenna of the radar sensor. Thus by comparing the transmitted frequency to the frequency of the reflected signal from the water surface, the local velocity can be determined.

The radar sensor has an opening angle of 12°. Therefore, the signals of an area are measured. The size of the area depends on the inclination angle and the distance from the sensor to the reflecting water surface. The velocities appearing in this area have a specific distribution depending on the current conditions. The velocity distribution is determined with a digital signal processor via spectral analysis, and the dominant velocity in the measurement area is calculated. Spectra can be output and used to evaluate measurements at gauging sites. Radar sensor movements can appear in directions either toward or away from the radar sensor. Depending on the direction, a frequency shift to higher or lower frequencies occurs. This phenomenon allows the radar sensor to distinguish the flow directions and accordingly evaluate the velocity distribution. As the radar sensor is directed in a specific angle to the water surface, an angle correction has to be applied. The radar sensor internally measures its vertical inclination and uses this value for automatic angle correction.

4.2 Principle of Water Level Measurement

The contact-free water level measurement uses the principle of transit time measurement of reflected signal [3, 4]. The radar sensor is installed above a river and transmits a short microwave impulse in the direction of the water surface. This impulse is reflected from the water surface and is recorded by the same sensor now working as receiver. The time between transmitting and receiving the impulse is directly proportional to the distance from sensor to water surface.

5 Specification of Contact-Free Radar Type Discharge Sensor

Using the CMRT facility, contact-free radar type discharge sensor (stationery) type current meters first time calibrated in India at CWPRS. These contact-free radar type discharge sensors are RQ30A [3] type and manufactured by Sommer Messtechnik GmbH, Austria. Detailed specifications of radar sensor for velocity measurement and water level measurement sensor are given in Table 1. Figure 3 shows a schematic view of contact-free radar type discharge sensor.

Table 1 Specification of radar sensor for velocity and water level measurement

Description	Velocity measurement	Water level measurement
Detectable measurement range	0.10…15 m/s (depending on the flow conditions)	0…15 m—standard version 0…35 m—extended measurement range (optional)
Accuracy	±0.02 m/s	±2 mm; ±0.025% FS (15 m)
Resolution	1 mm/s	1 mm
Direction recognition	±	
Measurement duration	5…240 s	
Measurement interval	8 s…5 h	
Measurement frequency (GHz (K-Band))	24	26
Radar opening angle	12°	10°
Distance to water surface	0.50…35 m	
Vertical inclination	Measured internally	

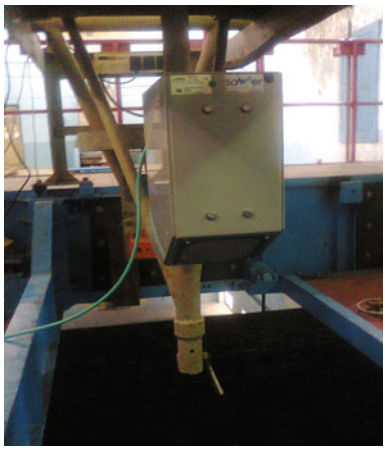

Fig. 3 Schematic view of contact-free radar type discharge sensor (R30A)

6 Test Setup for Velocity Measurement

The measuring instrument is mounted on the towing carriage by rigid rod suspension above the tank water surface. The radar sensor is mounted in such way that it emits a frequency signal through an adequate angle and distance from the water surface [4–6]. Contact-free radar type sensor senses the velocity of flowing water from distant place. However, rating tank water is in still/tranquil condition. In order to simulate river-like flow conditions, three cup type current meters at a specific depth by rigid rod suspension were immersed at front, middle and rear sides of the trolley to propagate surface water currents. Different trial runs were made to assess the optimum location and depth of immersion of these current meters to simulate

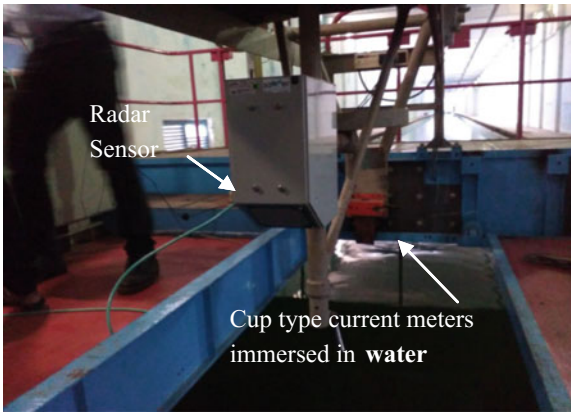

Fig. 4 Experiment test setup

Fig. 5 Readout unit radar sensor

exact field flow conditions. Figures 4 and 5 shows the mounting setup comprising of contact-free radar type discharge sensor, its read out unit and locations of current meters on rigid rods at front, middle and rear sides of the trolley.

7 Calibration Procedure for Velocity Measurement

The radar sensor mounted on current meter rating trolley is towed through still water at a constant speed (reference velocity, V_t). The measured values are stored up in readout unit of contact-free radar type discharge sensor shown in Fig. 5. During the steady speed of trolley, corresponding velocity indicated by the sensor on display unit is observed. In similar way, CMRT is towed through water different constant speeds ranging from 0.5 to 3.5 m/s and measured values were stored at 15 s interval in readout unit continuously.

7.1 Test Results for Velocity Measurement

Calibration of contact-free radar type discharge sensors, current meter type: RQ-30A, Make: Sommer Messtechnik GmbH, Austria, having Sr. nos. 11151444–11151447 was carried out at CWPRS for THDC India Limited, Tehri, Uttarakhand. Table 2 shows calibration value of water velocity. Figure 6 shows calibration curve for trolley velocity versus velocity indicated by the sensor. The sensors were calibrated in the velocity range of 0.5 to 3.5 m/s due to limitation of CMRT system.

8 Test Setup for Water Level Measurement

The radar sensor is mounted on CMRT with long rigid rod with clamps. The sensor can slide over this rod at different elevation from the surface of water level of the tank. Parallel to this rigid rod, a standard metric gauging rod is attached to compare the water level. The water level depth indicated by the sensor and measured by gauge is compared, and measurement error is shown in the result. Figure 7 shows the setup for water level measurement.

Table 2 Velocity measurement result of radar sensors

Sensor Sr. no. 11151444				Sensor Sr. no. 11151445		
Sr. no.	Trolley velocity V_t (m/s)	Velocity by sensor V_c (m/s)	$V_t - V_c$ V_d (m/s)	Trolley velocity V_t (m/s)	Velocity by sensor V_c (m/s)	$V_t - V_c$ V_d (m/s)
1	0.501	0.502	−0.001	0.513	0.513	0.000
2	1.014	1.025	−0.011	1.014	1.012	0.002
3	1.503	1.502	0.001	1.494	1.505	−0.011
4	2.010	2.000	0.010	1.998	1.943	0.055
5	2.505	2.470	0.035	2.494	2.493	0.001
6	2.995	2.995	0.000	3.000	2.990	0.010
7	3.490	3.520	−0.030	3.499	3.515	−0.016
Sr. no. 11151446				Sr. no. 11151447		
1	0.513	0.495	0.018	0.510	0.517	−0.007
2	1.017	0.965	0.052	1.005	0.993	0.012
3	1.512	1.550	−0.038	1.515	1.535	−0.020
4	2.010	2.035	−0.025	2.019	2.020	−0.001
5	2.508	2.515	−0.007	2.505	2.510	−0.005
6	3.050	3.055	−0.005	3.038	2.955	0.083
7	3.496	3.480	0.016	3.505	3.540	−0.035

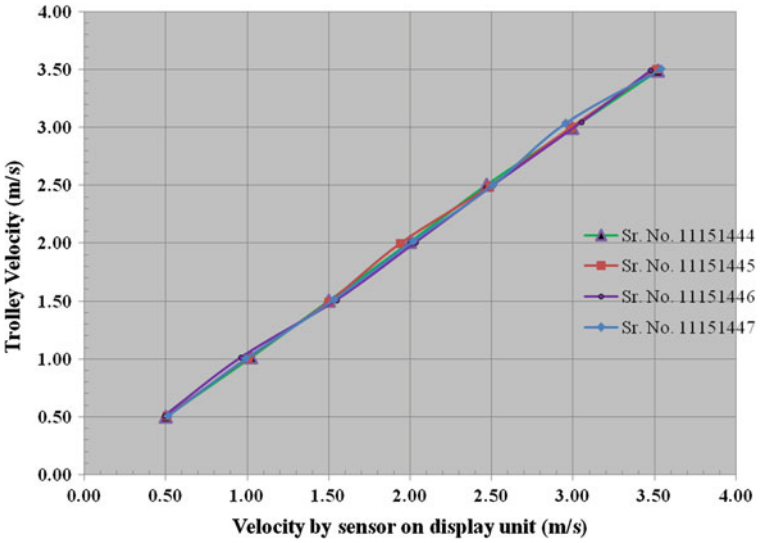

Fig. 6 Calibration curve for trolley velocity versus velocity indicated by the sensor

Fig. 7 Test setup for water level measurement

8.1 Test Result for Water Level Measurement

Water level measurement for contact-free radar type discharge sensors, having Sr. nos. 11151444–11151447, was taken. Table 3 shows the water level indicated by sensor and measured by gauge.

Table 3 Water level indicated by sensor Sr. no. 11151444—11151447

Water level measured by gauge	Water Level indicated by sensor	$D_0 - D_1$	Water level measured by gauge	Water Level indicated by sensor	$D_0 - D_1$
D_0 (m)	D_1 (m)	D_d (m)	D_0 (m)	D_1 (m)	D_d (m)
Water level for sensor Sr. no. 11151444			Water level for sensor Sr. no. 11151445		
1.730	1.730	0	2.118	2.118	0
2.556	2.555	−0.001	2.964	2.964	0
3.650	3.649	−0.001	3.559	3.564	0.005
Water level for sensor Sr. no. 11151446			Water level for sensor Sr. no. 11151447		
2.131	2.131	0	2.425	2.425	0
2.954	2.956	0.002	3.277	3.279	0.002
3.655	3.656	0.001	3.873	3.872	−0.001

9 Conclusion and Recommendation

Contact-free radar type sensor senses the velocity of flowing water from a distant place. However, rating tank water is in still/tranquil condition. In order to simulate river-like flow conditions, three cup type current meters at a specific depth by rigid rod suspension were immersed at front, middle and rear sides of the trolley to propagate surface water currents. Different trial runs were made to assess the optimum location and depth of immersion of these current meters to simulate exact field flow conditions. Velocity and water level depth measurements were taken for four number of contact-free discharge sensor using CMRT facility. From the measurements, it is concluded that

(a) The speed of rating trolley and corresponding water velocity indicated by the sensor show close agreement with each other and are well within the specified accuracy of ±0.02 m/s for the most of values.
(b) The water level measured by the metric gauge and indicated by sensor is within specified accuracy of ±0.002 m.
(c) Periodical calibration of the sensor is necessary to check its consistency and accuracy in performance.

Acknowledgements We wish to express our deep sense of gratitude to Dr. Mukesh Kumar Sinha, Director CWPRS, for encouragement and giving permission to publish this paper.

References

1. ISO 3455.: Liquid flow measurement in open channels—Calibration of rotating—element current meters in straight open tanks (1976)
2. IS 13371.: Code of practice for calibration (Rating) of rotating element current meters in open tank (1992)

3. User Manual of RQ-30, RQ-30a.: Discharge Measurement System, Firmware version 1.8x, Sommer Messtechnik, GmbH, A-6842 Koblach, Manual version: V02 (2014)
4. Federal Institute of Metrology.: Calibration of RQ 30A, Sommer make contact free radar discharge sensor. METAS Laboratory for Hydrometry Lindenweg 50, 3003 Bern-Wabern, Switzerland (2015)
5. Costa, J.E., Cheng, R.T., et.al.: Use of radars to monitor strem discharge by noncontact methods. J. Am. Geophys. California, USA, Water Resour. Res. **42**, W07422 (2006)
6. Lee, M.-C., Lai, C.-J., et.al.: Non contact flood discharge measurements using an X-band pulse radar (I) theory. J. Elsever Sci. Ltd, Flow Measur. Instrum. **13**, 265–270 (2002)

Turbulent Structures in Open-Channel Flow with Emergent and Sparse Vegetation

Soumen Maji, Nooka Raju Gompa, Prashanth Reddy Hanmaiahgari and Vikas Garg

Abstract Important turbulent characteristics are compared between upstream, interior and downstream of a sparse and emergent vegetation patch along the centerline in an open-channel flow. The emergent vegetation patch is made up of seventy uniform rigid acrylic cylindrical rods with regular spacing between two cylinders along streamwise and lateral directions. Along the centerline from upstream to downstream through the interior of the vegetation patch, time-averaged streamwise and lateral velocities are decreasing whereas vertical velocities are increasing. The profiles of streamwise lateral and vertical normal stresses, and turbulent kinetic energy increase in downstream direction through the vegetation patch along the centerline but slightly decrease in the wake region immediate downstream of the trailing edge as compared the values in the middle region of the vegetation patch. The dominant Reynolds shear stress $-\overline{u'w'}$ profiles show decreasing trend in the downstream direction inside the vegetation patch and in the wake region downstream of trailing edge. The vertical distribution of $-\overline{u'v'}$ shows negative values at the leading edge of the vegetation patch, but positive at interior and immediate downstream of the vegetation patch, which demonstrates increased lateral momentum transfer in downstream direction along the vegetation patch.

Keywords Turbulent flow · Streamwise variation · Emergent vegetation · Sparse vegetation · Open-channel

S. Maji (✉) · N.R. Gompa · P.R. Hanmaiahgari
Department of Civil Engineering, IIT Kharagpur, Kharagpur 721302, India
e-mail: soumen@civil.iitkgp.ernet.in; soumen.maji184@gmail.com

N.R. Gompa
e-mail: rajugompa1@gmail.com

P.R. Hanmaiahgari
e-mail: hpr@civil.iitkgp.ernet.in

V. Garg
Department of Civil Engineering, UPES, Dehradun 248007, India
e-mail: gargvikas27@gmail.com

V. Garg et al. (eds.), *Development of Water Resources in India*,
Water Science and Technology Library 75, DOI 10.1007/978-3-319-55125-8_36

1 Introduction

Emergent vegetation in open-channel flow affects mass and momentum transfer, roughness, sedimentation, velocity of flow, bed shear, turbulence quantities, biological processes and aquatic life. In addition to that, flow through emergent vegetation is characterized by significant velocity gradients and drag discontinuity at the interface resulting in shear layer formation between the vegetation stems and flow outside the vegetation. The shear layer in turn produces large coherent vortices due to Kelvin–Helmholtz instability and continues to grow in downstream due to vortex pairing and the creation of vortex street and eventually dissipate into the flow (Chen et al. [2]). The invalidity of log law in the roughness sub-layer of sparse emergent vegetation patch is demonstrated numerically by Lopez and Garcia [6]. Stone and Shen [13] and Vargas-Luna et al. [14] indicated that the flow resistance in rigid emergent vegetation depends on density of cylinders per unit area. Musleh and Cruise [9] have shown the importance of stem diameter of the vegetation to compute the flow resistance. Rominger and Nepf [12] have introduced a normalized parameter 'canopy flow blockage' which depends on the solid volume fraction and width of the vegetation patch and described its significant effect on the upstream flow velocity. On the other hand, a length scale is proposed by Cheng et al. [3] for the normalization of vegetated open-channel turbulent flow. In spite of having several attempts on the prediction of hydrodynamics in vegetated flow, no comprehensive investigation has been done so far to compare the turbulent hydrodynamics at interior and exterior of a sparse and emergent vegetation patch.

To attempt the aforementioned overlooked research problem, the objective of this study is to compare important turbulent features at upstream, interior and downstream of a vegetation patch which is sparse, rigid and emergent.

The paper consists four sections. A brief description of experimental methodology is given in Sect. 2. The physics of the measured profiles of important turbulent features is described elaborately in Sect. 3, and the study ends with some concluding remarks given in Sect. 4.

2 Experimental Methodology

The experiments were performed in a flume (12 m long, 0.91 m width, 0.61 m deep and 0.002 longitudinal slope) of Hydraulic and Water Resources Engineering Laboratory, Department of Civil Engineering, Indian Institute of Technology Kharagpur, India. A constant water depth $h = 20$ cm was maintained during the experiment. The flow can be visualized by 8-m-long and 1.5-cm-thick sidewalls made by transparent glass. For the recirculation of the flow between flume and

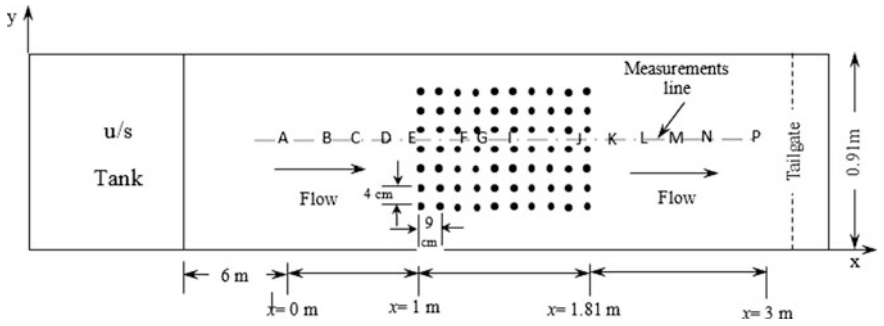

Fig. 1 *Top* view of experimental setup

underground sump, two centrifugal pumps were used. The flume was made rough by cladding sand particles whose weighted mean diameter d_{50} = 0.25 cm. A honeycomb baffle wall was provided at the entrance of the flume to reduce the turbulence, vorticity and non-uniformity in the incoming flow.

To prepare the sparse vegetation patch, 70 uniform acrylic cylindrical rods (0.64 cm diameter and 30 cm length) were perpendicularly planted with an arrangement of an array 7 × 10 over a fixed perspex sheet into the channel bed. The dimensions of vegetation patch were 81 cm length and 24 cm width as the regular spaces between two consecutive cylinders along streamwise and lateral directions were 9 cm and 4 cm, respectively. The front area of vegetation per unit volume was calculated as λ = 0.0178/cm which corresponds to a percentage of solid volume fraction Ø = 0.89%. The schematic diagram of the top view of experimental setup is shown in Fig. 1. The depth averaged flow velocity was kept 23 cm/s together with the flow discharge as 4 × 10^4 cm^3/s. The Reynolds number of fully developed flow is 43,500, stem Reynolds number is 1470, and wake Reynolds number is 28,050.

A Nortek VectrinoPlus ADV with one emitter and four down-looking probes was used to measure the instantaneous three-dimensional velocity components by analyzing the sound echoes received from the suspended particles in flowing water. At every point, data were collected with a sampling rate of 100 Hz and sampling period of 2 min which implies that 100 × 60 × 2 = 12000 instantaneous measurements were collected at the point. The data obtained were processed by a three-dimensional coordinate system where x, y and z axes represent streamwise, lateral and vertical directions, respectively. The time-averaged velocities along x, y and z directions are represented by u, v and w, respectively, together with fluctuation parts u', v' and w', respectively. The accurate prediction of experimental measurements is secured through rigorous data quality testing processes like spike filtering, signal-to-noise ratio (SNR) thresholding technique proposed by previous researchers [1, 4, 5, 7–10, 15].

3 Results and Discussion

Figures 2, 3, 4, 5, 6, 7, 8, 9, 10 and 11 illustrate the distribution of important turbulent parameters along the centerline (y = 47.4 cm) of the sparsely vegetated open-channel flow across its cross section. In these figures, the normalized vertical height on ordinate is represented by $\xi\,(=z/h)$ which lies between 0 and 1, x = 100 cm represents upstream of the vegetation patch, x = 150 cm represents the interior of the vegetation patch in flow direction, and x = 190 cm represents the wake region immediate downstream of the vegetation patch.

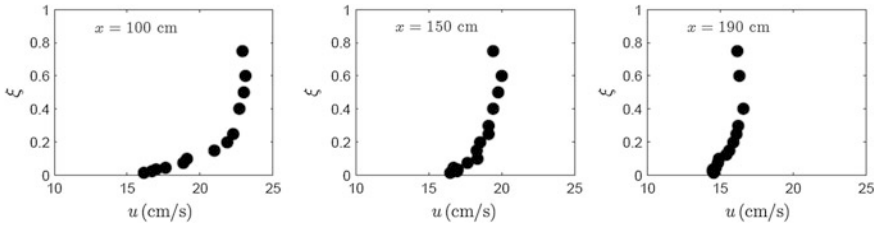

Fig. 2 Profiles of streamwise time-averaged velocity u at the entrance (x = 100 cm), interior (x = 150 cm) and immediate downstream (x = 190 cm) of the vegetation patch

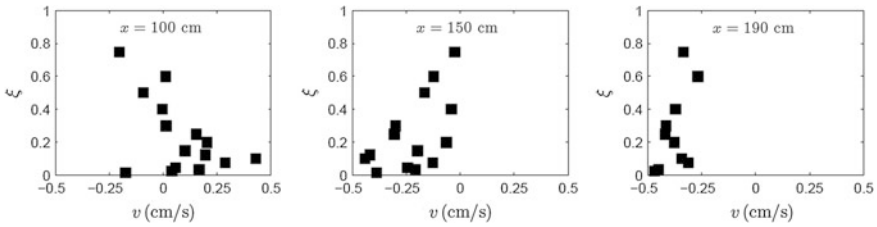

Fig. 3 Profiles of lateral time-averaged velocity v at the entrance (x = 100 cm), interior (x = 150 cm) and immediate downstream (x = 190 cm) of the vegetation patch

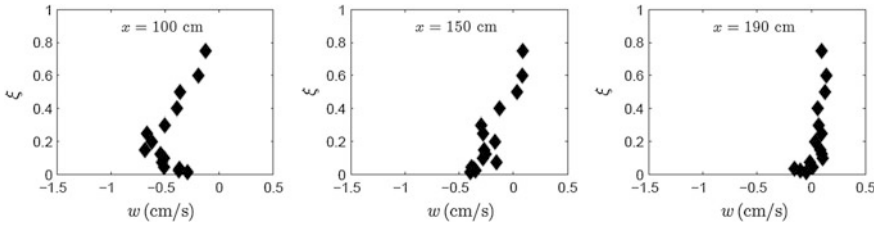

Fig. 4 Profiles of vertical time-averaged velocity w at the entrance (x = 100 cm), interior (x = 150 cm) and immediate downstream (x = 190 cm) of the vegetation patch

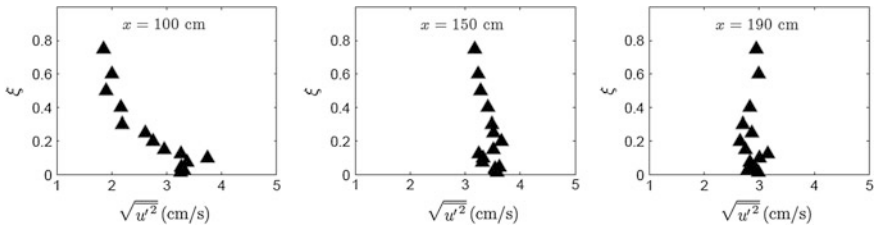

Fig. 5 Profiles of streamwise normal stress in terms of $\sqrt{u'^2}$ at the entrance (x = 100 cm), interior (x = 150 cm) and immediate downstream (x = 190 cm) of the vegetation patch

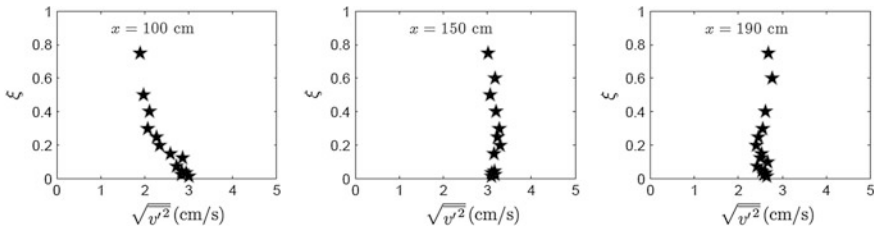

Fig. 6 Profiles of lateral normal stress in terms of $\sqrt{v'^2}$ at the entrance (x = 100 cm), interior (x = 150 cm) and immediate downstream (x = 190 cm) of the vegetation patch

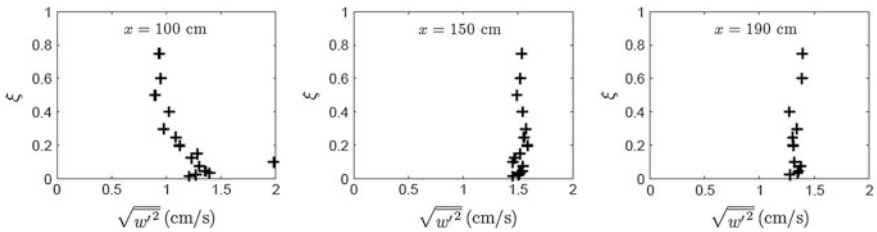

Fig. 7 Profiles of vertical normal stress in terms of $\sqrt{w'^2}$ at the entrance (x = 100 cm), interior (x = 150 cm) and immediate downstream (x = 190 cm) of the vegetation patch

3.1 Time-Averaged Velocities

The nature of time-averaged streamwise velocity u can be observed from Fig. 2 where at the leading edge of vegetation, i.e., x = 100 cm, a nature of fully developed turbulent flow over a rough bed without vegetation is shown. In the middle region of vegetation patch (x = 150 cm), the magnitude of u decreases considerably

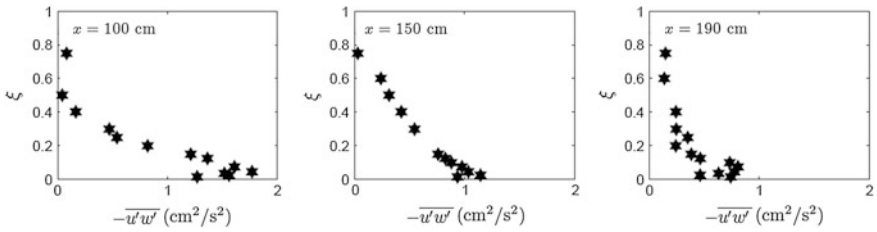

Fig. 8 Profiles of Reynolds shear stress $-\overline{u'w'}$ at the entrance (x = 100 cm), interior (x = 150 cm) and immediate downstream (x = 190 cm) of the vegetation patch

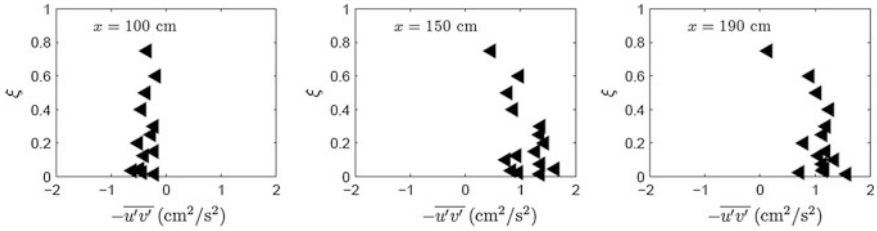

Fig. 9 Profiles of Reynolds shear stress $-\overline{u'v'}$ at the entrance (x = 100 cm), interior (x = 150 cm) and immediate downstream (x = 190 cm) of the vegetation patch

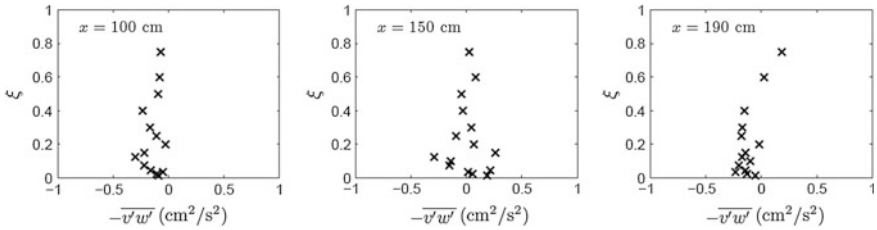

Fig. 10 Profiles of Reynolds shear stress $-\overline{v'w'}$ at the entrance (x = 100 cm), interior (x = 150 cm) and immediate downstream (x = 190 cm) of the vegetation patch

in comparison with the upstream profile and this characteristic is continued even at downstream of the vegetation patch (x = 190 cm). The reason behind this characteristic is that, inside the vegetation patch, the flow in streamwise direction is obstructed due to vegetation stems. Hence, the flow continuously losses its intensity along the interior and downstream of vegetation patch and results in decreasing magnitude of u profile. Figure 2 illustrates increase in velocity along the streamwise distance in the gaps between vegetation patch and side walls.

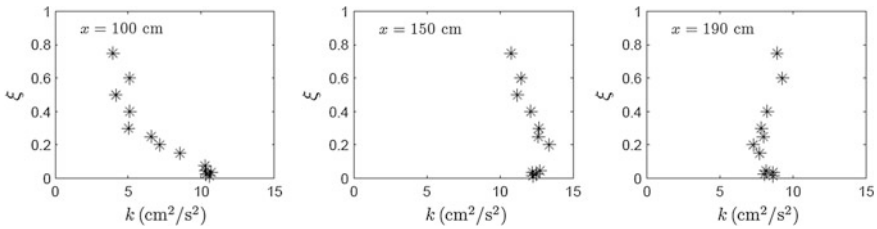

Fig. 11 Profiles of turbulent kinetic energy k at the entrance (x = 100 cm), interior (x = 150 cm) and immediate downstream (x = 190 cm) of the vegetation patch

It is observed from Fig. 3 that the time-averaged lateral velocity v values are approached to zero at the entrance of the vegetation patch (x = 100 cm). In the interior of the vegetation patch (x = 150 cm), the magnitude of v decreases. However, at the immediate vicinity after leaving the vegetation patch (x = 190 cm), lateral velocities are further decreased as compared to the profile at x = 150 cm. In the interior of the vegetation patch, the obstruction due to cylinders causes the flow to deviate from the central region to the gaps between the vegetation patch and the sidewalls, resulting in increase in value of v profile. On the other hand, the flow is free of obstructions in the wake region, causing magnitude of v becomes small due to the less lateral flow.

Figure 4 shows negative values of time-averaged vertical velocity w at leading edge of vegetation patch. Moreover, an increasing characteristic of downward w is observed with increasing downstream length.

This nature of the flow implies that the cylinders inside the vegetation patch have a significant role to continuously reduce the strength of downward w profile along the downstream in the interior of the vegetation patch and wake region downstream of the patch. The increasing characteristic of downward w profile explains that, in a turbulent flow over an erodible bed with sparse vegetation patch, the scouring occurs in the vicinity of leading edge and the scoured sediment would have been deposited in interior region near to the trailing edge of the vegetation patch.

3.2 Normal Stresses

The calculated profiles of Reynolds normal stresses in terms of root-mean-square (RMS) fluctuating velocities $\sqrt{\overline{u'^2}}$, $\sqrt{\overline{v'^2}}$ and $\sqrt{\overline{w'^2}}$ are shown in Figs. 5, 6 and 7, respectively. Similar kind of characteristics is observed though the profiles of $\sqrt{\overline{u'^2}}$, $\sqrt{\overline{v'^2}}$ and $\sqrt{\overline{w'^2}}$. The magnitude of RMS fluctuating vertical velocity $\left(0.75 \leq \sqrt{\overline{w'^2}} \leq 1.75\right)$ shows lesser value in comparison with the RMS fluctuating streamwise and lateral velocities $\left(1.5 \leq \sqrt{\overline{u'^2}}, \leq 4\right)$, $\left(2 \leq \sqrt{\overline{v'^2}} \leq 3.5\right)$. But, the

magnitudes of root-mean-square velocities increase in the middle of the vegetation patch (x = 150 cm) in comparison with the respective profiles of fully developed flow at the leading edge (x = 100 cm) of the vegetation patch. The peaks of root-mean-square fluctuating velocities are located near the channel bed for fully developed flow (x = 100 cm). However, the peak values of root-mean-square fluctuating velocities are shifted away from the channel bed for inside the vegetation patch. On the other hand, these values decrease further at the trailing edge (x = 190 cm) as compared to the same profiles in the interior of the vegetation patch (x = 150 cm). Hence, the phenomena can be explained as follows. Due to the interaction between cylinders and flow, large number of vortices are generated inside the sparse vegetation patch and interaction of these vortices causes higher fluctuations in three-dimensional instantaneous velocities resulting in increase in root-mean-square fluctuating velocities. At the downstream of the vegetation patch, the flow is affected by wake region of the vegetation patch resulting in decreased vorticity and root-mean-square velocities in comparison with profiles at interior of the vegetation patch.

3.3 Reynolds Shear Stresses

The flow is strongly influenced by Reynolds shear stress $-\overline{u'w'}$ than the other Reynolds shear stresses $-\overline{u'v'}$ and $-\overline{v'w'}$. The vertical distributions of $-\overline{u'w'}$ at different locations are shown in Fig. 8. The maximum values of $-\overline{u'w'}$ are located near the channel bed along the centerline of vegetation patch. Though the profile of $-\overline{u'w'}$ exhibits a characteristic of fully developed flow at leading edge of the vegetation patch (x = 100 cm), its magnitude decreases in the vegetation patch (x = 150 cm).

At downstream of trailing edge of the vegetation patch (x = 190 cm), the magnitude of $-\overline{u'w'}$ further decreases in comparison with the profile at interior of the vegetation patch. As the intensity of flow decreases through the patch in the streamwise direction and wake region at immediate downstream of the trailing edge cause decrease in magnitude of $-\overline{u'w'}$.

It is obtained from Fig. 9 that the vertical distribution of $-\overline{u'v'}$ shows negative values at the leading edge of the vegetation patch. However, $-\overline{u'v'}$ is positive at interior and immediate downstream of the vegetation patch. The increasing trend of $-\overline{u'v'}$ illustrates the increased lateral momentum transfer caused by the flow diversion from the vegetation patch toward the gap between the vegetation patch and side walls.

Unlike the vertical distributions of $-\overline{u'w'}$ and $-\overline{u'v'}$, the observed vertical distribution of $-\overline{v'w'}$ is not conclusive and scattered as shown in Fig. 10. As expected, $-\overline{v'w'}$ are positive near the free surface in the wake region immediate downstream

of the vegetation patch. The near-zero values of $-\overline{v'w'}$ throughout the depth along the centerline of vegetation patch prove negligible transfer of momentum in the vertical direction in and around the emergent sparse vegetation patch.

3.4 Turbulent Kinetic Energy

The plots of turbulent kinetic energy $k = 0.5\left(\overline{u'^2} + \overline{v'^2} + \overline{w'^2}\right)$ are shown in Fig. 11. At the upstream of the vegetation patch (x = 100 cm), the peak value of k occurs near the channel bed due to the influence of velocity defect layer. Interior of the vegetation patch (x = 150 cm), the values of k increase throughout the depth due to the increased vorticity and the intense mixing. On the other hand, the magnitude of k decreases at the downstream of the trailing edge of vegetation patch (x = 190 cm) is due to the effect of wake region. In the wake region, the peak of k is occurring far from the channel bed and irregular variation of peak value of k is caused by the passing detached eddies from upstream cylinder [11].

4 Conclusions

A detailed comparison analysis of important turbulent parameters at upstream, interior and downstream of a sparse vegetation patch has been carried out along the centerline of an open-channel flow. The conclusions obtained from this study are as follows.

- The time-averaged values of streamwise velocity u and lateral velocity v decrease, whereas the vertical velocity w increases in the downstream direction along the centerline of the vegetation patch.
- The profiles of streamwise, lateral and vertical normal stresses and turbulent kinetic energy increase in downstream direction through the vegetation patch along the centerline but slightly decrease in the wake region immediate downstream of the trailing edge as compared to the values in the middle region of the vegetation patch because inside the vegetation patch, the increased vorticity owing to the intense interactions between cylinders and flow causes higher fluctuations in 3D instantaneous velocities and produces larger magnitude of normal stresses and turbulent kinetic energy profiles.
- The profiles of Reynolds shear stresses $-\overline{u'w'}$ display decreasing trend with increasing streamwise distance through interior of the vegetation patch. The decreased flow inside the vegetation patch and in the wake region is responsible for the aforementioned decreasing behavior of $-\overline{u'w'}$ profiles.

- The vertical distribution of $-\overline{u'v'}$ shows negative values at the leading edge of the vegetation patch. However, $-\overline{u'v'}$ is positive at interior and immediate downstream of the vegetation patch.
- The near-zero values of $-\overline{v'w'}$ throughout the depth along the centerline of vegetation patch prove negligible transfer of momentum in the vertical direction in and around the emergent sparse vegetation patch.
- Finally, this study might be useful to understand the behavior of turbulent characteristics in interior and exterior of emergent and sparse vegetated open-channel turbulent flow.

References

1. Chanson, H., Trevethan, M., Aoki, S.I.: Acoustic Doppler velocimetry (adv) in small estuary: field experience and signal post-processing. Flow Meas. Instrum. **19**(5), 307–313 (2008)
2. Chen, Z., Ortiz, A., Zong, L., Nepf H.: The wake structure behind a porous obstruction and its implications for deposition near a finite patch of emergent vegetation. Water Resour. Res. **48** (9) (2012)
3. Cheng, N.S., Nguyen, H.T., Tan, S.K., Shao, S.: Scaling of velocity profiles for depth-limited open-channel flows over simulated rigid vegetation. J. Hydraul. Eng. **138**(8), 673–683 (2012)
4. Goring, D.G., Nikora, V.I.: Despiking acoustic Doppler velocimeter data. J. Hydraul. Eng. **128**(1), 117–126 (2002)
5. Kose, O.: Various filtering algorithms used to eliminate outliers in velocity time series obtained by advs (acoustic Doppler velocimeter). Arab. J. Geosci. **6**(7), 2691–2697 (2013)
6. Lopez, F., Garcia, M.H.: Mean flow and turbulence structure of open-channel flow through nonemergent vegetation. J. Hydraul. Eng. **127**(5), 392–402 (2001)
7. Lu, H., Wang, B., Zhang, H.Q., Wang, X.L.: Acoustic Doppler velocimeter in measurements of turbulent boundary layer flows. Appl. Mech. Mater. **239**, 100–103 (2012)
8. Mori, N., Suzuki, T., Kakuno, S.: Noise of acoustic Doppler velocimeter data in bubbly flows. J. Eng. Mech. **133**(1), 122–125 (2007)
9. Musleh, F.A., Cruise, J.F.: Functional relationships of resistance in wide flood plains with rigid unsubmerged vegetation. J. Hydraul. Eng. ASCE **132**(2), 163–171 (2006)
10. Parsheh, M., Sotiropoulos, F., Porté-Agel, F.: Estimation of power spectra of acoustic-doppler velocimetry data contaminated with intermittent spikes. J. Hydraul. Eng. **136**(6), 368–378 (2010)
11. Ricardo, A.M., Koll, K., Franca, M.J.: The terms of turbulent kinetic energy budget within random arrays of emergent cylinders. Water Resour. Res. **50**(5), 4131–4148 (2014)
12. Rominger, J.T., Nepf, H.M.: Flow adjustment and interior flow associated with a rectangular porous obstruction. J. Fluid Mech. **680**, 636–659 (2011)
13. Stone, B.M., Shen, H.T.: Hydraulic resistance of flow in channels with cylindrical roughness. J. Hydraul. Eng. **128**(5), 500–506 (2002)
14. Vargas-Luna, A., Crosato, A., Uijttewaal, W.S.J.: Effects of vegetation on flow and sediment transport: comparative analyses and validation of predicting models. Earth Surf. Proc. Land. **40**(2), 157–176 (2015)
15. Wahl, T.L.: Discussion of despiking acoustic Doppler velocimeter data by Derek g. Goring and Vladimir i. Nikora. J. Hydraul. Eng. **129**(6), 484–487 (2003)

Experimental Investigation of Turbulent Hydrodynamics in Developing Narrow Open Channel Flow

Debasish Pal, Minakshee Mahananda, Prashanth R. Hanmaiahgari and Mrinal Kaushik

Abstract In the present study, a detailed experimental investigation of turbulent hydrodynamics is carried out on developing flow along the centreline of a narrow open channel. The characteristics of flow velocity, normal stresses and Reynolds stresses have been investigated. At the beginning of the modelled region, the time-averaged streamwise velocity increases up to 20% of the flow depth from the channel bed and decreases with further increase in vertical height. With increasing streamwise length, vertical location of the maximum time-averaged streamwise velocity is shifting away from the bed. The time-averaged lateral velocities are positive along the midsection in the modelling region, whereas the time-averaged vertical velocities exhibit negative value. In the modelled region, the maximum value of time-averaged lateral velocity occurs either near the channel bed or in the vicinity of the free surface; however, the peak value of time-averaged vertical velocity appears in the neighbourhood of the channel bed. In the developing flow region, the values of normal stresses in streamwise and lateral directions are maximum near the bed and decrease with vertical distance up to 40% of the flow depth from the channel bed and after that normal stresses increase with further increase in vertical distance from the channel bed. Moreover, the observed magnitudes of streamwise normal stresses are greater than the corresponding values of lateral normal stress. The normal stress in vertical direction increases with

D. Pal · M. Mahananda · P.R. Hanmaiahgari
Department of Civil Engineering, IIT Kharagpur, Kharagpur 721302, India
e-mail: minakshee.mahananda1@gmail.com

P.R. Hanmaiahgari
e-mail: hpr@civil.iitkgp.ernet.in

M. Kaushik
Department of Aerospace Engineering, IIT Kharagpur, Kharagpur 721302, India
e-mail: mkaushik@aero.iitkgp.ernet.in

Present Address:
D. Pal (✉)
Pillar of Engineering Systems and Design, Singapore University of Technology and Design, 8 Somapah Road, Singapore 487372, Singapore
e-mail: bestdebasish@gmail.com

V. Garg et al. (eds.), *Development of Water Resources in India*,
Water Science and Technology Library 75, DOI 10.1007/978-3-319-55125-8_37

increasing vertical height from the channel bed; however, the increasing trend decreases with increasing streamwise distance. Before attaining the fully developed profile, the Reynolds shear stress exhibits a decreasing trend with increasing vertical height up to 60% of the flow depth from the channel bed, and with further increase in vertical distance, the Reynolds shear stress trend starts increasing. An important finding is that in the modelled region, the developing flow zone, the transition zone from developing flow to fully developed flow and the fully developed flow zone are detected. The present study provides a good quality data for further investigations of developing flow in a narrow open channel.

Keywords Turbulence · Hydrodynamics · Open channel flow · Narrow channel · Reynolds stresses · Flow development

1 Introduction

Understanding the hydrodynamics of open channel flow is very important as it has huge impact on human society. A voluminous amount of research on open channel hydraulics exists in the literature; however, investigators are still re-searching this topic due to its complex nature. In the vertical distribution of streamwise velocity profile, the classical log-law is applicable up to 20% of the flow depth from the channel bed [2, 9, 13]. On the other hand, investigators reported that above 20% of the flow depth from the channel bed, the log-law deviates from the experimental data and the most reasonable formula to account the velocity together with deviation is the log-wake law where the wake function was introduced by Coles [4]. It is worth mentioning here that the log-wake is not valid for narrow open channel where the value of aspect ratio, being defined by the ratio of width to height of the open channel, is less than 5. Moreover, it needs to be mentioned here that for wide open channel where the aspect ratio is greater than 5, the log-wake is not valid near the sidewalls. A century ago, researchers [5, 11] reported that in fully developed narrow open channel flow, the maximum velocity occurs below the free surface of the open channel which is known as dip phenomenon. In the last few decades, several experimental investigations proved the existence of dip phenomenon in narrow open channel [7, 10, 14]. Apart from the experimental study, available theoretical literature had predicted the velocity distribution together with dip phenomenon in narrow open channel [1, 16]. It is well known that to perform an experimental or theoretical study in narrow open channel flow, it is very important to know about the characteristic length by which the flow would acquire a fully developed nature. According to the best of our knowledge, till date, the understanding of the turbulent hydrodynamics of developing open channel flow is not reached up to the desired level and for the narrow open channel flow, the available knowledge on this topic is limited. Moreover, good quality experimental data in developing narrow open channel turbulent flow and the characteristic length required to get a fully developed nature are still lacking in the literature.

To attempt the aforementioned overlooked research problem, this paper presents preliminary experimental results of an ongoing larger project on narrow open channel turbulent flow where the different dimensionless parameters such as aspect ratio, Reynolds number are proposed to be varied in a sizeable range. First, the experimental set-up, experimental methodology, collection of data and the data filtering methodologies are discussed. After that, the observed turbulent characteristics and the reasons behind their behaviour are explained. This study ends by presenting conclusions.

2 Experimental Methodology

The experiments were carried out in an open channel which is located in the Hydraulic and Water Resources Engineering Laboratory of Indian Institute of Technology Kharagpur, India. The dimensions of the flume were 700 cm long, 61 cm width and 70 cm deep, and its longitudinal slope was 0.0002. To avoid the vibration of the flume, it was supported on a steel frame attached to the ground. During the flow in the flume, the structural rigidity of the flume was strengthened by two glass sidewalls with length 300 cm and thickness 1.5 cm. Moreover, the sidewalls were used for the clear visualization of the flow. Looking at the flow along streamwise direction by standing in the middle of the flume, then according to the right and left hands of a person, the two glass sidewalls were treated as right-hand side (RHS) wall and left-hand side (LHS) wall, respectively. At the inlet of the flume, a honeycomb baffle wall was provided to reduce the disturbance by converting the large eddies into small eddies. The test section in the flume was considered as 300 cm long which initial point was started from 150 cm downstream from the inlet. Sand particles of size $D_{50} = 0.25$ cm were coated over the bed surface to make it rough. Two centrifugal pumps were used to recirculate the water between the underground sump and the flume, and the average flow velocity was maintained as 38 cm/s. The flow depth h was maintained as 20 cm by providing a tailgate at the downstream end of the flume. The aspect ratio $A_r(=b/h, b$ is the width of the channel) was calculated as 3.05 which is smaller than 5; therefore, the flow in the channel was treated as a narrow open channel flow. A point gauge with accuracy of ± 0.01 cm was used for the measurement of the flow depth. To measure the flow velocity, a Nortek Vectrino Plus acoustic Doppler velocimeter (ADV) with a fixed probe and four side-looking beams was used. Rails on the sidewalls of the flume were provided for the easy positioning of the ADV and the point gauge. The flow was assumed to be stabilized after 30 min from its commencement, and then, the measurements of flow velocity were taken. A three-dimensional coordinate system was used where the origin was represented by the intersection point of the channel bed and the RHS wall. In the coordinate system, x-axis was represented in the streamwise direction, y-axis was denoted as the lateral direction from the RHS wall to the LHS wall, and z-axis was expressed as the vertical direction from the channel bed. In the modelling region, along the streamwise centreline of the flume,

the measurements of flow velocity were taken at seven stations which were represented by x = 0, 50, 100, 150, 200, 250 and 300 cm. The test section x = 0 is located at 2.15 m downstream of the inlet chamber. For each location of x, the velocity data by ADV were collected at twenty vertical locations along the flow depth which were z = 0.3, 0.5, 0.7, 0.9, 1.5, 2, 2.5, 3, 4, 5, 6, 7, 8, 9, 10, 11, 12, 13, 14 and 10 cm from the channel bed. The flow velocity at each and every vertical point was recorded with the duration of 300 s, sampling frequency of 100 Hz and sampling volume of 2.5 cm^3. The random spikes in the data were removed by the available spike filtering technique [6, 8, 12], and the spikes were replaced by cubic interpolation method. To obtain good quality data, the proposed signal-to-noise ratio method of Chanson et al. [3] was employed where the ratio value was maintained as 20. After that, the data with correlation values greater than 75% were used to investigate the turbulent hydrodynamics of developing flow in narrow open channel. Experimental conditions are given in Table 1 where R_e and Fr represent the Reynolds number and Froude number, respectively, and U expresses the depth-averaged velocity in the fully developed flow region. A picture of the experimental set-up together with the flow is shown in Fig. 1.

Table 1 Summary of experimental conditions

A_r	h (cm)	U (cm/s)	R_e	Fr
3.05	20	37.97	7.59×10^4	0.27

Fig. 1 A picture of experimental set-up together with the flow

3 Results and Discussion

In this section, vertical distribution of normalized time-averaged velocity components, turbulent intensities and Reynolds shear stresses is explained. In addition, the physics behind those characteristics has been discussed. The time-averaged streamwise, lateral and vertical velocity components are represented by u, v and w, respectively, and corresponding fluctuation components are expressed as u', v' and w', respectively. The vertical height z from the channel bed is normalized by the flow depth h as $\xi = z/h$. The time-averaged velocities along streamwise, lateral and vertical directions are normalized by the shear velocity u_* as $u^+ = u/u_*, v^+ = v/u_*$, and $w^+ = w/u_*$, respectively. The computed u_* values at different locations are given in Table 2.

3.1 Time-Averaged Velocity of Flow

ADV data have been used for shear velocity determination from Reynolds shear stress distribution. Figure 2 shows the profiles of normalized time-averaged streamwise velocity u^+ at different streamwise stations along the centreline of the open channel. At the beginning of the modelled section (x = 0 cm), the magnitude of u^+ increases up to 20% of the flow depth from the channel bed and from that position, u^+ decreases further with increasing vertical height. With increasing streamwise distance (x = 50, 100, 150 and 200 cm), it is observed that the vertical location of the maximum u^+ is shifting away from the bed which shows thickening of boundary layer. In developing flow, along streamwise distance, a developed flow phenomenon is observed at $x = 250$ cm and the fully developed characteristic of the flow is confirmed by the profile of u^+ at $x = 300$ cm. In the modelled region (x = 0–300 cm), the dip phenomenon of the flow is observed where the maximum streamwise velocity occurs below the free surface of the open channel. The exact reason of the occurrence of dip phenomenon is not available in the literature;

Table 2 Estimated shear velocity u_* at different locations

x (cm)	0	50	100	150	200	250	300
u_* (cm/s)	3.04	2.84	2.80	2.62	2.49	2.40	2.40

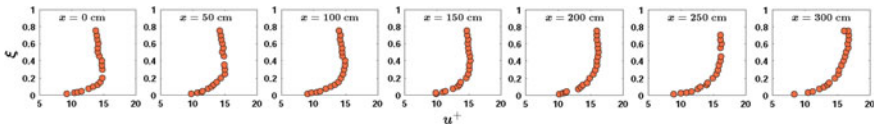

Fig. 2 Profiles of time-averaged streamwise velocity u in developing flow along the centreline of narrow open channel turbulent flow

however, it can be claimed that in narrow open channel flow, the phenomenon is governed by the presence of the secondary current [15, 16]. In addition, it is observed that the range of the magnitude of u^+ increases with increasing streamwise distance.

The vector of lateral and vertical velocities of the flow is known as secondary current. The profiles of normalized time-averaged lateral velocity v^+ at different streamwise stations are shown in Fig. 3. The positive values of v^+ are observed at all locations which implies that the lateral velocity moves from the RHS wall to the LHS wall. Near the inlet at $x = 0$ cm, it is observed that v^+ shows increasing characteristic with increasing vertical height near the channel bed and then, it decreases up to 40% of the flow depth; however, further increasing nature of v^+ is followed from 40 to 80% of the flow depth. With increasing streamwise distance between $x = 50$ and 100 cm, the nature of v^+ is slightly changed where its increasing characteristic near the channel bed is not followed. Moreover, the range of v^+ magnitude at $x = 50$ cm is found smaller than that at $x = 100$ cm, and the reason is due to increased strength of secondary current with increasing streamwise length in developing flow. The profiles of v^+ at $x = 150$ and 200 cm show same trend as observed at $x = 100$ cm though the range of v^+ magnitude decreases in comparison with the preceding profile. It needs to be mentioned here that after crossing a certain streamwise length, the developing flow endeavours to reduce its developing nature and converges to a fully developed flow. This characteristic is pronounced more clearly at $x = 250$ and 300 cm where v^+ increases with increasing vertical height from the channel bed unlike the characteristic found at x = 50, 100, 150 and 200 cm. The range of v^+ magnitude observed at $x = 300$ cm is smaller than that of $x = 250$ cm which shows that the flow is attaining the fully developed nature between $x = 250$–300 cm.

The nature of time-averaged vertical velocity w^+ at different streamwise stations is shown in Fig. 4. Negative values of w^+ are observed in the modelled section,

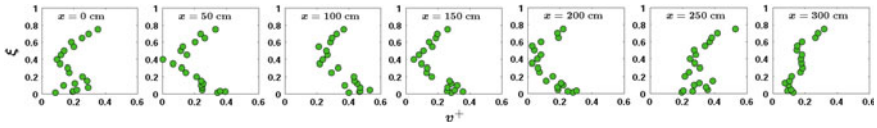

Fig. 3 Profiles of time-averaged lateral velocity v in developing flow along the centreline of narrow open channel turbulent flow

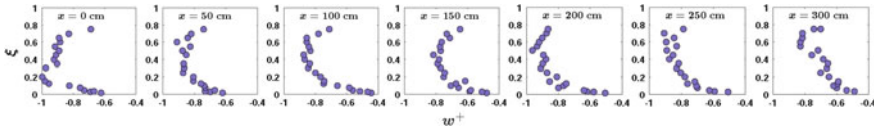

Fig. 4 Profiles of time-averaged *vertical* velocity w in developing flow along the centreline of narrow open channel turbulent flow

and this characteristic indicates that the direction of w^+ is downward in the developing flow. Near the entrance at $x = 0$ cm, the value of w^+ decreases with increasing vertical height up to 20% of the flow depth; however, after that it increases with further increase in vertical height from the channel bed. With increasing streamwise length ($x = 50$–200 cm), the profiles of w^+ show same trend and it is observed that w^+ decreases with increasing vertical distance from the channel bed and this trend is continued till 50% of the flow depth and after that, it decreases up to the vicinity of the free surface. At $x = 250$ and 300 cm, w^+ is maximum near the channel bed and decreases in the direction of the free surface. This trend is similar to fully developed flow. Hence, the non-uniformity of the normalized time-averaged streamwise, lateral and vertical velocities in the entrance region of the flow is due to strong rotational flow and robust mixing.

It is concluded that with respect to a developing flow in a narrow open channel, the strength of secondary current (v^+, w^+) decreases with increasing streamwise length. This phenomenon indicates that over an erodible sediment bed, the erosion ability of developing flow in narrow open channel decreases with increasing streamwise length. A characteristic length is found which is required for the flow to become fully developed in a narrow open channel.

3.2 Normal Stresses

Understanding the variation of non-dimensional normal stress along the flow depth is very important to understand the fluctuations in flow velocity. The non-dimensional normal stresses along streamwise, transverse and vertical directions are denoted by $\overline{u'^2}^+ = \overline{u'^2}/u_*^2$, $\overline{v'^2}^+ = \overline{v'^2}/u_*^2$ and $\overline{w'^2}^+ = \overline{w'^2}/u_*^2$, respectively. Figures 5, 6 and 7 represent the profiles of $\overline{u'^2}^+$, $\overline{v'^2}^+$ and $\overline{w'^2}^+$, respectively, at different streamwise stations in developing narrow open channel turbulent flow.

In Fig. 5, it is followed that the magnitudes of $\overline{u'^2}^+$ at different streamwise stations lie between 0–6. Near the inlet ($x = 0$ cm), the magnitude of $\overline{u'^2}^+$ decreases up to 40% of the flow depth from the channel bed and then increases with further increase in the vertical height. In the region between $x = 50$–150 cm, the

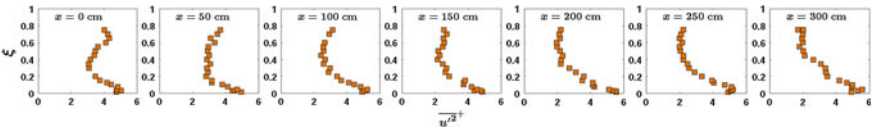

Fig. 5 Profiles of streamwise normal stress $\overline{u'^2}$ in developing flow along the centreline of narrow open channel turbulent flow

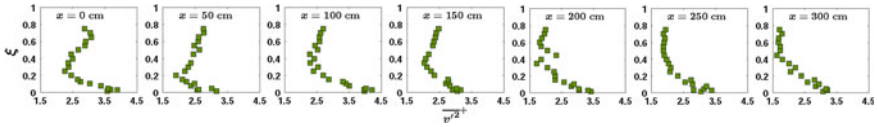

Fig. 6 Profiles of lateral normal stress $\overline{v'^2}$ in developing flow along the centreline of narrow open channel turbulent flow

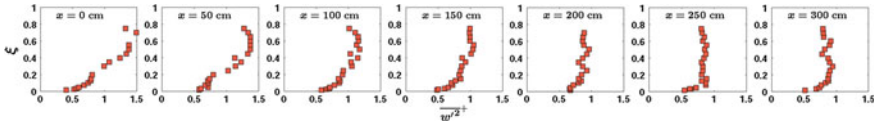

Fig. 7 Profiles of vertical normal stress $\overline{w'^2}$ in developing flow along the centreline of narrow open channel turbulent flow

range of $\overline{u'^2}^+$ magnitude decreases with increasing streamwise distance. An interesting phenomenon observed in this region is that with increasing streamwise distance, the increasing characteristic of $\overline{u'^2}^+$ from 40% of the flow depth above the bed decreases and is disappeared at $x = 200$ cm. In this region, the magnitude of $\overline{u'^2}^+$ decreases with increasing vertical height from the channel bed and this trend is continued up to $x = 300$ cm. Moreover, in the region between $x = 200$–300 cm, the range of $\overline{u'^2}^+$ magnitude is constant with increasing streamwise distance. Therefore, it is claimed that at $x = 200$ cm, the flow is becoming fully developed and the 100% fully developed flow is attained at $x = 250$ cm.

Similar to the characteristics of $\overline{u'^2}^+$, the non-dimensional normal stress in lateral direction $\overline{v'^2}^+$ which magnitudes lie within 0–4.5 shows the same nature except at the beginning of the flow where the increasing characteristic of $\overline{v'^2}^+$ is observed from 30% of the flow depth from the channel bed instead of 40% of the flow depth as found in the profiles of $\overline{u'^2}^+$.

Unlike the nature of $\overline{u'^2}^+$ and $\overline{v'^2}^+$, the normal stress $\overline{w'^2}^+$ along the vertical direction exhibits a completely different behaviour. The magnitude of $\overline{w'^2}^+$ lies within 0–1.5. Near the inlet at $x = 0$ cm, the magnitude of $\overline{w'^2}^+$ increases with increasing vertical from the channel bed except near the free surface where a decreasing trend is observed because of the suppression. It is followed that with increasing streamwise distance, the increasing characteristic decreases because of boundary layer development. At $x = 250$ and 300 cm, the magnitude of $\overline{w'^2}^+$ lies between 0.5–1 which are smaller than the values of $\overline{w'^2}^+$ at other streamwise stations. The result might be because the flow becomes a fully developed flow at $x = 250$ cm.

Overall, in developing narrow open channel flow, the ranges of the magnitudes of $\overline{u'^2}$, $\overline{v'^2}$ and $\overline{w'^2}$ are observed as 0–6, 0–3.5 and 0–1, respectively. Therefore, it can be claimed that the ascending order of turbulent intensities in developing narrow open channel flow is $w' < v' < u'$.

3.3 Reynolds Shear Stresses

It is a well-known fact that the three Reynolds shear stresses significantly influence the flow region and their characteristics in developing narrow open channel flow are discussed here.

The Reynolds shear stress $\overline{-u'w'}^+$ has a leading role in the flow region, and its profiles at different streamwise stations are shown in Fig. 8. Near the inlet ($x = 0$ cm), the values of $\overline{-u'w'}^+$ are decreasing up to 50% of the flow depth from the channel bed and then increase with further increase in vertical height. At this point, the values of $\overline{-u'w'}^+$ lie between -0.5 to 1. Between $x = 50$–150 cm, the values of $\overline{-u'w'}^+$ are decreasing up to 40% of the flow depth from the channel bed and then increase with further increasing vertical height; however, the increasing rate far from the channel bed is smaller than that of $x = 0$ cm. An interesting phenomenon is that with increasing streamwise distance, the negative values of $\overline{-u'w'}^+$ increase and become positive. At $x = 200$ cm, the increasing characteristic far from the channel bed almost disappears and the negative values of $\overline{-u'w'}^+$ converge to zero. The nature of $\overline{-u'w'}^+$ in fully developed flow is observed at $x = 250$ and 300 cm, where its values are positive and decrease with increasing vertical height from the channel bed. This characteristic indicates that in developing flow, the values of Reynolds shear stress $\overline{-u'w'}^+$ are greater than those of fully developed flow.

In comparison with $\overline{-u'w'}^+$, the other two Reynolds shear stresses $\overline{-u'v'}^+$ and $\overline{-v'w'}^+$ have less significant role in the flow region. The profiles of $\overline{-u'v'}^+$ and $\overline{-v'w'}^+$ at different stations are shown in Figs. 9 and 10, respectively. Figure 9 exhibits that from $x = 0$–150 cm, no consistent nature of $\overline{-u'v'}^+$ is observed in terms of magnitude and vertical distribution throughout the flow depth. From $x = 200$–300 cm, the values of $\overline{-u'v'}^+$ lie between -0.2 to 0.6 and they first

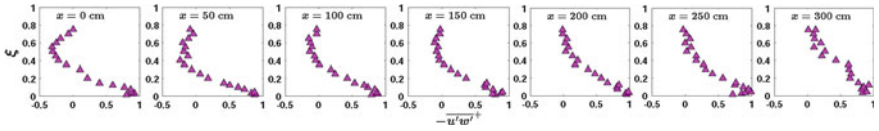

Fig. 8 Profiles of Reynolds shear stress $\overline{-u'w'}^+$ in developing flow along the centreline of narrow open channel turbulent flow

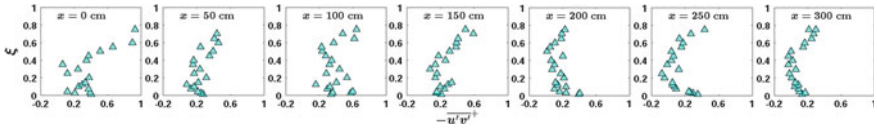

Fig. 9 Profiles of Reynolds shear stress $\overline{-u'v'}^+$ in developing flow along the centreline of narrow open channel turbulent flow

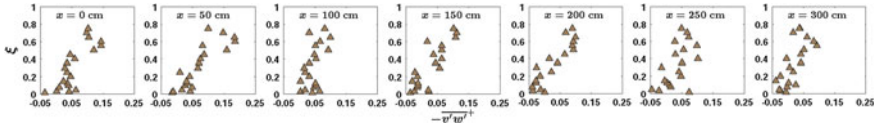

Fig. 10 Profiles of Reynolds shear stress $\overline{-v'w'}^+$ in developing flow along the centreline of narrow open channel turbulent flow

decrease up to 30% of the flow depth from the channel bed and increase with further increase in vertical height. The profiles of $\overline{-v'w'}^+$ show scattered nature, and their values lie between −0.05 to 0.2 as shown in Fig. 10. Near the channel bed, the values of $\overline{-v'w'}^+$ are negative; however, with increasing vertical height from the channel bed, $\overline{-v'w'}^+$ exhibits increasing phenomenon with positive values.

4 Conclusions

An experimental investigation of developing flow in narrow open channel has been carried out. Several important characteristics of turbulent hydrodynamics of developing turbulent open channel flow are explored in normalized form. An important result is observed that in between the modelled region (x = 0–300 cm), the developing flow zone is 0 cm $\leq x < 200$ cm, the transition zone from developing flow to fully developed flow is 200 cm $\leq x < 250$ cm, and the fully developed flow zone is 250 cm $\leq x \leq$ 300 cm. In the developing flow region, the values of normalized time-averaged streamwise velocity increase up to 20% of the flow depth from the channel bed and then decrease with further increase in vertical height. On the other hand, in the modelled section, the values of normalized time-averaged lateral and vertical velocities first decrease up to 40% of the flow depth from the channel bed and then decrease with further increase in vertical height. The direction of time-averaged lateral velocity is from the RHS wall to the LHS wall, whereas the time-averaged vertical velocity is in downward direction. The normalized normal stresses along streamwise and lateral directions decrease up to 40% of the flow depth from the channel bed and then increase with further

increase in vertical height in the developing flow. In addition, the normal stress along vertical direction increases with increasing vertical height from the channel bed in the developing flow region. In the modelled region, the Reynolds shear stress $\overline{-u'w'}^{+}$ shows negative value above 30% of the flow depth from the channel bed in the developing flow region and with increasing streamwise distance, those negative values converge to zero. The Reynolds shear stress $\overline{-u'v'}^{+}$ exhibits random nature in the modelled region; however, an increasing phenomenon with increasing vertical height from the channel bed is observed in the characteristic of the Reynolds shear stress $\overline{-v'w'}^{+}$ in all three flow regimes. At the end, it can be claimed that the data presented in this study will be useful for the verification of future theoretical models in developing narrow open channel turbulent flow.

Acknowledgements The first author thanks SRIC of IIT Kharagpur for being funded from project FVP. The authors express sincere thanks to two summer interns Ms. GayatriSahoo and Mr. Parag K. Baro for their assistance in collecting the experimental data.

References

1. Absi, R.: An ordinary differential equation for velocity distribution and dip-phenomenon in open channel flows. J. Hydraul. Res. **49**(1), 82–89 (2011)
2. Cardoso, A.H., Graf, W.H., Gust, G.: Uniform flow in a smooth open channel. J. Hydraul. Res. **27**(5), 603–616 (1989)
3. Chanson, H., Trevethan, M., Aoki, S.I.: Acoustic Doppler velocimetry (ADV) in small estuary: field experience and signal post-processing. Flow Measur. Instrum. **19**(5), 307–313 (2008)
4. Coles, D.: The law of the wake in the turbulent boundary layer. J. Fluid Mech. **1**(2), 191–226 (1956)
5. Francis, J.B.: On the cause of the maximum velocity of water flowing in open channels being below the surface. Trans. Am. Soc. Civ. Eng. **7**(1), 109–113 (1878)
6. Goring, D.G., Nikora, V.I.: Despiking acoustic Doppler velocimetry data. J. Hydraul. Eng. **128**(1), 117–126 (2002)
7. Kirkgöz, M.S., Ardiçlioglu, M.: Velocity profiles of developing and developed open channel flow. J. Hydraul. Eng. **123**(12), 1099–1105 (1997)
8. Mori, N., Suzuki, T., Kakuno, S.: Noise of acoustic Doppler velocimetry data in bubbly flows. J. Eng. Mech. **133**(1), 122–125 (2007)
9. Nezu, I., Rodi, W.: Open-channel flow measurements with a laser Doppler anemometer. J. Hydraul. Eng. **112**(5), 335–355 (1986)
10. Sarma, K.V.N., Prasad, B.V.R., Sarma, A.K.: Detailed study of binary law for open channels. J. Hydraul. Eng. **126**(3), 210–214 (2000)
11. Stearns, F.: On the current meter together with a reason why the maximum velocity of flowing in open channels is below the surface. Trans. Am. Soc. Civ. Eng. **12**, 331–338 (1883)
12. Wahl, T.L.: Discussion of despiking acoustic Doppler velocimetry data by Derek G. Goring and Vladimir **I**. **N**ikora. J. Hydraul. Eng. **129**(6), 484–487 (2003)
13. Xinyu, L., Changzhi, C., Zengnan, D.: Turbulent flows in smooth-wall open channels with different slope. J. Hydraul. Res. **33**(3), 333–347 (1995)

14. Yan, J., Tang, H.W., Xiao, Y., Li, K.J., Tian, Z.J.: Experimental study on influence of boundary on location of maximum velocity in open channel flows. Water Sci. Eng. **4**(2), 185–191 (2011)
15. Yang, S.Q.: Interactions of boundary shear stress, secondary currents and velocity. Fluid Dyn. Res. **36**(3), 121–136 (2005)
16. Yang, S.Q., Tan, S.K., Lim, S.Y.: Velocity distribution and dip-phenomenon in smooth uniform open channel flows. J. Hydraul. Eng. **130**(12), 1179–1186 (2004)

Lateral Variation of Turbulent Features in Developing and Developed Narrow Open-Channel Flow

Minakshee Mahananda and Prashanth R. Hanmaiahgari

Abstract In the present study, a detailed experimental investigation of lateral variation of turbulent characteristics is carried out in developing and fully developed flow over a fixed rough bed. Experiments are conducted in a rectangular flume of aspect ratio $(b/h = 3.05)$ and bed roughness $d_{50} = 2.5$ mm. Instantaneous three-dimensional velocities were measured using a Nortek Vectrino plus down-looking ADV. The characteristics of normalized flow velocity, turbulent intensities, Reynolds shear stresses and TKE distribution have been investigated. Raw velocity data have been filtered as prescribed in the recent literature. From the experimental data, it is observed that boundary-layer thickness increases along the streamwise distance in the developing flow region and reaches maximum in fully developed flow. On the contrary, boundary-layer thickness decreases in the lateral direction from the centreline of the channel towards sidewalls in both developing flow and fully developed flow. Local shear velocities are estimated from the Reynolds shear stress distribution in intermediate layer. Lateral variation of shear velocity shows decreasing trend in both developing and fully developed flow from the centreline towards sidewalls. Velocity dip phenomenon due to secondary current is observed in both the vertical distribution of normalized streamwise velocity profiles and RSS distribution along the lateral direction near to the side wall in both the developing flow and fully developed flow. Normalized Reynolds shear stress decreases in the lateral direction from the centreline of the channel towards the side wall in the developing flow with retardation of flow in the outer layer.

Keywords Turbulence · Hydrodynamics · Free surface flow · Aspect ratio · Lateral variation · Developing flow

M. Mahananda (✉) · P.R. Hanmaiahgari
Department of Civil Engineering, IIT Kharagpur, Kharagpur 721302, India
e-mail: minakshee.mahananda1@gmail.com

P.R. Hanmaiahgari
e-mail: hpr@civil.iitkgp.ernet.in

V. Garg et al. (eds.), *Development of Water Resources in India*,
Water Science and Technology Library 75, DOI 10.1007/978-3-319-55125-8_38

1 Introduction

It is essential to understand the flow characteristics in the developing and developed open-channel flow in order to address the hydraulic engineering problems such as fluid–sediment interactions, sediment erosion and deposition which are directly linked to the hydrodynamic characteristics such as vertical distribution of time-averaged velocities, effect of secondary currents, turbulent intensities, variation of Reynolds shear stresses along streamwise and lateral direction and turbulent kinetic energy. However, mostly open-channel flows are non-uniform/fully developed flows because of ever changing boundary conditions such as changes in discharge, changes in geometry, bed roughness and vicinity of hydraulic structures. Flow becomes disturbed whenever there is a change in boundary condition because of imbalance of viscous, gravitational and inertial forces. Subsequently, flow tries to attain fully developed flow conditions in the downstream direction. The developing turbulent flow in open channel is a complex three-dimensional flow which is influenced by aspect ratio, bed roughness, flow parameters and downstream distance from the inlet. Therefore, comprehensive study of lateral variation of turbulent characteristics of developing narrow open-channel flow on rough surfaces, which are often encountered in field, is of vital importance in hydraulic engineering. Researchers are still working on this important problem due to its complexity.

In the vertical distribution of streamwise velocity profile, the classical log law is applicable up to 20% of the flow depth from the channel bed [3, 12, 17]. On the other hand, investigators reported that above 20% of the flow depth from the channel bed, the log law deviates from the experimental data and the most reasonable formula to account the velocity together with deviation is the log-wake law where the wake function was introduced by Coles [5]. It is worth mentioning here that the log wake is not valid for narrow open channel where the value of aspect ratio, being defined by the ratio of width to height of the open channel, is less than 5. Moreover, it needs to be mentioned here that for wide open channel where the aspect ratio is greater than 5, the log-wake law is not valid near the sidewalls. A century ago, researchers [6, 14] reported that in fully developed narrow open-channel flow, the maximum velocity occurs below the free surface of the open channel which is known as dip phenomenon. In the last few decades, several experimental investigations proved the existence of dip phenomenon in narrow open channel [8, 10, 13, 18]. Apart from the experimental study, available theoretical literature had predicted the velocity distribution together with dip phenomenon in narrow open channel [1, 19]. Recently, Bonakari et al. [2] investigated the impact of relative roughness, Froude number and the Reynolds number on the establishment length using CFD analysis. They found that the effect of Froude number is negligible on the establishment length, whereas with increase in relative roughness the establishment length decreases. They also suggested a dimensionless establishment length which follows a linear relationship with Reynolds number. It is well known that to perform an experimental or theoretical study in narrow open-channel flow, it is very important to know the characteristic length by which

the flow would acquire a fully developed condition. According to the best of our knowledge, till date, the understanding of the lateral variation of the turbulent hydrodynamics of developing open-channel flow is not reached up to the desired level and for the narrow open-channel flow; the available knowledge on this topic is limited. To attempt the overlooked research problem, the aim of the study is to investigate the lateral variation of turbulent characteristics of the flow in developing and fully developed open-channel flow over fixed rough bed. First, the experimental set-up, experimental methodology, collection of data and the data filtering methodologies have been discussed. In Results and discussion section, the observed turbulent characteristics and reasons behind their trends have been explained. This study ends by presenting the conclusions.

2 Experimental Methodology

Experiments were conducted in the Hydraulic and Water Resources Engineering Laboratory, IIT Kharagpur, India. The experiments were carried out in a rectangular flume of width 0.61 m, depth 0.71 m and length 7 m. To enable the visualization of flow, the rectangular flume is provided with glass sidewalls. The flume was provided with railings on both the sidewalls throughout the length of the flume and also provided with a carriage in order to take readings at different locations. Along the length of the flume from the inlet of the channel, a uniform streamwise bed slope of 0.002 was maintained. Bed is cladded with uniform sand of median diameter 2.5 mm to simulate hydraulically rough surface. Overhead tank supplies the water to the flume. Two centrifugal pumps are used to recycle the water between underground sump and overhead tank. A honeycomb baffle wall was provided at the entrance of the channel in order to break larger eddies. Flow depth was maintained as 0.2 m above the channel bed by adjusting the tailgate height. As the aspect ratio, i.e. ratio of width to depth of flow for the present study, was calculated as 3.05 which is less than 5, the flow was treated as a narrow open-channel flow.

The streamwise bed slope and the depth of the flow were measured by using a point gauge provided with a Vernier scale with precision 0.1 mm. The velocity measurements were taken after flow initiation in order to ensure the flow stability. All the velocity measurements were taken by using a Nortek Vectrino Plus downlooking acoustic Doppler velocimeter (ADV) which was mounted on a point gauge fixed to the carriage to take velocity readings at different vertical depths, towards the sidewall and along the flow direction. Vectrino comprises of four downlooking probes and operates with an acoustics frequency of 10 MHz. Vectrino takes the measurement at a location 5 cm below the probe emitter. Hence, the influence of the probes on the measuring data is minimal. The sampling rate taken for the experiments was 100 Hz and the sampling volume height was 6 mm diameter. The sampling duration was taken as 3 min, but near the side walls depending upon the turbulence level, the sampling duration was taken between 6 and 10 min. The noise in the raw Vectrino data was despiked by the phase-space

method [7, 16], and the spikes were replaced by cubic interpolation method. To obtain good quality Vectrino data, the proposed SNR method of Chanson et al. [4] was followed where the ratio value was maintained as greater than 20. After that, the data with Vectrino correlation signal value greater than 75% were used to analyse the turbulence characteristics of developing flow in narrow open channel. Photographic view of the experimental set-up along with the flow is shown in Fig. 1.

A schematic diagram of the experimental set-up is presented in Fig. 2. As the main motive of the present study is to investigate turbulence along lateral sections at three different streamwise locations in flow development region, the measurements were taken along the various cross sections in the developing flow region. Three-dimensional velocities were measured at three cross sections (x = 2.15 m, x = 3.65 m and x = 5.15 m) along the developing region, and these are represented as CS1, CS2 and CS3, respectively. At each cross section, the measuring points were chosen from the centreline of the flume towards the sidewall as shown in Fig. 3.

For that, a three-dimensional coordinate system is adopted to represent the direction, i.e. x-, y- and z-axes are representing the streamwise, lateral and vertical directions, respectively. The origin of the x-axis, y-axis and z-axis were located at the entrance of the channel $(x = 0)$, at the centreline of the flume $(y/(0.5b) = 0)$ and at the bed level $(z/h = 0)$, respectively, where b is defined as flume width and h is defined as the depth of the flow. For a given streamwise and lateral location towards the sidewall from the centreline of the flume, four verticals were chosen for the data measurements (Fig. 3).

Fig. 1 Photographic view of experimental set-up

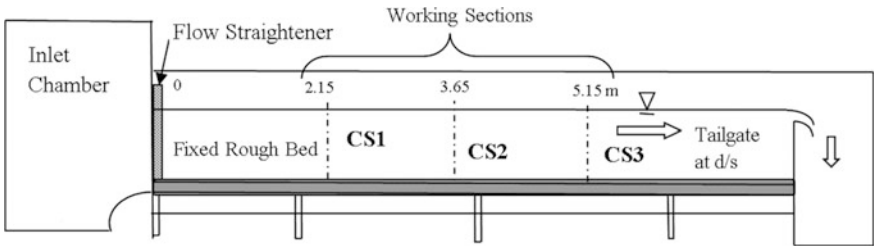

Fig. 2 Schematic diagram of experimental set-up showing working sections

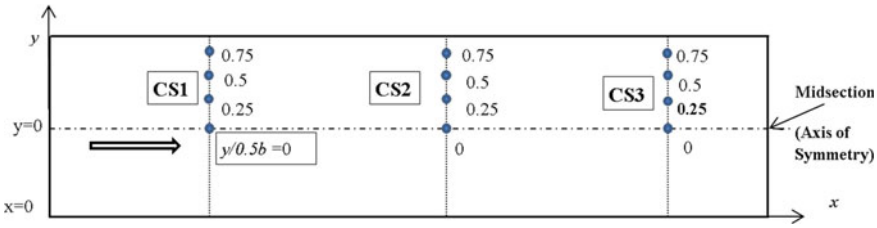

Fig. 3 *Top view* of measurement plane

Table 1 Details of experimental condition

Exp. run	h (m)	b (m)	Ar	U (m/s)	Re	Fr
1	0.2	0.61	3.05	0.357	71519	0.268

These measuring verticals are $(y/0.5b = 0, 0.25, 0.5, 0.75)$, respectively, for all three cross sections. Therefore, a total of 12 verticals were chosen for the data capturing on either side of the centreline to study lateral variation of turbulence. In this study at every location in $x - y$ plane, velocity measurements were taken at 19 vertical locations z = (0.3, 0.5, 0.7, 0.9, 1.5, 2, 2.5, 3, 4, 5, 6, 7, 8, 9, 10, 11, 12, 13 and 14) cm. The flow conditions of the present experimental study are summarized in Table 1.

3 Results and Discussion

In this section, the vertical distribution of normalized time-averaged streamwise velocity, turbulent intensities, Reynolds shear stresses and turbulent kinetic energy along the streamwise and lateral directions in developing and developed flow has been explained. To ascertain this, a three-dimensional coordinate system has been used, where u, v and w are time-averaged streamwise velocity, lateral and vertical velocity components, respectively; u', v' and w' are the fluctuations of corresponding velocity components. The flow velocities and all the turbulence quantities

Table 2 Estimated shear velocities

$y/0.5b$	Shear velocity u_* (m/s)		
	CS1	CS2	CS3 (fully developed flow)
0	0.0331	0.0235	0.02254
0.25	0.315	0.0228	0.0222
0.5	0.0287	0.0221	0.0187
0.75	0.0254	0.0217	0.0171

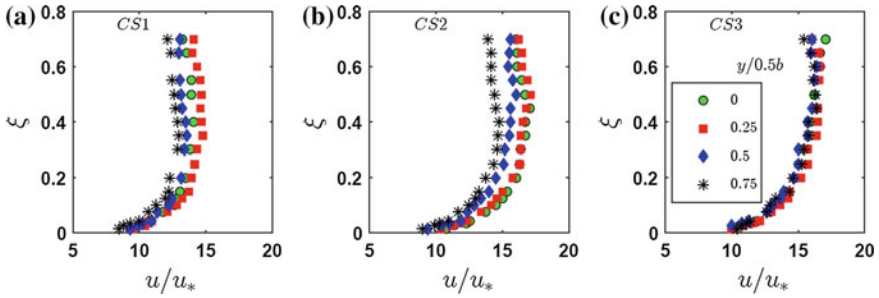

Fig. 4 Lateral variations of normalized time-averaged streamwise velocity u/u_* in developing flow

were normalized by local shear velocity u_*. Local shear velocities were obtained from Reynolds shear stress distributions. Vertical distance (z) of any location in the flow was normalized as z/h where h is defined as the total flow depth. The computed u_* values at different locations are listed in Table 2.

As mentioned above, u/u_*, v/u_* and w/u_* are defined as the normalized time-averaged velocities in streamwise, lateral and vertical directions, respectively; $\sqrt{\overline{u'u'}}/u_*$, $\sqrt{\overline{v'v'}}/u_*$ and $\sqrt{\overline{w'w'}}/u_*$ are defined as the normalized streamwise turbulent intensity u' or u_{rms}/u_*, turbulence intensity in lateral direction v' or v_{rms}/u_* and vertical turbulent intensity w' or w_{rms}/u_*, respectively. Similarly, normalized Reynolds stresses are denoted by $\overline{-u'w'}^{+} = \overline{-u'w'}/u_*^2$, $\overline{-u'v'}^{+} = \overline{-u'v'}/u_*^2$ and $\overline{-v'w'}^{+} = \overline{-v'w'}/u_*^2$, and the turbulent kinetic energy k^{+} is normalized as k/u_*^2.

3.1 Time-Averaged Velocity of Flow

Figure 4a–c depicts the vertical distribution of normalized time-averaged streamwise velocity (u/u_*) at various lateral stations of three different cross sections CS1, CS2 and CS3 in the developing open-channel flow.

Figure 4a shows that near to the inlet of the channel, at section CS1 profiles of u/u_* are showing similar trend. However, at the mid-vertical $(y/0.5b = 0)$ of CS1 $(x = 2.15\,\text{m})$, the magnitude of u/u_* increases with increase in vertical height up to 0.4 h from the channel bed and then u/u_* decreases with further increase in vertical

height because of instability of flow (inflection point in the velocity profile). With increasing lateral distance $(y/0.5b = 0.25, 0.5, \text{and } 0.75)$ at CS1, it is observed that the location of maximum time-averaged streamwise velocity is approaching boundary of inner layer. That means the boundary-layer thickness in developing region decreases towards the sidewall from the centre line of the channel which is also observed at sections CS2 and CS3 (shown in Fig. 4b, c). Figure 4b and c shows that with increasing streamwise distance (CS2, $x = 3.65$ m; CS3, $x = 5.15$ m), the location of maximum value of u/u_* of mid-vertical is shifting away from the channel boundary. Along the streamwise distance, a developed flow phenomenon is observed at CS3 and the developed flow characteristics is confirmed by the thickness of boundary layer at the mid-vertical (y/$0.5b$ = 0) of CS3 which is equal to the depth of flow [8]. Hence, the length of the boundary-layer development in the present study is found to be around 5.15 m. By examining the profiles of velocities at CS3 (Fig. 4c), it is found that for the lateral distances $y/0.5b > 0.5$, the velocity data in the outer layer $(z/h > 0.6)$ signify the dip phenomena where the maximum streamwise velocity is observed below the free surface of the open channel. Dip phenomenon is caused by the secondary currents in the flow. In addition, by observing the velocity data at all sections, it may be concluded that the peak magnitude of time-averaged streamwise velocity decreases with increase in streamwise distance along the centreline of the flow and also decreases with increase in lateral distance from the centreline of the channel towards the sidewall due to the sidewall effect.

3.2 Turbulence Intensities

A comprehensive understanding of the distribution of turbulent intensities is very important to analyse the level of turbulence in any open-channel flow. Figures 5, 6 and 7 show the vertical distribution of u_{rms}/u_*, v_{rms}/u_* and w_{rms}/u_*, respectively, at various lateral stations of three different cross sections CS1, CS2 and CS3 along the developing flow. Figure 5a–c shows that the magnitudes of u_{rms}/u_* at different cross sections lie between 0 and 2.5 times the local shear velocity. Near the entrance of the channel, at the mid-vertical $(y/0.5b = 0)$ of CS1, it is observed that close to the boundary region the streamwise turbulence intensity is maximum and then decreases rapidly up to $0.2h$ and again decreases gradually from $0.2h$ to $0.5h$ and again increases towards the free surface as shown in Fig. 5a. Similar trend is also observed near the sidewall at $y/0.5b = 0.75$. On the other hand, at $y/0.5b = 0.25$ and 0.5, the profiles remain invariant from $0.4h$ to $0.6h$ and then decrease with increasing vertical height towards the free surface. As the lateral distance increases that from $y/0.5b = 0, 0.25$ and 0.5, u_{rms}/u_* increases, but profile at $y/0.5b = 0.75$ shows slightly different trends due to the sidewall effect and in the free surface layer the magnitude of normalized streamwise turbulent intensity is found to be higher near to the sidewall (Fig. 5a).

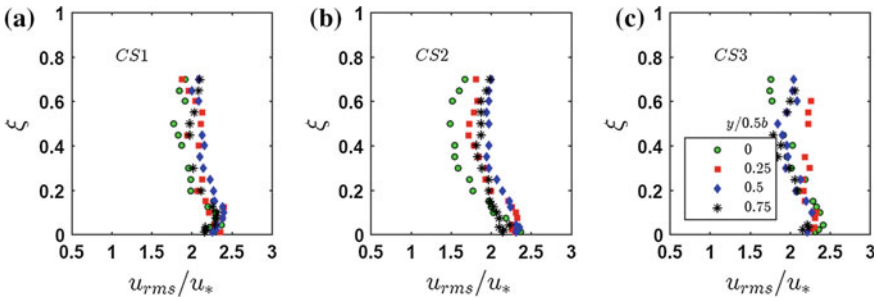

Fig. 5 Lateral variations of normalized streamwise turbulent intensity u_{rms}/u_* in developing flow

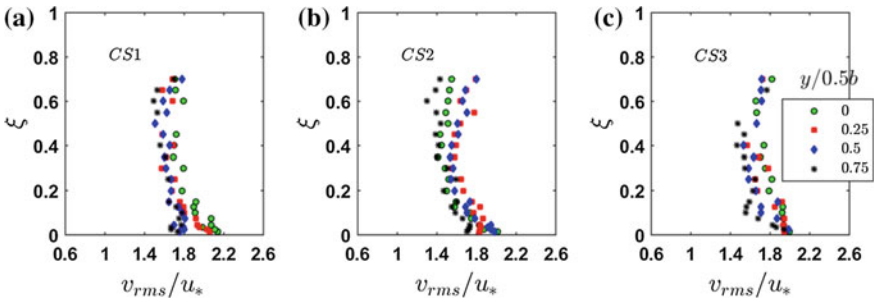

Fig. 6 Lateral variations of normalized lateral turbulent intensity v_{rms}/u_* in developing flow

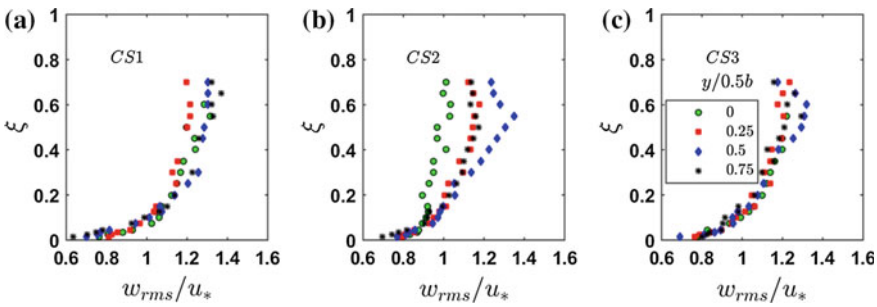

Fig. 7 Lateral variations of normalized vertical turbulent intensity w_{rms}/u_* in developing flow

Figure 5b shows that profiles of u_{rms}/u_* at CS2 follow similar trend as CS1 but trends are more pronounced at CS2. An interesting phenomenon observed in Fig. 5c is that with increasing streamwise distance from the channel inlet, the increasing characteristics of u_{rms}/u_* from $0.4h$ above the bed decreases and becomes invariant of flow depth at lateral distance $y/0.5b = 0.25$. At mid-vertical of CS3, the magnitude of streamwise turbulence intensity decreases with increasing vertical heights from the channel bed which is similar to the trend found in the fully

developed hydraulically rough wide channel flow. Therefore, it may be claimed that at section CS3 ($x = 5.15$ m), the flow is fully developed. However, in the outer region $z/h > 0.4$, the streamwise turbulent intensity profiles at $y/0.5b = 0.5$ and 0.75 of section CS3 are showing increasing trend with increase in vertical height of flow, which may be due to increase in shear at the intersection of sidewall and free surface. In addition, it may be concluded that the normalized streamwise turbulent intensity follows increasing trend along the lateral distance from the centreline of channel only up to $y/0.5b < 0.5$. By examining the experimental data, it is found that near the channel boundary among the peak values of u_{rms}/u_*, the magnitude of u_{rms}/u_* is maximum at the mid-verticals at any cross section and decreases along the lateral distance from the mid-vertical towards the sidewall except at section (CS1) near to the entrance of the channel, and this is due to the domination of the inertial forces over the viscous forces which negating the sidewall effect. The location of peak value of u_{rms}/u_* is not changing along the streamwise distance which shows viscous sublayer thickness is constant along the flow development length.

Figure 6a–c depicts the vertical distribution of normalized lateral turbulent intensities v_{rms}/u_* along the developing flow in a narrow open channel. Profiles are showing similar trend as u_{rms}/u_*, and it is observed that the magnitude of v_{rms}/u_* lies between 0 and 2.2 times of local shear velocities. But in the outer region, $z/h > 0.4$ for sections CS1 and CS2, all profiles are showing increasing trend with increase in vertical heights. Near to the entrance of the channel, i.e. section CS1, the magnitude of v_{rms}/u_* decreases with increase in lateral distance from the mid-verticals ($y/0.5b$ = 0, 0.25, 0.5 and 0.75); however, this characteristic is not shown up at sections CS2 and CS3 due to increased mixing in lateral direction. The peak value of v_{rms}/u_* observed near to the channel bed decreases with increase in streamwise distance along the flow. By comparing the data of v_{rms}/u_* and u_{rms}/u_*, it is found that the peak value of v_{rms}/u_* is lesser than u_{rms}/u_*. However, the ratio between them is close to 1.0, which shows flow is anisotropic but to a lesser degree. Unlike the nature of u_{rms}/u_* and v_{rms}/u_*, the normalized vertical turbulent intensity w_{rms}/u_* exhibits a complete different behaviour.

Figure 7a–c shows the vertical distribution of normalized vertical turbulent intensity. The magnitude of w_{rms}/u_* lies between 0 and 1.4 times of local shear velocities. Moreover, at sections CS1, CS2 and CS3, the data trends of w_{rms}/u_* along all the lateral distances show an increasing tendency with z/h in the inner layer and decreasing in the free surface region ($z/h > 0.6$) because of suppression. On the other hand, at section CS3, it is observed that the data trend of w_{rms}/u_* becomes invariant of lateral distance up to $/h < 0.4$; similarly, decreasing tendency is found in the free surface layer due to suppression. The suppression of vertical turbulent intensities generally explains about the characteristic patterns of secondary currents in open-channel flow [15]. Generally, in the present study of developing narrow open-channel flow, the magnitudes of u_{rms}/u_*, v_{rms}/u_* and w_{rms}/u_* are observed in the ranges of 0−2.5, 0−2.2 and 0−1.4 times of local shear velocities, respectively. Therefore, it can be claimed that the ascending order of

turbulent intensities in developing narrow open-channel rough flow is $w_{rms} < v_{rms} < u_{rms}$ that proves the existence of secondary currents in the region under investigation.

3.3 Reynolds Shear Stresses

Figure 8a–c depicts the vertical distribution of normalized Reynolds shear stress $\tau_{uw}^{+} = \overline{-u'w'}/u_*^2$ along the developing flow at three different cross sections CS1, CS2 and CS3. Near the entrance of the channel at section CS1 ($x = 2.15$ m), the profiles of τ_{uw}^{+} are showing sudden increasing trend near to the channel boundary and reach a peak value, then decrease with increase in vertical height up to $0.5h$ and again follow an increasing trend with further increase in vertical height as shown in Fig. 8a. The increase in τ_{uw}^{+} near the free surface is associated with the secondary flow. At the section CS1 near the channel boundary, the peak values of τ_{uw}^{+} decrease with increase in lateral distance from $y/0.5b$ = 0 to 0.75. It is observed that for $\xi > 0.2$, τ_{uw}^{+} are negative, which shows flow retardation. In addition, the vertical distribution of τ_{uw}^{+} is deviating from $1 - \xi$ except near the bed which shows $1 - \xi$ is not applicable to approximate τ_{uw}^{+} in the developing flow region. At section CS2 (Fig. 8b), it is observed that the values of τ_{uw}^{+} after reaching peak values near the channel bed follow decreasing trend up to $0.6h$ and then increase with further increase in vertical height.

Contrary to section CS1, the near boundary values of τ_{uw}^{+} are same at CS2 irrespective of lateral distance. At CS2, τ_{uw}^{+} profiles are trying to align with $1 - \xi$, however, deviated above $\xi > 0.2$, which shows $1 - \xi$ is not applicable to approximate τ_{uw}^{+} in the developing flow region. At section CS3 (Fig. 8c), the negative values of τ_{uw}^{+} near the free surface disappear at lateral distances $y/0.5b \geq 0.5$. Hence, the changes in sign of τ_{uw}^{+} from positive to negative at $y/h \geq 0.6$ for sections CS1, CS2 and $y/0.5b = 0.75$ of CS3, signify the existence of

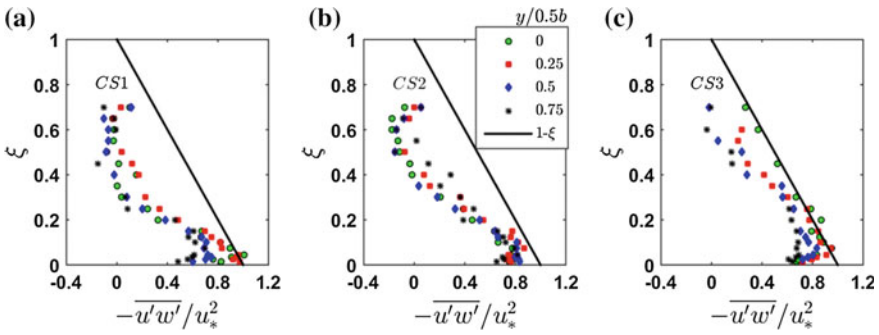

Fig. 8 Lateral variations of Reynolds shear stress $\overline{-u'w'}/u_*^2$ in developing flow

dip phenomena in narrow open-channel flow [19]. The negative values of normalized Reynolds shear stress are observed in the region where the velocity retardation takes place [9, 11]. Nevertheless, the retardation region is decreasing with increase in streamwise distance. Vertical distribution of τ_{uw}^{+} at $y/0.5b = 0$ of section CS3 ($x = 5.15$ m) reasonably follows the linearly decreasing trend with increase in vertical height from the channel bed which shows fully developed flow (Fig. 8c).

3.4 Turbulent Kinetic Energy

The plots of normalized turbulent kinetic energy k/u_*^2 are shown in Fig. 9a–c. At section CS1 ($x = 2.15$ m), the peak values of k/u_*^2 occur close to the channel bed as shown in Fig. 9a. The profiles have shown sharply increasing trend near to the channel bed, decrease with further increase in vertical height up to $0/4h$ and increase with further increase in vertical height. With increasing lateral distances, the magnitude of k/u_*^2 increases, however, that increasing trend found to be prominent at section CS2 (Fig. 9b). On the other hand, at section CS3 ($x = 5.14$ m) as shown in Fig. 9c, the increasing variation of k/u_*^2 with lateral distances is observed to be diminished that means k/u_*^2 of different lateral distances are falling on each other which shows establishment of fully developed flow.

In addition, by examining the turbulent kinetic energy data, it can be claimed that the magnitude of k/u_*^2 decreases with increase in streamwise distance along the developing flow. It can be inferred that turbulence is very high in the developing flow region which increases the mixing of the flow and by the time flow reaches fully developed it is already well mixed at section CS3. It can be understood that flow has more eroding power near the inlet and eroding power reduces as the flow attains fully developed state. The TKE increases with increase in lateral distance in the developing flow region, but invariant of lateral distances at section close to

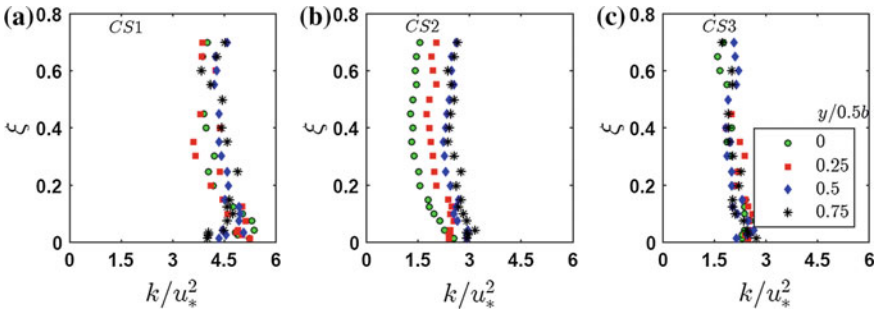

Fig. 9 Lateral variations of TKE in developing flow

developed flow or fully developed. It is also observed that the locations of peak values of k/u_*^2 are shifting towards the channel bed with increase in streamwise distance along the developing flow which proves reduced lateral flow in the fully developed flow.

4 Conclusions

An experimental investigation of lateral variation of turbulent characteristics in developing and developed flow in a narrow open channel has been carried out in the proposed research. A detailed study of the turbulent characteristics along the developing flow has been portrayed as follows. By examining the local shear velocities, it may be concluded that shear velocity decreases along the streamwise direction in the developing flow region. Lateral variation of local shear velocities shows decreasing trend from the centre line of the channel towards sidewalls in both developing flow and fully developed flow. Boundary-layer thickness decreases in the lateral direction from the centreline of channel, in both developing and fully developed flow. For $(y/0.5b > 0.5)$, it is found that the normalized streamwise velocity profile shows dip phenomena in the outer layer of the fully developed flow, which confirms the existence of secondary currents near to the sidewall of the flume. For $(y/0.5b < 0.5)$, normalized streamwise turbulent intensity decreases along the streamwise direction of the developing flow; however, it increases along the lateral direction from the centreline of the channel towards the sidewall. Normalized lateral turbulent intensity is found to be decreasing in the lateral direction of the developing flow. On the other hand, normalized turbulent intensity is invariant of lateral distance in the fully developed flow. In addition, turbulence anisotropy is found in the developing flow. Normalized Reynolds shear stress decreases from the centreline of the channel towards the sidewall in the developing flow and flow retardation takes place in the outer layer. The vertical distribution of normalized Reynolds shear stress deviates from theoretical linear distribution of RSS except near the bed and with increase in streamwise distance, normalized Reynolds shear stress profiles along the developing flow try to align with theoretical linear distribution. However, at the mid-vertical of the channel in the fully developed flow, normalized Reynolds shear stress follows reasonably well with the theoretical line. TKE increases along the lateral distance in the developing flow. On the other hand, it is invariant of lateral distance in the fully developed flow. Finally, it can be claimed that the present study can be used to find out the relation between the turbulence characteristics with the establishment length of flow in order to reduce the development length to get fully developed flow.

References

1. Absi, R.: An ordinary differential equation for velocity distribution and dip-phenomenon in open channel flows. J. Hydraul. Res. **49**(1), 82–89 (2011)
2. Bonakdari, H., GislainLipeme-Kouyi, G.L.A.: Developing turbulent flows in rectangular channels: a parametric study. J. Appl. Res. Water Wastewater **1**(2), 53–58 (2014)
3. Cardoso, A.H., Graf, W.H., Gust, G.: Uniform flow in a smooth open channel. J. Hydraul. Res. **27**(5), 603–616 (1989)
4. Chanson, H., Trevethan, M., Aoki, S.I.: Acoustic Doppler velocimetry (ADV) in small estuary: field experience and signal post-processing. Flow Meas. Instrum. **19**(5), 307–313 (2008)
5. Coles, D.: The law of the wake in the turbulent boundary layer. J. Fluid Mech. **1**(2), 191–226 (1956)
6. Francis, J.B.: On the cause of the maximum velocity of water flowing in open channels being below the surface. Trans. Am. Soc. Civ. Eng. **7**(1), 109–113 (1878)
7. Goring, D.G., Nikora, V.I.: Despiking acoustic Doppler velocimeter data. J. Hydraul. Eng. **128**(1), 117–126 (2002)
8. Kirkgöz, M.S., Ardic¸lioglu, M.: Velocity profiles of developing and developed open channel flow. J. Hydraul. Eng. **123**(12), 1099–1105 (1997)
9. Kironoto, B., Graf, W.H.: Turbulence characteristics in rough uniform open channel flow. Proc. Inst. Civ. Eng.—Water Maritime Eng. **106**(4), 333–344 (1994)
10. Nezu, I.: Open-channel flow turbulence and its research prospect in the 21st century. J. Hydraul. Eng. **131**(4), 229–246 (2005)
11. Nezu, I., Nakagawa, H.: Turbulence in Open-Channel Flows. IAHR/AIRH Monograph Series. Balkema, Rotterdam (1993)
12. Nezu, I., Rodi, W.: Open-channel flow measurements with a laser Doppler anemometer. J. Hydraul. Eng. **112**(5), 335–355 (1986)
13. Sarma, K.V.N., Prasad, B.V.R., Sarma, A.K.: Detailed study of binary law for open channels. J. Hydraul. Eng. **126**(3), 210–214 (2000)
14. Stearns, F.: On the current meter together with a reason why the maximum velocity of flowing in open channels is below the surface. Trans. Am. Soc. Civ. Eng. **12**, 331–338 (1883)
15. Tominaga, A., Nezu, I., Ezaki, K., Nakagawa, H.: Three-dimensional turbulent structure in straight open channel flows. J. Hydraul. Res. **27**(1), 149–173 (1989)
16. Wahl, T.L.: Discussion of despiking acoustic Doppler velocimeter data by Derek G. Goring and Vladimir **I**. **N**ikora. J. Hydraul. Eng. **129**(6), 484–487 (2003)
17. Xinyu, L., Changzhi, C., Zengnan, D.: Turbulent flows in smooth-wall open channels with different slope. J. Hydraul. Res. **33**(3), 333–347 (1995)
18. Yan, J., Tang, H.W., Xiao, Y., Li, K.J., Tian, Z.J.: Experimental study on influence of boundary on location of maximum velocity in open channel flows. Water Sci. Eng. **4**(2), 185–191 (2011)
19. Yang, S.Q., Tan, S.K., Lim, S.Y.: Velocity distribution and dip-phenomenon in smooth uniform open channel flows. J. Hydraul. Eng. **130**(12), 1179–1186 (2004)

Turbulent Hydrodynamics Along Lateral Direction in and Around Emergent and Sparse Vegetated Open-Channel Flow

Soumen Maji, Susovan Pal, Prashanth Reddy Hanmaiahgari and Vikas Garg

Abstract Jute plantation is one of the important crops in India and Bangladesh region. The vegetation density of Jute plantations is usually sparse. No comprehensive experimental study has been carried out till date to investigate turbulent characteristics in the lateral direction at interior and exterior of sparse and emergent vegetation patch. The proposed study investigates important turbulent characteristics at different cross sections at upstream, interior and downstream of emergent and sparsely vegetated open-channel flow. An array of seventy uniform rigid acrylic cylindrical rods with regular spacing was used to represent the emergent sparse vegetation patch. Three-dimensional instantaneous velocities were measured by a Nortek VectrinoPlus ADV. From this study, it was evident that time-averaged streamwise velocities were decreasing in interior of the vegetation along the streamwise direction. Inside the vegetation patch, time-averaged lateral velocities were directed towards the nearest sidewall. Time-averaged vertical velocities were negative throughout the cross section at upstream of the vegetation patch. But absolute magnitudes are decreasing in interior and downstream of the vegetation patch. Turbulent kinetic energy was decreasing inside the vegetation patch, and the peak values were located far from the channel bed in interior and downstream cross sections through the vegetation.

Keywords Turbulence · Hydrodynamics · Emergent vegetation · Sparse vegetation · Open-channel flow · Lateral variation

S. Maji (✉) · S. Pal · P.R. Hanmaiahgari
Department of Civil Engineering, IIT Kharagpur, Kharagpur 721302, India
e-mail: soumen@civil.iitkgp.ernet.in; soumen.maji184@gmail.com

S. Pal
e-mail: susovan9046@gmail.com

P.R. Hanmaiahgari
e-mail: hpr@civil.iitkgp.ernet.in

V. Garg
Department of Civil Engineering, UPES, Dehradun 248007, India
e-mail: gargvikas27@gmail.com

V. Garg et al. (eds.), *Development of Water Resources in India*,
Water Science and Technology Library 75, DOI 10.1007/978-3-319-55125-8_39

1 Introduction

It is very important to understand the turbulent features along lateral direction of flow through the sparsely emergent vegetated open channel as they affect mass and momentum transfer, sedimentation, nature of flow, aquatic life and several other environmental activities. The flow of water through a sparse and emergent vegetation is characterized by turbulent intensities, significant gradients of three-dimensional velocity components and Reynolds stresses across the cross-sectional area. At the interface between sparse vegetation patch and flow adjacent to it, shear flow and drag discontinuity result in shear layer formation between the vegetation stems and flow outside the vegetation. The shear layer along transverse direction in turn generates sweeps directing into interior of the flow and ejections directed towards exterior of the vegetation patch [8]. Nezu and Onitsuka [6] calculated horizontal vortices between channel flow and the edge of vegetated flood plain. Jimenez et al. [4] used mathematical modelling to observe coherent vortices due to Kelvin–Helmholtz shear instability at the sparse vegetated canopy interface. Chen et al. [2] experimentally investigated flow structure in the wake region of an emergent vegetation patch. Yang et al. [9] estimated the bed shear stress in emergent vegetated flow with smooth bed. The objective of this study is to compare important turbulent features in lateral direction at upstream, interior and downstream of an emergent, rigid and sparse vegetation patch. In this paper, a brief description of experimental methodology is given in Sect. 2. The physics of the measured distributions of important turbulent features in lateral direction is described in Sect. 3, and the study ends by presenting conclusions in Sect. 4.

2 Experimental Methodology

Experiment was conducted in a flume with dimensions 12 m long, 0.91 m wide, 0.61 m deep and 0.002 longitudinal slope at Hydraulic and Water Resources Engineering Laboratory, Department of Civil Engineering, Indian Institute of Technology Kharagpur, India. The flume consists of two 8-m-long and 1.5-cm-thick sidewalls made by transparent glass. Sand particles (d_{50} = 0.25 cm) were used for cladding the channel bed of the flume for making it rough and comparable to natural condition. Two centrifugal pumps were used to recirculate the flow in the flume. At inlet, a honeycomb baffle was used to make the flow uniform and free of vortex. The uniform and fully developed flow was observed at 7 m downstream of the inlet along streamwise direction. At the middle region through the cross section of the flume, a rectangular sparse and emergent vegetation patch was created at 1 m downstream of fully developed flow. Seventy uniform acrylic cylindrical rods with dimensions of 30 cm long and 0.64 cm diameter were arranged as an array of 7 × 10 on a Perspex sheet attached to the channel bed as a representation of the vegetation patch. Each of the seven rows along flow direction

contains ten cylinders. For implementing the sparse characteristic to the set-up, uniform spacing of 9 cm and 4 cm was maintained between centres of two consecutive cylinders along streamwise and lateral directions, respectively. The dimension of the vegetation patch was kept as 81 cm long and 24 cm wide. The solid volume fraction of the patch was calculated as $\Phi = 0.0089$. The experiment was performed with a depth averaged flow velocity (U) = 24 cm/s, discharge (Q) = 4.4 × 10^4 cm^3/s, a constant water depth (h) = 20 cm and Re = 48,000.

A Nortek VectrinoPlus Acoustic Doppler Velocimeter (ADV) with four down-looking probes was used to measure 3D velocity components along depth which were measured at different lateral stations through upstream, interior and downstream of the vegetation patch. The ADV receives echos from the suspended particles in flowing water and converts those sounds into the velocity values using the Doppler effect. Thirty minutes were allowed for stabilization of the flow field after setting the required flow conditions. Then, instantaneous velocity components were measured with sampling rate of 100 Hz and a sampling period of 2 min. A three-dimensional coordinate system was chosen where x, y and z axes represent streamwise, lateral and vertical directions, respectively. The time-averaged velocity components along x, y and z directions were represented by u, v and w, respectively, together with their corresponding fluctuation parts as u', v' and w', respectively. Spike filtering and signal-to-noise ratio thresholding techniques are applied for the accurate measurement of obtained experimental data [1, 3, 5].

3 Results and Discussion

A schematic top view of the streamwise and cross-sectional locations where experimental data were collected is shown in Fig. 1. Here the normalized vertical height from the channel bed is represented by $\xi(= z/h)$.

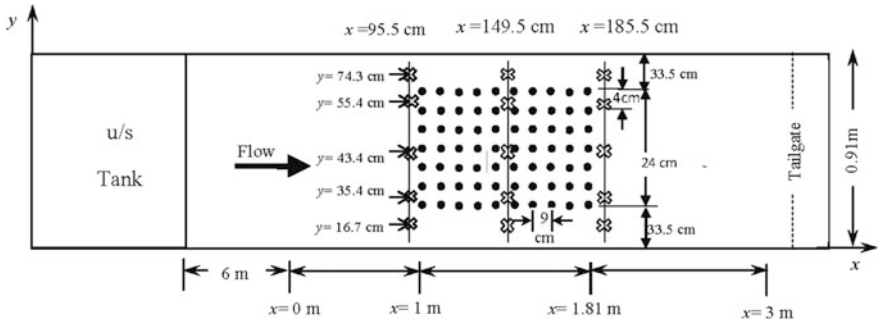

Fig. 1 *Top view* of experimental set-up with locations of measurement

3.1 Time-Averaged Streamwise Velocity

Figure 2 shows the variation of time-averaged streamwise velocity component u in upstream, interior and downstream of the vegetation patch. As the region at immediate vicinity of upstream leading edge of the vegetation patch (denoted by x = 95.5 cm) is free from the effect of sidewalls and vegetation patch, the flow shows fully developed nature at middle region of cross section, i.e. at y = 43.4 cm.

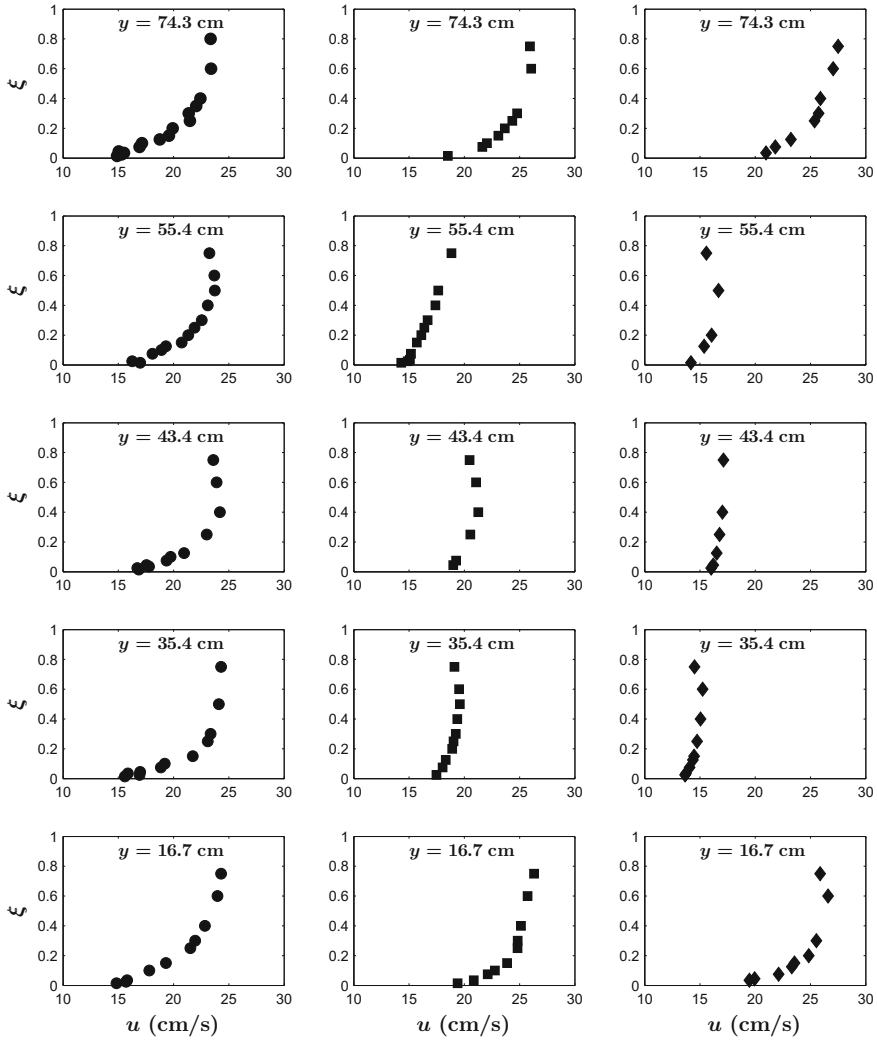

Fig. 2 Variation of time-averaged streamwise velocity u along lateral direction at upstream (*first column* and x = 95.5 cm), interior (*second column* and x = 149.5 cm) and downstream (*third column* x = 185.5 cm) of sparse vegetation patch

The profiles of u between sidewalls and two streamwise edges of vegetation patch (y = 16.7 and 74.3 cm) do not show the effects of sidewalls. Further, at y = 35.4 and 55.4 cm the flow does not show any effect of vegetation on the downstream. A flow separation is caused by the deviation at the leading edge, and it is also responsible for the scattering of u components at y = 35.4 and 55.4 cm. The vicinity of middle cross section of the vegetation patch is denoted by x = 149.5 cm, and the values of u inside the vegetation patch (y = 35.4, 43.4 and 55.4 cm) decrease in comparison with the corresponding components at x = 95.5 cm. At x = 185.5 cm, the flow leaves the vegetation patch. Here u maintains the preceding decreasing behaviour with reference to the relevant profiles at x = 149.5 cm. Inside the vegetation patch, the cylinders cause a barrier for the flow resulting decreased magnitude of u inside the vegetation patch and immediate downstream of the vegetation patch. It is observed that decreasing the components of u is lesser at middle cross-sectional region of vegetation patch (y = 43.4 cm) than the edges (right edge (y = 35.4 cm) and left edge (y = 55.4 cm)) of the vegetation patch. This can be explained by two counter-rotating horizontal eddies in either side of the measuring location. An obstructing effect on the velocity at x = 149.5 cm and y = 55.4 cm is created by the simultaneous action of two eddies, a clockwise eddy on the left shoulder side and an anticlockwise-rotating eddy on interior side. Similarly, anticlockwise eddy on the side of right shoulder and clockwise eddy in the interior of the vegetation obstruct streamwise velocity at x = 149.5 cm and y = 35.4 cm. This is also applicable for the intense wake region (x = 185.5 cm) immediate downstream of the trailing edge, although von Kármán vortices are generated at downstream of both the corners of the patch thereby decreasing u velocity components at those two locations (x = 185.5 cm, y = 35.4 cm and x = 185.5 cm, y = 55.4 cm). The magnitudes of corresponding u components increase with increasing streamwise length at y = 16.7 and 74.3 cm as here the flow faces no obstruction by the vegetation patch. The flow inside the vegetation patch has a tendency to come out from that patch due to the blockage of cylinders, and a part of the flow gets released at exterior of that patch due to its lateral movement. The released part of the flow adds a momentum in streamwise velocity. It results in increased magnitude of u at y = 16.7 and 74.3 cm.

3.2 Time-Averaged Lateral Velocity

The time-averaged lateral velocity v components varying with cross-sectional region in upstream, interior and downstream of the sparse vegetation patch are shown in Fig. 3. The lateral velocities between centreline and LHS wall are positive as the flow deflected towards left. On the contrary, lateral velocities of flow between centreline and RHS wall are negative because flow deflected towards RHS wall. It has been observed that lateral velocity at the centreline, i.e. at y = 43.4 cm, is almost zero. Here the maximum negative value is observed for y = 43.4 cm located at middle region of cross-sectional area. It indicates that v has an intensity to move

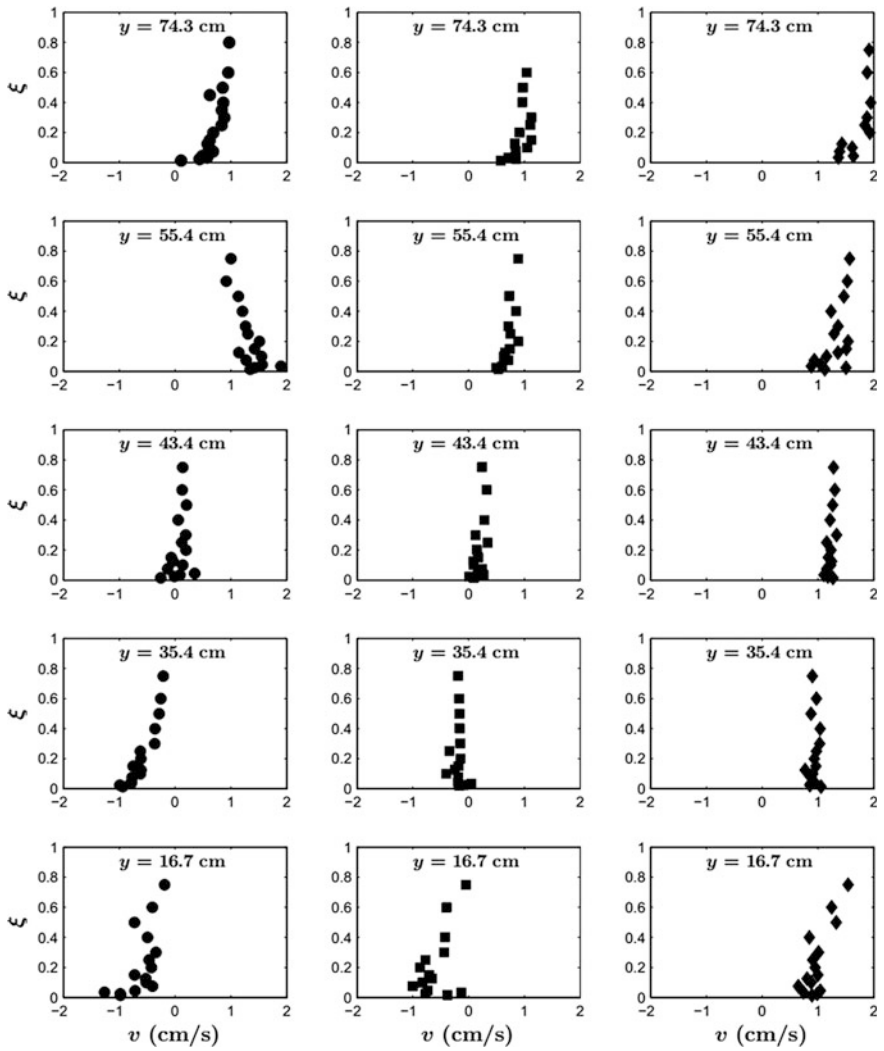

Fig. 3 Variation of time-averaged lateral velocity v along lateral direction at upstream (*first column* and x = 95.5 cm), interior (*second column* and x = 149.5 cm) and downstream (*third column* x = 185.5 cm) of sparse vegetation patch

near the right sidewall along negative direction. This tendency is highest at mid-portion of cross section due to maximum streamwise velocity. Along the cross-sectional area in the middle of the vegetation patch denoted by x = 149.5 cm, the components of v increase in reference to the corresponding profiles at x = 95.5 cm. Positive values are observed for y = 55.4 and 74.3 cm, although the profiles at y = 16.7, 35.4 and 43.5 cm provide negative values. Moreover, immediate downstream of trailing edge of the vegetation patch (x = 185.5 cm), positive

values of v are observed at all cross-sectional stations together with increased value with respect to the corresponding profiles at $x = 149.5$ cm. From the behaviour of measured v distributions at those cross sections, it can be said that the flow is directed towards the right sidewall at upstream of the vegetation patch. In middle of the patch, flow is diverted towards the left and right sidewalls. Hence, v is positive in half cross-sectional area ($y > 45.5$ cm) and negative in other half cross-sectional area ($y < 45.5$ cm). The reason for this behaviour is due to the serpentine pattern of flow inside the vegetation patch. In the middle cross-sectional region of the vegetation patch, the direction of v towards both the sidewalls can be explained by the diffusion of vortices from the interior of the patch to the sidewalls. The components of v are positive in immediate downstream of leading edge of the vegetation patch as the direction of flow is directed towards the left sidewall.

Also, v is found to be uniform across the cross section which shows thorough mixing of flow caused by the fully developed turbulence in the wake region. The scatter in the lateral velocity profiles found interior of the vegetation patch is caused by the vortex shedding.

3.3 Time-Averaged Vertical Velocity

Figure 4 shows the components of time-averaged vertical velocity w at all streamwise and cross-sectional locations. The components of w are negative at immediate upstream of leading of the vegetation patch ($x = 95.5$ cm) which indicates downward flow similar to the flow over hydraulically rough surfaces. The cross section at $x = 149.5$ cm interior of the vegetation patch, w, shows maximum negative values near the channel bed at $y = 43.4$ cm, i.e. middle of the cross-sectional area. It indicates possible scour at that location due to the action of sweeps. The profiles of w are similar in shape and consistent across the cross section at $x = 185.5$ cm, i.e. immediate downstream of trailing edge of the vegetation patch. The consistent nature represents the intense mixing of turbulence in the wake region. The positive w away from the wall at $x = 185.5$ cm indicates the deposition of sediment for a sediment-laden open-channel turbulent flow over an erodible bed. Similar to the lateral velocity profiles, vertical velocity profiles are scattered due to vortex shedding in the vegetation patch.

3.4 Reynolds Shear Stress

Reynolds shear stresses have a significant role in characterization of the flow field. Within three Reynolds shear stresses, the $-\overline{u'w'}$ has more dominating role in the flow field in comparison with the remaining two $-\overline{u'v'}$ and $-\overline{v'w'}$. The components of $-\overline{u'w'}$ were measured at all streamwise and lateral directions as shown in Fig. 5.

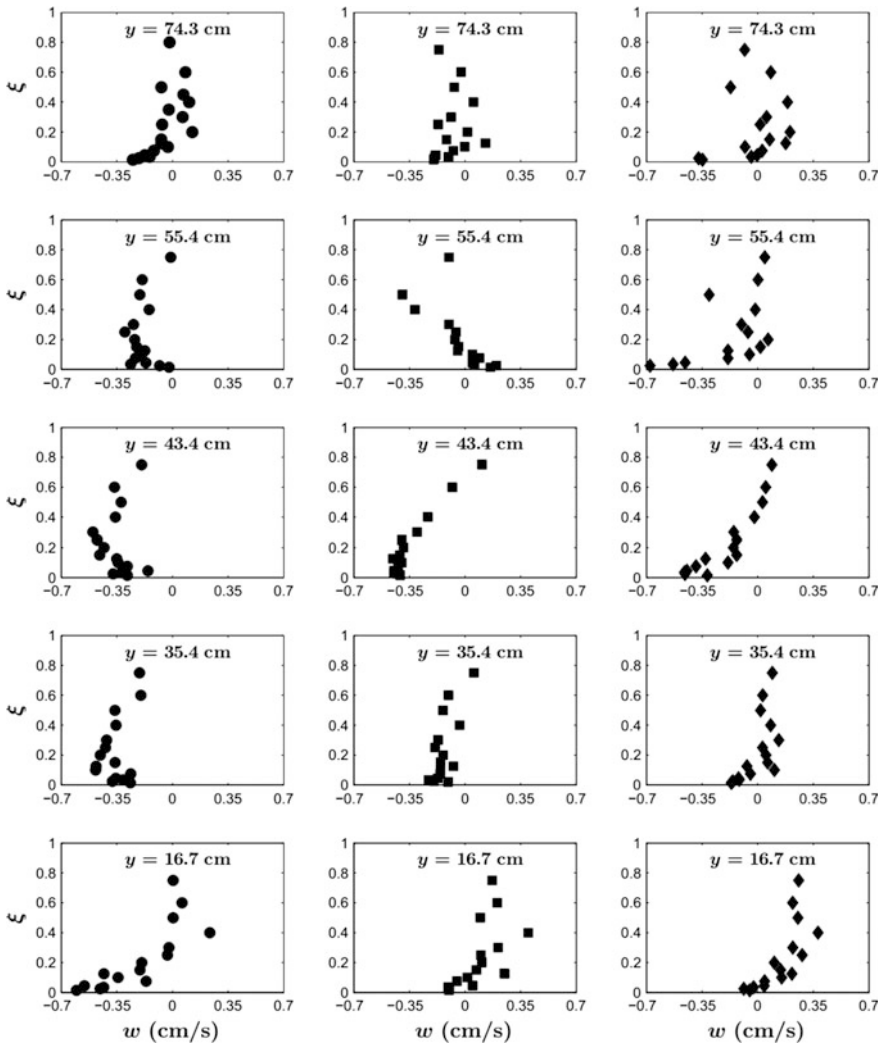

Fig. 4 Variation of time-averaged vertical velocity w along lateral direction at upstream (*first column* and x = 95.5 cm), interior (*second column* and x = 149.5 cm) and downstream (*third column* x = 185.5 cm) of sparse vegetation patch

It is noticed that at x = 95.5 cm at upstream of leading edge of the vegetation patch, the components of $-\overline{u'w'}$ appear to be same shape as in fully developed flow. In the interior of the vegetation patch, the components of $-\overline{u'w'}$ follow decreasing trend with increasing streamwise length for x = 149.5 and 185.5 cm. Moreover, $-\overline{u'w'}$ is

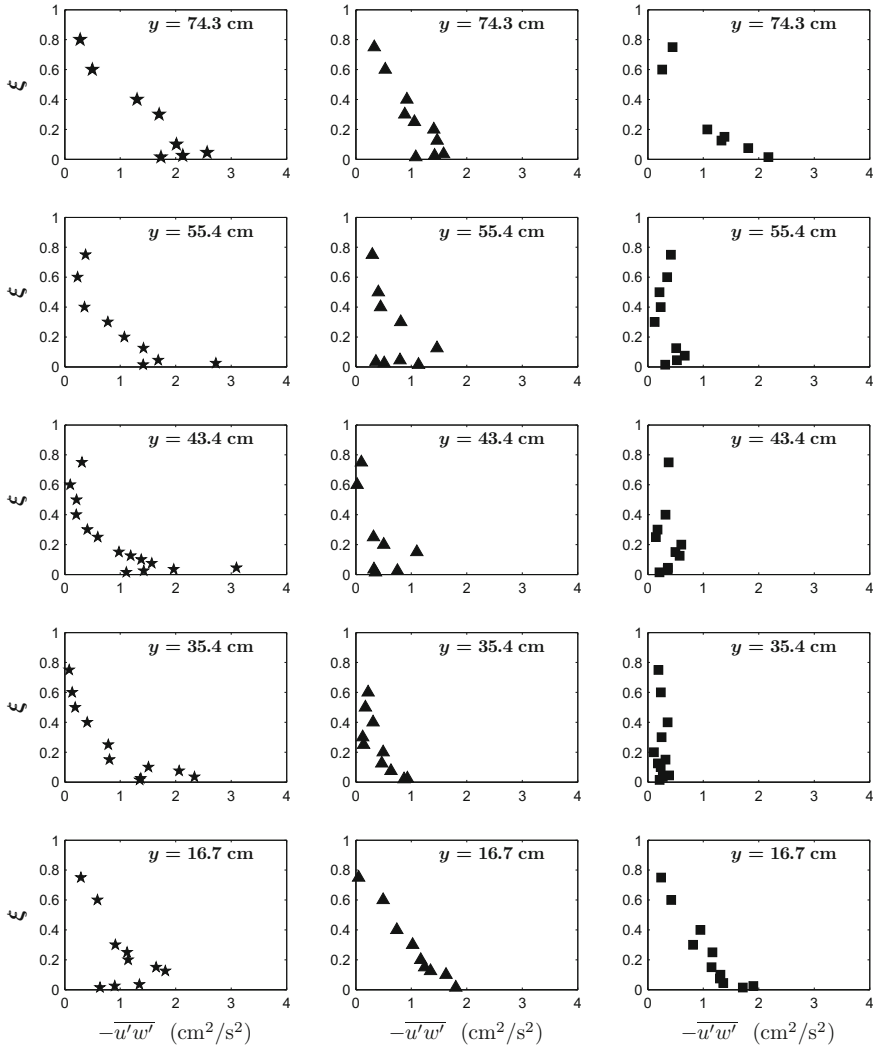

Fig. 5 Variation of Reynolds shear stress $-\overline{u'w'}$ along lateral direction at upstream (*first column* and x = 95.5 cm), interior (*second column* and x = 149.5 cm) and downstream (*third column* x = 185.5 cm) of sparse vegetation patch

uniform throughout the cross section at middle of the vegetation patch, i.e. x = 149.5 cm and in the wake region at x = 185.5 cm which could be due to intense mixing caused by interaction of eddies. However, $-\overline{u'w'}$ increases at y = 16.7 and 74.3 cm due to increased flow velocity in that region due to blockage

effect of vegetation patch. Due to the wake effect at downstream of trailing edge of the patch (x = 185.5 cm), the components of $-\overline{u'w'}$ show minimum value throughout the depth for y = 35.4, 43.4 and 55.4 through the vegetation patch; however, $-\overline{u'w'}$ gives maximum value at y = 16.7 and 74.3 cm due to the flow diversion through the region.

3.5 Turbulent Kinetic Energy

Normal stresses ($\overline{u'^2}, \overline{v'^2}$ and $\overline{w'^2}$) have important roles to influence the hydrodynamics in and around the vegetation patch. Due to the highly irregular behaviour of three-dimensional velocity components, the analysis of $\overline{u'^2}, \overline{v'^2}$ and $\overline{w'^2}$ requires huge space and also involves difficulty in drawing conclusions. So, here the normal stresses are investigated in terms of turbulent kinetic energy $k\left(=0.5\left[\overline{u'^2}+\overline{v'^2}+\overline{w'^2}\right]\right)$ which provides important information regarding the variation of normal stresses and turbulent kinetic energy of the flow. The components of k obtained from all streamwise and lateral locations are plotted in Fig. 6. At upstream of leading edge of the vegetation patch represented by x = 95.5 cm, the components of k at all cross-sectional stations decrease with increasing vertical height from the channel bed. Similarly, for x = 149.5 and 185.5 cm and y = 16.7 and 74.3 cm, the components of k maintain the same nature as the flow faces no barrier of cylinders at those regions. At x = 149.5 cm which is the middle cross-sectional area inside the patch, the components of k at y = 35.4, 43.4 and 55.4 cm are scattered. Here k increases with increase in ξ. Unlike the peak values found near the bed in fully developed flow at x = 95.5 cm, the maximum value of k occurs far from the channel bed for x = 149.5 cm. This may be due to the vortex stretching caused by the mean shear which converts energy from mean flow to turbulent kinetic energy. It has been observed that the vortex stretching increases upwards from the bed. Ricardo et al. [7] proposed that high values of k in the wake region are caused by shed vortices. The irregular variation of k along the depth is caused by passing vortices in von Kármán vortex street. The distribution of k is found to be similar at immediate downstream of the vegetation patch denoted by x = 185.5 cm. The distribution of k reaches its peak values near the bed at y = 16.4 and 74.3 cm because of flow diversion through that region.

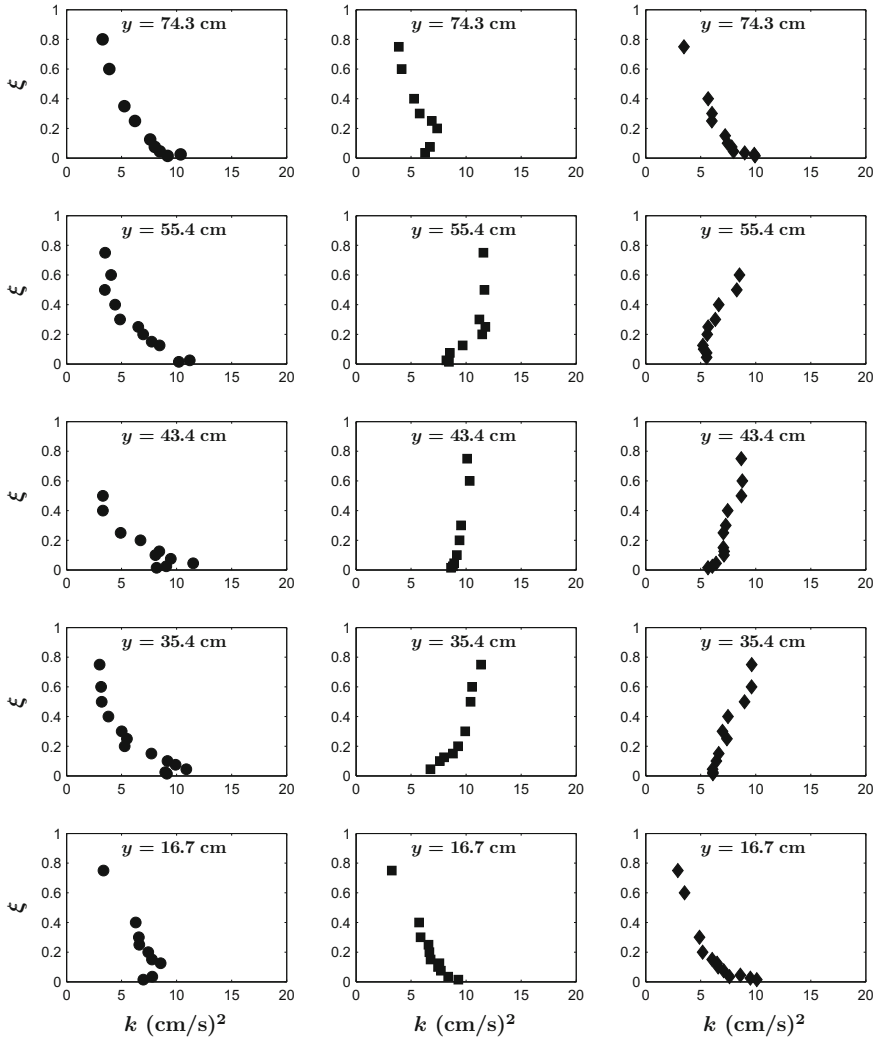

Fig. 6 Variation of turbulent kinetic energy k along lateral direction at upstream (*first column* and x = 95.5 cm), interior (*second column* and x = 149.5 cm) and downstream (*third column* x = 185.5 cm) of sparse vegetation patch

4 Conclusions

The variation of different turbulent features across the cross sections in upstream, interior and downstream of a sparse and emergent vegetation patch has been thoroughly investigated in this paper. The physics behind the variation of the turbulent characteristics is discussed. The conclusions obtained from this study are:

- The time-averaged streamwise velocity components just upstream of the sparse vegetation patch are similar across the section; however, the components through the interior of the vegetation patch decrease with increasing streamwise direction. Streamwise velocity components measured in the middle of gaps between vegetation patch and sidewalls are increasing with increasing streamwise direction.
- The cross sections upstream and interior of the vegetation patch, the lateral velocities are directed towards nearest sidewalls; however, positive values are observed throughout the cross-section just downstream of the vegetation patch. The characteristics indicate the serpentine pattern of flow when it moves past through the vegetation patch.
- The time-averaged vertical velocity component values are negative upstream of the vegetation patch. On the contrary, the components are positive throughout the cross section at the immediate downstream of the vegetation patch. Time-averaged vertical velocities across the middle cross section in the vegetation patch are negative, but absolute magnitudes are less than those of immediate upstream of the vegetation patch. The lateral and vertical velocities inside the vegetation are found to be scattered due to the vortex shedding.
- The profiles of Reynolds shear stresses $-\overline{u'w'}$ just upstream of the sparse vegetation patch are similar like fully developed flow; however, the components through interior of the vegetation are decreasing with increasing streamwise length.
- At upstream of the vegetation patch, turbulent kinetic energy follows the same trend across the cross section with the maximum values occurring near the bed. On the contrary, in the interior of the vegetation patch k values are increasing towards the free surface. However, k values are found to be maximum near the bed in the gaps between the vegetation patch and side walls.

These results from this study should be useful in helping further the understanding of the behaviour of turbulent flow in the interior and exterior of an emergent and sparse vegetation patch.

References

1. Chanson, H., Trevethan, M., Aoki, S.I.: Acoustic Doppler velocimetry (ADV) in small estuary: field experience and signal post-processing. Flow Meas. Instrum. **19**(5), 307–313 (2008)
2. Chen, Z., Ortiz, A., Zong, L., Nepf, H.: The wake structure behind a porous obstruction and its implications for deposition near a finite patch of emergent vegetation. Water Resour. Res. **48**(9) (2012)
3. Goring, D.G., Nikora, V.I.: Despiking acoustic doppler velocimeter data. J. Hydraul. Eng. **128** (1), 117–126 (2002)
4. Jimenez, J., Uhlmann, M., Pinelli, A., Kawahara, G.: Turbulent shear flow over active and passive porous surfaces. J. Fluid Mech. **442**, 89–117 (2001)
5. Mori, N., Suzuki, T., Kakuno, S.: Noise of acoustic Doppler velocimeter data in bubbly flows. J. Eng. Mech. **133**(1), 122–125 (2007)

6. Nezu, I., Onitsuka, K.: Turbulent structures in partly vegetated open-channel flows with LDA and PIV measurements. J. Hydraul. Res. **39**(6), 629–642 (2001)
7. Ricardo, A.M., Koll, K., Franca, M.J.: The terms of turbulent kinetic energy budget within random arrays of emergent cylinders. Water Resour. Res. **50**(5), 4131–4148 (2014)
8. White, B.L., Nepf, H.M.: Shear instability and coherent structures in shallow flow adjacent to a porous layer. J. Fluid Mech. **593**, 1–32 (2007)
9. Yang, J.Q., Kerger, F., Nepf, H.M.: Estimation of the bed shear stress in vegetated and bare channels with smooth beds. Water Resour. Res. **51**(5), 3647–3663 (2015)

Turbulent Scale and Mixing Length Measurement in Mobile Bed Channel

Anurag Sharma, Dengkhw Brahma, Mahesh Patel and Bimlesh Kumar

Abstract This paper describes a laboratory study of turbulence scales in mobile bed channel. The experimentation has been carried on curvilinear cross-section mobile bed channel with median sand size (d_{50} = 0.418 mm). The present result investigated the different turbulence scale such as Kolmogorov, Taylor and integral scales. The percentage decrease in between Kolmogorov and Taylor scale has been increased as compared to the percentage decrease in between Taylor and integral scale, but the result is quite opposite in velocity scale. Flow turbulent scales indicate that the eddy size increases in integral scale because of increase in momentum transfer and decrease in energy dissipation linked to the evolution of the sediment transport. Evaluated Prandtl mixing length is well satisfied with theoretical curves given by Nezu and Nakagawa (Turbulence in open-channel flows, 1993) [1]. Sediment transport influenced decreased in von Karmann constant indicates the reduction in the mobile bed resistance to flow.

Keywords Velocity · Turbulence scale · Mixing length

1 Introduction

Turbulent motion occurs to an extensive range of length and velocity scale. Turbulence can consist of eddies of different sizes. The eddy sizes generally define the characteristics turbulence scale which can be characterized by length scale and velocity scale. Kolmogorov, Taylor and integral are the basic type of length scale, and corresponding velocity scale is used in turbulence model. The area captured by large size eddy may have the small size eddy. Large size eddy is unstable and split into smaller eddy till Reynolds number is small so that kinetic energy is dissipated

A. Sharma (✉) · D. Brahma · M. Patel · B. Kumar
Indian Institute of Technology Guwahati, Guwahati 781039, Assam, India
e-mail: anurag.sharma@iitg.ernet.in

V. Garg et al. (eds.), *Development of Water Resources in India*,
Water Science and Technology Library 75, DOI 10.1007/978-3-319-55125-8_40

with the effect of molecular viscosity [2]. The size of smallest scale of the flow is determined by viscosity, and at these small scales, kinetic energy of turbulence is converted into heat. The energy dissipated at the small scale must equal to energy shift by the larger scale in steady turbulent flow. Kolmogorov's first similarity hypothesis states that the scale of dissipated energy will depend on both viscosity and the dissipation rate. Taylor scale indicates the size of the eddy in the inertial sub-range. Since Taylor scale is related to turbulent fluctuation, so this scale is also named by turbulence length scale and it is first length scale derived to describe the turbulence. At this scale, the dissipation rate depends on the viscosity and the velocity gradient in the turbulent eddies. Length scale can be obtained from single-point timescale measurement using Taylor hypothesis [3] and the condition under which this is valid are hardly satisfied in practical turbulent flows. Direct measurement of the length scale requires simultaneous, two-point measurements of the spatial correlation from which integral and microscales of turbulence can be calculated [3]. Previous study [4] used LDV for making velocity length scale measurement in non-reacting and reacting turbulent flows. The researcher [5] described about the turbulence and random process in fluid mechanics. In the present research work, mobile bed streams used to collect experimental data that has been employed to investigate the turbulence scales and mixing length measurement and compare between different types of turbulence scales. The present studies also investigate the link between turbulence scale and sediment transport. The present study in fact the extension of study by Sharma et al. [6] on turbulent parameters of flow in curved cross-section sand bed channel.

2 Experimental Setup

In this study, experiment was conducted in a tilting flume of dimension 17.24 m length, 1 m width and 0.72 m deep (Fig. 1). The flume has upstream tank of sizes 2.8 m in long, 1.5 m in wide and 1.5 m in deep which provide the flow into the flume. The upstream tank collects water from the overhead tank where water was driven by three pumps having capacities of 10 HP each. The flow depth is controlled by a tail gate located at the downstream section of the channel. The depth of flow over the rectangular notch at the downstream collection tank is used to measure the flow discharge. Water is gradually introduced into the channel by opening a valve located at the overhead tank. When the bed was fully submerged, the tail gate was operated so that flow depth is approximately equal to bank depth in the channel. At the same time, the upstream discharge was also adjusted to achieve incipient motion condition. The discharge Q and flow depth y are registered corresponding to incipient motion.

The cross-check of incipient motion was done with the visual observation suggested by Yalin [7]. The threshold condition was also confirmed with [8] diagram. Most of the stable channel predictors were empirical or semiempirical excluding [9]. The geometric profiles with 0.70 m (shape 70) were used at which

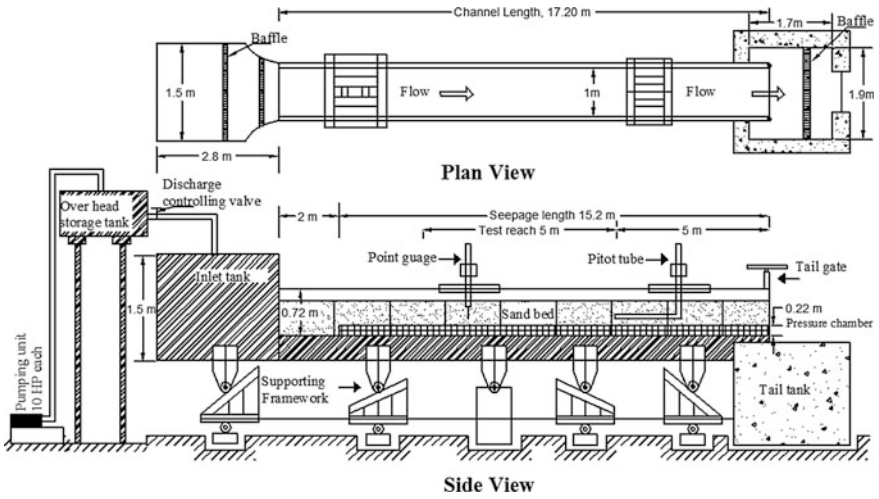

Fig. 1 Tilting flume setup

Table 1 Summary of flow measurement

Median grain size, d_{50} (mm)	Discharge, Q (m^3/s)	Depth of flow, y (m)	Hydraulic radius, R (m)	Bed slope, S_0
0.418	0.0169	0.14	0.075	0.0015

maximum flow depth of 0.142 m is calculated by Lane [9] equation. A wooden shaper was used to prepare curved cross-section profile of 0.7 m shape. Experimental data were taken at a distance of 7.5 m from the downstream section of the flume; the details of flow parameter are tabulated in Table 1. Acoustic Doppler velocimeter (ADV) was used to measure 3D water velocity in the main channel. ADV made sampling volume at a vertical distance of 5 cm from the central transmitter, while velocity components were sampled in the remote sampling volume at the rate of 200 Hz for the duration of 300 s. A digital point gauge connected to a trolley was used to measure the flow depth of water in the channel. Water surface slope and bed slope in experiments were measured with the help of Pitot-static tube and total station, respectively. Correlation and signal-to-noise ratio (SNR) were selected for reconstructed the velocity data points. In the experiment, minimum SNR and correlation were kept as 15 and 70, respectively. Correlation was reduced to 65 at near the bed [10]. The ADVdata is suffered from spikes due to which data were reconstructed by the acceleration thresholding method using spike removal algorithm [3]. The threshold value lies in between 1 and 1.5 so that velocity power spectra in inertial sub-range should satisfy Kolmogorov −5/3 scaling law [11].

3 Results and Discussion

Mean streamwise velocity profile is shown in Fig. 2. In order to describe the linkage between turbulent flow and sediment transport, turbulence scale and mixing length were studied for velocity profile by considering the turbulence-scale motions that are at isotropic condition.

3.1 Turbulence Scale

Largest size eddies are called integral scale which are defined by length scale l and velocity scale u_1 having an order of $(2\ k/3)^{1/2}$ where K is the turbulence kinetic energy (TKE). Integral scale is the scale at which energy is produced from time-average velocity and transferred to smaller eddy which is calculated based on the TKE dissipation rate (ε) and turbulent kinetic energy (K).

$$l = K^{3/2}/\varepsilon \tag{1}$$

$$u_l = (K)^{1/2} \tag{2}$$

At sufficiently large flow Reynolds number, small-scale motions are isotropic which indicates that size of small eddies cannot be discriminated by a specific spatial direction [1]. Since TKE dissipation rate (ε) and viscosity (υ) are simply two parameters to determine small-scale motions, there are unique in Kolmogorov length scale (η) and velocity scale (u_η) that can be expressed by dimensional analysis.

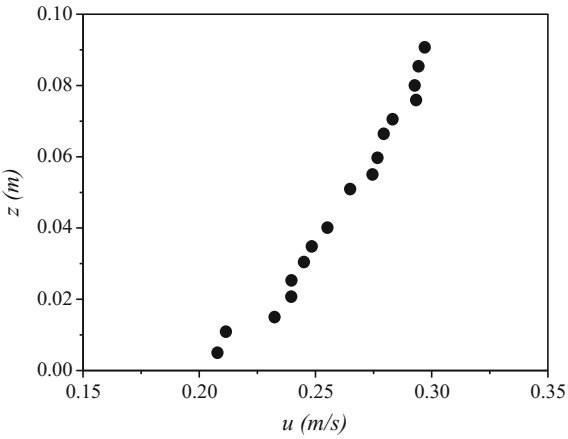

Fig. 2 Profile of mean streamwise velocity

$$\eta = \left(\upsilon^3/\varepsilon\right)^{1/4} \tag{3}$$

$$u_\eta = (\varepsilon\upsilon)^{1/4} \tag{4}$$

Taylor scale is calculated based on the Kolmogorov's second similarity hypothesis which states that at sufficiently high Reynolds number of every turbulent flow, the statistics of motion of scale have a common form that is uniquely calculated by ε independent of υ.

$$\lambda = \left(15\upsilon\sigma_u^2/\varepsilon\right)^{0.5} \tag{5}$$

$$u_\lambda = \sigma_u \tag{6}$$

where σ_u is standard deviation in streamwise direction. TKE dissipation rate ε is measured based on Kolmogorov's second hypothesis. The same is plotted in Fig. 3. Kolmogorov, Taylor and integral length and velocity scale with respect to depth from the bed (z) are shown in Fig. 4. Figure 4 presents the results of percentage decrease from Taylor to Kolmogorov length scale which is about 97.6%, while integral to Taylor length scale is about 98.2%. The percentage decrease from Taylor to Kolmogorov velocity scale is about 91%, while integral to Taylor velocity scale is about 18%. The result presented that velocity scale reduces as length scale increases. The present results indicate that influence of moving sand bottom decreases the turbulence length scale while increases in case of velocity scale. The experimental results conclude that the size of largest eddies in the flow is given by integral scale, while range of intermediate and smaller eddies is given by Taylor and Kolmogorov scale, respectively. Integral eddy length is increased as compared to other scales in the vicinity of bed surface.

The beginning of bed structures is mainly due to larger size eddies within the near-bed surface [12]. Compared to Taylor and Kolmogorov scales, integral scale is

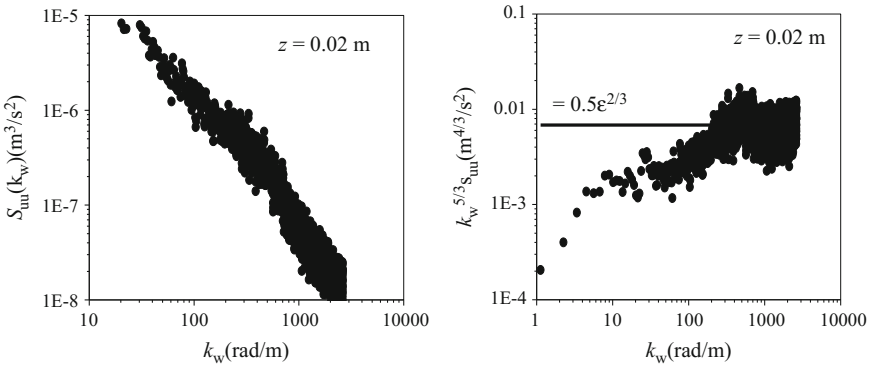

Fig. 3 Velocity power spectra $S_{uu}(k_w)$ and estimation of turbulent dissipation rate ε

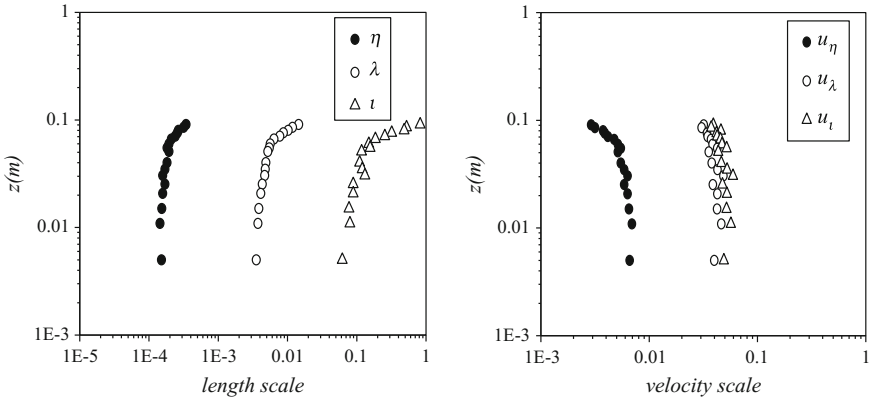

Fig. 4 Vertical distribution of length and velocity scale

of comparatively larger in the near-bed zone which corresponds to higher energy production and less energy dissipation of turbulent motions. Thus, higher degree of turbulence achieved in the vicinity of bed surface with an increased eddy size, which results in the initiation of sediment transport in channel. The rate of transfer of the higher turbulence kinetic energy, i.e., energy dissipation, can be related to characteristic length scale for turbulent motion. It is observed that integral scales are higher than Taylor and Kolmogorov scale which implies that the introduction of large size eddies in the flow reduces the energy dissipation rate. As observed from Reynolds stress profiles [6], an increase in Reynolds stress toward the bed surface implies transfer of momentum increased from the flow to the bed particles. An increase in momentum transfer decreases the energy dissipation rate leading to a gain in turbulence length scales.

3.2 Turbulent Mixing Length

Prandtl mixing length (L) is the length at which fluid parcels retain its original form before dispersed into surrounding fluid, which is given by $L = (\overline{-u'w'})^{0.5}/du/dz$. To determine the mixing length, velocity profiles were used to measure the velocity gradient du/dz and the values of $\overline{-u'w'}$ were obtained directly from Reynolds stress profiles. The non-dimensional variations of mixing length L/y with z/y are presented in Fig. 5. Experimental data points fit satisfactorily with the theoretical equation $L/y = kz/y(1 - z/y)^{0.5}$ given by Nezu and Nakagawa [1].

The slope of lined portion called as von Karmann constant $k = L/z$ is observed as 0.36 which is same as calculated with velocity logarithmic law [6]. The estimate k is found as less than universal value (= 0.41). This result suggested that eddy traversing length decreases with sediment transport and reduction in the mobile bed resistance to flow.

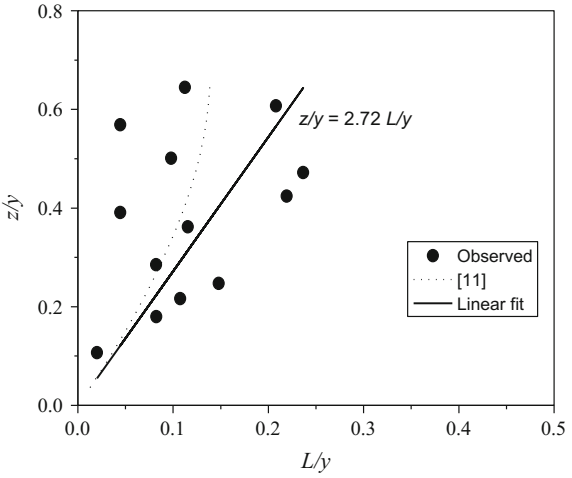

Fig. 5 Mixing length distributions

4 Conclusions

In this present study, measurement of turbulence scales in curvilinear mobile bed has been the main concern. The parameter used for the calculation of turbulence scales was measured by conducting the experiment using Vectrino probe. Different turbulent scales were also analyzed to obtain information regarding eddies size. The experimental observation concludes that percentage decrease in between Kolmogorov and Taylor length scale is increased as compared to the percentage decrease in between Taylor and integral scale, but the result is quite opposite in the field of velocity scale. The result concludes that length scale increases as velocity scale decreases. The integral length scale is more as compared to Kolmogorov and Taylor scale in the vicinity of bed surface which advises higher energy production and less energy dissipation in the near-bed zone. These findings contribute to the coherent structure of flows that correspond to increase in bed load transport. The calculated Prandtl mixing length satisfies the theoretical equation given by Nezu and Nakagawa [1]. The von Karmann constant has been decreased with sediment transport as compared to clear water which suggested that there is the deduction in the transverse length of the fluid parcel and mobile bed resistance to flow.

References

1. Nezu, I., Nakagawa, H.: Turbulence in Open-Channel Flows. Balkema, Rotterdam (1993)
2. Pope, S.B.: Turbulent Flows. Cambridge University Press, Cambridge (2000)
3. Goring, D.G., Nikora, V.I.: Despiking acoustic Doppler velocimeter data. J. Hydraul. Eng. **128**, 117–126 (2002)

4. Fraser, R., Pack, C.J., Santavicca, D.A.: An LDV system for length scale measurement. In: Experiments in Fluids, vol. 4, pp. 150–152. Springer (1986)
5. Landahl, M.T., Christensen, E.M.: Turbulence and Random Process in Turbulence. Cambridge University Press (1986)
6. Sharma, A., Patel, M., Kumar, B.: Turbulent parameters and corresponding sediment transport in curved cross section channel. ISH J. Hydraul. Eng. **21**, 333–342 (2015)
7. Yalin, M.S.: Mechanics of Sediment Transport. Pergamon, Oxford, U.K. (1976)
8. Shields, A.: Application of Similarity Principles and Turbulence Research to Bed-Load Movement. California Institute of Technology, Pasadena (1936)
9. Lane, E.W.: Progress report on studies on the design of stable channels by the bureau of reclamation. Proc. ASCE **79**, 1–31 (1953)
10. Deshpande, V., Kumar, B.: Turbulent flow structures in alluvial channels with curved cross-sections under conditions of downward seepage. ESPL **41**, 1073–1087 (2016)
11. Lacey, R.W.J., Roy, A.G.: Fine-scale characterization of the turbulent shear layer of an in stream pebble cluster. J. Hydraul. Eng. 925–936 (2008)
12. Venditti, J.G., Church, M.A., Bennett, S.J.: Bed form initiation from a flat sand bed. J. Geophys. Res. **110**, F1 (2011)

CFD Prediction of Loss Coefficient in Straight Pipes

Abdullah Haroon, Shahbaz Ahmad and Ajmal Hussain

Abstract Loss of head in pipes is an important factor to be considered in design of engineering systems to reduce energy costs. This loss is either due to viscous effect called friction loss or due to change in geometry like bends, elbows, expansion and contraction. The pressure loss is a function of the type of flow of the fluid, i.e., laminar, turbulent; material of the pipe; and the fluid flowing through the pipe. In present study, straight pipes of various materials, namely PVC, steel and cast iron, are analyzed using ANSYS. Equations of mass, momentum and k-ε turbulence model are solved using the finite volume method. To validate the numerical tool friction, loss coefficient is determined and compared with existing experimental results. Furthermore, the effect of variation of Reynolds number on the friction loss coefficient is studied. The contours of turbulence eddy dissipation at various Reynolds number are also presented to investigate the effect of Reynolds number on turbulent kinetic energy.

Keywords Friction loss · CFD · k-ε turbulence model · ANSYS-CFX

1 Introduction

In any pipe assembly, there are two types of resistance against the flow of fluid, namely dynamic losses and frictional losses. Frictional losses are caused mainly due to the shearing stress between the layers of fluid in the laminar sublayer, which are in the vicinity to the surface of the pipe walls. Friction is also caused when the fluid domain in the turbulent flow strikes against the protrusions of the pipe wall. This causes eddy formation and contributes to energy loss. Friction losses take place along the entire length of a pipe. On the other hand, when fluid passes through fitting components such as elbows, curves, tee joints, contractions, expansions,

A. Haroon · S. Ahmad · A. Hussain (✉)
Zakir Husain College of Engineering & Technology, Aligarh Muslim University, Aligarh, UP, India
e-mail: ajmalamin.iitr@gmail.com

V. Garg et al. (eds.), *Development of Water Resources in India*,
Water Science and Technology Library 75, DOI 10.1007/978-3-319-55125-8_41

exits and entrances, a change in direction or velocity of flow occurs. This change leads to separation of flow from the walls of the pipe and the formation of eddies and turbulence in that area. The loss of energy resulting from these eddies and turbulences constitutes what are called as dynamic losses. Friction losses also known as major losses are unavoidable in any pipe system as they occur throughout the entire length of the pipe and hence very important to keep a track for the estimation of energy losses in the assembly. Since the shear stress of a flow also depends on whether the flow is laminar or turbulent, friction loss also depends on type of flow. For turbulent flow, the losses due to pressure drop depends on the protuberance of the surface, while in laminar flow, the protuberance effects of the walls are insignificant. This is because in turbulent flow, a thin viscous layer (laminar sublayer) is formed close to the pipe wall which causes a loss in energy, while in laminar flow any such layer is absent.

Studies have been performed to get the knowledge about velocity distribution, pressure drop and turbulent flow behavior in the vicinity of rough walls [1–3]. In rough pipes, the inspection of fluctuating velocity spectra is used to find the turbulence profile in all coordinate directions. A significant observation of this study was that the nature of the solid boundary has negligible effect on the flow in the core of the pipe. On the other hand, the flow in the vicinity of the wall is dependent on the nature of the solid boundary [4]. In literature, different approaches were proposed by several researchers to study the relationship of turbulent flow and rough surfaces. The behavior of turbulent flow in pipes by implementing roughness element drag coefficient is studied by Wang et al. [5]. Recently formula for the mean velocity calculation across the inner layer of turbulent boundary is proposed [6]. The velocity profile obtained by busing this formula is used to formulate the friction factor correlation for the fully developed turbulent pipe flow. Saleh [7] observed the effects of roughness by using k-ε turbulence model in conjunction with empirical wall function. Other significant works with the implementation of k-ε turbulence model were studied by Cardwell et al. [8]. K-ε model can be used with moderate roughness within a suitable degree of accuracy. The researchers concluded that among the different turbulence models k-ε model gives the most suitable prediction.

This study focuses on the possibility of employing computational fluid dynamics (CFD) techniques for prediction of friction factor in pipes of various materials. Since every material has a characteristic roughness, friction factor is different for different materials. For the numerical model validation, the Moody's diagram was used [9]. Friction loss coefficient was predicted using standard k-ε turbulence model and was validated from the results appearing in Moody's diagrams. The absolute roughness coefficient for various materials was also read from Moody's diagram. This paper also investigates the effects of Reynolds number on friction loss coefficient and turbulent kinetic energy. ANSYS-CFX is used to solve the RANS equations to achieve convergence residuals of 10E-5.

2 Mathematical Modeling

2.1 Governing Equations

The equation of continuity in differential form can be represented as:

$$\frac{\partial u}{\partial x} + \frac{\partial v}{\partial y} + \frac{\partial w}{\partial z} = 0 \tag{1}$$

The momentum equation for the incompressible viscous fluids can be written as:

$$\frac{\partial u}{\partial t} + (u \,.\, \nabla)u = -\frac{1}{\rho}\nabla p + v\nabla^2 u \tag{2}$$

2.2 Turbulence Model

The standard k-ε turbulence model is most famous and simple turbulence model. This model employs the calculation of the turbulent velocity and length scales independently by using the solution of different transport equations. The standard k-ε model has been used widely for solving the turbulence model of practical engineering flow problems [10]. This model is based upon a semiempirical model approach which utilizes model transport equations for the calculation of turbulence kinetic energy k and its dissipation rate ε. The transport equation for turbulence kinetic energy (k) in the model is derived from the exact equation, whereas the transport equation for dissipation rate of kinetic energy (ε) is obtained using physical reasoning and has little resemblance to its mathematically exact counterpart. These equations are as follows:

$$u_i \frac{\partial k}{\partial x_i} = \frac{\partial}{\partial x_i}\left(\frac{v_t}{\sigma_k}\frac{\partial k}{\partial x_i}\right) - v_t\left(\frac{\partial u_i}{\partial x_j} + \frac{\partial u_j}{\partial x_i}\right)\frac{\partial u_i}{\partial x_j} - \varepsilon \tag{3}$$

$$u_i \frac{\partial \varepsilon}{\partial x_i} = \frac{\partial}{\partial x_i}\left(\frac{v_t}{\sigma_\varepsilon}\frac{\partial \varepsilon}{\partial x_i}\right) + c_{1_\varepsilon}\frac{\varepsilon}{k}P - c_{2_\varepsilon}\frac{\varepsilon^2}{k} \tag{4}$$

where

$$P = v_t\left(\frac{\partial u_i}{\partial x_j} + \frac{\partial u_j}{\partial x_i}\right)\frac{\partial u_i}{\partial x_j}$$

In the above equations, σ_k, σ_ε, $c_{1\varepsilon}$, $c_{2\varepsilon}$ are empirical constants having standard values as: σ_k = 1.0, σ_ε = 1.3, $c_{1\varepsilon}$ = 1.44, $c_{2\varepsilon}$ = 1.92.

2.3 Other Basic Equations

The Reynolds number is expressed as:

$$Re = \rho UD/\mu, \tag{5}$$

Friction factor (f) can be written as:

$$f = \frac{2\Delta PD}{L\rho U^2} \tag{6}$$

Head loss for fully developed flow is determined by Hagen–Poiseuille's co-relation:

$$H = \frac{fLU^2}{2Dg} \tag{7}$$

3 Numerical Modeling

In the present problem, pipe of length 2 m and diameter 75 mm was used as shown in Fig. 1. The geometry was discretized using a structured hexagonal mesh throughout. O-grid scheme with linearly varying nodal space in the radial direction was used near the wall surface to capture accurately the effect near the walls as shown in Fig. 2. ICEM-CFD was used to generate a 3D geometry and meshing. Material of the pipe was modeled by defining the roughness of walls. Standard roughness of materials was read from Moody's diagram, and the relative roughness was calculated by dividing this value by diameter of pipe as shown in Table 1.

The boundary conditions employed at the boundaries of the domain are as follows:

(1) Boundary condition at inlet: The inlet flow rate is decided by velocity, and the direction is normal to the inlet. The velocities in the other two directions are zero. The temperature is kept as 25 °C.

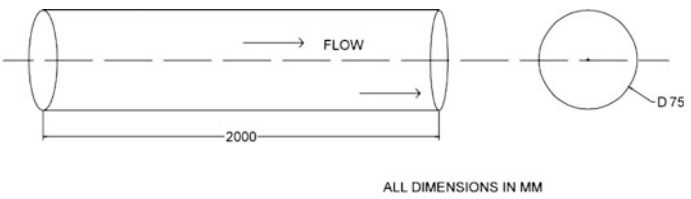

Fig. 1 Schematic view of pipe of length 2 m and diameter 75 mm

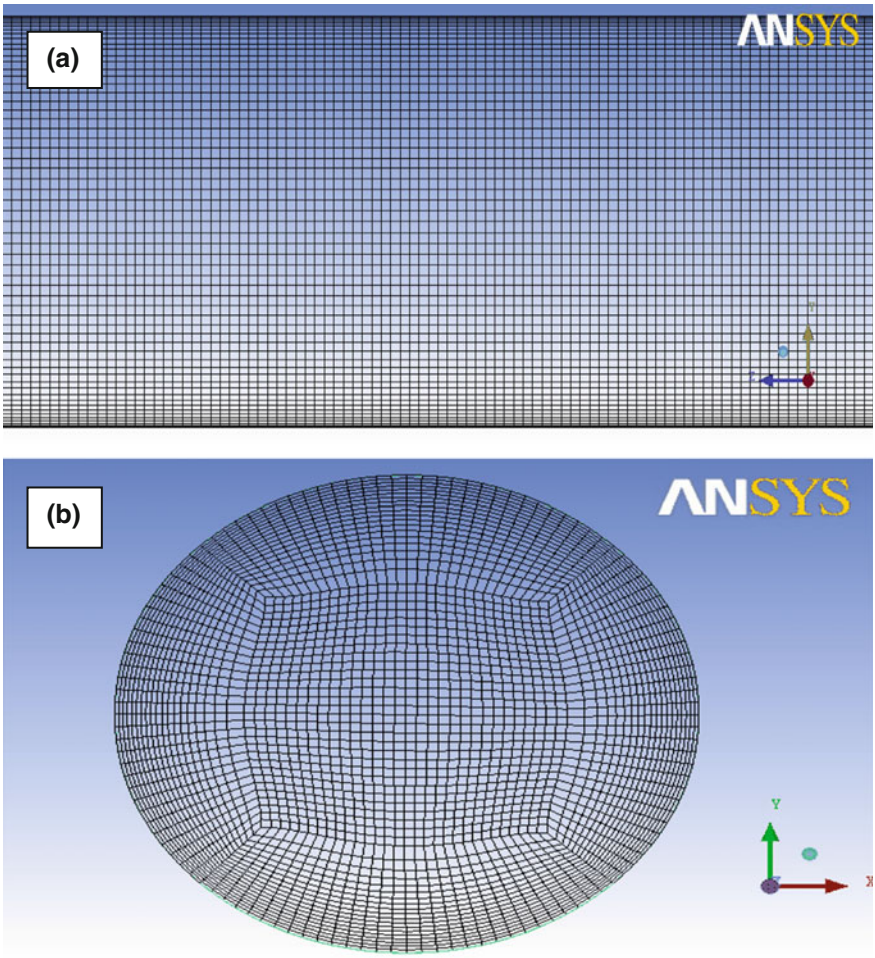

Fig. 2 Meshing of the test pipe **a** side view, **b** inside view

Table 1 Absolute and relative roughness of different materials

Material	Absolute roughness (mm)	Relative roughness (mm)
PVC	0.0025	0.0001
Steel	0.025	0.001
Cast iron	0.15	0.006

(2) Boundary condition at outlet: The outlet boundary condition is kept at zero relative pressure which means that the fluid is flowing out at atmospheric pressure.

(3) Boundary conditions at walls: No-slip wall is chosen as the wall condition. This assumes relative velocity to be equal to zero at the interface of the surface and the fluid, which means that $u = v = w = 0$ at the surface. The wall roughness is altered as per the choice of material.

The governing equations were solved using the finite volume method. The convergence is set such that the scaled residuals decrease to 10E-4 for all the variables. Comparison of friction factor obtained from simulation and Moody's charts is presented in Table 2.

Figure 3 shows the effect of Reynolds number on friction factor of pipes of various materials. It can be inferred from the graph that the friction factor for each pipe decreases as the Reynolds number is increased, which is in corroboration with the friction factor determined from co-relation reported in Moody's diagram.

Table 3 shows the comparison of head loss of this model for PVC pipe with the results obtained by co-relation as shown in Eq. (7). The difference between the co-relation values and simulation results is negligible. Similar comparison can be made for other materials as well.

Table 2 Friction factor comparison for different materials

Material	Absolute roughness (mm)	f (Simulated)	f (Moody's diagram)
PVC	0.0025	0.01788	0.01807
Steel	0.025	0.01914	0.01966
Cast iron	0.15	0.02386	0.02533

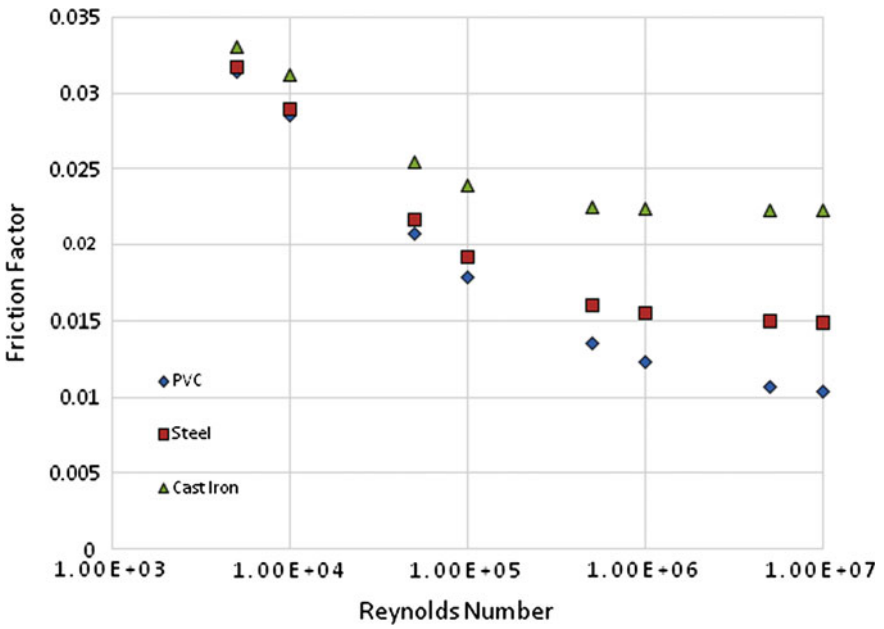

Fig. 3 Effect of changing Reynolds number on friction factor of various materials

Table 3 Comparison of head loss for PVC pipe

Velocity	Head loss (Simulated)	Head loss (Correlation)	% Difference
0.0595	7.54712E-05	7.92015E-05	4.709964895
0.119	0.000274217	0.000279611	1.929346551
0.595	0.004984811	0.005028045	0.85985222
1.19	0.01720683	0.017395463	1.084381008
5.95	0.324415902	0.326237105	0.558245162
11.9	1.186091743	1.1827298	0.284252887
59.5	25.76766565	25.35314611	1.634982641
119	99.94943935	97.77489636	2.224029955

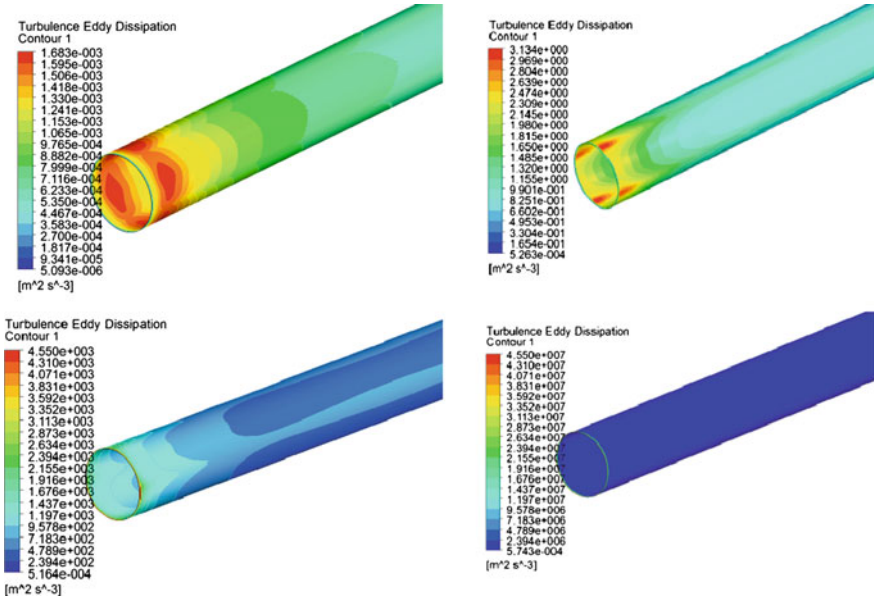

Fig. 4 Effect of different Reynolds number on the turbulence eddy dissipation near the inlet

Effect of different Reynolds number on the turbulence eddy dissipation near the inlet is illustrated in Fig. 4. It is clear from these figures that turbulence at inlet decreases with the increase in Reynolds number.

Figure 5 shows the variation of velocity with Reynolds number at a plane passing through the cross section of the pipe in the middle. In can be observed that as the Reynolds number increases the velocity gradient in the radial direction becomes steeper.

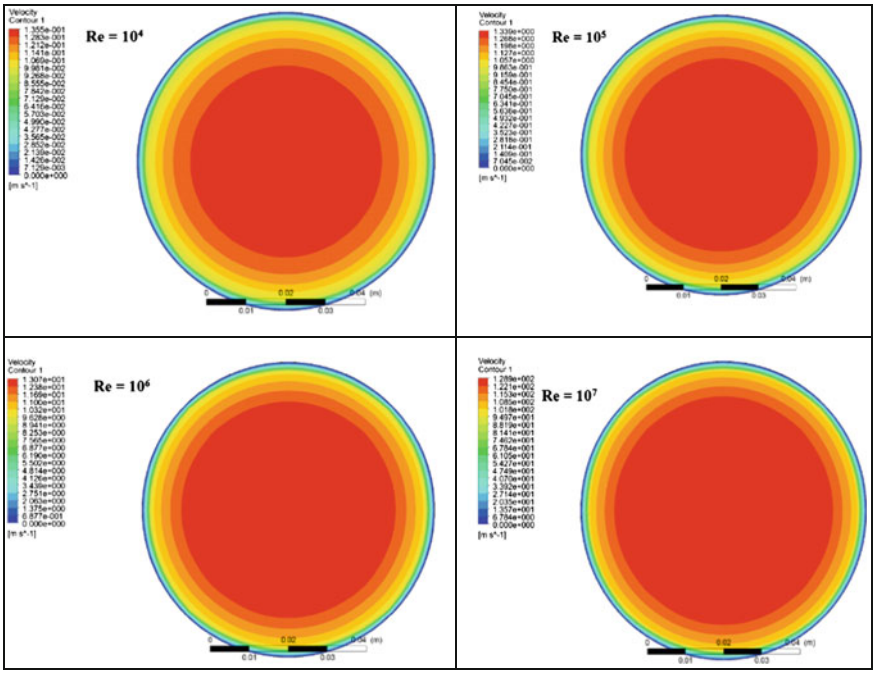

Fig. 5 Variation of velocity with Reynolds number at a plane passing through the cross section of the pipe in the middle

4 Conclusion

In the present study, the extrapolative abilities of the standard *k*-ε turbulence model have been tested as they implemented to the calculation of friction factor of turbulent flow in a 3D pipe with good agreement. This model has been used to predict the various aspects of the fluid flow in a straight pipe, including the wall roughness, friction factor at various Reynolds number and head loss. The advantage of using k-ε turbulence model is that it is computationally cheap. The presented results show a fairly good agreement with the available literature, implying that CFD techniques are mature enough nowadays to predict flow of fluids with standard turbulence models.

References

1. Reif, B.P., Andersson, H.: Prediction of turbulence-generated secondary mean flow in a square duct. Flow Turbul. Combust. **68**, 41 (2002)
2. Vijiapurapu, S., Cui, J.: Simulation of turbulent flow in a ribbed pipe using large eddy simulation. Numer. Heat Transf. Part A: Appl. **51**(12), 1137–1165 (2007)

3. Vijiapurapu, S., Cui, J.: Performance of turbulence models for flows through rough pipes. Appl. Math. Model. **34**(6), 1458–1466 (2010)
4. Rao, A.R., Kumar, B.: Transition of turbulent pipe flow. J. Hydraul. Res. **47**(4), 529–533 (2009)
5. Wang, et al.: Direct simulation of surface roughness effects with RANS and DES approaches on viscous adaptive Cartesian grids. AIAA Paper 2420 (2004)
6. Scibilia, M.-F.: Heat transfer in a forced wall jet on a heated rough surface. J. Therm. Sci. **9**(1), 85–92 (2000)
7. Di Nucci, C., Spena, A.R.: Mean velocity profiles of two-dimensional fully developed turbulent flows. C R Mec **340**(9), 629–640 (2012)
8. Cardwell, N.D., Vlachos, P.P., Thole, K.A.: Developing and fully developed turbulent flow in ribbed channels. Exp. Fluids **50**(5), 1357–1371 (2011)
9. Moody, L.F.: Friction factors for pipe flow. Trans. ASME **66**(8), 671–684 (1944)
10. Rolander, N., Rambo, J., Joshi, Y., Allen, J.K., Mistree, F.: An approach to robust design of turbulent convective systems. ASME J. Mech. Des. **128**(4), 844–855 (2006)

Performance Analysis of Cross-Flow Turbine: Variation in Shaft Diameter

Virendra Kumar Yadav and S.K. Singal

Abstract Presently, the major contribution in energy generation comes from conventional sources. Micro-hydropower is found to be a promising source of the future for rural electrification which can be economical and ecologically acceptable where conventional turbines are neither economical nor ecologically undisputed and cross-flow turbine is found most suitable. Many studies have been done in the past for different parameters in cross-flow turbine. Efficiency of turbine was found to be in lower range. In present study, CFD analysis is done for performance analysis of cross-flow turbine with variation in shaft diameter. From the results, it is found that on decreasing the diameter of shaft, pressure is found to be decreasing at the nozzle inlet. Maximum power output is obtained when the shaft diameter approaches zero value. Hydraulic efficiency of cross-flow turbine is found to be inversely proportional to shaft diameter. The increase in the value of hydraulic efficiency is about 5% when there is no shaft present as compared to the case when there is shaft of diameter 50 mm inside the runner.

Keywords Cross-flow turbine · Efficiency · Shaft diameter · CFD · Power output

1 Introduction

Energy is a vital component of the life of every human being. Be it cooking food, heating a house, lighting a street, running a factory; everything requires energy. Energy influences one's quality of life and economic competitiveness. Global population and energy demand grow hand in hand. Consequently, energy crisis is being faced by every part of the country. Presently major share is contributed by fossil fuel-based energy systems which not only affect the environment adversely but also lay a huge financial burden on the government as they rely heavily on import from other countries; therefore, focus should be shifted toward harnessing

V.K. Yadav (✉) · S.K. Singal
Alternate Hydro Energy Center, Indian Institute of Technology, Roorkee, India
e-mail: virendrayadav09@gmail.com

V. Garg et al. (eds.), *Development of Water Resources in India*,
Water Science and Technology Library 75, DOI 10.1007/978-3-319-55125-8_42

more renewable energy sources such as solar, wind, biomass and small hydro. Small hydropower is well-proven technology, and potential is available on small streams as well as big rivers. Small capacity project up to 100 kW in micro-hydrorange can also be useful for rural electrification in the remote areas. Among type of turbines, cross-flow turbine is found suitable in micro-hydrorange. It is seen that the maximum efficiency of the cross-flow turbine having different combination of flow and head increases with the increase in the nozzle entry arc or decrease in the aspect ratio for turbine runner [1]. From the study of previous work experimentally conducted on the physical model of simplified cross-flow turbine, the optimum efficiency obtained was more than 70% for given conditions of 5 m head and 80% valve opening, with speed variations from 10 to 18 [2]. To study the effect on efficiency with variations in the ratio of runner diameter and gate opening for two dissimilar turbine nozzles operating under different heads, investigation was made experimentally. The highest efficiency obtained was 72% for the runner with a diameter ratio of 0.67 [3]. A cross-flow turbine is developed to optimize the efficiency and shaft fatigue life of a cross-flow turbine for micro-hydropower. The priority of hydraulic efficiency and shaft fatigue life was altered by defining different objective functions in the optimization process. In one of the cases, comparison of initial and optimal turbine showed a hydraulic efficiency improvement of 10.14% and relative shaft FOS improvement of 4.86% [4]. In the present study, performance analysis of cross-flow turbine was performed with variation in the shaft diameter by computational flow dynamics (CFD) analysis.

2 Cross-Flow Turbine

Cross-flow turbine is known as Ossberger or Banki-Michell turbine and developed by the German Fritz Ossberger, Australian Anthony Michell and Hungarian Donat Banki. Patent was obtained by Mihell for his turbine design in 1903. Ossberger manufactured the turbine as a standard product, which was granted first patent by him in 1922. In cross-flow turbine, water passes across the turbine blades, whereas in other turbines, water flows axially or radially over the turbine blades. In case of waterwheel, water is admitted at its edge. Water leaves turbine runner at opposite side from entrance after passing through the runner. Additional efficiency was provided by the turbine, when water passes in both stages of runner. The nozzle of cross-flow turbine is simple in construction, and it is low-speed machine. It is designed in such a way that water does not get deflected via turbine shaft [5–7].

3 Methodology

Typical site data are considered with design head as 10 m, design discharge 65 l/s and rotational speed 375 rpm. The steps for sizing cross-flow turbine are given below, and the design parameters of the cross-flow turbine are given in Table 1:

Table 1 Sizing of cross-flow turbine

S. no.	Parameter	Value
1	Outer runner diameter	338 mm
2	Inner runner diameter	224 mm
3	Runner width	64 mm
4	No. of blades	24
5	Shaft diameter	50 mm

(i) Find out the outer diameter (d1) and inner diameter (d2) of turbine runner.
(ii) Design of profile of nozzle.
(iii) Design blade profile.
(iv) Find out runner width.

Using the data determined in Table 1, model is constructed using workbench 15 and analysis is performed with Workbench 15 under ANSYS software. The numerical analysis procedure involves the following steps:

(i) Problem formulation.
(ii) Model the geometry and flow domain.
(iii) Grid generation.
(iv) Establish the boundary conditions.
(v) Establish the simulation strategy.
(vi) Perform the simulation and monitor the simulation for completion.

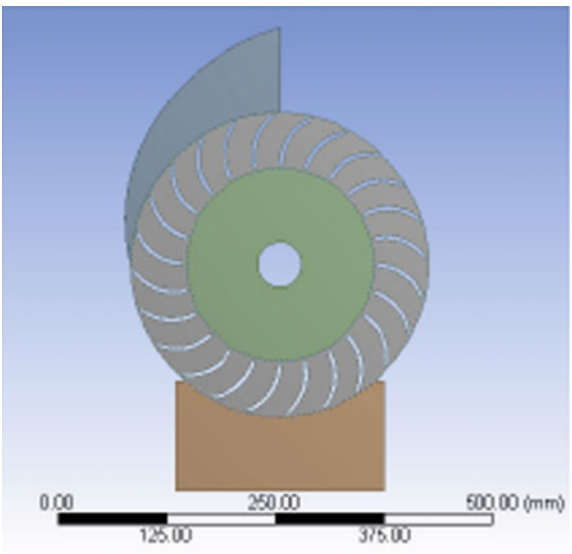

Fig. 1 3D model of cross-flow turbine

vii) Post-process the simulation to get the results and make comparisons of the results.

CFD is fundamentally based on the governing equations of fluid dynamics, which represent the mathematical statement of the conservation laws of physics such as conservation of mass, conservation of momentum and conservation of energy. Figure 1 shows the model of turbine as developed by using above methodology where unstructured meshing is done. Further, meshed models of all

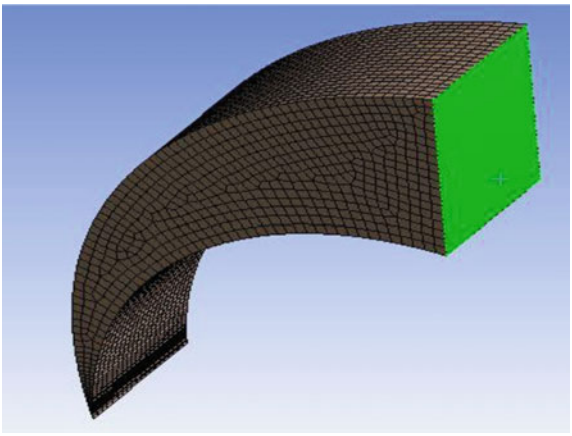

Fig. 2 Nozzle with inlet

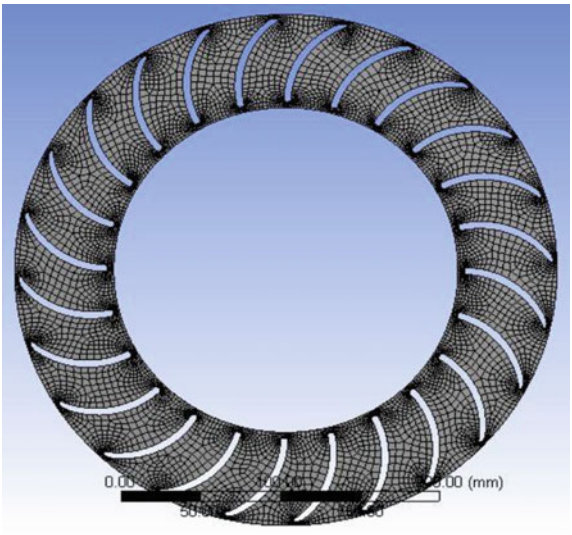

Fig. 3 Runner

the components of cross-flow turbine were developed and are shown in Figs. 2, 3, 4 and 5. The value of nodes and elements formed in the mesh for cross-flow the turbine are given in Table 2.

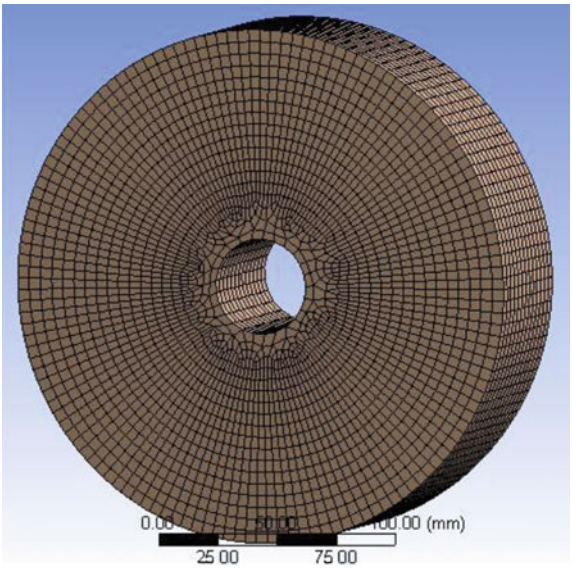

Fig. 4 Solid body

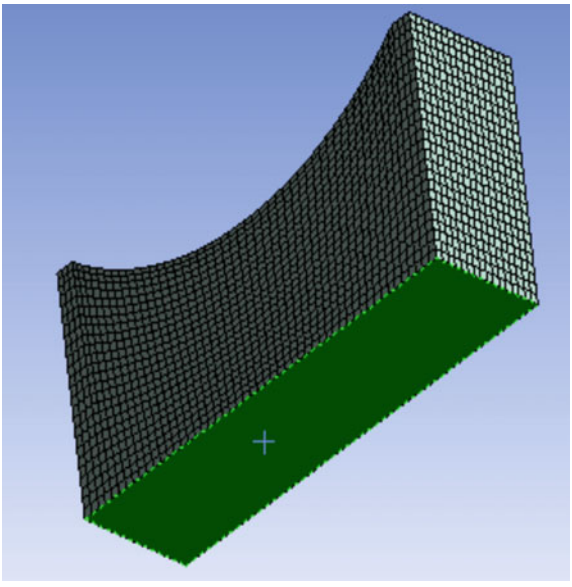

Fig. 5 Channel with outlet

Table 2 Value of nodes and elements formed in the mesh for cross-flow turbine

Shaft dia. (mm)	Runner		Nozzle		Channel		Solid body		All domains	
	Nodes	Elements	Nodes	Elements	Nodes	Elements	Nodes	Elements	Nodes	Elements
50	1172192	1015428	15687	13120	22984	20400	31780	28418	1242643	1077366
40	1172192	1015428	15687	13120	22984	20400	34104	30615	1244967	1079563
30	1172192	1015428	15687	13120	22984	20400	35294	31798	1246157	1080746
20	1172192	1015428	15687	13120	22984	20400	30315	27272	1241178	1076220
10	1172192	1015428	15687	13120	22984	20400	34224	30990	1245087	1079938
0	1172192	1015428	15687	13120	22984	20400	34230	30888	1245093	1079836

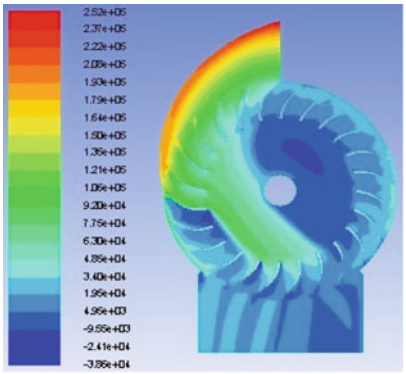

Shaft diameter 50 mm

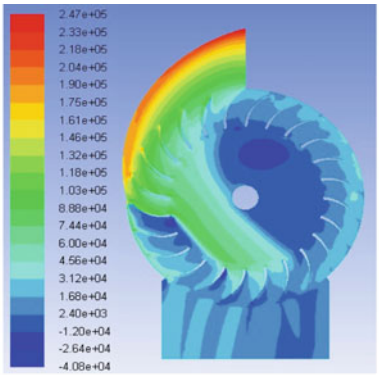

Shaft diameter 40 mm

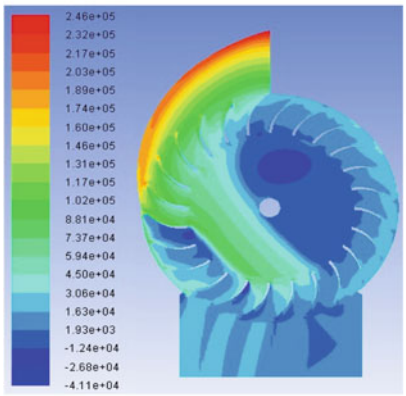

Shaft diameter 30 mm

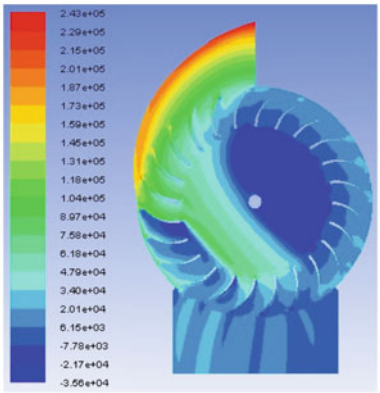

Shaft diameter 20 mm

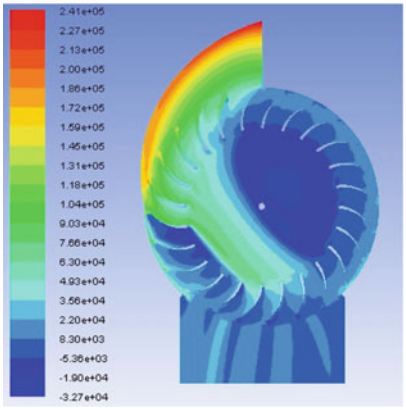

Shaft diameter 10 mm

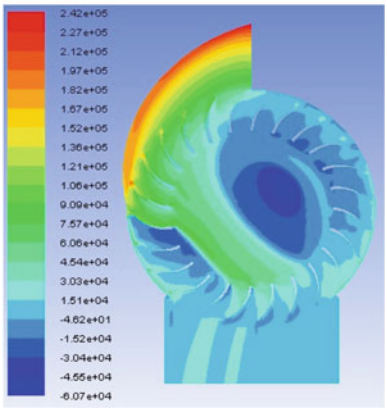

Shaft diameter 0 mm

Fig. 6 Pressure distribution at different shaft diameters of turbine

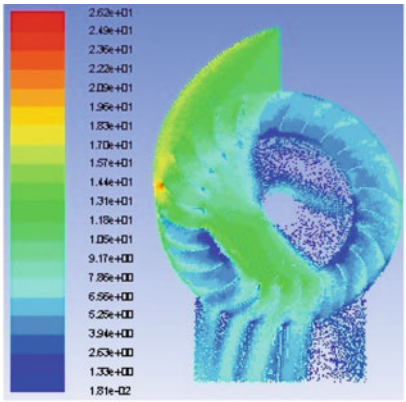

Shaft diameter 50 mm

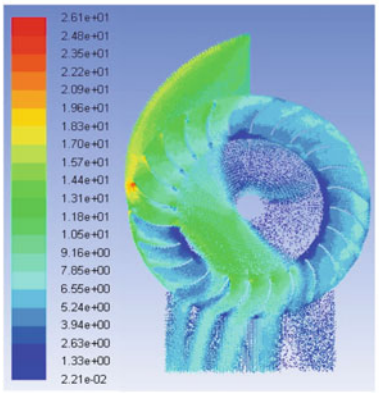

Shaft diameter 40 mm

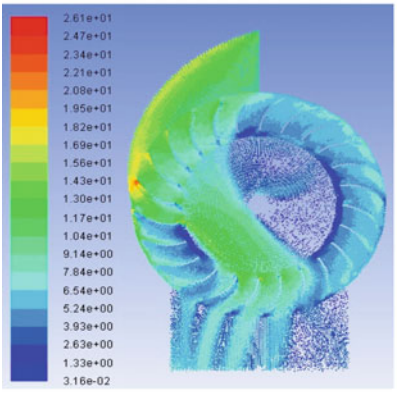

Shaft diameter 30 mm

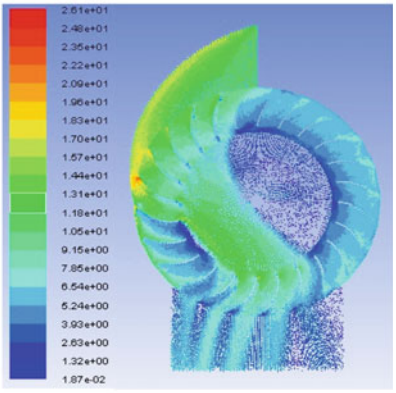

Shaft diameter 20 mm

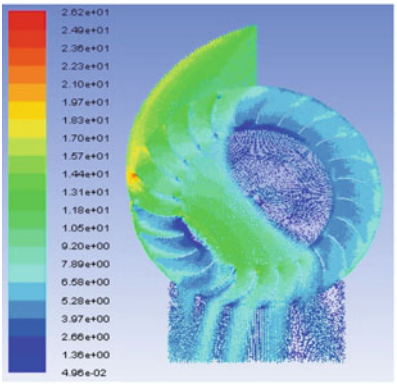

Shaft diameter 10 mm

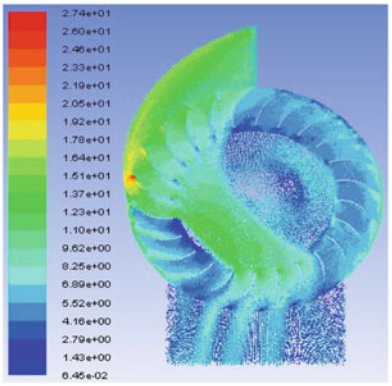

Shaft diameter 0 mm

Fig. 7 Velocity distribution at different shaft diameters of turbine

4 Results and Discussion

In order to predict the effect of variation in shaft diameter on the performance of a cross-flow turbine, CFD analysis has been carried out. The performance has been evaluated by studying the variations in pressure, power output and turbine efficiency. The variation in these parameters has been observed at design conditions for the turbine model considered in the study.

The pressure contours of the turbine for varying shaft diameter are shown in Fig. 6. Figure 6 shows that the value of the pressure does not remain constant at all parts of the turbine.

The velocity contours of the turbine for varying shaft diameter are shown in Fig. 7. Figure 7 shows that the value of the velocity does not remain constant at all parts of the turbine.

Figure 8 shows the variation of inlet pressure with shaft diameter. Inlet pressure is used to determine the net head working at the turbine runner.

The power output of the turbine under different shaft diameters has been worked out as shown in Fig. 9.

Figure 10 shows the variation of turbine efficiency with variation in shaft diameter. It has been found that the efficiency of turbine increases with the decrease in shaft diameter. In this study, shaft diameter within the runner is taken in decreasing order from 50 mm to zero mm, which shows that the value of efficiency increases with the decrease in shaft diameter.

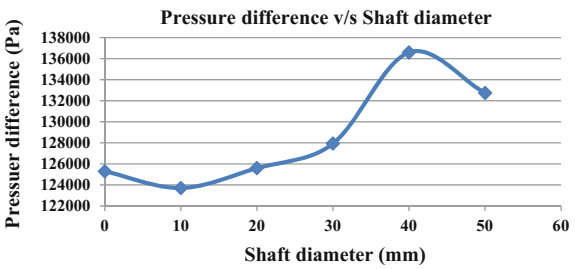

Fig. 8 Variation of pressure difference with shaft diameter

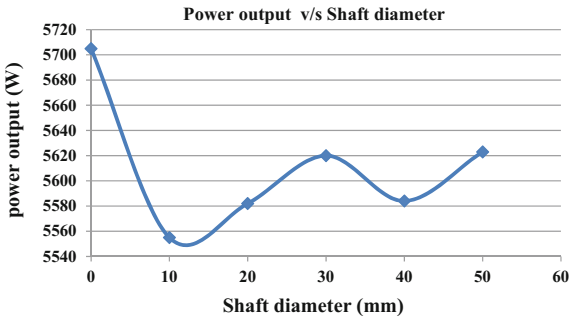

Fig. 9 Variation of power output with shaft diameter

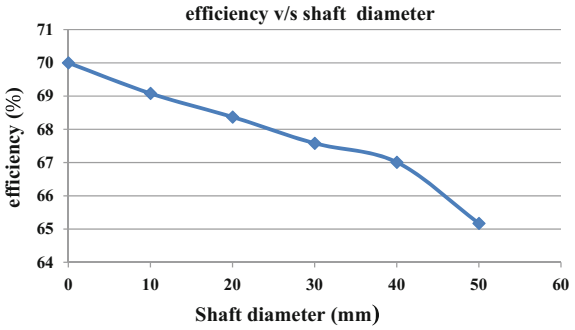

Fig. 10 Variation of efficiency with shaft diameter

Using the data shown in Fig. 10, a quadratic co-relation is developed from the results between efficiency and shaft diameter of cross-flow turbine as given below. This correlation has the value of R^2 as 0.9785, thus having a good agreement.

$$\eta = -0.0007d^2 - 0.0529d + 69.853 \quad (1)$$

where

η efficiency of cross-flow turbine
d shaft diameter

5 Conclusions

In the present study, 3-D models of cross-flow turbine were prepared with variation in shaft diameter inside runner and analyzed using FLUENT software. The turbine has been designed for a design head of 10 m and design discharge of 65 lps. The simulations have been carried out using the k-turbulence model. From the analysis, it is observed that maximum output power is obtained when the shaft diameter approaches zero value or in other words when there is no shaft. The hydraulic efficiency of cross-flow turbine is found inversely proportional to variation in the shaft diameter. The increase in the value of hydraulic efficiency is found about 5% when there is no shaft present as compared to the case when there is shaft of diameter 50 mm inside the runner. A co-relation of the efficiency with the shaft diameter is also determined by using the results of the study of cross-flow turbine through CFD and can be useful for further research work and commercial installations.

References

1. Khosrowpanah, S., Fluzat, A.A., Member, ASCE, Albertson, M.L.: Experimental study of cross-flow turbine **114**(3), 299–314 (1988)
2. Kaunda, C.S., Kimambo, C.Z., Nielsen, T.K.: Experimental study on a simplified crossflow turbine. Int. Energy Environ. Found. **5**(2), 155–182 (2014)
3. Olgun, H.: Investigation of the performance of a cross-flow turbine. Int. J. Energy Res. **22**(11), 953–964 (1998)
4. Reihani, A., Ojaghi, A., Derakhshan, S., Beigzadeh, B.: Shaft fatigue life and efficiency improvement of a micro cross flow turbine. Eng. Solid Mech. **2**(1), 1–14 (2014)
5. Haurissa, J., Wahyudi, S., Irawan, Y.S., Soenoko, R.: The cross flow turbine behavior towards the turbine rotation quality, efficiency, and generated power. J. Appl. Sci. Res. **8**(1), 448–453 (2012)
6. De Andrade, J., Curiel, C., Kenyery, F., Anguillón, O., Vásquez, A., Asuaje, M.: Numerical investigation of the internal flow in a bamki turbine. Int. J. Rotating Mach. (2011)
7. Fukutomi, J., Nakase, Y., Ichimiya, M., Ebisu, H.: Unsteady fluid forces on a blade in a cross-flow turbine. JSME Int. J. B **38**(3), 404–410 (1995)

Hydropower Sites Investigation and Sensitivity Analysis of Assessed Potential Using Geospatial Inputs

Pramod Kumar, Suraj Kunwar and Vikas Garg

Abstract Hydroelectric power (HEP) sites in Balephi River valley, Nepal, were identified using remote sensing and ancillary data. Historical discharge data were used to identify 50% (2004–05) and 90% (2003–04) dependable years. Temporal snow cover, temperature and precipitation for dependable years were assessed using MODIS snow cover, LST and NOAA-CPC data, respectively. Snowmelt runoff model was used to estimate discharge with Nash–Sutcliffe model efficiency coefficient obtained as 0.86 and 0.89 for 50% and 90% dependable years, respectively. While combining design discharge corresponding to 50th percentile flow with hydraulic head determined from digital elevation model, the power potential was computed for dependable years. Five HEP sites were identified with power potential varying from 7.49 to 13.48 MW (50% dependable year) and 4.81 to 8.37 MW (90% dependable year). Sensitivity analysis of assessed potential was analyzed, and up to 31% variation in discharge and consequent changes in power potential were observed.

Keywords Hydropower · DEM · Geospatial · Cartosat-1 · Snowmelt runoff

1 Introduction

Hydroelectric power (HEP) systems produce electrical energy from the potential and kinetic energy of water in rivers and streams. This renewable source is one of the clean energy options without causing any air pollution and depletion of fossil

P. Kumar (✉)
Indian Institute of Remote Sensing, Kalidas Road, Dehradun, India
e-mail: pramodvaish@gmail.com

S. Kunwar
Pancheshwar Multipurpose Project, Kathmandu, Nepal
e-mail: surajlink@gmail.com

V. Garg
University of Petroleum and Energy Studies, Dehradun, India
e-mail: gargvikas27@gmail.com

V. Garg et al. (eds.), *Development of Water Resources in India*,
Water Science and Technology Library 75, DOI 10.1007/978-3-319-55125-8_43

fuels. HEP projects have long lives, offering stable product cost, low operating cost, and provide spin-off advantages in the form of irrigation, recreation and flood control. Perennial inflow of water and suitable location providing sufficient head are the primary factors for a potential HEP scheme. These must be complemented with favourable geological, environmental and socio-economic parameters. A landlocked country, Nepal, is blessed with snow-capped mountains and glaciers in Himalayas. The perennial nature of Nepalese rivers and steep gradient of country's topography provide ideal conditions for hydropower development [27]. Although, Nepal has 225 billion cubic metres (BCM) of water available annually, only a small part of it, estimated at 15 BCM, has been so far utilized for economic and social purposes [28]. Using satellite imagery, information about Land Use/Land Cover (LULC), river morphology and geology can be easily prepared as compared to conventional means of field survey and can be utilized for HEP sites suitability analysis. Digital elevation models (DEMs) have many applications in HEP site suitability analysis as they can be used to assess hydraulic head, delineate the catchment area and derive topographic characteristics and water conveyance path from diversion to power house. The present study has been carried out in Balephi River, Nepal with the following objectives: (i) HEP sites suitability analysis based on drainage, topography, geology and LULC, (ii) hydraulic head, discharge and power potential assessment for identified HEP sites and (iii) sensitivity analysis of hydropower potential due to changes in hydro-meteorological parameters.

Hydropower sites investigations using geospatial data and tools have been attempted in USA, using geographic information system (GIS)-based proximity analysis, and the information on small hydropower potential (<1 MW) was made available in public domain [10]. Punys et al. [24] compared several software tools for the planning and design of small hydropower plants (SHP). Jorgensen et al. [15] carried out GIS-based study to determine the quantity and size of potential HEP sites within a sample county in USA using property ownership and boundaries, elevation, stream locations and federal and state protected areas. Preliminary HEP sites assessment in a Brazilian river catchment has been carried out using a DEM along with river flow data [17]. Rojanamon et al. [25] proposed a combination of engineering, economic and environmental criteria, as well as social impact analysis in the upper Nan River Basin, north of Thailand, to select small run-of-river HEP projects using GIS technology. A preliminary assessment of HEP potential in South Africa was undertaken by estimating actual energy potential calculated using digital slope and runoff data [4]. The HEP potential at a regional scale in France was attempted by combining hydrologic and hydrographic characteristics of sub-basins and rainfall maps [5]. Rapid hydropower assessment model (RHAM) was developed using GIS to identify over 8,000 potential HEP sites in the Province of British Columbia, Canada [20]. Alterach et al. [1] proposed a methodology to evaluate the residual hydropower potential in Italy, taking into account the current uses (such as irrigation and drinking water) with a numerical technique coupled with GIS. However, only a few studies have been carried out on remote sensing and GIS-based HEP site suitability analysis and potential assessment in Nepal. Pathak [22] described the importance of GIS and remote sensing to make hydropower

development environment-friendly and to create less impact upon rural livelihood in Nepal. He also described the hydro-climatic variability and its uncertainty for hydropower development, and the mitigation of uncertainties for sustained hydropower production in Nepal. Prajapati [23] assessed the run-of-river HEP potential of Karnali Basin in Nepal using GIS and continuous semi-distributed hydrological model, Hydrological Modeling System (HMS), but the study did not consider HEP site characteristics evaluation (based on geology, LULC, etc.) and sensitivity analysis of assessed potential. As the temporal snow cover in Nepal varies from 7 to 33% of the total area [2], studies on snowmelt runoff model (SRM)-based discharge prediction for prospecting HEP schemes are required for snowfed valleys [21].

2 Study Area

Balephi River is located in Sindhupalchowk District of Bagmati Zone in the Central Development Region of Nepal. Geographically, the project area is located between 27°43′N to 28°12′N latitude and from 85°41′E to 85°54′E longitude (Fig. 1). Balephi is a snowfed and perennial river, which originates from Jugal Mountain of the great Himalayan range of Nepal with a catchment area of 689 km^2. The catchment boundary has been delineated using ASTER Global Digital Elevation

Fig. 1 Location map of Dangri River watershed

Model (GDEM) up to the confluence of Balephi River with Sunkoshi River. The elevation ranges from 777 to 6938 m in Balephi catchment. Its catchment has more than 50% area under snow cover at the beginning of melt season that contributes to good perennial inflow even during dry season. The monsoon causes major annual precipitation over the region and in the catchment. The average melt duration in the Eastern Himalayas starts from early May and continues up to mid-October. The low flow period starts from November and continues till April. The Jalbire Gauge and Discharge (G&D) site is located approximately 10 km upstream of the confluence point of Balephi River. Therefore, SRM calibration was done for catchment area up to Jalbire G&D site, but for HEP sites investigation, the catchment boundary was extended up to the confluence of Balephi River with Sunkoshi River.

3 Materials and Methods

3.1 Data Collection

In the present study, the following data have been used: (i) ASTER GDEM (ASTGDEMV2_0N27E085 & ASTGDEMV2_0N28E085) with 1 arc-second spatial resolution prepared using data acquired from the beginning of observation until the end of August 2010, (ii) Cartosat-1 stereo data (Path/Row: 570/268 and 570/269 acquired on 25 December 2010), (iii) MODIS snow cover (MOD10A2, 500 m spatial resolution, 8-day temporal resolution for the period June 2003 to May 2005), (iv) MODIS Land Surface Temperature (LST) (MOD11A1, $\sim$1 km spatial resolution, daily for the period June 2003 to May 2005), (v) CPC precipitation data (daily, 0.5 $\times$ 0.5 degree spatial resolution) for the period June 2003 to May 2005 and (vi) Landsat ETM+ (L1T, LE71410412003063SGS00, acquired on 4 March 2003, Path/Row:141/41 with 30 m spatial resolution.

ASTER GDEM and Landsat ETM+ data have been downloaded from the U.S. Geological Survey (USGS) Earth Resources Observation and Science (EROS) Center archive's website EarthExplorer (http://earthexplorer.usgs.gov/). MODIS data have been downloaded from NASA's website (http://reverb.echo.nasa.gov/reverb/). Global precipitation data have been downloaded from NOAA's Climate Prediction Center GIS Portal (ftp://ftp.cpc.ncep.noaa.gov/GIS/GRADS_GIS/GeoTIFF/GLB_DLY_PREC/DLY-HISTORICAL/). Cartosat-1 stereo data have been obtained from National Remote Sensing Centre, India. Following ancillary data have been used in the present study: (i) Hydro-meteorological data, i.e. daily discharge data of Balephi River at Jalbire G&D site and temperature data for Jalbire, and other stations outside Balephi catchment were purchased from Department of Hydrology and Meteorology, Nepal, (ii) Detailed geological map for the study area was procured from Department of Mines and Geology, Govt. of Nepal and (iii) Topographical maps from Department of Survey, Nepal (scale 1: 50,000/1:25,000).

3.2 DEM Generation

Cartosat-1 stereo data are supplied as ortho kit that enables view geometry in the form of rational polynomial coefficients (RPCs). RPCs define the relationship between normalized pixel coordinates (l_N and s_N) and normalized ground coordinates (φ_N, λ_N and h_N), where h_N is normalized height above the ellipsoid and usually given with respect to world geodetic system (WGS84) as defined below [8, 9]:

$$l_N = Num_l(\varphi_N, \lambda_N, h_N)/Den_l(\varphi_N, \lambda_N, h_N) \quad (1)$$

$$s_N = \frac{Num_s(\varphi_N, \lambda_N, h_N)}{Den_s(\varphi_N, \lambda_N, h_N)} \quad (2)$$

where Num_l, Den_l, Num_s and Den_s are third-order polynomials in lieu of sensor and satellite parameters. The RPC-based stereo model has systematic offsets, which influences its accuracy for location determination [8, 9]. The accuracy of the RPC-based stereo model can be further improved by using control points. In this study, after setting up project definition, interior and exterior orientations were performed using Leica Photogrammetry Suite (LPS) based on RPC information provided in Cartosat-1 stereo ortho kit and control points. Triangulation was performed with control points to check model accuracies at all the tie points. The information resulting from triangulation was used as input for DEM generation and ortho-rectification.

Sahu et al. [26] have used the control points collected from Google Earth image to georeference Cartosat-1 stereo data at 2.5 m resolution. The DEM was generated using LPS at 10 m resolution to extract terrain parameters such as elevation, slope, aspect, hill shade and drainage. Widhalm et al. [29] carried out local scale photogrammetric processing of ALOS-Prism triplets at ground sampling distance of 2.5 m using LPS for surface point extraction. Google Earth images were used to derive longitude and latitude, and DEM available at 100 m resolution was used to obtain heights of control points. In the present study, the hydraulic head measurement, i.e. the elevation difference between diversion and power house site, has been carried out through stereoscopic visualization of HEP sites using Terrain Editor (TE) module of LPS. Therefore, Cartosat-1 stereo data were used to generate the 3D stereo model. The control points for generating stereo model were obtained from high-resolution Google Earth images (longitude and latitude) and ASTER GDEM for point heights. The control and checkpoints were well distributed throughout the image at different altitudes.

3.3 Land Use/Land Cover (LULC)

The HEP sites investigation needs LULC information to understand its feasibility in terms of areas affected, especially the loss of agricultural or forest land and the cost

for the rehabilitation of affected population. Satellite remote sensing data are extremely helpful in carrying out LULC mapping due to their explicit manifestation on images. In the present study, Landsat Enhanced Thematic Mapper+ (ETM+) data have been used to delineate LULC classes by following Iterative Self-Organizing Data Analysis Technique (ISODATA) clustering algorithm. Using ISODATA classifier, the initial number of cluster was fixed as 50 and unsupervised classification was carried out. During post-processing of classified data, the clusters labelling was attempted and 10 major LULC classes were identified. The output LULC map was later verified using ground truth information and also using high-resolution Google Earth images. The stratified random sampling design was adopted for the accurate assessment, and sample points were collected based on multinomial probability theory. With an expected accuracy of 85% and an allowable error of 5%, 204 sample points are required for a 95% two-sided confidence probability [7]. The sample points collected were used to prepare error matrix and to estimate map accuracy and kappa statistic.

3.4 Geology

The geological studies of potential HEP sites are essential to ensure that the location, design, structural safety and stability are adequate. In reservoir projects, the water-tightness of submergence area and geological stability of dam site are accounted by geological investigation. Zaruba and Mencl [31] have defined the following factors from geological and geomorphological point of view in selecting a HEP site: (i) dam sites are chosen in constricted parts of the valleys with steep rocky slopes, (ii) dam site is structurally, lithologically and tectonically sound, (iii) nature and depth of overburden to suitable foundation bed are conducive, (iv) slopes above crest of dam must be stable as excavations for abutments and floor may disturb the equilibrium, (v) availability of suitable construction material, (vi) reservoir area is water tight and (vii) reservoir area has stable valley banks, and siltation is minimum in the reservoir. In the present study, the geological map procured from Department of Mines and Geology, Govt. of Nepal and the topographical maps procured from Department of Survey, Nepal (scale 1:50,000/1:25,000) were scanned, georeferenced and used for the HEP sites characterization.

3.5 Snowmelt Runoff Model

Using energy-budget method, the snowmelt is estimated by calculating the available heat flux to snow pack from radiative, latent, sensible, precipitation and geothermal heat transfer. Magnusson et al. [18] have evaluated the numerous

energy balance models. Temperature index or degree-day models, on the other hand, rest upon a relationship between snow or ice melts and air temperature. Since air temperature generally is most readily available data, such models have been most widely used for ice and snowmelt computations, ice dynamic modelling or climate sensitivity studies. The temperature index models have proven to be powerful tools for melt modelling, often on a catchment scale outperforming energy balance models due to their simplicity [12]. SRM is a temperature index model which was originally developed by Martinec [19] to simulate and forecast daily stream flow in mountain basins, where snowmelt is a major runoff factor. The model has been applied and performed very well in over 100 basins in 29 different countries. The water produced from snowmelt and rainfall is computed as given in Eq. (3):

$$Q_{n+1} = [C_{sn} a_n (T_n + \Delta T_n) S_n + C_{Rn} P_n] \frac{A \cdot 10,000}{86,400} (1 - K_{n+1}) + Q_n K_{n+1} \quad (3)$$

where Q = average daily discharge (m^3/s), C = runoff coefficient expressing losses as a ratio (runoff/precipitation) with C_S referring to snowmelt and C_R to rain, a = degree-day factor (cm/°C/d) indicating snowmelt depth resulting from 1 degree day, T = number of degree days (°C d), ΔT = adjustment by temperature lapse rate when extrapolating temperature from the station to average hypsometric elevation of the basin or zone (°C d), S = ratio of snow covered area to total area, P = precipitation contributing to runoff (cm), T_{CRIT} determines whether this contribution is rainfall or snow, A = area of the basin or zone (km^2), k = recession coefficient indicating decline of discharge without snowmelt or rainfall, where $k = Q_{m+1}/Q_m$ (m, m + 1 are the sequence of days during a true recession flow period). The adjustment ΔT (°C d) for temperature lapse rate was computed from the base station elevation to the hypsometric mean elevations of each elevation zone using the relationship given in Eq. (4):

$$\Delta T = \gamma(h_{st} - h) \frac{1}{100} \quad (4)$$

where γ = temperature lapse rate (°C per 100 m), h_{st} = altitude of temperature station (m) and h = hypsometric mean elevation of a zone (m).

The model parameters and value of coefficients were obtained as follows: (i) MODIS snow cover for the dependable years was used for Snow Cover Area (SCA) estimation, (ii) MODIS LST data were used to assess mean temperature for each elevation zone, (iii) NOAA-CPC has been used to assess mean precipitation for each elevation zone, (iv) Runoff coefficient values have been iteratively obtained as 0.15–0.9 (C_s) and 0.1–0.9 (C_r) for 50% dependable year (2004–05), whereas for 90% dependable year (2003–04), both coefficients have been estimated to vary from 0.1 to 0.9. Degree-day factor converts the number of degree days, T (°C d), into daily snowmelt. Iteratively, its value was observed to vary from 0.3 to 0.7 °C/day for 50% dependable year (2004–05) and from 0.2 to 0.8 °C/day for 90% dependable year

(2003–04), (vi) The temperature lapse rate indicates the change in temperature with respect to change in altitude. In the present study, variable lapse rate has been used and observed to vary from 0.01 to 1.14 for 90% dependable year (2003–04) and from 0.03 to 1.21 for 50% dependable year (2004–05), (vii) The critical temperature determines whether the measured or forecasted precipitation is rain or snow. In this study, 0 °C has been assumed to be critical temperature for both dependable years, (viii) Recession coefficient (k) values have been obtained by using historical discharge data, and Q_n and Q_{n+1} were plotted against each other where the lower envelope line of all points is considered to indicate the k-values. Accordingly, $K_{n+1} = x \cdot Q_n - Y$ was solved to obtain the value of constants x and y. The value of constants was estimated as x = 0.7511 and y = 0.011 for 50% dependable year and x = 0.7418 and y = 0.015 for 90% dependable year, (ix) Time lag expresses the time taken by snowmelt runoff or direct runoff to reach the gauging station. As there was lack of hourly hydrological data, the actual lag time could not be calculated. Therefore, an average lag time of 6 h was assumed for this study, and (xi) Rainfall contributing area is a parameter used in SRM to determine whether runoff is added to snowmelt runoff only from snow-free area (option 0) or from entire basin or zone area (option l). In this study, a threshold of 0.1 mm was chosen, the value less than threshold considered as 0 and the value more than it as 1.

3.5.1 Model Validation

The SRM model is validated using two well-established accuracy criteria namely the coefficient of determination, R^2 (or, the Nash–Sutcliffe model efficiency coefficient), and the volume difference, D_v [19]. The coefficient of determination is computed as shown in Eq. (5):

$$R^2 = 1 - \frac{\sum_{i=1}^{n}(Q_i - Q_i')^2}{\sum_{i=1}^{n}(Q_i - \bar{Q})^2} \tag{5}$$

where Q_i is the measured daily discharge, Q_i' is the computed daily discharge, $\bar{Q}(Q)$ is the average measured discharge of the given year or snowmelt season and n is the number of daily discharge value [19]. The deviation of runoff volumes, D_v is computed as given in Eq. (6):

$$D_v(\%) = \frac{V_R - V_{R'}}{V_R} * 100 \tag{6}$$

where V_R is the measured yearly or seasonal runoff volume and V_R' is the computed yearly or seasonal runoff volume.

3.6 HEP Sites Identification

The HEP site analysis requires information on drainage, topography, hydrology, geology (lithology and structure), LULC characteristics, etc. The power potential estimates of HEP sites are directly dependent on hydraulic gradient and discharge of river, and they are also considered as the critical factor in sites suitability analysis. Figure 2 shows the methodology for identifying HEP sites, and Fig. 3 shows the methodology for estimating discharge at HEP sites. The base map for Balephi river catchment was prepared using ortho-rectified Cartosat-1 data and topographical maps. ASTER GDEM data were used for the delineation of watershed and sub-watersheds boundaries of the identified HEP sites using ArcSWAT model. The decision rules as mentioned by Zaruba and Mencl [31] were used for the HEP sites suitability analysis using DEM, theme maps and ancillary data. The potential HEP sites were overlaid on LULC and geological (lithology and geological structure) layers to analyze their characteristics. Time series analysis of 12-year daily discharge data of Balephi River was carried out to identify 50 and 90% dependable years following Weibull's distribution. MODIS snow cover and temperature data were downloaded for these years. The SRM model used in the present study requires elevation zone-wise input parameters; therefore, ASTER GDEM was also used to divide the catchment into 12 elevation zones of about 500 m each. MODIS LST data were analyzed to derive elevation zone-wise mean temperature and CPC precipitation data for mean precipitation. These parameters were used in SRM to estimate discharge for 50% and 90% dependable years for identified HEP sites. Ten percentage of total flow has been considered as environment release at each scheme. While combining the design discharge corresponding to 50th percentile flow with the gross hydraulic head determined from

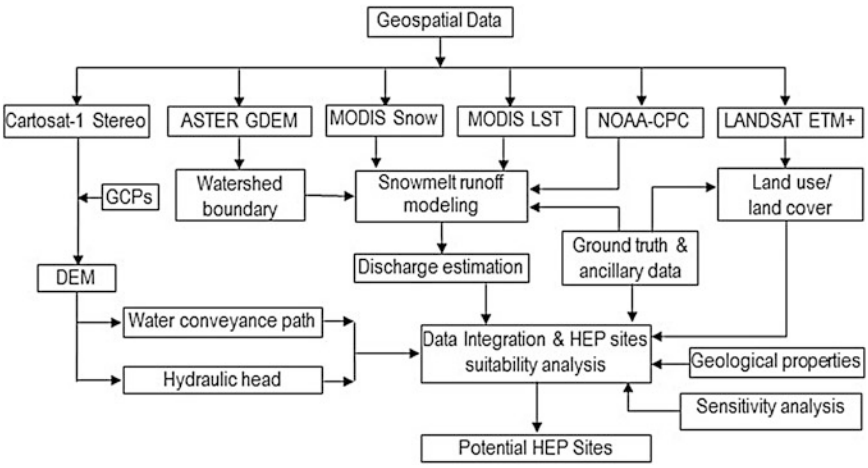

Fig. 2 Methodology for identifying potential hydropower sites

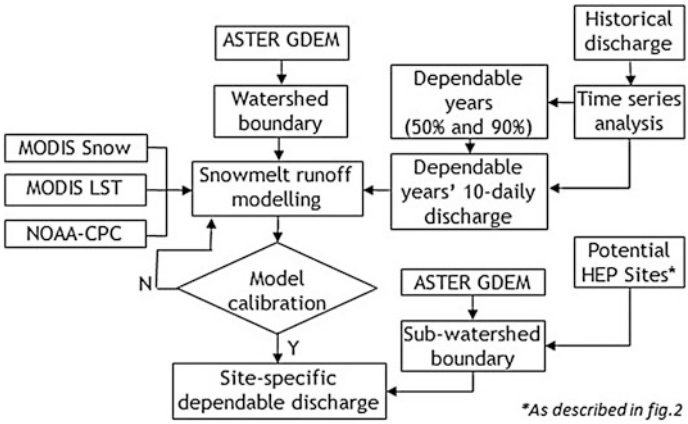

Fig. 3 Methodology for estimating discharge at potential hydropower sites

DEM, the power potential was determined for each dependable year. Sensitivity analysis of design discharge by varying temperature and precipitation was carried out for each identified HEP site. Cartosat-1 stereo model was used to determine the hydraulic head available between each pair of diversion and power sites through stereoscopic visualization. DEM derived from Cartosat-1 stereo data was also used to identify the water conveyance path based on longitudinal profile drawn between diversion and the penstock inlet.

3.7 Power Potential

The hydropower potential is estimated using dependable inflows and the hydraulic head. The design consideration for determining power potential is as follows: (i) Net head is considered as 90% of gross head which is common practice in Nepal for power potential assessment at pre-feasibility level, (ii) Efficiency considered for turbines, generators and transmission is 90%, 95% and 98%, respectively, which yields to overall efficiency of 84%, (iii) Downstream release of 10% is considered for environmental consideration and (iv) 10% seasonal outage is considered for both dry and wet period [6]. The power potential of HEP sites has been estimated as given in Eq. (7):

$$P_e = r \cdot g \cdot h \cdot Q \cdot \eta \tag{7}$$

where P_e is electric power output (kW), r is density of water (1000 kg/m^3), g is acceleration due to gravity (9.81 m/s^2), h is water head (m), Q is volumetric flow rate (m^3/s) and η is turbine-generator conversion efficiency (%) [6].

3.8 Sensitivity Analysis

Climate variability and global climate change have brought significant impact on the high mountainous glacial environment [3, 30]. Continued greenhouse gas emissions at or above current rates would cause further warming and induce many changes in the global climate system during the twenty-first century that would very likely be larger than those observed during the twentieth century. Thus, it is necessary to look into the sensitivity of the reserve and glacier mass balance to climate warming. Hong and Guodong [13] used SRM for the Gongnaisi River Basin in the western Tianshan Mountains, and a comparison was made between snowmelt runoff hydrographs under present and future climatic conditions. In their study, the SRM was proven to be ideal method in data-scarce regions, particularly in remote and inaccessible high mountain watersheds in arid areas. HEP generation in the Upper Danube Basin was modelled for two future decades (2021–2030 and 2051–2060) by Koch et al. [16] using a special hydropower module coupled with the physically based hydrological model PROMET. To cover a possible range of uncertainties, 16 climate scenarios were taken as meteorological drivers which were defined from different ensemble outputs of a stochastic climate generator, based on the IPCC-SRES-A1B emission scenario (2007) and four regional climate trends [14]. Depending on the trends, the results showed a slight to severe decline in HEP generation. While the mean summer values indicated a decrease, the mean winter values displayed an increase. Hamududu and Killingtveit [11] studied the climate change impacts on global hydropower. They predicted that globally hydropower generation shall change very little by the year 2050 as compared to hydropower system in operation today. This change amounts to an increase of less than 1% of the current (2005) generation level although it is necessary to carry out basin level detailed assessment for local impacts which may differ from the country-based values.

In the present study, sensitivity analysis of hydropower potential was assessed due to changes in hydro-meteorological parameters. The variations in river discharge for 50 and 90% dependable years were studied due to changes in rainfall and temperature variation induced snow cover to compute the resultant changes in hydropower potential. The average temperature was varied from 1 °C to 4 °C and the precipitation from 20% decrease to 20% increase for both dependable years. For these climate change scenarios, analysis has been done using SRM model and the simulation results were analyzed for design discharge and consequent power output generation.

4 Results and Discussion

4.1 Dependable Year Analysis

Flow duration curve (FDC) is widely used to identify the dependable flow; it acts as one of the governing factors for HEP sites potential computation. FDC is a relationship between the discharge and the percentage of time the given stream flow

was equalled or exceeded over historical period. Historical discharge data (from 1999 to 2011) from gauge station on Balephi river have been rearranged as water budget year (June–May), and 90% (2003–04) and 50% (2004–05) dependable years were identified following Weibull's distribution.

4.2 DEM

Two Cartosat-1 stereo pairs have been used to generate a DEM using LPS for the catchment of Balephi River. The photogrammetric block orientation was done using 14 control points and 13 checkpoints. Using the image matching principles, the tie points were generated to establish relationships between images. During the triangulation process, the ground coordinates for these tie points were calculated. The root-mean-square errors (RMSE) of control points were obtained as 2.48 m, 2.41 m and 6.49 m in along-track, across-track and height, respectively. Similarly, the RMSE errors using 13 checkpoints were obtained as 2.13 m, 2.11 m and 12.72 m in along-track, across-track and height, respectively. The model's total RMSE was obtained as 0.13 pixels. After the satisfactory model accuracy was achieved, DEM was generated with a cell size of 10 m. The ortho-rectified image was produced at a spatial resolution of 2.5 m using AFT image because of its near nadir acquisition angle. Using TE module of LPS, the hydraulic head at each identified HEP site was estimated using elevation difference between intake and power house site through 3D stereoscopic visualization.

4.3 Drainage and Geology

Balephi River is one of the major tributaries of Sunkoshi River. It has a narrow V-shaped valley, which comprises of steep rocky slopes and river banks flowing from north to south. The river has dendritic drainage pattern, and the rivulets show more or less parallel pattern. The shape of the valley is structurally controlled by joints and foliation of rock. Recent and old gently dipping alluvial deposits were observed along the both banks. Selang, Deurali, Mahabhir, Ale and Guhe are the major tributaries of Balephi River. The understanding of river morphology helps in HEP identification as broader river sections are generally avoided for smaller HEP schemes.

The Balephi catchment belongs to Nuwakot Complex and Higher Himalayan Group. The rock of Nuwakot Complex has been subdivided into Lower and Upper Nuwakot Groups and separated by an erosional unconformity. Nuwakot Complex of Lesser Himalayan Crystalline Zone is separated from Higher Himalayan Zone in the north by Main Central Thrust and Siwalik Himalayas in the south by Main Boundary Thrust. The project area lies within the Robang Phyllite, Benighat Slates, Dhading Dolomite of Upper Nuwakot Group and Fagfog Quartzite, Kunchha

Formation of Lower Nuwakot Group of Lesser Himalayan Crystalline Zone and Hadi Khola Schist, Dhad Khola Gneiss, Sermathang Formation, Simpani Formation of Higher Himalayan Zone. Detailed geological characteristics (group, type and lithology) for each site have been given in Table 2. These information will help in prioritizing the sites for detailed investigation in subsequent stages of the HEP sites planning.

4.4 Land Use/Land Cover

LULC map was prepared using Landsat ETM+ data and ISODATA clustering algorithm. Balephi River catchment is largely covered under snow (35.44%), forest (22.96%), cultivated land (18.12%), bush/shrub land (13.18%) and grassland (7.7%). At the higher reaches, the catchment is well covered with snow cover and glaciers. The catchment has large area under forest cover constituting both coniferous and deciduous species. Grasslands occur below the snowline with sporadic occurrence of bushes or shrub land. Cultivated land is observed in catchment mainly at lower reaches with intermittent patches of settlement. Overall kappa accuracy was obtained as 0.82 which means that classification accuracy was 82% greater than chance. The dominant LULC classes surrounding the identified HEP sites are given in Table 2.

4.5 Snowmelt Runoff Modelling

In Balephi catchment, the elevation ranges from 777 m to 6938 m. Using ASTER GDEM, the catchment was subdivided at 500 m interval into 12 hypsometric mean elevations zones. Variables namely temperature, precipitation and snow cover area were used zone-wise for each day as input to SRM, and the model was operated to obtain year-round simulations. Mean daily values of these variables (precipitation, temperature and SCA) were extracted using zonal statistics tool of spatial analyst in GIS for each elevation zone. The zone-wise SCA was divided by each zonal area to calculate conventional depletion curve. The temperature data for each zone were acquired by applying varying temperature lapse rate obtained from MODIS LST data. The simulated discharge on daily basis was compared to measured discharge to evaluate the accuracy of simulation. The volume difference (%) was obtained as 7.20 and the coefficient of determination (or, the Nash–Sutcliffe model efficiency coefficient) as 0.89 for 50% dependable year (2004–05). Similarly, for 50% dependable year (2004–05), the volume difference was obtained as 2.49 and the coefficient of determination as 0.86. The model parameters for entire watershed estimated through iterative process were used to simulate runoff for sub-watersheds delineated at each HEP site. The discharge versus percentage of exceedance graph was plotted for each site and dependable year, and design discharge at 50% and 90% probability was

Table 1 Design discharge and energy outputs computation for Jhulkedada–Seguli HEP (50% dependable year)

(i) Design discharge

Month	Mean	Rank	Descending order	% exceedance	
June	34.97	1	147.15	7.69	$Q_{50\%}$ = 26.79
July	86.70	2	135.74	15.38	
August	135.74	3	86.70	23.08	
September	147.15	4	71.68	30.77	
October	71.68	5	34.97	38.46	
November	30.95	6	30.95	46.15	
December	21.47	7	22.63	53.85	
January	21.74	8	21.74	61.54	
February	14.89	9	21.47	69.23	
March	13.32	10	19.73	76.92	
April	19.73	11	14.89	84.62	
May	22.63	12	13.32	92.31	

(ii) Installed capacity and power outputs

1	*River data*		*Power output*		
	Basin	Balephi	Installed capacity	13.4761	MW
	Intake	Jhulkedada			
	Powerhouse	Sugeli	Wet energy	66.2753	GWH
	Intake elevation	1196.00 m	Dry energy	20.9996	GWH
	Powerhouse elevation	1128.00 m	Total energy	87.2749	GWH
	Length	2795 m			
2	*Head*				
	Gross head	68.00 m			
	Net head	61.20 m	Considering 10% head loss		
3	*Efficiency (η)*				
	$\eta_{turbine}$	90%			
	$\eta_{Generator}$	95%			
	$\eta_{Transmission}$	98%			
	$\eta_{overall}$	83.79%			
4	*Discharge (Q)*			Dry season outage	10%
	$Q_{Calculated}$	26.79 m^3/s	50th percentile	Wet season outage	10%

(iii) Seasonal and annual energy produced

Month	River flow	Release flow	Available flow	Design flow	Generation capacity	Dry season energy	Wet season energy
	m^3/s	m^3/s	m^3/s	m^3/s	MW	MWH	MWH
June	34.97	3.50	31.47	26.79	13.4761		8732.5303
July	86.70	8.67	78.03	26.79	13.4761		9023.6146
August	135.74	13.57	122.17	26.79	13.4761		9023.6146
September	147.15	14.72	132.44	26.79	13.4761		8732.5303

(continued)

Table 1 (continued)

(iii) Seasonal and annual energy produced							
Month	River flow	Release flow	Available flow	Design flow	Generation capacity	Dry season energy	Wet season energy
	m^3/s	m^3/s	m^3/s	m^3/s	MW	MWH	MWH
October	71.68	7.17	64.52	26.79	13.4761		9023.6146
November	30.95	3.10	27.86	26.79	13.4761		8732.5303
December	21.47	2.15	19.32	19.32	9.7183	3253.6777	3253.6777
January	21.74	2.17	19.57	19.57	9.8436	6591.2690	
February	14.89	1.49	13.40	13.40	6.7431	4223.8998	
March	13.32	1.33	11.98	11.98	6.0286	4036.7422	
April	19.73	1.97	17.76	17.76	8.9321	2893.9908	2893.9908
May	22.63	2.26	20.36	20.36	10.2437		6859.1973
Maximum power generation (MW)					13.4761		
Total seasonal energy (GWH)						20.9996	66.2753
Annual energy (GWH)						87.2749	

estimated. A typical calculation for Jhulkedada–Seguli HEP site for 50% dependable year is shown in Table 1. The design discharge for this site corresponding to 50th percentile flow was obtained as 26.79 cumec. Similar calculations for other HEP sites were carried out.

4.6 HEP Sites Characteristics

Five potential HEP sites have been identified in the Balephi River catchment after the site suitability analysis. The identified sites are as follows: Jhulkedada–Sugeli, Tarke–Kubheswa, Sera (Selang)–Katakuti, Sera (Batase)–Kubhinde River and Simle–Bhainse, where the first name indicates the diversion or intake and the second as power house site. Table 1 shows the typical design discharge and power potential computation for Jhulkedada–Seguli HEP site corresponding to 50% dependable year. The discharge and HEP potential for 50% and 90% dependable years, and site characteristics for the identified sites are shown in Table 2. Figure 4 shows the theme maps used in HEP sites identification and potential HEP sites identified in Balephi River catchment. The geographic coordinates of the identified sites are given in Table 2. The elevation difference between the diversion or intake and the power house for each site was observed through 3D visualization using TE module of LPS, and the gross head was estimated. The net head was estimated as 90% of gross head which is common practice in Nepal for power potential assessment at pre-feasibility level. The design discharge at 50th and 90th percentile flows was estimated as demonstrated for Jhulkedada–Sugeli site in Table 1. Using

Table 2 HEP sites discharge, power potential and characteristics

S. No.	Scheme location		Location		Elevation (m)	Gross head (m)	Net head (m)	Design discharge $Q_{50\%}$ (m^3/s)	Installed capacity $Q_{50\%}$ (MW)	Design discharge $Q_{90\%}$ (m^3/s)	Installed capacity $Q_{90\%}$ (MW)
	Intake	Power house	Latitude (m)	Longitude (m)							
1	Jhulkedada		379463.76	3089510.76	1196	68	61.2	26.79	13.48	16.64	8.37
		Sugeli	378571.78	3087365.21	1128						
2	Tarke		377840	3086027	1026	53	47.7	26.8	10.51	17.09	6.7
		Kubheswar	377239.34	3082900.1	973						
3	Sera (Selang)		377810	3082127	899	66	59.4	26.99	13.18	17.37	8.48
		Katakuti	378740.28	3077947.71	833						
4	Sera (Batase)		378650	3077191.19	793	37	33.3	27.36	7.49	17.59	4.81
		Kubhinde River	378159.64	3073700.8	756						
5	Simle		379460	3070038.72	705	40	36	27.56	8.16	17.93	5.3
		Bhaise	379550.42	3067161.58	665						

S. No.	Scheme location		Location		Elevation (m)	Dominant land use	Geology		
	Intake	Power house	Latitude (m)	Longitude (m)			Group	Type	Lithology
1	Jhulkedada		379463.76	3089510.76	1196	Forest/Agriculture/Bush/Shrub	Lower Nuwakot Group	Kunchha Formation	Sericitic-chloritic green to grey, thinly bedded phyllites, gritty phyllites with thin intercalation of white quartzite and amphibolites
		Sugeli	378571.78	3087365.21	1128				

(continued)

Table 2 (continued)

S. No.	Scheme location		Location		Elevation (m)	Dominant land use	Geology		
	Intake	Power house	Latitude (m)	Longitude (m)			Group	Type	Lithology
2	Tarke		377840	3086027	1026	Forest/Agriculture/Bush/Shrub	Lower Nuwakot Group/Upper Nuwakot Group/Higher Himalayan Group	Benighat Slate with Jhiku Carbonate/Kunchha Formation/Fagfog Quartzite	Thinly bedded, dark grey to black slate, grey phyllites with bands of jhiku carbonate; Sericitic-chloritic green to grey, thinly bedded phyllites, gritty phyllites with thin intercalation of white quartzite and amphibolites; Thinly bedded, white fine-grained quartzite with thin intercalation of slate
		Kubheswar	377239.34	3082900.1	973				
3	Sera (Selang)		377810	3082127	899	Forest/Agriculture/Bush/Shrub	Upper Nuwakot Group/Higher Himalayan Group	Hadi Khola Schist/Robang Phyllite/Benighat Slate	Thin to medium bedded, fine garnet-biotite schist, calc. schist and gneiss bands; Chloritic-sericitic garnetiferous phyllite with thin intercalation of white quartzite and chloritic gneiss; Thinly bedded, dark grey to black slate, grey phyllites
		Katakuti	378740.28	3077947.71	833				

(continued)

Table 2 (continued)

S. No.	Scheme location		Location		Elevation (m)	Dominant land use	Geology		
	Intake	Power house	Latitude (m)	Longitude (m)			Group	Type	Lithology
4	Sera (Batase)		378650	3077191.19	793	Forest/Grassland	Higher Himalayan Group	Dhad Khola Gneiss	Porphyroblastic gneiss, augen gneiss with thin bands of quartzite and schists, migmatitic gneiss
		Kubhinde River	378159.64	3073700.8	756				
5	Simle		379460	3070038.72	705	Forest/Grassland/Agriculture	Higher Himalayan Group	Hadi Khola Schist/Dhad Khola Gneiss	Thin to medium bedded, fine garnet-biotite schist, calc. schist and gneiss bands; Porphyroblastic gneiss, augen gneiss with thin bands of quartzite and schists, migmatitic gneiss
		Bhaise	379550.42	3067161.58	665				

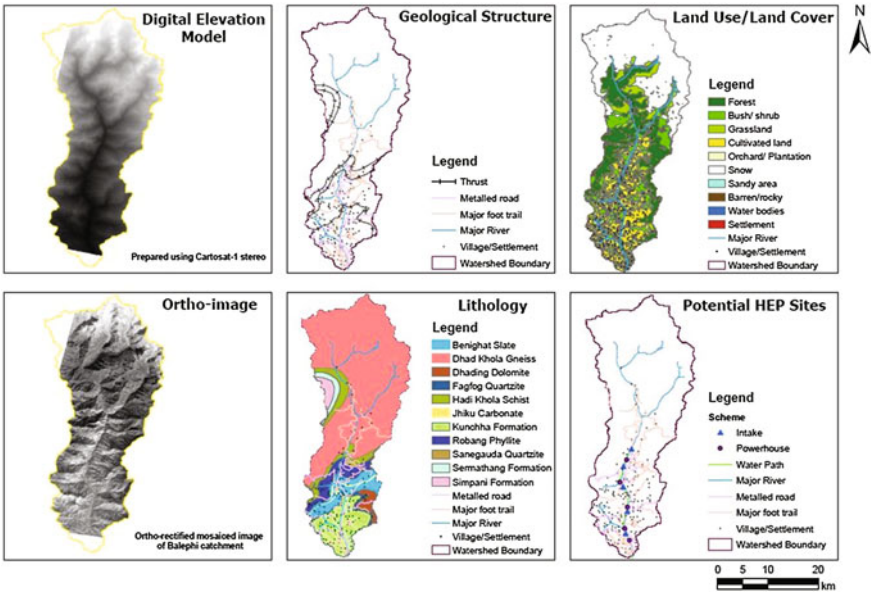

Fig. 4 Potential hydropower sites identified and their characteristics

Eq. (7), the installed capacity for each HEP site was computed as shown in Table 1 (ii). The expected energy output generation during dry and wet seasons was computed as shown in Table 1 (iii). A typical calculation is shown for Jhulkedada–Seguli HEP site, where the wet, dry and total energy output corresponding to 50% dependable year is computed as 66.2753 GWH, 20.9996 GWH and 87.2749 GWH, respectively. The total length of the water conveyance path has been computed by following the longitudinal profile drawn between diversion and the penstock inlet. For the Jhulkedada–Seguli HEP site, the water conveyance path length has been computed as 2795 m (Table 1). The dominant LULC surrounding the HEP sites has also been given in Table 2.

4.7 Sensitivity Analysis

The sensitivity analysis of runoff as the sum of snow and glacier melt, and rainfall to changes in temperature and precipitation has been performed. In the present study, the changes in temperature and precipitation intensity are considered as core variables to represent climate change effect on runoff and consequently on power generation. The percentage increase or decrease in design discharge and power potential due to changes in temperature and precipitation for each potential HEP site and dependable years is presented in Table 3. From the Table, it is inferred that there is increase in discharge due to increase in temperature but there is relatively

Table 3 Sensitivity analysis of installed capacity due to changes in meteorological parameters

Scheme	Jhulkedada–Sugeli	Tarke–Kubheswar	Sera (Selang)–Katakuti	Sera (Batase)–Kubinde River	Simle–Bhainse
Power, MW (2004–05, 50% dependable year)					
Designed	*13.48*	*10.51*	*13.18*	*7.49*	*8.16*
T+1	14.35	10.78	13.45	7.62	8.30
T+2	15.44	11.57	14.44	8.18	8.90
T+3	16.54	12.36	15.42	8.73	9.50
T+4	17.63	13.15	16.41	9.28	10.10
P+10%	13.52	10.55	13.23	7.52	8.20
P+20%	13.57	10.60	13.29	7.56	8.25
P−10%	13.51	10.53	13.19	7.49	8.15
P−20%	13.46	10.48	13.13	7.45	8.10
Power, MW (2003–04, 90% dependable year)					
Designed	*8.37*	*6.70*	*8.48*	*4.81*	*5.30*
T+1	8.88	7.10	8.91	5.03	5.54
T+2	9.53	7.62	9.56	5.34	5.78
T+3	10.19	8.15	10.21	5.70	6.18
T+4	10.85	8.67	10.86	6.07	6.57
P+10%	8.42	6.75	8.55	4.85	5.36
P+20%	8.48	6.80	8.63	4.90	5.42
P−10%	8.36	6.69	8.46	4.79	5.27
P−20%	8.30	6.63	8.38	4.74	5.21

T temperature, *P* precipitation

insignificant change in discharge with the change in precipitation. The Balephi catchment is largely snowfed; therefore, discharge increases as a result of higher snowmelt with an increase in temperature and shows relatively insignificant changes in discharge with the changes in rainfall magnitude. The variation in discharge has led up to 31% variation in power potential (Table 3) when compared to design power potential for various sites. The variation is highest for the Jhulkedada–Sugeli HEP site.

4.8 Limitations of the Study

The present study demonstrates the applications potential of geospatial techniques in HEP sites suitability analysis using open source data, discharge and potential estimates, and sensitivity analysis of assessed potential. The only commercial data used in the present study were Cartosat-1 stereo to generate high-resolution DEM and to visualize the identified HEP site in 3D environment. It has helped in further improving the geographic coordinates of identified HEP site and also to assess the

hydraulic head available between diversion and probable power house site. The DEM derived from Cartosat-1 data was used to determine the water conveyance path between diversion and penstock inlet. The outputs of the study are desirable for any pre-feasibility level survey of potential HEP sites. During the detailed investigation, the HEP site characteristics are studied at higher scale where each component of water diversion, conveyance path and power house site in terms of design and stability is given importance to understand its feasibility.

The study carries some limitations due to relatively coarser resolution of geospatial data and limited field inputs used. As the terrain is largely inaccessible, the ground control points could not be collected using Differential Global Positioning System (DGPS) survey. Therefore, the control points for generating DEM from Cartosat-1 stereo data have been obtained from Google Earth images and ASTER DEM. As the triangulation results were reasonable and the aberrations in stereo model were not observed during the stereoscopic visualization of HEP sites, it is assumed that hydraulic head assessed in 3D environment is fairly good. However, it is recommended that during the detailed survey of any identified HEP site, the hydraulic head assessed should be verified using field based survey methods. LULC characteristics surrounding the identified HEP site have been studied using open-source ETM+ data. It is, therefore, recommended that during the detailed survey, the LULC characteristics of HEP sites should be studied using higher resolution remote sensing data. SRM was used to estimate discharge with Nash–Sutcliffe model efficiency obtained as 0.86 and 0.89 for 50% and 90% dependable years, respectively. The model accuracy obtained is reasonably good; however, it is recommended that during detailed survey, field data available from other sources should be incorporated to study the site-specific discharge.

5 Conclusions

Balephi River is primarily snowfed with many tributaries meeting the main river. Being a perennial river, flow is available throughout the season which is favourable for hydropower development. Present study was undertaken to utilize geospatial data and tools for HEP sites identification, discharge and power potential computation, and sensitivity analysis of assessed potential in the catchment of Balephi River. Historical discharge data (1999–2011) were analyzed to identify 50% and 90% dependable years. Temporal snow cover and temperature have been assessed using MODIS snow cover and LST products for these dependable years, and precipitation has been assessed using NOAA-CPC data. Higher resolution DEM prepared using Cartosat-1 stereo data has been used for the lower reaches of catchment for HEP sites investigation and also to estimate hydraulic head. The watershed boundary for entire Balephi River and sub-watershed boundaries for each HEP site were delineated using ASTER GDEM. The existing geological and topographical maps and derived drainage and LULC maps were used for HEP sites characterization. The discharge was computed using SRM model, and the values of

percentage deviation and Nash–Sutcliffe model efficiency coefficient were obtained as 2.4912 and 0.86 for 50% dependable year (2004–05) and 7.1986 and 0.89 for 90% dependable year (2003–04). The calibrated model parameters were used to estimate discharges from sub-watersheds delineated for each identified HEP site corresponding to 50% and 90% dependable years. Different climate change scenarios have been created in the model for sensitivity analysis of HEP sites.

The integrated information on topographical, hydrological and geological characteristics has helped to identify five potential hydropower sites with installed capacity ranging from 7.5 MW to 13.5 MW and from 4.81 MW to 8.37 MW corresponding to 50% and 90% dependable years, respectively. The dependable discharge corresponding to 50% and 90% dependable years with reference to 50% exceedance varies from 26.79 cumec to 27.56 cumec and 16.64 cumec to 17.93 cumec, respectively. Sensitivity analysis of assessed potential has been analyzed by varying average temperature from 1 °C to 4 °C and precipitation from 20% decrease to 20% increase. Changes in meteorological parameters have led up to 31% variation in discharge and consequent changes in installed capacity. The LULC and geological characteristics for each identified sites have been analyzed. The study has helped to understand that geospatial data and techniques are extremely helpful in Nepal to carry out pre-feasibility level study for hydropower development due to its rugged and inaccessible terrain. Further, detailed investigation in terms of techno-economic feasibility analysis is recommended for the identified HEP sites. This study is limited to run-of-river scheme; therefore, it is recommended that the analysis for reservoir type scheme shall also be carried out in future for Balephi River valley.

Acknowledgements The authors express their heartfelt gratitude to Dr. Y.V.N. Krishna Murthy, Director, National Remote Sensing Centre (NRSC), and former Director, Centre for Space Science and Technology Education in Asia and the Pacific (CSSTEAP), Dehradun, India, for constant guidance and encouragements to demonstrate the utility of geospatial techniques for societal benefits. The authors are grateful to Dr. A. Senthil Kumar, Director, Indian Institute of Remote Sensing and CSSTEAP, Dehradun, India for his inspiration to explore niche areas in geospatial technology and applications. The authors express their gratefulness to Dr. Sarnam Singh, former Programme Coordinator, CSSTEAP, India, for coordinating the education and research programmes of CSSTEAP. The second author acknowledges the authorities in Pancheshwar Multipurpose Project, Kathmandu, Nepal, for their permission to conduct research using geospatial techniques at CSSTEAP, India.

References

1. Alterach, J., Peviani, M., Davitti, A., Vergata, M., Ciaccia, G., Fontini, F.: Evaluation of the remaining hydro potential in Italy. Int. J. Hydropower Dams **16**(5), 56–59 (2009)
2. Anon: Snow cover statistic—Nepal, Cryosphere Knowledge Hub. International Centre for Integrated Mountain Development (ICIMOD) E-Bulletin, vol. 1, no. 2. http://www.icimod.org/?q=12193 (2013). Accessed 5 Aug 2016

3. Bajracharya, S.R., Mool, P.K., Shrestha, B.R.: Global climate change and melting of Himalayan Glaciers. In: Ranade, P.S. (ed.) Melting Glaciers and Rising Sea Levels: Impacts and Implications, pp. 28–46. ICFAI University Press, Hyderabad (2008)
4. Ballance, A., Stephenson, D., Chapman, R.A., Muller, J.: A geographic information systems analysis of hydro power potential in South Africa. J. Hydroinform. **2**(4), 247–254 (2000)
5. Crépon, O.: Re-assessing French hydropower potential. Int. J. Hydropower Dams **15**(5), 47–49 (2009)
6. Duffy, A., Rogers, M., Ayompe, L.: Renewable Energy and Energy Efficiency: Assessment of Projects and Policies. Wiley (2015)
7. Fitzpatrick-Lins, K.: Comparison of sampling procedures and data analysis for a land-use and land-cover map. Photogram. Eng. Remote Sens. **47**, 343–351 (1981)
8. Giribabu, D., Kumar, P., Mathew, J., Sharma, K.P., Murthy, Y.V.N.K.: DEM generation using Cartosat-1 stereo data: issues and complexities in Himalayan Terrain. Eur. J. Remote Sens. **46**, 431–443 (2013)
9. Grodecki, J., Dial, G.: Block adjustment of high-resolution satellite images described by rational polynomials. Photogram. Eng. Remote Sens. **69**(1), 59–68 (2003)
10. Hall, D.: Water Energy Resources of the United States with Emphasis on Low Head/Low Power Resources: Appendix B-Assessment Results by State. EERE Publication and Product Library (2004)
11. Hamududu, B., Killingtveit, A.: Assessing climate change impacts on global hydropower. Energies **5**(2), 305–322 (2012)
12. Hock, R.: Temperature index melt modelling in mountain areas. J. Hydrol. **282**(1), 104–115 (2003)
13. Hong, M.A., Guodong, C.: A test of snowmelt runoff model (SRM) for the Gongnaisi River basin in the Western Tianshan Mountains, China. Chin. Sci. Bull. **48**(20), 2253–2259 (2003)
14. IPCC: Climate Change 2007: Working Group I: The Physical Science Basis. IPCC Fourth Assessment Report: Climate Change. https://www.ipcc.ch/publications_and_data/ar4/wg1/en/spmsspm-projections-of.html (2007). Accessed 5 Aug 2016
15. Jorgensen, J.: On trial in Clackamas County. Int. Water Power Dam Constr. Mag. 30–33. http://www.waterpowermagazine.com/features/featureon-trial-in-clackamas-county/ (2009). Accessed 5 Aug 2016
16. Koch, F., Prasch, M., Bach, H., Mauser, W., Appel, F., Weber, M.: How will hydroelectric power generation develop under climate change scenarios? A case study in the upper Danube basin. Energies **4**(10), 1508–1541 (2011)
17. Larentis, D.G., Collischonn, W., Olivera, F., Tucci, C.E.: GIS-based procedures for hydropower potential spotting. Energy **35**(10), 4237–4243 (2010)
18. Magnusson, J., Farinotti, D., Jonas, T., Bavay, M.: Quantitative evaluation of different hydrological modelling approaches in a partly glacierized Swiss watershed. Hydrol. Process. **25**(13), 2071–2084 (2011)
19. Martinec, J.: Snowmelt-runoff model for stream flow forecasts. Hydrol. Res. **6**(3), 145–154 (1975)
20. Monk, R., Joyce, S., Homenuke, M.: Rapid hydropower assessment model: identify hydroelectric sites using geographic information systems. In: Proceedings of the Small Hydro Conference. http://www.kwl.bc.ca/sites/default/files/SmallHydro2009_RJM_SFJ_MEH_AbstractPaper_0.pdf (2009). Accessed 5 Aug 2016
21. Panday, P.K., Frey, K.E., Ghimire, B.: Detection of the timing and duration of snowmelt in the Hindu Kush-Himalaya using Quikscat, 2000–2008. Environ. Res. Lett. **6**(2) (2011)
22. Pathak, M.: Application of GIS and remote sensing for hydropower development in Nepal. Hydro Nepal: J. Water Energy Environ. **26**(3), 42–45. http://www.nepjol.info/index.php/HN/article/viewArticle/1920 (2009). Accessed 5 Aug 2016
23. Prajapati, R.N.: Delineation of run of river hydropower potential of Karnali Basin Nepal using GIS and HEC-HMS. Eur. J. Adv. Eng. Technol. **2**(1) 50–54. http://www.ejaet.com/PDF/2-1/EJAET-2-1-50-54.pdf. Accessed on 5 Aug 2016

24. Punys, P., Dumbrauskas, A., Kvaraciejus, A., Vyciene, G.: Tools for small hydropower plant resource planning and development: a review of technology and applications. Energies **4**(9), 1258–1277 (2011)
25. Rojanamon, P., Chaisomphob, T., Bureekul, T.: Application of geographical information system to site selection of small run-of-river hydropower project by considering engineering/economic/environmental criteria and social impact. Renew. Sustain. Energy Rev. **13**(9), 2336–2348 (2009)
26. Sahu, N., Obireddy, G.P., Kumar, N., Nagaraju, M.S., Srivastava, R., Singh, S.K.: Characterization of landforms and land use/land cover in basaltic terrain using IRS-P6 LISS-IV and Cartosat-1 DEM data: a case study. Agropedology **24**(2), 166–178 (2014)
27. Shrestha, S., Khatiwada, M., Babel, M.S., Parajuli, K.: Impact of climate change on river flow and hydropower production in Kulekhani hydropower project of Nepal. Environ. Process. **1** (3), 231–250 (2014)
28. WECS: Water Resources of Nepal in the Context of Climate Change. Water and Energy Commission Secretariat (WECS), Singha Durbar, Kathmandu, Nepal, p. 90 (2011)
29. Widhalm, B., Hogström, E., Ressl, C., Trofaier, A., Heim, B., Biasi, C., Bartsch, A.: PAGE21 WP5-Land Surface Hydrology from Remotely Sensed Data at PAGE21 Sites. http://epic.awi.de/35990/ (2014). Accessed 5 Aug 2016
30. Yu, P.S., Yang, T.C., Kuo, C.M., Chou, J.C., Tseng, H.W.: Climate change impacts on reservoir inflows and subsequent hydroelectric power generation for cascaded hydropower plants. Hydrol. Sci. J. **59**(6), 1196–1212 (2014)
31. Zaruba, Q., Mencl, V.: Engineering Geology. Developments in Geotechnical Engineering, vol. 10, p. 504. Elsevier, Amsterdam (1976)

Torrent Areas' Change Dynamics and Vulnerability Analysis

Pramod Kumar, Vikas Garg and T.M.B.P.K. Tennakoon

Abstract Torrents are ephemeral mountainous streams which flow with high velocity run-off, usually carrying large size particles and cause extensive damage due to meandering and lateral migration. An attempt was made to study temporal changes and vulnerability analysis in Dangri river watershed, Panchkula district, India. Temporal satellite data were used to map torrents and surroundings. It was observed that due to conservation activities ongoing in watershed, 447.6 ha of land got converted to more productive use which were hitherto categorized as dry river bed or under grass/scrub cover. The torrent vulnerability was assessed by integrating surrounding land use/land cover, channel and upstream characteristics and proximity to structural measures using geographical information system. The study area has been categorized into five classes ranging from low to very high vulnerability due to torrential activities. The methodology proposed is useful to identify vulnerable areas for undertaking reclamation measures and to monitor watershed conservation efforts.

Keywords Torrents · Remote sensing · GIS · Vulnerability analysis

P. Kumar (✉)
Indian Institute of Remote Sensing, Dehradun, India
e-mail: pramodvaish@gmail.com

V. Garg
University of Petroleum and Energy Studies, Dehradun, India
e-mail: gargvikas27@gmail.com

T.M.B.P.K.Tennakoon
Centre for Space Science and Technology Education in Asia and the Pacific, Dehradun, India
e-mail: biyanka_2004@yahoo.com.sg

V. Garg et al. (eds.), *Development of Water Resources in India*,
Water Science and Technology Library 75, DOI 10.1007/978-3-319-55125-8_44

1 Introduction

Large, infrequent fluxes of sediment to streams by mass wasting are intrinsic to the erosion regime of mountainous river basins. To elucidate the role of mass wasting in the construction and evolution of steep land and channel environments, it is crucial that we identify the processes involved and recognize their legacy on the valley floor. Miller and Benda [6] reported that the sediments move downstream as a wave-like pulse or pulses, overwhelming the channel and causing it to braid with flooding and alluvial deposition over the valley floor, based on analysis of resulting channel morphologies and bed textures. These seasonal mountainous streams (torrents) originating from outer Himalayas/Siwalik Hills in Indian subcontinent are termed as '*Choes*' in Punjab, '*Kholas*' in Himachal Pradesh and Nepal, '*Jhora*' in Sikkim and West Bengal and '*Dong*/*Jhora*' in Assam and Bhutan. The riverine lands are known as '*Bet*' in Punjab and Haryana, '*Khadar*' in Himachal, '*Char*' and *'Diara*' in Uttar Pradesh and Bihar and '*Char*' and '*Beet*' in West Bengal and Assam [2, 7, 8, 13, 15].

The land degradation caused due to infrequent sedimentation in and around torrents in the Siwaliks and outer Himalayas, and its impact on economic activities in the plains calls for precise mapping and analysis of torrential areas. The sequential scanning of the earth's surface by remote sensing satellites provide an opportunity to map parameters related to torrent risk assessment, physiography, land cover and erosional status and also to monitor seasonal and year-to-year changes in land degradation due to torrent activity as well as planform analysis of river system wherein the different river reaches such as straight, braided and meander can be identified [1]. Several studies have been carried out in the past to study the torrent and their ecosystem. Kaul and Dohru [3] reported that anthropogenic activities are most responsible factors, which are detrimental to the soil and property particularly on the southern slopes of Siwaliks. Samra and Agnihotri [12] have evaluated runoff control measures, exposure of watershed to biotic interference, adoption of mechanical-cum-vegetative measures and the integrated watershed management programmes in the Siwalik area. Mazari [5] analysed functional aspect of the fluvial system of torrents that is governed by various inherent factors such as equilibrium, base level and complex response, tectonic uplift and denudation, etc. Ravishankar et al. [9] used remote sensing data and GIS-based methodology to assess the soil losses from a hilly watershed. Kumar et al. [4] analysed temporal remote sensing data and change detection techniques to assess the LULC changes in some selected watersheds of Uttar Pradesh, India. However, the knowledge on temporal change in torrents' areal extent and its impact on surrounding environment are limited. Hence, an attempt has been made in the present study to understand the dynamics of torrential areas and its surroundings using temporal satellite data. The torrent vulnerability analysis has been carried out using surrounding land use/land cover (LULC), channel and upstream characteristics, proximity to structural measures undertaken and current torrent floodplain in geographical information system (GIS) environment. The objectives of the present

study have been to map torrential areas using temporal satellite data and to conduct torrent vulnerability analysis using various channel and watershed physiographic characteristics.

2 Study Area

The present study has been carried out in Dangri river watershed, located in Panchkula district, Haryana, India (Fig. 1). The watershed covers a total of 9757 ha and lies between 30°35′ to 30°42′N latitude and 77°00′ to 77°05′E longitude. It falls in Survey of India (SOI) topographical map no. 53 F/2 on 1:50,000 scale. The *Ratta tibbi* and *Thathar ki Nadi* are the main tributaries of Dangri river, and they ultimately offload to Ghaggar, a tributary of river Yamuna. The north and north-east part of the watershed are under steep and dissected slope with a maximum elevation of 1200 m. The south and central part of the watershed is under gently sloping piedmont and alluvial areas and is intersected by broad beds of seasonal rivers. The watershed has a subtropical continental monsoon climate where seasonal rhythm lies i.e. hot summer (starting from April to end of June), cool winter, unreliable rainfall and higher variation in diurnal temperature. The northern part of the watershed is bestowed with tropical dry deciduous and subtropical forests.

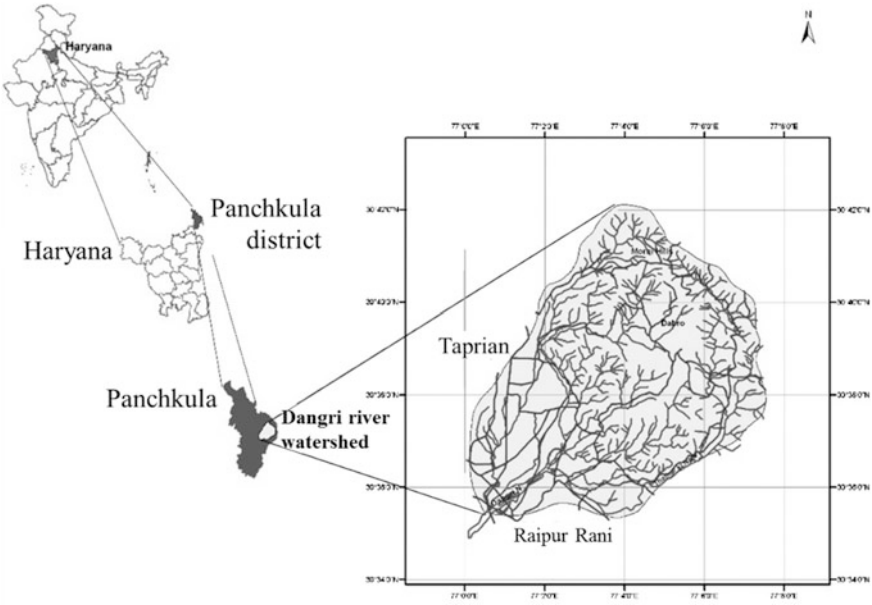

Fig. 1 Location map of Dangri river watershed

Physiographically, the area is divided into four major units: Lesser Himalayas, Siwaliks, piedmont and alluvial plain. The geological milieu in area represents rock/lithological formations of extremely wide ranging age groups, i.e. from Precambrians in lesser Himalayan region to recent deposits of Indo-Gangetic plains through upper Tertiary formations of Siwaliks. Soils of hilly region (lesser Himalaya and Siwaliks) as well as upper piedmont (foothill of Siwaliks) are shallow, stony, excessively drained and poorly developed, whereas in Indo-Gangetic plains, they have medium permeability and moderate profile development and are highly productive.

3 Materials and Methods

3.1 Data Collection

Following data have been used in the present study: Landsat TM digital and hard copy data of February 1987; IRS-1D LISS-III digital and hard copy data of February 2003; Resourcesat P-6 LISS-III of March 2012 and SOI topographical map no. 53 F/2. Temporal satellite data were geo-referenced and co-registered with accuracy better than a pixel using ground control points (GCPs). LULC mapping of the watershed was carried out using supervised classification technique. The drainage density map (stream length per km^2) was prepared using the drainage map digitized with the conjugate use of SOI topographical map and satellite data. The soil map was prepared using digital classification of satellite data with stratified approach and extensive field information. The buffer zones surrounding the torrents were generated using distance values from 100 to 500 m (as 5 classes) for torrent vulnerability analysis. The sites of spurs and other structural measures existing in the field were collected using global positioning system (GPS) device and transferred to GIS database. The stream width was measured at several places on the ground. The torrents' meander angles were estimated interactively using the satellite data at numerous river sections. The temporal LULC maps prepared were overlaid for change detection analysis. The torrent vulnerability analysis has been carried out based on six parameters, viz., (i) slope, (ii) channel characteristics, (iii) proximity to current torrent floodplain, (iv) upstream characteristics, (v) proximity to structural measures to torrents and (vi) surrounding land use/land cover.

3.2 Methodology

Saaty's analytical hierarchy process (AHP) is a widely used method for scaling the weights of parameters by constructing a pair-wise comparison matrix of parameters whose entries indicate the strength with which one element dominates another vis-

à-vis the criteria under consideration [10, 11, 14]. Hence, Saaty's AHP procedure was adopted to assign weightages to various parameters for the preparation of torrent vulnerability map. In order to compute weights for different criteria, the AHP starts creating a pair-wise comparison matrix, A. Each entry a_{jk} of matrix A represents importance of *j*th criterion relative to *k*th criterion. If $a_{jk} > 1$, then *j*th criterion is more important than *k*th criterion, while if $a_{jk} < 1$, then *j*th criterion is less important than *k*th criterion. If two criteria have the same importance, then entry a_{jk} is 1.

$$\bar{a}_{jk} = \frac{a_{jk}}{\sum_{k=1}^{m} a_{jk}} \tag{1}$$

Once the matrix A is built, it is possible to derive from A, the normalized pair-wise comparison matrix A_{norm} by making equal to 1, the sum of entries on each column, i.e. each entry $\bar{a}_{jk}$ of matrix A_{norm} is computed as

$$w_j = \frac{\sum_{k=1}^{m} \bar{a}_{jk}}{m} \tag{2}$$

Consistency index (CI) is obtained by first computing the scalar x as the average of elements of vector whose *j*th element is the ratio of *j*th element of vector $A \cdot w$ to the corresponding element of vector w. A perfectly consistent decision-maker should always obtain CI = 0, but small values of inconsistency may be tolerated. CI is defined as:

Table 1 Importance matrix for torrent vulnerability analysis

Parameter	Importance
Slope	• Less important than channel characteristics • Slightly more important than proximity to current torrent floodplain • Very important than upstream characteristics • Strongly very important than proximity to structural measures • Slightly more important than LULC
Channel characteristics	• Less important than proximity to current torrent floodplain • Less important than upstream characteristics • More important than proximity to structural measures for torrents • Very important than LULC
Proximity to current torrent floodplain	• Less important than upstream characteristics • Very important than proximity to structural measures for torrents • More important than LULC
Upstream characteristics	• Slightly more important than proximity to structural measures • Very important than LULC
Proximity to structural measures	• Strongly very important than LULC

Table 2 Weights for various parameters derived using Saaty's AHP

Parameter	1	2	3	4	5	6
1	1	1/6	1/3	1/7	1/9	3
2	6	1	4	1/2	1/5	7
3	3	1/4	1	1/4	1/7	5
4	7	2	4	1	1/3	7
5	9	5	7	3	1	9
6	1/3	1/7	1/5	1/7	1/9	1

1 Slope, *2* Channel characteristics, *3* Proximity to current torrent floodplain, *4* Upstream Characteristics, *5* Proximity to structural measures to torrents, *6* LULC

Table 3 Weights of parameters used in the vulnerability analysis

Parameter	Subcategory	Weight	Parameter	Subclass	Subcategory	Weight
Slope (%)	0–1	20	Channel characteristics	Bed width (m)	0–10	100
	1–3	20			10–20	80
	3–5	40			20–30	60
	5–10	60			30–40	40
	10–15	60			50–75	20
	15–35	80		Meander (deg.)	0–30	20
	35–50	80			30–60	40
	50–75	100			60–90	60
	>75	100			90–135	80
Soil	A1	12			135–180	100
	A2	13		LULC	Bare	20
	P11	13			Grass/Scrub	40
	P12	13			Plantation	60
	P13	12			Agriculture	100
	P21	13				
	P22	13	Proximity to structural measures	Retaining wall		20
	T	13		Spur-attractive		20
	H11	15		Spur-deflective		20
	H12	15				
	H13	18	Land use/cover	Settlement		100
	H21	19		Agricultural land		80
	H22	18		Plantation		60
	M1	15		Fallow land		40
	M2	18		Scrub land		20
	V	12		Water body		20
				Open forest		20
				Dense forest		40
				Terrace cultivation		60
Drainage density	0–0.008	20				
	0.008–0.028	40	Proximity to current torrent floodplain (m)		500	20
	0.028–0.037	60			400	40
	0.037–0.049	80			300	60
	0.049–0.096	100			200	80
					100	100

$$CI = \frac{x - m}{m - 1} \tag{3}$$

Using importance matrix for torrent vulnerability analysis (Table 1) and using online tool [16], weights for six parameters based on Eigen vector method were derived (Table 2). These weightages were multiplied with feature class attributes (Table 3) to compute composite vulnerability index (CVI). The CVI coverage was reclassified into six categories to prepare the torrent vulnerability classes. The procedure for torrent vulnerability analysis is shown as flow chart in Fig. 2. Various kinds of conservation activities have been implemented by the developmental agencies in the watershed e.g. retaining wall, spurs, rejuvenation of water bodies, plantation of grasses and plants, etc. Along the *Thathar ki Nadi*, near its confluence with Dangri, 36 spurs and the retaining wall have been constructed. At other places too, some conservation measures were noticed. These locations were

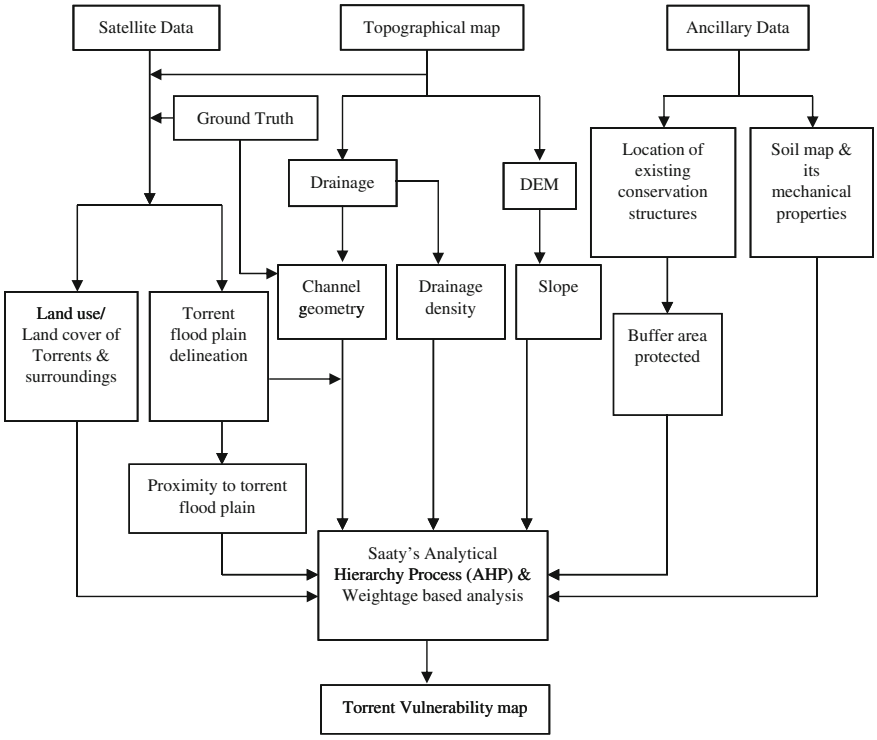

Fig. 2 Methodology followed for torrent vulnerability analysis

mapped using a mobile GPS and added to GIS database to carry out torrent vulnerability analysis.

4 Results and Discussion

The present study on temporal change dynamics of torrent areas and torrent vulnerability analysis in a hilly watershed of Himalayan region was carried using temporal satellite data and various theme properties that affect torrential region. The torrent-affected areas in the entire watershed were categorized into four categories, viz., torrents under agriculture, orchard/plantation, grass/scrub and dry river bed. The temporal dynamics of torrential areas revealed that some areas of the torrents and surroundings have been converted into agricultural land, grass land and land under orchard/plantation. As a consequence, the area under torrents bed has reduced significantly (Table 4 and Fig. 3). The change detection of torrents in Dangri river watershed is presented in Fig. 3. The changes in torrent-affected areas are due to various management interventions carried out by several agencies. Thus, the torrent land under orchard/plantation or agriculture has increased over a period of 16 years. During 1987, 44.1 ha of torrent lands were under plantation and have increased up to 91 ha in year 2003. By overlaying and analysis of both the maps (1987 and 2003), it was observed that area under bare torrent has decreased from 545.1 to 311.1 ha. On the other hand, the torrent areas under grass and scrub had undergone minimal change i.e. 12.8 ha only. The conversion of bare torrent bed to grass/scrub land, agricultural land and plantation are due to conservation practices adopted by various implementing agencies. The area under torrent and associated land use which has remained unchanged is 239.9 ha of bare torrent lands, 504.7 ha of grass lands and scrub, 44.1 ha of plantation and 66.3 ha of agricultural lands. Most of these changes can be seen along the main Dangri river and its downstream areas (Fig. 3).

The torrent vulnerability map based on CVI has been categorized into five classes, viz., very high, high, moderate to high, moderate and moderate to low (Table 3). The map shows that very high category occupies small fraction of the

Table 4 Torrent area change dynamics in Dangri river watershed (1987–2012) (Unit: ha)

Land use class	1987				
2012	Dry river bed	Grass scrub	Orchard/Plantation	Agriculture	Total
Dry river bed	239.9	64.0	0.0	7.1	311.1
Gras/Scrub	182.8	504.7	0.0	10.7	698.3
Orchard/Plantation	29.3	17.7	44.1	0.0	91.0
Agriculture	93.1	124.7	0.0	66.3	284.1
Total	545.1	711.1	44.1	84.1	1384.4

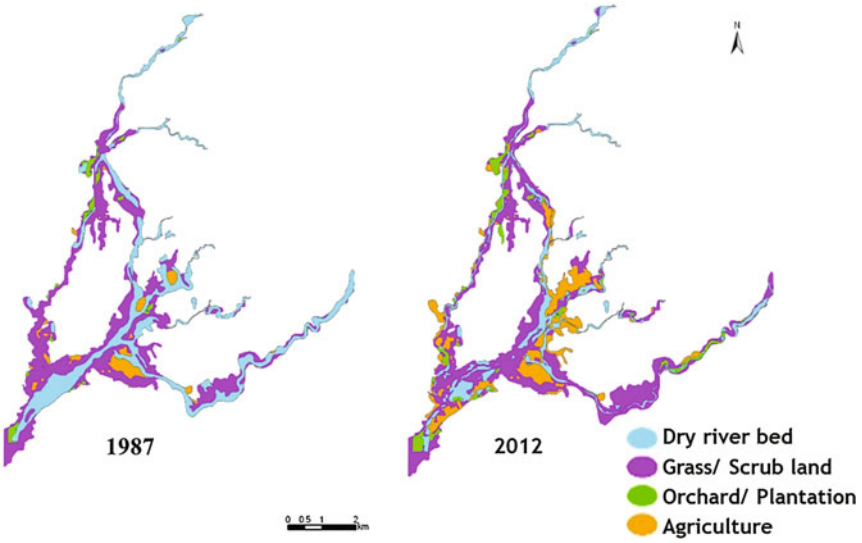

Fig. 3 Change detection of torrents and surroundings in Dangri river watershed

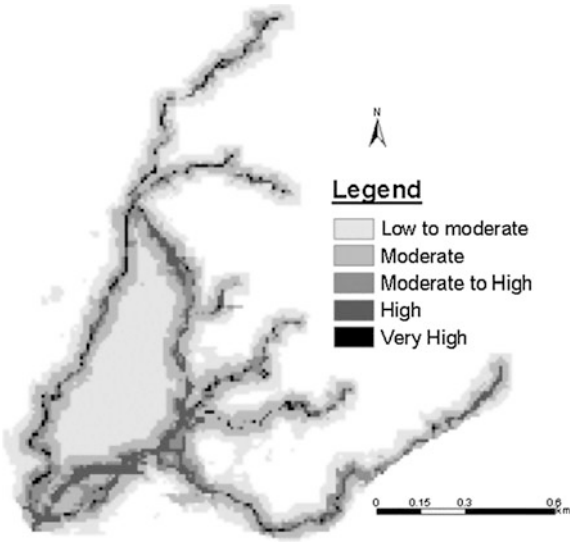

Fig. 4 Torrent vulnerability analysis of Dangri river watershed

watershed (Fig. 4). These areas are located in the downstream region of the Dangri river watershed. The moderate-to-high vulnerable area is located in the lower part (alluvial plain) of the watershed. These are spread out along the main Dangri river and its tributaries and are caused due to heavy bed load emanating from the hilly areas and finally contribute to the main Dangri river. Moderately vulnerable areas

have spread out all along the whole watershed. Areas under moderate-to-low vulnerability are located in the middle part of the watershed due to moderate slope and low drainage density of this area. Other areas in the watershed fall under low vulnerable category.

5 Conclusions

This study has been carried out for assessing changes in torrential watershed and to prepare torrent vulnerability map. Landsat TM (1987), IRS-1D LISS-3 data (2003) and Resourcesat LISS-3 (2012) were used to map torrent-affected area of Dangri river watershed. By overlaying the temporal LULC maps, temporal changes in the watershed were assessed. It was observed that due to conservation activities ongoing in watershed on torrent beds and surroundings, 447.6 ha of land have been reclaimed which were earlier categorized as bare and torrent under grass/scrub cover. Due to various management interventions, area under plantation and agriculture has increased by 46.9 ha and 200 ha in torrential areas, respectively. Using various parameters such as channel characteristics, LULC, slope, upstream characteristics, proximity to structural measures for torrents and proximity to current torrent floodplain, torrent vulnerability map was prepared. It was observed that highly vulnerable areas are located in torrential zones having higher slopes with narrow streams beds as well as at few places in lower part of the watershed. Moderate and moderate to highly vulnerable areas are located all over the watershed. Rest of the watershed area belongs to low vulnerable category. The methodology demonstrates its potential for adoption by conservation agencies to identify vulnerable areas for undertaking reclamation and to monitor the effects of conservation measures.

Acknowledgements The authors express their heartfelt gratitude to Dr. Y.V.N. Krishna Murthy, Director, National Remote Sensing Centre (NRSC) and former Director, Centre for Space Science and Technology Education in Asia and the Pacific (CSSTEAP), Dehradun, India, for constant guidance and encouragements to demonstrate the utility of geospatial techniques for societal benefits. Authors are grateful to Dr. A. Senthil Kumar, Director, Indian Institute of Remote Sensing and CSSTEAP for constant encouragements and extending facilities.

References

1. Bhan, S.K., Pande, L.M., Saha, S.K.: Erosion risk assessment due to torrents in lower Himalayas using remote sensing techniques. In: Sastry, G., Sharda, V.N., Guyal, G.P., Samra, J.S. (eds.) Torrent Menace: Challenges and Opportunities, pp. 13–19. CSWCR&TI Publication (1995)
2. Das, D.C.: Torrent problem-causative factors and control measures for eco-stability in Himalayan watershed—an overview. In: Sastry, G., Sharda, V.N., Guyal, G.P., Samra, J.S.

(eds.) Torrent menace: challenges and opportunities, pp. 1–12. CSWCR&TI Publication (1995)
3. Kaul, B.K., Dohru, R.K.: Torrential streams eco-system of Himachal Pradesh: its ecology and utilization. In: Sastry, G., Sharda, V.N., Guyal, G.P., Samra, J.S. (eds.) Torrent Menace: Challenges and Opportunities, pp. 66–71. CSWCR&TI Publication (1995)
4. Kumar P., Manchanda, M.L.: Monitoring watersheds, remote sensing approach: case studies from U.P., India. In: Proceedings of International Conference on Land Resources Management, New Delhi, India, Nov 2000 (2000)
5. Mazari, R.K.: Geomorphological perspective of the fluvial system with special reference to torrent control in the Himalaya. In: Sastry, G., Sharda, V.N. Guyal, G.P., Samra, J.S. (eds.) Torrent Menace: Challenges and Opportunities, pp. 21–221. CSWCR&TI Publication (1995)
6. Miller, D.J., Benda, L.E.: Effect of punctuated sediment supply on valley-floor landforms and sediment transport. J.: Geol. Soc. Am. Bull. **112**(12), 1814–1824 (2000)
7. Mittal, S.P., Aggarwal, R.K., Samra, J.S.: Fifty Years of Research on Sustainable Resource Management in Siwaliks. CSWCRT&TI, Chandigarh (2000)
8. National Commission on Agriculture: Report of National Commission on Agriculture, Part V, Chaps. 17 & 18. Ministry of Agriculture & Irrigation, New Delhi (1976)
9. Ravishankar, H.M., Srivastava, S.K., Saha, S.K., Kumar, P., Prasad, J.: Watershed prioritization through USLE using digital satellite data—an integration approach. Asian-Pac. Remote Sens. J. **6**(2), 101–108 (1994)
10. Saaty, L.: The Analytical Hierarchy Process. McGraw-Hill, New York (1980)
11. Saaty, T.L.: Decision making with the analytic hierarchy process. Int. J. Services Sci. **1**(1), 83–98. http://www.colorado.edu/geography/leyk/geog_5113/readings/saaty_2008.pdf (2008). Accessed 05 Aug 2016
12. Samra, J.S., Agnihotri, Y.: Torrent management in Siwaliks. In: Sastry, G., Sharda, V.N., Guyal, G.P., Samra, J.S. (eds.) Torrent menace: challenges and opportunities, pp. 146–155. CSWCR&TI Publication (1995)
13. Sastry, G., Sharda, V.N., Juyal, G.P., Samra, J.S.: Torrent Menace: Challenges and Opportunities. Central Soil & Water Conservation Research & Training Institute, Dehra Dun (1995)
14. Sastry, S.V.C., Rao, M., Pathan, S.K., Yadav, P.D., Majumdar, K.L.: A Comparative Study of the Priority Weighing Methods in a Multi Criteria Based GIS Application. Space Applications Centre, Ahmedabad, India (1991)
15. Singh, G., Venkataramanan, C., Sastry, G., Joshi, B.P.: Manual of Soil and Water Conservation Practices, pp. 306–308. Oxford and IBH Publishing Co. Pvt. Ltd., New Delhi (1996)
16. http://bpmsg.com/academic/ahp_calc.php. Accessed 05 Aug 2016

Index

V. Garg et al. (eds.), *Development of Water Resources in India*,
Water Science and Technology Library 75, DOI 10.1007/978-3-319-55125-8